THÈSE

En vue de l'obtention du

DOCTORAT DE L'UNIVERSITÉ DE TOULOUSE

Délivré par l'Institut National Polytechnique de Toulouse

Présentée et soutenue par

Anne-Marie TOBIE

Le 25 février 2021

Hybridation GNSS/5G pour la navigation en milieu urbain

Ecole doctorale : **EDMITT - Ecole Doctorale Mathématiques, Informatique et Télécommunications de Toulouse**

Spécialité : **Informatique et Télécommunications**

Unité de recherche :
Laboratoire de Recherche ENAC

Thèse dirigée par
Axel Javier GARCIA PENA et Paul THEVENON

Jury

M. Gonzalo SECOS GRANADOS, Rapporteur
M. Lian CHENG, Rapporteur
Henk WYMEERSCH, Examinateur
M. Didier BELOT, Examinateur
Mme Corinne MAILHES, Examinatrice
M. Axel Javier GARCIA PENA, Directeur de thèse

A ma famille

Maman, Papa

Anne-Cécile, Marie-Josée,

Jean-Christophe, Sophie

Axel, Emilie, Ethan

Parce que rien n'aurait été possible sans vous, je vous aime

Acknowledgments

This work has been carried out in the Signal Processing and Navigation Group of the TELECOM Lab at the ENAC.

A lot of people have played an important role in this Ph.D. thesis that I would like to deeply acknowledge.

First and foremost, I want to thank my thesis supervisors Axel GARCIA PENA for his constant supervision over these years and Paul THEVENON who joined the adventure along the way. Both of you provide me with greats support and greatest patience.

I acknowledge Thalès Alenia space, through the supervision of Damien SERANT, and the CNES (Centre National d'Etudes Spatiales), through the supervision of Marion AUBAULT, for funding this thesis.

I am grateful to Lian CHENG and Gonzalo SECOS GRANADOS for accepting to review the thesis, and to Henk WYMEERSH, Didier BELOT and Corinne MAILHES for accepting to be part of the jury. Thank you for the interest you have shown in my thesis, for your comments and advices on the manuscript, and of course for assisting to my Ph.D. defense.

Je remercie particulièrement mes collègues du laboratoire SIGNAV et EMA qui m'ont accueillie très chaleureusement au sein du labo (moi ou mes désormais célèbres « gâteaux du lundi» peut-être !...). Merci à Jérémy pour le support GénéIQ et Kalman, Capucine et Xiao mes co-bureaux, Maxandre pour nos séances d'escalades, Thomas pour ses histoires sans chutes, Hélène mangeuse de graines, Florian, Anaïs, Antoine, Ikhlas, Rémi, Alexandre, Christophe…

Enfin, aucun mot ne sera suffisant pour vous remercier : maman, papa, votre soutien et votre amour inconditionnel dans les bons comme dans les mauvais moments m'ont permis d'en arriver là, merci. Merci également à mes frère et sœurs pour leur soutien sans failles : Anne-Cécile, Marie-Josée, Jean-Christophe, Sophie.

Abstract

Over the past few years, the need for positioning, and thus the number of positioning services in general, has been in constant growth. This need for positioning has been increasingly focused on constrained environments, such as urban or indoor environments, where GNSS (Global Navigation Satellite System) is known to have significant limitations: multipath as well as the lack of Line-of-Sight (LOS) satellite visibility degrades the GNSS positioning solution and makes it unsuitable for some urban or indoor applications. In order to improve the GNSS positioning performance in constrained environments, many solutions are already available: hybridization with additional sensors, [1], [2] or the use of signals of opportunity (SoO) for example, [3], [4], [5], [6], [7], [8]. Concerning SoO, mobile communication signals, such as the 4G Long Term Evolution (LTE) or 5G, are naturally envisioned for positioning, [3], [9], [10]. Indeed, a significant number of users are expected to be "connected-users" and 5G systems offers promising opportunities.

5G technology is being standardized at 3GPP [11]; the first complete release of 5G specifications, Release-15, was provided to the community in March 2018. 5G is an emerging technology and its positioning performance, as well as a potential generic receiver scheme to conduct positioning operations, is still under analysis. In order to study the potential capabilities provided by 5G systems and to develop a 5G-based generic positioning module scheme, the first fundamental step is to develop mathematical models of the processed 5G signals at each stage of the receiver for realistic propagation channel models: the mathematical expression of the useful received 5G signal as well as the AWG (Additive White Gaussian) noise statistics. In the Ph.D., the focus is given to the correlation operation which is the basic function implemented by typical ranging modules for 4G LTE signals [12], DVB signals [7], [8], and GNSS [13]. In fact, the knowledge of the correlation output mathematical model could allow for the development of optimal 5G signal processing techniques for ranging positioning.

Previous efforts were made to provide mathematical models of received signals at the different receiver signal processing stages for signals with similar structures to 5G signals – Orthogonal Frequency Division Multiplexing (OFDM) signals as defined in 3GPP standard, [14]. OFDM signal-type correlator output mathematical model and acquisition techniques were derived in [7], [15]. Moreover, in [8], [15], tracking techniques were proposed, analyzed and tested based on the correlator output mathematical model of [7]. However, these models were derived by assuming a constant propagation channel over the duration of the correlation. Unfortunately, when the Channel Impulse Response (CIR) provided by a realistic propagation channel is not considered to be constant over the duration of the correlation, the correlator output mathematical models are slightly different from the mathematical models proposed in [7], [8].

Therefore, the first main point considered in the Ph.D. consists in the development of mathematical models and statistics of processed 5G signals for positioning. In order to derive accurate mathematical models, the time evolution impact of the 5G standard compliant propagation channel is of the utmost importance. Note that, in the Ph.D., the continuous CIR will be approximated by a discretized CIR, and the continuous time-evolution will be replaced by the propagation channel generation sampling rate notion. This approximation makes sense since, in a real transmission/reception chain, the received time-continuous signal is, at the output of the Radio-Frequency (RF) front-end, sampled. Therefore, a preliminary step, prior to derive accurate mathematical models of processed 5G signals, consists in determining the most suitable CIR-generation sampling interval for a selected 5G standard compliant propagation channel, QuaDRiGa: trade-off between having a realistic characterization and its complexity. Complexity is especially important for 5G compliant channels with multiple emitter and receiver antennas, and high number of multipath. Then, the impact of a time-evolving propagation channel inside

an OFDM symbol duration is studied. A method to select the most appropriate CIR sampling interval for accurate modelling of symbol demodulation, correlator outputs and delay tracking will also be proposed.

Based on the correlator output mathematical models developed for realistic multipath environments for both GNSS and 5G systems, ranging modules are then developed. These ranging modules outputs the pseudo ranging measurements required to develop navigation solution. In order to improve the positioning availability and GNSS positioning performance in urban environment through the exploitation of 5G signals, both systems, GNSS and 5G communication systems, must be optimally combined. In fact, in order to achieve this optimal combination, both types of signals must be optimally processed, and the mathematical model of their generated pseudo range measurements must be accurately characterized. The second main objective of the Ph.D. aims thus at realistically characterizing GNSS and 5G pseudo range measurement mathematical models and at developing hybrid navigation modules exploiting/adapted to the derived pseudo range measurements mathematical models. In order to validate, the mathematical models developed in the Ph.D., a simulator is designed. The pseudo range measurements mathematical models are derived from a realistic simulator which integrates a typical GNSS receiver processing module and a typical 5G signal processing module proposition; moreover, in order to achieve a realistic characterization, the simulator implements highly realistic propagation channels for GNSS, SCHUN [16], and for 5G, QuaDRiGa [17] is developed. The hybrid navigation modules to be implemented and compared in this work are an Extended Kalman Filter (EKF) and an Unscented Kalman Filter (UKF). The performances of these hybrid navigation modules are then studied to quantify the improvements bringing by 5G TOA measurements.

List of acronyms

3GPP	Third Generation Partnership Project
5GC	5G Core
5G PPP	5G infrastructure Public Private Partnership
ADC	Analog to Digital Convertor
AE	Absolute Evolution
AMF	Access and mobility Management Function
AoA	Angle of Arrival
AoD	Angle of Departure
ARNS	Aeronautical Radio Navigation Service
AWGN	Additive White Gaussian Noise
BER	Bit Error Rate
BOC	Binary Offset Carrier
BPSK	Binary Phased Shift Keying
BS	Base Station
C/A	Coarse Acquisition
CBOC	Composite Binary Offset Carrier
CDF	Cumulative Density Function
CDMA	Code Division Multiple Access
CFE	Carrier Frequency Estimator
CFO	Carrier Frequency Offset
CIR	Channel Impulse Response
CN0	Carrier to Noise ratio
CP	Cycle Prefix
CRB	Cramer Rao Bound
CIR	Channel Impulse Response
CSI	Channel State Information

D2D	Device-To-Device
DCI	Downlink Control Information
DCO	Digitally Controlled Oscillator
DFT-s-OFDM	Discrete Fourier Transform-spread-OFDM
DL	Down Link
DLL	Delay Lock Loop
DoA	Direction of Arrival
DS-SS	Direct Sequence Spread Spectrum
E2E	End to End
EKF	Extended Kalman Filter
eMBB	enhanced Mobile BroadBand
EML	Early Minus Late
EMLP	Early Minus Late Power
eNB	Evolved Node B
E-UTRA	Evolved Universal Terrestrial Radio Access Network
FDD	Frequency Division Duplex
FDMA	Frequency Division Multiple Access
FFT	Fast Fourier Transform
FIM	Fischer Information Matrix
FLL	Frequency Lock Loop
GEO	Geostationary Earth Orbit
GLONASS	GLObal Navigation Satellite System
GNSS	Global Navigation Satellite System
GPS	Global Positioning System
GSM	Global System for Mobile communications
HEO	Highly Elliptical Orbit
ICI	Inter Carrier Interference
iFFT	Inverse Fast Fourier Transform

IGSO	Inclined Geo Synchronous Orbit
IoT	Internet of Things
IP	Internet Protocol
IRNSS	Indian Regional Navigation Satellite System
ITU	International Telecommunication Union
KF	Kalman Filter
LDPC	Low Density Parity Check
LOS	Line Of Sight
LS	Least Square
LTE	Long Term Evolution
MAC	Medium Access Control
MAP	Maximum a Posteriori
MEO	Medium Earth Orbit
MIMO	Multiple Input Multiple Output
ML	Maximum Likelihood
mMIMO	Massive MIMO
MMSE	Minimum Mean Square Error
mMTC	massive Machine Type Communication
mmW	Millimeter Wave
MSP	Mobile Service Providers
MTTA	Mean Time To Acquire
NLOS	Non Line Of Sight
NR	New Radio
OFDM	Orthogonal Frequency Division Multiplexing
OS	Open Service
PBCH	Physical Broadcast Channel
PDCCH	Physical Downlink Control Channel
PDCP	Packet Data Convergence Protocol

PDF	Probability Density Function
PDSCH	Physical Downlink Shared Channel
PF	Particle Filter
PLL	Phase Lock Loop
PRACH	Physical Random Access Channel
PRBS	Pseudo Random Binary Sequence
PRN	Pseudo Random Noise
PRS	Public Regulated Service
PSD	Power Spectral Density
PSS	Primary Synchronization Signal
PTRS	Phase Tracking Reference Signal
PUCCH	Physical Uplink Control Channel
PUSCH	Physical Uplink Shared Channel
PVT	Position Velocity Time
QAM	Quadrature Amplitude Modulation
QoS	Quality of Service
QPSK	Quadrature Phase-Shift Keying
QuaDRiGa	Quasi Deterministic RadIo channel GenerAtor
QZSS	Quasi Zenith Satellite System
RAN	Radio Access Network
RE	Relative Evolution
RF	Radio Frequency
RLC	Radio Link Control
RMSE	Root Mean Square Error
RRC	Radio Resource Control
SDAP	Service Data Adaptation Protocol
SINR	Signal to Interference plus Noise Ratio
SNR	Signal to Noise Ratio

SRS	Sounding Reference Signal
SS	Synchronization Signal
SSPBCH	Synchronization Signal Physical Broadcast Channel
SSS	Secondary Synchronization Signals
TCP	Transmission Control Protocol
TDD	Time Division Duplex
TDoA	Time Difference of Arrival
ToA	Time of Arrival
TTI	Transmission Time Interval
TUT	Tampere University of Technology
UCI	Uplink Control Information
UDN	Ultra-Dense Network
UDP	User Datagram Protocol
UE	User Equipment
UKF	Unscented Kalman FIlter
UL	Up Link
UMi	Urban Micro Cell
UMTS	Universal Mobil Telecommunication System
UPF	User Plane Function
URLLC	Ultra-Reliable and Low Latency Communication
UTC	Universal Time Coordinate
UWB	Ultra-Wide Band
V2X	Vehicle to everything
WER	Word Error Rate
WLS	Weighted Least Square
WRC	World Radio communication Conference

Table of content

List of figures

List of tables

Chapter 1. Introduction

1.1. Context and motivation

Over the past few years, the need for positioning, and thus the number of positioning services in general, has been in constant growth. This need for positioning has been increasingly focused on constrained environments, such as urban or indoor environments. In those challenging environments, GNSS (Global Navigation Satellite System) is known to have significant limitations mostly due to multipath and the lack of Line-of-Sight (LOS) satellite visibility.

More specifically, a GNSS receiver needs at least 4 LOS signals to provide a position. However, this ideal situation is rarely fulfilled in urban canyons. On one hand, due to high buildings and narrow streets, a lot of satellite signals are obstructed; this phenomenon is called lack of LOS satellite visibility. This blockage impacts the geometry of satellites viewed by the receiver: most of satellite signals coming from “across the street” are blocked, leaving only those “along the street”. The result is thus a degradation of the Dilution of Precision (DOP) of the solution.

On the other hand, the presence of high buildings and narrows streets is also going to create multipath. Multipath is a phenomenon produced by the superposition of the direct LOS signal with its reflected or diffracted replicas. The path travelled by a multipath being, by definition, longer than the direct path, it is always received after the direct path and its impact on the tracking will depend on the multipath received delay, phase and relative amplitude. If the multipath delay is very large, the multipath can be easily removed. Indeed, the correlation function between the received signal (direct path and multipath) and the local replica will leave the main peak (corresponding to the direct path) “clean” or, in other words, not distorted. However, if the delay is short, the multipath will distort this correlation function and will make it harder to perform an efficient tracking loop until the point to cause a loss of lock. And even if the loss of lock situation is not reached, multipath phenomenon introduces a non-negligible error on the pseudo range measurement.

Moreover, the combination of the lack of LOS satellite visibility and the apparition of multipath generates a potentially even worse situation. The satellite transmitted signal can only be received via reflection: a constant bias is added to the pseudo range measurement which, in its turn, creates a bias on the positioning solution. This phenomenon is referred as NLOS reception.

In summary, due to the multipath phenomenon, the lack of LOS satellite visibility, and the combination of the two, NLOS signal reception, the GNSS positioning solution can be highly degraded and thus can be unsuitable for some urban or indoor applications.

In order to improve the GNSS positioning performance in constrained environments, many solutions are already available: hybridization with additional sensors, [1], [2] or the use of signals of opportunity (SoO) for example, [3], [4], [5], [6], [7], [8]. Concerning SoO, mobile communication signals, such as the 4G Long Term Evolution (LTE) or 5G, are naturally envisioned for positioning, [3], [9], [10]. Indeed, a significant number of users are expected to be “connected-users” and 5G systems offers promising opportunities.

5G technology is being standardized at 3GPP [11]; the first complete release of 5G specifications, Release-15, was provided to the community in March 2018. 5G is an emerging technology and its positioning performance, as well as a potential generic receiver scheme to conduct positioning operations, is still under analysis. In order to study the potential capabilities provided by 5G systems and to develop a 5G-based generic positioning module scheme, the first fundamental step is to develop mathematical models of the processed 5G signals at each stage of the receiver for realistic propagation channel models: the mathematical expression of the useful received 5G signal as well as the AWG (Additive White Gaussian) noise statistics. In the Ph.D., the focus is given to the correlation operation which is the basic function implemented by typical ranging modules for 4G LTE signals [12], DVB signals [7], [8], and GNSS [13]. In fact, the knowledge of the correlation output mathematical model could allow for the development of optimal 5G signal processing techniques for ranging positioning.

Previous efforts were made to provide mathematical models of received signals at the different receiver signal processing stages for signals with similar structures to 5G signals – Orthogonal Frequency Division Multiplexing (OFDM) signals as defined in 3GPP standard, [14]. OFDM signal-type correlator output mathematical model and acquisition techniques were derived in [7], [15]. Moreover, in [8], [15], tracking techniques were proposed, analyzed and tested based on the correlator output mathematical model of [7]. However, these models were derived by assuming a constant propagation channel over the duration of the correlation. Unfortunately, when the Channel Impulse Response (CIR) provided by a realistic propagation channel is not considered to be constant over the duration of the correlation, the correlator output mathematical models are slightly different from the mathematical models proposed in [7], [8].

Therefore, the first main point considered in the Ph.D. consists in the development of mathematical models and statistics of 5G signals correlators outputs to be used for positioning. In order to derive accurate mathematical models, the study of the time evolution impact of the 5G standard compliant propagation channel is of the utmost importance. Note that, in the Ph.D., the continuous CIR will be approximated by a discretized CIR, and the continuous time-evolution will be replaced by the propagation channel generation sampling rate notion. This approximation makes sense since, in a real transmission/reception chain, the received time-continuous signal is, at the output of the Radio-Frequency (RF) front-end, sampled. Therefore, a preliminary step, prior to derive accurate mathematical models of processed 5G signals, consists in determining the most suitable CIR-generation sampling interval for the selected 5G standard compliant propagation channel: QuaDRiGa, which proposes a trade-off between having a realistic characterization and its complexity. Complexity reduction is especially important for 5G compliant channels with multiple emitter and receiver antennas, and high number of multipath. Then, the impact of a time-evolving propagation channel inside an OFDM symbol duration is studied. A method to select the most appropriate CIR sampling interval for accurate modelling of delay tracking will also be proposed.

The correlator output mathematical models developed for realistic multipath environments for both GNSS and 5G systems are then used to proposed and develop ranging modules; this is the second main objective of the Ph.D. These ranging modules outputs the pseudo ranging measurements required to develop navigation solution. The proposed 5G signal ranging module is based on the use of a classic Delay Lock Loop (DLL) and of a Frequency Lock Loop (FLL) (which usefulness is defined according to the configurations adopted). A C/N_0 estimator is also proposed to assess whether the signal is locked or not and to determine the measurement noise covariance value to be used in the navigation filters.

In order to improve the positioning availability and GNSS positioning performance in urban environment through the exploitation of 5G signals, both systems, GNSS and 5G communication systems, must be optimally combined. In fact, in order to achieve this optimal combination, both types of signals must be

optimally processed, and the mathematical model of their generated pseudo range measurements must be accurately characterized. The third main objective of the Ph.D. aims thus at realistically characterizing GNSS and 5G pseudo range measurement mathematical models and at developing hybrid navigation modules exploiting/adapted to the derived pseudo range measurements mathematical models. In order to validate the mathematical models developed in the Ph.D., a simulator is designed. The pseudo range measurements mathematical models are derived from a realistic simulator which integrates a typical GNSS receiver processing module and a typical 5G signal processing module proposition; moreover, in order to achieve a realistic characterization, the simulator implements highly realistic propagation channels for GNSS, SCHUN [16], and for 5G, QuaDRiGa [18]. The hybrid navigation modules to be implemented and compared in this work are an Extended Kalman Filter (EKF), a classical filter used in the literature and an Unscented Kalman Filter (UKF), which could outperform the EKF. The performances of these hybrid navigation modules are then studied to quantify the improvements brought by 5G TOA measurements.

1.2. Objectives

The global objective of the thesis is the design of hybrid navigation modules using both GNSS and 5G measurements. In order to do so, the thesis can be divided into 4 phases:

- The development of highly realistic 5G signals correlator outputs for ranging based positioning considering a realistic propagation channel
    - The realism of the propagation channel is of the utmost importance; it must be carefully selected and precisely modelled. The selected one is QuaDRiGa, [18]. Studies have shown that the propagation channel generated by QuaDRiGa cannot be considered as constant over the duration of an OFDM symbol. Therefore, a complete methodology has been derived in order to determine: the evolving parameters of the propagation channel and the generation sampling rate required to accurately model the propagation channel.
    - Determination of a highly realistic correlator output mathematical model. The derived model can be split into a useful term and an interference term. However, the resulting complete model is quite complex and to derive a simplified model could be beneficial for practical purposes, for example to implement less time-consuming simulations. This simplified model will be less accurate but easier to manipulate; its derivation is split into the useful term simplification and the interference term model.
    - A simplified model for the useful contribution in the previously presented model has been proposed and validated in the thesis
    - Statistical studies have shown the possibility to model the interference and the noise terms by an additive Gaussian variable. The Gaussian variables can be seen as an enhanced noise power and thus as a potential decrease of the available SNR or C/N_0.
- The development of ranging modules
    - The objective of the 5G signal ranging module is to estimate the time-of-arrival (TOA) of the signal.
    - The proposed 5G signal ranging module is based on the use of a classic Delay Lock Loop (DLL); a FLL is also proposed and the configuration for which a FLL is useful are described.

    - Studies have been led to assess the necessity to implement the carrier frequency estimator, a FLL for example. In fact, it will be shown that the implementation of the FLL is not required to improve the performance of the tracking estimation but can still be used in some cases.
- The precise characterization of pseudo range errors due to the propagation channels
    - Derivation of the methods. In absence of precise methods in the literature, two methods have been designed to characterize the pseudo range errors due to the propagation channels and thermal noise referred as a Gaussian fitting and a Gaussian over bounding methods.
    - Definition of scenarios and determination of the characteristics. Two systems are considered in the thesis: GNSS and 5G systems; both with a proper propagation channel: SCHUN for GNSS and QuaDRiGa for 5G. Use case scenarios have been defined in order to derive through simulations the characterizations.
- The development of hybrid navigation modules exploiting/adapted to the derived pseudo range measurements mathematical models.
    - 2 navigation filters have been studied in the thesis: an Extended Kalman Filter (EKF) and an Unscented Kalman Filter (UKF).
    - Determination of the benefit of the 5G measurements in a navigation module. The EKF and UKF have been studied for both 5G standalone and GNSS/5G hybrid cases. The benefit of the use of 5G measurement has been proved

1.3. Contributions

The contributions of the Ph.D. are listed below.

”Hybrid Navigation Filters Performances Between GPS, Galileo and 5G TOA Measurements in Multipath Environment” September, 23rd 2020 in the Session D1: Alternative Technologies for GNSS-Denied Environments 1 at ION GNSS + virtual conference, Anne-Marie TOBIE (TéSA), Axel GARCIA-PENA (ENAC), Paul THEVENON (ENAC), Marion AUBAULT (CNES), François Xavier MARMET (CNES)

“Processed 5G Signals Mathematical Models for Positioning considering a Non-Constant Propagation Channel” Anne-Marie TOBIE (TéSA), Axel GARCIA-PENA (ENAC), Paul THEVENON (ENAC), Marion AUBAULT (CNES) – International Workshop on Reliable Ubiquitous Navigation in Smart Cities - co-located with the IEEE Vehicular Technology Conference (IEEE VTC-Fall 2019).

1.4. Thesis outline

The manuscript is structured as follows.

Chapter 2 provides the description of GNSS systems with the emphasis on the GPS L1 C/A and the Galileo E1 signals. The signal structures and receiver processing are carefully described. A particular attention is also given to the selection of a realistic propagation channel.

Chapter 3 provides the description of the 5G systems. An overall description is provided but the main focus is done on the physical layer. This physical layer description comprises the definition of the modulation scheme, the waveform or again physical signals; all required information to derive a correct receiver. Based on this description a receiver is designed for an AWGN channel. Special attention is also provided to the selection of a realistic propagation channel.

Chapter 4 provides the derivation of mathematical models and statistics of processed 5G signals for ranging based positioning for a realistic propagation channel. In details, the impact of the propagation channel is first studied and according to this, new mathematical models of the correlator output of a 5G signals for positioning purposes is derived.

Chapter 5 describes the proposed synchronization module. The delay and the carrier tracking loops are first precisely presented. In this chapter, we also want to implement a C/N_0 estimator; to check its validity, the relationship between the SNR and the C/N_0 must be perfectly established.

Chapter 6 is dedicated to the realistic characterization of the pseudo range measurement errors due to propagation channels. The first step consists in precisely described the pseudo range measurements. 3 systems are considered in this thesis: GPS, Galileo and 5G systems; each of them has its own reference time frame. Therefore, a particular attention has been dedicated to the realist description of the synchronization between systems. Second, two methods to characterize the pseudo range errors are proposed. These methods are then applied to characterize the pseudo range measurement errors due to a realistic 5G propagation channel, QuaDRiGa, and due to a realistic GNSS propagation channel, SCHUN.

Chapter 7 provides the detailed performances of the proposed navigation filters in a realistic urban environment. In this chapter, the navigation modules envisioned are theoretically presented. Two navigation modules have been studied in this thesis: Extended Kalman Filter and Unscented Kalman Filter. The performances of the Kalman filters in a realistic urban environment are studied for different parameterization: the approximation used, the synchronization module defined and the C/N_0 estimation used, etc. in order to derive the optimal navigation solution.

Chapter 8 draws conclusion based on the results obtained in this thesis and present possible research work topics that could be addressed in the future.

Chapter 2. GNSS signals, measurement model and positioning

Global Navigation Satellite Systems (GNSS) refer to the navigation systems with global coverage capable of providing the user with a three-dimensional positioning and timing solution by radio signals ranging transmitted by orbiting satellites.

The aim of this chapter is to provide a global overview of GNSS systems and to present the signal processing implemented in the receiver which is in charge of obtaining the measurements required by the navigation block to provide the Position Velocity Time (PVT) solution. In this regard, the precise mathematical modelling of the received signal is of the utmost importance to determine the most optimal signal processing techniques to be implemented. The received signal is the result of the transmission of the signal generated by the satellite through the propagation channel and thus, the propagation channel should also be carefully modelled in order to have a realistic mathematical model of the received signal. In this chapter, the transmitted signal, the propagation channel and the received signal mathematical model descriptions are provided.

The organization of the chapter is as follow. First, the GNSS system is presented. Second, the GNSS signals are presented, since the thesis focus on GPS L1 C/A and Galileo E1 OS, only those 2 signals are detailed. Third, the GNSS signal propagation channel selected for the thesis is presented. Fourth, the GNSS receiver signal processing is explained. Fifth, the GNSS measurement model is detailed and finally, the GNSS positioning principle is explained.

2.1. GNSS system

The GNSS system is a passive system for the user; satellites send signals and the user receivers passively receive and process them; the term passive means that the user receivers cannot interact with the satellites. This passive characteristic allows an unlimited number of users to use GNSS systems at the same time. The GNSS system is composed of 3 segments: the user segment, the control segment and the space segment, they are detailed in this section and illustrated in Figure 2.1.

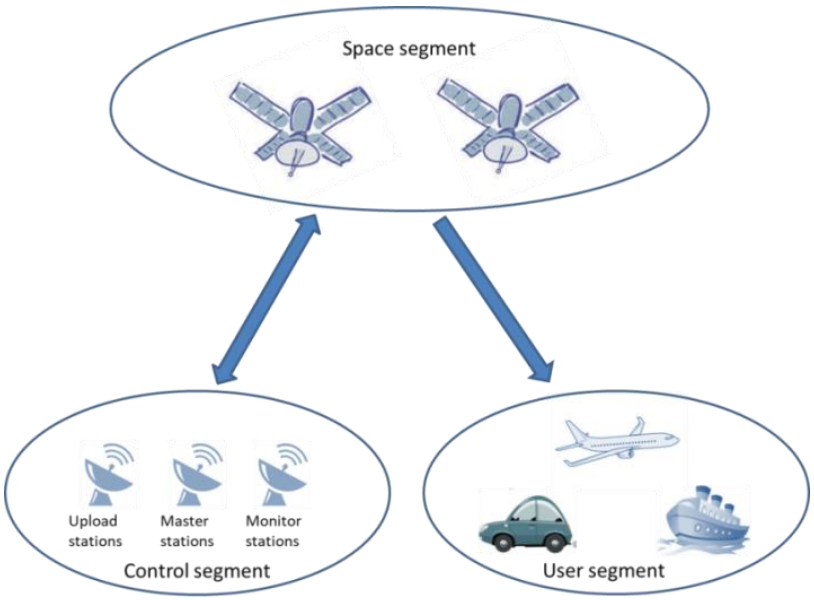

Figure 2.1 – GNSS System

2.1.1. Space segment presentation

The space segment corresponds to the constellation of satellites from which the users generate ranging measurements. Several GNSS constellations are already deployed; only the constellations which signals are used in this work are briefly detailed in this section.

2.1.1.1. GPS constellation

The Global Positioning System (GPS) is the first constellation being developed and remains the most famous nowadays. The first GPS satellites were launched in the late 1970s by the United State Department of Defence. Since that time several satellite generations or blocks have been deployed. GPS constellation consists in 31 satellites (24 mandatory to obtain Full Operation Capability (FOC)) in 6 orbit planes with a 55°-inclination (angle of the orbit with respect to the equatorial plane), see Figure 2.2. The orbits are nearly circular Medium Earth Orbit (MEO) orbits with a 20 200 km-radius and an orbit period for each satellite of approximately 12 hours.

Three frequency bands are used by GPS satellites. The L1 band, with a carrier frequency equal to 1575.42 MHz, is used to transmit two signals: the L1 C/A signal (Coarse/Acquisition) and the L1P(Y) (Precision) which is encrypted for military and other authorized users. From the Block III, a new signal L1C is also transmitted. The L2 band, with a carrier frequency equals to 1227.60 MHz, is used to transmit two signals: the L2P(Y) and the L2C (civilian) code since the Block IIR M satellites (2005). A M-codes (Military) signal is transmitted from IIR-M. The L5 band, 1176.45 MHz carrier frequency, is available from with Block IIF satellites (2009). Note that L1 and L5 bands are also Aeronautical Radio Navigation Service (ARNS) frequency bands; that is to say, bands reserved for civil aviation applications whereas L2 bands is not.

The GPS navigation message for L1 C/A, P and L2 P signals is presented in Figure 2.3. It is composed of 25 frames repeating every 12.5 minutes. Each frame is composed of 5 sub-frames and each sub-frame is composed of 10 words of 30 bits. Binary data are transmitted at 50 bit/s on L1CA, L1P(Y) and L2P(Y) signals by each satellite. The content of every sub-frame is as follows:

- The first sub-frame contains information about the clock corrections to be applied to the satellite, the transmitting satellite health and the user range accuracy
- The sub-frames 2 and 3 contain the transmitting satellite ephemeris
- The sub-frame 4 provides ionospheric model parameters as well as universal time coordinate (UTC) information and part of the almanac.
- The sub-frame 5 contains data from the almanac and the constellation status. It allows to identify the satellite that should be visible from the receiver (once it has computed a first position), thus simplifying and accelerating the acquisition or re-acquisition process. 25 frames are needed to complete the almanac.

The three first sub-frames content is specific to each satellite and the type of content (clock error corrections, ephemerides, etc) is always the same. However, sub-frames 4 and 5 content is common for all satellites whereas the type of content can vary from page to page among the 25 possible different pages (transmitted at a sequential order and generating a super frame).

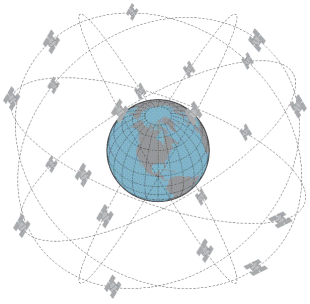

Figure 2.2 – The GPS constellation – [19]

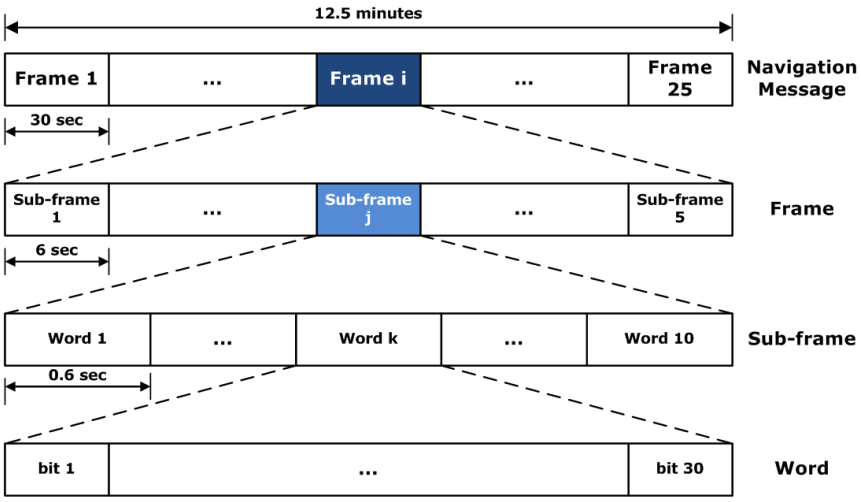

Figure 2.3 – Navigation Frame illustration - Source [19]

Even if the other constellations have different navigation message formats; the same main information is transmitted.

2.1.1.2. Galileo constellation

The Galileo constellation, deployed by the European Commission, comprises 30 satellites placed in MEO orbits. Three orbital planes are used at 56° inclination and a 23 222 km orbit altitude; 10 satellites are placed in each orbit.

Galileo system proposes 4 services:

- An Open Service (OS) which provides open and free of charge service set up for positioning, navigation and precise timing services.
- A High Accuracy Service (HAS) which completes the OS by providing an additional navigation signal and added-value services in a different frequency band. The HAS signal can be encrypted in order to control its access.
- A Public Regulated Service (PRS) which is a service restricted to government-authorised users, for sensitive applications that require a high level of service continuity.
- A Search And Rescue (SAR) service; this is the Europe contributions to the international COSPAS SARSAT cooperative system, which is an international satellite-based search and rescue distress alert detection system.

Galileo signals are transmitted over 4 frequency bands: the E1 band, 1575.42 MHz carrier frequency, E5a with a carrier frequency equal to 1176.45 MHz, E5b with a carrier frequency equal to 1207.14 MHz, and E6 with a carrier frequency equal to 1278.75 MHz.

2.1.2. Control segment presentation

The control segment is in charge of controlling the characteristics of the transmitted signals from each satellite, computing the ephemeris data (Keplerian elements) and satellite clock corrections, and then uploading the navigation message to each satellite.

It is composed of a ground network of master control stations, upload stations and monitor stations. The monitor stations installed all over the world monitor the satellites' signals and status and relay this

information to the master control stations. The master control analyses the signals then transmits the orbit and time corrections to the satellites through the uploading station.

As an example, for the GPS system, there are 2 master control stations (one is for back up), 4 upload stations and 16 monitor stations; their locations is presented in Figure 2.4.

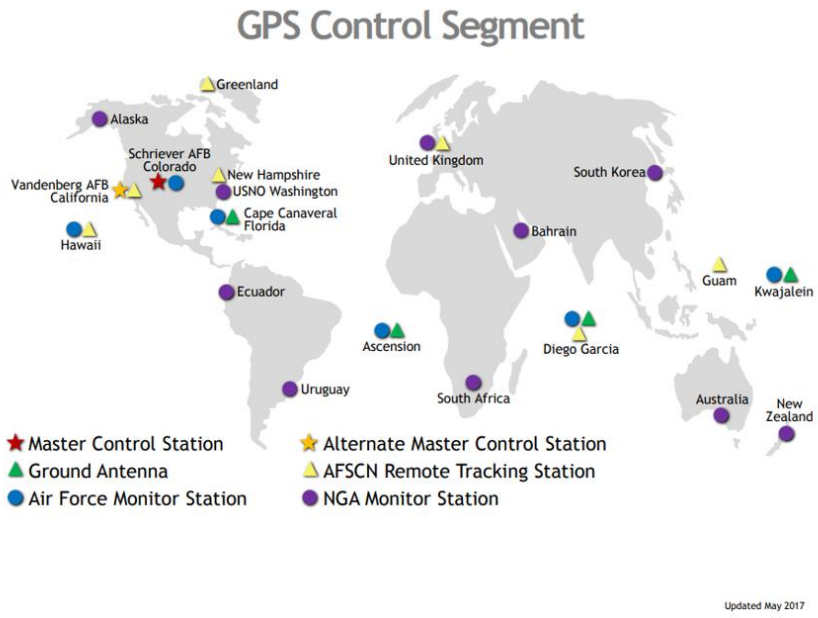

Figure 2.4 – GPS control segment

2.1.3. User segment presentation

The user segment is composed of all GNSS's user receivers. The user receiver processes the signal transmitted from the space segment to obtain positioning, velocity and timing solution usually referred as PVT solution. GNSS receivers are used in many of our daily life's equipment: car, smartphones, sport-related devices, etc. Moreover, the general trend in components' miniaturization leads to the proliferation of low-cost receivers.

The general structure of a receiver, illustrated in Figure 2.5, can be decomposed into 3 blocs:

- The Radio Frequency (RF) Front-End block
- The signal processing block
- The data processing block

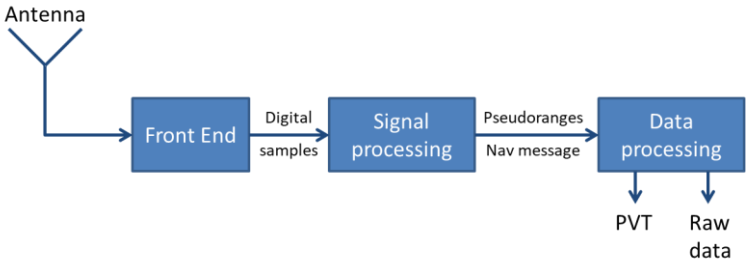

Figure 2.5 – User segment: receiver architecture

The working principle and thus, the functions of each of the three blocks are defined next.

The signal from the satellite is received at the antenna; then, it is processed by the front end. Basically, the front end aims to amplify the incoming signal, to filter the undesired part of the spectrum, to down-convert the received signal frequency around the intermediate frequency (IF) and to digitize the signal (sampling and quantizing).

The received signal digital samples are then processed by the signal processing block. This block aims to recover from the received signal the navigation message coming from each satellite in view and aims to calculate pseudo range (and potentially the pseudo range rate) measurement from each received satellite signal.

Finally, pseudo-ranges (and potentially the pseudo range rate) and navigation messages are processed to obtain the PVT on the data processing block (with the navigation solution filter).

2.2. GNSS signals

In order to continue the description of GNSS, the focus is now on the GNSS signals transmitted by the satellites and processed on the ground. The precise knowledge of the transmitted signal is of the utmost importance to design the optimal receiver and associated signal processing techniques.

This section introduces thus the GNSS signals with an emphasis on the signals of interest in this Ph.D. thesis, namely the GPS L1 C/A and Galileo E1 OS signals.

The design of GNSS signals has several goals. On one hand, the GNSS signal has to deliver the useful data (ephemeris, satellite clock correction, etc.) to the user with a convenient data rate, while ensuring an acceptable Bit/Word Error Rate (BER/WER). On the other hand, the GNSS signal also has to enable accurate ranging for the user within the range of reception conditions. For that purpose, GNSS uses Direct Sequence Spread Spectrum (DS-SS) techniques, a technique described in the first sub-section. The second and third sections aim at presented the GPS L1 C/A signal and the Galileo E1OS signal respectively.

2.2.1. Direct Sequence Spread Spectrum techniques

Direct Sequence Spread Spectrum (DS-SS) uses a known Pseudo Random Binary Sequence (PRBS) to spread the useful signal spectral occupation. Moreover, if the PRBS is used to distinguish the useful signal of several emitters of a same system sharing the same frequency band and the same transmission time, a multiple-access referred as Code Division Multiple Access (CDMA) is implemented. All GNSS systems but GLONASS (excepted for modernized signals) implement CDMA. In order to describe the working principle of DS-SS, a generic simple signal model is used in the section. GNSS signals can be slightly different from this generic signal model but the general description of the DS-SS impact on any GNSS signal remains valid.

2.2.1.1. PRN code

In this section, a description of the PRBS is proposed. Those PRBS sequences are finite and periodic, their design is such that they possess statistical properties similar to those of random white noise sequences in terms of autocorrelation (a Dirac function) and Power Spectral Density (PSD) (constant over all frequencies). In the following they are referred to Pseudo Random Noise sequence (PRN).

The PRN discrete sequence is defined, in the continuous time domain, as $c(t) = \sum_{k=-\infty}^{+\infty} c(k)\delta(t - kT_c)$; where $c(k)$ represents the bits, referred as chips, of the discrete PRN sequence, T_c is the duration between two PRN chips and $\delta(t)$ is the Dirac function. An illustration is proposed in Figure 2.6.

This PRN is then materialized using a shaping waveform $m(t)$; an illustration is proposed in Figure 2.7, for a rectangular shaping waveform, the mathematical model is provided in (2.1).

$$c_m(t) = \left(\sum_{k=-\infty}^{+\infty} c(k)\delta(t - kT_c) \right) * m(t - kT_c) = \sum_{k=-\infty}^{+\infty} c(k)m(t - kT_c) \quad (2.1)$$

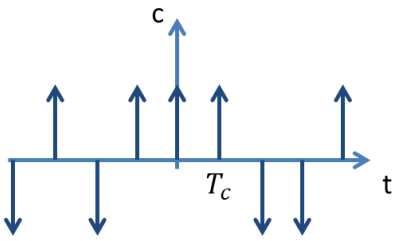

Figure 2.6 – PRN discrete sequence

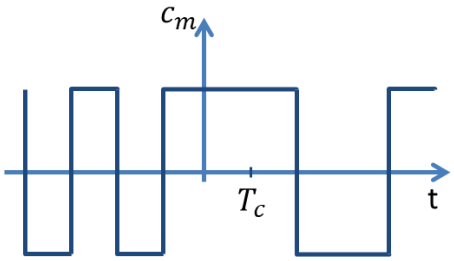

Figure 2.7 – Pulse shaping – a rectangular shaping waveform

2.2.1.2. *Transmission of the information*

The transmission of information is typically conducted by using the polarity of the transmitted PRN sequences. More specifically, a BPSK data modulation is implemented where the fundamental waveform (or vector of the signal space basis), $m_d(t)$, is a PRN sequence, or a repetition of PRN sequences, K, and where the symbol coordinates in the signal space basis are $d(k) = \{-1, +1\}$.

However, the mathematical model which is used to represent the data transmission for a DS-SS GNSS signal is a bit different in order to analyse independently the transmitted data modulation from the PRN sequence (and the inclusions of the subcarrier element for more advanced chip modulations such as the BOC modulation). In GNSS signals, the data modulation is mathematically modelled as a multiplicative signal, $d(t)$, to the PRN sequence (or signal), $c_m(t)$: $d(t) \cdot c_m(t)$. Using this mathematical model, $m_d(t)$ is simply a square pulse of length equal to the number of PRN sequences modulating the same BPSK symbol (or bit). Noting T_d the duration of one navigation message data bit and $T_R = LT_C$ the duration of one PRN sequence, where L is the number of chips per PRN sequence, which results in $T_D = KT_R$, $d(t)$ can be modelled as.

$$d(t) = \sum_{k=-\infty}^{+\infty} d(k) \cdot rect_{T_D}(t - k \cdot T_D) \quad (2.2)$$

For GPS L1 C/A, there are $K = 20$ PRN code sequences within one (binary) data bit; an illustration is proposed with the 2 first drawings in Figure 2.8.

Finally, note that the duration of one chip is significantly shorter than that of a data bit $T_c \ll T_d$.

2.2.1.3. *Final signal model*

The general simple time-domain structure of the transmitted DS-SS signal can be finally derived by modulating in frequency the signal resulting from the multiplication of the data signal, $d(t)$, and the PRN sequence or signal, $c_m(t)$. The general model is presented in equation (2.3). Note that the term "simple" used to describe this model is required due to the lack of more advanced signal structure elements such as the subcarrier term (used to include BOC modulations) or the data/pilot components.

$$s_T(t) = \Re\left(Ad(t)c_m(t)e^{-j2\pi f_L t}\right) = Ad(t)c_m(t)\cos(2\pi f_L t) \quad (2.3)$$

Where:

- f_L is the carrier frequency
- A is the amplitude of the transmitted signal
- $d(t)$ is the data signal carrying the binary information data to be transmitted to the user. The chip duration, T_c, is much smaller than the duration of a data symbol, T_d
- $c_m(t)$ is the PRN signal of the m^{th} satellite
- $s_{low\ pass}(t) = Ad(t)c_m(t)$ is the low pass representation or complex envelop of the signal

In practice, for the DS-SS GPS L1 C/A signal, the following representation can be done, see Figure 2.8. As presented below, there is an integer number of PRN sequences within one data bit. The data, the PRN sequence and the carrier are synchronized.

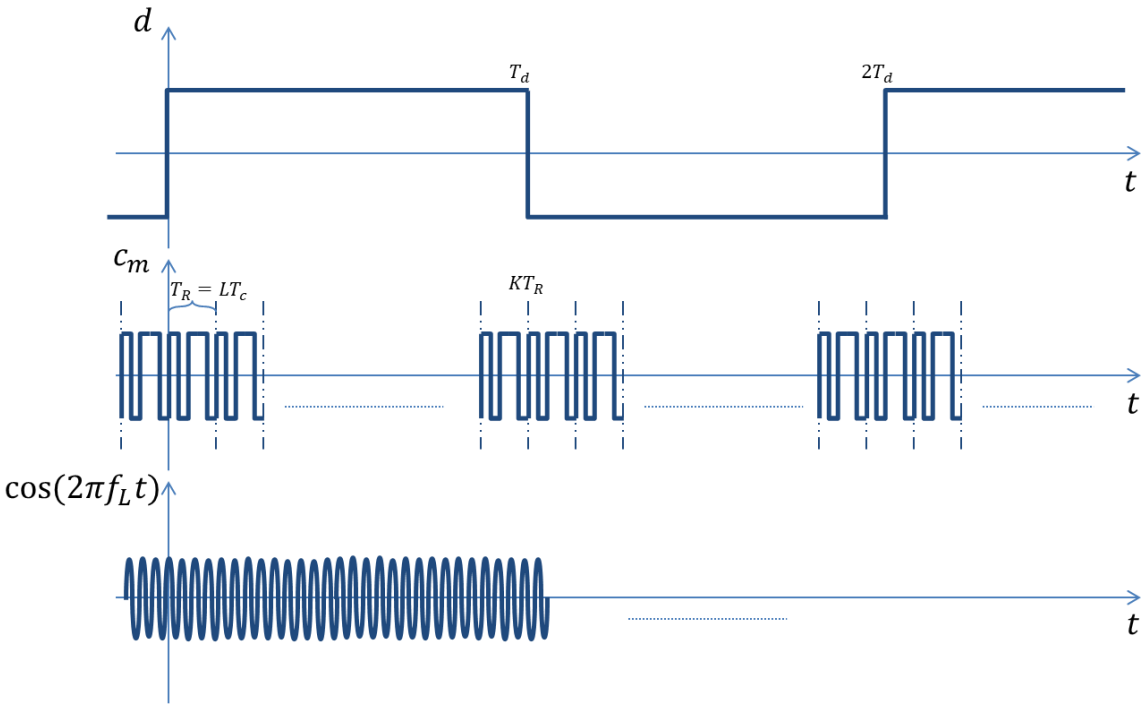

Figure 2.8 – Spread Spectrum communication

2.2.1.4. Power Spectrum density

To clearly visualise the spreading effect, the PSD of $s_T(t)$ must be observed. Assuming that the chip shaping waveform is rectangular and that the used chip modulation is BPSK modulation, the signal PSD can be modelled as in (2.4).

$$S_{s_T}(f) = TF[s_T(t)](f) = TF[Ad(t)c_m(t)\cos(2\pi f_L t)](f) = \frac{A}{2}\left[S_{dc_m}(f - f_L) + S_{dc_m}(f + f_L)\right] \quad (2.4)$$

Where $TF[\cdot]$ is the Fourier Transform operator and $S_{dc_m}(f) = S_d(f) * S_{c_m}(f)$. Note that $S_{c_m}(f) = S_{c_l}(f) \cdot S_m(f)$, where $S_m(f)$ is the chip waveform PSD and $S_{c_l}(f)$ is the PSD of $c_l(t)$.

In Figure 2.9, the PSD of the transmitted signal S_{s_T} is given when assuming a BPSK chip modulation and when assuming a fully random PRN sequence, $S_{c_l}(f) = 1$. In Figure 2.10, a comparison between S_d and S_{dc_m} (at baseband) is proposed, it can be observed that the bandwidth increase is approximately $KL = \frac{T_d}{T_c}$ (thus explaining its name "spread spectrum") and that the maximum amplitude of the transmitted signal S_{dc_m} is significantly lower than that of S_d.

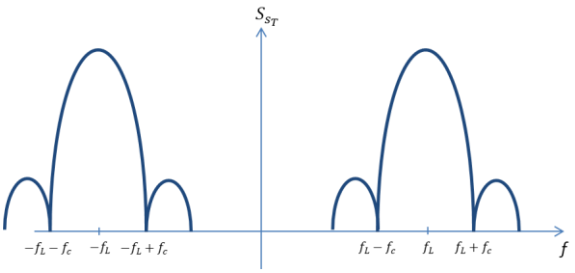

Figure 2.9 – Representation of the PSD of the transmitted GNSS signal – PRN sequence assumed fully random

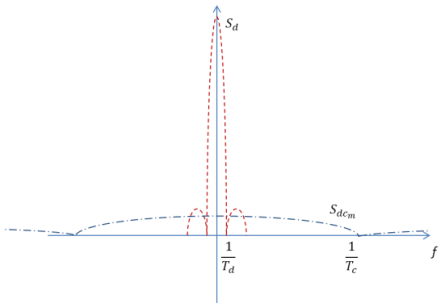

Figure 2.10 – Comparison of S_d and S_{dc_m}

The DS-SS technique is presented in this section for a general case, but it is at the basis of every GNSS signal generation. In the next sections, GPS L1 C/A and Galileo E1 OS signals are presented.

2.2.2. GPS L1 C/A

GPS sends several signals in the L1 band (carrier frequency $f_{L_1} = 1575.42\ MHz$), the C/A code (Coarse/Acquisition) signal, the L1P(Y)-(Precision) signal and M-codes (Military) signal which are encrypted for military and other authorized users, and from the Block III, the L1C signal, composed of a data component and a pilot component. These signals PSD are presented in Figure 2.11. The thesis focuses on the GPS L1 C/A signal and thus, only the exact description of this signal is provided in the following.

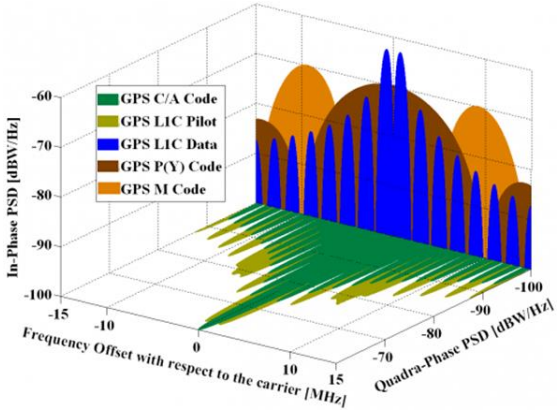

Figure 2.11 – GPS L1 signals – source [19]

The GPS L1 C/A signal mathematical model is the same as the one presented in equation (2.3) and its derivation is fully detailed in [20]. GPS L1 C/A implements a $BPSK(1)$ modulation for the chip modulation; this is equivalent to having a shaping waveform, $m(t)$, equal to a square pulse with the length of a chip. The PRN code is composed of $N = 1023\ chips$ and the chipping rate is $f_c = \frac{1}{T_c} = 1.023\ Mchip/sec$. The duration of a PRN code repetition is $T_R = 1\ ms$ and the shaping waveform is rectangular. Hence, the autocorrelation of the PRN code can be approximated by a triangle ($rect_T * rect_T = tri_T$) with a base within [-1; +1] chip and a repetition every 1023 chips. Regarding the data, the duration of a data bit is $T_d = 20\ ms$ (data rate is 50 bit/s) and there are $K = 20$ PRN code repetitions per data bit.

2.2.3. Galileo E1 OS

Galileo transmits two signals in its E1 band ($f_{L_1} = 1575.42\ MHz$): E1 OS (Open Service) and PRS, both illustrated in Figure 2.12. Only the Galileo E1 OS signal is commented in this section since the PRS signal is restricted to authorized users.

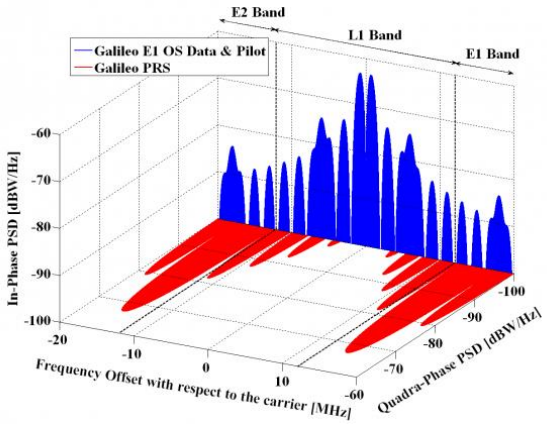

Figure 2.12 – Galileo E1 signals – source [19]

The structure of Galileo E1 OS is more advanced than GPS L1 C/A signal structure. In fact GPS L1 C/A signal is considered as the GNSS legacy signal, since its development several innovations have been developed to improve some of the GPS L1 C/A signal performance. Among them, three are used by the Galileo E1 OS signal: the Binary Offset Carrier (BOC) modulation, the data/pilot architecture and the use of secondary codes.

2.2.3.1. BOC modulation

The BOC modulation is a modulation (or materialization with memory) applied to the PRN sequence chips. The BOC modulation can be mathematically modelled as the multiplication of the PRN sequence materialized with a square pulse, $c_m(t)$, with a square wave sub-carrier, $sc(t)$. A square wave is a function representing the sign of a continuous wave. The sub-carrier is such that it is synchronized with the spreading code, and there is an integer number of half cycles of the sub-carrier within one PRN code chip. The BOC modulation is particularly interesting because it allows to add a frequency offset on the location of the main PSD signal lobe. For example, the $BOC(2,1)$, illustrated in Figure 2.13, has the main PSD lobe not located on the centre of the band but offset by 2 MHz from this centre. This offset allows to add a signal on a band with mitigated interference effect on the other signals already present in the band. Therefore, as illustrated in Figure 2.14, GPS and Galileo, which (partially) uses a $BOC(1,1)$ modulation, can both transmit a signal on the L1 band with reduced/mitigated interference from one signal over the other.

Another advantage of the BOC modulation is the sharper peak of the correlation function (see Figure 2.15), which results in a better accuracy compared to a BPSK modulation, notably in terms of robustness against noise and multipath.

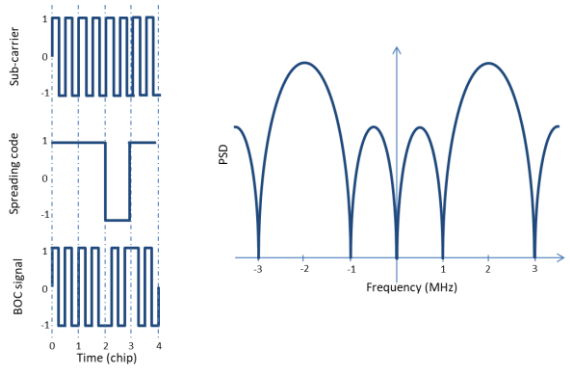

Figure 2.13 – BOC (2,1) modulation illustration

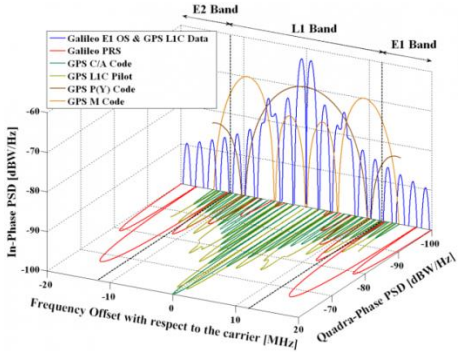

Figure 2.14 – Spectra of GPS and Galileo signals in L1 – source [19]

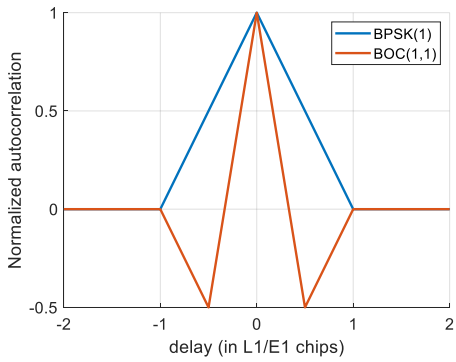

Figure 2.15 – Autocorrelation of BPSK51) and BOC(1,1) signals

2.2.3.2. Data/pilot architecture

Until now, the transmitted signal was composed of the data modulated by a carrier and a code. The presence of data in the signal leads to several limits; indeed, it is necessary to avoid data bit transition when conducting the correlation operation; therefore, the correlation time, also known as coherent integration time, is limited. Moreover, when conducting the carrier tracking, it is necessary to wipe off those data (discriminator insensitive to data bit transitions).

A data/pilot architecture can be used to overcome these listed limitations. A pilot component is a signal that does not carry any useful information. This signal is always transmitted along with a data signal; both are perfectly synchronized and use different PRN codes to avoid interference. The power is split between those two signals. In this architecture, the normalized baseband signal can be expressed as in (2.5).

$$s(t) = \alpha d(t) c_D(t) + \beta c_P(t) \;\; with\; \alpha^2 + \beta^2 = 1 \qquad (2.5)$$

The main advantage of the pilot signal is to remove data bit transitions. Hence longer integration can be done, which leads to correlators outputs with higher Signal to Noise Ratio (SNR) (better thermal noise filtering), and more optimal tracking algorithms can be used. However, as the power is split between the data and the pilot components, the data demodulation performance is affected (this effect is compensated by the introduction of more robust channel codes).

2.2.3.3. Secondary codes

Secondary codes are binary known codes; they are shorter than the spreading PRN code. An example is proposed in Figure 2.16, the duration of a secondary code chip is the same as the duration of the whole PRN (primary) code. The secondary code artificially extends the length of the spreading code; those longer codes allow for better correlation properties.

The product of the PRN code by the secondary code is called a tiered code. Secondary codes help fighting narrowband interferences and are also beneficial for data bit synchronization when used on a data component.

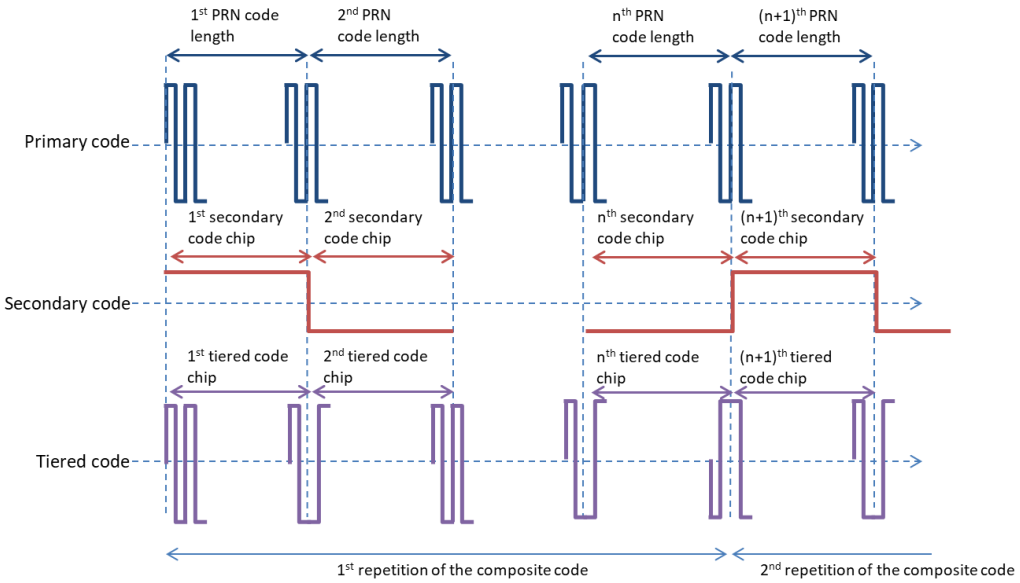

Figure 2.16 – Secondary codes principle

2.2.3.4. *Galileo E1 OS signal structure*

The E1 OS signal uses the data/pilot architecture and is modulated by a Composite BOC modulation (CBOC). The expression of the transmitted signal is provided in (2.6) and is described in [21].

$$s_{E1}(t) = \frac{1}{\sqrt{2}} c_{E1-B}(t) d_{E1-B}(t) CBOC_{\left(6,1,\frac{1}{11},+\right)}(t) - \frac{1}{\sqrt{2}} c_{E1-C}(t) c_{Sec,E1-C}(t) CBOC_{\left(6,1,\frac{1}{11},-\right)}(t) \qquad (2.6)$$

Where:

- $c_{E1-B}(t)$ and $c_{E1-C}(t)$ are the primary codes with a length of 4092 chips and a chipping rate of 1.023 MHz; hence a code last 4 ms (1 ms for GPS L1 C/A). The use of longer code with respect to GPS L1 C/A improves the correlation isolation.
- $d_{E1-B}(t)$ is the data transmitted on the data component. The data bit rate is 250 symbols per second, the symbol duration is 4 ms (20 ms for GPS L1 C/A).
- $c_{Sec,E1-C}(t)$ the secondary code modulating the pilot component, it is 25 bits long and has a rate of 250 Hz.
- $CBOC_{\left(6,1,\frac{1}{11},+\right)}(t) = \sqrt{\frac{10}{11}} BOC_{(1,1)}(t) + \sqrt{\frac{1}{11}} BOC_{(6,1)}(t)$, the time representation of this sub-carrier is given in Figure 2.17 on the left
- $CBOC_{\left(6,1,\frac{1}{11},-\right)}(t) = \sqrt{\frac{10}{11}} BOC_{(1,1)}(t) - \sqrt{\frac{1}{11}} BOC_{(6,1)}(t)$, the time representation of this sub-carrier is given in Figure 2.17 on the right

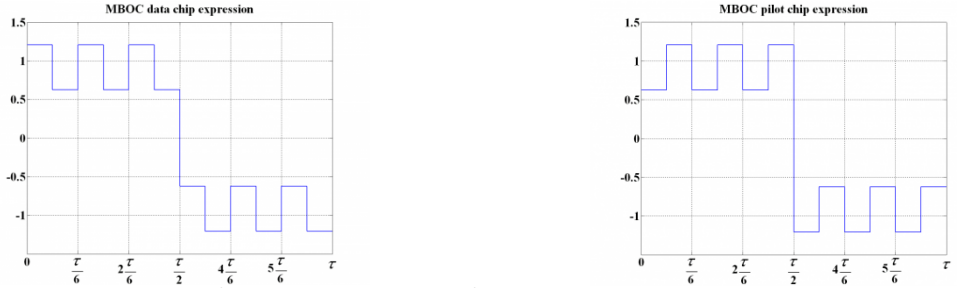

Figure 2.17 – $CBOC(6,1,\frac{1}{11},+)$ (left) and $CBOC(6,1,\frac{1}{11},-)$ (right) sub carrier time representation – source [19]

2.3. GNSS propagation channel

The GNSS signals presented in the previous section are the signals transmitted by the satellites; however, before being received by the users, these signals go through the propagation channel which can highly corrupt/distort them. This section aims to present the propagation channel used in this thesis for GNSS signals. Remind that one of the objectives of the chapter is to precisely model the received signals and its impairments in order to adopt the optimal signal processing techniques.

Recently, the need for a precise and accurate positioning has become the main objectives of new GNSS signal generations. To fulfill these objectives, the development of highly sophisticated GNSS signals and advanced processing techniques is performed. However, the development/improvements of these new signals must be made by taking into account the propagation channel impacting the signal. That is why, while developing and testing new signals, a realistic propagation channel model is required. This area of research is wide.

In this section, first the Channel Impulse Response (CIR) principle is presented, second a brief presentation of a propagation channel is presented then, the propagation channel adopted in the Ph.D. is presented. A deep study of propagation channel can be found in [16].

2.3.1. Channel Impulse Response

The received complex envelope signal mathematical model at the receiver antenna input can be expressed in (2.7) by the convolution between the incoming signal and the propagation channel complex envelope Channel Impulse Response (CIR). The CIR mathematical model is usually expressed as $h_c(t,u)$, where u is a mathematical variable used for the convolution operation, t is used to model the complex amplitude evolution and delay of each multipath.

$$r_l(t) = h_c(t,u) * s_l(u)|_{u=t} \tag{2.7}$$

In order to define a precise received signal model it is thus of the utmost importance to precisely model the CIR mathematical model, $h_c(t,u)$. Therefore, in order to design the CIR model, it is of the utmost importance to first select a GNSS compliant propagation channel model.

2.3.2. Propagation channel study

2.3.2.1. Definition

From its transmission to its digital processing the GNSS signal is impacted by impairments. The sources of these impairments include:

- The satellite payload and antenna. The payload comprises all reference oscillators, Digital to Analogue Converters, Filters and amplifiers used to transmit the signal s_T defines above.
- Free space loss. Linked with the distance between the transmitter and the receiver, the power loss during the propagation is mainly due to the free space loss.
- Atmospheric propagation. Atmospheric delays are due to the propagation of the signal through the lower atmospheric layers: the ionosphere and the troposphere.
- Reflections and diffractions. In presence of multipath, the Line Of Sight (LOS) signal is mixed with delayed replicas of the LOS, which implies difficulties to recognize the LOS when processing the signal.

- Blockage and shadowing of the direct path. Due to the environment, the LOS path can be shadowed, or even completely blocked.
- Interferences. There can be a very wide variety of interference received at the same time as the useful GNSS signal.
- Receiver antenna and RF front end. As for the first item, the receiver uses oscillators, Digital to Analogue Converters, Filters and amplifiers that disturb the signal.

The free space loss, atmospheric propagation, reflections and diffractions impairments are usually referred to as the propagation channel. All the above mentioned impairments are usually referred to the transmission channel.

2.3.2.2. Modelling of the propagation channel

Getting a precise and realistic model of the propagation channel is mandatory to develop new signals model and signal processing techniques. Therefore, a high amount of information can be found in the literature to model the effect of the propagation channel. For example, a deep study of the propagation channel modelling methods can be found in [22].

Three main approaches can be found in the literature to model the Land Mobile Satellite propagation channel. The choice of the method is a trade-off between computation time and accuracy.

- A deterministic approach will use the environment model to precisely compute, by ray tracing method, the interactions between the impinging waves and the local environment. It requires a precise model of the environment and a huge computation time.
- A statistical approach reproduces the global channel behaviour. It is based on statistical distributions and derived models coming from measurements campaigns. It is less accurate than the deterministic approach but requires less computation time.
- A hybrid approach is simply a hybrid deterministic-statistical approach; several models exist in the literature, each of them is the result of a balance between statistical and deterministic modelling

2.3.3. SCHUN

For the purpose of this thesis, the adopted propagation channel model is SCHUN. SCHUN stands for Simplified Channel for Urban Navigation. The complete description of the model can be found in [22].

The propagation channel simulator SCHUN has been implemented to compute the wide-band parameters of the Land Mobile Satellite (LMS) channel corresponding to the motion of a receiver in an urban canyon. SCHUN is a hybrid deterministic-statistical LMS propagation channel; the implementation of the statistical and deterministic modules optimizes the trade-off between accuracy and computational resource.

The macro architecture of SCHUN is provided in Figure 2.18; two components can be identified: a statistical and a deterministic component. Basically, the statistical component of the simulator is dedicated to the generation of the virtual city, which depends on the parameters provided by the user. Then, based on this generated environment, SCHUN models the interactions between impinging signals and the environment by using simple Electromagnetic (EM) interaction models; this is the deterministic aspect of the model. More specifically, the LOS contribution is estimated using an optical ray approach, whereas the echoes are generated using the Three Components Model developed in [16].

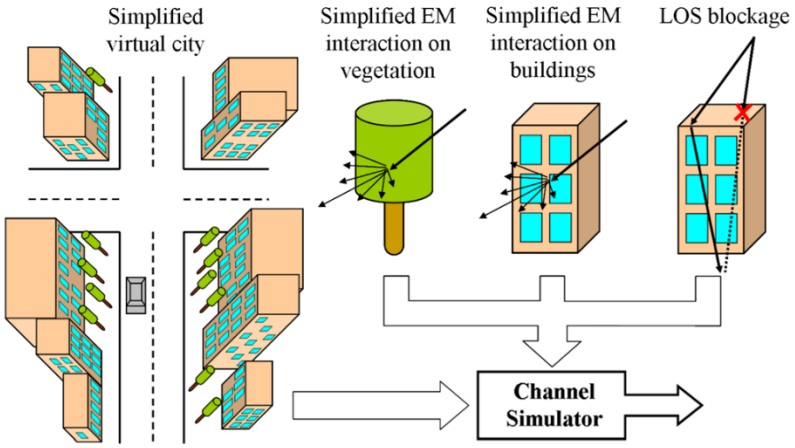

Figure 2.18 – SCHUN macro architecture – source [22]

The SCHUN time evolving complex envelop Channel Impulse Response (CIR), $h(t,\tau)$, adopted from now on is given in (2.8).

$$h(t,\tau) = \sum_{l=0}^{N} \gamma_l(t) e^{-j\Phi_l(t)} \delta\big(\tau - \tau_l(t)\big) \tag{2.8}$$

Where:

- t is the time variable
- τ is the convolution variable
- N is the number of multipath
- l is the index corresponding to a particular ray
- γ_l is the ray amplitude
- Φ_l is the phase of the ray including delay and reflection shifts
- τ_l is the ray delay

A complete example of a propagation channel generation will be presented in chapter 7.

2.4. Receiver signal processing

In the first sections, the GNSS system and the signal transmitted has been presented. The impairments degrading the transmitted signal have been explained. Therefore, the model of the received signal at the antenna input is now precisely defined.

In this section, the processing of received signal made by the receiver is described. However, before reaching the signal processing block the signal must pass through the RF front-end block as explained in section 2.4.1. Therefore, before explaining the signal processing techniques, the distortions introduced by the antenna and RF front-end block to the received signal at the antenna input must be characterized in this section to obtain the received signal mathematical model at the signal processing block input.

Finally, note that the outputs of the signal processing block will then be used by the data processing block to calculate the PVT solution as commented in section 2.4.3. The principle of the PVT solution exploited in the data processing block is presented in section 2.6.1.

First, the Radio Frequency Front-End is presented; then the signal processing applied to the legacy signal GPS L1 C/A is detailed step by step: acquisition, tracking and data demodulation.

2.4.1. Radio Frequency front-end block

The RF front-end role is to provide a sampled signal as clean as possible to the signal processing block. It has to select the useful signal, to mitigate out-of-band interference and multipath. Basically, the RF front end consists of:

- a low noise amplifier which is used to amplify the incoming signal
- a down converter to take the signal to intermediate frequency (IF) or baseband (depending on the receiver), the down conversion is achieved by mixing the incoming signal with local oscillators
- a selective filter (bandpass filter centred around IF or a lowpass filter) which removes all the unwanted signal
- an analogue to digital converter, which samples then quantizes the incoming signal, coupled with an Automatic Gain Control (AGC) device,

A general architecture of a RF front end is provided in Figure 2.19.

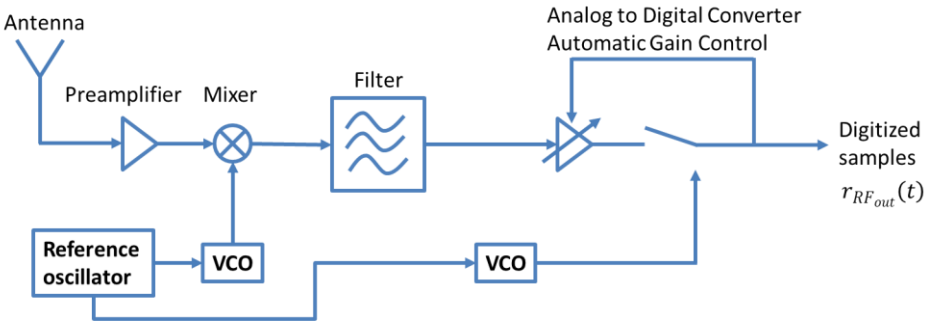

Figure 2.19 – Radio Frequency Front End

The mathematical model of the received signal at the RF front end output, $r_{RF_{out}}(t)$, is derived next. The derivation is proposed for one ray only; the final model at the output of SCHUN is the linear combination of rays. For simplification, in the following demonstrations, the propagation channel will be modelled as a pure delay. The development for a SCHUN propagation channel is provided in Annex B. The generic received signal model is given in (2.9).

$$r_{RF_{out}}(t) = h_{RF}(t) * [h_c(u,t) * s_T(t) + n(t)] \tag{2.9}$$

Where:

- h_c is the impulse response of the propagation medium modelled by a pure delay which can vary in time. It is assumed that $h_c(u,t) = \delta\big(u - \tau(t)\big)$.
- h_{RF} is the impulse response of the equivalent RF Front-End filter. It is assumed that its impulse response is h_{RF} and its transfer function is $H_{RF}(f) = rect_B(f) * [\delta(f - f_{IF}) + \delta(f + f_{IF})]$, where f_{IF} is the intermediate frequency. The equivalent low-pass RF Front-End is thus $H_{RF,BB}(f) = rect_B(f)$
- n is an additive perturbation. In the following it is assumed that the only additive perturbation is the noise created by the RF Front-End; which creates an additional white Gaussian noise (AWGN) whose PSD is $S_n(f) = \frac{N_0}{2} W/Hz$

Hence the model can be re-written as given in (2.10).

$$r_{RF_{out}}(t) = \Big(\big(s_T\big(u - \tau(t)\big) + n(u)\big) * h_{RF}\Big)(t) = \underbrace{(s_r * h_{RF})}_{u_{RF_{out}}}(t) + n_{RF_{out}}(t) \tag{2.10}$$

Where:

- $s_r(t) = s_T\big(t - \tau(t)\big) = Ad\big(t - \tau(t)\big)c_m\big(t - \tau(t)\big)\cos(2\pi f_L t)$
- $u_{RF_{out}}$ is the useful part of the signal coming out of the RF front-end
- $n_{RF_{out}} = (h_{RF} * n)$ is the thermal noise filtered by the RF front-end

Hence, the signal model, over the integration time, is provided by (2.11).

$$r_{RF_{out}}(t) = Ad\big(t - \tau(t)\big)c_m\big(t - \tau(t)\big)\cos\big(2\pi f_L t + 2\pi f_D(t)t + \theta_0(t)\big) + n_{RF_{out}}(t) \qquad (2.11)$$

2.4.2. Signal processing block

The signal processing block aims to generate a local replica of the signal perfectly synchronized with the incoming signal. Therefore, estimates of the signal parameters (delay, phase, Doppler, power) are available and can be used to produce measurements: pseudo range, phase, navigation message, SNR, etc.

GNSS signal processing is based on correlator outputs, these correlator outputs are used for the three main functions of the signal processing: the acquisition, the tracking and the data demodulation. The principle of the correlation operation is to de-spread the incoming signal and to integrate, over a certain period referred to as correlation time. The de-spreading of the signal is achieved by multiplying the incoming signal with a synchronized local replica of the same PRN sequence.

In order to estimate the signal parameters, the signal processing block can be divided into 3 sub blocks: the acquisition block, the tracking block and the data demodulation, an illustration is proposed in Figure 2.20.

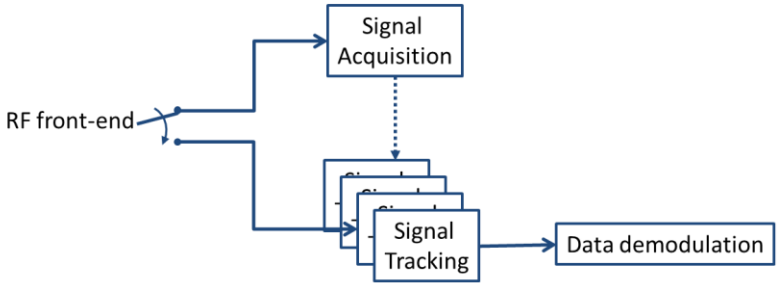

Figure 2.20 – signal processing architecture

The acquisition block aims at identifying the received signal and at achieving a rough time and frequency synchronization with the incoming signal. The signal tracking block aims at achieving a fine synchronization with the incoming signal; each identified signal is processed independently. The data demodulation aims at decoding the navigation message. In order to do so, the receiver must detect the location of the edges of the navigation data bit; this is the bit synchronization step. Then the receiver must find the beginning of the frame inside the flow of broadcasted bit; this is the frame synchronization step. Finally the demodulation of the navigation data can be conducted and the pseudo ranges can be computed.

2.4.2.1. Correlation in a GNSS receiver

GNSS signal processing is based on correlator outputs. Those correlator outputs are used in the three following steps: the acquisition, the tracking and the demodulation steps.

The principle of the correlation operation is firstly to de-spread the incoming signal by multiplying it with a synchronized local replica of the same PRN sequence and a synchronized local replica of the carrier frequency. Secondly, the de-spread signal is integrated, over a correlation time T_I, in order to have a positive Signal to Noise Ratio (SNR) at the correlator output. This integration is equivalent to a low pass filter with a $\frac{1}{T_I} Hz$-bandwidth. T_I is called the coherent integration time and is a multiple of the PRN code duration T_R.

The principle of the correlation operation, for a GPS L1 C/A signal, is illustrated in Figure 2.21.

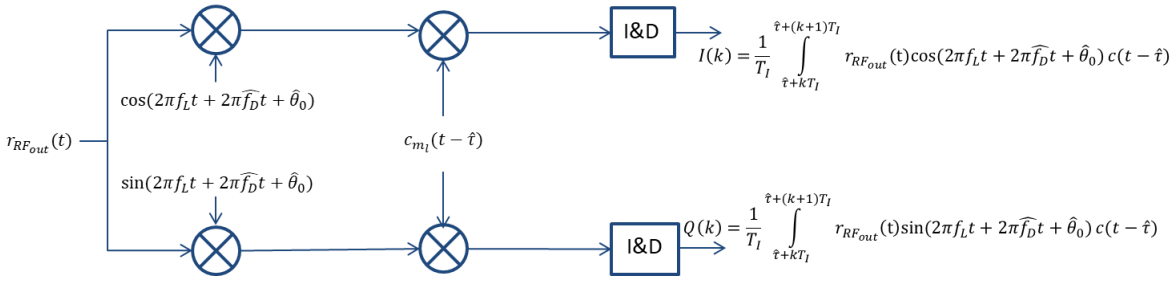

Figure 2.21 – General structure of a correlator

In Figure 2.21:

- $\hat{\tau}$ corresponds to the delay of the local replica
- $\widehat{f_D}$ corresponds to the Doppler of the local replica
- $\hat{\theta}_0$ corresponds to the phase of the local replica at the beginning of the coherent integration time interval
- I, Q correspond to the In-phase and In-Quadrature correlator outputs
- T_I is the correlation duration, the integration time
- $I\&D$ stands for Integrate and dump

The In-Phase and Quadrature-phase correlator output mathematical model, for a GPS L1 C/A signal, are given in (2.12) and (2.13). These models are well known and their complete derivation can be found in [23].

$$I(k) = \frac{Ad(k)}{2}\mathrm{sinc}\left(\pi\varepsilon_f T_I\right)\cos(\pi\varepsilon_f T_I + \varepsilon_\theta)K_{c_m,c_{m_l}}(\varepsilon_\tau) + n_I(k) \tag{2.12}$$

$$Q(k) = \frac{Ad(k)}{2}\mathrm{sinc}\left(\pi\varepsilon_f T_I\right)\sin(\pi\varepsilon_f T_I + \varepsilon_\theta)K_{c_m,c_{m_l}}(\varepsilon_\tau) + n_Q(k) \tag{2.13}$$

Where:

- $K_{c_m,c_{m_l}}(\tau-\hat{\tau}) = \int_{\hat{\tau}+kT_I}^{\hat{\tau}+(k+1)T_I} c_m(u-\tau)c_{m_l}(u-\hat{\tau})\,du$ represents the correlation value between the PRN code of the incoming signal and the locally generated PRN code
- $\varepsilon_\tau = \tau - \hat{\tau}$ the delay estimation error
- $\varepsilon_f = f_D - \widehat{f_D}$ the carrier frequency estimation error
- $\varepsilon_\theta = \theta_0 - \hat{\theta}_0$ the carrier phase estimation error at the beginning of the coherent integration time interval
- n_I and n_Q are uncorrelated and Gaussian noises, $n_I, n_Q \sim N\left(0, \frac{N_0}{4T_I}\right)$.

This development is proposed here for a propagation channel assumed to be a pure delay, the development for an advanced channel (as SCHUN) is given in Annex B.

2.4.2.2. Acquisition

The goal of the acquisition process is to detect the presence of the useful signal and to give a rough estimate of the Doppler frequency and the code delay. There are several methods to perform this search process. The usual way to detect the presence of a signal is to compute a detector to be compared against a threshold. Each signal is processed separately, since each signal has its own PRN sequence (a satellite is identified by a unique PRN code), see [23].

Basically, the acquisition process consists in testing, for each satellite, a set of code delay, $\hat{\tau}$, and Doppler frequency, $\hat{f}$, and finding the couple that maximise the selected detector. For that purpose, the adopted strategy is to define an acquisition 2D search matrix, which will depend on the code delay and the Doppler frequency. This search matrix is presented in Figure 2.22. As it can be seen, the size of the matrix depends on the total uncertainty on the code delay, which is 1023 chips for GPS L1 C/A, and on the total uncertainty on the Doppler frequency, which depends on the available information. To be precise, if the receiver has some information on its position, the position of the satellite and its clock; then it will perform a warm start, and the Doppler uncertainty can be reduced. However, if the receiver has no information, it will perform a cold start. In that case, the uncertainty is maximal. By doing this detection process, either the signal is present (and detected) and a peak is a priori visible in the acquisition detector output (see Figure 2.23), or the signal is absent and the acquisition output is only composed of noise.

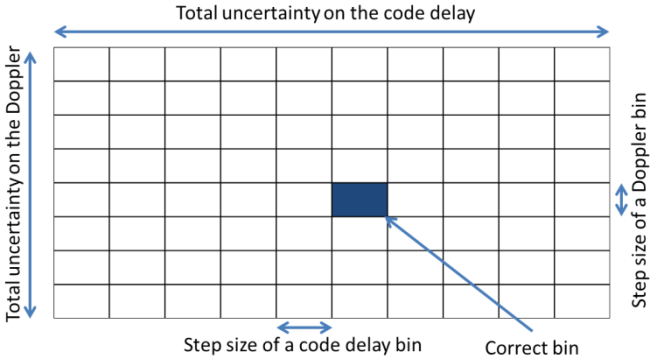

Figure 2.22 – Acquisition matrix – source [19]

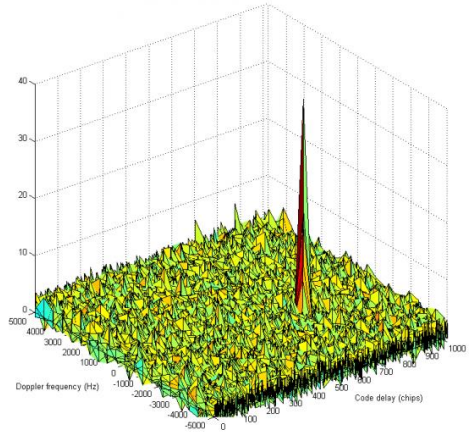

Figure 2.23 – Acquisition detector output – source [19]

The acquisition performances are characterized through the detection performance and the time to acquire the signal. Theoretically, detection performance is based on the classic Neyman-Pearson test, which details can be found in [23].

Finally, at the end of the acquisition process, the receiver knows, for each detected satellite, an estimate of its code delay and of its Doppler frequency. The uncertainty of the code delay depends on the size of the code bin and the uncertainty of the Doppler frequency depends on Doppler bin, which is deduced from the integration time.

2.4.2.3. GSP L1 C/A Tracking process

While the acquisition process gives rough estimates of the code delay and Doppler frequency, the tracking process aims at generating local replica perfectly synchronized with the incoming signal (obtaining of fine estimates). As two parameters have to be tracked, two tracking processes are defined: the carrier tracking (1st part) and the code delay tracking (2nd part).

2.4.2.3.1. Carrier tracking

The goal of the carrier tracking loop is to generate a local carrier that is perfectly synchronized with the incoming signal. Once the phase is tracked ($\varepsilon_\theta \to 0, \varepsilon_f \to 0$) then the In-Phase and the Quadrature-Phase correlator output models can be simplified as in (2.14).

$$\begin{cases} I(k) = \frac{A}{2} d(k) \cos\left(\pi \varepsilon_f T_I + \varepsilon_\theta\right) K_{c_m, c_{m_l}}(\varepsilon_\tau) sinc\left(\pi \varepsilon_f T_I\right) + n_I(k) \to \frac{A}{2} d(k) K_{c_m, c_{m_l}}(\varepsilon_\tau) + n_I(k) \\ Q(k) = \frac{A}{2} d(k) \sin\left(\pi \varepsilon_f T_I + \varepsilon_\theta\right) K_{c_m, c_{m_l}}(\varepsilon_\tau) sinc\left(\pi \varepsilon_f T_I\right) + n_Q(k) \to n_Q(k) \end{cases} \quad (2.14)$$

This means that, if the code delay estimate is precise ($\varepsilon_\tau \sim 0$), the Quadrature-Phase correlator output will only contain noise and the data, $d(k)$, can be recovered from the In-Phase correlator.

The generic GPS receiver carrier tracking loop block diagram is given in Figure 2.24. The carrier loop discriminator defines the type of tracking loop: a Phase Lock Loop (PLL) or Frequency Lock Loop (FLL).

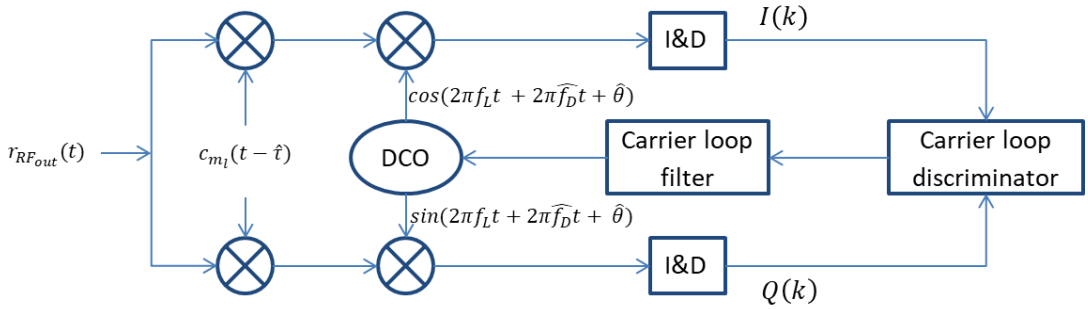

Figure 2.24 – Generic GPS carrier tracking loop block diagram

2.4.2.3.1.1. Phase Lock Loop (PLL)

The goal of a PLL is to generate a local replica which phase is perfectly synchronized with the carrier phase in the incoming signal. The phase discriminator estimates the phase error between the local replica and the incoming signal carrier, this error is then filtered using a low pass filter F_{PLL}. Finally, this filtered error is fed to a Digitally Controlled Oscillator (DCO) that will generate the new local carrier. Two kinds of PLL are usually defined; the pure PLL when there is no data modulation on the GPS signal (the discriminator used is sensitive to data) and the Costas PLL which is a PLL that tolerates the presence of data modulation on the baseband signal (the discriminator used is insensitive to data). For each of them, [23] provides several discriminator algorithm, each having its own characteristics.

2.4.2.3.1.2. Frequency Lock Loop (FLL)

The PLL might not be able to track the signal phase in case of high dynamics, or when the Doppler uncertainty is high. The goal of the FLL is to try to lower the frequency error to a level acceptable for phase tracking. The functioning of a FLL is very similar to that of a PLL. The correlator outputs are used by the frequency discriminator which estimates the frequency error between the incoming carrier and the locally generated carrier. Then the estimate is filtered with a low pass filter and the new carrier estimate is generated thanks to the DCO. Here again, several discriminators can be defined, some are given in [23]. Typically, the FLL is used just after the acquisition process to track the important frequency error. Once it is tracked, a PLL has to be used. A classical structure used is the FLL-aided PLL. The FLL absorbs the major part of the frequency error and then the PLL should easily lock on the residual phase error.

2.4.2.3.2. Code Delay tracking

The goal of the DLL is to generate a local replica of the PRN that is perfectly synchronized with the PRN code delay of the incoming signal. The principle is similar to that of the carrier tracking loop. Correlator outputs are used by a code delay discriminator to estimate the synchronisation error between the local replica and the incoming signal. The error is then filtered and used to control a DCO that commands the shift register generating the local replica (see Figure 2.26).

Contrary to the carrier tracking loop, the DLL uses two more correlators: an early and a late (in addition to the prompt used in the carrier tracking loop). The first one correlates the signal with an early version of the local PRN code replica, the delay is $\frac{d}{2}$. The second correlates the signal with a late version of the local PRN code replica, the delay is $-\frac{d}{2}$. The DLL uses the output of the prompt correlator to normalize the discriminator. d refers to the Early-Late spacing, as illustrated in Figure 2.25, the DLL principle is to look for the alignment in amplitude of the Early and Late correlators.

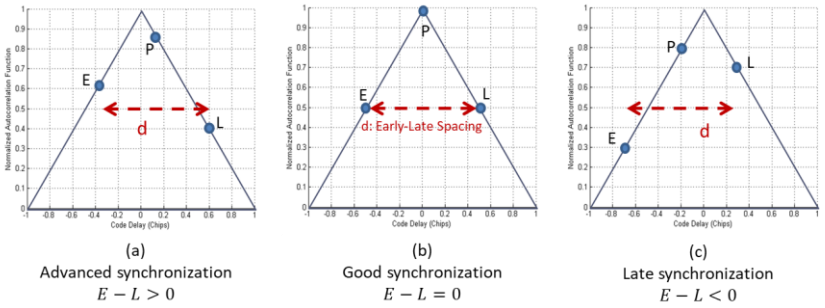

(a) Advanced synchronization $E - L > 0$ (b) Good synchronization $E - L = 0$ (c) Late synchronization $E - L < 0$

Figure 2.25 – DLL principle

The complete tracking process can thus be summarized as in Figure 2.26, more details can be found in [23].

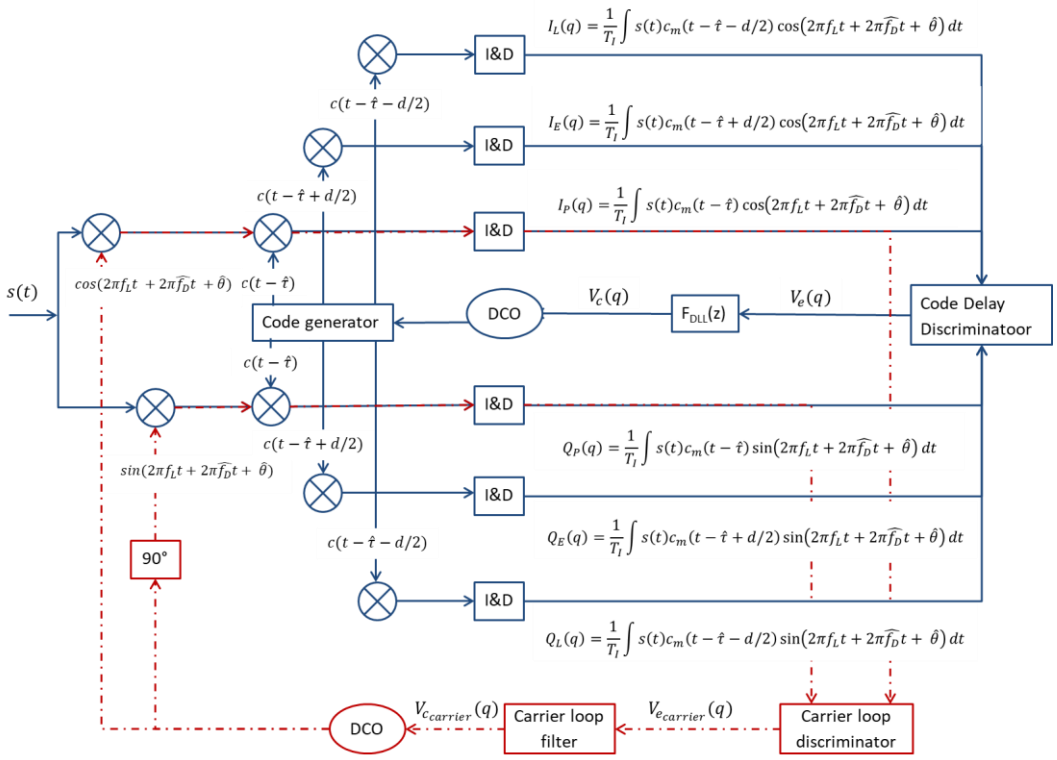

Figure 2.26 – GPS receiver – tracking loop

2.4.3. GPS L1 C/A data demodulation

The tracking loop process that has just being presented aimed at creating local replicas perfectly synchronized with the incoming signal that is to say: $\varepsilon_\theta \approx 0$, $\varepsilon_\tau \approx 0$, $\varepsilon_f \approx 0$. Hence, the correlator outputs provided in (2.14) can be simplified as given in (2.15).

$$\begin{cases} I(k) = \dfrac{A}{2}d(k) + n_I(k) \\ Q(k) = n_Q(k) \end{cases} \tag{2.15}$$

The last step is now to estimate the data, and as it can be seen from above, data can be estimated from the In-Phase correlator output. For that purpose, it is necessary to perform bit synchronization. Bit synchronization aims at determining the start of the navigation message data bits in order to observe the prompt correlation value over 20 ms and therefore, estimate the navigation message. GPS L1 C/A uses a BPSK data modulation; hence $d(k) \in \{-1,1\}$. Then the In-Phase correlator becomes:

$$I(k) = \begin{cases} \dfrac{A}{2} + n_I(k)\ if\ d(k) = 1 \\ -\dfrac{A}{2} + n_I(k)\ if\ d(k) = -1 \end{cases} \tag{2.16}$$

It is thus possible to determine the sign of the navigation message data bit. Basically, the bit synchronization algorithm is based on the detection of a change in the sign between two successive In-Phase prompt correlator outputs. A common way to achieve symbol synchronization is by means of histograms and counters, details in [23]. Once the bit synchronization is achieved, 20 ms long integration can be done, that will permit to reduce the power of the noise affecting correlator outputs. The receiver knows when the start of each bit of the navigation message is; it can then start the demodulation of the navigation message. For that purpose, it has to know when a sub-frame starts, i.e. it has to perform frame

synchronization. In GPS L1 C/A, all sub-frames begin using the same preamble. When the receiver has found this preamble, it begins reading and using the data.

2.5. Measurement model

The aim of the chapter is to precisely model the received signal in order to apply the optimal signal processing techniques which will permit to obtain the required measurements. The objective of this section is to present the pseudo range measurements models obtained and used after the signal processing step. Only the models are presented, the method to obtain the measurements by using the estimated values obtained from the tracking loops is not detailed here. Second, the metrics used to assess their quality is presented.

2.5.1. Pseudo range measurement

The receiver computes pseudo-range measurements of three kinds:

- The code pseudo-range measurement $P^i(k)$ for a satellite i at epoch k obtained as the time difference between the emission time and the reception time of the signal
- The carrier phase pseudo-range measurement which represents the phase of the local carrier associated to the Doppler term only. The phase measurement can also be referred to as integrated Doppler
- The Doppler pseudo-range measurement

The raw pseudo-range measurement models for the code, the phase and the Doppler can be modelled as given in (2.17).

$$\begin{cases} code\ [m] & P^i(k) = \rho^i(k) + c\left(\Delta t_u(k) - \Delta t^i(k)\right) + d_I^i(k) + d_T^i(k) + D_{mult}^i(k) + n_P^i(k) + b_P^i(k) \\ phase\ [m] & \varphi^i(k) = \rho^i(k) + c\left(\Delta t_u(k) - \Delta t^i(k)\right) - d_I^i(k) + d_T^i(k) \\ & \quad +\varphi_{mult,\varphi}^i(k) + N^i\lambda^i + n_\varphi^i(k) + b_\varphi^i(k) \\ Doppler[m] & D^i(k) = \lambda(\delta\rho^i(k) + c\left(\delta\Delta t_u(k) - \delta\Delta t^i(k)\right) - \delta d_I^i(k) + \delta d_T^i(k) + \delta D_{mult}^i(k) + n_D^i(k) \end{cases} \quad (2.17)$$

Where:

- $\rho^i = \sqrt{(x - x^i)^2 + (y - y^i)^2 + (z - z^i)^2}$ is the geometrical distance
  - (x, y, z) the user position to determine
  - (x^i, y^i, z^i) the known satellite position
- Δt_u and Δt^i are the user and satellite clock offset with regards to the system reference time respectively
- d_I^i and d_T^i are the ionospheric and tropospheric delay respectively
- $D_{mult}^i$and $\varphi_{mult,\varphi}^i$ are the multipath component affecting the code and phase measurements, respectively
- n_P^i, n_φ^i and n_D^i represent noise
- b_P^i and b_φ^i are RF code and phase bias respectively
- N^i is the ambiguity of the phase measurement
- δX indicates that for the Doppler measurement, the measures are actually time variations

Before PVT computation, these raw measurements are corrected by a prediction of the satellite clock offset, predictions of the ionospheric and tropospheric delays. All above errors are still there in the model of corrected pseudo-range measurements but less important. The models are presented in (2.18).

$$\begin{cases} code\ [m] & P^i(k) = \rho^i(k) + c\left(\Delta t_u(k) - \Delta t^i(k)\right) + \varepsilon_I^i(k) + \varepsilon_T^i(k) + \varepsilon_{mult}^i(k) + \varepsilon_P^i(k) + \varepsilon_P^i(k) \\ phase\ [m] & \varphi^i(k) = \rho^i(k) + c\left(\Delta t_u(k) - \Delta t^i(k)\right) - \varepsilon_I^i(k) + \varepsilon_T^i(k) \\ & \quad +\varepsilon_{mult,\varphi}^i(k) + N^i\lambda^i + \varepsilon_\varphi^i(k) + \varepsilon_\varphi^i(k) \\ Doppler[m] & D^i(k) = \lambda(\delta\rho^i(k) + c\left(\delta\Delta t_u(k) - \delta\Delta t^i(k)\right) - \delta\varepsilon_I^i(k) + \delta\varepsilon_T^i(k) + \dot{\delta}\varepsilon_{mult}^i(k) + \varepsilon_D^i(k) \end{cases} \quad (2.18)$$

Where ε_X referred to the residual errors.

2.5.2. Pseudo range quality – UERE

The UERE, presented in (2.19), is the sum of all equivalent residual errors affecting the corrected pseudo-range measurements used by the PVT algorithm. As presented above, these errors are the satellite clock bias error, the ionospheric and tropospheric delays, the multipath, the thermal noise and the equivalent range error due to satellite position error (which comes from the use of an estimated satellite position in the PVT computation).

$$\sigma_{UERE}^2{}^i = \sigma_{iono}^2{}^i + \sigma_{tropo}^2{}^i + \sigma_{multipath}^2{}^i + \sigma_{noise}^2{}^i + \sigma_{sat/eph}^2{}^i \quad (2.19)$$

The accuracy of the measurement depends on three main factors: the elevation of the satellites, the user antenna gain and the environment (multipath, obstruction, etc.).

2.6. GNSS positioning

The final objective of a GNSS system is to allow to a user to calculate its precise and accurate positioning solution. The first section aims to explain how the measurements previously descried can be used to provide the PVT solution to the user. Moreover, this Ph.D. thesis is dedicated to urban positioning, therefore the second part focuses on the problematics related to this kind of environment.

2.6.1. GNSS positioning principles

The basic principle of GNSS is based on the trilateration principle. If the user is able to determine its distance with respect to three emitters then it is located at the intersection of the three spheres, each centred at the emitter location and with a radius equal to the distance receiver-emitter. To determine the distance emitter-receiver, the receiver measures the transition time from the transmitter to the receiver and multiplies it by the speed of light. It implies that the receiver and the transmitter are perfectly time-synchronized.

However, as inferred in the previous section, for a GNSS system, the synchronization's condition is not fulfilled. Therefore, it is of the utmost importance to express the satellites and users time measurement models in the same GNSS reference time. The clock shift between the satellites and the GNSS time is corrected thanks to the ephemerides, thus only the bias between the receiver and the GNSS time remains. The corrected measured signal propagation delay is thus systematically biased by an unknown clock offset. For that purpose, in GNSS it is not question of range measurements but rather pseudo-range measurements.

To compute the PVT, 4 parameters have thus to be estimate: $[x, y, z, \Delta t_u]$, where Δt_u is the user clock offset with regards to a reference time. Hence at least 4 pseudo-ranges measurements are needed. The principle of the PVT computation (dropping the estimation of the velocity for simplification reason) is to search for $[\hat{x}, \hat{y}, \hat{z}, \widehat{\Delta t_u}]$ so that the prediction error of the measurement vector is minimal; typically, least squares methods or Kalman filtering are used, the latter is further described in Chapter 7.

2.6.2. Expected accuracy of GNSS positioning

There are two factors impacting the accuracy of GNSS positioning: the measurement quality, assessed by the UERE, and the satellite geometry relative to the user, assessed by the DOP. The UERE has been briefly mentioned in 2.5.2.

The satellite geometry is quantified by the DOP value. If the satellites are well distributed, the DOP is low, the positioning more precise. On the contrary, a high DOP means bad satellites geometry and a less precise positioning. It is possible to visualise this in 2D in Figure 2.27. In the situation (a), the satellites are not well distributed; hence, since their position is not perfectly known, the receiver position uncertainty region (area in red) is bigger than the one in situation (b) where the geometry is better.

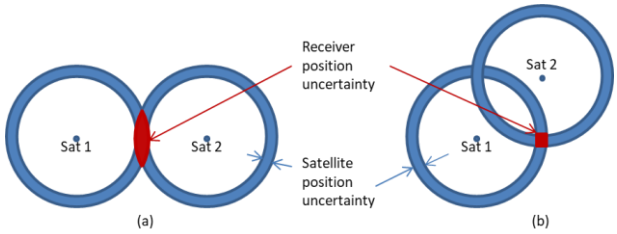

Figure 2.27 – Satellite geometry

There are several DOP values:

- The GDOP used to quantify the 4D standard deviation of the error
- The PDOP (Position DOP) used to quantify the 3D position standard deviation of the error
- The HDOP (Horizontal DOP) used to quantify the horizontal position standard deviation of the error
- The VDOP (Vertical DOP) used to quantify the vertical position standard deviation of the error
- The TDOP (Time DOP) used to quantify the receiver time standard deviation of the error

Since the visible satellites are all above the user, the VDOP is generally better than the HDOP, leading to a worse accuracy in the vertical direction than in the horizontal plane.

2.6.3. Urban environment challenges

According to the previously presented sections, in order to provide an accurate positioning solution to the user, the receiver must have at least four pseudo range measurements. Since the accuracy of the positioning solution is linked to the quality of the measurements, 2 cases can be easily identified: an open sky environment and a non-open sky environment, the latter can be for example urban, sub-urban or indoor environment. The open sky environment is usually modelled as an AWGN case, satellites are visible and much less subject to link disturbances (blocking/shadowing) caused by buildings for example; in this environment, there are usually no difficulties to obtain an accurate positioning solution. The situation in urban environment is completely different and presents a challenge from the positioning process point of view.

A further inspection of the signal link disturbances encountered in an urban environment is commented next since this environment is the main target of this Ph.D. work. Figure 2.28 presents a graphical summary. Several situations can be considered:

- The signal is received in line of sight (LOS) (blue in the illustration)

- The signal received is a reflected one (red and cyan in the illustration): a multipath (associated to a received LOS – red) or a NLOS (the direct path is not received – cyan)
- The signal is obstructed by buildings (violet in the illustration)

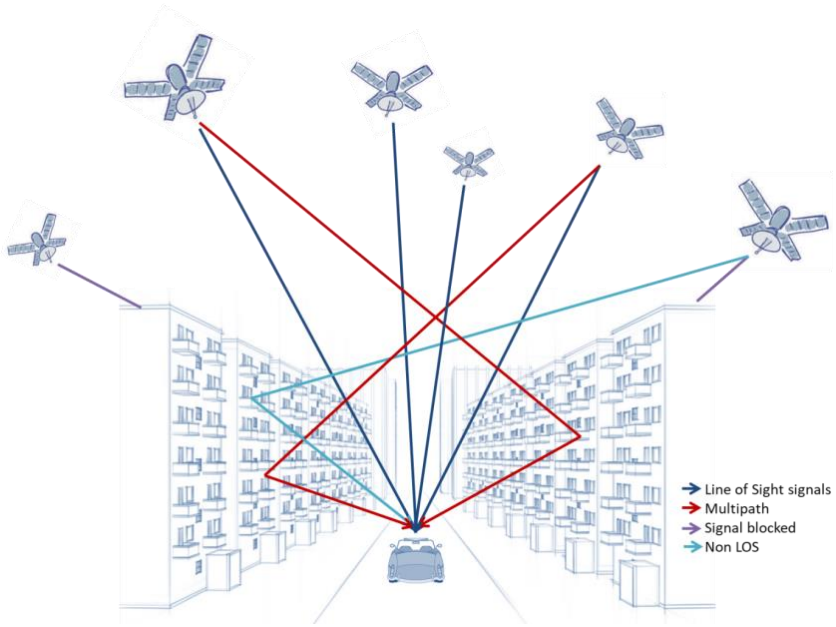

Figure 2.28 – Urban positioning challenges

Ideally, the receiver needs 4 LOS signals to provide a position, however this situation is rarely fulfilled in urban canyons. Due to the presence of high buildings and of narrow streets, a high quantity of satellite signals is usually obstructed. This impacts the geometry of satellites viewed by the receiver, since most of satellite signals coming from “across the street” are blocked, leaving only those “along the street” (the situation becomes close to the (a) on Figure 2.27). Moreover, the receiver can receive a high quantity of multipath and NLOS signals, which degrade the UERE.

As multipath and NLOS signals are the worst interference in the urban case, it is of interest to understand the impact of those interferences. The next sub sections aim thus to define these interferences and to describe their impact on the signal processing blocks.

2.6.3.1. Multipath

A multipath is a reflected or diffracted replica of the desired signal; since the path travelled by a multipath is longer than the direct path, it is always received after the direct path. If the multipath delay is very large (as presented in the left part of Figure 2.29) then the multipath can be easily removed. Indeed, the correlation function between the received signal (direct path and multipath) and the local replica will leave the main peak (corresponding to the direct path) “clean”, not distorted. However, if the delay is short, the multipath will distort this correlation function (right part on the Figure 2.29); and therefore will make it harder to perform an efficient DLL or, in other words, to track the actual delay of the LOS path. Indeed, as a reminder, a DLL is based on two delayed correlators; the objective of the DLL loop is to equalize the power of the Early and Late correlators. As illustrated on Figure 2.29 (b), with a distorted correlation function, the LOS propagation delay estimation will not be correct.

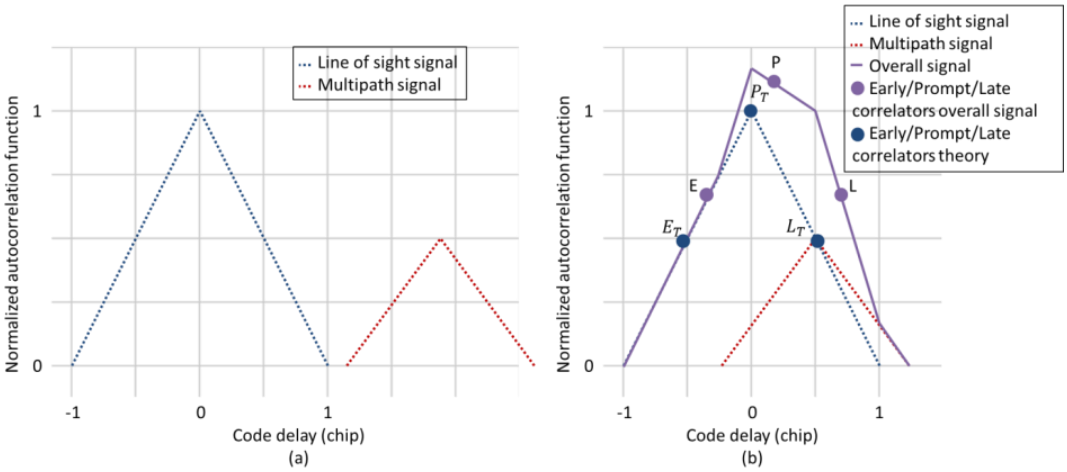

Figure 2.29 – Multipath impact on the correlation function for GPS L1 C/A

Hence, the impact of multipath depends on the delay with respect to the direct path but also on its power and carrier phase with respect to the direct path; the higher the power, the worst the impact.

2.6.3.2. NLOS

Non-Line-of-Sight tracking is said to occur when the receiver tracks a NLOS signal while the LOS signal is very attenuated or blocked. This phenomenon results in a measurement that can be very erroneous as the tracking error will be a function of the extra distance travelled by the tracked NLOS with respect to the distance travelled LOS. This erroneous tracking situation is very common in urban environment.

Nevertheless, note that tracking a NLOS signal is not always a bad situation if the tracking error is low (meter level). More accurately, if the tracking error is low, to conserve the measurement will permit to increase the number of measurement and therefore to potentially improve the PVT solution. The problem is however very serious if the bias is large.

2.6.3.3. Methods to improve GNSS positioning

Several methods exist to improve positioning in urban environment. First of all, using multi-constellation and/or multi-frequency measurements help by providing more GNSS signals.

Second, to hybridize the GNSS solution with other sensors such as inertial sensors for example is a typical solution. It is also common to hybridize the GNSS solution with other signals called Signal of Opportunity (SoO); it can be telecommunication signals such as 4G LTE, 5G or Wi-fi signals, etc. This is the solution explored in this Ph.D. thesis.

Finally, multipath mitigation techniques are also an important research theme. There are mostly 4 types of multipath mitigation techniques: the location of the antenna, the choice of the antenna (isolation with respect to multipath), signal processing techniques and data processing techniques.

2.7. Chapter conclusion

The aim of the chapter is to provide a global overview of GNSS systems and to present the signal processing techniques adopted in the receiver in order to obtain the required measurements. In order to determine the most optimal signal processing techniques it is of the utmost importance to precisely know the mathematical model of the transmitted signal. The generated signal goes through the propagation channel which should also be carefully modelled in order to have a realistic mathematical model of the

received signal. The aim of the receiver is then to process the received signal and to extract several information such as the ephemeris or pseudo range measurements. Finally, the joint exploitation of the pseudo range measurements and the ephemeris, etc., allow the receiver to calculate its PVT solution.

To achieve this objective, in the first section, the definition of the GNSS systems has been provided. As presented, there is a wide variety of GNSS systems; nevertheless, since the Ph.D. emphasis on 2 particular signals: GPS L1 C/A and Galileo E1 OS, only these two systems are presented. The second section focused only on the description of these 2 signals. Before being processed by the user, the transmitted signal is disturbed by several sorts of interferences. These interferences, described in section 3, have to be modelled in order to analyse the received signals, thus a propagation channel model must be defined; for the purpose of the thesis, the SCHUN propagation channel has been selected. SCHUN is a hybrid deterministic-statistical LMS propagation channel; the implementation of the statistical and deterministic modules optimizes the trade-off between accuracy and computational resource. The signal is then processed by the receiver, which has been presented in the fourth section. The main 3 signal processing functions of the receiver are based on the correlation operation: the acquisition, the tracking and the demodulation. The correlation aims to locally generate a replica perfectly synchronized with the incoming signal.

Finally, the receiver provides pseudo range measurements which have been presented in section 5. These measurements are used to allow the user to calculate its PVT solution. In the last section, it has been highlighted that a special care must be taken for a non-open sky environment since the conditions, with respect to an open sky, can be highly degraded.

Chapter 3. 5G systems

Over the past few years, the need for positioning, and thus the number of positioning services in general, has been in constant growth. This need for positioning has been increasingly focused on constrained environments, such as urban or indoor environments, where GNSS is known to have significant limitations: multipath as well as the lack of LOS satellite visibility degrades the GNSS positioning solution and makes it unsuitable for some urban or indoor applications. These problematics have been presented in chapter 2. In order to improve the GNSS positioning performance in constrained environments, many solutions are already available: hybridization with additional sensors, [1], [2] or the use of signals of opportunity (SoO) for example, [3], [4], [5], [6]. [7], [8]. Concerning SoO, mobile communication signals, such as 4G Long Term Evolution (LTE) or 5G, are naturally envisioned for positioning, [3], [9], [10], [24]. In order to mitigate the issues linked to an urban environment, the thesis focuses on 5G signals.

The aim of the chapter is to provide a global overview of 5G systems and to present the signal processing adopted in the receiver in order to obtain the required measurements assuming an AWGN channel. In order to determine the most optimal signal processing techniques, it is of the utmost importance to precisely know the mathematical model of the transmitted signal. The generated signal goes through the propagation channel which should also be carefully modelled in order to have a realistic mathematical model of the received signal. The aim of the designed signal processing block of the receiver is to extract Time Of Arrival (TOA) measurements from the received signal.

First, the interest in developing a new radio system is presented. Second, a general overview of the 5G system architecture is given. The third section focuses on the physical layer of the system; it allows to clearly define the signal transmitted by the Base Station. Before being received by the user, the signal goes through the propagation channel, the fourth section presents the propagation channel considered in the Ph.D. The distorted signal is then processed by the receiver, presented in the fifth section. The receiver aims at providing the pseudo range measurement (presented in section six) which are used to determine a positioning solution.

3.1. 5G systems objectives

In this section, the interest in developing a new radio system is presented. The first sub-section gives several definitions required for the rest of the chapter. Second, the current state (as of Q2 2020) of the telecommunication network is presented. Finally, the 5G requirements are presented.

3.1.1. Some definitions

All along this report, expression such as Base Station (BS), User Equipment (UE), etc. are used. This first section aims at defining those expressions.

Cellular network: A cellular network consists of a set of base stations (BS) and a set of user equipment (UE). Each UE is connected to one BS, which provides services to it.

Base Station (BS): A base station is defined as a fixed communication location and is part of a network's wireless telephone system. It relays information to and from a transmitting/receiving unit, such as a mobile phone. Often referred to as a cell site, a base station allows mobile phones to work within a local area, as long as it is linked to a mobile or wireless service provider.

User Equipment (UE): User equipment is defined as any device used directly by an end-user to communicate. It can be a hand-held telephone, a laptop computer with a mobile broadband, or any other device.

Downlink (DL): Downlink is defined as the ensemble of signals sent from the BS to their respective UE

Uplink (UL): Uplink is defined as the ensemble of the signals sent from the UE to the respective BS

3.1.2. 5G system status

For the record, a brief network history is given (first part), then the needs to evolve from 4G to 5G are highlighted (second part) and finally, the current state of the development of the 5G is given (third part).

3.1.2.1. Network history

Wireless communications have evolved very fast during the years and have become more performant with every subsequent evolution. In 1970, the first wireless communication system appeared, the 1G, which achieved basic analogue communications (voice). Then, there was the Global System for Mobile (GSM) communications (also called 2G), which introduced digital communication and internet services. The third generation (3G), optimized mobile for data enabling mobile broadband services, gave faster and better connectivity at lower cost to the users. About ten years ago, the 4G Long Term Evolution (LTE) – and, more recently, its evolution the LTE-Advanced – which delivers more capacity for faster and better mobile broadband experiences, was designed. And now, the fifth generation is developed, a new radio system willing to be even more performant than the current 4G LTE (-A); it is not yet deployed.

3.1.2.2. The needs for 5G

The driven idea behind 5G systems is to provide communication services for a large panel of applications; this means that there are economic (new applications/market) and technical (traffic growth demand) needs for the design of the 5G. Some identified needs are presented next and illustrated in Figure 3.1 and [25].

Figure 3.1 – The needs for 5G – source [25]

The mobile data traffic is rising exponentially mostly due to video streaming. In addition, users are more and more connected, with several connected devices most of the time. Due to these two aspects, a growing number of mobiles and increased data traffic, mobiles and networks need to increase the energy efficiency. Moreover, in addition to the traditional mobile communications, 5G enables the development of new use cases and new applications for the industry (automation, automated driving, etc.). Therefore, new categories of users and markets are interested in using 5G.

However, these new use cases and applications are also generating new challenges such as an increase of the traffic demand, big data management issues, energy management, etc.

3.1.2.3. 5G status

The standardization of the 5G systems is conducted in the Third Generation Partnership Project (3GPP). This project has started in 2016 with the ambition of making 5G systems commercially available around 2020 and widely adopted by 2025. The first release dealing with 5G systems is the Release 15. As show in Figure 3.2, this release has been frozen since June 2018. As the Release 15 work has matured and drawn close to completion, the group's focus is now shifting on to the first stage of Release 16.

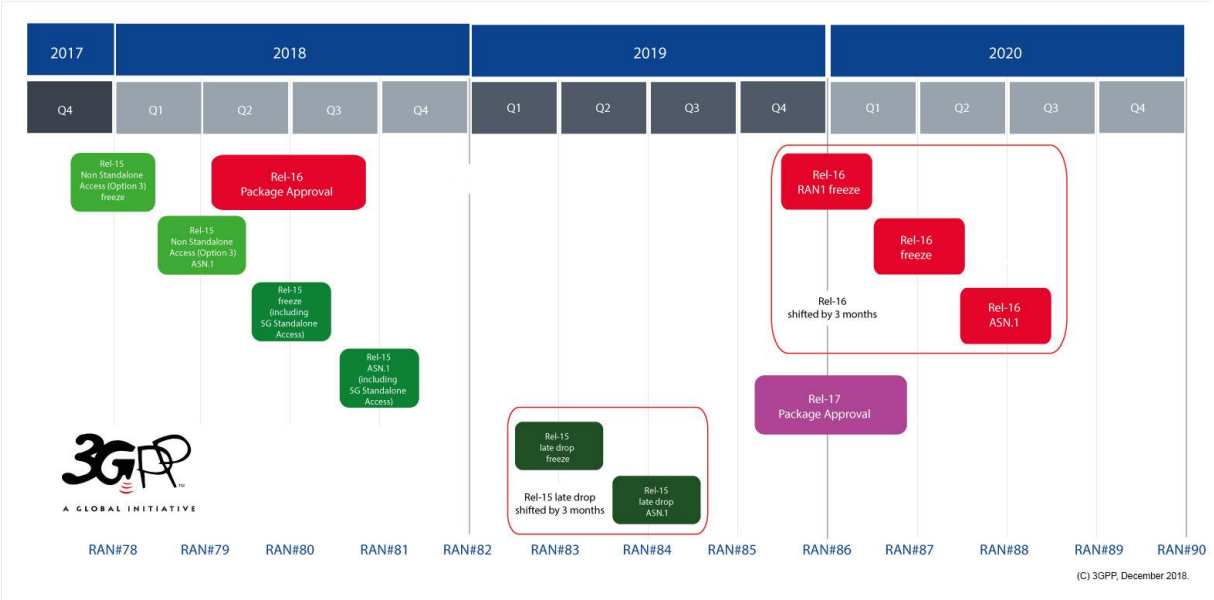

Figure 3.2 – 3GPP timeline for Release 15 – source [11]

Regarding the frequency bands that will be used for 5G systems, the International Telecommunications Union (ITU) has made recommendations during the World Radio communication Conference 2019 (WRC-19), [26]. In total, 17.25 GHz of spectrum has been identified for International Mobile Telecommunication (IMT) by the Conference, in comparison with 1.9 GHz of bandwidth available before WRC-19. Out of this number, 14.75 GHz of spectrum has been harmonized worldwide, reaching 85% of global harmonization. From a general point of view, three ranges have been widely identified:

- Sub-1GHz: to support widespread coverage across urban, suburban and rural areas and help support IoT
- 1-6GHz: which offers a good mixture of coverage and capacity benefits
- Above 6GHz: to meet ultra-high broadband speeds envisioned for 5G in a limited coverage

From the 3GPP point of view, in TS 38.101 ([27] and [28]), two frequency ranges are identified and, on each one, expected transmitter and receiver characteristics are defined:

- FR1: 410 MHz – 7125 MHz
- FR2: 24250 MHz – 52600 MHz

Those operating ranges are themselves split into smaller bands, [14].

3.1.3. 5G requirements

5G systems must meet the requirements of a highly mobile and fully connected society. Indeed, the number of connected devices is growing exponentially, as well as the traffic demand, and the wide range of related applications.

The ITU identified in September 2015 three scenarios to describe those requirements; they are summarized in Figure 3.3 (see [29]):

1. enhanced Mobile BroadBand (eMBB). The future 5G systems will require massive system capacity to meet the predicted future traffic growth. Densification with more network nodes, the use of more spectrum, and spectral efficiency enhancements are needed. The eMBB category focuses on services that have high requirements for bandwidth, such as high definition videos, virtual reality, and augmented reality.
2. massive Machine Type Communication (mMTC). The future 5G systems will address applications with a very large number of sensors, actuators, and similar devices typically associated with little traffic as well as requirements on low devices cost and very long battery life. Together with network enhancements, such as improved coverage and signalling reductions, they enable the vision of a networked society with billions of connected things. This use case family is also known as Massive IoT. Monitoring and automation of buildings and infrastructure, smart agriculture, logistics, tracking and fleet management are examples belonging to this service category.
3. Ultra-Reliable and Low Latency Communication (URLLC). Considering URLLC implies fulfilling very tough requirements on reliability, availability, and latency in order to offer connectivity that is always available. Application examples include health applications, traffic safety and control, control of critical infrastructures, connectivity for industrial processes but also assisted and automated driving.

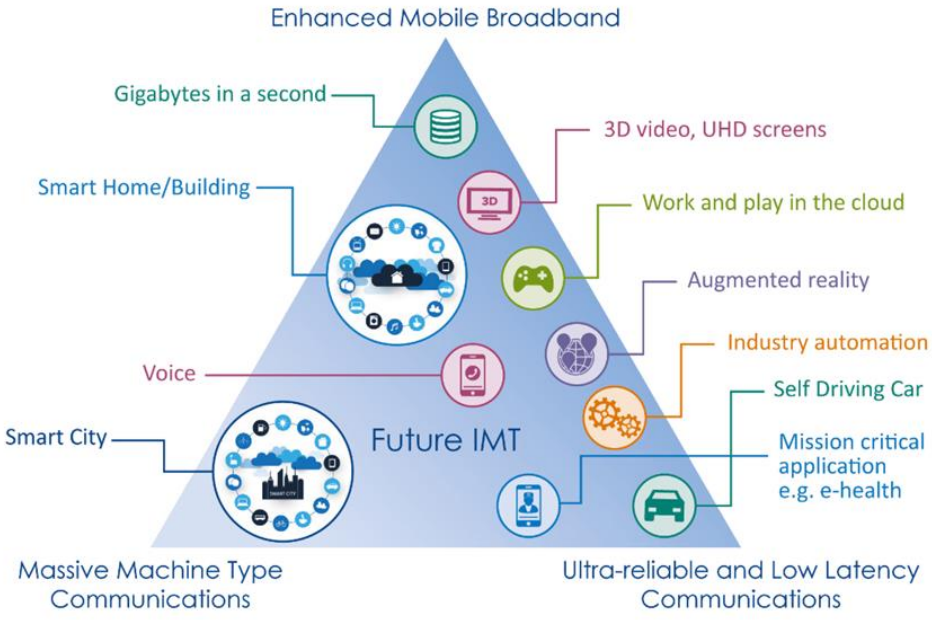

Figure 3.3 – 5G requirements – source [29]

Quite naturally, there are applications that do not fit in a unique use case family. Think of cars applications that require connecting a large number of sensors that have to be monitored in a reliable way; hence, that fit in mMTC as well as the URLLC use case families.

3.2. 5G system general architecture

This section provides a general presentation of the innovative technologies used for 5G system and their benefits for 5G positioning.

3.2.1. Innovative technologies

To meet all 5G requirements, new technologies have to be designed. Three technical directions for 5G are identified: the spectrum efficiency, the spectrum extension and the network density. The spectrum efficiency refers to the information rate that can be transmitted over a given bandwidth in a specific communication system. The spectrum extension refers to the exploration of new wavelength, new spectrum (frequency higher than 20 GHz for example). The network density refers to the number of BS for a given area. Two technologies appeared to fulfil these expectations: millimetre-waves frequencies and massive Multiple-Input-Multiple-Output systems.

As illustrate in Figure 3.4, to address 5G requirements, there is three technical key approaches to increase system capacity:

- Use ultra-dense network (UDN): a denser network can further boost the network capacity
- Large quantities of new bandwidth: higher frequencies will release a large amount of bandwidth available to support higher throughput transmission → mmW
- High spectrum efficiency: mMIMO can significantly improve the spectrum efficiency by extensively harnessing the available space resources

First, millimetres waves are presented, then principle of massive MIMO are explained. Finally, the interest to use both mmW and mMIMO for 5G systems is given.

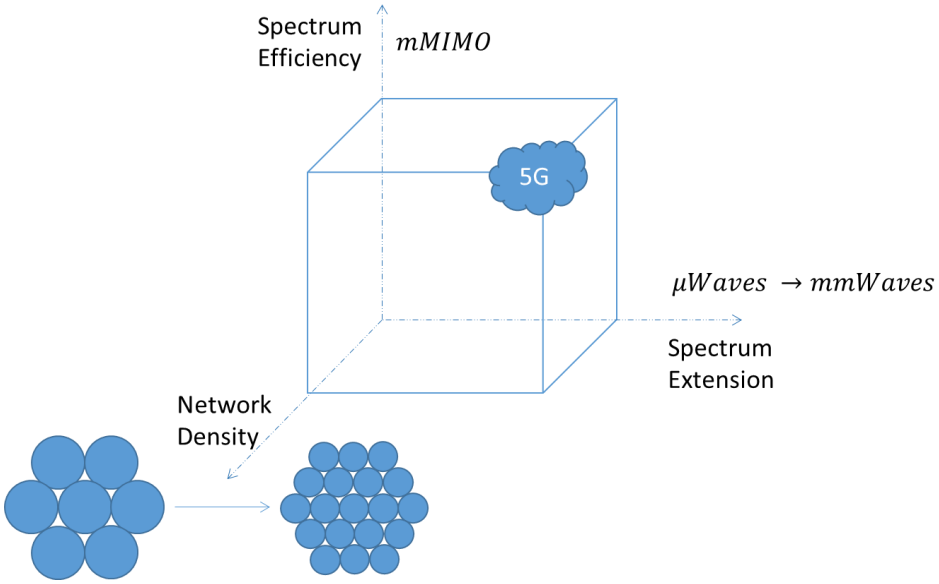

Figure 3.4 – Technical directions to meet 5G requirements

3.2.1.1. *Millimeter waves (mmW)*

Regarding the current state of the electromagnetic spectrum, it can be seen that the spectra below 3 GHz is packed and the cost per Hertz of bandwidth is huge. Moreover, in nowadays cellular systems, bandwidth (and rate) is lacking. With those considerations, 5G communication networks will likely adopt millimetre wave's technology. Indeed, the millimetre wave's spectrum is rather unused, and thus, larger bandwidths are available. Millimetre-wave frequencies often refer to the frequency range from 30 GHz to 300 GHz, the corresponding wavelength is between 10 mm to 1 mm ($\lambda = \frac{c}{f}, where\ c\ is\ the\ celerity$).

3.2.1.1.1. Advantages

There are several advantages of using mmW for 5G systems. First of all, the radio spectrum at mmW frequencies is still rather unused, as shown in Figure 3.5; more bandwidth is available at these frequencies than at microwave frequencies. Second, the physical size of antennas at mmW frequencies becomes small; therefore, it is possible to use large antennas arrays. Third, as very wide bandwidth is available, high data rates can be reached (as the capacity of a link is function of the bandwidth and the Signal to Noise Ratio (SNR)). Finally, due to the propagation characteristics of mmW, i.e. limited scattering because a few clusters exist, the channel is sparse; hence efficient channel equalization techniques exist.

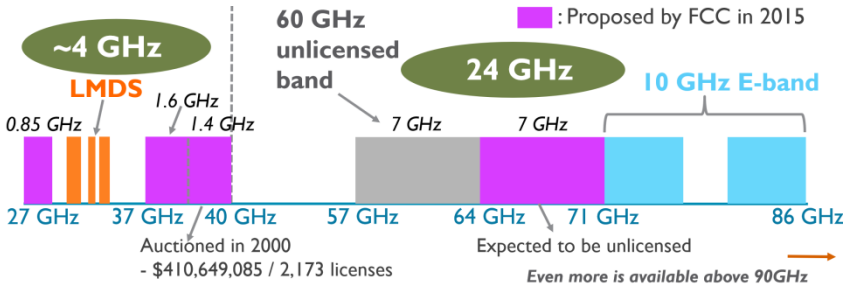

Figure 3.5 – Electromagnetic Spectrum: millimetre waves – source [30]

3.2.1.1.2. Drawbacks

There are also several drawbacks of using mmW for 5G systems. The main drawback for the use of mmW frequencies concerns their propagation characteristics. A comparison between mmW and sub-6 GHz propagations is given in Figure 3.6 in order to understand the differences between both. Basically, blockage is a major impairment at mmW. To sum up, at lower frequency there are better propagation conditions and so the range is higher, but there is not much bandwidth. At mmW, there is large available bandwidth, but the propagation conditions are not very good, and so is the range.

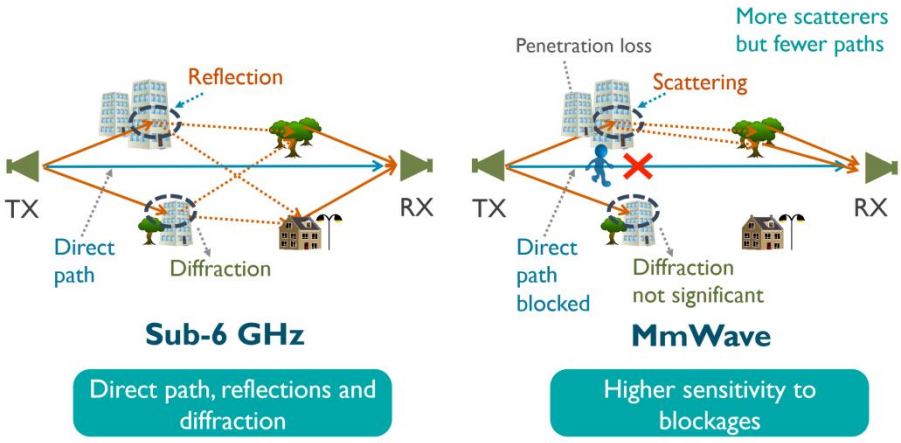

Figure 3.6 – Propagation characteristics of mmW – source [30]

The second important drawback is related to the actual implementation of mmW for 5G communications since with mmW, as large bandwidth will be used, the hardware will thus potentially consume a lot of power and have a huge complexity. Using mmW frequency means that the received power at the transmitter side is lower than with classical wavelength (free space losses formula). This translates into a network of emitters with a higher density, and cost (both for capital and operational expenditures) for the mobile operator.

3.2.1.2. Massive Multiple Input Multiple Output

In Massive MIMO, each BS is equipped with a large number of antennas, M, and serves a cell with a large number of terminals, K, see Figure 3.7. Different BSs serve different cells, and except for power control and pilot assignment, there is no cooperation between BS. On UL, the BS has to recover the individual signals transmitted by each terminal. On the DL, the BS has to ensure that each terminal receives only the signal intended for it (to mitigate interference). The BS's multiplexing and de-multiplexing signal processing is made possible by utilizing a large number of antennas and by its possession of Channel State Information (CSI).

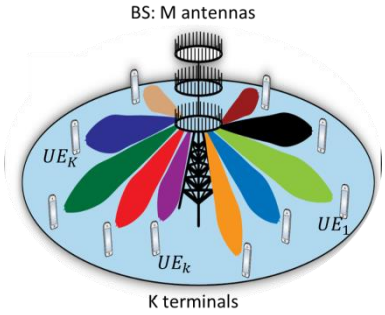

Figure 3.7 – massive MIMO model

Massive MIMO is often linked to the beamforming concept; beamforming is the ability to adapt the radiation pattern of the antenna array to a particular scenario. This is illustrated in Figure 3.7, where the BS generates beams steering at each user. In analogue beam-forming, the transmission is done in one direction a time. In digital beam-forming, it is possible to transmit in different sub-bands in different directions at the same time; it is possible to receive in all directions at the same time (see Figure 3.8). Hence regarding the scenario envisioned for 5G, that is serves multiple users simultaneously, the digital beam forming has to be applied, [31].

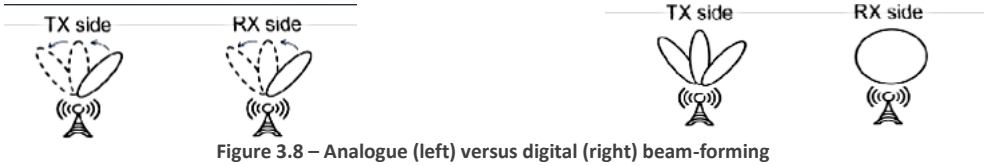

Figure 3.8 – Analogue (left) versus digital (right) beam-forming

3.2.1.2.1. Advantages

mMIMO is seen as a promising key technology for 5G, several advantages can be noted. First, by using more antennas and denser cells (thus more power), mMIMO provides highly improved cell edge coverage, hence it can provide uniformly good service to everyone in the cell. Second, mMIMO provides high multiplexing gain by improving considerably the spectrum efficiency as well as the energy efficiency and the channel quality with simple linear processing such as maximum-ratio transmission or zero-forcing. mMIMO improve the spectral efficiency by simultaneously serving many user terminals in the cell, over the same bandwidth, by means of space division multiple access, see [32] and [33]. Third, mMIMO

functions equally well in rich scattering environment as in line-of-sight. Finally, an additional consequence of using large numbers of antennas is that the required signal processing and resource allocation simplifies, owing to a phenomenon known as channel hardening. Basically, the significance of channel hardening is that small scales fading effects and frequency dependence disappear when M is large.

3.2.1.2.2. Drawbacks

However, mMIMO faces some challenges. First, pilot contamination exists because of the practical necessity to reuse the time frequency resources across cells. Second, preferably, Massive MIMO operates in TDD and exploits uplink/downlink reciprocity. However, 5G is also intended to use FDD; therefore mMIMO will have to operate in FDD too, see [34] for more details. Third, power control is extremely important in mMIMO to reduce the near far effect. Finally, the design of mMIMO systems has to be well optimized in order to reduce the power consumption of Radio Frequency (RF) chains.

3.2.2. Interest of 5G for positioning

In this section, the objective is to identify potential methods that can be used in positioning and to select the one later used for the Ph.D. In a first part, the basics of radio-based positioning are reminded as well as the current positioning solution. In a second part, the selected method for the Ph.D. upon the methods derived in the first section is presented. Third, the currently led studies among the scientific community are mentioned.

3.2.2.1. Radio-based positioning

First, the basics of radio-based positioning are presented; then, the current positioning solutions are presented. The basic idea of radio-based positioning is to use the fact that waveforms convey information. This information can be related to signal strength, time or angle.

3.2.2.1.1. Signal Strength based measurements

The basic methodology for the signal strength based measurement is to estimate the propagation loss thanks to the path loss models (link budget); then, from the measured signal strength, it is possible to determine a distance. However this method has an uncertainty of several meters. The usual method to exploit signal strength measurement is through fingerprinting. The idea is to compare the signal strength measured with respect to many RF emitters with a pre-existing data base of geo-located signal strength measurements. Based on these set of measurements it is possible to locate the receiver by triangulation.

3.2.2.1.2. Time-based measurements

The most famous time-based positioning system is the GNSS. The idea of such measurements is quite simple. The transmitter transmits the signal at a certain time $s(t)$ and the receiver receives it at $s(t+\tau)$ where τ is dependent on the distance and the speed of light. By estimating the time of arrival (ToA), it is possible to determine distance up to a clock bias, due to the fact that the receiver and the transmitter may not be perfectly synchronized. While the transmitter clock bias may be controlled and corrected (thanks to a synchronization process of the emitter networks, or thanks to corrections provided by a monitoring segment), the receiver clock bias remains unknown and is generally estimated along with the position. The receiver then requires at least 4 ToA measurements to compute its 3D position and clock bias. A derived technique based on the use of Time Difference of Arrival (TDoA), consisting of differentiating 2 ToA measurements, allows to avoid estimating the receiver clock bias, but still requires the transmitters clock biases to be known and the same number of ToA measurements.

One challenge with this kind of measurement is the obstacles. If there is an obstacle in the Line of Sight (LoS) path, two cases are possible: either the signal passes through it (in that case, it will be delayed) or the LoS signal is completely blocked (then the first received signal is a reflected one). In both cases, huge biases can be obtained in the distance estimates.

3.2.2.1.3. Angle-base measurements

In Figure 3.9 (left and middle), the UE is supposed to have one antenna and the BS has multiple antennas. Basically, the received waveform at the antenna (left picture) depends on the transmitted waveform ($s(t)$), the time difference (τ) and also the response at the receiver side ($a(\theta)$). After some processing it is possible to determine the Angle of Arrival (AoA). Similarly, middle picture, it is possible to determine the Angle of Departure (AoD). With those measurements, it is necessary to use multiples antennas and the antenna orientation must be known. After obtaining the angle of arrival, and by using the transmission time, τ, the position of the mobile device is determined as the intersection of multiple bearings, a highly simplified illustration is proposed in Figure 3.9 right part.

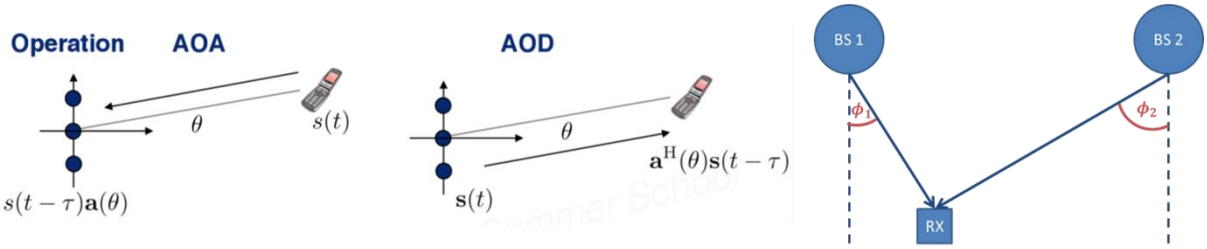

Figure 3.9 – AoA and AoD principles

3.2.2.2. Selected solution

With regards to the three methods presented in section 32.2.1., choices have to be made. The radio-based positioning method based on signal strength measurements will not be used for the Ph.D. The uncertainty linked to the method is of several meters, much higher than the expectancy of the Ph.D. Moreover, it also requires pre-existing data base of geo-located strength measurements which is not available yet for 5G.

The AoA radio-based positioning also required a lot of hypothesis regarding the antenna. At the time to decide which method will be used for the rest of the Ph.D., the standard at the 3GPP regarding the emitted antenna was still at the beginning. Several studies was led around the community regarding the MIMO antenna but insufficient for the Ph.D. The design of the received antenna was even less available. Moreover, the algorithms complexity to process AoA measurements is much higher than for ToA measurements. Consequently, the rest of the Ph.D. will focus of radio-based positioning using ToA measurements

3.2.2.3. State-of-the-Art: 5G positioning solutions

An overview of the projects led over the scientific community regarding 5G positioning have been performed. Some of them are presented in the section.

3.2.2.3.1. Cascaded Extended Kalman Filter

In [35], the authors seek to develop appropriate frame and reference signal structures to support high-efficiency positioning, as well as signal processing solutions to obtained accurate Direction of Arrival (DoA) and ToA.

Hereafter, the main positioning solution they are working on is explained; see [36], [37], [38] for details. Their method is based on Extended Kalman Filter (EKF), due to its highly accurate estimation performance and its low computational complexity compared to the Particle Filter (PF) and the Unscented Kalman Filter (UKF). It also has to be noted that it is based on a network centric approach, in order to save energy.

The scenario considered is shown in Figure 3.10. The UE, which have one or multiple antennas, is moving in an Ultra Dense Network area. Periodically, it sends pilot signals/sequences to the BSs around it. Those BS have antenna arrays and, their position is assumed to be known. The bandwidth used is centred around 3.5 GHz.

The method's idea is to estimate both UE position and UE clock offset (by-product) in a network centric manner using a cascaded EKF. The general steps are:

1. The UE sends periodically UL pilots (the nature of this pilots is not defined)
2. The BSs receiving UL pilot determine if they are in LoS conditions or not. For that, the Rice factor, which is a power ratio between LoS component and all other propagation paths, is estimated; by using, for example, a Particle Filter (PF).
3. Each BS in LoS conditions estimates the DoA and ToA and sends them to a central unit; this is the first step of the cascaded EKF.
4. The DoA and ToA measurements obtained from the first part of the cascaded EKF are fused into UE's location estimates as well as clock offset and skews of both UE's location and BS in the second part of the cascaded EKF.

Those steps are summarized on Figure 3.11, more details can be found in [37]. It has to be noted that they have define 2 main cases. In the first one, BS are supposed synchronized, UE unsynchronized ("Pos&Clock" in Figure 3.11). In the second one, both BS and UE are supposed unsynchronized ("Pos&Sync" in Figure 3.11).

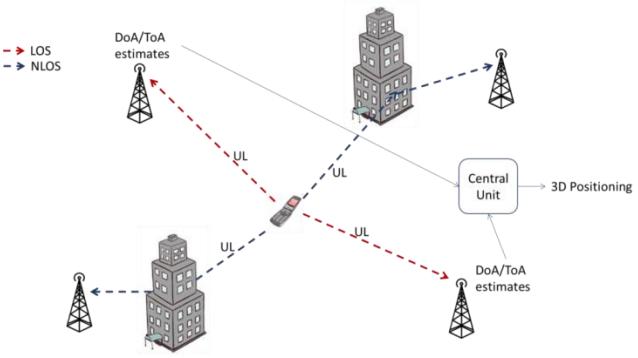

Figure 3.10 – Scenario description for 5G positioning – source [37]

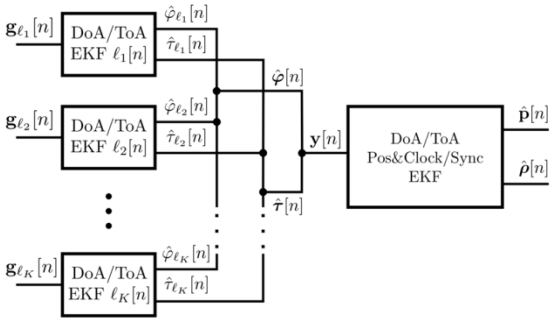

Figure 3.11 – Cascaded EKFs for joint UE positioning and network clock synchronization – source [37]

3.2.2.3.2. Cascaded Unscented Kalman Filter

In [39], an UKF cascaded solution for joint DoA and ToA estimation, and simultaneously 3D device positioning and network synchronisation in future 5G UBNs is proposed. The principle is the same as the one presented in section 5.3.1.1:

1. In a first phase, a UKF estimates DoAs and ToAs at each BS in LoS condition
2. Then, the obtained estimates are fused within the joint 3D device positioning and network synchronization UKF

As the previous one, this method provides 3D position estimates for a UE but also clock offset estimates for the UE and BSs in LoS conditions. In this study, performances obtained by the cascaded EKF and by the cascaded UKF are compared. With both methods, the sub 1 meter accuracy is fulfilled; however, the cascaded EKF slightly outperforms the cascaded UKF.

3.3. 5G system: physical layer description

The description of the 5G system and architecture in the previous sections permits to identify the layer where the 5G signals is defined and designed. Thus this section focuses on the description, step by step, of the physical layer.

3.3.1. Modulation schemes

The 4G-LTE supports different data modulation formats: QPSK, 16 QAM, 64 QAM and 256 QAM. It is envisioned that 5G will support all these modulations in both UL and DL, plus in the UL the π/2-BPSK modulation. The definition of each modulation is given in [40].

3.3.2. Waveform

The waveform envisioned for 5G system is based on an Orthogonal Frequency Division Multiplexing (OFDM) modulation with a scalable numerology (subcarrier spacing and cycle prefix). For the UL, Discrete Fourier Transform-spread-OFDM (DFT-s-OFDM) with a cycle prefix is also supported. The section is organised as follow; first, the OFDM are presented, then the envisioned numerology.

3.3.2.1. OFDM modulation

3.3.2.1.1. General overview

The OFDM modulation is a telecommunication multicarrier modulation technique; it consists in transmitting in parallel N complex data symbols over N orthogonal narrowband subcarriers. More specifically, in OFDM, each sub-carrier transmits a low rate data signal modulation (in comparison to the complete OFDM signal bandwidth) where its pulse shape is a rectangular pulse ($sinc$ in frequency domain). Each sub-carrier is frequency spaced so that the zeros of one sub-carrier spectrum correspond to the peaks of the neighbouring sub-carriers; see Figure 3.12 and Figure 3.13. This permits to avoid sub-carrier interferences and this is the reason why the term orthogonal is used. In practice, the digital modulation process is achieved by applying doing an inverse Fast Fourier Transform (iFFT) and the demodulation by doing a Fast Fourier Transform (FFT). The first main advantage of OFDM modulation is thus its easy implementation.

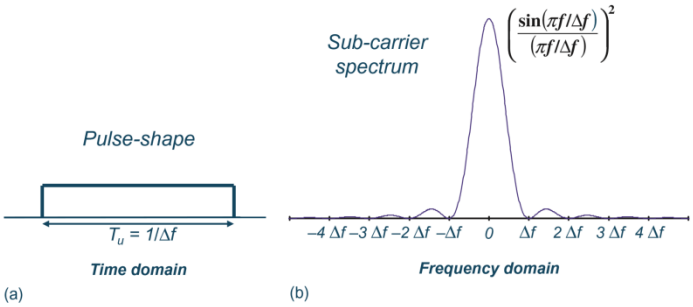

Figure 3.12 – (a) subcarrier pulse shape, (b) spectrum for basic OFDM transmission

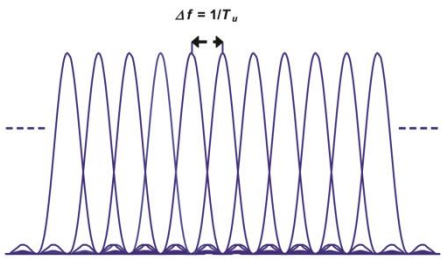

Figure 3.13 – OFDM subcarrier spacing

3.3.2.1.2. Modulation/demodulation process

The mathematical aspects of the OFDM transmission chain are detailed next. The transmission chain is presented in Figure 3.14. The stream of data symbols (symbols previously modulated with a modulated scheme such as QPSK or M-QAM) passes through a series-to-parallel converter (S/P); each data symbol is then OFDM modulated by the application of the iFFT. After the Cycle Prefix (CP) inclusion, and passing through a parallel to series converter, the signal is transmitted through the transmission channel. The CP is a repetition of a part of the signal that provides several advantages to the signal; it is presented in the next sections. Conversely, at the receiver part, all these steps are performed again in a reversed order.

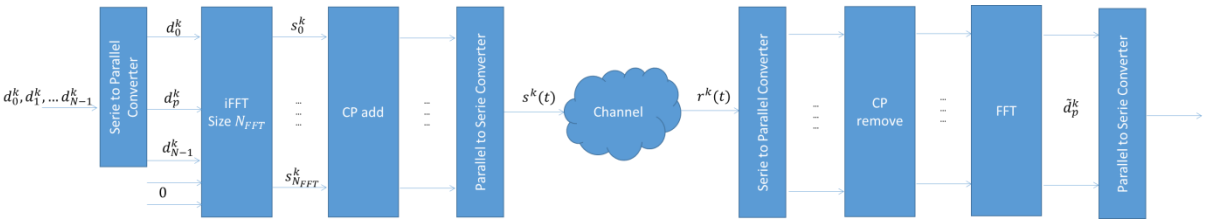

Figure 3.14 – OFDM transmission chain

The transmitted signal, $s(t)$, in the time period $[(k-1)\cdot T_{OFDM}, k\cdot T_{OFDM}]$, can be noted as $s^k(t)$ and represents the part of the OFDM signal carrying the k^{th} OFDM symbol, where T_{OFDM} represents the duration of an OFDM symbol. $s^k(t)$ is composed of all the modulated subcarriers where the symbols modulated by each subcarrier in the period $[(k-1)\cdot T_{OFDM}, k\cdot T_{OFDM}]$ are denoted as d_p^k (e.g. QAM symbols). $s^k(t)$ is modelled in (3.1) and is graphical representation is shown in Figure 3.15.

$$s^k(t) = \sum_{p=0}^{N-1} s_p^k(t) = \sum_{p=0}^{N-1} d_p^k e^{i2\pi p\Delta f t} \tag{3.1}$$

Where:

- s_p^k is the p^{th} modulated subcarrier
- d_p^k is the k^{th} modulated symbol carried by the p^{th} subcarrier
- N is the number of transmitted subcarriers
- Δf is the subcarrier spacing
- p is the subcarrier index
- k is the OFDM symbol number

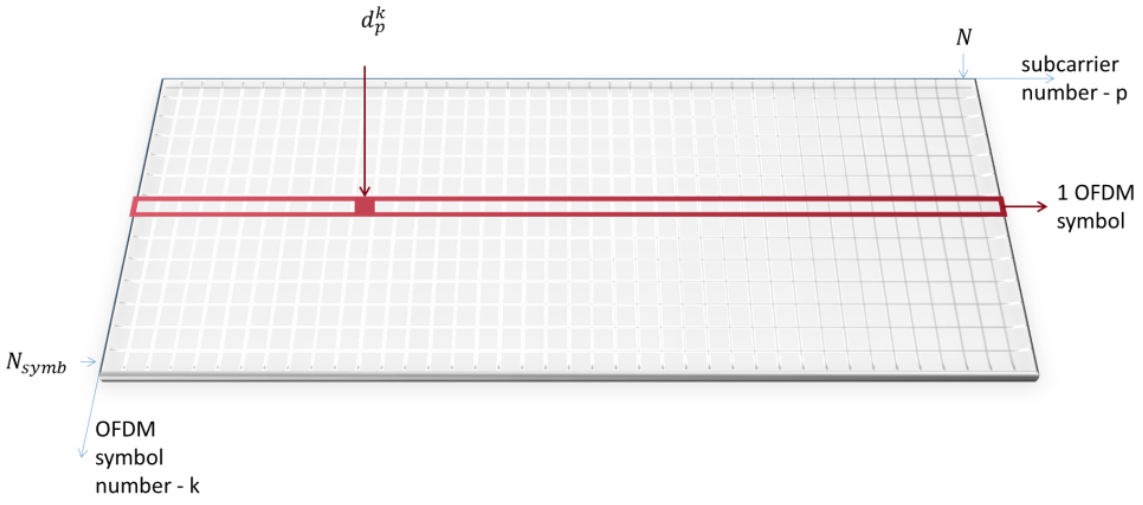

Figure 3.15 – Illustration of the OFDM signal to transmit

Considering a time-discrete (sampled) OFDM signal in the time period $[(k-1)\cdot T_{OFDM}, k\cdot T_{OFDM}]$ with sampling rate f_s being a multiple of the subcarrier spacing: $\frac{1}{f_s} = T_s = \frac{1}{N\cdot\Delta f}$. Its expression, s_n^k, can then be defined as in (3.2) using the inverse Fourier Transform (iFT).

$$s_n^k = iFT_N\left(d_p^k\right)[n] = s(nT_s) = \sum_{p=0}^{N-1} s_p^k(nT_s) = \sum_{p=0}^{N-1} d_p^k e^{i2\pi p\Delta f nT_s} = \sum_{p=0}^{N-1} d_p^k e^{\frac{i2\pi np}{N}} \quad (3.2)$$
$$n \in [0, N-1]$$

Moreover, assuming a higher sampling rate, f_s, $\frac{1}{f_s} = T_s = \frac{1}{N_{FFT}\cdot\Delta f}$ with $N_{FFT} > N$ and $N_{FFT} = 2^K$, $K \in \mathbb{Z}$, the previous expression can be rewritten using the targeted iFFT instead of the iFT as:

$$s_n^k = iFFT_{N_{FFT}}\left(d_p^k\right)[n] = \sum_{p=0}^{N_{FFT}-1} d_p'^k e^{\frac{i2\pi np}{N_{FFT}}}, n \in [0, N_{FFT}-1] \quad (3.3)$$

Where:

- n is the sample index
- N_{FFT} is the iFFT size
- $d_p'^k = \begin{cases} d_p^k & for\ 0 \le p < N \\ 0 & for\ N \le p < N_{FFT} \end{cases}$ is the complex data symbol carried by the p^{th} subcarrier
- s_n^k is the n^{th} sample of the k^{th} OFDM symbol

The demodulation process is performed using a direct FFT. Suppose that the channel do not perturb the signal, hence $s^k(t) = \sum_{p=0}^{N-1} s_p^k(t) = r^k(t)$. The demodulated signal is given in (3.4).

$$\begin{aligned} \tilde{d}_{p'}^k = FFT_{N_{FFT}}(r_n^k)[p'] &= \sum_{n=0}^{N_{FFT}-1} r_n^k\, e^{-i2\pi\frac{np'}{N_{FFT}}} = \sum_{n=0}^{N_{FFT}-1}\sum_{p=0}^{N_{FFT}-1} d_p'^k e^{\frac{i2\pi np}{N_{FFT}}} e^{-i2\pi\frac{np'}{N_{FFT}}} \\ &= \sum_{p=0}^{N_{FFT}-1} d_p'^k \sum_{n=0}^{N_{FFT}-1} e^{\frac{i2\pi n(p-p')}{N_{FFT}}} = \sum_{p=0}^{N_{FFT}-1} d_p'^k \delta(p-p') = d_{p'}^k \end{aligned} \quad (3.4)$$

For notation simplification purposes, in the remaining part of this PhD, the number of samples used to conduct the iFFT and FFT operations will always be assumed to be equal to N_{FFT}.

3.3.2.1.3. OFDM in multipath environment

The second main advantage of OFDM modulation is its robustness in multipath environment. Indeed, it combats frequency selectivity as well as time dispersity, 2 characteristics of multipath environment. The frequency selectivity is the distortion of the signal due to the echo of a symbol over itself. The time dispersity is the distortion of the signal due to the echo of a symbol over the next one. These two characteristics are now detailed.

3.3.2.1.3.1. Frequency selectivity

Frequency selectivity appears when signal replicas arrive with a delay larger than the inverse of the signal bandwidth. In other word, when the multipath component arrive at the receiver with a large delay. This is illustrated in Figure 3.16. On the left illustration, the multipath arrives with a very short delay; it will distort a little bit the signal. This distortion is called “flat” fading (in the spectral domain, it can be considered constant) and can be easily corrected. However, in the right part of Figure 3.16, the multipath arrives with a large delay, the received signal is highly distorted and the correction to apply is very costly.

This phenomenon is an issue for wideband telecommunication in urban or indoor environment since the bandwidth used is large.

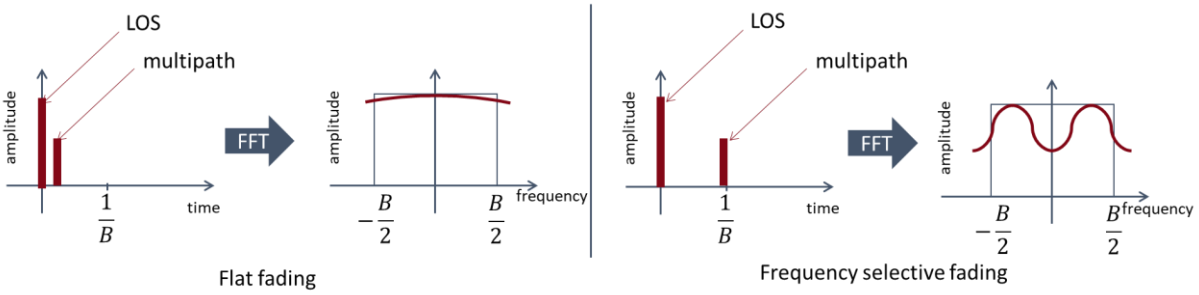

Figure 3.16 – Frequency selectivity illustration

By using narrow bandwidths for each sub-carrier, OFDM allows to combat frequency selectivity. Indeed, as illustrated Figure 3.17, the fading can be considered as "flat" on each subcarrier, for a maximum subcarrier bandwidth with respect to the multipath delay, and can be easily corrected by channel estimation and correction (aka channel equalization).

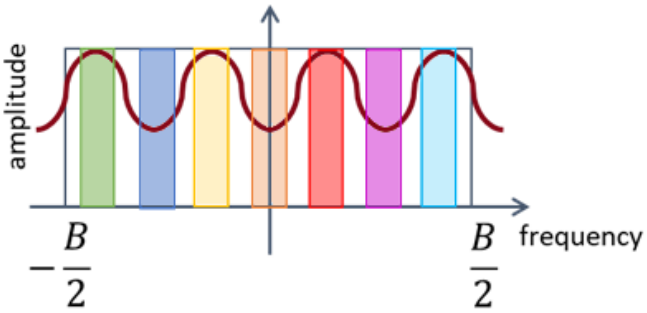

Figure 3.17 – OFDM combats frequency selectivity

3.3.2.1.3.2. Time dispersity

The second main phenomenon linked to the multipath environment is time dispersity. Time dispersity is due to the spreading of the symbols' power in time. The solution usually adopted to correct this distortion is to introduce an interval between two consecutive symbols, to avoid inter-symbol interferences. In OFDM, the interval is filled with a cycle prefix before the OFDM actual symbol, see Figure 3.18.

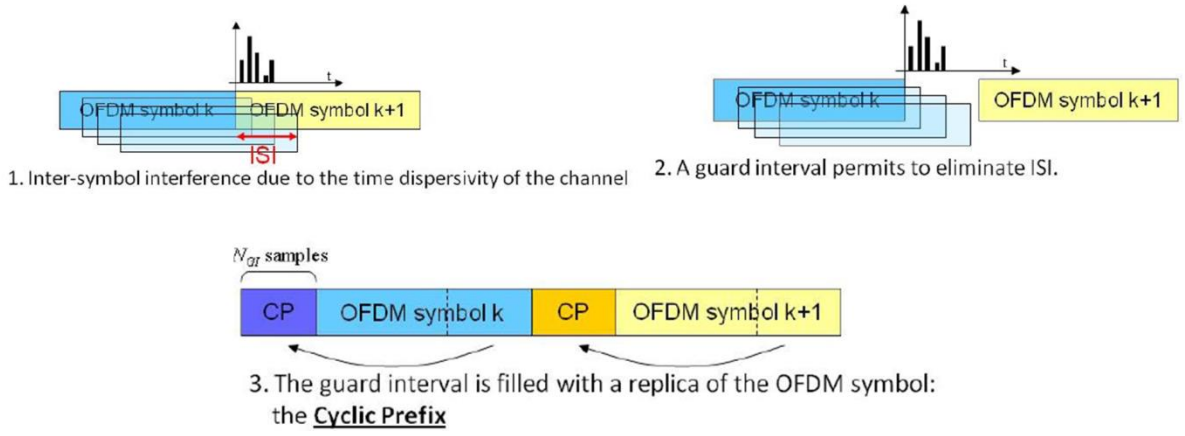

Figure 3.18 – Cycle prefix introduction to combat time dispersity – source [41]

The cycle prefix is composed of the last N_{CP} samples of the OFDM symbol; hence the total length of the OFDM symbol becomes: $N_{CP} + N_{FFT}$. The samples belonging to the cycle prefix can be expressed as in (3.5).

$$s_n^k = s_{n+N_{FFT}}^k \; for - N_{CP} \leq n < 0 \tag{3.5}$$

This property is interesting for the demodulation process. Indeed, the demodulation (i.e. the FFT) is done over N_{FFT} samples. In the ideal case, assuming a perfect synchronization process, the beginning of the FFT window would be placed just at the beginning of the symbol, (a) in Figure 3.19. If so, the received signal is expressed as in (3.6).

$$r_n^k{}_{with\ CP} = \sum_{p=-N_{CP}}^{N_{FFT}-1} s_p^k(nT_s) \tag{3.6}$$

The cycle prefix is removed from the previous equation and therefore the received signal to be processed is given below.

$$r_n^k = \sum_{p=0}^{N_{FFT}-1} s_p^k(nT_s) \tag{3.7}$$

Where $p = 0$ denotes the beginning of the OFDM symbol.

If there is a delay in the choice of the beginning of the FFT window (i.e. synchronization delay), case (b) in Figure 3.19, it will create a phase shift in the demodulation process. Indeed, let's consider the case (b); then noting N_s the advance in samples from the start of the OFDM symbol, the demodulated symbol is given in (3.8). Detailed derivation can be found in Annex C.3.

$$\tilde{d}_{p'}^k = FFT_{N_{FFT}}(r_n^k)[p'] = \sum_{n=0}^{N_{FFT}-1} r_{n+N_s}^k \, e^{-i2\pi\frac{np'}{N_{FFT}}} \tag{3.8}$$

Therefore, the demodulated symbol obtained is given in (3.9). In fact, it is the actual demodulated symbol (or symbols), affected by a phase shift. This phase shift can be easily compensated through the adequate use of training sequence or pilot symbols.

$$\tilde{d}_{p'}^k = d_{p'}^k e^{-\frac{i2\pi N_s p'}{N_{FFT}}} \tag{3.9}$$

As explained before, this property can be applied in the case of multipath, as long as the multipath falls into the cycle prefix the time delay becomes a phase shift. The demonstration is proposed below.

To recover the signal, suppose the FFT window starts just after the cycle prefix and has a N_{FFT}-size, see Figure 3.20. Suppose now that in addition to the LOS path, there is also a multipath component; hence the received signal can be model as in (3.10).

$$r_n^k = s_n^k + s_{n-N_\tau}^k \tag{3.10}$$

Where N_τ is the delay in samples between the direct and reflected paths. The demodulated symbol is thus given in (3.11).

$$\tilde{d}_{p'}^k = FFT(r_n^k)[p'] = \sum_{n=0}^{N_{FFT}-1} s_n^k \, e^{-i2\pi\frac{np'}{N_{FFT}}} + \sum_{n=-N_\tau}^{N_{FFT}-1-N_\tau} s_n^k \, e^{-i2\pi\frac{(n+N_\tau)p'}{N_{FFT}}} \tag{3.11}$$

With the previous results, the demodulated symbol obtained is given in (3.12). Again, the output of the demodulator is the expected demodulated symbol, multiplied by a complex factor, which can be easily compensated with the use of pilot symbols and channel estimation techniques.

$$\tilde{d}_{p'}^{k} = d_{p'}^{k}\left(1 + e^{-\frac{i2\pi p' N_\tau}{N_{FFT}}}\right) \tag{3.12}$$

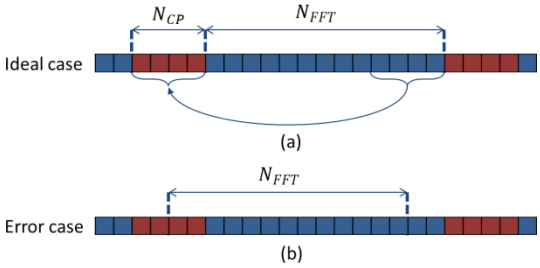

Figure 3.19 – Demodulation of an OFDM signal

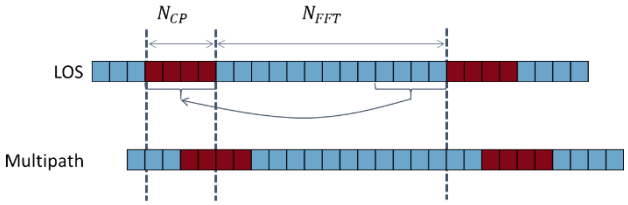

Figure 3.20 – OFDM combats time dispersity

3.3.2.2. 5G Numerology

As presented in the previous section, 5G implements an OFDM modulation; the modulation is parameterized by the window size, N_{FFT}, the subcarrier spacing, Δf, and the cycle prefix. These parameters are referred as the numerology.

The subcarrier spacing determines the sampling frequency at the receiver. The sampling frequency is usually defined as (3.13), where f_s is the sampling frequency, Δf is the subcarrier spacing, n is a positive integer and N is the number of sub-carriers.

$$f_s = n \cdot N \cdot \Delta f, n \in \mathbb{Z}^+ - \{0\} \tag{3.13}$$

The cycle prefix, as already presented, provides a guard interval to eliminate inter symbol interference from the previous symbol.

5G is envisioned to operate from sub 1 GHz to 100 GHz for a wide range deployment options and to support a variety of services. It is not possible for single waveform numerology to fulfil all these requirements. Hence, multiple OFDM numerologies must be supported. In Table 3.1, all the numerologies envisioned for 5G are presented. For the record 4G-LTE uses a $15kHz$ sub-carrier spacing only. Higher sub-carrier spacing are well-adapted for higher carrier frequencies, where the available bandwidth is larger and the multipath delay is shorter. [42] specifies that the FFT window size reference is $N_{FFT} = 2048$.

Table 3.1 – Supported numerologies – source [38]

μ	$\Delta f = 2^{\mu} \cdot 15$ [kHz]	Cyclic prefix
0	15	Normal
1	30	Normal
2	60	Normal, Extended
3	120	Normal
4	240	Normal

3.3.3. Duplexing mode

To support transmission in paired and unpaired spectrum, both Frequency Division Duplex (FDD) and Time Division Duplex (TDD) are enabled. FDD and TDD are duplexing methods; they define the method employed to separate the DL and UL transmissions. This section aims at describing them.

3.3.3.1. *Frequency Division Duplex*

FDD consists in separating the DL and UL in the frequency domain: both links share the same time slots but are transmitted in different frequency bands, see Figure 3.21. UL and DL are separated by a frequency guard; the guard band characterization can be found in [11]. The advantages of such a duplexing method are: low latency due to continuous UL and DL transmissions and higher immunity to intra-system interference.

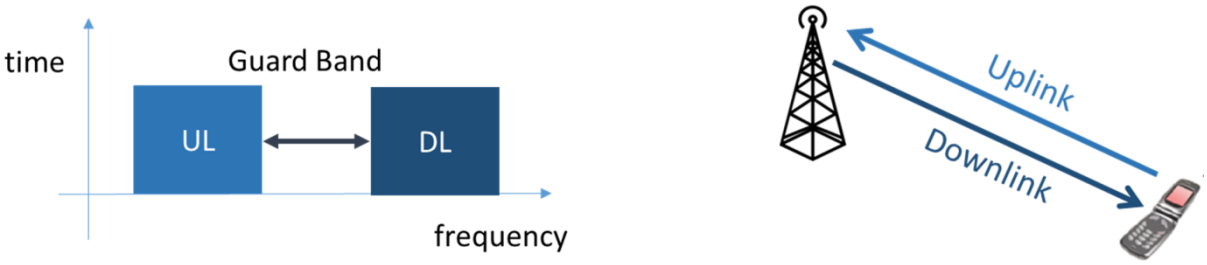

Figure 3.21 – Frequency Division Duplex principle

3.3.3.2. *Time Division Duplex*

TDD consists in separating the DL and UL in the time frame domain: both link share the same frequency band but are transmitted in different time slots, see Figure 3.22. The advantages of such a duplexing method are: channel reciprocity, high frequency diversity, unpaired band allocation and limited number of spectrum licences to be bought by mobile telecommunication operators.

Figure 3.22 – Time Division Duplex principle

3.3.4. Frame structure

The frame structure refers to the structure of the transmitted signal. In a first part, some general information is provided; then the frame and sub-frame structures are presented. Third, the focus is on the slots definition. Finally, the symbol characteristics are provided.

3.3.4.1. *General information*

The 3GPP, [43], defines the size of various fields in the time domain as a number of time units as followed.

$$T_s = \frac{1}{\Delta f_{ref}\, N_{f,ref}} = \frac{1}{30\,720\,000} \cong 32.55\, ns \tag{3.14}$$

$$T_c = \frac{1}{\Delta f_{max}\, N_f} = \frac{1}{1\,966\,080\,000} \cong 0.509\, ns \tag{3.15}$$

$$\kappa = \frac{T_s}{T_c} = 64 \tag{3.16}$$

Where $\Delta f_{max} = 480\ kHz$, $N_f = 4096$, $\Delta f_{ref} = 15\ kHz$, and $N_{f,ref} = 2048$.

3.3.4.2. Frame and sub-frame structures

Downlink and uplink transmissions are organized into frames of 10 ms-duration, (3.17).

$$T_f = \frac{\Delta f_{max}\, N_f}{100} T_c = 10\ ms \tag{3.17}$$

Each frame is composed of ten sub-frames of 1 ms-duration, (3.18).

$$T_{sf} = \frac{\Delta f_{max}\, N_f}{1000} T_c = 1\ ms \tag{3.18}$$

Each sub-frames is composed of K slots, each slot is composed of 14 OFDM symbols. The number of consecutive slots (and by extension OFDM symbols) per sub-frame depends on the numerology adopted. The Figure 3.23 shows a general frame structure. Each frame is divided into two equally-sized half-frames of five sub-frames each with half-frame 0 consisting of sub-frames 0 – 4 and half-frame 1 consisting of sub-frames 5 – 9.

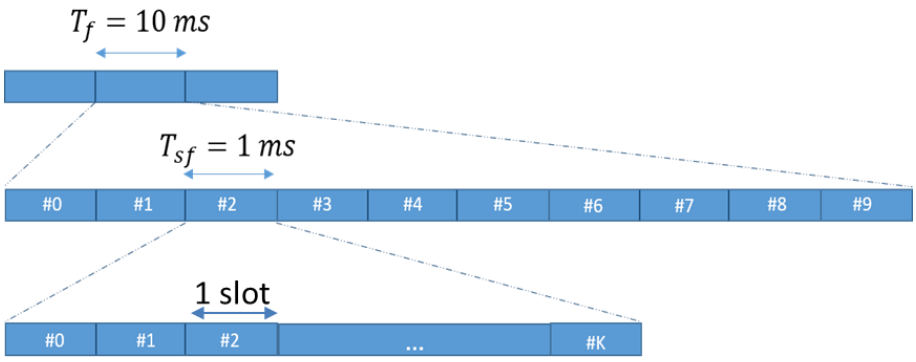

Figure 3.23 – Frame structure

3.3.4.3. Slots

The number of OFDM symbols per sub-frame is given by (3.19).

$$N_{symb}^{subframe,\mu} = N_{symb}^{slot} N_{slot}^{subframe,\mu} \tag{3.19}$$

Where N_{symb}^{slot} is the number of symbol per slot (14 for a normal cycle prefix, 12 for the extended one) and $N_{slot}^{subframe,\mu}$ is the number of slot per sub-frame, it depends on the sub-carrier spacing

In Table 3.2, the number of OFDM symbol per slot is given for each numerology.

Table 3.2 – Number of OFDM symbols per slot – source [43]

μ	Cyclic prefix	N_{symb}^{slot}	$N_{slot}^{subframe,\mu}$	$N_{slot}^{frame,\mu}$
0	Normal	14	1	10
1	Normal	14	2	20
2	Normal	14	4	40
2	Extended	12	4	40
3	Normal	14	8	80
4	Normal	14	16	160

As an example, in Figure 3.24, the frame structure is represented for 2 numerologies: $\mu = 0$ and $\mu = 2$, both with normal Cycle prefix.

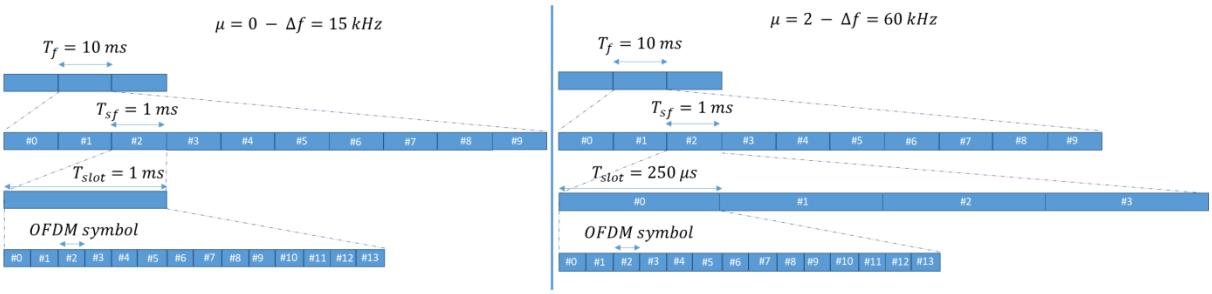

Figure 3.24 – Frame structure example for two numerologies

3.3.4.4. *Symbol and cycle prefix durations*

In this part, the durations of the OFDM symbols and of the CP are given for all numerologies. Their duration can be extracted regarding the information given in [43]. The complete demonstration for each numerology is provided in Annex C.1.

A brief example is provided here assuming the first numerology: $\mu = 0$. The subcarrier spacing is $\Delta f = 15\ 000\ Hz$, there is one slot per sub-frame and each slot is composed of 14 symbols.

The OFDM duration is fixed by the carrier spacing: $T_{OFDM} = 2048\ T_s \approx 66.67\ \mu s$; where $T_s = \frac{1}{2048*15000} = \frac{1}{30\ 720\ 000} \approx 32.55\ ns$. As it is shown in Figure 3.25, a slot is composed of 14 OFDM symbols and 14 cycle prefix: $T_{subframe} = 14\ T_{OFDM} + T_{CP}$. Hence, to fully occupy the slot, the cycle prefixes have to verify: $T_{CP} = (30\ 720 - 2048 * 14)\ T_s = 2048\ T_s$.

Two CP lengths are defined (the same principle is applied for 4G-LTE). Hence symbols 0 and 7 have extended length. As defined in [43]: $2048 = 12 * 144 + 2 * 160$. Therefore, the length of the first and seventh OFDM symbols CP is then $160\ T_s \approx 5.208\ \mu s$ and the length of the remaining OFDM symbols CP is $144\ T_s \approx 4.687\ \mu s$.

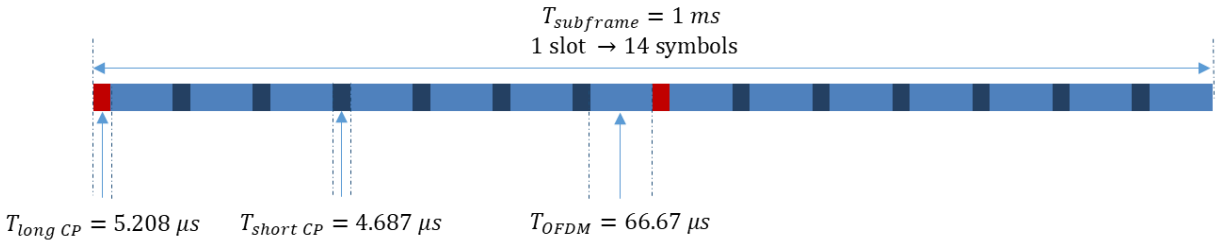

Figure 3.25 – Slot structure

In Table 3.3, the durations of the OFDM symbols and of the CP for each numerology are provided.

Table 3.3 – OFDM and CP duration for each numerology

μ	CP	Number of slot	OFDM symbol duration	1^{st} and $(7.2^{\mu})^{th}$ CP duration	Other CP duration
0	Normal	1	66.67 µs	5.208 µs	4.687 µs
1	Normal	2	33.33 µs	2.865 µs	2.376 µs
2	Normal	4	16.67 µs	1.692 µs	1.172 µs
2	Extended	4	16.67 µs	4.167 µs	4.167 µs
3	Normal	8	8.333 µs	1.106 µs	585.9 ns
4	Normal	16	4.167 µs	813.8 ns	292.9 ns

3.3.5. Physical resources

The physical resources refer to the time and frequency resource associate to each BS/UE to transmit/receive the signal. Basically an antenna port is associated to a resource grid which is composed of resource blocks which are composed of resource element. In this section, concepts of antenna port, resource grid, resource block and resource element are explained. These concepts are necessary to understand how the signal is transmitted

3.3.5.1. Antenna port

The official definition given by the 3GPP is the following one:

> *"An antenna port is defined such that the channel over which a symbol on the antenna port is conveyed can be inferred from the channel over which another symbol on the same antenna port is conveyed. "*

Quote 1 – Antenna port's definition – source [43]

Hence, these antenna ports do not correspond to physical antennas, but rather are logical entities distinguished by their reference signal sequences. Multiple antenna port signals can be transmitted on a single transmit antenna. Correspondingly, a single antenna port can be spread across multiple transmit antennas. It is a general concept introduced, for example, to allow for beam-forming using multiple physical antennas without the terminal being aware of the beam-forming carried out at the transmitter side. The way in which these logical antenna ports are assigned to the physical transmit antennas of a base station is up to the base station, and can vary between base stations of the same type (because of different operating conditions) and also between base stations from different manufacturers.

3.3.5.2. Resource grid

A resource grid is composed of resource blocks which are divided into resource elements. For each numerology and carrier, a resource grid of $N_{grid,x}^{size,\mu}N_{sc}^{RB}$ subcarriers and $N_{symb}^{subframe,\mu}$ OFDM symbols is defined, where x is DL or UL, N_{sc}^{RB} is the number of subcarriers per resource block and $N_{grid,x}^{size,\mu}$ refers to the carrier bandwidth. There is one resource grid per antenna port p, per subcarrier spacing configuration μ, and per transmission direction (DL or UL).

3.3.5.3. Resource elements

A resource element represents each element in the resource grid for antenna port p and subcarrier spacing μ. It identifies a specific subcarrier-OFDM symbol (k,l) where k is the index in the frequency domain and l refers to the symbol position in the time domain relative to some reference point. A resource element $(k,l)_{p,\mu}$ corresponds to the complex value $a_{k,l}^{(p,\mu)}$. It is the smallest physical resource block, see Figure 3.26.

3.3.5.4. Resource blocks

A resource block is defined as $N_{symb}^{subframe,\mu}$ consecutive OFDM symbols in the time domain and $N_{sc}^{RB} = 12$ consecutive subcarriers in the frequency domain (see Figure 3.26). A physical resource block thus consists of $N_{symb}^{subframe,\mu}N_{sc}^{RB}$ resource elements. A Resource Element is the smallest defined unit which consists of one OFDM sub-carrier during one OFDM symbol interval.

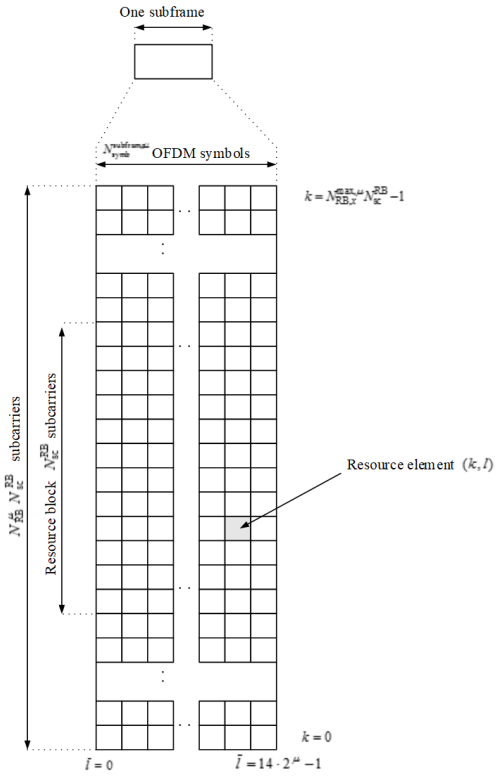

Figure 3.26 – Resource grid and resource block – source [43]

Regarding the resource blocks, the specification distinguishes four resource blocks: the reference resource blocks, the common resource blocks, the Physical resource blocks and the virtual resource blocks. Each of them is described in [42].

The distinction between these four blocks has its importance when trying to map physical channels and signals according to each user to the resource grid. Anyway, a mapping is possible without this distinction. In other words, it is possible to map physical channels and signals by restricting to one or more resource block.

3.3.6. Physical channels and physical signals

The previous sections have permitted to present the characteristics of the transmitted signals based on the OFDM modulation. It has been explained that the content of the transmitted symbols in the time and frequency domain is made thanks to the design of resource grids. It is now of interest to describe the content of the resource grid; this is done thanks to the definition of the physical channel and physical signals.

In this section and in the following one, physical channels and physical signals concepts are presented. Before giving the actual details of which physical channels and which physical signals are sent, their definition must be given first by visually understanding the problem. Note that only the DL physical channel and signal will be described, as they are the main focus of this study. The interest in presenting the physical channels is to be able to select the candidate to perform positioning.

In the previous section, it has been explained that the signal transmitted by the UE and BS can be defined with resource grids. The resource grids are constituted of resource elements and thus, in order to understand the content of the transmitted signal, the content of these resource elements must be defined and how the content of the different resource elements is linked. The objective is to fill each grid

as presented in Figure 3.27 (this illustration serves as an illustration and in no way represent what will be done).

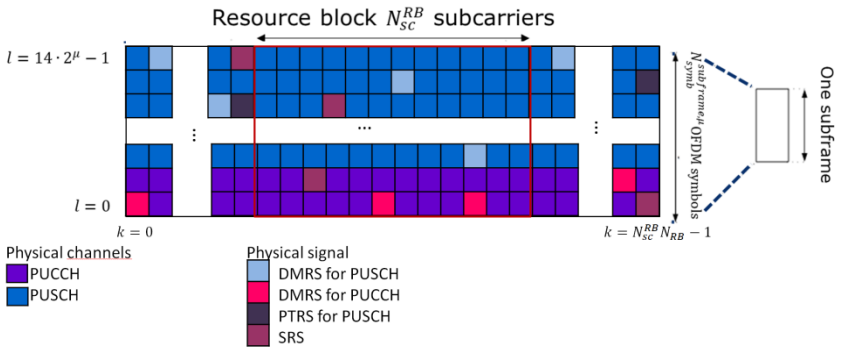

Figure 3.27 – Illustration of physical channels and physical signals

3.3.6.1. Vocabulary

The information flows between the different protocols are known as channels and signals. There are different types of channels (logical, transport and physical) distinguished by the kind of information they carry and by the way in which the information is processed.

- A logical channel defines what type of information is transmitted over the air.
- A transport channel define the way something is transmitted over the air (encoding, interleaving options used to transmit data).
- A physical channel define where is something transmitted over the air (which symbol in the resource grid).

Each physical channel corresponds to a set of resource elements in the time-frequency grid that carry information from higher layers. The basic entities that make a physical channel are resource elements and resource blocks.

Physical channels (UL or DL) carry layer 2 information but physical signals (UL or DL) are only used by the physical layer. In other words, physical channels will serve to transmit/receive actual information (data from user or control information) and physical signals are pilots, they do not contain information but are used for synchronization purpose. The concepts of physical channels and signals being presented, the focus is now on the physical channels.

3.3.6.2. Physical channels in the DL

In the DL, the following physical channels are defined:

- Physical Downlink Shared Channel – PDSCH: it contains actual user data
- Physical Downlink Control Channel – PDCCH: this is a physical layer control channel; it informs the UE about the resource allocation. It is used for DL control information, mainly scheduling decisions, required for reception of PDSCH, and for scheduling grants enabling transmission on the Physical Uplink Shared Channel (PUSCH)
- Physical Broadcast Channel – PBCH: this channel carries system information required by the terminal in order to access the network

3.3.6.3. Physical signals

The physical layer uses physical signals. Those signals do not carry information from upper layer. There are two types of physical signals: Reference and Synchronization signals. Basically, they are pilot signals.

3.3.6.3.1. DL reference signals

Reference signals carry some predefined symbol sequences; those sequences are known from the receiver and help the receiver to estimate the transmission channel.

3 reference signals are defined in the DL:

- The demodulation reference signal – DM-RS. It is used to estimate the radio channel in order to coherently demodulate the signal at the UE. It is associated with transmission of PDSCH and PDCCH and is mandatory. The UE may assume that at least one symbol with DMRS is present on each layer in which PDSCH is transmitted to a UE. The number of DMRS symbols and resource element mapping is configured by higher layers.
- The phase tracking reference signal – PT-RS. PTRS may be transmitted on additional symbols to aid receiver phase tracking.
- The channel state information reference signal – CSI-RS. It gathers several different types of indicators: the channel quality indicator (how good/bad the communication channel quality is), the precoding matrix indicator, the precoding type indicator, the rank indication. It is used by the UE to estimate the channel and report channel quality information to the base station.

It has to be noted that DM-RS (for PDSCH and for PDCCH) is always transmitted; whereas, PTRS is only transmitted if the transmitting procedure indicates it.

As an example, TS 38.211 specifies that the UE may assume that at least one symbol with demodulation reference signal is present on each layer in which PDSCH is transmitted to a UE. The number of DMRS symbols and resource element mapping is configured by higher layers.

3.3.6.3.2. Synchronization signals

Synchronization signals allow the synchronization between the UE and the BS; they are available in the DL only. Several can be cited as the physical cell ID, the Primary Synchronization Signal or the Secondary Synchronization Signal: their complete description can be found in Annex C.4.

A deep study of the 3GPP standards has shown that the only set of pilots that are fixed in the resource grid is the SS/PBCH block. Therefore, in the following the pilot candidate retained is the SS PBCH. This section aims at describing precisely their location in the time and frequency domain.

3.3.6.3.2.1. Structure

In the time domain, an SS/PBCH block consists of 4 OFDM symbols, numbered in increasing order from 0 to 3 within the SS/PBCH block, where PSS, SSS, and PBCH with associated DM-RS occupy different symbols as given by Table 3.4.

In the frequency domain, an SS/PBCH block consists of 240 contiguous subcarriers with the subcarriers numbered in increasing order from 0 to 239 within the SS/PBCH block. Subcarrier 0 in an SS/PBCH block corresponds to subcarrier k_0 in common resource block $N_{\text{CRB}}^{\text{SSB}}$, where $N_{\text{CRB}}^{\text{SSB}}$ is obtained from the higher-layer parameter *offset-ref-low-scs-ref-PRB*.

In Figure 3.28, the frequency domain allocation is represented, considering $v = N_{ID}^{cell} mod 4 = 0$. This choice is just for visualization purpose.

Any common resource block partially or fully overlapping with an SS/PBCH block shall be viewed as occupied and not used for transmission of PDSCH or PDCCH.

For an SS/PBCH block, the UE shall assume

- antenna port $p = 4000$,
- the same cyclic prefix length and subcarrier spacing for the PSS, SSS, and PBCH,
- for SS/PBCH block type A, $k_0 \in \{0,1,2 \dots 23\}, \mu \in \{0,1\}$ and N_{CRB}^{SSB} is expressed in terms of 15 kHz subcarrier spacing, and
- for SS/PBCH block type B, $k_0 \in \{0,1,2 \dots 11\}, \mu \in \{3,4\}$ and N_{CRB}^{SSB} is expressed in terms of 60 kHz subcarrier spacing.

Table 3.4 – Resources within an SS/PBCH block for PSS, SSS, PBCH and DMRS for PBCH – source [38]

Channel or signal	OFDM symbol number l relative to the start of an SS/PBCH block	Subcarrier number k relative to the start of an SS/PBCH block
PSS	0	56, 57, …, 182
SSS	2	56, 57, …, 182
Set to 0	0	0, 1, …, 55, 183, 184, …, 236
	2	48, 49, …, 55, 183, 184, …, 191
PBCH	1, 3	0, 1, …, 239
	2	0, 1, …, 47, 192, 193, …, 239
DM-RS for PBCH	1, 3	$0+v,4+v,8+v,\dots,236+v$
	2	$0+v,4+v,8+v,\dots,44+v$ $192+v,196+v,\dots,236+v$

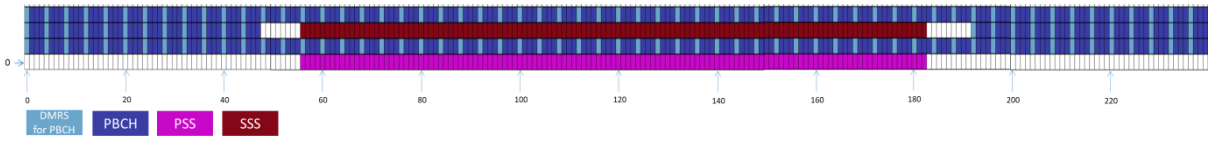

Figure 3.28 – Frequency domain allocation

Remind that DMRS are reference signals and PBCH are physical channel. More specifically, PBCH DMRS is a special type of physical layer signal which functions as a reference signal for decoding PBCH.

3.3.6.3.2.2. Time location of an SS/PBCH block

The locations in the time domain where a UE shall monitor for a possible SS/PBCH block are described in [44]. These synchronization signals are received at the UE side to perform cell search. Cell search is a procedure by which a UE acquires time and frequency synchronisation with a cell and detects the physical layer cell ID of that cell. The location in the time domain depends on two main parameters: the numerology and the frequency band.

As such 5 cases are defined in [44], in the following an example is detailed. Let's consider the first numerology: $\Delta f = 15\ kHz$. Then the standard specifies:

"For a half frame with SS/PBCH blocks, the number and first symbol indexes for candidate SS/PBCH blocks are determined according to the subcarrier spacing of SS/PBCH blocks as follows.

- *Case A - 15 kHz subcarrier spacing: the first symbols of the candidate SS/PBCH blocks have indexes of {2, 8} + 14*n. For carrier frequencies smaller than or equal to 3 GHz, n=0, 1. For carrier frequencies larger than 3 GHz and smaller than or equal to 6 GHz, n=0, 1, 2, 3."*

Quote 2 – Time allocation SS/PBCH block – source [44]

Visually this can be represented in Figure 3.29; the allocation for the other cases is presented in Annex C.2. Note that the indexes represented are "candidates".

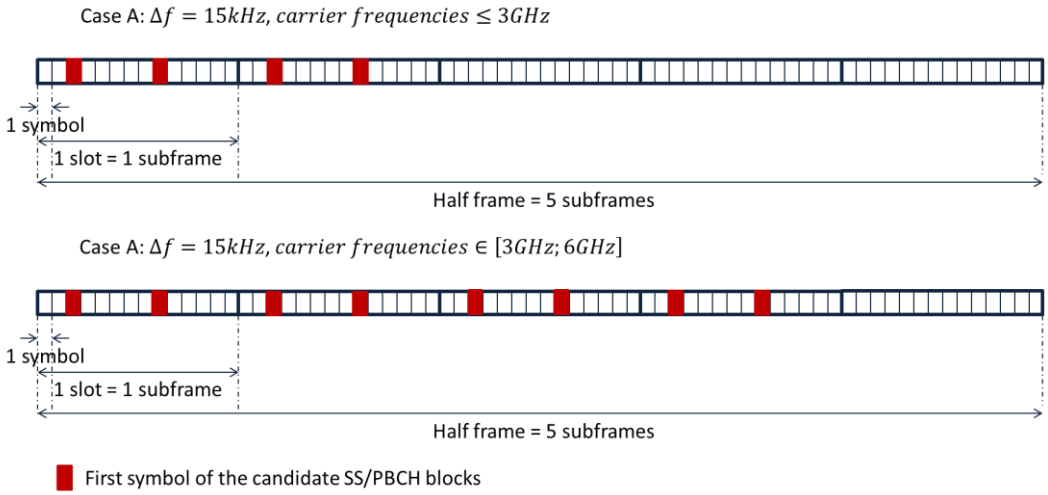

Figure 3.29 – Time allocation of the first SS/PBCH symbol candidate

For initial cell selection, a UE may assume that half frames with SS/PBCH blocks occur with a periodicity of 2 frames. Otherwise, the periodicity of the SS/PBCH block can be configured by the network.

3.3.7. Simplified 5G signal selected for this Ph.D. thesis

All along this Ph.D., a simplified 5G frame is considered. In fact, since 5G signal is being developed, to design a precise and realistic resource grid is almost impossible. Therefore, in the following the 5G signal is composed one OFDM symbol repeated every symbol. The considered symbol corresponds to the 2nd or 4th symbol of the SSPBCH block presented above. Remind that this symbol is composed of one pilot every 4 subcarriers over 240 subcarriers.

3.3.8. Conclusion

In this section, the 5G physical layer and part of the MAC layer have been presented. By doing so, the design of the 5G signals and the way the signals are transmitted are understood. The section also illustrates the complexity of the 5G signal design. The resource grid is so flexible that it is almost impossible to design a reference resource grid. More specifically, only one set of pilots can be precisely described. Therefore in the following the focus will be made on SSPBCH signals, explaining why their precise descriptions have been given.

3.4. Transmission channel

In the previous section, the transmitted signal model has been precisely modeled. This signal is disturbed by the transmission channel before being received and processed by the receiver. It is of the utmost importance to precisely describe these disturbances and therefore to precisely model the transmission channel.

In this section, the received signal model is reminded; second, the selection of a 5G compliant propagation channel is provided. Third, QuaDRiGa, the transmission channel simulator selected for the thesis is presented.

3.4.1. Received signal

The noiseless received complex envelope signal mathematical model at the receiver antenna input can be thus expressed in (3.20) by the convolution between the incoming signal and the propagation channel complex envelope Channel Impulse Response (CIR). The CIR mathematical model is usually expressed as $\alpha^k(t,u)$, where u is a mathematical variable used for the convolution operation, t is used to model the complex amplitude evolution and delay of each multipath, k is the index of the OFDM symbol, and the sub-index nl for "noiseless" permits to distinguish this noiseless model and the model with noise.

$$r_{nl}^k(t) = \alpha^k(t,u) * s^k(u)\Big|_{u=t} \tag{3.20}$$

In order to define a precise received signal model it is thus of the utmost importance to precisely model the CIR mathematical model, $\alpha^k(t,u)$. Therefore, in order to design the CIR model, it is of the utmost importance to first select a 5G compliant propagation channel model.

3.4.2. Selection of a 5G compliant propagation channel

The selection of a 5G compliant propagation channel has been made with regards to 2 aspects: the fulfilling of 5G requirements and its complexity.

First, the 5G requirements in term of transmission channel depend on several parameters: the scenarios in which the radio system is expected to be used (indoor, outdoor, rural, and urban), the frequencies used, the bandwidths, the antenna, etc. These requirements are described in Annex C.5.

Second, when designing a wireless transmission system, it is useful to evaluate its performance over at least a minimum number of channel realizations. The high computational complexity of deterministic modelling prohibits the intensive link or system level simulation required during system design. This is one of the main reasons why Geometry based Stochastic Channel Models (GSCM) modelling is the most used type of propagation channel model in practice.

According to these parameters, and after a deep study of the literature, the propagation channel model selected is QuaDRiGa. The QuaDRiGa project is an open free project, allowing the design of particular trajectory and high level scenario propagation. It is a GSCM that fulfills the main requirements identified for 5G regarding the frequency range, millimeter waves as well as sub-6 GHz carrier frequency can be modelled, the envisioned scenarios, dense urban as well as indoor environment can be modelled, and antenna considerations, MIMO antennas can be modelled. The complete study is available in Annex C.5.

3.4.3. QuaDRiGa

The Quasi-Deterministic Radio channel Generator (QuaDRiGa) is a model evolved from the WINNER II project; it can even be seen as a 3GPP 3D and 3GPP 38.901 reference implementation. It is used for generating realistic radio channel impulse responses for system-level simulations of mobile radio networks. QuaDRiGa was developed at Fraunhofer HHI to enable the modeling of MIMO radio channels for specific network configurations, such as indoor, satellite or heterogeneous configurations. QuaDRiGa is a 3D-GSCM.

3.4.3.1. General presentation

The QuaDRiGa channel model follows a geometry-based stochastic channel modeling approach, which allows the creation of an arbitrary double directional radio channel. It is based on the statistical ray-tracing model. The channel model is antenna independent, hence different antenna configurations and different element patterns can be inserted.

The QuaDRiGa approach can be understood as a "statistical ray-tracing model". Unlike the classical ray tracing approach, it does not use an exact geometric representation of the environment but distributes the positions of the scattering clusters (the sources of indirect signals such as buildings or trees) randomly. A simplified overview of the model is depicted in Figure 3.30. For each path, the model derives the angle of departure (the angle between the transmitter and the scattering cluster), the angle of arrival (the angle between the receiver and the scattering cluster) and the total path length which results in a delay τ of the signal. For the sake of simplicity, only two paths are shown in the figure.

The channel parameters are determined stochastically, based on statistical distributions extracted from channel measurements. The distributions are defined for, e.g. delay spread, delay values, angle spread, shadow fading, and cross-polarization ratio. The trajectory is split into segments, for each segment the channel parameters are calculated from the distributions. Specific channel realizations, or CIR, are generated by summing contributions of rays with specific channel parameters like delay, power, angle-of-arrival and angle-of-departure. Different scenarios are modeled by using the same approach, but different parameters.

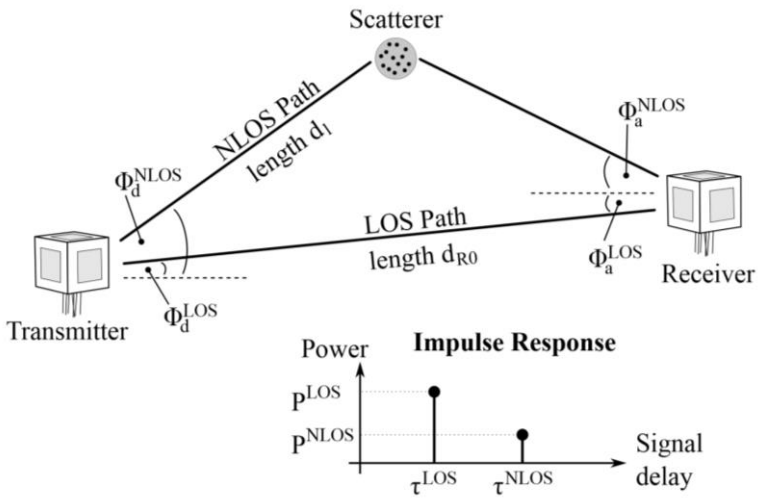

Figure 3.30 – Simplified overview of the modelling approach in QuaDRiGa – source [45]

3.4.3.2. Program flow

The QuaDRiGa program flow is provided in Figure 3.31 and is extracted from [45].

1. The user configures the network layout. It sets the TX position and defines the RX and TX antenna properties. It also defines the user trajectory; more specifically, it defines the states or segments along the user trajectory and associates to each segment a propagation environment.
2. The statistical properties of the Large Scale Parameters (LSP) are defined, for each state, thanks to a configuration file. There are typically two configuration files used in QuaDRiGa, one for LOS scenarios and the other one for the NLOS scenarios.

3. Clusters are calculated, for each segment of the trajectory, according to the values of the LSPs at the UE position. The number of clusters depends on the high-level scenario selected. The cluster positions are random within the limits given by the LSP.
4. Each cluster is split into 20 sub-paths and the arrival angles are calculated for each sub-path and for each positions of the UE on the trajectory.
5. The antenna response for each of the arrival/departure angles and for each of the antenna element is calculated.
6. The phases are calculated based on the position of the terminal antennas in relation to the clusters. The terminal trajectory defines how the phases change. This results in the Doppler spread.
7. The coefficients of the 20 sub-paths are summed. At this point, the MIMO channel response is created. In the software, the correlated LSP values are taken as input and the Channel Impulse Response is calculated for each user position. In other words, for each cluster, one path is created and associated to a set of parameters (delay, AoA, complex envelop, etc.)
8. The channel coefficients of adjacent segment are merged.
9. The channel coefficients together with the path delays are formatted and returned to the user for further analysis.

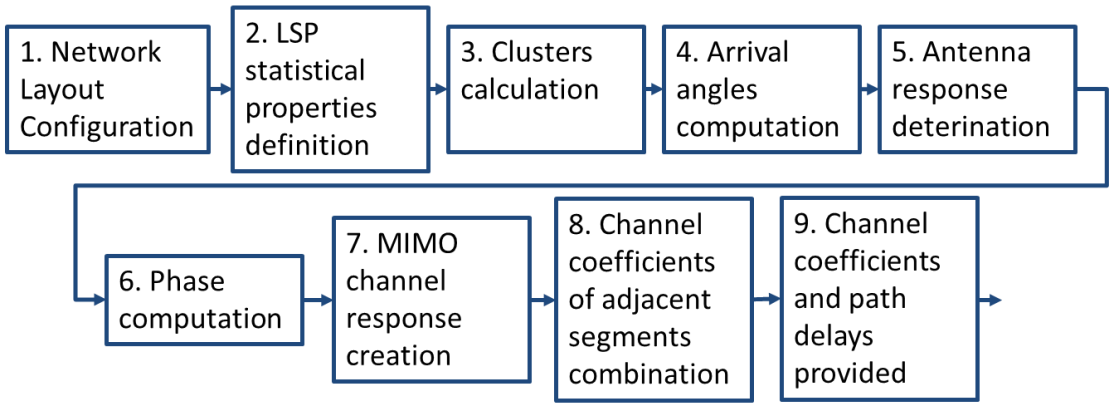

Figure 3.31 – QuaDRiGa program flow

QuaDRiGa is mostly the model described by the 3GPP standard, [43], however, in order to make the model consistent, slight modifications have been made and are detailed in [45]. In chapter 7, an example of propagation channel generation is provided.

3.5. Receiver signal processing

The signal received by the receiver is modelled as the convolution between the transmitted signal and propagation channel. The received signal is processed by the receiver in order to obtain ToA or TDoA measurements which are then used to compute the PVT solution as shown, for example, in section 3.6. The detailed signal processing leading to the ToA and TDoA computations is presented in this section.

First the general systems and signals characteristics used in the thesis are presented. Second the envisioned 5G ranging module is detailed. Third a focus is given on the correlator output mathematical models in Additive White Gaussian Noise (AWGN).

3.5.1. Systems characteristics

The complex envelope transmitted signal mathematical model (consisting in only one OFDM time symbol) has been presented in section 3.3.2.1.2. The time-continuous transmitted signal is sampled and the discrete signal mathematical model is reminded in (3.21) for the duration of an OFDM symbol.

$$s^k[n] = \sum_{q=0}^{N_{FFT}-1} d_q^k e^{\frac{i2\pi pn}{N_{FFT}}} \quad -N_{CP} \leq n \leq N_{FFT} - 1 \tag{3.21}$$

Where d_p^k is the k^{th} modulated symbol carried by the p^{th} subcarrier, N_{FFT} is the size of the FFT window, N_{CP} is the number of CP samples.

As explained in section 3.3.6, a resource grid is composed of 2 types of symbols: data and pilots. The data symbols corresponds the useful information for the user – a-priori unknown. The pilot symbols are known symbols in terms of time/frequency localization and value. Due to the knowledge of their location, pilot symbols are used to compute the correlation; thus the mathematical model presented in this thesis is based on correlation operations over reference pilot signals, a method already used in [7], [8]. In this work, the SSPBCH pilots presented in section 3.3.6.3.2 and Figure 3.28 are selected. More specifically, the focus is put on the 2nd and 4th symbols which are composed of 1 Demodulation Reference Signal (DMRS) every 4 subcarriers over 240 subcarriers, details in [14] (see Figure 3.28).

The defined OFDM signal in (3.21) is then transmitted through the propagation channel. For simplification purposes, and in order to follow the studies proposed in [7], [8], the propagation channel is assumed to be first an AWGN channel, and second is assumed to be constant over the duration of the correlation. The noiseless received signal for both cases is presented below.

3.5.1.1. Received signal in AWGN

The complex envelope CIR mathematical model of an AWGN channel can be expressed as

$$\alpha^k(t,u) = \alpha^k(u) = \alpha\delta(u - \tau_0) \tag{3.22}$$

Where α is the complex amplitude of the AWGN propagation channel and τ_0 is the propagation delay. $r_{nl}^k(t)$ can be derived as given by (3.20) (assuming $u = t$). The process has already been presented in chapter 2 section 2.3.1.

In order to simplify the notation, from now on, the term noiseless will be used to denote the mathematical models associated to the signals processing of the useful received signal without considering the noise.

$$r_{nl}^k(t) = s^k(t) * \alpha^k(t) \tag{3.23}$$

The discrete version, $r_{nl}^k[n]$, is provided in (3.24). Where $\tilde{\tau}_0 = \tau_0/T_s$ is the continuous time parameter normalized by the sampling interval.

$$r_{n_{nl}}^k = \alpha \sum_{q=0}^{N_{FFT}-1} d_q^k e^{\frac{i2\pi q(n-\tilde{\tau}_0)}{N_{FFT}}} \tag{3.24}$$

3.5.1.2. Received signal for a constant propagation channel over the correlation duration

The complex envelope CIR mathematical model of a propagation channel which is constant for the correlation's duration is given in (3.25). From now on, this type of propagation channel will be called constant propagation channel. Moreover, since the correlation will always be conducted over only one OFDM symbol, the notion of constant propagation channel over the duration of an OFDM symbol will also be used.

$$\alpha^k(t,u) = \alpha^k(u) = \sum_{l=0}^{L-1} \alpha_l^k \delta(u - \tau_l) \;\; 0 \leq u \leq T_{OFDM} \tag{3.25}$$

Where α_l^k is the channel complex amplitude for the k^{th} OFDM symbol and for the l^{th} path, and $\mathrm{T}_{\mathrm{OFDM}}$ is the OFDM symbol duration. Applying (3.23), the final expression of the received signal is provided in (3.26).

$$r_{n_{nl}}^k = \sum_{l=0}^{L-1} \alpha_l^k \sum_{q=0}^{N_{FFT}-1} d_q^k e^{\frac{i2\pi q(n-\tilde{\tau}_l)}{N_{FFT}}} \tag{3.26}$$

3.5.2. Envisioned 5G ranging module

In this section, the envisioned 5G ranging module is presented. The aim of the ranging module, as for GNSS systems (see chapter 2 section 2.4.2), is to estimate the transmitted signal propagation delay between the 5G emitter and receiver, τ_0, or in other words, to estimate the time-of-arrival (TOA).

In order to design a 5G signal ranging module performing the time-of-arrival (TOA) estimation, a classic Delay Lock Loop (DLL) is used. Remember that a DLL is a feedback closed-loop structure which, in this case, is used to maximized the Maximum Likelihood (ML) function defined as the distance between the received signal, $r^k[n]$, and the local replica, LR, $\|r^k[n] - LR(\hat{\tau})\|^2$, where $\hat{\tau}$ is the propagation delay estimated by the DLL. Moreover, remember that the synchronization block structures that solve the maximization of the ML function are optimal estimation solutions; therefore, the proposed DLL is an optimal propagation time delay estimation solution for an AWGN propagation channel. In the specific case of this Ph.D. thesis, the local replica signal only contains pilot (known) symbols; therefore, the proposed DLL correspond to a Data-Aided (DA) closed loop structure solution. Non-Data-Aided (NDA) solutions are not explored in this work. Additionally, note that the same structure could be used for time-difference-of-arrival (TDOA) but at least two 5G signals should be received; [46], [47].

The DLL block scheme is illustrated in Figure 3.32; as previously said, this scheme is adapted for an AWGN channel, and was studied in [8]. Note that the tracking step provided by Figure 3.32 must be preceded by an acquisition step to achieve an initial rough synchronization with the incoming signal. A possible example of the acquisition process consists in using first the Van de Beek algorithm (before CP removal), [48], followed by the matching pursuit algorithm (after CP removal, using correlator outputs), presented in [8]. The tracking of the roughly estimated propagation delays obtained during the acquisition phase is then conducted by the DLL. In order to illustrate the structure of the generic DLL diagram block, the case of an AWGN channel will be presented.

As presented in Figure 3.32, to implement the discriminator, the DLL makes use of the correlation operation between the incoming signal, r_n^k, which contains the desired code delay to be estimated $\tilde{\tau}_0$, and

a local replica, LR, which contains the propagation delay estimated by the DLL denoted as $\hat{\tau}$. The correlation is performed on the pilot symbols that are present in the 5G Synchronization Signals. More specifically, the correlation is computed at three points spaced by a distance d called the correlator spacing.

- $LR[\hat{\tau} - \delta/2]$ for the early correlator output: $R_E(\varepsilon_\tau)$
- $LR[\hat{\tau}]$ for the prompt correlator output: $R_P(\varepsilon_\tau)$
- $LR[\hat{\tau} + \delta/2]$ for the late correlator output: $R_L(\varepsilon_\tau)$

Where $\varepsilon_\tau = \tilde{\tau}_0 - \hat{\tau}$ is defined as the propagation delay estimation error. The chosen discriminator is the Early Minus Late Power (EMLP) defined in (3.27) and studied in [6]:

$$D_{EMLP}^{norm}(\varepsilon_\tau) = \frac{|R_E(\varepsilon_\tau)|^2 - |R_L(\varepsilon_\tau)|^2}{K_{norm}|R_P(\varepsilon_\tau)|^2} \tag{3.27}$$

This discriminator is normalized by K_{norm} such that $D_{EMLP}^{norm}(\varepsilon_\tau) \approx \varepsilon_\tau$ for ε_τ close to 0, its expression is derived in Annex F.1. The discriminator output is then filtered by a low-pass filter. Finally, the new delay estimate, $\hat{\tau}$, is determined by using a DCO (Digitally Controlled Oscillator), the new local replica signals are generated and new Early, Prompt and Late correlator outputs are computed.

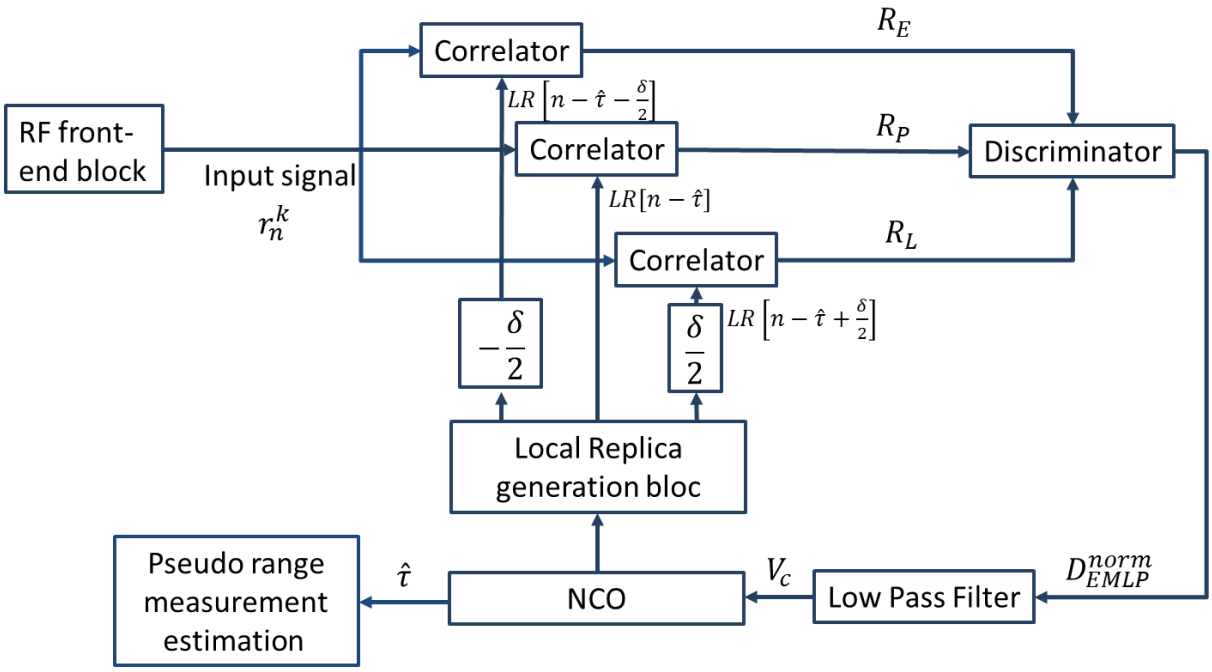

Figure 3.32 – Delay Lock Loop architecture

3.5.3. Correlator output mathematical model in AWGN

In this section, the correlation operation is first presented; then the application in the case of an AWGN is provided.

3.5.3.1. General correlator output mathematical model

The correlation operation can be defined for an OFDM symbol from its direct time-domain expression or from the equivalent frequency-domain expression, see Figure 3.33. In the time domain, the incoming signal is multiplied with the local replica, and then accumulated (integration and dump) to get the correlation result. In the frequency domain, a FFT is applied to the incoming signal, multiplied with the

FFT of the local replica, LR, and, an iFFT evaluated in 0 (first term of the iFFT output) is performed to the previous multiplication result in order to come back to the time domain. Remind that the local replica is generated according to the pilot sequence only.

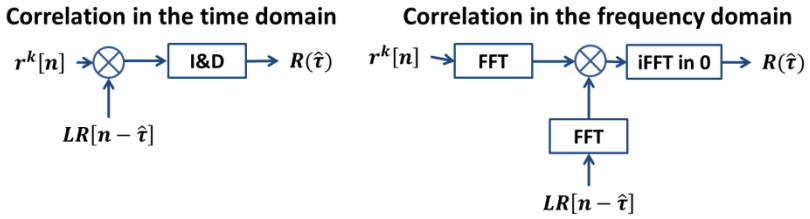

Figure 3.33 – Correlation operation presentation

Additionally, note that the received signal is also demodulated by applying a FFT; therefore, to conduct the correlation process in the frequency domain will not require more complexity to the receiver.

$$\hat{d}_{q'}^{k} = FFT(r^k[n])[q'] = \frac{1}{N_{FFT}} \sum_{n=0}^{N_{FFT}-1} r_n^k \, e^{-i2\pi \frac{nq'}{N_{FFT}}} \tag{3.28}$$

For an AWGN channel, if $\tilde{\tau}_0$ is accurately estimated ($\tilde{\tau}_0 \approx \hat{\tau}$), the demodulated symbol is equal to the transmitted one (corrupted by the presence of noise, $b_{q'}^k$): $\hat{d}_{q'}^k = d_{q'}^k + b_{q'}^k$.

Due to the reutilization of the FFT module and due to the facility to tune the propagation delay estimation, $\hat{\tau}$, the frequency domain correlation is preferred in this work.

The general correlation formula is presented in (3.29):

$$R(\varepsilon_\tau) = \frac{1}{N_P} \sum_{q' \in P} \hat{d}_{q'}^k \cdot FLR_{q'}^{k*}[\hat{\tau}] \tag{3.29}$$

$$FLR_{q'}^{k}[\hat{\tau}] = \mathrm{FFT}(LR^k[\hat{\tau}])_{q'} = p_{q'}^k e^{-\frac{2i\pi q'}{N_{FFT}}\hat{\tau}} \tag{3.30}$$

Where $FLR_{q'}^k[\hat{\tau}]$ is the local replica with $p_{q'}^k$ the pilot symbol localized in the q'^{th} subcarrier on the k^{th} OFDM symbol, N_p is the number of pilot symbols, $\hat{d}_{q'}^k$ is the demodulated symbols and P is the set of pilots. Note that the local replica only includes pilot symbols and does not consider the data symbols. In order to have a generic formula, the set of pilots P can be defined as: $P = \gamma q' + \beta$. Where γ is the period of repetition of the pilots in the OFDM symbol, $q' \in [0 \dots N_P - 1]$ and β is the subcarrier index of the first pilot in the symbol.

3.5.3.2. Correlator output mathematical model for a constant channel

For a constant propagation channel, in order to obtain the demodulated symbols mathematical model, (3.26) is used in (3.28); it leads to (3.33). Note that the following demonstration is performed assuming a useful received signal without the noise.

$$\hat{d}_{nl,q'}^k = \frac{1}{N_{FFT}} \sum_{n=0}^{N_{FFT}-1} \sum_{l=0}^{L-1} \alpha_l^k \sum_{q=0}^{N_{FFT}-1} d_q^k e^{\frac{i2\pi q(n-\tau_l)}{N_{FFT}}} e^{-i2\pi \frac{nq'}{N_{FFT}}} \tag{3.31}$$

$$\hat{d}_{nl,q'}^k = \frac{1}{N_{FFT}} \sum_{l=0}^{L-1} \alpha_l^k \sum_{q=0}^{N_{FFT}-1} d_q^k e^{-\frac{i2\pi q\tau_l}{N_{FFT}}} \sum_{n=0}^{N_{FFT}-1} e^{\frac{i2\pi n(q-q')}{N_{FFT}}} \tag{3.32}$$

$$\hat{d}_{nl,q'}^{k}=\begin{cases}\sum_{l=0}^{L-1}\alpha_l^k\sum_{\substack{q=0\\q\neq q'}}^{N_{FFT}-1}d_q^k e^{-\frac{i2\pi q\tau_l}{N_{FFT}}}\cdot\dfrac{\sin\left(\pi(q-q')\right)}{\sin\left(\dfrac{\pi(q-q')}{N_{FFT}}\right)}e^{\frac{i\pi(q-q')(N_{FFT}-1)}{N_{FFT}}}=0 & q\neq q'\\ \sum_{l=0}^{L-1}\alpha_l^k d_{q'}^k e^{-\frac{i2\pi q'\tau_l}{N_{FFT}}} & q=q'\end{cases} \tag{3.33}$$

The correlation is then obtained by using (3.33) in (3.29), the correlator output is derived in the next equations.

$$R_{nl}(\varepsilon_\tau)=\frac{1}{N_P}\sum_{q'\in P}\sum_{l=0}^{L-1}\alpha_l^k d_{nl,q'}^k e^{-\frac{i2\pi q'\tau_l}{N_{FFT}}}\cdot p_{q'}^{k*}e^{\frac{2i\pi q'}{N_{FFT}}\hat{\tau}} \tag{3.34}$$

$$R_{nl}(\varepsilon_\tau)=\sum_{l=0}^{L-1}\frac{\alpha_l^k}{N_P}\sum_{q'\in P}d_{nl,q'}^k\cdot p_{q'}^{k*}e^{\frac{i2\pi q'(\hat{\tau}-\tau_l)}{N_{FFT}}} \tag{3.35}$$

From now on, $\varepsilon_{\tau_l}=\hat{\tau}-\tau_l$ represents the estimation delay error.

In order to have a general formula, the set of pilots P is noted as $P=\gamma q'+\beta$, where γ is the period of repetition of the pilots $q'\in[0\dots N_P-1]$ and β is the subcarrier index of the first pilot in the symbol. In order to visualize this, note that Figure 3.28 corresponds to the case where $\gamma=4,\beta=0$. Note that in (3.35) the sum is performed over the pilots symbols thus the data symbols, $d_{nl,q'}^k$, are actually pilots and can be written, $p_{q'}^k$, as in (3.36).

$$R_{nl}(\varepsilon_\tau)=\sum_{l=0}^{L-1}\frac{\alpha_l^k}{N_P}\sum_{q'=0}^{N_P-1}p_{q'}^k\cdot p_{q'}^{k*}e^{\frac{i2\pi(\gamma q'+\beta)\varepsilon_{\tau_l}}{N_{FFT}}} \tag{3.36}$$

The pilot power is normalized, $p_{q'}^k\cdot p_{q'}^{k*}=1$.

$$R_{nl}(\varepsilon_\tau)=\sum_{l=0}^{L-1}\frac{\alpha_l^k}{N_P}e^{\frac{i2\pi\beta\varepsilon_{\tau_l}}{N_{FFT}}}\sum_{q'=0}^{N_P-1}e^{\frac{i2\pi\gamma q'\varepsilon_{\tau_l}}{N_{FFT}}} \tag{3.37}$$

$$R_{nl}(\varepsilon_\tau)=\sum_{l=0}^{L-1}\alpha_l^k R_{nl,l}(\varepsilon_{\tau_l}) \tag{3.38}$$

$$R_{nl,l}(\varepsilon_{\tau_l})=\frac{1}{N_P}e^{\frac{i2\pi\beta\varepsilon_{\tau_l}}{N_{FFT}}}\sum_{q'=0}^{N_P-1}e^{\frac{i2\pi\gamma q'\varepsilon_{\tau_l}}{N_{FFT}}} \tag{3.39}$$

$$R_{nl,l}(\varepsilon_{\tau_l})=\begin{cases}\dfrac{1}{N_P}e^{\frac{i2\pi\beta\varepsilon_{\tau_l}}{N_{FFT}}}\dfrac{sin\left(\frac{\pi\gamma\varepsilon_{\tau_l}N_P}{N_{FFT}}\right)}{sin\left(\frac{\pi\gamma\varepsilon_{\tau_l}}{N_{FFT}}\right)}e^{\frac{i\pi\gamma(N_P-1)\varepsilon_{\tau_l}}{N_{FFT}}} & \varepsilon_{\tau_l}\neq 0\\ 1 & \varepsilon_{\tau_l}=0\end{cases} \tag{3.40}$$

Finally, the correlator output mathematical model for a constant propagation channel is provided in (3.41).

$$R_{nl}(\varepsilon_\tau)=\sum_{l=0}^{L-1}\alpha_l^k R_{nl,l}(\varepsilon_{\tau_l})$$

$$R_{nl,l}(\varepsilon_{\tau_l})=\begin{cases}\frac{1}{N_P}\,e^{\frac{i\pi\left(2\beta+\gamma(N_P-1)\right)\varepsilon_{\tau_l}}{N_{FFT}}}\dfrac{sin\left(\frac{\pi\gamma\varepsilon_{\tau_l}N_P}{N_{FFT}}\right)}{sin\left(\frac{\pi\gamma\varepsilon_{\tau_l}}{N_{FFT}}\right)} & \varepsilon_{\tau_l}\neq 0\\ 1 & \varepsilon_{\tau_l}=0\end{cases} \tag{3.41}$$

This formula has been validated using the second symbol of the SSPBCH block ($\gamma=4,\beta=0$). Note that for simplification purposes, it is assumed that each consecutive symbol is identical and corresponds to the second symbol of the SSPBCH block. Therefore, a simplified 5G frame is considered.

In Figure 3.34, the correlator output mathematical model (3.41) is compared to the true correlator output (simulation of the complete generation/reception signal chain until the correlation operation for a QuaDRiGa constant propagation channel) in terms of modulus and phase. The left side of the figure presents the 2 results, which are superimposed, and the right side presents the difference from one to the other:

- Up: in terms of modulus: $|Real| - |Model|$, the averaged relative error equals $5.8782.10^{-13}\%$
- Bottom: in terms of phase: $\theta_{Real} - \theta_{Model}$, the averaged relative error equals $1.1526.10^{-12}\%$

These results prove the validity of the mathematical model.

The correlator outputs derived in the section are used by the ranging module to track the signal delays which determine the pseudo range measurements. As it has been shown on this sub-section, the correlation operation is the basis of the ranging module. Therefore, the correct mathematical modelling of its output is mandatory in order to develop a ranging module adapted to the targeted propagation channel and 5G signal.

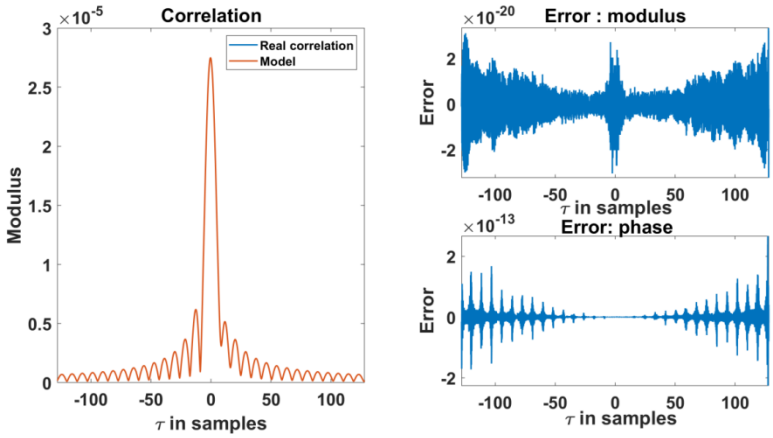

Figure 3.34 – Correlation model validation

3.6. Pseudo range measurement model

The receiver presented in the previous section makes use of correlator outputs to track the signal delay. This delay is then used to determine the pseudo range measurement model. These pseudo range measurements are then used by the navigation filter presented in Chapter 7 in order to determine the receiver position. In this section the 5G pseudo range measurement model is presented.

Ideally, the distance between the receiver and the transmitter can be computed by determining the transmission time of the signal. In other words, the distance can be obtained by subtracting the transmission and reception time and multiplying by the speed of light as shown in (3.42).

$$r_{5G_j} = c \cdot \left(t_{Reception} - t_{Transmission}\right) \tag{3.42}$$

However as for GNSS systems, the receiver clock time frame and the Base Station time frame are not necessarily synchronized. Moreover, each Base Station with respect to the reference 5G time frame might not be synchronized either. Therefore, for 5G systems as well, a pseudo distance is defined as proposed in (3.43) by the difference between the received time (in the receiver time frame) as for GNSS and the emission time which is, as for GNSS, the BS clock reading at time which the signal left the BS.

$$\rho_{5G_j} = c \cdot \left(t_{user,RX} - t_{BS_j,TX}\right) \tag{3.43}$$

Where:

- ρ_{5G_j} is the pseudo-distance measured for the j^{th} Base Station by the receiver
- c is the speed of the light
- $t_{user,RX}$ is the reception time expressed in the receiver clock time frame
- $t_{BS_j,TX}$ is the emission time expressed in the emitter clock time frame

Each time can be expressed in the 5G reference clock time frame as follow

- The reception time is expressed in the 5G reference time frame as $t_{user,RX} = t_{5G,RX} + \Delta t_{5G/user}$ where $\Delta t_{5G/user}$ is the time shift of the receiver clock with respect to the 5G clock time frame.
- The emission time is expressed in the reference time frame as $t_{BS_j,TX} = t_{5G,TX} + \Delta t_{5G/BS_j}$, where $\Delta t_{5G/BS_j}$ is the time shift of the j^{th} Base station clock with respect to the 5G clock time frame

The pseudo distance measured for the j^{th} Base Station by the user in 5G reference clock time frame is thus modeled as:

$$\rho_{5G_j} = c \cdot \left(t_{user,RX} - t_{BS_j,TX}\right) \tag{3.44}$$

$$\rho_{5G_j} = c \cdot \left(t_{5G,RX} + \Delta t_{5G/user} - t_{5G,TX} - \Delta t_{5G/BS_j}\right) \tag{3.45}$$

$$\rho_{5G_j} = c \cdot \left(t_{5G,RX} - t_{5G,TX}\right) + c \cdot \Delta t_{5G/user} - c \cdot \Delta t_{5G/BS_j} \tag{3.46}$$

$$\rho_{5G_j} = c \cdot dt_j + c \cdot \Delta t_{5G/user} - c \cdot \Delta t_{5G/BS_j} \tag{3.47}$$

Where $c \cdot dt_j = r_{5G_j}$ is the geometric distance between the receiver and the j^{th} 5G base station. Finally the pseudo range model is expressed as (3.48).

$$\rho_{5G_j} = r_{5G_j} + c \cdot \Delta t_{5G/user} - c \cdot \Delta t_{5G/BS_j} \tag{3.48}$$

Note that contrary to the GNSS pseudo range measurement model, since 5G transmissions are at the ground level, there are no tropospheric or ionospheric delays. Nevertheless, multipath components can create an additional delay, $\varepsilon_{multipath}$. Thus, the pseudo range model can be expressed as

$$\rho_{5G_j} = r_{5G_j} + c \cdot \Delta t_{5G/user} - c \cdot \Delta t_{5G/BS_j} + \varepsilon_{multipath} \tag{3.49}$$

3.7. Chapter conclusion

The aim of the chapter is to provide a global overview of 5G systems and to present the signal processing adopted in the receiver in order to obtain the required measurements when an AWGN channel is considered. The aim of the designed receiver is to extract Time Of Arrival (TOA) measurements from the received signal. The chapter provides a thorough description of the 5G systems. Since 5G is an emerging technology, the 5G systems history has been given as well as the envisioned use cases.

Three radio-based positioning methods have been presented in the chapter: the signal strength based method, the Angle of Arrival method and the Time of Arrival method. The first two has not been selected for the Ph.D., the signal strength method requires data base and has an uncertainty of several meters and the AoA method requires a lot of hypothesis regarding the receiving and emitting antennas. Therefore, the rest of the Ph.D. will be based on ToA measurements.

The signal transmitted by 5G BS has been precisely described. In order to determine the most optimal signal processing techniques, it is of the utmost importance to precisely know the mathematical model of the transmitted signal. The generated signal goes through the propagation channel which should also be carefully modelled in order to have a realistic mathematical model of the received signal. For realism purposes, a deep state of the art has been performed in order to identify the potential propagation

channel projects that could be used for the Ph.D. The objective of the study is to identify a 5G compliant and an easy-to-use propagation channel. The final choice is QuaDRiGa; it is an open-source simulator following the 3GPP standard, [43]. It fulfills the 5G propagation channel requirements; moreover, it is a GSCM, thus proposes a fair trade between complexity and realism. Then a description of the main techniques for ToA measurements on OFDM signals has been provided. The focus has been made on the 5G synchronization signal SSPBCH. In the fifth section the envisioned 5G ranging module has been presented with a particular application for an AWGN case. Finally, the pseudo range model in AWGN channel has been derived. This model will be completed in later chapter with the impact of the multipaths.

Chapter 4. Mathematical Models and Statistics of Processed 5G Signals for Ranging Based Positioning for a Realistic Propagation Channel

The OFDM signal-type correlator output mathematical model presented in the previous chapter is derived by assuming a constant propagation channel over the duration of the correlation (which is performed over one OFDM symbol). Nevertheless, as it will be shown in this chapter, the Channel Impulse Response (CIR) of a 5G signal propagation channel (QuaDRiGa is selected in this Ph.D. thesis) cannot be considered as constant over the duration of the correlation: the expected correlator output of a 5G signal is thus different between a time-evolving propagation channel and a constant one over the duration of the correlation, performed over an OFDM symbol.

However, in order to precisely characterize the performances of the 5G signals for ranging purposes, a precise and realistic correlator output mathematical model is required. This means that the correlation output model presented in chapter 3 section 3.5.3 obtained when assuming a constant propagation channel over the duration of an OFDM symbol may be insufficient, and that new correlator output mathematical models in time-evolving propagation channel must be derived.

In order to derive this precise and realistic correlator output mathematical model, it is thus of the utmost importance to precisely model the received 5G signal and, by extension, the interferences distorting the signal introduced by the propagation channel with as much realism as possible; or in other words, the CIR.

Note that, although the ultimate goal of this chapter is to derive the correlator output mathematical model of a 5G signal for ranging purposes, intermediates steps such as the correct characterization of the CIR propagation channel, the effect of the time-evolving CIR on the symbol demodulation process as well as the impact of the noise along all the 5G processing stages, up to the correlator output, must be correctly modelled. Moreover, since the ultimate goal is to derive the correlator model mathematical model for ranging purposes, the general criterion used along this chapter to determine whether the derived models and parameters models are sufficiently tuned will be based on the inspection of the time delay tracking results.

The structure of this chapter is thus as follows. First, the impact of a realistic time evolving propagation channel is presented; this impact analysis includes the inspection of the signal parameters evolution in time and the determination of the CIR sampling time. Second, the correlator output mathematical model for a time-evolving propagation channel is derived.

4.1. Impact of a time evolving channel

5G standard compliant propagation channel impulse responses evolve in time and thus, a new correlator output mathematical model should be derived for them. The first step to answer this question consists thus in correctly modeling the propagation channel and its parameters in order to analyze their impact on the correlator output of a 5G signal.

In this work, the chosen propagation channel model is QuaDRiGa, [17]. Moreover, the time-continuous propagation channel is approximated by a time-discrete model (discrete CIR). Therefore, the determination of the sampling rate to be applied to the time-continuous channel to derive the discrete channel, denoted CIR sampling rate, is one of the key parameters and is of the utmost importance. The targeted sampling rate must be high enough to allow a realistic approximation of the time-continuous

propagation channel, but at the same time, it is of interest to have a low sampling rate to simplify the mathematical model. Note that this approximation does not affect the impact of the time-continuous propagation channel on the received signal since at the ADC/AGC block output, the time-continuous propagation channel CIR is indeed sampled. Moreover, note that the ADC sampling rate and the CIR sampling rate are different, and that the former one is going to be much higher than the latter one as is shown in this work. Finally, note that the CIR sampling rate determination is made in this work for the QuaDRiGa propagation channel model; however, the applied methodology can be reused for any other propagation channel model.

In order to conduct this study, first the CIR sampling rate is formally defined; second, the trajectories (which generate different propagation channels and associated CIR as seen in section 4.1.2) used later on for testing purpose are described. Third, the CIR candidates are presented. Fourth, the propagation channel time-varying parameters are analyzed. Fifth, the CIR sampling interval is determined to accurately model the correlator outputs mathematical models to be used for ranging purposes. A summary concludes this section.

4.1.1. CIR sampling rate

4.1.1.1. CIR sampling rate definition

In this work, the CIR sampling rate is defined as the sampling rate applied to the time-continuous CIR to derive the discrete CIR; in other words, it is the number of CIR samples directly generated by the discrete propagation channel model (QuaDRiGa in this case) over the duration of an OFDM symbol, T_{OFDM}. However, the number of signal samples per OFDM symbol at the Radio Frequency Front-End (RFFE) block output of a receiver is not determined by the CIR sampling rate but rather by the ADC sampling rate. This means that the role of the CIR sampling rate in the received signal model is to determine the number of RFFE output signal samples affected by the same CIR coefficient(s).

For example, Figure 4.1 shows the time evolution of a given CIR for different CIR sampling rate values: assuming that an OFDM symbol is composed of N signal samples and assuming a CIR sampling rate of X samples/OFDM symbol, then, the applied channel coefficients are constant over N/X RFFE output samples.

In the following, the notation “XCIR samples per OFDM symbol” is equivalent to a CIR sampling rate of X samples per OFDM symbol. Moreover, a “XCIR propagation channel” means a propagation channel with a CIR sampled at a CIR sampling rate of X samples per OFDM symbol.

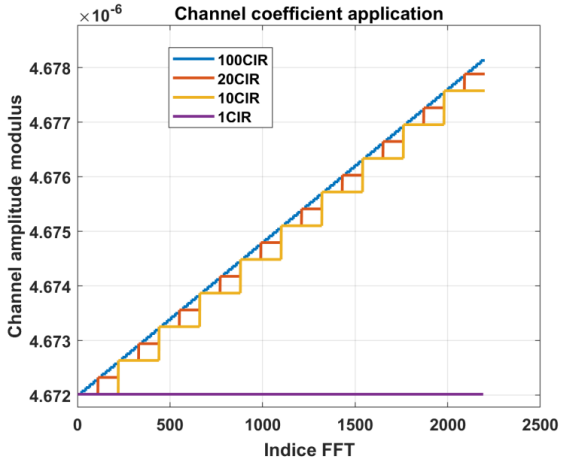

Figure 4.1 – Channel coefficients modulus over the OFDM symbol

4.1.1.2. CIR sampling rate impact

The CIR sampling rate has a non-negligible impact on the correlator output mathematical model of a 5G signal and must be considered. This statement is illustrated in Figure 4.2, where the study of the correlation function with several CIR sampling rates is illustrated.

The correlation function provided in Figure 4.2 is determined for a QuaDRiGa propagation channel composed of a LOS path and 33 multipaths for one random instant. The symbol considered corresponds to the 2nd symbol of the SS PBCH block described in chapter 3 (one pilot every 4 subcarriers over 240 subcarriers). On the left, the correlation functions moduli are provided for $X = 100, 20, 10$ and 1 CIR sampling rates. On the upper right, the absolute evolutions of the correlation functions moduli (denoted AE) obtained for 20, 10 and 1 CIR with respect to 100 CIR are provided. On the bottom right, the same is provided but in terms of phase. Naturally, as the sampling interval increases, the AE gets closer to 0. In order to quantify these impacts, the Root Mean Square Errors (RMSE) are provided in Table 4.1.

These differences between correlation functions will naturally impact the DLL discriminator outputs, defined in chapter 3 section 3.5.2, and thus the delay estimates and finally the tracking performances. Remember that the targeted correlator output mathematical model is desired for ranging purposes and thus the final selection criterion will be the tracking results as discussed in 4.1.5. In order to numerically quantify the example presented in Figure 4.2, Table 4.1 is provided. The first two lines present the RMSE difference between the correlation function computed over a delay range of 15 OFDM samples (centered on the peak of the correlation function) using 100 CIR and the 3 others sampling rates; the difference is given in term of modulus and phase. The last line presents the difference between the tracking loop discriminator outputs obtained for 100 CIR and the 3 other samplings, for an Early-Minus-Late-Power discriminator with a correlator spacing of 4 samples.

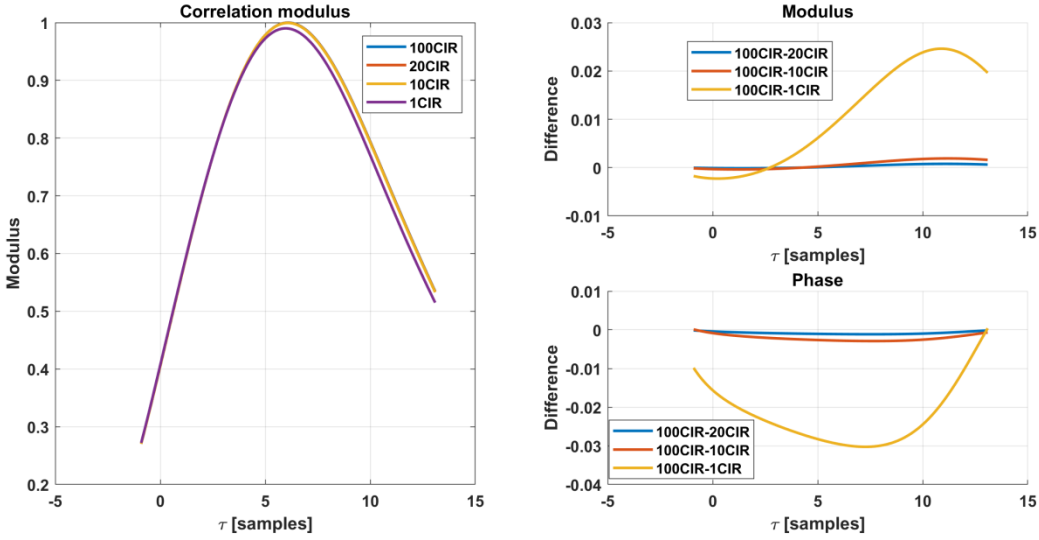

Figure 4.2 – Comparison of the correlation function when different CIR sampling intervals are applied

Table 4.1 – Root Mean Square Error of the correlation function CIR impact

	100CIR-20CIR	100CIR-10CIR	100CIR-1CIR
Modulus RMSE	5.0781e-04	0.0013	0.0127
Phase RMSE	0.0015	0.0033	0.0408
Discriminator outputs [m]	0.0378	0.0952	1.0895

In the following part of this chapter, several CIR sampling rate values have been compared in order to choose the most suitable CIR sampling rate in terms of time-continuous propagation channel representativeness for 5G signal ranging purposes and mathematical model simplification purposes.

Finally, the reader must be aware that simulations have shown that the propagation channel generated for 200 CIR per OFDM symbol is equivalent to the propagation channel generated for 100 CIR per OFDM symbol since the difference between the propagation channels generated at 100 CIR and at 200 CIR per OFDM symbol in terms of DLL discriminator output is negligible. Therefore, in this work, it has been assumed that using 100 CIR per OFDM symbol is equivalent to, or enough to represent, a time-continuous channel. From now on, the 100 CIR propagation channel is considered as the reference channel. In other words, it can be said that the coherence time (time interval while the propagation channel is constant) of the QuaDRiGa propagation channel corresponds to 100 CIR per OFDM symbol.

4.1.2. Simulated scenarios presentation

CIR sampling rate determination process must be valid regardless of the considered scenarios. To guarantee this validity, extra care must be taken on the selection of the analyzed scenarios. Note that, as presented in the previous chapter, the propagation channel model selected for the thesis is QuaDRiGa. The scenario design of the propagation channel to be simulated by QuaDRiGa is made through the selection of 3 parameters: high-level scenario, receiver's trajectory and signal characteristics.

First, concerning the high-level scenarios, two configurations proposed by QuaDRiGa, [17], have been selected: 3GPP_38.901_UMi_NLOS and 3GPP_38.901_UMi_LOS. Both configurations model typical terrestrial pico-base stations deployed below rooftop in densely populated urban areas covering carrier frequencies from 500 MHz to 100 GHz. The interest in choosing these high-level scenarios is twofold. First, both follow the 3GPP standard on 5G propagation channel: TS.38.901, [49], especially regarding the frequency range. Second, they model Urban Micro-Cell environment which fits with the targeted problematic (constrained environment). The LOS scenario is a favorable case: LOS signal has higher power than multipath. The Non-Line-Of-Sight (NLOS) scenario is a non-favorable case: multipath signals are more powerful than the LOS.

Second, concerning the trajectories, since the selected scenario simulates pico-base stations which have typically a 4-to-200 m-radius-size, 4 trajectories have been studied. The first one is a radial trajectory beginning at 75 m from the Base-Station and moving away (trajectory 1), the last 3 represent a few meter-long arc of a 50 m (trajectory 2), 100 m (trajectory 3) and 150 m-radius circle (trajectory 4) at $v = 50\ km/h$. They are all illustrated in Figure 4.3. The length of trajectory is 25 m approximately.

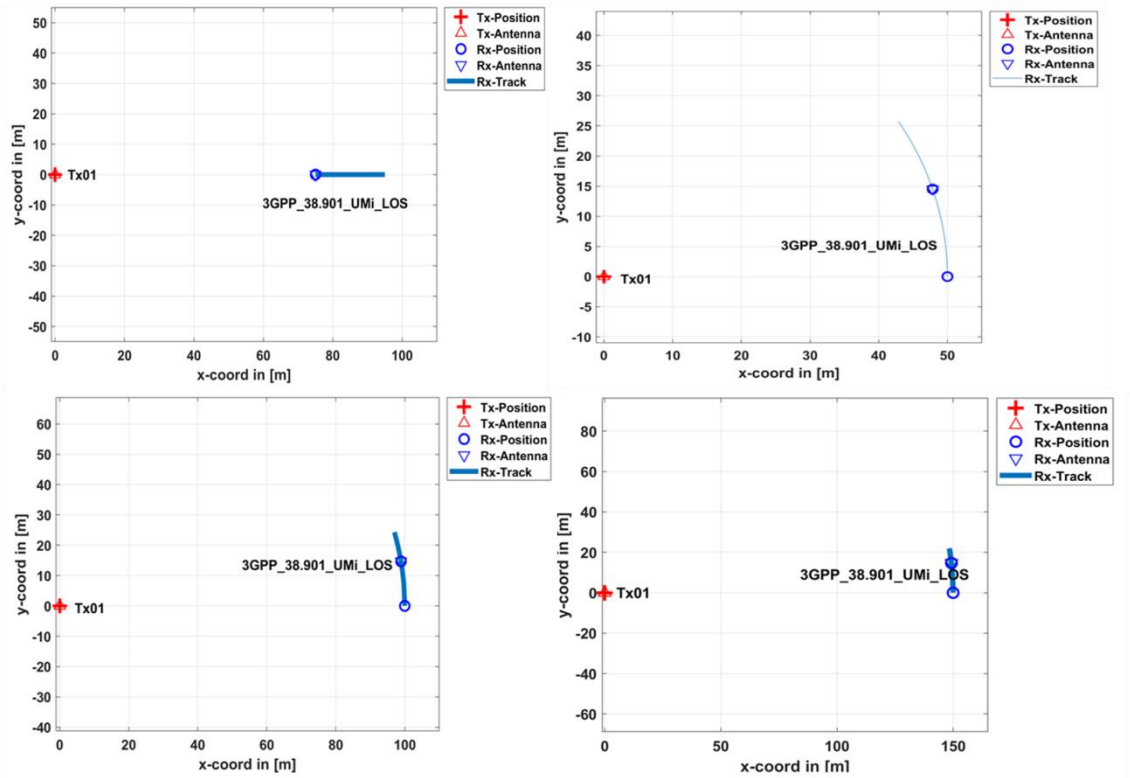

Figure 4.3 – Trajectories of the simulated scenarios

Third and last, regarding the 5G signal characteristics, 2 cases are considered, which are assumed to be representative 5G system configurations:

- Case 1: carrier frequency set to 2 GHz, subcarrier spacing to 15 kHz.
- Case 2: carrier frequency set to 60 GHz, subcarrier spacing to 120 kHz.

A simplified 5G frame is considered, it is the repetition of one symbol which corresponds to the 2nd (or 4th) symbol of the SS PBCH synchronization block presenting in chapter 3 section 3.3.6.3.2. As a reminder, this symbol is composed of one pilot (DMRS) every 4 subcarriers over 240 subcarriers.

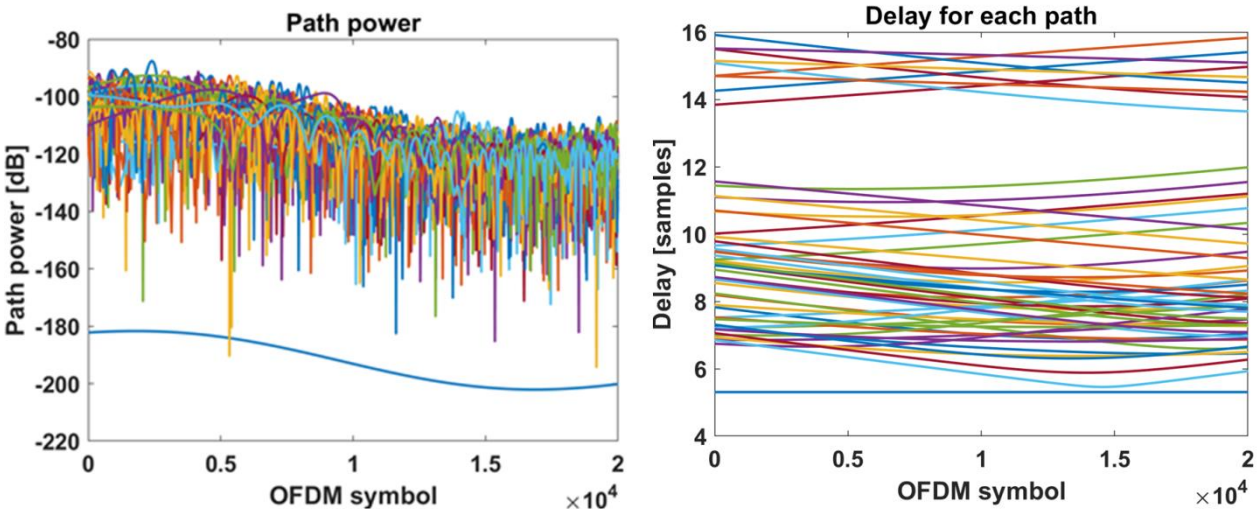

Figure 4.4 – "3GPP_38.901_UMi_NLOS" scenario Case 1 – trajectory 2 – QuaDRiGa

In Figure 4.4, an example of the path powers and delays simulated for the NLOS scenario, Case 1 and trajectory 2 is provided.

An additional comment must be given concerning the interest of the association between the 5G signal characterization and the high-level scenario. The 4 possible associations are:

- Case 1 and LOS scenario.
- Case 1 and NLOS scenario.
- Case 2 and LOS scenario.
- Case 2 and NLOS scenario.

As stated in chapter 3 section 3.2.1.1, the use of millimeter waves has consequences on the propagation properties and the ranges for which the signal can be exploited are shorter than for Case 1. Moreover, the expected 5G deployment implies a dense network and therefore a high number of BS available at each instant. It is thus assumed that case 2 in NLOS scenario is not representative in terms of potential 5G signal use for positing purposes with respect to the 3 other scenarios. Nevertheless, for the sake of completeness, case 2 in NLOS scenario will be still analyzed along the other scenarios.

4.1.3. CIR sampling rate candidates

In order to be able to determine the most suitable CIR sampling rate, different figures of merit are evaluated and compared to a reference. The sampling rate of 100 CIR per OFDM symbol is considered as the reference in this work (equivalent to a time-continuous channel as confirmed by simulations with higher CIR sampling rates, it is the coherence time of the channel). Three CIR sampling rates are investigated and compared to this reference: 1, 10, 20 CIR per OFDM symbol. Note that 1 CIR sampling rate simulates a constant channel, assumed a priori to be insufficient to model appropriately the 5G propagation channel for ranging purpose.

4.1.4. Analysis of the propagation channel time varying parameters

To properly model the evolution of the propagation channel, and to be able to determine the most suitable CIR sampling rate, the first step to conduct is to identify the significant time-varying channel parameters. Note that this analysis is similar to inspect the channel parameters evolution with respect to a coherence time of the channel but restricted to the duration of the coherent integration (correlation) time. To do so, the evolution of the channel is studied with respect to the delay τ_l^k and the complex amplitude (phase and modulus) α_l^k of the LOS and multipaths CIR, in terms of absolute evolution (denoted AE) and relative evolution (denoted RE). In other words, the time coherency of the channel is analyzed for the mentioned parameters.

4.1.4.1. Evolution of the path delays

In order to study the evolution of the path delays over one OFDM symbol, the first step to conduct is to derive the mathematical model of the demodulated symbol considering non-constant path delays. The propagation channel model adopted for this study is defined in (4.1).

$$\alpha^k(t,\tau) = \sum_{l=0}^{L-1} \alpha_l^k(t,\tau)$$
$$\alpha_l^k(t,\tau) = \alpha_l^k(t) \cdot \delta\big(\tau - \tau_l(t)\big), 0 \le t \le T_{OFDM} \tag{4.1}$$

The noiseless digital received signal, $r_{n\ nl}^k$, presented in (3.26) as a function of the transmitted signal and of the CIR mathematical model, is consequently defined as in (4.2).

$$r_{n\ nl}^k = \sum_{l=0}^{L-1} \alpha_l^k(n) \sum_{q=0}^{N_{FFT}-1} d_q^k e^{\frac{i2\pi q(n-\tilde{\tau}_l(n))}{N_{FFT}}} \tag{4.2}$$

Where $\tilde{\tau}_l(n) = \frac{\tau_l(nT_s)}{T_s}$ is the normalized evolving path delay for the l^{th} path. Assuming that the path delay's evolution is linear over 1 OFDM symbol, $\tilde{\tau}_l(n)$ can be modelled as $\tilde{\tau}_l(n) = n\dot{\tilde{\tau}}_l + \tilde{\tau}_{l_0}$. Where $\tilde{\tau}_{l_0}$ is the initial delay and $\dot{\tilde{\tau}}_l$ the delay's evolution rate over the OFDM symbol.

In order to study the impact of the evolution of the delay over the duration of an OFDM symbol, for simplification purposes, the complex amplitude of the propagation channel is assumed to be constant over an OFDM symbol: $\alpha_l^k(n) = \alpha_l^k\ for\ n \in [0, N_{FFT}-1]$.

Finally, the FFT is applied to demodulate the signal and the obtained model is provided in (4.5). In (4.5), assuming that $\alpha_l^k(n)$ is constant over the duration of a symbol, the sum over n is a geometric sum which can be derived as in (4.6).

$$\hat{d}_{q'}^k = \frac{1}{N_{FFT}} \sum_{n=0}^{N_{FFT}-1} r_{n\ nl}^k e^{\frac{-2i\pi q' n}{N_{FFT}}} \tag{4.3}$$

$$\hat{d}_{q'}^k = \frac{1}{N_{FFT}} \sum_{n=0}^{N_{FFT}-1} \left(\sum_{l=0}^{L-1} \alpha_l^k \sum_{q=0}^{N_{FFT}-1} d_q^k e^{\frac{i2\pi q(n-\tilde{\tau}_l(n))}{N_{FFT}}} \right) e^{\frac{-2i\pi q' n}{N_{FFT}}} \tag{4.4}$$

$$\hat{d}_{q'}^k = \sum_{l=0}^{L-1} \frac{\alpha_l^k}{N_{FFT}} \sum_{q=0}^{N_{FFT}-1} d_q^k\, e^{-\frac{i2\pi q\tilde{\tau}_{l_0}}{N_{FFT}}} \sum_{n=0}^{N_{FFT}-1} e^{\frac{i2\pi(q(1-\dot{\tilde{\tau}}_l)-q')n}{N_{FFT}}} \tag{4.5}$$

$$\sum_{n=0}^{N_{FFT}-1} e^{\frac{i2\pi(q(1-\dot{\tilde{\tau}}_l)-q')n}{N_{FFT}}}$$
$$= \begin{cases} \dfrac{1-e^{i2\pi(q(1-\dot{\tilde{\tau}}_l)-q')}}{1-e^{\frac{i2\pi(q(1-\dot{\tilde{\tau}}_l)-q')}{N_{FFT}}}} = e^{\frac{i\pi(q(1-\dot{\tilde{\tau}}_l)-q')}{N_{FFT}}(N_{FFT}-1)} \cdot \dfrac{\sin\left(\pi\left(q\left(1-\dot{\tilde{\tau}}_l\right)-q'\right)\right)}{\sin\left(\dfrac{i\pi\left(q\left(1-\dot{\tilde{\tau}}_l\right)-q'\right)}{N_{FFT}}\right)} & \left(q\left(1-\dot{\tilde{\tau}}_l\right)-q'\right) \neq 0 \\ N_{FFT} & \left(q\left(1-\dot{\tilde{\tau}}_l\right)-q'\right) = 0 \end{cases} \tag{4.6}$$

Using the first line in (4.6); it can be seen that the normalized evolution of the path delays has an impact on the demodulated symbol only if they are significant compared to 1: if $\dot{\tilde{\tau}}_l \ll 1$, the last term of equation (4.6) can be approximated as $\delta[q-q']N_{FFT}$ and the constant delay demodulation mathematical model can be applied. Therefore, the second step of the study is to compare the normalized path delays evolution rate, $\dot{\tilde{\tau}}_l$, with respect to 1 for all trajectories.

The method used to study the evolution of the path delays consists in comparing the evolution of the delay applied to the sample n, $\tau_l(n)$, and the delay applied to sample $n+100$, $\tau_l(n+100)$, with the

sampling time, T_s, using (4.7). By analyzing delays 100 samples apart, the evolution is studied over 1 OFDM symbol for the reference case (100 CIR-generation sampling rate is assumed to be equivalent to a continuous propagation channel) with a sliding window over the trajectory (sample by sample).

$$AE_{l,n} = \frac{|\tau_l(n) - \tau_l(n+100)|}{T_s} = |\tilde{\tau}_l(n) - \tilde{\tau}_l(n+100)|, n \in [1 \dots N] \quad (4.7)$$

Results for the L paths generated by QuaDRiGa are then averaged over the N computed $AE_{l,n}$ on multipath only, where $N + 100$ is defined as the number samples of the discrete propagation channel being analyzed; the LOS is considered separately because a lower variation is expected. Results for the 4 trajectories, the 2 QuaDRiGa scenarios and the 2 cases described in section 4.1.2 are provided in Table 4.2 with $N = 20000$.

From Table 4.2, it can be concluded that the multipath evolution is in average independent from the trajectory and of the order of 10^{-5}. The worst evolution of the LOS path is found for the radial trajectory, 10^{-4} in average, close to the evolution of the observed multipath delay. For the circular trajectories, it is significantly lower, 10^{-6} for the fourth trajectory and even lower for trajectories 2 and 3. This study proves the negligibility of the path delays evolution with respect to symbol duration: the path delay can thus be considered as constant over an OFDM symbol.

Table 4.2 – Evolution rate of QuaDRiGa propagation channel delays

$AE = E[AE_{l,n}]$ [s]			LOS path		MP	
			μ	σ	μ	σ
Trajectory 1	Scenario LOS	Case 1	-1e-4	1 e-7	-7e-5	7e-6
		Case 2	-9e-5	2e-8	1e-5	3e-6
	Scenario NLOS	Case 1	-1e-4	1e-7	-3e-5	2e-5
		Case 2	-9e-5	2e-8	-4e-5	5e-6
Trajectory 2	Scenario LOS	Case 1	1e-11	4e-8	1e-5	3e-5
		Case 2	3e-10	4e-7	1e-5	5e-6
	Scenario NLOS	Case 1	1e-11	4e-8	2e-5	2e-5
		Case 2	3e-10	4e-7	-1e-6	2e-6
Trajectory 3	Scenario LOS	Case 1	1e-10	3e-7	8e-6	1e-5
		Case 2	1e-6	7e-7	1e-5	4e-6
	Scenario NLOS	Case 1	1e-10	3e-7	1e-5	2e-5
		Case 2	1e-6	7e-7	3e-5	5e-6
Trajectory 4	Scenario LOS	Case 1	-1e-8	4e-7	2e-5	3e-5
		Case 2	1e-6	4e-7	2e-5	1e-6
	Scenario NLOS	Case 1	-1e-8	4e-7	9e-6	1e-5
		Case 2	1e-6	4e-7	2e-6	1e-6

4.1.4.2. Evolution of the path complex amplitudes

The path complex amplitudes' evolution analysis is split in 2: the modulus evolution analysis and the phase evolution analysis. For each simulated path, the AE and RE are computed for 100 CIR-generation sampling rate between CIR samples being 100 samples apart (one OFDM symbol) over the whole considered trajectory (N samples), $AE_{l,n}$ and $RE_{l,n}$, $n \in [1 \dots N]$. Note that a sliding window is used to assume any potential symbol position on the CIR. Finally, the sample-by-sample results are then averaged over the whole trajectory (N samples) and over the number of multipath to obtain the final results,

$AE = E[AE_{l,n}]$ and $RE = E[RE_{l,n}]$; the focus is made on the multipath since their evolutions are larger than the LOS evolution.

The $AE_{l,n}$ and $RE_{l,n}$ formulas applied for the modulus comparison between samples n and $n + 100$ are presented in (4.8) and (4.9). The same methodology is used for the phase by adapting (4.8) and (4.9) expressions.

$$AE_{l,n} = \big||\alpha_l(n)| - |\alpha_l(n+100)|\big|, n \in [1 \dots N] \tag{4.8}$$

$$RE_{l,n} = \frac{\big||\alpha_l(n)| - |\alpha_l(n+100)|\big|}{\big||\alpha_l(n)|\big|} \cdot 100 \tag{4.9}$$

Results are provided in Table 4.3 for each configuration presented in section 4.1.2 over $N = 20000$ samples. The RE is not relevant for the phase results; indeed, due to the formula itself, if the complex amplitude angles at n and $n + 100$ are close to 0, the RE will be really high. Therefore, only the REs are provided for the modulus evolution and only the AE are provided for the phase evolution. From Table 4.3, it can be observed that the channel complex amplitude cannot be neglected. The REs of the modulus tend to increase as the receiver goes away from the BS. For the fourth trajectory for a NLOS scenario in the case 2 the RE of the modulus is in average close to 4% with a standard deviation of 13%; the worst evolution of the four cases. It can also be observed that the REs of the modulus increase along with the subcarrier spacing (case 2 REs are higher than case 1 REs).

Table 4.3 – Propagation Channel Complex Amplitude Evolution

Trajectory		Trajectory 1				Trajectory 2			
Scenario		LOS		NLOS		LOS		NLOS	
Case		1	2	1	2	1	2	1	2
Modulus RE (%)	μ	0,440	1,675	0,798	2,823	0,513	1,934	0,936	3,554
	σ	1,117	4,383	1,976	7,642	1,233	4,576	2,284	9,731
Phase AE (rad)	μ	0,063	0,182	0,046	0,171	0,038	0,163	0,052	0,148
	σ	0,433	0,713	0,373	0,701	0,326	0,677	0,396	0,651
Trajectory		Trajectory 3				Trajectory 4			
Scenario		LOS		NLOS		LOS		NLOS	
Case		1	2	1	2	1	2	1	2
Modulus RE (%)	μ	0,995	2,192	0,884	3,629	0,641	2,479	1,406	3,820
	σ	3,636	5,367	2,766	11,14	1,537	6,782	3,713	13,15
Phase AE (rad)	μ	0,047	0,144	0,053	0,130	0,051	0,159	0,037	0,161
	σ	0,370	0,631	0,400	0,610	0,389	0,658	0,339	0,679

In conclusion, the evolution of the propagation channel complex amplitude is not negligible over one OFDM symbol and thus, it must be included in the correlator output mathematical model.

4.1.5. Determination of the CIR sampling interval for accurate modeling of symbol demodulation

In the previous section the non-negligibility of the propagation channel complex amplitude has been shown. Therefore, the last remaining step to realistically characterize 5G signal propagation channels for ranging purposes, and more specifically, to realistically model the propagation channel complex amplitude evolution over the OFDM symbol, is to determine the CIR sampling interval of the propagation channel. Moreover, note that a trade-off must be made between the generation computing time and the realism of the modelling.

4.1.5.1. Methodology

The following method is applied to determine the required CIR sampling interval of a 5G signal propagation channel with complex amplitude evolving over 1 OFDM symbol. Remind that this CIR sampling interval is required in section 4.2 to determine the correlator output mathematical model for ranging purposes.

1. The second or fourth 5G SSPBCH reference OFDM symbols presented in Figure 3.28 is generated (pilots and random data).
2. The propagation channel is generated considering 1, 10, 20 and 100 CIR and applied to the generated symbol.
3. The DLL discriminator outputs, (3.27), obtained with each considered X CIR sampling rate, are compared to the 100 CIR samples case per symbol (reference). The comparison metrics is presented in section 4.1.5.2.
4. The results are analyzed with respect to two different criterions, described in section 4.1.5.3, to determine the minimum X CIR sampling rate which will be used on this work.

Additionally, the same comparison has been made with respect to the demodulated symbols, (3.28), and the correlator, (3.29). The results are shown in Annex D.1.

4.1.5.2. Comparison metrics

The average degradations (AE and RE) of the DLL discriminator output with respect to the reference case are used as the key figures of merit for determining the CIR sampling rate. More specifically, the relevant parameter for the discriminator output is the AE. The degradation of a parameter is calculated by averaging the individual parameters degradation computed on each generated OFDM symbol, $AE_{X,m}$ and $RE_{X,m}$, according to (4.10) and (4.11).

$$AE_{X,m} = |D_{100} - D_X|_m, m \in [1 \dots M] \tag{4.10}$$

$$RE_{X,m} = \frac{|D_{100} - D_X|_m}{|D_{100}|_m} \cdot 100 \tag{4.11}$$

Where D_X represents the discriminator output values, the subscript *X*, defines the CIR generation sampling rate, and the subscript m represents the analyzed OFDM symbol. Note that the method presented to compute the degradation is not limited to DLL discriminator outputs; it can easily be extrapolated to any features.

For example, the REs for the demodulated symbols and correlator outputs are also computed (with respect to the reference). The comparison is given Annex D.1.

4.1.5.3. Selection criteria

Two selection criteria have been inspected it this work. Remember that the used criteria tackles the selection of the CIR sample rate from ranging perspectives. The two criteria are given below:

A given X CIR sampling rate is only accepted if

1) The discriminator output AE mean and standard deviation are lower than 10 cm for a LOS scenario and lower than 20 cm for a NLOS scenario.

2) The discriminator output AE values are lower than 0.5 m 95% of time and lower than 1m 99% of time.

The first criterion is used to inspect the statistics of the discriminator outputs difference between reference CIR and inspected X CIR. The second criterion was introduced in order to remove the influence of the potential outliers from the selection criterion.

4.1.5.4. Results

The metrics evaluation is conducted with the following configuration: unless stated otherwise, $M = 5000$ OFDM symbols, and for the DLL configuration $\delta = 4$ samples (EMPL discriminator correlator spacing) and $B_l = 10\ Hz$ (DLL's loop bandwidth); the DLL is justified and carefully presented in chapter 5 section 5.1. Note that the DLL, or in this case, the DLL's discriminator is applied to only 1 symbol which implies a coherent integration time of one symbol. This choice is also justified in chapter 5 section 5.1.

In Table 4.4 and Table 4.5, the first selection criterion is inspected. On these tables, the averaged mean and standard deviation of the AE are provided. Results are provided for all trajectories in both LOS (Table 4.4) and NLOS (Table 4.5) scenarios. The color code adopted for all tables represents the following conditions:

- in red, differences between reference and tested X-CIR sampling rate are deemed unacceptable
- in orange, differences between reference and tested X-CIR sampling rate are deemed at the acceptance limit
- in blue, differences between reference and tested X-CIR sampling rate fulfill the criteria and the CIR configuration is the selected one
- in green, differences between reference and tested X-CIR sampling rate are better than the criteria

From Table 4.4, the first relevant conclusion of the CIR sampling rate determination can be extracted for the LOS scenario: 10 CIR per OFDM symbol is suitable candidate for all cases. However, results are less convincing for 10 CIR as seen in Table 4.5 for the NLOS scenario. In fact, no CIR generation sampling rate is satisfying except for a small group of cases.

Table 4.4 – LOS scenario – CIR generation rate impact on the discriminator output – δ=4 samples – $B_l = 10Hz$

Trajectory			Trajectory 1		Trajectory 2		Trajectory 3		Trajectory 4	
Scenario			LOS		LOS		LOS		LOS	
Case			1	2	1	2	1	2	1	2
Discriminator AE (m)	μ	1	0,12	0,21	0,08	0,05	0,18	0,04	0,06	0,37
		10	0,00	0,02	0,00	0,00	0,01	0,00	0,00	0,04
		20	0,00	0,00	0,00	0,00	0,00	0,00	0,00	0,01
	σ	1	0,28	0,18	0,09	0,09	0,14	0,03	0,05	0,65
		10	0,02	0,02	0,00	0,00	0,01	0,00	0,00	0,13
		20	0,00	0,00	0,00	0,00	0,00	0,00	0,00	0,03

Table 4.5 – NLOS scenario – CIR generation rate impact on the discriminator output – δ=4 samples – $B_l = 10Hz$

Trajectory			Trajectory 1		Trajectory 2		Trajectory 3		Trajectory 4	
Scenario			NLOS		NLOS		NLOS		NLOS	
Case			1	2	1	2	1	2	1	2
Discriminator AE (m)	μ	1	0,72	1,40	0,75	2,20	1,98	13,4	2,39	17,0
		10	0,04	0,29	0,05	0,61	0,15	1,36	0,36	1,43
		20	0,01	0,09	0,02	0,07	0,05	0,56	0,15	1,44

	σ	1	1,99	6,93	4,79	21,9	16,0	24,4	56,4	289,
		10	0,19	4,30	0,32	14,2	1,73	18,4	9,04	29,0
		20	0,08	0,73	0,17	0,63	0,49	7,26	3,69	35,9

In Table 4.6, the second selection criterion is inspected. In this table, the percentage of time when the discriminator output AE is less than 0.5 m (upper part) and less than 1 m (lower part) is presented. The same color code as for Table 4.4 and Table 4.5 is used. The criterion is thus satisfied when using 10 CIR per OFDM symbol for the 0.5 m criterion, and when using 20 CIR per OFDM symbol for the 1 m criterion; for all cases but the NLOS case 2.

Table 4.6 – Percentage of symbol where the discriminator output AE is less than 0.5m and 1 m – δ=4 samples – $B_l = 10Hz$

AE <0.5m	Trajectory 1				Trajectory 2				Trajectory 3				Trajectory 4			
	LOS		*NLOS*		*LOS*		*NLOS*		*LOS*		*NLOS*		*LOS*		*NLOS*	
	1	*2*	*1*	*2*	*1*	*2*	*1*	*2*	*1*	*2*	*1*	*2*	*1*	*2*	*1*	*2*
1CIR	96.5	91.8	65.8	54.5	99.7	99.3	77.8	36.4	96.1	100	65.8	1.93	99.9	78.3	62.9	8.2
10CIR	100	100	99.1	91.6	100	100	98.5	66.7	100	100	96.6	72.8	100	99.6	91.1	84.6
20CIR	100	100	99.8	97.6	100	100	99.1	72.9	100	100	98.9	94.1	100	99.8	95.7	84.2
AE <1m	Trajectory 1				Trajectory 2				Trajectory 3				Trajectory 4			
	LOS		*NLOS*		*LOS*		*NLOS*		*LOS*		*NLOS*		*LOS*		*NLOS*	
	1	*2*	*1*	*2*	*1*	*2*	*1*	*2*	*1*	*2*	*1*	*2*	*1*	*2*	*1*	*2*
1CIR	98.8	99.7	81.5	74.1	99.9	99.6	89.0	55.1	99.9	100	78.5	4.2	100	94.8	79.8	15.7
10CIR	100	100	99.7	95.7	100	100	99.2	71.1	100	100	98.4	87.9	100	99.8	94.7	91.0
20CIR	100	100	99.9	99.2	100	100	99.5	74.9	100	100	99.4	96.2	100	99.9	98.8	89.3

Finally, in order to have a better understanding of the discriminator outputs behavior, another DLL configuration is studied and results for the first criterion are provided in Table 4.7 and Table 4.8, and in Table 4.9 for the second criterion. Remind that in Table 4.6, the DLL is run with a correlator spacing equal to 4 samples and a 10 Hz-loop bandwidth. In Table 4.7, Table 4.8 and Table 4.9, the DLL is run with a correlator spacing equal to 4 samples and a 1 Hz-loop bandwidth. By doing so, the DLL is less reactive to the propagation channel evolutions.

From Table 4.7, the first relevant conclusion of the CIR sampling rate determination can be extracted for the LOS scenario: 1 CIR per OFDM symbol could be a suitable candidate for all cases (although some values do not completely fulfill the criterion). However, in Table 4.8 for the NLOS scenario, no CIR generation sampling rate is satisfying the first criterion. However, by looking at the 2nd criterion it can be seen that outliers highly degrade the statistics.

Regarding the second criterion, for all cases but NLOS case 2 and trajectory 4, using 10 CIR per OFDM symbol permits to satisfy the second criteria. This study highlights that the DLL configuration highly influence the results; the remaining problematic point is for the NLOS scenario case 2 where even with 20CIR per OFDM symbol the discriminator output AE remains too high; a higher sampling would be required.

Table 4.7 – LOS scenario – CIR generation rate impact on the discriminator output – δ =4 samples – $B_l = 1Hz$

Trajectory			Trajectory 1		Trajectory 2		Trajectory 3		Trajectory 4	
Scenario			LOS		LOS		LOS		LOS	
Case			1	2	1	2	1	2	1	2
Discriminator AE (m)	μ	1	0,10	0,03	0,08	0,01	0,20	0,01	0,03	0,02
		10	0,01	0,00	0,00	0,00	0,01	0,00	0,00	0,00
		20	0,00	0,00	0,00	0,00	0,00	0,00	0,00	0,00
	σ	1	0,21	0,02	0,11	0,00	0,28	0,00	0,03	0,01
		10	0,02	0,00	0,00	0,00	0,02	0,00	0,00	0,00

		20	0,00	0,00	0,00	0,00	0,01	0,00	0,00	0,00

Table 4.8 – NLOS scenario – CIR generation rate impact on the discriminator output – δ =4 samples – $B_l = 1Hz$

Trajectory			Trajectory 1		Trajectory 2		Trajectory 3		Trajectory 4	
Scenario			NLOS		NLOS		NLOS		NLOS	
Case			1	2	1	2	1	2	1	2
Discriminator AE (m)	μ	1	4,19	1,88	30,4	76,7	2,23	1,20	2,53	11,8
		10	1,60	0,12	1,07	54,3	0,66	0,89	0,27	1,74
		20	0,91	0,05	0,44	226	0,31	0,04	0,11	1,09
	σ	1	220	82,7	1991	3751	76,0	23,4	68,1	240
		10	106	3,45	56,2	2893	38,1	1,30	9,33	53,3
		20	60,9	1,33	22,3	1377	17,4	0,70	4,00	40,6

Table 4.9 – Percentage of symbol where the discriminator output AE is less than 0.5m and 1 m – δ =4 samples – $B_l = 1Hz$

AE <0.5m	Trajectory 1				Trajectory 2				Trajectory 3				Trajectory 4			
	LOS		*NLOS*		*LOS*		*NLOS*		*LOS*		*NLOS*		*LOS*		*NLOS*	
	1	*2*	*1*	*2*	*1*	*2*	*1*	*2*	*1*	*2*	*1*	*2*	*1*	*2*	*1*	*2*
1CIR	96.9	100	82.4	89.3	98.3	100	84.4	82.9	92.5	100	87.3	88.7	99.9	100	72.5	48.4
10CIR	100	100	98.1	98.5	100	100	98.5	97.8	100	100	98.8	98.7	100	100	98.8	89.8
20CIR	100	100	99.0	98.9	100	100	99.2	98.6	100	100	99.3	99.3	100	100	99.6	94.3
AE <1m	Trajectory 1				Trajectory 2				Trajectory 3				Trajectory 4			
	LOS		*NLOS*		*LOS*		*NLOS*		*LOS*		*NLOS*		*LOS*		*NLOS*	
	1	*2*	*1*	*2*	*1*	*2*	*1*	*2*	*1*	*2*	*1*	*2*	*1*	*2*	*1*	*2*
1CIR	98.5	100	90.2	94.7	99.9	100	93.1	90.8	97.3	100	93.6	94.9	100	100	87.7	68.5
10CIR	100	100	99.0	99.0	100	100	99.2	98.6	100	100	99.3	99.2	100	100	99.5	94.0
20CIR	100	100	99.4	99.5	100	100	99.7	99.1	100	100	99.6	99.5	100	100	99.7	96.9

Therefore, from Table 4.6 and Table 4.9, the second relevant conclusion about CIR sampling rate determination can be extracted: 10 CIR per OFDM symbol sampling rate is a suitable candidate for NLOS conditions and case 1, and a very high CIR sampling rate will be required for case 2.

However, as already evoked in the configurations section, this problematic case 2 must be weighed against the interest in using such a degraded received signal for ranging applications. Indeed, NLOS scenario for case 2 (large subcarrier spacing and thus fast variation of the multipath characteristics) will provide high ranging error values, fast C/N_0 variations and thus will not be probably used in a navigation solution. Therefore, this case will not be considered in this Ph.D. due to its lack of relevance.

In order to complete the results, the study has been repeated for a DLL using a 6 samples correlator spacing for the 2 loop bandwidths ($B_l = 10\,Hz$ and $B_l = 1\,Hz$); the complete results are provided in Annex D.2.

To conclude, considering the application of the 1st and 2nd selection criteria, in this work and for the targeted cases of study, the 10 CIR sampling rate candidate is selected.

4.1.6. Summary

To summarize, in this section, it has been shown that the 5G compliant propagation channel, QuADRiGa, is not constant over the duration of one OFDM symbol. A study of its parameters proves that the evolution of the delay can be considered as constant but not the evolution of the complex amplitude: channel coherence time of the complex amplitude is shorter than one OFDM symbol whereas the channel coherence time of delays is longer for ranging purposes. The CIR-generation sampling rate required to simulate a realistic propagation channel by limiting as much as possible the generator computational

burden / mathematical model has been then determined. The adopted CIR generation sampling rate is equal to 10 CIR per OFDM symbol for the signal conditions considered relevant in the analysis of this work. The choice of this CIR sampling rate induces a degradation of less than 10 cm on the mean and standard deviation of the discriminator output in the LOS case (for both a sub-6 GHz and a mmW system), and a degradation of less than 20 cm in the NLOS case (for a sub-6 GHz system).

4.2. Correlator output mathematical model for positioning

Remember that the ultimate goal of this chapter is to derive the correlator output mathematical model of a 5G signal for ranging purposes. In order to derive this precise and realistic correlator output mathematical model, it is of the utmost importance to precisely model the received 5G signal and, by extension, the interferences distorting the signal introduced by the propagation channel with as much realism as possible. Section 4.1 has permitted to correctly characterize the CIR propagation channel.

Therefore, an accurate model of the received signal is available. In order to determine the correlator output mathematical model accordingly to the pilot sequence illustrated in Figure 3.28, the noiseless received signal must be first demodulated and then correlated (using an abusive language) over the pilot symbols presented in chapter 3 section 3.3.6.3.2. The derivation of the noiseless correlator output mathematical model is presented in the first section. The second section presents the mathematical model of the noise. Third, the final correlator output mathematical model, combining the noiseless correlator output mathematical model and the noise model, is presented.

4.2.1. Derivation of the correlator output mathematical model associated to the received useful signal

In order to simplify the notation, from now on, the term noiseless will be used to denote the mathematical models associated to the signals processing of the useful received signal without considering the noise.

In this section, first, the consequences of a time-evolving propagation channel on the OFDM symbols are detailed. Second, the noiseless mathematical models of the demodulated symbols and of the correlator output over a time-evolving propagation channel are derived in subsection 4.2.1.2 and 4.2.1.3. Fourth, the statistics of the noiseless correlator output mathematical model are provided. Finally, a simplified model for the correlator output mathematical model is proposed.

4.2.1.1. Loss of subcarrier orthogonality due to a time varying channel

The objective of this subsection is to explain the consequences of a complex amplitude time-evolving propagation channel over the OFDM symbol duration on the OFDM demodulated symbols as well as on the correlation function.

For a time-evolving propagation channel model over the duration of the OFDM symbol, the complex envelope CIR is modelled as (4.12).

$$\alpha^k(t,\tau) = \sum_{l=0}^{L-1} \alpha_l^k(t,\tau)\,, 0 \leq t \leq T_{OFDM} \tag{4.12}$$

The complex envelope CIR of the received multipath l, $\alpha_l^k(t,\tau)$, can be expressed as (4.13) when assuming a constant time delay over the duration of the OFDM symbol (validated in previous section

4.1.4.1). Please note that contrary to the model derived in (3.25), the propagation channel complex amplitude is evolving, therefore, α_l^k depends on t.

$$\alpha_l^k(t,u) = \alpha_l^k(t) \cdot \delta(u - \tau_l), 0 \leq t \leq T_{OFDM} \tag{4.13}$$

Where u is a mathematical variable used for the convolution, t is used to model the complex amplitude evolution of each multipath and $\alpha_l^k(t)$ is the evolving complex amplitude for the k^{th} OFDM symbol and for the l^{th} multipath. The received signal for the l^{th} multipath and k^{th} symbol, the noiseless received useful signal mathematical model, ${r_l^k}_{nl}(t)$ is then calculated as (4.14).

$${r_l^k}_{nl}(t) = \alpha_l^k(t) \cdot \delta(u - \tau_l) * s(u)\big|_{u=t} = \alpha_l^k(t) \cdot s(t - \tau_l) \tag{4.14}$$

Where $s(t)$ is the transmitted complex envelope signal mathematical model. Assuming for simplification purposes $\tau_l = 0$, the received signal Fourier Transform is equal to (4.15).

$$R_l^k(f) = A_l^k(f) * S(f) \tag{4.15}$$

Where $A_l^k(f) = FT[\alpha_l^k(t)]$ and $S_l(f) = FT[s_l(t)]$. If the propagation channel is constant over the duration of the correlation, $\alpha_l^k(t) = \alpha_l^k$, $A_l^k(f)$ is a Dirac delta function. However, if the propagation channel evolves, $\alpha_l^k(t) \neq \alpha_l^k$, $A_l^k(f)$ is no longer a Dirac (see Figure 4.6) and the convolution in the frequency domain will create a spectral broadening effect. This spectral broadening implies the loss of the orthogonality among the OFDM signal subcarriers. This process is illustrated in Figure 4.5.

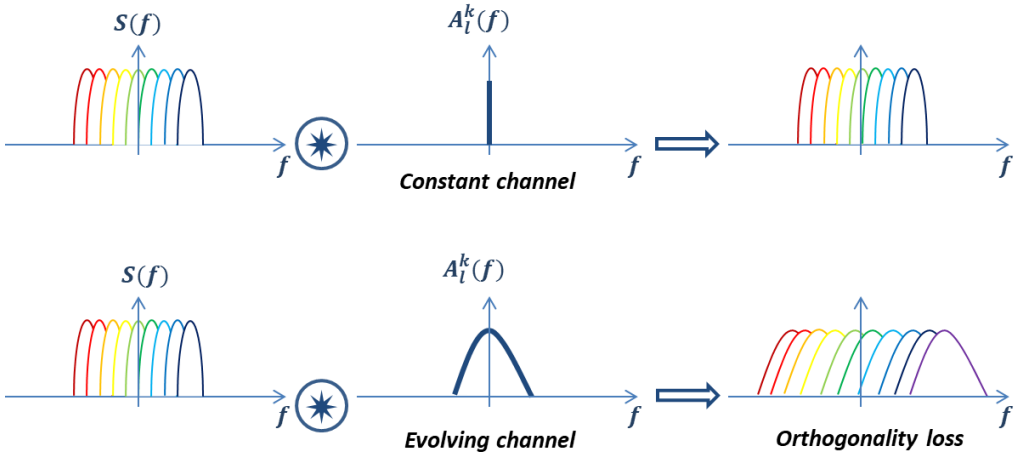

Figure 4.5 – Consequence of the evolution of the channel on the orthogonality of the OFDM signal

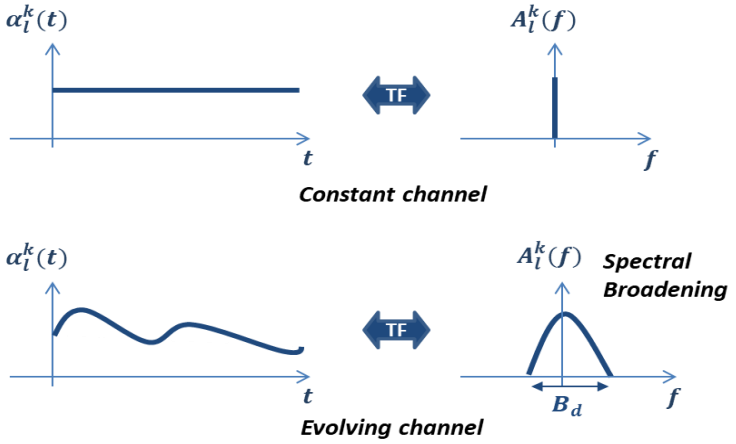

Figure 4.6 – Consequence of the evolution of the channel on the Fourier Transform

4.2.1.2. *Noiseless demodulated symbols mathematical model*

The channel model defined in (4.12) is applied to the signal model presented in (3.23) in order to obtain the new noiseless received signal model, $r_{nl}^k(t)$. After sampling (quantization is neglected for simplification purposes), the new noiseless discrete received signal model, $r_{n\,nl}^k$, at the RF front-end output is provided in (4.16).

$$r_{n\,nl}^k = r_{nl}^k(nT_s) = \sum_{l=0}^{L-1} \alpha_l^k(n) \sum_{q=0}^{N_{FFT}-1} d_q^k e^{\frac{i2\pi q(n-\tilde{\tau}_l)}{N_{FFT}}} \tag{4.16}$$

Where $\tilde{\tau}_l = \frac{\tau_l}{T_s}$ is the normalization of the continuous parameter by the sampling time T_s. In order to demodulate this signal, a FFT is applied; the mathematical model of the q'^{th} noiseless demodulated symbol is:

$$\hat{d}_{nl,q'}^k = \sum_{q=0}^{N_{FFT}-1} \frac{d_q^k}{N_{FFT}} \sum_{l=0}^{L-1} e^{\frac{-2i\pi q\tilde{\tau}_l}{N_{FFT}}} \sum_{n=0}^{N_{FFT}-1} \alpha_l^k(n) e^{\frac{-2i\pi(q'-q)n}{N_{FFT}}} \tag{4.17}$$

In order to keep this formula readable, the following terms are defined:

$$A_l^k(q'-q) = \sum_{n=0}^{N_{FFT}-1} \alpha_l^k(n) e^{-\frac{2i\pi(q'-q)n}{N_{FFT}}} \tag{4.18}$$

$$A^k(q',q) = \sum_{l=0}^{L-1} e^{-\frac{2i\pi q\tilde{\tau}_l}{N_{FFT}}} A_l^k(q'-q) \tag{4.19}$$

These formulations give a physical meaning to the demodulation since $A_l^k(q'-q)$ is the Discrete Fourier Transform of the CIR complex amplitude over the symbol duration of path l. By doing so, the noiseless demodulated symbol mathematical model is:

$$\hat{d}_{nl,q'}^k = \frac{1}{N_{FFT}} \sum_{q=0}^{N_{FFT}-1} d_q^k A^k(q',q) \tag{4.20}$$

It is possible to split the noiseless demodulated symbol mathematical model into a useful contribution and an Inter-Carrier Interference (ICI) contribution as presented in (4.21). The useful term $\hat{d}^k_{nl,q'_{useful}}$ is the contribution of the desired symbol to be demodulated; the ICI term $\hat{d}^k_{nl,q'_{interf}}$ is the contribution of the symbols of the subcarriers other than the targeted one.

$$\hat{d}^k_{nl,q'} = \frac{A^k(q',q')}{N_{FFT}} d^k_{q'} + \sum_{\substack{q=0 \\ q\neq q'}}^{N_{FFT}-1} \frac{A^k(q',q)}{N_{FFT}} d^k_q \qquad (4.21)$$

$$\hat{d}^k_{nl,q'} = \hat{d}^k_{nl,q'_{useful}} + \hat{d}^k_{nl,q'_{interf}}$$

4.2.1.3. Noiseless correlator output mathematical model

As for a constant propagation channel, the correlation is performed over pilots only following (3.29). Similar to the demodulation process, the noiseless correlation output mathematical model can be split into a noiseless useful term and an ICI term as presented below.

$$R_{nl}(\varepsilon_\tau) = \frac{1}{N_P} \sum_{q'\in P} \left(\hat{d}^k_{nl,q'_{useful}} + \hat{d}^k_{nl,q'_{interf}} \right) p^{k*}_{q'} e^{\frac{2i\pi\hat{\tau}q'}{N_{FFT}}} \qquad (4.22)$$

$$R_{nl}(\varepsilon_\tau) = R_{useful}(\varepsilon_\tau) + R_{interf}(\varepsilon_\tau) \qquad (4.23)$$

The expression of the noiseless useful term can be developed as proposed in equations (4.24) to (4.28). This formula can be linked to the noiseless correlator output mathematical model for a constant channel developed in chapter 3 section 3.5.3.2. Note that in order to derive (4.27) from (4.26) it must be reminded that the sum indexed by q' is a sum over the pilots therefore $d^k_{q'} = p^k_{q'}$. Moreover, $\sigma^2_{pilot} = p^k_{q'} \cdot p^{k*}_{q'}$ is assumed to be equal to 1.

$$R_{useful}(\varepsilon_\tau) = \frac{1}{N_P} \sum_{q'\in P} d^k_{nl,q'_{useful}} p^{k*}_{q'} e^{\frac{2i\pi\hat{\tau}q'}{N_{FFT}}} \qquad (4.24)$$

$$R_{useful}(\varepsilon_\tau) = \frac{1}{N_P} \sum_{q'\in P} \frac{1}{N_{FFT}} d^k_{q'} A^k(q',q') p^{k*}_{q'} e^{\frac{2i\pi\hat{\tau}q'}{N_{FFT}}} \qquad (4.25)$$

$$R_{useful}(\varepsilon_\tau) = \frac{1}{N_P} \sum_{q'\in P} \frac{1}{N_{FFT}} d^k_{q'} \sum_{l=0}^{L-1} e^{-\frac{2i\pi q'\tau_l}{N_{FFT}}} A^k_l(0)\, p^{k*}_{q'} e^{\frac{2i\pi\hat{\tau}q'}{N_{FFT}}} \qquad (4.26)$$

$$R_{useful}(\varepsilon_\tau) = \frac{1}{N_P} \frac{1}{N_{FFT}} \sum_{l=0}^{L-1} A^k_l(0) \sum_{q'\in P} e^{\frac{2i\pi(\hat{\tau}-\tau_l)q'}{N_{FFT}}} \qquad (4.27)$$

$$R_{useful}(\varepsilon_\tau) = \sum_{l=0}^{L-1} \frac{A^k_l(0)}{N_{FFT}} R_{nl,l}(\varepsilon_{\tau_l}) \qquad (4.28)$$

Where, $R_{nl,l}(\varepsilon_{\tau_l})$ is provided in (3.41). It must be noted that the noiseless useful term, (4.28), is different from the correlator output derived in (3.41) for a constant channel. For a constant channel, only one coefficient is considered for each path l for each symbol k, α^k_l (see violet curve Figure 4.1); while for an evolving channel, the impact of the l^{th} path on symbol k is modelled by the sum $A^k_l(0) = \sum_{n=0}^{N_{FFT}-1} \alpha^k_l(n)$, where the $\alpha^k_l(n)$ values are constant over a period shorter than the OFDM symbol, and thus depend on the chosen CIR sampling rate.

The expression of the ICI term is derived in (4.29), (4.30) and (4.31). First, remember that the set of pilots can be expressed as $P = \gamma q' + \beta$, where γ is the period of repetition of the pilots in the OFDM symbol, $q' \in [0 \dots N_P - 1]$ and β is the subcarrier index of the first pilot in the symbol. For simplification purposes, in the following, $\beta = 0$.

In (4.29), symbols $\{d_q^k\}$ are either pilots $d_{q_{pilot}}^k = p_q^k$ if $q \bmod \gamma = 0$ where $q \in [0 \dots \gamma N_P - 1]$ or data $d_{q_{data}}^k = D_q^k$ if $q \bmod \gamma \neq 0$ where $q \in [0 \dots N_{FFT} - 1]$. Therefore, the sum over q can be split in two, see (4.30), a first sum over the data, the second over the pilot.

$$R_{interf}(\varepsilon_\tau) = \sum_{q' \in P} \sum_{\substack{q=0 \\ q \neq q'}}^{N_{FFT}-1} d_q^k \frac{A^k(q, q')}{N_P N_{FFT}} p_{q'}^{k*} e^{\frac{2i\pi\hat{\tau}q'}{N_{FFT}}} \tag{4.29}$$

Then, in (4.30), the sum over $q' \in P$ can be defined as $q' = \gamma q'' + \beta$ where $q'' \in [0, \dots, N_P - 1]$, for the sake of simplicity, q'' is kept as q' and $\beta = 0$. The ICI term final expression is provided in (4.31).

$$R_{interf}(\varepsilon_\tau) = \frac{1}{N_P N_{FFT}} \sum_{q' \in P} \left(\sum_{\substack{q=0 \\ q \neq q' \\ q \bmod \gamma \neq 0}}^{N_{FFT}-1} d_{q_{data}}^k A^k(q, q')\, p_{q'}^{k*} e^{\frac{2i\pi\hat{\tau}q'}{N_{FFT}}} + \sum_{\substack{q=0 \\ q \neq q'}}^{N_P-1} d_{q_{pilot}}^k A^k(\gamma q, q')\, p_{q'}^{k*} e^{\frac{2i\pi\hat{\tau}q'}{N_{FFT}}} \right) \tag{4.30}$$

$$R_{interf}(\varepsilon_\tau) = R_{interf_{pilot}}(\varepsilon_\tau) + R_{interf_{data}}(\varepsilon_\tau)$$

$$\begin{cases} R_{interf_{pilot}}(\varepsilon_\tau) = \dfrac{1}{N_P N_{FFT}} \displaystyle\sum_{l=0}^{L-1} \sum_{q'=0}^{N_P-1} \sum_{\substack{q=0 \\ q \neq q'}}^{N_P-1} e^{\frac{-2i\pi\gamma q\tilde{\tau}_l}{N_{FFT}}} p_q^k p_{q'}^{k*} e^{\frac{2i\pi\hat{\tau}\gamma q'}{N_{FFT}}} \sum_{n=0}^{N_{FFT}-1} \alpha_l^k(n) e^{\frac{2i\pi\gamma(q-q')n}{N_{FFT}}} \\ R_{interf_{data}}(\varepsilon_\tau) = \dfrac{1}{N_P N_{FFT}} \displaystyle\sum_{l=0}^{L-1} \sum_{q'=0}^{N_P-1} \sum_{\substack{q=0 \\ q \neq \gamma q' \\ q \bmod \gamma \neq 0}}^{N_{FFT}-1} e^{\frac{-2i\pi q\tilde{\tau}_l}{N_{FFT}}} D_q^k p_{q'}^{k*} e^{\frac{2i\pi\hat{\tau}\gamma q'}{N_{FFT}}} \sum_{n=0}^{N_{FFT}-1} \alpha_l^k(n) e^{\frac{2i\pi(q-\gamma q')n}{N_{FFT}}} \end{cases} \tag{4.31}$$

In Figure 4.7, the validation of the noiseless correlator output mathematical model is provided for the 100 m-radius-circle trajectory, for Case 1, and scenario LOS. The symbols considered correspond to the 2nd (or 4th) symbol of the SS PBCH block presented in chapter 3 (one pilot every 4 subcarriers over 240 subcarriers). On the left, the true correlation and the analytical model are plotted. On the right, the difference between the two in terms of modulus (upper part) and phase (lower part) are provided. From Monte Carlo simulations, the averaged relative errors (computed similarly to (4.9)) are of the order of 10^{-13}% in term of modulus and phase. This validation process has been performed over all trajectories defined before and it confirms the model's validity.

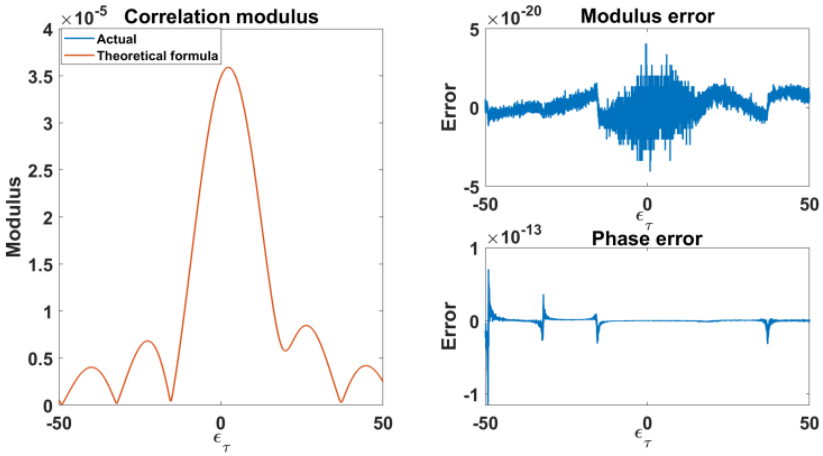

Figure 4.7 – Validation of the correlator output mathematical model

4.2.1.4. *Determination of the noiseless correlator output mathematical model probabilistic distribution*

In the previous section, it was seen that the noiseless correlator output mathematical model can be divided in two parts, a noiseless useful part and an ICI part. The ICI part depended on the transmitted data as seen in equation (4.31). This means that the noiseless correlator output mathematical model when assuming a time-evolving propagation channel over an OFDM symbol is no longer a deterministic mathematical model, as it was the case for a constant channel, but rather a stochastic process. Therefore, in order to completely determine the noiseless correlator output mathematical model and in order to potentially simplify it, the distribution and statistic moments of the noiseless useful and ICI correlator output mathematical models are analyzed. Moreover, the determination of the statistics and probably density function of this term will ultimately allow to probabilistically combine it with the mathematical model of the correlator output noise distribution.

In this section, the noiseless correlator output mathematical models are modeled by a Gaussian variable. This is possible since the ICI term in (4.31) (random variable of the noiseless correlator output mathematical model) can be, due to the Central Limit Theorem, modelled by a Gaussian variable. In order to prove this, the Skewness and Kurtosis statistics have been computed for 10000 Monte Carlo and over the Early, Prompt and Late correlator outputs; results are provided in Table 4.10. As a reminder, for a Gaussian distribution, the Skewness is equal to 0 and the Kurtosis to 3.

Table 4.10 – Skewness and Kurtosis measurements

Trajectory		1	3		
scenario		LOS	LOS	LOS	NLOS
Case		1	1	2	1
		Skewness measures			
$R(\varepsilon_\tau)$	Early	0.0456	-0.0365	-0.0133	-0.0197
	Prompt	0.0237	-0.0152	-0.0449	-0.0261
	Late	-0.0128	-0.0042	-0.0187	-0.0225
		Kurtosis measures			
$R(\varepsilon_\tau)$	Early	2.8743	2.9322	3.0247	3.0453
	Prompt	3.0175	2.9608	3.0447	3.0412
	Late	3.2130	3.0214	2.9834	3.1001

The Skewness and Kurtosis statistics have proved that the correlator output mathematical model can be modeled by a Gaussian variable which is completely described by its mean and variance. The mean of the noiseless correlator output mathematical model ICI term is defined in (4.32).

According to (4.31), the interference term can be split into an interference contribution due to the pilot, $R_{interf_{pilot}}(\varepsilon_\tau)$, and an interference contribution due to the data, $R_{interf_{data}}(\varepsilon_\tau)$. The interference contribution due to the pilot is a deterministic term; thus $E\left[R_{interf_{pilot}}(\varepsilon_\tau)\right] = R_{interf_{pilot}}(\varepsilon_\tau)$. The mean of the interference contribution due to the data is null since the data symbols are QPSK symbols; thus $E\left[D_q^k\right] = 0$.

$$E\left[R_{interf}(\varepsilon_\tau)\right] = E\left[R_{interf_{data}}(\varepsilon_\tau)\right] + E\left[R_{interf_{pilot}}(\varepsilon_\tau)\right] \tag{4.32}$$

After derivation, the variance of the correlator output mathematical model is given in (4.38). This variance is exclusively due to the ICI term, $R_{interf}(\varepsilon_\tau)$.

Classically, the variance can be expressed as (4.33). The development of (4.33) leads to (4.34). Using the expression of $R_{interf_{data}}(\varepsilon_\tau)$ in (4.31), and the statistics of QPSK symbols detailed in (4.36), the final expression of the variance of the correlator output can be derived, (4.38).

$$Var\left[R_{interf}(\varepsilon_\tau)\right] = E\left[\left(R_{interf}(\varepsilon_\tau) - E\left[R_{interf}(\varepsilon_\tau)\right]\right)^2\right] \tag{4.33}$$

$$Var\left[R_{interf}(\varepsilon_\tau)\right] = E\left[R_{interf_{data}}(\varepsilon_\tau) R_{interf_{data}}^{*}(\varepsilon_\tau)\right] \tag{4.34}$$

$$\begin{aligned} &Var\left[R_{interf}(\varepsilon_\tau)\right] \\ &= \frac{1}{N_P^2 N_{FFT}^2} \sum_{l=0}^{L-1} \sum_{q'=0}^{N_P-1} \sum_{\substack{q=0 \\ q\ mod\ \gamma \neq 0 \\ q \neq \gamma q'}}^{N_{FFT}-1} e^{\frac{-2i\pi q \tilde{\tau}_l}{N_{FFT}}} p_{q'}^{k*} e^{\frac{2i\pi \hat{\tau} \gamma q'}{N_{FFT}}} \sum_{n=0}^{N_{FFT}-1} \alpha_l^k(n) e^{\frac{2i\pi(q-\gamma q')n}{N_{FFT}}} \\ &\cdot \sum_{l'=0}^{L-1} \sum_{v'=0}^{N_P-1} \sum_{\substack{v=0 \\ v\ mod\ \gamma \neq 0 \\ v \neq \gamma v'}}^{N_{FFT}-1} e^{\frac{2i\pi v \tilde{\tau}_{l'}}{N_{FFT}}} p_{v'}^{k} e^{-\frac{2i\pi \hat{\tau} \gamma v'}{N_{FFT}}} \sum_{n'=0}^{N_{FFT}-1} \alpha_{l'}^{k*}(n') e^{-\frac{2i\pi(v-\gamma v')n'}{N_{FFT}}} E\left[D_q^k D_v^{k*}\right] \end{aligned} \tag{4.35}$$

$$E\left[D_q^k D_v^{k*}\right] = \begin{cases} 1 & v = q \\ 0 & v \neq q \end{cases} \tag{4.36}$$

$$\begin{aligned} &Var\left[R_{interf}(\varepsilon_\tau)\right] \\ &= \frac{1}{N_P^2 N_{FFT}^2} \sum_{\substack{q=0 \\ q\ mod\ \gamma \neq 0}}^{N_{FFT}-1} \left(\sum_{l=0}^{N_{FFT}-1} \sum_{\substack{q'=0 \\ q \neq \gamma q'}}^{N_P-1} e^{\frac{-2i\pi q \tilde{\tau}_l}{N_{FFT}}} p_{q'}^{k*} e^{\frac{2i\pi \hat{\tau} \gamma q'}{N_{FFT}}} \sum_{n=0}^{N_{FFT}-1} \alpha_l^k(n) e^{\frac{2i\pi(q-\gamma q')n}{N_{FFT}}} \right) \\ &\cdot \left(\sum_{l=0}^{N_{FFT}-1} \sum_{\substack{q'=0 \\ q \neq \gamma q'}}^{N_P-1} e^{\frac{-2i\pi q \tilde{\tau}_l}{N_{FFT}}} p_{q'}^{k*} e^{\frac{2i\pi \hat{\tau} \gamma q'}{N_{FFT}}} \sum_{n=0}^{N_{FFT}-1} \alpha_l^k(n) e^{\frac{2i\pi(q-\gamma q')n}{N_{FFT}}} \right)^* \end{aligned} \tag{4.37}$$

$$\begin{aligned} &Var\left[R_{interf}(\varepsilon_\tau)\right] \\ &= \frac{1}{N_P^2 N_{FFT}^2} \sum_{\substack{q=0 \\ q\ mod\ \gamma \neq 0}}^{N_{FFT}-1} \left| \sum_{l=0}^{L-1} e^{\frac{-2i\pi q \tilde{\tau}_l}{N_{FFT}}} \sum_{\substack{q'=0 \\ q \neq \gamma q'}}^{N_P-1} p_{q'}^{k*} e^{\frac{2i\pi \hat{\tau} \gamma q'}{N_{FFT}}} \sum_{n=0}^{N_{FFT}-1} \alpha_l^k(n) e^{\frac{2i\pi(q-\gamma q')n}{N_{FFT}}} \right|^2 \end{aligned} \tag{4.38}$$

In order to validate the expectation formula (4.32) and the variance formula (4.38), 50000 Monte Carlo simulations (trajectory 3, scenario LOS/NLOS, Case 1) have been run for three values of ε_τ: $\varepsilon_\tau = -5$, $\varepsilon_\tau = 0$ and $\varepsilon_\tau = 5$. For all values, the relative error between the theoretical mean and variance and the simulated mean and variance are provided in Table 4.11. The relative errors between the true mean and the theoretical model is lower than 0.065%, the model is thus validated. The relative errors between the theoretical variance and the simulated one are mostly below 3% which is an acceptable confidence level. Therefore, the mathematical models of the mean and variance of the noiseless correlator output mathematical model are validated.

Table 4.11 – Relative error between the theoretical mean and variance and the simulated mean and variance

		$\varepsilon_\tau = -5$		$\varepsilon_\tau = 0$		$\varepsilon_\tau = 5$	
		LOS	NLOS	LOS	NLOS	LOS	NLOS
μ RE %	Complex	0.055	0.064	0.042	0.049	0.052	0.037
	Phase	3e-04	0.007	0.011	0.012	6e-04	0.098
	Mod	0.055	0.062	0.040	0.047	0.052	0.032
σ	value	1e-15	8e-16	1e-15	8e-16	1e-15	8e-16
	RE %	1.598	2.131	1.867	2.476	1.093	3.257

Therefore, the proposed correlator output mathematical model is composed of a useful part, derived in (4.28), and a Gaussian random variable whose mean and variance mathematical model have been derived and validated in this section. These models are dependent on the propagation channel generated and thus are trajectory- and scenario-dependent.

The relevance of the interference term with respect to the noiseless useful term is initially assessed in the next section when a simplified model for the noiseless useful term is presented.

4.2.1.5. Presentation of a simplified model for the noiseless useful correlator output and ICI term impact analysis

The noiseless correlator output mathematical model previously described can be split into a noiseless useful term and an interference term. However, the resulting complete model is still quite complex and to derive a simplified model could be beneficial for theoretical purposes, for example to derive optimal signal processing techniques, and for practical purposes, for example to implement less time-consuming simulations. As presented in section 4.2.1.4, the interference term can be modelled as a Gaussian variable which mean and variance mathematical model have been previously derived; therefore, in this section a simplified model of the noiseless useful correlator output mathematical model provided in (4.28) is derived. This simplified model will be less accurate but easier to manipulate, and could not be applicable to all situations or scenarios. Moreover, during the derivation of this simplified model, the analysis of the relevance of the ICI term in front of the useful term will be preliminary assessed.

The noiseless useful correlator output mathematical model term differs from the constant channel model by the inclusion of the addition, $A_l^k(0) = \sum_{n=0}^{N_{FFT}-1} \alpha_l^k(n)$, which represents the time-evolution of the propagation channel over one OFDM symbol for the l^{th} path, see (4.18).The objective of this section is thus to simplify this term to reduce the final mathematical model complexity and to reduce the QuaDRiGa channel model generation process time.

In order to do so, the following hypotheses are considered:

- The sum of the complex amplitudes over the duration of an OFDM symbol is split in two sums, the sum over the modulus and the sum over the phases. Note that this approximation is only accurate when modulus does not change significantly during the duration of an OFDM symbol. This is the case in the analyzed cases since, as shown in section 4.1.5.4, the modulus varies of a few % over an OFDM symbol:

$$A_l^k(0) \cong \left(\sum_{n=0}^{N_{FFT}-1} \left|\alpha_l^k(n)\right| \right) \left(\frac{1}{N_{FFT}} \sum_{n=0}^{N_{FFT}-1} e^{i\theta(n)} \right) \tag{4.39}$$

- The sum over the modulus is replaced by the mean of the first modulus of symbols k and k+1:

$$\sum_{n=0}^{N_{FFT}-1} \left|\alpha_l^k(n)\right| \cong \frac{\left|\alpha_l^k(0)\right| + \left|\alpha_l^{k+1}(0)\right|}{2} N_{FFT} \tag{4.40}$$

- The phase variation is assumed linear over one symbol (assumption verified through simulations for a QuaDRiGa propagation channel, case 1 and 2, in both LOS/NLOS conditions, and all 4 trajectories):

$$\theta_l(n) \cong \theta_{0_l}^k + 2\pi {\delta_f}_l^k \cdot n \tag{4.41}$$

  Where $\theta_{0_l}^k$ is the phase of the first propagation channel sample applied to the k^{th} OFDM symbol and ${\delta_f}_l^k = \frac{\theta_{0_l}^k - \theta_{0_l}^{k+1}}{2\pi(N_{FFT}+N_{CP})}$ is the normalized (by the sampling time) Doppler frequency of the k^{th} OFDM symbol.

This simplification would allow the generation of only 1 CIR sample per OFDM symbol instead of 10 CIR samples. Finally, the channel contribution term can be simplified as presented in (4.42).

$$A_l^k(0) \cong \frac{\left|\alpha_l^k(0)\right| + \left|\alpha_l^{k+1}(0)\right|}{2} e^{i\theta_{0_l}} e^{i\pi {\delta_f}_l^k \cdot (N_{FFT}-1)} \frac{sin\left(\pi {\delta_f}_l^k N_{FFT}\right)}{sin\left(\pi {\delta_f}_l^k\right)} \tag{4.42}$$

In order to validate this new model, a comparison is performed between the correlation operation using 10 CIR for a complete channel, the initial derived correlator output mathematical model without taking into account the interference term (4.28) using 10 CIR and the proposed simplification (4.42) with respect to the correlation operation using 100 CIR. The correlation operation corresponds to the actual correlation between the received signal and the local replica.

More accurately, first the comparison between the initial model and the correlation operation is performed. The correlation operation includes the interference term, while the initial model does not. Therefore, the comparison aims to provide the impact of interference term with respect to the noiseless useful term (which is either modelled with the initial model or with the simplified one).

Second, the comparison between the initial model and the simplified model is performed. The comparison with the initial model without interference aims to validate the applicability of the simplified model: the simplified model does not target nor include the interference term; therefore, the two models are equivalent if they are statistically equivalent.

The comparison method which has been used is the same as the one used to determine the CIR sampling rate: for the four trajectories defined in section 4.1.2 case 1 and 2, in both LOS/NLOS conditions, the four correlation output time series are computed over 5000 symbols over the main peak of the correlation; then for each symbol the DLL outputs are inspected but in terms of AE. A simplified 5G frame is considered, it is the repetition of one symbol which corresponds to the 2nd (or 4th) symbol of the SS PBCH synchronization block presenting in chapter 3 section 3.3.6.3.2. As a reminder, this symbol is composed of one pilot (DMRS) every 4 subcarriers over 240 subcarriers. The two selected criteria are studied here.

4.2.1.5.1. Impact of the interference term

In this first sub-section, the impact of the interference term is studied by comparing the initial model and the correlation operation.

In Table 4.12, the first criterion and the used color code is the one described in section 4.1.5.4. From Table 4.12, it can be seen that the statistics of the initial model are different from the statistics obtained with 10 CIR per OFDM symbol. This difference is due to the interference term which is not modelled in the initial model. This ICI term impact highly depends on the simulation (trajectory, scenario and case); the worst case is found in the NLOS case 2 simulations. Note that here again, the presented results must be further inspected to limit the outliers' influence using Table 4.13 and Table 4.14 where two DLL configurations are presented, respectively $B_l = 10\ Hz$ and $B_l = 1\ Hz$.

Table 4.12 – Comparison of the DLL absolute evolution in meter – δ=4 samples – $B_l = 10Hz$ – ICI study

Noiseless discriminator output		Trajectory 1				Trajectory 2			
		LOS		NLOS		LOS		NLOS	
		1	2	1	2	1	2	1	2
μ	10	0,008	0,025	0,046	0,290	0,008	0,002	0,056	0,611
	Initial 10	0,028	0,345	0,074	1,391	0,011	0,031	0,084	11,65
σ	10	0,021	0,021	0,194	4,305	0,008	0,002	0,320	14,23
	Initial 10	0,049	0,263	0,162	7,357	0,010	0,058	0,376	103,4
Noiseless discriminator output		Trajectory 3				Trajectory 4			
		LOS		NLOS		LOS		NLOS	
		1	2	1	2	1	2	1	2
μ	10	0,019	0,003	0,153	1,368	0,005	0,043	0,366	1,431
	Initial 10	0,063	0,064	1,362	1,987	0,020	1,863	0,601	13,29
σ	10	0,014	0,002	1,738	18,46	0,003	0,134	9,045	29,03
	Initial 10	0,052	0,051	13,81	24,06	0,014	1,962	8,515	101,2

In Table 4.13 and Table 4.14, the second selection criterion is applied. Focusing on Table 4.14, the 0.5 m criterion is fulfilled, for all cases but the NLOS case 2 and trajectory 4; note that the initial model is at the acceptance limit for NLOS case 1 and radial trajectory. The 1 m criterion is fulfilled for the LOS scenario and it is at the acceptance limit for the NLOS scenario but for case 2 and trajectory 4. This last case assumed to be irrelevant for the envisioned ranging application. The 1 Hz DLL loop bandwidth is more performant than the 10 Hz DLL loop bandwidth. Indeed, it can be seen from Table 4.16 that the 0.5 m and the 1 m criteria are not fulfilled for barely all cases 2 LOS and NLOS.

Therefore, for the 1 Hz DLL loop bandwidth, even if the percentages obtained with the initial case are lower than the ones obtained for the correlation operation, the criterion fulfilled by the correlation operation are mainly fulfilled by the initial model.

In conclusion, the interference term has a very small impact with respect to the noiseless useful term in the LOS scenario case 1 independently from the DLL loop bandwidth and for any NLOS scenario with a 1 Hz DLL loop except for the NLOS case 2 and trajectory 4. For any other configuration, the interference term impact becomes relevant with respect to the noiseless useful term.

Table 4.13 – Percentage of symbol where the discriminator output AE is less than 0.5m and 1 m – δ=4 samples – $B_l = 10Hz$ – ICI study

AE <0.5 m	Trajectory 1				Trajectory 2				Trajectory 3				Trajectory 4			
	LOS		*NLOS*		*LOS*		*NLOS*		*LOS*		*NLOS*		*LOS*		*NLOS*	
	1	*2*	*1*	*2*	*1*	*2*	*1*	*2*	*1*	*2*	*1*	*2*	*1*	*2*	*1*	*2*
10CIR	100	100	99.1	91.6	100	100	98.5	66.7	100	100	96.6	72.8	100	99.6	91.1	84
Initial	99.7	76.1	98.2	55.3	100	99.6	97.9	6.02	100	100	77.3	66.8	100	19.5	83.2	3.8
AE <1 m	Trajectory 1				Trajectory 2				Trajectory 3				Trajectory 4			
	LOS		*NLOS*		*LOS*		*NLOS*		*LOS*		*NLOS*		*LOS*		*NLOS*	

	1	*2*	*1*	*2*	*1*	*2*	*1*	*2*	*1*	*2*	*1*	*2*	*1*	*2*	*1*	*2*
10CIR	100	100	99.7	95.7	100	100	99.2	71.1	100	100	98.4	87.9	100	99.8	94.7	91
Initial	100	97.9	99.7	74.5	100	99.9	99.2	10.9	100	100	86.4	83.8	100	38.4	89.1	8.2

Table 4.14 – Percentage of symbol where the discriminator output AE is less than 0.5m and 1 m – δ =4 samples – $B_l = 1Hz$ – ICI study

AE <0.5 m	Trajectory 1				Trajectory 2				Trajectory 3				Trajectory 4			
	LOS		*NLOS*		*LOS*		*NLOS*		*LOS*		*NLOS*		*LOS*		*NLOS*	
	1	*2*	*1*	*2*	*1*	*2*	*1*	*2*	*1*	*2*	*1*	*2*	*1*	*2*	*1*	*2*
10CIR	100	100	98.1	98.5	100	100	98.5	97.8	100	100	98.8	98.7	100	100	98.8	89.8
Initial	100	100	97.0	96.9	100	100	96.6	91.8	100	100	98.5	95.8	100	100	97.8	9.0
AE <1m	Trajectory 1				Trajectory 2				Trajectory 3				Trajectory 4			
	LOS		*NLOS*		*LOS*		*NLOS*		*LOS*		*NLOS*		*LOS*		*NLOS*	
	1	*2*	*1*	*2*	*1*	*2*	*1*	*2*	*1*	*2*	*1*	*2*	*1*	*2*	*1*	*2*
10CIR	100	100	99.0	99.0	100	100	99.2	98.6	100	100	99.3	99.2	100	100	99.5	94.0
Initial	100	100	98.4	98.3	100	100	98.6	95.9	100	100	99.1	97.7	100	100	99.1	17.8

4.2.1.5.2. Applicability of the simplified model

In this second sub-section, the validity of the simplified model is studied by comparing the initial model and the simplified model.

Table 4.15 – Comparison of the DLL absolute evolution in meter – δ=4 samples – $B_l = 10Hz$ – validity study

Noiseless discriminator output		Trajectory 1				Trajectory 2			
		LOS		NLOS		LOS		NLOS	
		1	2	1	2	1	2	1	2
μ	Initial 10	0,028	0,345	0,074	1,391	0,011	0,031	0,084	11,65
	simplified	0,024	0,345	0,078	1,391	0,010	0,030	0,066	2,577
σ	Initial 10	0,049	0,263	0,162	7,357	0,010	0,058	0,376	103,4
	simplified	0,039	0,261	0,188	7,273	0,010	0,057	0,318	39,12
Noiseless discriminator output		Trajectory 3				Trajectory 4			
		LOS		NLOS		LOS		NLOS	
		1	2	1	2	1	2	1	2
μ	Initial 10	0,063	0,064	1,362	1,987	0,020	1,863	0,601	13,29
	simplified	0,064	0,063	1,343	1,724	0,018	1,859	0,462	11,35
σ	Initial 10	0,052	0,051	13,81	24,06	0,014	1,962	8,515	101,2
	simplified	0,054	0,050	13,74	19,17	0,013	1,963	4,444	35,55

From Table 4.15, it can be seen that the statistics obtained with the initial and the simplified models are roughly equivalent. The simplified model is slightly better. To understand this result, see Figure 4.1. This figure illustrates the method used to model the propagation channel time evolution over one OFDM symbol. It can be seen that the 1st complex amplitude of symbol k+1 is closer to the last complex amplitude applied to symbol k by the reference than the last complex amplitude of symbol k obtained with 10 CIR. It means that the complex amplitudes considered in the simplified model are closer to the reference, which explains its better behavior.

In Table 4.16 and Table 4.17, the second selection criterion is applied. From these tables, it can be seen that the initial and the simplified models are statistically equivalent; the simplified model slightly outperforms the initial one in some cases. Basically, the observations have already been made in 4.2.1.5.1.

In conclusion, the simplified model can be used instead of the initial one for the noiseless useful term for all scenarios since the simplified model is statistically equivalent to the initial model.

Table 4.16 – Percentage of symbol where the discriminator output AE is less than 0.5m and 1 m – δ =4 samples – $B_l = 10Hz$

AE <0.5 m	Trajectory 1				Trajectory 2				Trajectory 3				Trajectory 4			
	LOS		*NLOS*		*LOS*		*NLOS*		*LOS*		*NLOS*		*LOS*		*NLOS*	
	1	*2*	*1*	*2*	*1*	*2*	*1*	*2*	*1*	*2*	*1*	*2*	*1*	*2*	*1*	*2*
Initial	99.7	76.1	98.2	55.3	100	99.6	97.9	6.02	100	100	77.3	66.8	100	19.5	83.2	3.8
simpli	99.9	76.1	98.2	54.9	100	99.7	98.5	30.9	100	100	78.1	68.9	100	19.7	85.3	4.6
AE <1m	Trajectory 1				Trajectory 2				Trajectory 3				Trajectory 4			
	LOS		*NLOS*		*LOS*		*NLOS*		*LOS*		*NLOS*		*LOS*		*NLOS*	
	1	*2*	*1*	*2*	*1*	*2*	*1*	*2*	*1*	*2*	*1*	*2*	*1*	*2*	*1*	*2*
Initial	100	97.9	99.7	74.5	100	99.9	99.2	10.9	100	100	86.4	83.8	100	38.4	89.1	8.2
simpli	100	97.9	99.7	74.3	100	99.9	99.4	50.6	100	100	86.8	84.7	100	38.4	91.8	9.2

Table 4.17 – Percentage of symbol where the discriminator output AE is less than 0.5m and 1 m – δ =4 samples – $B_l = 1Hz$

AE <0.5m	Trajectory 1				Trajectory 2				Trajectory 3				Trajectory 4			
	LOS		*NLOS*		*LOS*		*NLOS*		*LOS*		*NLOS*		*LOS*		*NLOS*	
	1	*2*	*1*	*2*	*1*	*2*	*1*	*2*	*1*	*2*	*1*	*2*	*1*	*2*	*1*	*2*
Initial	100	100	97.0	96.9	100	100	96.6	91.8	100	100	98.5	95.8	100	100	97.8	9.0
simpli	100	100	96.9	97.2	100	100	96.8	92.0	99.9	100	98.4	95.9	100	100	97.7	8.9
AE <1m	Trajectory 1				Trajectory 2				Trajectory 3				Trajectory 4			
	LOS		*NLOS*		*LOS*		*NLOS*		*LOS*		*NLOS*		*LOS*		*NLOS*	
	1	*2*	*1*	*2*	*1*	*2*	*1*	*2*	*1*	*2*	*1*	*2*	*1*	*2*	*1*	*2*
Initial	100	100	98.4	98.3	100	100	98.6	95.9	100	100	99.1	97.7	100	100	99.1	17.8
simpli	100	100	98.3	98.4	100	100	98.7	95.9	100	100	99.0	97.7	100	100	99.2	17.8

4.2.2. Noise correlator output model

In order to complete the development of the evolved 5G signal correlator output mathematical model, the mathematical distribution of the noise at the correlator output must be modelled. Since the noise at the RF front-end output is modelled as an additive white Gaussian distribution, and the demodulation and correlation operations are linear operations, the distribution of the noise at the correlator output is also a Gaussian distribution. Therefore, the analysis of the statistics of the noise, mean and variance, suffices to completely determine its distribution or probability density function. This statistical analysis (development and validation) is split into 3 steps:

- Statistics of the noise at the RF front-end block output
- Statistics of the noise of the OFDM demodulated symbols
- Statistics of the noise at the correlation operation output

4.2.2.1. Complete received signal at the RF front end output

The discrete received signal model at the RF front-end output over one OFDM symbol duration is provided in (4.43).

$$r_n^k = {r_n^k}_{nl} + w_n^k \tag{4.43}$$

Where $w_n^k = w_{n_I}^k + j w_{n_Q}^k$, with $w_{n_I}^k$ and $w_{n_Q}^k$ two independent zero-mean Gaussian variables with $N\left(0, \frac{\sigma_{noise}^2}{2}\right)$, σ_{noise}^2 is determined by the RF front-end block.

4.2.2.2. Noise model of the demodulated OFDM symbol

The method used to study ${r_n^k}_{nl}$ is repeated for w_n^k. Applying the FFT, the noise contribution at the demodulated symbols is:

$$b_q^k = \frac{1}{N_{FFT}} \sum_{n=0}^{N_{FFT}-1} w_n^k e^{-\frac{2i\pi qn}{N_{FFT}}} \tag{4.44}$$

The noise is a Gaussian variable since it is the result of the application of a linear operation of Gaussian variables. It is centered in 0 and the variance and covariance of the correlation between two demodulated noise symbols are provided in (4.45); the derivation can be found in Annex E.1.

$$E\left[b_q^k b_{q'}^{k,*}\right] = \begin{cases} 0 & if\ q \neq q' \\ \sigma_{noise}^2/N_{FFT} & if\ q = q' \end{cases} \tag{4.45}$$

In order to validate this formula, 50000 Monte Carlo are run. The relative error between the theoretical and true variance is equal to 0.0048%.

4.2.2.3. Statistics of the noise at the correlator output

Similarly to (3.29), the correlation of the demodulated noise and the local replica is defined by (4.46). The correlation noise expectation and variance are provided in (4.47) and (4.48) respectively; the derivation can be found in Annex E.2.

$$R_{noise}(\hat{\tau}) = \frac{1}{N_P} \sum_{q \in P} b_q^k p_q^{k*} e^{\frac{2i\pi\hat{\tau}q}{N_{FFT}}} \tag{4.46}$$

$$E[R_{noise}(\hat{\tau})] = \frac{e^{\frac{2i\pi\hat{\tau}\beta}{N_{FFT}}}}{N_P} \sum_{q=0}^{N_P-1} E\left[b_q^k\right] p_q^{k*} e^{\frac{2i\pi\varepsilon_\tau\gamma q}{N_{FFT}}} = 0 \tag{4.47}$$

$$Var[R_{noise}(\hat{\tau})] = \sigma_{noise}^2/(N_{FFT}N_P) \tag{4.48}$$

In order to validate these formulas, 60000 Monte Carlo are run for three values of ε_τ tested. The relative errors between the theoretical and simulated mean and variance are provided in Table 4.17 for several $\hat{\tau}$ values.

Table 4.18 – RE between the theoretical and simulated correlator output noise statistics

	$\hat{\tau} = -5$	$\hat{\tau} = 0$	$\hat{\tau} = 5$
Mean	0.4384%	0.1361%	0.1558%
Variance	0.1290%	0.0796%	0.1666%

The synchronization module proposed in chapter 3 section 3.5.2 uses a DLL and consequently, the Early, and Late correlator output will be generated for the DLL discriminator. Therefore, it is required to determine the correlation of the noise generated between two correlator outputs spaced by a delay equal to $\Delta\tau$. This correlation is provided in (4.49); the derivation can be found in Annex E.3.

$$E[R_{noise}(\hat{\tau})R_{noise}{}^*(\hat{\tau}-\Delta\tau)] = \begin{cases} \frac{e^{\frac{i\pi\Delta\tau(2\beta+\gamma(N_P-1))}{N_{FFT}}}}{N_P^2} \frac{\sigma_{noise}^2}{N_{FFT}} \frac{sin\left(\frac{\pi\Delta\tau\gamma N_P}{N_{FFT}}\right)}{sin\left(\frac{\pi\Delta\tau\gamma}{N_{FFT}}\right)} & \Delta\tau \neq 0 \\ \frac{\sigma_{noise}^2}{N_{FFT}N_P} & \Delta\tau = 0 \end{cases} \tag{4.49}$$

In order to validate this formula, 100000 Monte Carlo are run. The relative error between the theoretical and simulated variance is provided in terms of modulus and in terms of phase in Table 4.19 for three different values of $\Delta\tau$. The relative errors are lower than 0.5% the model is validated.

Table 4.19 – RE between the theoretical and simulated correlation

	$\Delta\tau = -5$	$\Delta\tau = -1$	$\Delta\tau = 5$
Modulus	0.0685%	0.1440%	0.4188%
Phase	0.1122%	0.0924%	0.0417%

4.2.3. Complete correlator output mathematical model

In this section the complete correlator output mathematical model which includes the contribution of the useful received signal (denoted as noiseless contribution) and the contribution of the noise is derived.

The complete correlator output mathematical model derived for a propagation channel evolving over the duration of the correlation is presented in (4.50).

It is composed of three terms:

1. A term referred as noiseless useful term, $R_{useful}(\varepsilon_\tau)$; which is the correlation part linked to the desired received pilot symbols correlated with the local replica pilot symbols.
2. An ICI interference term, $R_{interf}(\varepsilon_\tau)$, which is composed of an interference term due to the pilots symbols and of an interference term due to the data symbols of the transmitted signal. This term can be modelled as a Gaussian variable as shown in section 4.2.1.4.
3. A noise term which is also modelled as a Gaussian variable

Therefore, the correlator output can be mathematically modelled as presented in equation (4.51), which includes the noiseless useful term, $R_{useful}(\varepsilon_\tau)$, and the addition of an equivalent Gaussian variable with mean and variance given in equation (4.52).

Note that correlator output mathematical model of equation (4.51), can be seen as a noiseless useful term, close to the correlator output mathematical model for a constant propagation channel (see chapter 3 section 3.5.3.2), plus a noise with an enhanced power. Therefore, the ICI term can be seen as a degradation of the available SNR or C/N_0 since the Gaussian variable mean part could only affect the DLL operation during the discriminator normalization operation. The value of this degradation depends on the considered case: LOS or NLOS, sub-6 GHz or mmW.

$$R(\varepsilon_\tau) = R_{useful}(\varepsilon_\tau) + R_{interf}(\varepsilon_\tau) + R_{noise}(\varepsilon_\tau) \tag{4.50}$$

$$R(\varepsilon_\tau) = R_{useful}(\varepsilon_\tau) + R_{noise+interf}(\varepsilon_\tau) \tag{4.51}$$

$$R_{noise+interf}(\varepsilon_\tau) \sim N\left(R_{interf_{pilot}}(\varepsilon_\tau), Var[R_{noise}(\hat{\tau})] + Var\left[R_{interf_{data}}(\varepsilon_\tau)\right]\right) \tag{4.52}$$

Finally, note that in order to further simplify the complete correlator output mathematical model, the simplified model of the noiseless useful correlator output mathematical model, which focus on the $A_l^k(0)$ term, can be applied instead of the initial model as justified in section 4.2.1.5.

4.3. Conclusion

The OFDM signal-type correlator output mathematical model presented in chapter 3 is derived by assuming a constant propagation channel over the duration of the correlation (which is performed over

one OFDM symbol). Nevertheless, as shown in this chapter, the CIR of a 5G signal propagation channel (QuaDRiGa) cannot be considered as constant over the duration of the correlation: the expected correlator output of a 5G signal is thus different between a time-evolving propagation channel and a constant one over the duration of an OFDM symbol. The ultimate goal of this chapter was thus to precisely derive the correlator output mathematical model of a 5G signal for ranging purposes; in other word, to improve the model presented in chapter 3 section 3.5.3. In order to derive this precise and realistic correlator output mathematical model, it is of the utmost importance to first precisely model the received 5G signal and, by extension, the interferences distorting the signal introduced by the propagation channel with as much realism as possible; or in other words, the CIR.

Therefore, the method followed in this chapter is divided in two: first the CIR characterization which has permitted to accurately model the propagation channel, second the derivation of the correlator output mathematical model.

In order to validate the results a simplified 5G frame is considered, it is the repetition of one OFDM symbol which corresponds to the 2^{nd} (or 4^{th}) symbol of the SS PBCH synchronization block presenting in chapter 3 section 3.3.6.3.2. As a reminder, this symbol is composed of one pilot (DMRS) every 4 subcarriers over 240 subcarriers.

The CIR characterization

To properly model the evolution of the propagation channel, and to be able to determine the most suitable CIR sampling rate, a two-step process has been followed: first to determine the propagation channel parameters significantly varying in time and second to determine the sampling rate evolution of these parameters.

The first step has permitted to identify the significant time-varying channel parameters. Section 4.1 has shown that the evolution of the propagation channel complex amplitude is not negligible over one OFDM symbol and thus, it must be included in the correlator output mathematical model. However, the evolution of the propagation channel time delay is negligible and may be neglected. In other words, the channel coherence time of the complex amplitude is shorter than one OFDM symbol whereas the channel coherence time of delays is longer for ranging purposes

The second step has allowed to determine the suitable CIR sampling interval of the propagation channel in terms of complex amplitude variation. One constraint to consider during the analysis was the trade-off between the generation computing time and the realism of the modelling.

This method implemented in this second step to determine the CIR sampling rate is based on the inspection of two criteria, which have been derived from a ranging perspective. The two criteria are reminded below:

1) A given X CIR sampling rate is only accepted if the discriminator output AE mean and standard deviation are lower than 10 cm for a LOS scenario and lower than 20 cm for a NLOS scenario.
2) The discriminator output AE values are lower than 0.5 m 95% of time and lower than 1 m 99% of time.

The first criterion is used to inspect the statistics of the DLL discriminator outputs difference between reference CIR and inspected X CIR. The second criterion was introduced in order to remove the influence of the potential outliers from the selection criterion.

Different simulation scenarios were considered, varying trajectories (radial, circular, receiver to emitter distance) and carrier frequencies (sub-6 GHz and mmW).

By applying this method, the CIR-generation sampling rate required to simulate a realistic propagation channel by limiting as much as possible the generator computational burden / mathematical model has been then determined. The adopted CIR generation sampling rate is equal to 10 CIR per OFDM symbol for the signal conditions considered relevant in the analysis of this work.

The correlator output mathematical model

The time-evolution of the propagation channel has important consequences on the OFDM symbol. Basically, as presented in section 4.2.1, the convolution in the frequency domain will create a spectral broadening effect. This spectral broadening implies the loss of the orthogonality among the OFDM signal subcarriers.

The first step proposed for the derivation of the correlator output mathematical model consisted in deriving the noiseless correlator output mathematical model. As shown in section 4.2.1, the noiseless correlator output mathematical model can be split into a noiseless useful term and an ICI term.

The noiseless useful part is deterministic and similar to the correlator output mathematical model derived in chapter 3 section 3.5.3 for a constant channel except for the contribution channel term $A_l^k(0)$. A simplified model for the contribution term has been proposed and validated through simulations.

The interference part can be modelled as a Gaussian variable with a mean depending on the received signal pilot symbols and a variance depending on the received signal data symbols. According to the simulations proposed in section 4.2.1, the interference term can be neglected for some scenario with respect to the useful term. More specifically, it has been shown that the interference term has a very small impact with respect to the noiseless useful term in the LOS scenario case 1 (sub-6 GHz) independently from the DLL loop bandwidth and for any NLOS scenario (sub-6 GHz and mmW) with a 1 Hz DLL loop except for the NLOS case 2 (mmW) and trajectory 4 (receiver at the limit of the range of an emitter coverage). The remaining analysis to be conducted is the impact of the interference term with respect to the noise. This analysis is conducted by a specific scenario in chapter 5.

The second step consisted in modelling the noise contribution to the correlator output mathematical model. The noise has been modelled by a Gaussian variable which statistics derived in section 4.2.2.

Finally, the final correlator output mathematical model is provided in section 4.2.3. This model is composed of the noiseless useful part for which a simplified model can be applied and an additive Gaussian variable. The Gaussian variables includes the noise and interference terms and can be seen as an enhanced noise power and thus as a potential decrease of the available SNR or C/N_0.

Chapter 5. Synchronization module of a 5G signal

As explained in the previous chapters, 5G technology is being standardized at 3GPP [11]; the first complete release of 5G specifications, Release-15, was provided to the community in June 2018. 5G is an emerging technology and its positioning performance, as well as a potential generic receiver scheme to conduct positioning operations, is still under analysis. In order to study the potential capabilities provided by 5G systems and to develop a 5G-based generic positioning module scheme, the first fundamental step is to develop the correlator output mathematical model of a 5G signal for realistic propagation channel models. This model has been derived in chapter 4 section 4.2. The knowledge of the correlation output mathematical model allows for the development of optimal 5G signal processing techniques for ranging positioning. The objective of this chapter is thus to present a potential signal processing ranging module and the elements constituting it.

The correlator output is then used in the synchronization block in order to generate locally a replica perfectly synchronized with the received signal. The synchronization block is usually composed of a delay estimator, or DLL, a potential carrier frequency estimator, a FLL for example, and also a C/N_0 estimator. The later one is required to determine the lock condition of the former ones and can also be used to determine the covariance noise measurement values required to implement the navigation filters. The potential signal processing steps of a 5G ranging module have already been briefly presented in chapter 3 section 3.5.2.

In the first section, the delay lock loop adopted in the thesis is reminded; it was briefly presented for an AWGN channel in chapter 3 section 3.5.3. Second the necessity to implement a carrier tracking loop is studied. Third, the relationship between the input 5G signals Signal to Noise Ratio (SNR) and the C/N_0 is derived and a C/N_0 estimator is proposed.

5.1. Time delay estimator

In this section, the time delay estimator implemented in the synchronization module is presented. More specifically, in this work a time delay estimation closed-loop structure or Delay Lock Loop (DLL) is presented in details. First, the architecture briefly presented in chapter 3 section 3.5.2 is detailed. Second, the discriminator and its characteristics are analyzed. Third, the time delay estimation performance is inspected. Fourth, the sensitivity of the DLL is presented.

5.1.1. DLL architecture

5.1.1.1. Considerations from the correlator output mathematical model

The correlator output mathematical model derived in the previous chapter and adopted for the study is reminded in (5.1). The noiseless useful contribution is reminded in (5.2) and as explained in chapter 4 section 4.2.1.5, the simplified channel contribution model, reminded in (5.3), is adopted. The noise-plus-interference term represents the contribution of the noise as well as the contribution of the ICI term due to the received signal complex envelope evolution over the duration of an OFDM symbol. This term has been modelled as a Gaussian variable with a mean and variance determined by the noise and ICI terms statistics, see chapter 4 section 4.2.1.4.

$$R(\varepsilon_\tau) = R_{useful}(\varepsilon_\tau) + R_{noise+interf}(\varepsilon_\tau) \tag{5.1}$$

$$R_{useful}(\varepsilon_\tau) = \sum_{l=0}^{L-1} \frac{A_l^k(0)}{N_{FFT}} R_l(\varepsilon_{\tau_l}) \tag{5.2}$$

$$A_l^k(0) \cong \frac{\left|\alpha_l^k(0)\right| + \left|\alpha_l^{k+1}(0)\right|}{2} e^{i\theta_{0_l}} e^{i\pi\delta_{f_l}{}^k \cdot (N_{FFT}-1)} \frac{sin\left(\pi\delta_{f_l}{}^k N_{FFT}\right)}{sin\left(\pi\delta_{f_l}{}^k\right)} \quad (5.3)$$

The joint modelling of the noise and ICI terms allows to interpret the correlator output as the correlator output of a constant propagation channel over the duration of an OFDM symbol (or more specifically over the correlation coherent integration time) with an enhanced noise power (potential degradation of the signal SNR or C/N_0). Therefore, since the ranging module in chapter 3 section 3.5.2 is the result of an optimal derivation (ML function maximization with a closed-loop structure) when assuming an AWGN propagation channel (a channel constant over the duration of an OFDM symbol), the same ranging module can still be re-used for the correlator output derived in (5.1) with the same optimal solution status. However, note that this proposed ranging module is still not the optimal solution in the presence of multipath; in this work this optimization has not been tackled. The impact of multipath on this ranging module will be assessed through simulation in Chapter 6.

5.1.1.2. DLL reminders

The selected DLL is a closed loop diagram block scheme and is reminded in Figure 5.1. The selected DLL is the optimal synchronization solution when no multipath is present in the received signal.

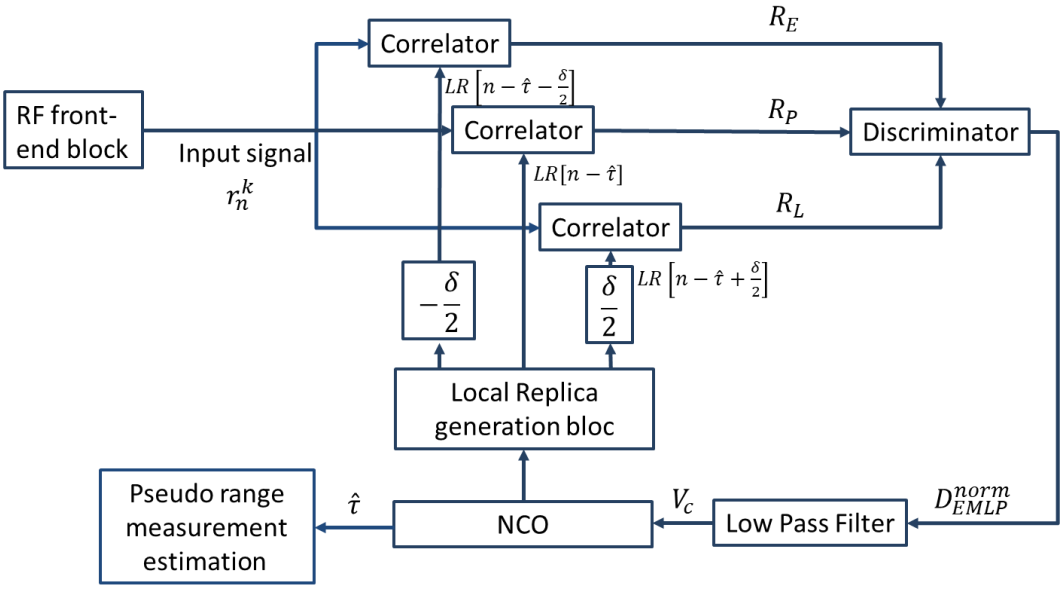

Figure 5.1 – Delay Lock Loop architecture

The DLL makes use of the correlation operation between the incoming signal, r_n^k, which contains the desired code delay to be estimated $\tilde{\tau}_0$ (τ_0 normalized by the sampling time, T_s: $\tilde{\tau}_0 = \tau_0/T_s$), and a local replica, LR, which contains the propagation delay estimated by the DLL denoted as $\hat{\tau}$. More specifically, the correlation is computed at three points spaced by a distance δ called the correlator spacing.

- $LR[\hat{\tau} - \delta/2]$ for the early correlator output: $R_E(\varepsilon_\tau)$
- $LR[\hat{\tau}]$ for the prompt correlator output: $R_P(\varepsilon_\tau)$
- $LR[\hat{\tau} + \delta/2]$ for the late correlator output: $R_L(\varepsilon_\tau)$

Where $\varepsilon_\tau = \tilde{\tau}_0 - \hat{\tau}$ is defined as the propagation delay estimation error. The discriminator output is then filtered by a low-pass filter. Finally, the new delay estimate, $\hat{\tau}$, is determined by using a DCO (Digitally Controlled Oscillator), the new local replica signals are generated and new Early, Prompt and Late correlator outputs are computed for the next loop iteration.

5.1.1.3. DLL general parameters

The configuration of the DLL depends on the parameters provided below. The value of each one of these parameters is commented individually in this section. These presented values are the values used along this work

5.1.1.3.1. DLL update rate

The DLL update rate, T_{update}, is at least equal to the correlator coherent integration time; it is comprised between the OFDM symbol duration, $T_{symbol} = \frac{N_{FFT}+N_{CP}}{\Delta f N_{FFT}}$, and 20 ms (which is the GNSS integration time). All along the thesis, the DLL update rate is set to its lowest possible value: T_{symbol}. Note that this also means that the correlation coherent time (or coherent integration time), T_I, is also set to 1 symbol along this thesis since $T_I \leq T_{update}$.

In Table 5.1, the DLL update rates used in the thesis are provided. Note that the highest subcarrier spacing ($\Delta f = 120\ kHz$) has been used in case 2 in section 4.1.2 in Chapter 4.

Table 5.1 – DLL update rate

N_{FFT}	N_{CP}	Δf	T_{symbol}
2048	144	$15\ kHz$	$7.1354 \cdot 10^{-5}\ s$
		$120\ kHz$	$8.9193 \cdot 10^{-6}\ s$

5.1.1.3.2. DLL discriminator

The chosen discriminator is the Early Minus Late Power (EMLP) defined in (5.4) and studied in [6].

$$D_{EMLP}^{norm}(\varepsilon_\tau) = \frac{|R_E(\varepsilon_\tau)|^2 - |R_L(\varepsilon_\tau)|^2}{K_{norm}|R_P(\varepsilon_\tau)|^2} \tag{5.4}$$

This discriminator is normalized by K_{norm} such that $D_{EMLP}^{norm}(\varepsilon_\tau) \approx \varepsilon_\tau$ for ε_τ close to 0, its expression is derived in the next section.

5.1.1.3.3. DLL order

A second order DLL is used, with the numerical controlled oscillator (NCO) command function, $V_c(k)$, given in (5.5) (which includes the low-pass filter and NCO processing). Note that a second order DLL is chosen since no carrier phase estimator or carrier frequency aided solutions could be implemented in the receiver, and thus the DLL itself must be able to follow the signal dynamics. More specifically, in this work, no carrier phase estimator is planned to be implemented and the implementation of a carrier frequency estimator is not mandatory (see section 5.2).

$$V_c(k) = V_c(k-1) + (K_{VCO\,1} + K_{VCO\,2}) \cdot D_{EMLP}^{norm}(k) - K_{VCO\,1} \cdot D_{EMLP}^{norm}(k-1) \tag{5.5}$$

Where:

- $K_{VCO\,1} = \frac{8}{3} B_l T_{update}$
- $K_{VCO\,2} = \frac{K_{VCO\,1}^2}{2}$

- k is the current sample index

Details can be found in [50]; in this case, the approximation of the discrete case describe in [50] is valid if T_{update} is small, if this was not the case the expression for $K_{VCO\,1}$ and $K_{VCO\,2}$ should be revised.

5.1.1.3.4. DLL one-sided noise equivalent bandwidth

Two loop bandwidths are tested in the thesis, $B_l = 10\ Hz$ and $B_l = 1\ Hz$.

5.1.1.4. DLL normalization factor

The EMLP discriminator defined in (5.4) is normalized by a factor K_{norm}, such that $D_{EMLP}^{norm}(\varepsilon_\tau) \approx \varepsilon_\tau$ for ε_τ close to 0, its expression is now derived. In this section an ideal discriminator is derived when no multipath is considered. The correlator output model can be obtained from (5.6).

$$R_{useful}(\varepsilon_\tau) = \frac{A_l^k(0)}{N_{FFT}} \frac{1}{N_P} e^{\frac{i2\pi\beta\varepsilon_{\tau_l}}{N_{FFT}}} \frac{sin\left(\frac{\pi\gamma\varepsilon_{\tau_l}N_P}{N_{FFT}}\right)}{sin\left(\frac{\pi\gamma\varepsilon_{\tau_l}}{N_{FFT}}\right)} e^{\frac{i\pi\gamma(N_P-1)\varepsilon_{\tau_l}}{N_{FFT}}} \tag{5.6}$$

The expression of the normalization factor, K_{norm}, is such that

$$D_{EMLP}^{norm}(\varepsilon_\tau) \sim \varepsilon_\tau \tag{5.7}$$

Supposing ε_τ is close to 0, the normalized discriminator output (5.4) can be simplified into (5.8). It is expressed in samples.

$$D_{EMLP}^{norm}(\varepsilon_\tau) = \frac{\left(\varepsilon_\tau + \frac{\delta}{2}\right)^2 \left(sin\left(\frac{\pi\gamma\left(\varepsilon_\tau - \frac{\delta}{2}\right)N_P}{N_{FFT}}\right)\right)^2 - \left(\varepsilon_\tau - \frac{\delta}{2}\right)^2 \left(sin\left(\frac{\pi\gamma\left(\varepsilon_\tau + \frac{\delta}{2}\right)N_P}{N_{FFT}}\right)\right)^2}{K_{norm}\left(\varepsilon_\tau - \frac{\delta}{2}\right)^2 \left(\frac{\pi\gamma}{N_{FFT}}\right)^2 \left(\varepsilon_\tau + \frac{\delta}{2}\right)^2} \tag{5.8}$$

Then by using classic trigonometric formula, the equation (5.8) can be rewritten as in (5.9).

$$\begin{aligned} &D_{EMLP}^{norm}(\varepsilon_\tau) \\ &= \frac{\varepsilon_\tau\delta - \left(\varepsilon_\tau^2 + \frac{\delta^2}{4}\right)\sin\left(\frac{\pi\gamma 4\varepsilon_\tau N_P}{N_{FFT}}\right)\sin\left(\frac{\pi\gamma 2\delta N_P}{N_{FFT}}\right) - \varepsilon_\tau\delta\cos\left(\frac{\pi\gamma 4\varepsilon_\tau N_P}{N_{FFT}}\right)\cos\left(\frac{\pi\gamma 2\delta N_P}{N_{FFT}}\right)}{K_{norm}\left(\varepsilon_\tau - \frac{\delta}{2}\right)^2 \left(\frac{\pi\gamma}{N_{FFT}}\right)^2 \left(\varepsilon_\tau + \frac{\delta}{2}\right)^2} \end{aligned} \tag{5.9}$$

Finally, the normalization factor is provided in (5.10).

$$K_{norm} = \frac{1 - \frac{\delta\pi\gamma N_P}{N_{FFT}}\sin\left(\frac{\pi\gamma 2\delta N_P}{N_{FFT}}\right) - \varepsilon_\tau\cos\left(\frac{\pi\gamma 2\delta N_P}{N_{FFT}}\right)}{\left(\frac{\pi\gamma}{N_{FFT}}\right)^2 \frac{\delta^3}{2^4}} \tag{5.10}$$

Where

- δ is the correlator spacing
- γ is used to describe the pilot architecture as presented in chapter 3 section 3.5.3

The complete derivation is provided in Annex F.1.

5.1.2. DLL discriminator study

An important feature to be defined when describing a DLL is the discriminator linearity zone. Figure 5.2 illustrates the discriminator linearity zone, $D_{th_{double-sided}}$, for an EMLP discriminator.

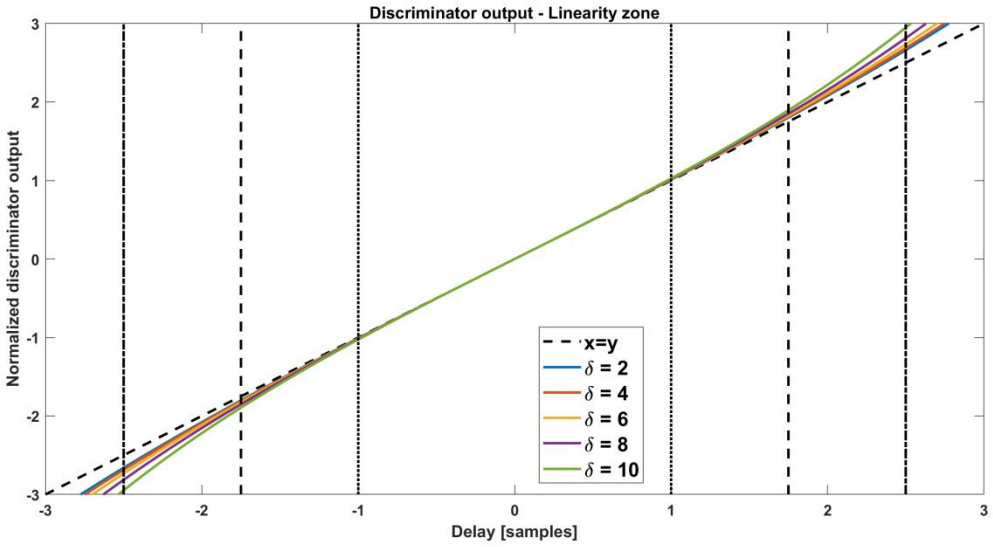

Figure 5.2 – EMLP linearity zone

From Figure 5.2, it can be seen that the choice of D_{th}, which is the one sided discriminator linearity zone, depends on the accepted error between the curve $y = x$ and the discriminator output at the threshold D_{th}. In Table 5.2, this error is quantified for several correlator spacing and D_{th} expressed in samples. In the following, the maximum accepted error is 5%, this choice permitted a fair trade-off between the highest reachable threshold while limiting the errors at the limits. According to the studies performed in chapter 4 section 4.2.1, the correlator spacing used in the following is $\delta = 4$. Therefore, it is assumed that the one-sided discriminator linearity zone is $D_{th} = 7/4$ samples.

Table 5.2 – Errors in % at the limits

	$\delta = 2$	$\delta = 4$	$\delta = 6$	$\delta = 8$	$\delta = 10$
$D_{th} = 1$	0,9349	1,0840	1,3599	1,8184	2,5846
$D_{th} = 7/4$	3,0018	3,4700	4,3387	5,7882	8,2230
$D_{th} = 5/2$	6,4414	7,4650	9,3677	12,550	17,915

5.1.3. Code delay estimation error performance

In this section the variance of the tracking error estimate for an AWGN propagation channel is studied; its expression is provided in (5.11) and the derivation can be found in Annex F.2.

$$var[\varepsilon_\tau] = \frac{2B_l T_s K_1}{N_P SNR}\left(1 + \frac{K_2}{N_P SNR}\right) \tag{5.11}$$

$$K_1 = \frac{4}{K_{norm}^2}\frac{1}{N_P^2}\left(\frac{\sin\left(\frac{\pi\delta\alpha N_P}{2N_{FFT}}\right)}{\sin\left(\frac{\pi\delta\alpha}{2N_{FFT}}\right)}\right)^2\left(1 - \frac{1}{N_P}\frac{\sin\left(\frac{\pi\delta\alpha N_P}{N_{FFT}}\right)}{\sin\left(\frac{\pi\delta\alpha}{N_{FFT}}\right)}\right) \tag{5.12}$$

$$K_2 = \frac{1}{2}\frac{\left(1+\frac{1}{N_P}\frac{\sin\left(\frac{\pi\delta\alpha N_P}{N_{FFT}}\right)}{\sin\left(\frac{\pi\delta\alpha}{N_{FFT}}\right)}\right)^2}{\frac{1}{N_P^2}\left(\frac{\sin\left(\frac{\pi\delta\alpha N_P}{2N_{FFT}}\right)}{\sin\left(\frac{\pi\delta\alpha}{2N_{FFT}}\right)}\right)^2} \quad (5.13)$$

Simulations have been made in order to validate (5.11). In those simulations, the receiver is assumed to be fixed at 20 m from the Base Station; an AWGN channel is considered. The 5G frame is a simplified frame which is composed of one symbol repeated for each symbol; the considered symbol is the 2nd symbol of the SS PBCH synchronization block, see chapter 3 section 3.3.6. The loop bandwidth is set to $B_l = 10\ Hz$; the correlator spacing is set to $\delta = 4$ and the DLL is updated every symbol, $T_s = \frac{N_{FFT}+N_{CP}}{\Delta f N_{FFT}} = 7.135 \cdot 10^{-5}\ s$. Results are provided in Table 5.3 and Figure 5.3. As it can be observed, the variances obtained by simulation fit the theoretical ones.

Table 5.3 – Validation of the variance of the tracking error estimate formula

$SNR_{demod}\ [dB]$	$var[\varepsilon_\tau]$ [m]	
	Theoretical	Simulated
0	0,0002678	0,0002778
10	2,63821e-05	2,73618e-05
20	2,63423e-06	2,73016e-06
30	2,63384e-07	2,74367e-07

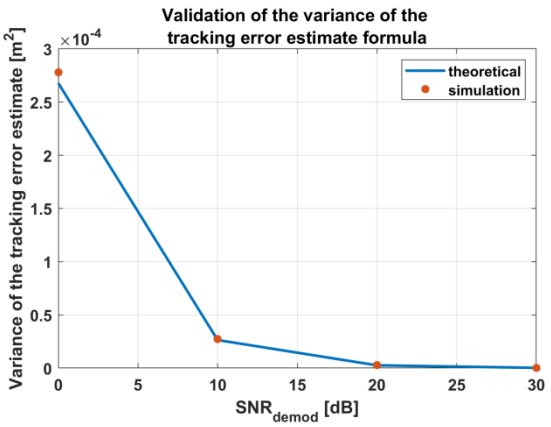

Figure 5.3 – Validation of the variance of the tracking error estimate formula

5.1.4. Sensitivity

In this section the sensitivity of the selected DLL, or DLL tracking threshold, is derived: the DLL tracking threshold is the SNR at the RF front end output, or equivalently the SNR at the demodulation output, value below for which the loop can be considered to have lost tracking. A rule-of-the-thumb criterion to decide that the tracking is lost, is when the 3-sigma value of the tracking error becomes greater than the one-sided linearity zone of the discriminator, D_{th}.

The tracking loss criterion specifies that the DLL has lost its lock if the tracking error falls outside the linearity zone of the discriminator, (5.14). Modelling the noise statistics as a Gaussian distribution and knowing that 99.7% of the values of a Gaussian distribution are inside 3σ, the previous criterion is mathematically modelled as having the discriminator linearity region being equal or smaller than 3 times the standard deviation of the noise. It is assumed that by using a second order DLL, the dynamic of the signal is perfectly tracked and no bias is created on the delay estimation error (short T_{update} will help in this regard). Note that the presented derivation is easily adapted to the presence of a bias on the delay estimation error by just adding the expected bias (depending on the DLL order and worst considered signal dynamic) to the left part of the equation.

$$3\sqrt{var[\varepsilon_\tau]} < \frac{7}{4} \tag{5.14}$$

Replacing (5.11) into the criterion (5.14) leads to (5.15). The complete derivation is provided in Annex F.3.

$$SNR_{demodulator_{th}} = \frac{12^2}{7^2}\frac{B_l T_s K_1}{N_p}\left(1 + \sqrt{1 + \frac{2 \cdot 7^2 K_2}{12^2 B_l T_s K_1}}\right) \tag{5.15}$$

Where:

- $T_s = \frac{N_{FFT}+N_{CP}}{\Delta f N_{FFT}}$, the OFDM symbol duration
- Δf, the subcarrier spacing
- N_{CP}, the Cycle Prefix length
- B_l, the loop bandwidth

The tracking threshold of the DLL, as a function of the correlator spacing and the subcarrier spacing, is provided in Figure 5.4 for a 1 Hz DLL loop bandwidth (left) and for a 10 Hz DLL loop bandwidth (right). Note that 5G systems envisioned the use of several subcarrier spacing: Figure 5.4 shows that the DLL tracking threshold decreases (in the sense of improving) as the subcarrier spacing increases. Moreover, the parameters of the DLL also impact this threshold, the influence of the correlator spacing is provided in Figure 5.4: the DLL tracking threshold decreases along the correlator spacing increase. Finally, the tracking threshold is lower for the 1 Hz DLL loop bandwidth than for the 10 Hz DLL loop bandwidth.

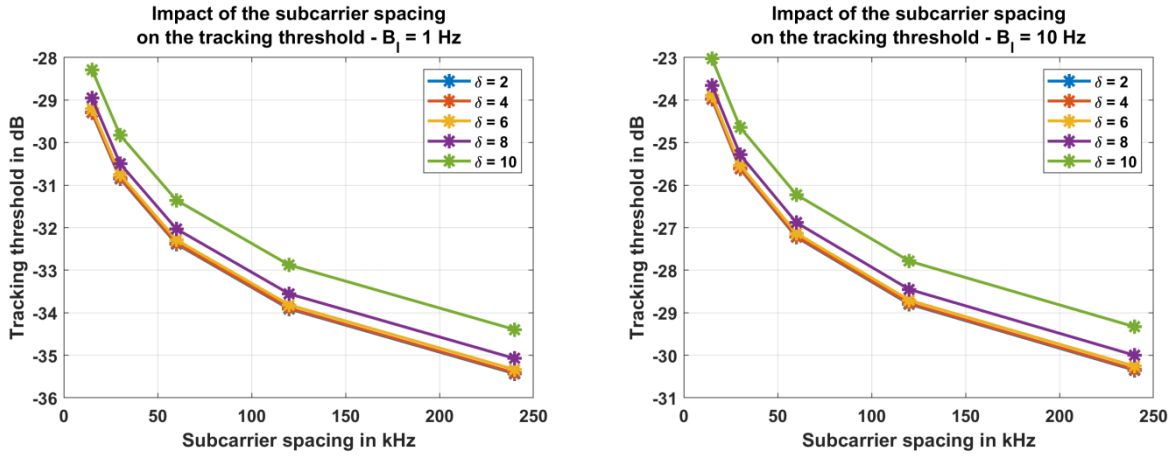

Figure 5.4 – DLL threshold ($SNR_{demodulation_{th}}$)

In chapter 7, the correlator spacing is set to 4 samples and the subcarrier spacing is set to 15 kHz; therefore, the tracking threshold equals -29 dB for a 1 Hz DLL loop bandwidth and -24 dB for the 10 Hz DLL loop bandwidth.

5.2. Carrier Frequency estimator

Two types of tracking loops are usually implemented in a synchronization module, delay and carrier tracking loops. The aim of a delay tracking loop, also denoted as DLL and presented in section 5.1, is to estimate the transmitted signal propagation delay between the emitter and receiver, in this case of analysis, a 5G emitter and a 5G receiver. In section 5.1, a DLL has been implemented and studied in order to design a 5G signal ranging module performing the synchronization. However, this study assumed a

perfect estimation of the 5G signals carrier frequency where this estimation, for example, could be obtained by a Frequency Lock Loop (FLL). Note that the frequency contribution appears in the contribution channel term: $A_l^k(0)$ for the useful term and $A^k(q,q')$ for the interference term in (4.19). Nevertheless, before implementing a FLL or any other carrier frequency estimation technique in a receiver, it is necessary to determine the benefits of such implementation, or in other words, which are the benefits in terms of time delay estimation brought by the existence of a carrier frequency estimator such as a FLL.

The aim of this section is first to study the degradation caused by a frequency estimation error on the time delay estimation conducted by the proposed DLL, and second to provide an in-depth analysis which should help to determine whether the implementation of a carrier frequency estimator is necessary in this work.

In order to conduct this study, the outline of the section is the following one. First, a FLL is presented as a potential carrier frequency estimator candidate. Second, the impact of the CFO on the tracking performances is studied. Third, the theoretical degradation on the delay estimation due to CFO is determined. Finally, the theoretical derivations are validated through simulations.

5.2.1. Presentation of the FLL

The considered FLL is a second order FLL running at twice the symbol rate, $2 \cdot T_{symbol}$. It uses a 10 Hz loop bandwidth, $B_{l_{fll}} = 10\ Hz$.

For each symbol the discriminator defined in (5.16) is computed and the local replica phase, θ_{acc}, is updated as in (5.17).

$$D_{FLL} = \frac{angle(R_P(k) \cdot R_P(k-1)^*)}{2\pi N_{FFT}} \tag{5.16}$$

$$\theta_{acc}(k) = \theta_{acc}(k-1) + 2\pi V_c(k) \tag{5.17}$$

The VCO, $V_c(k)$, is defined in (5.18), it is updated every two symbols (as said before). This equation includes the processing of the NCO and of the low-pass filter of the closed loop.

$$V_c(k) = 2V_c(k-1) - V_c(k-2) + (K_{VCO\,1} + K_{VCO\,2}) \cdot D_{FLL}(k) - K_{VCO\,1} \cdot D_{FLL}(k-1) \tag{5.18}$$

Where:

- $K_{VCO\,1} = 2\frac{8}{3} B_{l_{fll}} T_{update}$
- $K_{VCO\,2} = \frac{K_{VCO\,1}^2}{2}$

The FLL outputs, $\theta_{acc}(k)$ and $V_c(k)$, are then used to correct the phase and Doppler of the incoming signal; therefore these outputs are applied to the received symbol.

$$r_{n\,nl,corrected}^k = r_{n\,nl}^k e^{-i(\theta_{acc}(k-1) + 2\pi V_C(k) n)} \tag{5.19}$$

The impact on the demodulated symbols can be modelled as

$$\tilde{d}_{q'}^{k} = \frac{1}{N_{FFT}} \sum_{l=0}^{L-1} \sum_{q=0}^{N_{FFT}-1} d_q^k e^{-\frac{i2\pi q \tilde{\tau}_l}{N_{FFT}}} \sum_{n=0}^{N_{FFT}-1} \left|\alpha_l^k(n)\right| \cdot e^{i\left(\theta_l^k(n) - \theta_{acc}(k)\right)} e^{i2\pi n\left(\frac{(q-q')}{N_{FFT}} - V_C(k)\right)} \quad (5.20)$$

The correlator output mathematical model derived in chapter 4 is therefore slightly modified and more accurately, the contribution channel is modified as provided in (5.21).

$$A_l^k(0) \cong \frac{\left|\alpha_l^k(0)\right| + \left|\alpha_l^{k+1}(0)\right|}{2} e^{i\left(\theta_{0_l}^k - \theta_{acc}(k)\right)} e^{i\pi\left(\delta_{f_l}{}^k - V_c(k)\right)\cdot(N_{FFT}-1)} \frac{sin\left(\pi\left(\delta_{f_l}{}^k - V_c(k)\right)N_{FFT}\right)}{sin\left(\pi\left(\delta_{f_l}{}^k - V_c(k)\right)\right)} \quad (5.21)$$

5.2.2. Determination of the CFO impact

Mainly due to the Doppler effect and imperfect coarse acquisition, the baseband received signal is affected by a residual carrier frequency offset which impact must be analyzed, and corrected if necessary, in order to design the optimal 5G positioning module.

The studies led in chapter 4 section 4.2.1 prove that the evolution of the complex amplitude of the multipath coming from the propagation channel during the correlation operation impacts the correlator output mathematical model. The objective of this section is to determine the impact of the phase of the LOS tap, which is included on the complex amplitude term, by adapting the process developed in [7] for the CFO study.

5.2.2.1. Determination of the CFO impact on the demodulated symbol

The aim of this section is to determine the impact of a CFO on the demodulated symbol. The impact of the CFO is studied by first deriving the demodulator output in presence of a CFO. Afterwards, the CFO is split into an integer part and a fractional part. The impact of both is then studied independently.

In chapter 4 section 4.2.1.2, the demodulated symbol model has been derived in (4.17) and is reminded below, where $\tilde{\tau}_l = \frac{\tau_l}{T_s}$ is the normalization of the continuous parameter by the sampling time T_s.

$$\tilde{d}_{q'}^{k} = \frac{1}{N_{FFT}} \sum_{l=0}^{L-1} \sum_{q=0}^{N_{FFT}-1} d_q^k e^{-\frac{i2\pi q \tilde{\tau}_l}{N_{FFT}}} \sum_{n=0}^{N_{FFT}-1} \alpha_l^k(n)\, e^{\frac{i2\pi n(q-q')}{N_{FFT}}} \quad (5.22)$$

In order to simplify the study, only one path is considered from now on, $L = 1$.

$$\tilde{d}_{q'}^{k} = \frac{1}{N_{FFT}} \sum_{q=0}^{N_{FFT}-1} d_q^k e^{-\frac{i2\pi q \tilde{\tau}_0}{N_{FFT}}} \sum_{n=0}^{N_{FFT}-1} \alpha_0^k(n)\, e^{\frac{i2\pi n(q-q')}{N_{FFT}}} \quad (5.23)$$

The propagation channel complex amplitude, $\alpha_l^k(n)$, is rewritten as a modulus and a phase as in (5.24). Inserting (5.24) into (5.23) leads to (5.25).

$$\alpha_0^k(n) = \left|\alpha_0^k(n)\right| \cdot e^{i\theta_0^k(n)} \quad (5.24)$$

$$\tilde{d}_{q'}^{k} = \frac{1}{N_{FFT}} \sum_{q=0}^{N_{FFT}-1} d_q^k e^{-\frac{i2\pi q\tilde{\tau}_0}{N_{FFT}}} \sum_{n=0}^{N_{FFT}-1} \left|\alpha_0^k(n)\right| e^{i\theta_0^k(n)} e^{\frac{i2\pi n(q-q')}{N_{FFT}}} \quad (5.25)$$

Following the same method as for the development of the simplified correlator output mathematical model, the sum over the index n in (5.25) can be approximated as follows. The sum is split into a sum of the modulus and a sum over the phases, (5.26). This approximation has been proposed in Chapter 4 (4.39) for $q = q'$; it has been applied here for $q \neq q'$. Indeed, even if it does not reflect the exact numerical value of the contribution term (looser approximation for $q \neq q'$ than for $q = q'$), since the objective is to study the impact of the CFO, the approximation should be close enough to inspect the CFO impact tendency. The sum over the modulus can be approximated by the mean modulus value, (5.27). Finally, studies have proved (chapter 4 section 4.2.1.5) that the phase, $\theta_0^k(n)$, can be assumed linear and approximated by (5.28).

$$\sum_{n=0}^{N_{FFT}-1} \left|\alpha_0^k(n)\right| e^{i\theta_0^k(n)} e^{\frac{i2\pi n(q-q')}{N_{FFT}}} \cong \left(\sum_{n=0}^{N_{FFT}-1} \left|\alpha_0^k(n)\right|\right)\left(\frac{1}{N_{FFT}} \sum_{n=0}^{N_{FFT}-1} e^{i\theta_0^k(n)} e^{\frac{i2\pi n(q-q')}{N_{FFT}}}\right) \quad (5.26)$$

$$\sum_{n=0}^{N_{FFT}-1} \left|\alpha_0^k(n)\right| \cong \frac{\left|\alpha_0^k(0)\right| + \left|\alpha_0^{k+1}(0)\right|}{2} N_{FFT} \quad (5.27)$$

$$\theta_0^k(n) \cong \theta_{0\,0}^{k} + 2\pi\delta_{f\,0}^{\,k} \cdot n \quad (5.28)$$

Where:

- $\theta_{0\,0}^{k}$ is the phase of the first propagation channel sample applied to the k^{th} OFDM symbol
- $\delta_{f\,0}^{\,k} = \frac{\theta_{0\,0}^{k} - \theta_{0\,0}^{k+1}}{2\pi(N_{FFT}+N_{CP})}$ is the carrier frequency offset normalized by the sampling time, T_s

Following these assumptions, the model of the demodulated symbols can be derived as in (5.29) and (5.30).

$$\tilde{d}_{q'}^{k} = \left(\frac{\left|\alpha_0^k(0)\right| + \left|\alpha_0^{k+1}(0)\right|}{2}\right) \frac{1}{N_{FFT}} \sum_{q=0}^{N_{FFT}-1} d_q^k e^{-\frac{i2\pi q\tilde{\tau}_0}{N_{FFT}}} \sum_{n=0}^{N_{FFT}-1} e^{i\theta_{0\,0}^{k} + 2i\pi\delta_{f\,0}^{\,k} \cdot n} e^{\frac{i2\pi n(q-q')}{N_{FFT}}} \quad (5.29)$$

$$\tilde{d}_{q'}^{k} = \left(\frac{\left|\alpha_0^k(0)\right| + \left|\alpha_0^{k+1}(0)\right|}{2}\right) \frac{1}{N_{FFT}} e^{i\theta_{0\,0}^{k}} \sum_{q=0}^{N_{FFT}-1} d_q^k e^{-\frac{i2\pi q\tilde{\tau}_0}{N_{FFT}}} \sum_{n=0}^{N_{FFT}-1} e^{\frac{i2\pi n\left(q-q'+\delta_{f\,0}^{\,k}\right)}{N_{FFT}}} \quad (5.30)$$

As it can be seen in (5.30), the normalized carrier frequency offset, $\delta_{f\,0}^{\,k}$, appears. In order to study its impact, it is split into a integer part, p_{f_l}, and a fractional part, $\delta_{f_l} \in [-0.5, 0.5]$. The impact of both is then studied separately.

$$\delta_{f\,l}^{\,k} = p_{f_l} + \delta_{f_l} \quad (5.31)$$

5.2.2.1.1. Impact of an integer CFO

First, the impact of the integer part of the normalized Doppler frequency offset, p_{f_l}, is studied; for this purpose, the fractional part is assumed to be zero, $\delta_{f_l} = 0$.

The demodulated symbol mathematical model is thus expressed as (5.32). The sum over the index n is a geometric sum and it can be derived as in (5.33). Since p_{f_l} is an integer, the sum is limited to the case where $\left(q - q' + p_{f_l}\right) = 0$; thus the mathematical model the demodulated symbol is (5.34).

Remind that only one path is considered from now on, $L = 1$, therefore $l = 0$.

$$\tilde{d}_{q'}^{k} = \left(\frac{\left|\alpha_0^k(0)\right| + \left|\alpha_0^{k+1}(0)\right|}{2}\right)\frac{1}{N_{FFT}} e^{i\theta_{00}^k} \sum_{q=0}^{N_{FFT}-1} d_q^k e^{-\frac{i2\pi q\tilde{\tau}_0}{N_{FFT}}} \sum_{n=0}^{N_{FFT}-1} e^{\frac{2i\pi n\left(q-q'+p_{f_0}\right)}{N_{FFT}}} \tag{5.32}$$

$$\sum_{n=0}^{N_{FFT}-1} e^{\frac{2i\pi n\left(q-q'+p_{f_0}\right)}{N_{FFT}}}$$

$$= \begin{cases} e^{\frac{i\pi(N_{FFT}-1)\left(q-q'+p_{f_0}\right)}{N_{FFT}}} \dfrac{\sin\left(\pi\left(q-q'+p_{f_0}\right)\right)}{\sin\left(\frac{\pi}{N_{FFT}}\left(q-q'+p_{f_0}\right)\right)} & \left(q-q'+p_{f_0}\right) \neq 0 \\ N_{FFT} & \left(q-q'+p_{f_0}\right) = 0 \end{cases} \tag{5.33}$$

$$= \begin{cases} 0 & for\ \left(q-q'+p_{f_0}\right) \neq 0 \\ N_{FFT} & for\ \left(q-q'+p_{f_0}\right) = 0 \end{cases}$$

$$\tilde{d}_{q'}^{k} = \left(\frac{\left|\alpha_0^k(0)\right| + \left|\alpha_0^{k+1}(0)\right|}{2}\right) e^{i\theta_{00}^k} e^{-\frac{i2\pi\left(q'-p_{f_0}\right)\tilde{\tau}_0}{N_{FFT}}} d_{q'-p_{f_0}}^{k} \tag{5.34}$$

The model presented in (5.34) differs from the demodulated symbol mathematical model (4.19): no ICI term appears in (5.34) moreover, in place of the desired symbol, $d_{q'}^k$, modulated by subcarrier q', a symbol modulated by another subcarrier, $q' - p_{f_0}$, is obtained, $d_{q'-p_{f_0}}^k$.

In conclusion, an integer CFO, p_{f_l}, induces a shift on the demodulated symbol. In order to recover the transmitted symbol $d_{q'}^k$, p_{f_l} must be estimated; however, since the only impact is a shift, the estimation and correction of the integer p_{f_l}, can be easily achieved after the demodulation. Therefore, p_{f_l} impact is assumed to be corrected and its effect neglected in the remaining part of the work. Moreover, the mathematical model derived in chapter 4 section 4.2.3 remains correct (but the part of the ICI term associated to the LOS does not exist, only the ones of the multipath which are not considered in this section).

5.2.2.1.2. Impact of a fractional CFO

Second, the impact of the fractional part of the normalized Doppler frequency offset, δ_{f_l}, is studied; for this purpose, the integer part is assumed to be zero, $p_{f_l} = 0$.

Please note that in chapter 4 section 4.2.1.4, the ICI term has been modelled as a Gaussian variable. In this section, the precise mathematical model of the ICI term is carefully studied in order to quantify the influence of the CFO on this term.

The demodulated symbol mathematical model is thus expressed as (5.35). The sum over the index n is a geometric sum and it can be derived similarly to (5.33). Since δ_{f_0} is a fractional number, the sum is

limited to the case where $\left(q-q'+\delta_{f_0}\right)\neq 0$; therefore, the mathematical model the demodulated symbol is (5.36) (from equation (5.33)).

$$\tilde{d}_{q'}^{k}=\left(\frac{\left|\alpha_0^k(0)\right|+\left|\alpha_0^{k+1}(0)\right|}{2}\right)\frac{1}{N_{FFT}}e^{i\theta_{00}^{k}}\sum_{q=0}^{N_{FFT}-1}d_q^k e^{-\frac{i2\pi q\tilde{\tau}_0}{N_{FFT}}}\sum_{n=0}^{N_{FFT}-1}e^{\frac{i2\pi n\left(q-q'+\delta_{f_0}\right)}{N_{FFT}}} \tag{5.35}$$

$$\begin{aligned}&\tilde{d}_{q'}^{k}\\&=\left(\frac{\left|\alpha_0^k(0)\right|+\left|\alpha_0^{k+1}(0)\right|}{2}\right)\frac{e^{i\theta_{00}^{k}}}{N_{FFT}}\sum_{q=0}^{N_{FFT}-1}d_q^k e^{-\frac{i2\pi q\tilde{\tau}_0}{N_{FFT}}}e^{i\pi\left(q-q'+\delta_{f_0}\right)(N_{FFT}-1)}\frac{sin\left(\pi\left(q-q'+\delta_{f_0}\right)N_{FFT}\right)}{sin\left(\pi\left(q-q'+\delta_{f_0}\right)\right)}\end{aligned} \tag{5.36}$$

Following the method used in chapter 4 section 2, the mathematical sum over the symbols indexed by q can be split in two sums. This permits to define the useful contribution, for $q=q'$, and the interference contribution, for $q\neq q'$, as expressed in (5.37), (5.38) and (5.39).

$$\tilde{d}_{q'}^{k}=\tilde{d}_{q'_{useful}}^{k}+\tilde{d}_{q'_{interf}}^{k} \tag{5.37}$$

$$\tilde{d}_{q'_{useful}}^{k}=\left(\frac{\left|\alpha_0^k(0)\right|+\left|\alpha_0^{k+1}(0)\right|}{2}\right)\frac{1}{N_{FFT}}e^{i\theta_{00}^{k}}e^{-\frac{i2\pi q'\tilde{\tau}_0}{N_{FFT}}}e^{i\pi\delta_{f_0}(N_{FFT}-1)}\frac{sin\left(\pi\delta_{f_0}N_{FFT}\right)}{sin\left(\pi\delta_{f_0}\right)}d_{q'}^{k} \tag{5.38}$$

$$\begin{aligned}&\tilde{d}_{q'_{interf}}^{k}\\&=\left(\frac{\left|\alpha_0^k(0)\right|+\left|\alpha_0^{k+1}(0)\right|}{2}\right)\frac{e^{i\theta_{00}^{k}}}{N_{FFT}}\sum_{\substack{q=0\\q\neq q'}}^{N_{FFT}-1}d_q^k e^{-\frac{i2\pi q\tilde{\tau}_0}{N_{FFT}}}e^{i\pi\left(q-q'+\delta_{f_0}\right)(N_{FFT}-1)}\frac{sin\left(\pi\left(q-q'+\delta_{f_0}\right)N_{FFT}\right)}{sin\left(\pi\left(q-q'+\delta_{f_0}\right)\right)}\end{aligned} \tag{5.39}$$

As it can be seen on the useful term, a fractional CFO induces attenuation and phase rotation of the demodulated symbol. As it can be seen by the interference term, a fractional CFO determines the contribution of the non-desired symbol in the ICI term (and thus the mean and variance of this term).

Contrary to the section 5.2.2.1.1 for the integer CFO, the inter carrier interference (ICI) term appears in (5.37) (ICI term due to LOS does not appear for the integer CFO and the multipath are not considered). The ICI term corresponds to the model derived in (4.21) and reminded in (5.40). (5.40) is proposed assuming one path only as supposed for this derivation. By comparing (5.37) and (5.40), it can be seen that (5.37) is more developed since equation (5.37) proposes an approximation for the term $A_0^k(q'-q)$ (see equation (5.41)).

$$\begin{aligned}&\hat{d}_{n_l,q'}^{k}=\frac{A^k(q',q')}{N_{FFT}}d_{q'}^{k}+\sum_{\substack{q=0\\q\neq q'}}^{N_{FFT}-1}\frac{A^k(q',q)}{N_{FFT}}d_q^k\\&\hat{d}_{n_l,q'}^{k}=\frac{e^{-\frac{2i\pi q\tilde{\tau}_0}{N_{FFT}}}A_0^k(0)}{N_{FFT}}d_{q'}^{k}+\sum_{\substack{q=0\\q\neq q'}}^{N_{FFT}-1}\frac{e^{-\frac{2i\pi q\tilde{\tau}_0}{N_{FFT}}}A_0^k(q'-q)}{N_{FFT}}d_q^k\end{aligned} \tag{5.40}$$

$$A_0^k(q'-q) \approx \left(\frac{\left|\alpha_0^k(0)\right| + \left|\alpha_0^{k+1}(0)\right|}{2}\right) e^{i\theta_{0_0}^k} e^{i\pi\left(q-q'+\delta_{f_0}\right)(N_{FFT}-1)} \frac{sin\left(\pi\left(q-q'+\delta_{f_0}\right)N_{FFT}\right)}{sin\left(\pi\left(q-q'+\delta_{f_0}\right)\right)} \quad (5.41)$$

5.2.2.2. Determination of the CFO impact at the correlator output

The effects observed on the demodulated symbols can also be characterized at the correlator outputs. Since the impact of an integer CFO on the demodulated symbols is a shift, it has been explain that the correction can be easily achieved after the demodulation. Therefore, only the impact of a fractional CFO is described here.

In fact, this impact is easily predictable by following the method used in chapter 4 section 4.2.1.3. when dividing the noiseless demodulated symbol into a noiseless useful part and an interference part. Therefore, the degradation due to the CFO are the attenuation of the LOS path by the factor described in (5.41) and the inter carrier interference term. As already concluded in 5.2.2.1, the model derived for a fractional CFO is equivalent to the model derived in chapter 4 section 4.2.1.3 but more developed since it proposes an approximation for the term $A_l^k(q'-q)$.

In conclusion, a fractional CFO induces an attenuation and a phase rotation on the demodulated symbol and adds an additional ICI term; the same effect is propagated to the correlator outputs. Two impacts already observed in chapter 4 section 2. The fractional CFO cannot be corrected after the demodulation but instead requires be estimating and correcting before. Therefore, the necessity to apply this correction for time delay tracking purposes is the objective of this analysis.

5.2.3. Theoretical degradation of delay estimation performance due to CFO

5.2.3.1. Methodology

As shown in section 5.2.2, a fractional CFO induces distortion effects on the demodulation and on the correlation. The induced degradation on the delay estimation performance must thus be quantified in order to determine whether a carrier phase estimator, such a FLL, is required or not. The method adopted to determine the necessity to implement a carrier frequency estimator consists in deriving the degradation of the time delay estimation performance as a function of the Signal to Noise Ratio (SNR) and the Carrier Frequency Offset (CFO). Therefore, this work first determines and selects realistic CFO and SNR values to obtain realistic upper bounds on the time delay estimation performance.

More specifically, the section is organized as follows. First, the assumptions made regarding the propagation channel in order to perform the study are presented. Second, the theoretical degradation of the SNR due to the CFO is determined. In order to determine realistic values of the delay tracking degradation, realistic values of SNR and Doppler variation are determined in the third and fourth sections. Fifth, the SNR degradation due to the CFO is studied. Sixth the theoretical degradation on the time delay estimation due to CFO is determined.

5.2.3.2. Propagation channel assumptions

The propagation channel considered for the derivation is made of one path only. Its modulus is assumed constant however a Doppler frequency, and thus a CFO is considered.

5.2.3.3. *Theoretical degradation of SNR due to CFO*

The degradation due to the CFO, D, is analyzed by adapting the work developed in [51]; it can be shown that this degradation, D, is the ratio between the SNR and the SINR and can be expressed as a function of the SNR at the correlator output and the CFO. Note that in chapter 4, it was demonstrated that the ICI term could be modelled as a Gaussian variable and thus, the noise and the ICI term could be jointly modelled as a unique Gaussian variable with resulting variance equal to the addition of each individual term variances. Therefore, the methodology to directly add the interference power to the power of the noise is fully justified and validated in this work.

The SINR is modelled as $SINR = \frac{A^2 S}{N+P_{ICI}}$, where A represents the attenuation due to the fractionnal CFO. According to the study presented in section 5.2.2, A is represented by $A = \frac{1}{N_{FFT}} \frac{sin(\pi\delta_{f_l} N_{FFT})}{sin(\pi\delta_{f_l})}$.

In [52], the mathematical model of the P_{ICI} is derived for the ICI term present at the demodulated symbols, $P_{ICI}^{demod} = \frac{(\pi\delta)^2}{3}$. This model is valid for the demodulated symbols and for small values of δ_f, as illustrated in Figure 5.5.

In this study, a new mathematical model for the P_{ICI} has been empirically derived for the ICI term present at the correlator output for small values of δ_f: $P_{ICI}^{corr} = \frac{7(\pi\delta_f)^2}{2N_P}$. It is specific to the considered signal: the Fourier Transform window is set to 2048, the signal is composed of 240 subcarriers with a pilot every 4 subcarrier, it corresponds to the 2nd or 4th symbol of the SSPBCH synchronization block described in chapter 3 section 3.3.6.3.2. An ideal timing synchronization is assumed. The model is validated through simulation (empirical derivation), as illustrated in Figure 5.5.

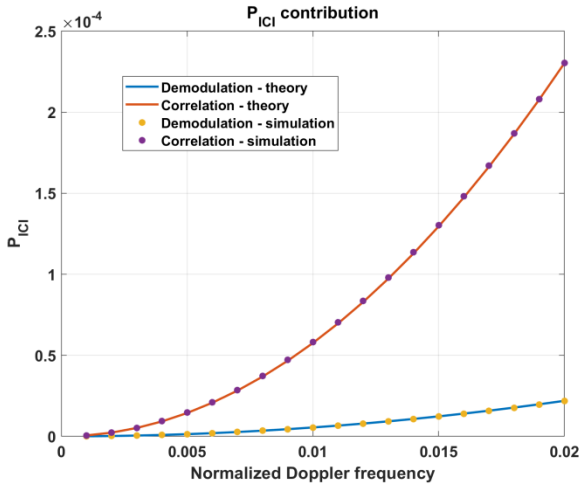

Figure 5.5 – Inter Carrier Interference term

The degradation due to the CFO, D, is therefore defined by (5.42).

$$D = \frac{SNR}{SINR} = \frac{\frac{S}{N}}{\frac{A^2 S}{N + P_{ICI}}} = \frac{1}{A^2}\left(1 + \frac{7(\pi\delta_f)^2}{2N_P} SNR\right) \text{where: } A = \frac{1}{N_{FFT}} \frac{sin\left(\pi\delta_{f_l} N_{FFT}\right)}{sin\left(\pi\delta_{f_l}\right)} \quad (5.42)$$

5.2.3.4. Determination of realistic SNR values

Concerning the derivation of realistic SNR values at the RF front end output, a lower bound for the SNR can be set by determining the sensitivity of the considered DLL; or in other words the DLL tracking threshold which has been derived in section 5.1.3.

In order to quantify the SNR degradation due to a CFO, three 5G signal configurations, defined from the signal carrier frequency and subcarrier spacing, are considered and presented in Table 5.4. In these configurations, two subcarrier spacings are considered, the correlator spacing is set to $\delta = 4$ and the DLL loop bandwidth is set to $B_l = 10\ Hz$. Thus the lower bounds of the SNR to be tested are:

- $SNR_{threshold} = -24\ dB$ for $\Delta f = 15\ kHz$
- $SNR_{threshold} = -29\ dB$ for $\Delta f = 120\ kHz$

5.2.3.5. Determination of the Doppler variation values

In order to quantify the degradation due to the CFO, the third step consists in determining a realistic worst value for the normalized (with respect to the sampling time) frequency error, δ_f. More specifically a worst δ_f is derived when the receiver goes away from a base station at high speed (50 km/h); this value is then multiplied by 2 to represent the case when the receiver goes back and forth. The maximum range of Doppler variation can be defined as a function of the Doppler frequency, f_d, and the subcarrier spacing, Δf.

$$\delta_{f,worst} = 2 f_d T_{sampling} = \frac{2 f_d}{\Delta f N_{FFT}} = \frac{2 f_c \cdot v}{N_{FFT} \cdot \Delta f \cdot c} \quad (cycle/sample) \tag{5.43}$$

Where f_c is the carrier frequency, N_{FFT} is the Fourier Transform size, v is the speed of the receiver and c is the celerity of light.

In order to determine a realistic range of Doppler variation with the previous formula, three 5G signal configurations, defined from the signal carrier frequency and subcarrier spacing, are considered and presented in Table 5.4. These configurations aim to represent realistic and generic 5G signal configurations – as envisioned in the 3GPP standard: sub-6 GHz band with a low subcarrier spacing (case 1) and millimeter wave bands with high subcarrier spacing (Case 2 and 3). Moreover, Table 5.4 provides typical Doppler variation values normalized by the sampling time, $\delta_{f,worst}$, that will be used in (5.41) to quantify the degradation of SNR due to the CFO. Note that the maximum values are far smaller than the maximum δ_f for which the empirical P_{ICI}^{corr} model was derived. Therefore, the validity of this model for the inspected cases is proven.

Table 5.4 – Determination of a realistic value of frequency error

Case	Speed v	Carrier frequency f_c	Subcarrier spacing Δf	$f_d = \frac{f_c \cdot v}{c}$ $Hz = (cycle/second)$	$\delta_{f,worst} = \frac{2 f_c \cdot v}{N_{FFT} \cdot \Delta f \cdot c}$ $(cycle/sample)$
1	50 km/h	2 GHz	15 kHz	92.6567 Hz	6.0323e-06
2		30 GHz	120 kHz	1389.85 Hz	1.1328e-05
3		60 GHz	120 kHz	2779.70 Hz	2.2607e-05

5.2.3.6. *Study of the CFO degradation*

By using the SNR and Doppler ranges determined in the 2 previous sections, it is possible to quantify the SNR degradation D (see equation (5.41)). Results obtained by the evaluation of (5.41) are presented in Figure 5.6. As illustrated, the degradation increases with the SNR; the worst degradation is obtained in case 3 and reaches 44 dB for $SNR_{correlator} = 157\ dB$.

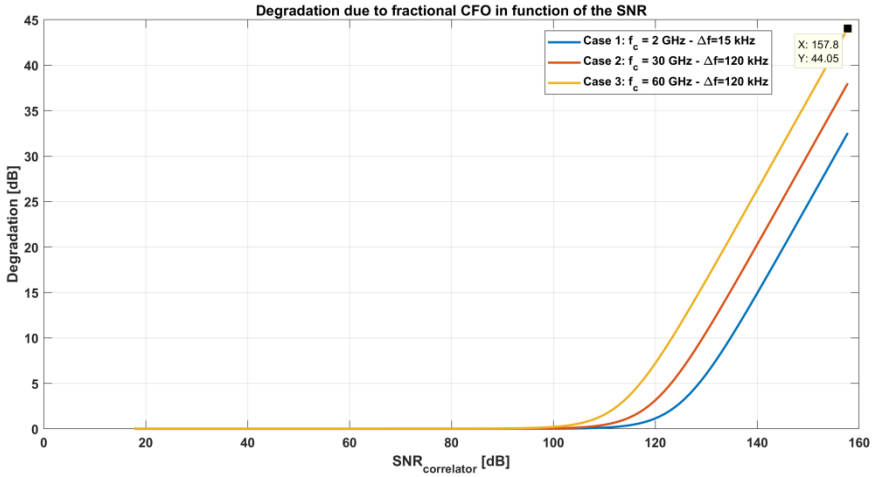

Figure 5.6 – Degradation due to a fractional CFO

From Figure 5.6, it can be observed that for the considered cases, for $SNR_{correlator} < 105\ dB$, the degradation is lower than 0.5 dB. Therefore, it is already possible to infer that for $SNR_{correlator}$ values lower than 105 dB, the degradation on the DLL tracking performance will be negligible.

The degradation's behavior could actually be problematic since it means that a CFO will induce a saturation phenomenon for high SNR values. In order to visualize this phenomenon, Figure 5.7 is proposed. In this figure, the case 1 presented in Table 5.4 is studied.

Figure 5.7 illustrates the effect of the Doppler derived for case 1 assuming that the DLL is updated every 7.13e-5 s, or at 15 kHz.

The effect of the CFO and the DLL rate is studied by inspecting the SNR at the correlator output when assuming an AWGN propagation channel. The following relationship is used to obtain the SNR at the correlator output: $SNR_{correlator_{degraded}} = SNR_{correlator} - D$.

From Figure 5.7, for the worst case scenario, when the normalized Doppler equals 6.0323e-06, it can be seen that the saturation is appearing for an input SNR at the correlator output of 120 dB which corresponds to a base station emitted power of $C \cong -15\ dBW$ which is close to the maximum base station emitted power provided in [53]: $C_{max} \cong -6\ dBW$.

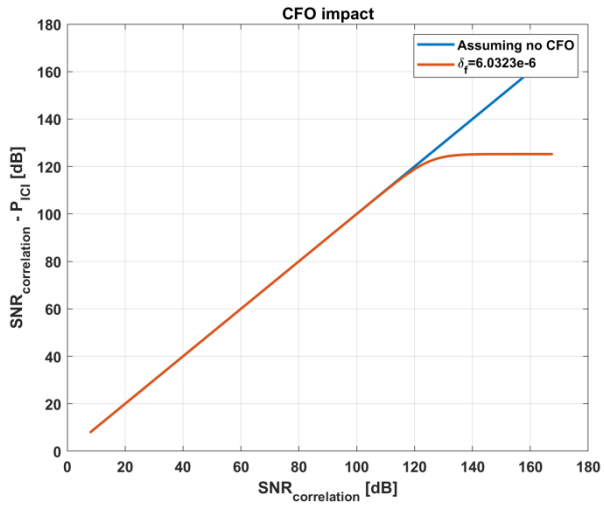

Figure 5.7 – Focus on case1: impact of the Doppler on the $SNR_{correlation}$

In the next sections, the emitted base station powers is assumed to be equal to $C \cong -30\ dBW$, which correspond to a SNR at the demodulation output of 96 dB. Therefore, this saturation phenomenon does not appear. Moreover, the same assumption has been taken along this thesis which means that this saturation effect does not appear during all the following analysis.

5.2.3.7. Theoretical degradation on the time delay estimation due to CFO

In this section, the theoretical degradation on the DLL precision due to the CFO is determined. By doing so, the potential theoretical benefits of the implementation of a carrier frequency estimator in terms of time delay estimation are determined. For this purpose, the variance of the tracking estimation error is derived for two cases:

- An input SNR, $SNR = SNR_{true}$
- A SNR degraded using the degradation term computed before, $SNR_{degraded} = SNR_{true} + D$

The error in terms of standard deviation of the tracking estimation error due to the CFO as a function of the SNR is illustrated in Figure 5.8 for the 3 cases described in Table 5.4. More specifically, the difference between σ_{true} and $\sigma_{degraded}$ as defined in (5.44) and (5.45) is presented.

$$\sigma_{true} = \sqrt{var(\tilde{\varepsilon}_\tau)_{SNR=SNR_{true}}} \tag{5.44}$$

$$\sigma_{degraded} = \sqrt{var(\tilde{\varepsilon}_\tau)_{SNR=SNR_{degraded}}} \tag{5.45}$$

As it can be seen, the error is of the order of the millimeters and thus, the degradation can be qualified as negligible. Therefore, it can be concluded that a carrier frequency estimator is theoretically not necessary in a AWGN channel even in the presence of a worst-case scenario CFO when the correlation is conducted over one OFDM symbol and when the DLL has an update rate of one OFDM symbol as well.

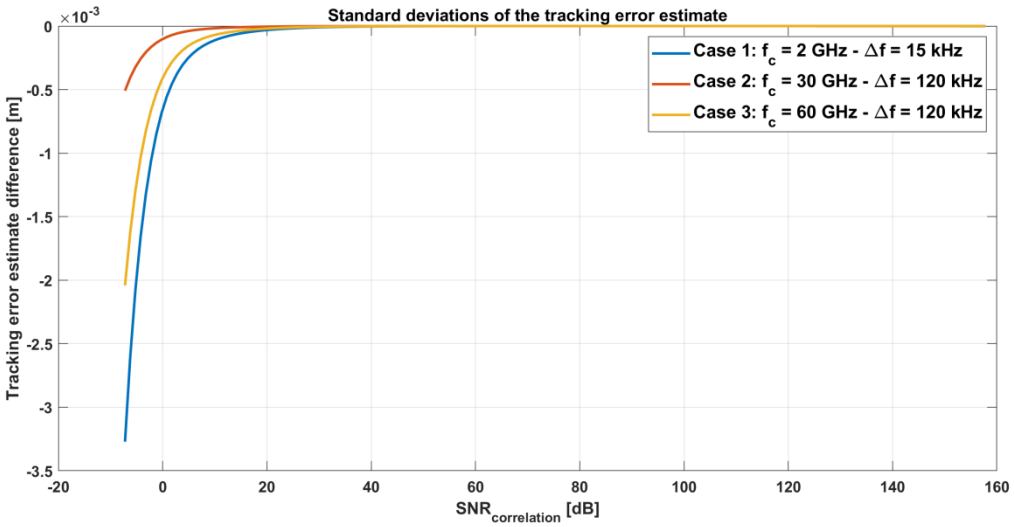

Figure 5.8 – Standard deviation of the tracking error estimate

It must be kept in mind that this study is conducted assuming an AWGN channel with a worst-case scenario CFO. Therefore, simulations are required to first validate these results and second to study the impact of the propagation channel: for a complete channel it might be useful to still implement a carrier frequency estimator, for example a FLL.

5.2.4. Validation through simulation

The previous theoretical analysis showed that the carrier frequency estimator implementation in a receiver brings no benefit in terms of time delay estimation performance for an AWGN channel with a worst-case scenario CFO. In order to validate these results, simulations are proposed using a 5G signal simulator presented in Annex A.

The section is structured as follows: first the tested configurations are presented. Second, the results obtained for an AWGN channel are presented; these results allow to validate the theoretical derivation proposed in section 5.2.3. Third, the previous study is performed for a complete QuaDRiGa propagation channel; this will permit to determine if, due to the degradation due to the multipath, the implementation of a FLL can improve the time delay estimation performance.

5.2.4.1. Tested configurations

In order to validate the theoretical results of section 5.2.3, 4 carrier frequency estimator configurations combined with 2 DLL configurations are tested. Note that not every combination of DLL configuration and carrier frequency estimator configuration will be tested. Only the configurations deemed more representatives for each inspected case.

5.2.4.1.1. DLL configurations

Two DLL configurations are used: the implemented DLL is always a second order DLL presented in section 5.1., the correlator spacing is set to 4 samples and the DLL loop bandwidth is set to 10 Hz or 1 Hz. Table 5.5 summarizes the DLL configurations.

Table 5.5 – DLL configurations

	Order	Correlator spacing	DLL loop bandwidth
Configurations	2nd	$\delta = 4$	$B_l = 1\ Hz$ $B_l = 10\ Hz$

5.2.4.1.2. Carrier frequency estimator configurations

Four carrier frequency estimator configurations are tested. The impact of these 4 configurations can all be modelled on the correlator output formula (5.46) where they differ from the expression of $A_l^k(0)$ of the noiseless useful term, (5.47), and on the ICI term power. Remember that the ICI term impact is jointly modelled with the noise in the term $R_{noise+interf}(\varepsilon_\tau)$.

For each carrier frequency estimator configuration, the contribution of channel expression of the LOS path is considered apart from the multipath (first and second line in Table 5.6 respectively). In order to distinguish both of them, the LOS contribution channel is referred as $A^k{}_{\substack{l \\ l=0}}(0)$ and the multipath contribution channel is referred as $A^k{}_{\substack{l \\ l\neq 0}}(0)$. Each configuration is characterized by a phase error $\boldsymbol{\theta_{case\ X}}$ and a Doppler error $\boldsymbol{\delta_{f_{case\ X}}}$ for both the LOS and the multipath. These phase and Doppler error depends on the type of carrier synchronization process assumed in the receiver. These configurations are described below and summarized in Table 5.6.

$$R(\varepsilon_\tau) = \sum_{l=0}^{L-1} \frac{A_l^k(0)}{N_{FFT}} R_l(\varepsilon_{\tau_l}) + R_{noise+interf}(\varepsilon_\tau) \tag{5.46}$$

$$A_l^k(0) \cong \frac{|\alpha_l^k(0)| + |\alpha_l^{k+1}(0)|}{2} e^{i\boldsymbol{\theta_{case\ X}}} e^{i\pi\boldsymbol{\delta_{f_{case\ X}}}\cdot(N_{FFT}-1)} \frac{sin(\pi\boldsymbol{\delta_{f_{case\ X}}}N_{FFT})}{sin(\pi\boldsymbol{\delta_{f_{case\ X}}})} \tag{5.47}$$

The 4 carrier frequency estimator (CFE) configurations are listed below and the associated phase error and Doppler error models are given in Table 5.6.

- **CFE CASE 1:** A fine carrier frequency acquisition process is not conducted (acquisition achieved at the nominal 5G signal carrier frequency) and no tracking carrier frequency estimator is implemented.
- **CFE CASE 2:** A fine carrier frequency acquisition process is conducted and no tracking carrier frequency estimator is implemented. However, the actual Doppler frequency of the LOS signal has the largest possible difference with the assumed Doppler frequency provided by the acquisition stage: for example, the acquisition was assumed to be conducted when the receiver was getting closer to the BS whereas now, the receiver is going further away from the BS. In order to determine this worst Doppler value, results from the previous study in Case 1 in Table 5.4 are reused and thus $\delta_{f_{worst}} = 6.0322e-06$.
- **CFE CASE 3:** A fine carrier frequency acquisition process is conducted and an ideal tracking carrier frequency estimator is implemented. In that case, the Doppler of the LOS path is perfectly estimated at each instant, $\delta_{f_{los}}^k = \frac{\theta_{0\ los}^k - \theta_{0\ los}^{k+1}}{2\pi(N_{FFT}+N_{CP})}$.
- **CFE CASE 4:** A fine carrier frequency acquisition process is conducted and the FLL presented in section 5.2.1 is implemented. The FLL loop bandwidth is equal to 10 Hz.

Table 5.6 – Configuration summary

CFE		Case 1	Case 2	Case 3	Case 4
Fine frequency acquisition process		Not conducted	Conducted	Conducted	Conducted
Carrier frequency tracking process		Not implemented	Not implemented	Ideal implementation	FLL described in section 5.2.1 implemented
phase $\boldsymbol{\theta_{case\ X}}$	LOS $A^k{}_{l\ l=0}$	θ_{0_l}	θ_{0_l}	θ_{0_l}	$\theta^k_{0_l} - \theta_{acc}(k)$
	Multipath $A^k{}_{l\ l\neq 0}$		$\theta_{0_l} + 2\pi\delta_{f_{worst}}$	$\theta_{0_l} + 2\pi\left(\delta_{f_l}{}^k - \delta^k_{f_{los}}\right)$	
Doppler $\boldsymbol{\delta_{f\ case\ X}}$	LOS $A^k{}_{l\ l=0}$	$\delta_{f_l}{}^k$	$\delta_{f_{worst}}$	$\delta_{f_l}{}^k = 0$	$\delta_{f_l}{}^k - V_c(k)$
	Multipath $A^k{}_{l\ l\neq 0}$		$\delta_{f_l}{}^k - \delta_{f_{worst}}$	$\delta_{f_l}{}^k - \delta^k_{f_{los}}$	

5.2.4.2. AWGN channel simulation results

In this section, the propagation channel is assumed to be an AWGN propagation channel. More accurately, the channel is composed of one path only with a constant complex amplitude and an evolving phase, therefore, a Doppler is modelled. The statistics of the pseudo range estimation error and of the discriminator are compared for the 4 CFE configurations combined with the DLL configuration with $B_l = 10\ Hz$.

The pseudo range estimation error statistics and the discriminator output statistics are illustrated in Figure 5.9 and Figure 5.10. As it can be observed, there are no significant differences among the cases. Nevertheless, the mean of the discriminator output for Case 4, when a FLL is implemented, is closer to 0 than for the other cases.

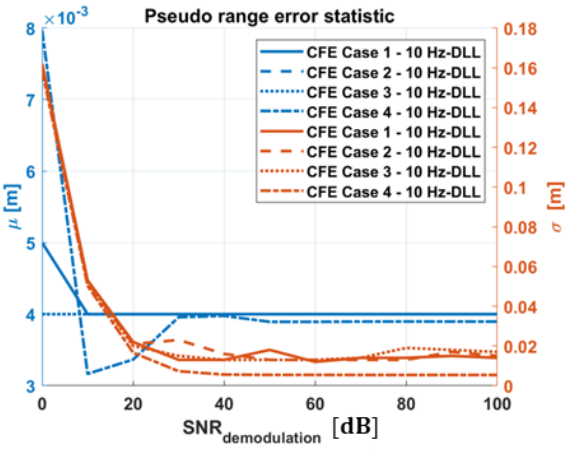

Figure 5.9 – Pseudo range error statistics

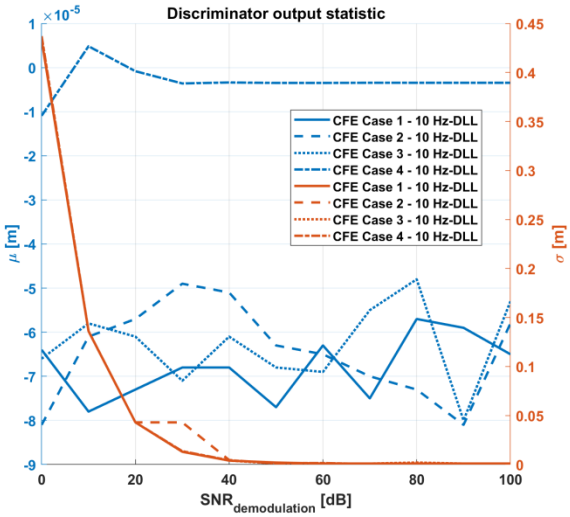

Figure 5.10 – Discriminator output statistics

The standard deviations of the tracking error estimate obtained in Figure 5.9 can also be compared to the theoretical standard deviation of the tracking error estimate in (5.44), the results are illustrated in Figure 5.11. The error between the theoretical standard deviation and the simulated standard deviations is

approximately equal to 1.5 cm for SNR higher than 40 dB, it decreases to 3 mm for 0 dB. When the FLL is used, Case 4 or green curve in Figure 5.11, the standard deviations of the tracking error estimate is even closer to the theoretical blue curve. The differences at high SNR are mostly due to numerical issues.

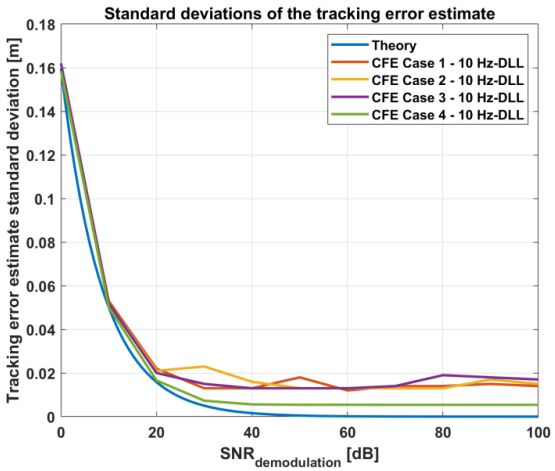

Figure 5.11 – Standard deviations of the tracking error estimate

These simulations confirm the theoretical derivations proposed in section 5.2.3 where the implantation of a carrier frequency estimator is deemed not mandatory for an AWGN propagation channel.

5.2.4.3. QuaDRiGa channel simulation results

The previous study proves the non-necessity of the carrier frequency estimator for an AWGN case; nevertheless, simulations must also be made for a complete QuaDRiGa propagation channel, where, due to the degradation linked to the multipath, a carrier frequency estimator could improve the tracking performances.

This comparison cannot be SNR specific since the true complex amplitude for each path is considered. Therefore, the statistics of the tracking error estimate are provided for the 4 CFE cases assuming a 10 Hz and a 1 Hz DLL loop bandwidth and for the first 300 m of the radial trajectory illustrated in Figure 5.12, independently of the SNR. The tracking after 300 m is mainly lost due to the multipath distortion on the signal; additionally, the QuaDRiGa scenario is assumed to be valid for Pico-cell scenario meaning 4-to-200-m radius circle.

The QuaDRiGa scenario used to generate the propagation channel is the 3GPP_38.901_UMi_LOS; the propagation channel path powers generated are provided in Figure 5.13.

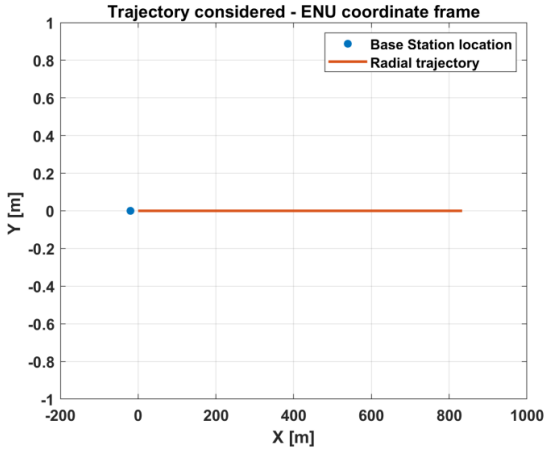

Figure 5.12 – Trajectory considered

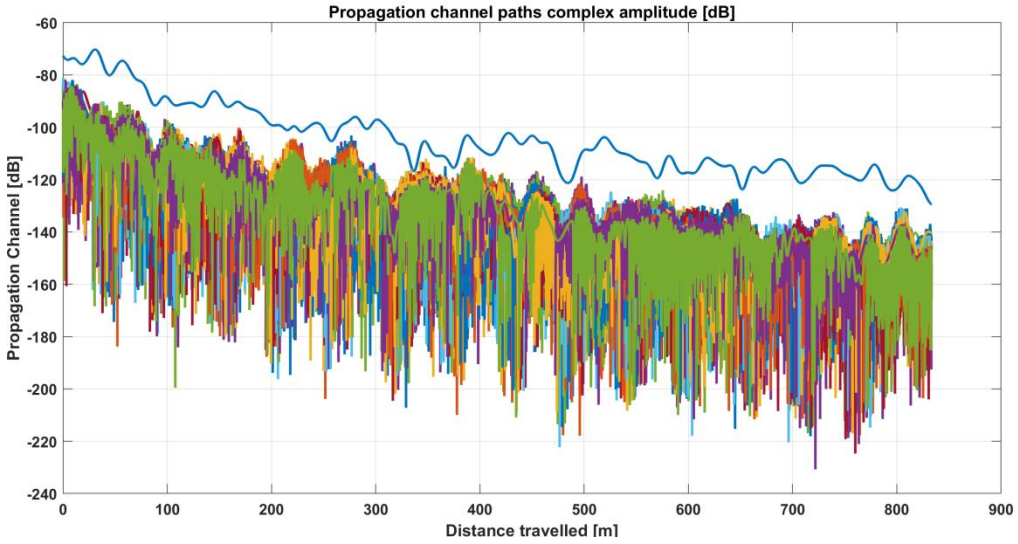

Figure 5.13 – Propagation channel path power for the radial trajectory

The pseudo range estimation errors obtained for the 4 cases and 10 Hz-DLL are illustrated in Figure 5.14 for the multipath case and the statistics are provided in Table 5.7. The 4 cases and 1 Hz-DLL have also been tested the statistics are provided in Table 5.7.

As it can be seen from Table 5.7, the statistics obtained for CFE case 3 using the ideal FLL are worse than the statistics obtained for CFE case 1, for both DLL loop bandwidth. These results can be explained by analyzing CFE case 4 results. Indeed, the ideal FLL perfectly is assumed to track the Doppler of the LOS path only without taking into account the Doppler of the multipath. However, a true FLL estimates the Doppler of the complete received signal (LOS plus multipath) and provides better results. In conclusion, the Doppler of the multipath cannot be neglected.

The statistics obtained by CFE case 4 (FLL of section 5.2.1) and a 10 Hz-DLL configuration are barely identical to the statistics obtained for CFE case 1 and 2. Nevertheless, CFE case 4 and a 1 Hz-DLL configuration, the statistics obtained for a complete channel are better than for CFE case 1 and a 1 Hz-DLL. In fact, the statistics obtained for the 1 Hz-DLL for CFE cases 1 and 4 are better than those obtained for the 10 Hz-DLL.

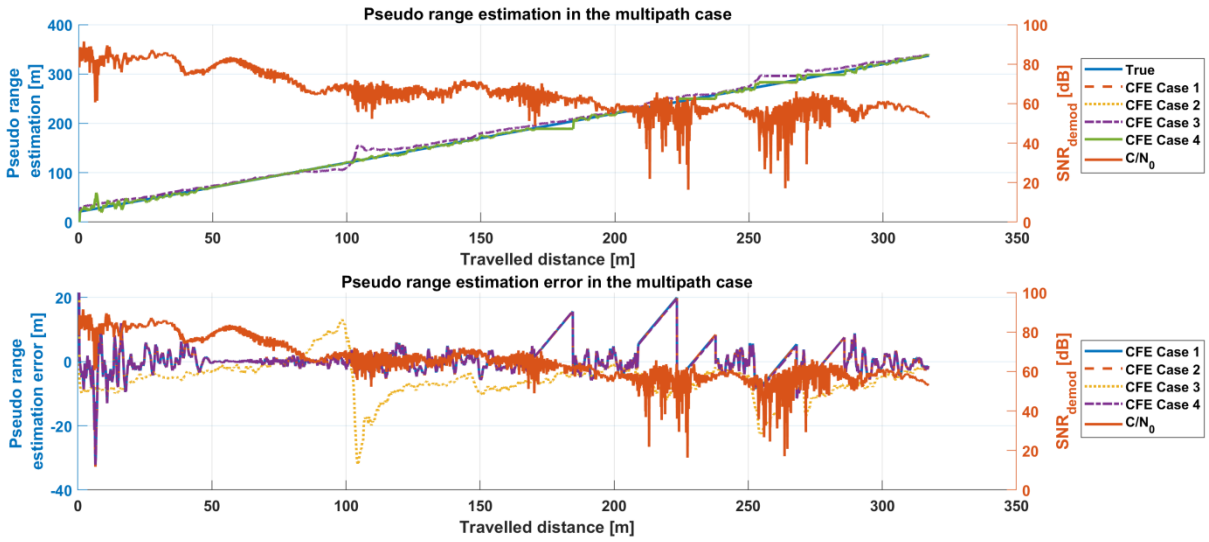

Figure 5.14 – Tracking performances in multipath environment

Table 5.7 – Pseudo range estimation error statistics

Cases	10 Hz-DLL			1 Hz-DLL		
	μ [m]	σ [m]	RMSE [m]	μ [m]	σ [m]	RMSE [m]
CFE Case 1	0,6325	4,7406	4,7826	-0,9938	4,1713	4,2880
CFE Case 2	0,6188	4,7234	4,7637	Not conducted		
CFE Case 3	-5,7921	5,7097	8,1332	-5,7249	6,1202	8,3804
CFE Case 4	0,5780	4,7198	4,7550	0,20943	2,7633	2,7713

The study proposed in this section shows that the implementation of a FLL is not required to improve the tracking performances of the ranging module for a 10 Hz DLL loop bandwidth. However, the tracking performances of the ranging module for a 1 Hz DLL loop bandwidth are improved when using a FLL for a complete channel. Therefore, the FLL is not required but can improve the performances of the ranging module according to the DLL loop bandwidth chosen (the improvement is not significant from a ranging perspective for a 10 Hz-DLL).

Therefore, in Chapter 7, the navigation filters performances will be studied for the 1 Hz DLL loop bandwidth with and without the implementation of a FLL.

5.3. C/N_0 estimator

In order to design a 5G synchronization module, it is required to have access to the C/N_0 value at each instant; the C/N_0 is typically used as an indicator to decide whether the tracking loops, DLL and FLL for example, are locked or not. In other words, the C/N_0 is used as a lock detector. Moreover, as it will be shown in chapters 6 and 7, the C/N_0 can also be used as the parameter which determines the pseudo range measurements error standard deviation to be used at each instant of time in the navigation solution filter. Therefore, a C/N_0 estimator must be implemented in the receiver. Several C/N_0 candidates are inspected in this work.

In order to verify the validity of the different C/N_0 estimator candidates, it is required to compare the estimators' outputs to the true C/N_0. However, all the previous derivations (e.g. thresholds) were provided with respect to the demodulator SNR whereas the C/N_0 estimation is calculated at the correlator output. Therefore, the link between the SNR and the C/N_0 must first be known all over the receiving process in order to verify the correct behavior of the different C/N_0 estimator candidates.

First the SNR relationships all along the path from the transmitter to the DLL input of the receiver are derived. Second the C/N_0 estimator candidate is presented.

5.3.1. 5G SNR relationship

First the relationship between the SNR and the C/N_0 all along the transmission chain must be derived, see Figure 5.15.

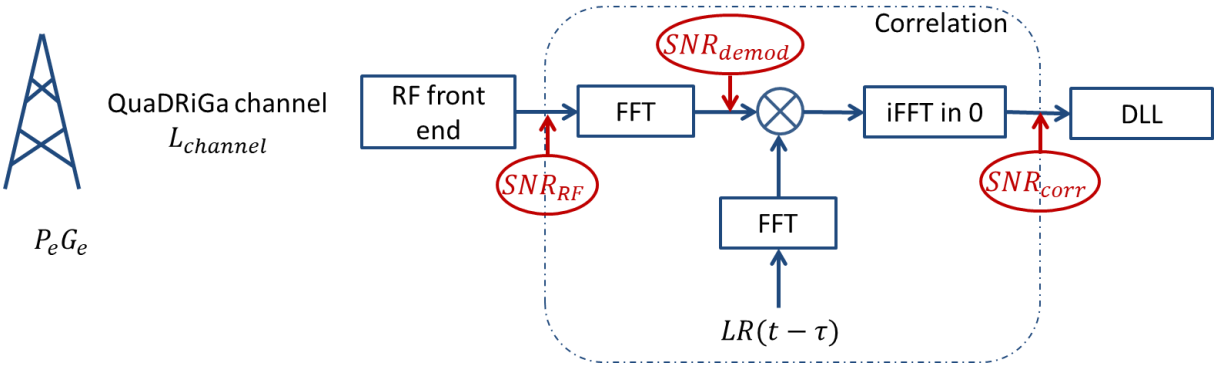

Figure 5.15 – SNR along the transmission chain

5.3.1.1. SNR at the RF front-end output

By definition, the SNR is defined as the ratio between the useful power and the noise power, (5.48). In this first section, the SNR at the RF front-end output is derived.

$$SNR_{RF} = \frac{P_{useful}}{P_{noise}} \tag{5.48}$$

In order to simplify the study, the path loss are modeled by a generic term, $L_{channel}$; according to [18], QuaDRiGa generates all the distortions of the propagation channel : from the antenna to the free space loss to the environment multipath. The useful power at the output of the RF front-end is:

$$P_{useful} = P_e G_e L_{channel} G_a L_{RF} \tag{5.49}$$

Where :

- $P_e = \sigma^2_{symbol} \cdot N_{FFT}$ is the emitted power at the BS
- σ^2_{symbol} is the power of the symbol on each subcarrier
- G_e is the gain of the antenna at the BS in the direction of the receiver
- $L_{channel}$ is the channel attenuation generated by QuaDRiGa
- G_a is the gain of the antenna at the user side in the direction of the received signal
- L_{RF} is the power loss due to the RF front end filter

The noise power at the Analog to Digital Converter input is:

$$P_{noise} = N_0 B \tag{5.50}$$

Where :

- N_0 is the noise term defines as : $N_0 = K_{boltz}(T_a + T_0(L_1 NF_1 - 1)$
  - ✓ K_{boltz} is the Boltzman constant $K_{boltz} = 1.38 \cdot 10^{-23}\, J/K$
  - ✓ T_a is the antenna temperature
  - ✓ T_0 is the standard noise temperature $T_0 = 290\ K$
  - ✓ L_1 is the cable loss, typically $L_1 = 1\ dB$
  - ✓ NF_1 is the Noise Factor term defines as $NF_1 = 1 + \frac{T_{comp}}{T_0}$ and is typically comprised in [1-4] dB
  - ✓ Finally, $N_0 = \begin{cases} -203.8\ dBw/Hz & if\ NF = 1dB \\ -199.8\ dBw/Hz & if\ NF = 4dB \end{cases}$
- $B = N_{FFT} \cdot \Delta f$ is the bandwidth

Finally, the expression of the SNR using the emitted power is

$$SNR_{RF} = \frac{P_{useful}}{P_{noise}} = \frac{P_e G_e L_{channel} G_a L_{RF}}{N_0 B} = \frac{\sigma^2_{symbol}}{\Delta f} \frac{G_e L_{channel} G_a L_{RF}}{N_0} \tag{5.51}$$

In the following, for simplification purposes, $G_e = 1$, $G_a G_{RF} = 1$

$$SNR_{RF} = \frac{P_{useful}}{P_{noise}} = \frac{\sigma^2_{symbol}}{\Delta f} \frac{L_{channel}}{N_0} \tag{5.52}$$

5.3.1.2. SNR at the demodulation output

By definition, the SNR after demodulation is defined as the ratio between the power of the data symbols and the power of the noise affecting the data symbol, (5.53). In this second section, the SNR at the demodulation output is derived.

$$SNR_{demod} = \frac{P_{useful,demod}}{P_{noise,demod}} \tag{5.53}$$

Where the useful power and the noise power are provided in (5.54) and (5.55).

$$P_{useful,demod} = \sigma^2_{symbol} L_{channel} \tag{5.54}$$

$$P_{noise,demod} = N_0 \Delta f \tag{5.55}$$

Finally, the SNR expression after the demodulation is provided in (5.56). As it can be seen, the SNR at the demodulator output is equal to the SNR at the RF Front End output: (5.52) is identical to (5.56).

$$SNR_{demod} = \frac{\sigma^2_{symbol} L_{channel}}{N_0 \Delta f} \tag{5.56}$$

5.3.1.3. SNR at the correlation output

By definition, the SNR at the correlator output is defined as the ratio between the power of the correlated symbols (in other words the pilot symbols power) and the power of the noise, (5.57).

$$SNR_{correlator} = \frac{P_{useful,correlator}}{P_{noise,correlator}} \tag{5.57}$$

Where the useful power and the noise power are provided in (5.58) and (5.59).

$$P_{useful,correlator} = \sigma^2_{symbol} L_{channel} \tag{5.58}$$

$$P_{noise,correlator} = \frac{N_0 \Delta f}{N_P} \tag{5.59}$$

Finally, the SNR at the correlator output is expressed as (5.60). Note that in (5.60), the loss due to the propagation channel is presented; however, it is important to keep in mind that this loss is later on considered within the C/N_0 term. In other word the C/N_0 estimator will estimate (5.61).

$$SNR_{correlator} = \frac{\sigma^2_{symbol} L_{channel}}{N_0 \Delta f} N_P \tag{5.60}$$

$$SNR_{correlator} = \frac{C}{N_0} \frac{1}{\Delta f} \tag{5.61}$$

5.3.2. C/N_0 estimator

In order to assess the C/N_0 at each instant of time, an estimator must be implemented. First, the analyzed C/N_0 estimator candidate (Narrow-to-Wideband-Power-Ratio (NWPR) estimator) is presented. Second, its observed limits are detailed, notably a saturation effect which depends on the presence of a

phase variation of the signal, and consequently on the type of trajectory followed be the receiver. Third, the solutions adopted to potentially overcome these limits are presented.

5.3.2.1. Theoretical presentation of the Narrow-to-wideband-Power-Ratio C/N_0 estimator

The C/N_0 estimator used in the simulator is proposed in [54] for GPS signals. The method is based on the comparison of total signal-plus-noise power in two different bandwidths; it is referred as the Narrow-to-Wideband-Power-Ratio- C/N_0 (NWPR) estimator. The fundamentals of the estimator are presented next.

The measurements of total power in $1/T$ (wide-band power) and $1/MT$ (narrow-band power) noise bandwidths are derived according to (5.62) and (5.63) respectively.

$$WBP_k = \left(\sum_{i=1}^{M}\left(I_i^2 + Q_i^2\right)\right)_k \tag{5.62}$$

$$NBP_k = \left(\sum_{i=1}^{M} I_i\right)_k^2 + \left(\sum_{i=1}^{M} Q_i\right)_k^2 \tag{5.63}$$

Where I is the real part of the prompt correlator output and Q is the imaginary part of the prompt correlator output. These measurements are computed over the same M samples. The normalized power is computed as (5.64).

$$NP_k = \frac{NBP_k}{WBP_k} \tag{5.64}$$

Then the Narrow-to-Wideband-Power-Ratio-C/N_0 estimator is defined as:

$$\widehat{C/N_0} = 10 \cdot \log_{10}\left(\frac{1}{T}\frac{\hat{\mu}_{NP} - 1}{M - \hat{\mu}_{NP}}\right) \tag{5.65}$$

Where $\hat{\mu}_{NP}$, named as the lock detector measurement in [54], is defined as (5.66), K is the number of time the NP_k is computed. In other words, the estimation of $\frac{\widehat{C}}{N_0}$ is made using $K \cdot M$ OFDM symbols. In the following, $K = 50$ and $M = 10$; this corresponds to a coherent integration time equal to $T_{I_{coherent}} = 7.1354e-04\ s$ and to a non-coherent integration time of $T_{I_{non-coherent}} = 0.0357\ s$; after deep studies, this is the best found set of values.

$$\hat{\mu}_{NP} = \frac{1}{K}\sum_{k=1}^{K} NP_k \tag{5.66}$$

5.3.2.2. Limits of the C/N_0 estimator candidate

5.3.2.2.1. Behavior of the NWPR estimator in AWGN channel

In order to study the C/N_0 estimator behavior, the estimator has been tested for an AWGN propagation channel using the simulator of Annex A. The user is assumed to be fixed, therefore the C/N_0 is constant over the simulation duration set to 60 s. The complex amplitude of the propagation channel is assumed to be equal to 1 ($\alpha = 1$, no phase or Doppler is simulated).

The input SNR corresponds to the SNR at the RF Front output, it allows to define the variance of the noise generated for the simulation at the correlator output, using (5.67), where N_P is the number of pilot

contained in the OFDM symbol. This noise variance corresponds to the variance of the two components considered in chapter 4 section 4.2.2.

$$\sigma_{noise} = \sqrt{\frac{1}{SNR_{demodulation} \cdot N_P \cdot 2}} \tag{5.67}$$

The maximum and minimum values of SNR to be tested as determined as follows:

- Minimum input SNR: According to Figure 5.4 and with the considered parameters, the DLL tracking threshold, which corresponds to the SNR at the demodulation output, is $DLL_{th} = SNR_{demod_{lower\ bound}} = -24\ dB$.
- Maximum input SNR: In order to define a higher bound for the SNR to be tested, a brief description of the 3GPP standard is required. In [53], the 3GPP standard defined 3 types of base stations: a Wide Area Base Station, for Macro cell scenario; a medium Area Base Station for Micro cell scenarios, and a local Area Base Station for Pico cell scenarios with a Base station to receiver minimum distance along the ground equal to 2 m. For each BS, the standard provides maximum power values requirements. In this thesis, the focus is on constrained environment and Pico-cell scenarios; therefore, the considered Base Station falls into the "local area Base station" category. For this type of BS, the power output at the antenna must be lower than $P_e = \sigma^2_{symbol} \cdot N_{FFT} = 24\ dBm$. Assuming this value, the SNR at the demodulation output must be lower or equal to $SNR_{demod_{higher\ bound}} = \frac{\sigma^2_{symbol}}{N_0 \Delta f} = 119\ dB$ (maximum value of $L_{channel}$ is assumed equal to 1 for simplification purposes).

The results of the study are provided in Figure 5.16 and Table 5.8. This behavior analysis has highlighted a first limit of the NWPR estimator. Indeed, as it can be observed, the NWPR estimator saturates when C/N_0 reaches 119 dBHz. In the second column of Table 5.8, the expected C/N_0 is provided. This expected C/N_0 is defined as (5.68) by using the derivation performed in section 5.3.1. Note that in AWGN case, $L_{channel} = 1$

$$C/N_0 = SNR_{correlator} \Delta f = SNR_{demodulation} \mathrm{N_P} \Delta f L_{channel} \tag{5.68}$$

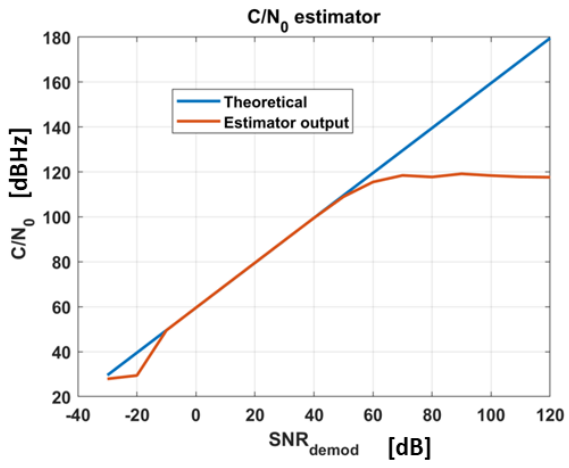

Figure 5.16 – AWGN case C/N_0 estimator study

Table 5.8 – AWGN C/N_0 estimator study

SNR_{demod} [dB]	Theoretical C/N_0 [dBHz]	Estimated C/N_0 [dBHz]
-20	39,54	29,407
-10	49,54	49,515
0	59,54	59,573
10	69,54	69,579
20	79,54	79,579
30	89,54	89,573
40	99,54	99,522
50	109,5	108,99
60	119,5	115,53
70	129,5	118,46
80	139,5	117,76
90	149,5	119,17
100	159,5	118,39
110	169,5	117,82
120	179,5	117,63

5.3.2.2.2. Behavior of the NWPR estimator in LOS channel for a radial trajectory

To further analyze this phenomenon, two other types of propagation channel are used: a LOS propagation channel composed of one path only with an evolving propagation channel complex amplitude and a complete channel composed of the LOS and multipath (the propagation channel model is provided in (4.1)). Moreover, in order to increase the number of test cases, 4 emitter powers are tested: from $P_e = -37dBW$ to $P_e = -7dBW$.

In Figure 5.17 and Figure 5.18, the true C/N_0 is compared with the C/N_0 estimation value provided by the NWPR estimator in order to further inspect its behavior. In these figures, the dot-lines represent the true C/N_0 assuming the different emitter powers, P_e, and the solid lines represent the estimation obtained with the estimator. In Figure 5.17, the LOS propagation channel is considered; in Figure 5.18, the complete channel is used. The true C/N_0 values at instant k is computed as shown in (5.69).

$$C/N_{0_{true}}^{k} = \frac{\left|R_P^{\mathrm{k}}(\varepsilon_\tau)\right|^2}{N_0}\sigma_{local}^2 N_P \tag{5.69}$$

Where $R_P^{\mathrm{k}}(\varepsilon_\tau)$ is the normalized complex noiseless prompt correlator output at instant k; N_0 is the noise value. Note that $R_P^{\mathrm{k}}(\varepsilon_\tau) = R_{useful}^{\mathrm{k}}(\varepsilon_\tau)$ described in equation (5.2).

From Figure 5.17 and Figure 5.18, it can be seen that when the true C/N_0 goes under 60 dBHz, the estimated C/N_0 fits with the true one. Moreover, the saturation phenomenon can also be observed when the true C/N_0 goes above at 60 dBHz. Note that this saturation value, 60dBHz, is different from the saturation value identified in the previous section which was around 119 dBHz. Therefore, it can be concluded that when considering a more complex propagation channel, the NWPR estimator reaches a saturation point, around 60dBHz, which is far inferior to the tested one for an AWGN channel.

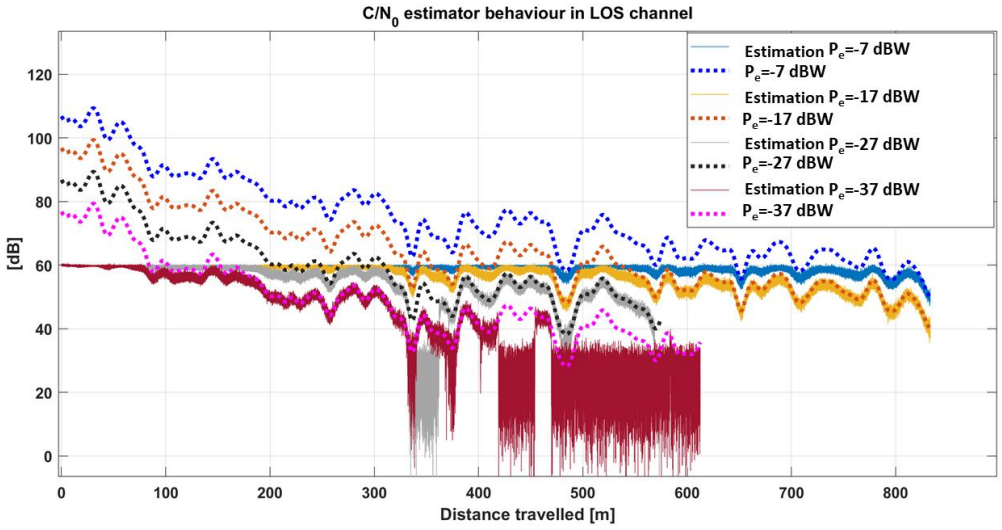

Figure 5.17 – LOS case C/N_0 estimator study – Radial trajectory

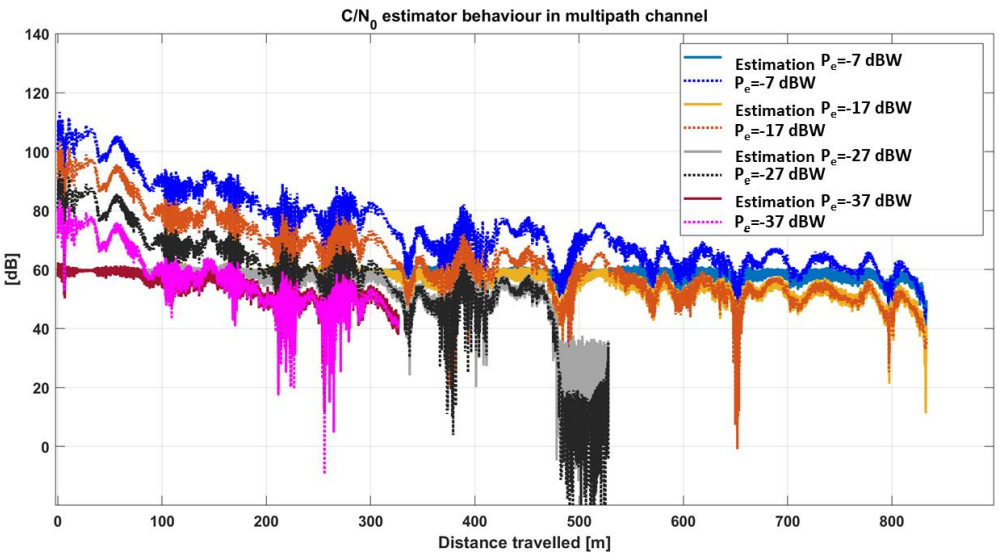

Figure 5.18 – Multipath case C/N_0 estimator study – Radial trajectory

5.3.2.2.3. Behavior of the NWPR estimator in LOS channel for a circular trajectory

In order to complete this study, the behavior of the estimator has been studied for a circular trajectory, illustrated in Figure 5.19. Similarly to the radial trajectory, 2 propagation channels have been tested: a LOS propagation channel and a multipath propagation channel. Results are provided in Figure 5.20 and Figure 5.21 respectively. As it can be seen in Figure 5.20 for the circular trajectory in the LOS case, the C/N_0 estimation is correct and no saturation is observed. However, in the multipath case Figure 5.21, the C/N_0 estimation is correct for an emitter power lower than $P_e = -37dBW$ which correspond to a SNR at the demodulation output lower than 90 dB; nevertheless, for higher C/N_0 values, the saturation phenomenon is still observed with a different saturation threshold: around 80 dBHz.

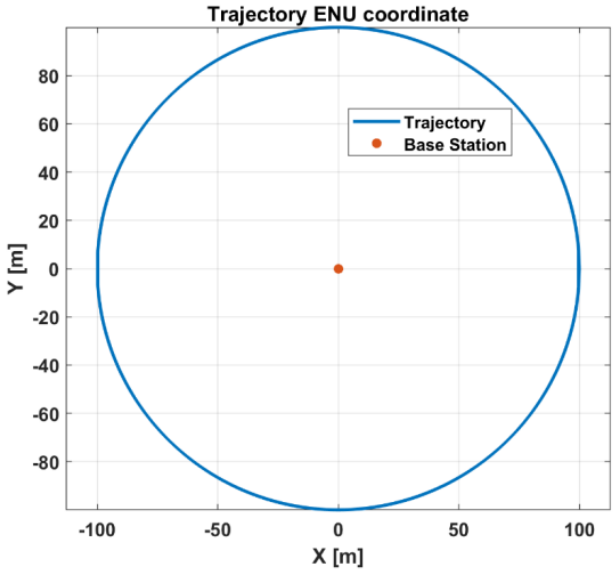

Figure 5.19 – Circular trajectory – ENU coordinates

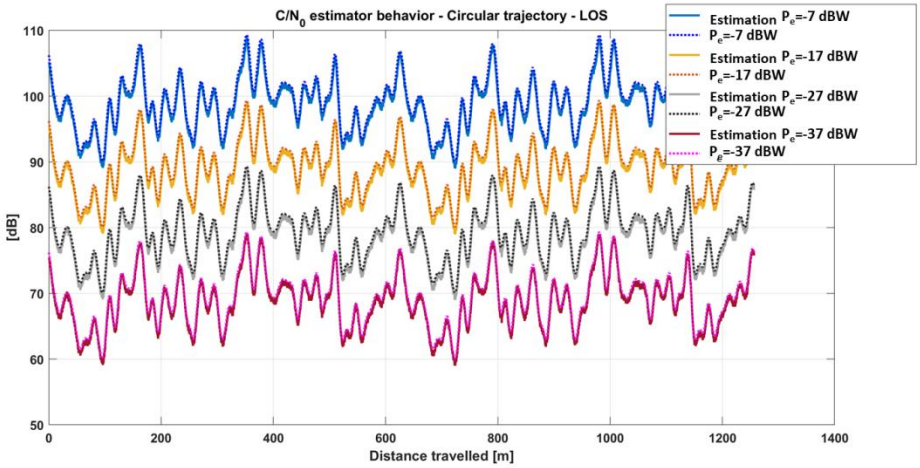

Figure 5.20 – C/N_0 estimator behavior in LOS case for a circular trajectory

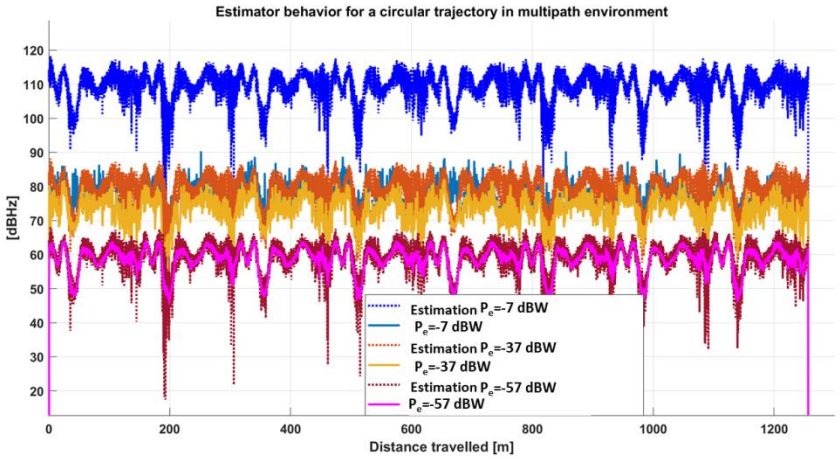

Figure 5.21 – C/N_0 estimator behavior in multipath case for a circular trajectory

5.3.2.2.4. Sensitivity of the NWPR estimator to phase variation

In order to explain the saturation phenomenon observed in the previous section, two parameters are analyzed: the phase evolution and the Doppler evolution. The phase evolution for the radial and the circular trajectory are provided in Figure 5.22 and in Figure 5.23 respectively. The Doppler evolution for the radial and the circular trajectory are provided in Figure 5.24 and in Figure 5.25 respectively. In order to ease the visualization, the evolution of the LOS path is not presented.

First, as it can be seen from Figure 5.22 to Figure 5.25 for the radial and the circular trajectory the Doppler and the phase for each path is evolving. Since, the NWPR- C/N_0 estimator works only for the circular trajectory in the LOS case where the LOS signal phase is constant, this phase evolution can be the potential reason why the estimator does not work on the other cases (trajectories and/or propagation channels).

Second, from Figure 5.22 and Figure 5.23, it can be seen that the evolution of the multipath phases for the radial trajectory is almost twice the evolution of the multipath phases for the circular trajectory. As an example, at 300 m in Figure 5.22, the worst phase is almost 10 000 rad whereas in Figure 5.23, the worst phase is 10 000 rad after 600 m. This lower phase evolution might explain why the NWPR- C/N_0 estimator behavior is better for the circular trajectory (higher saturation threshold).

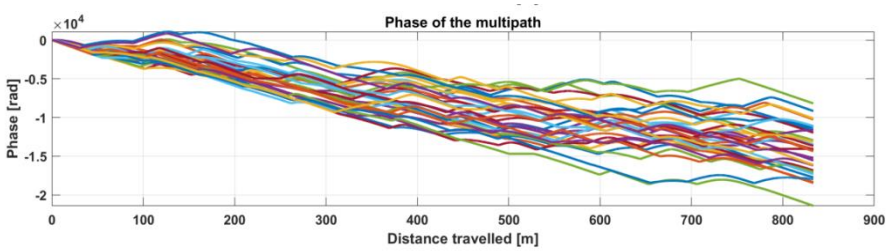

Figure 5.22 – Phase evolution for the radial trajectory

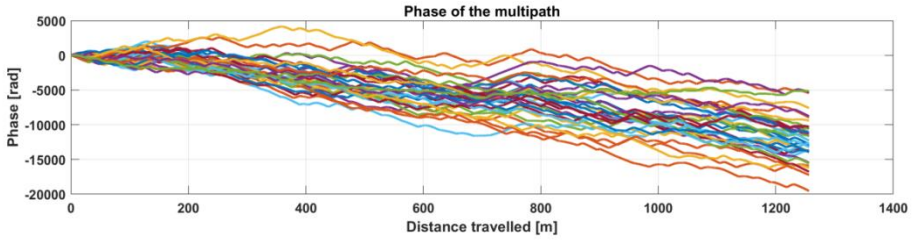

Figure 5.23 – Phase evolution for the circular trajectory

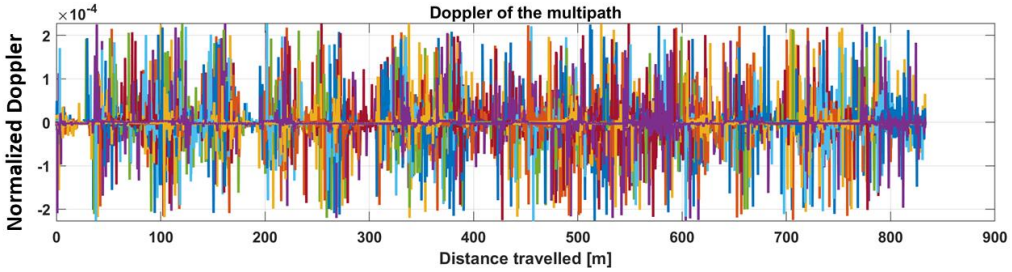

Figure 5.24 – Doppler evolution for the radial trajectory

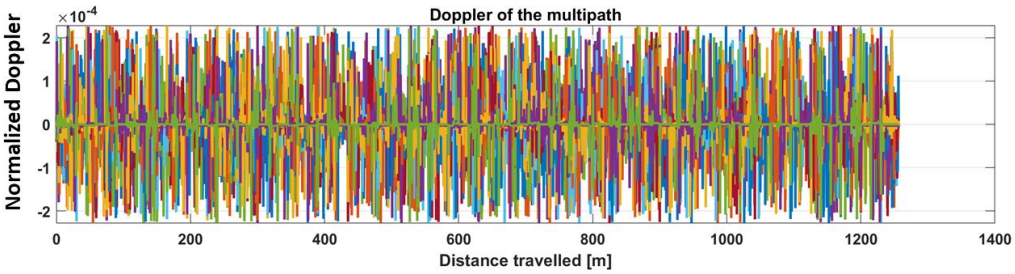

Figure 5.25 – Doppler evolution for the circular trajectory

In order to confirm these observations, the following tests are proposed for the radial trajectory. For both the LOS and the complete propagation channel, the 4 tests presented in Table 5.9 are performed. Case 1 presents the complete impact of the Doppler, Case 2 permits to identify the impact of the Doppler as a phase evolution between consecutive symbols, Case 3 permits to identify the impact of the Doppler as an attenuation (phase evolution inside a symbol), and in Case 4, the Doppler impact is completely removed.

Table 5.9 – Tests configuration – Doppler and phase impacts on the C/N_0 estimator

Case		Propagation channel contribution model	
1	Initial model	$A_l^k(0) \cong \frac{\left\|\alpha_l^k(0)\right\| + \left\|\alpha_l^{k+1}(0)\right\|}{2} e^{i\theta_{0_l}} e^{i\pi\delta_{f_l}{}^k \cdot (N_{FFT}-1)} \frac{sin\left(\pi\delta_{f_l}{}^k N_{FFT}\right)}{sin\left(\pi\delta_{f_l}{}^k\right)}$	(5.70)

2	Doppler as a phase evolution	$A_l^k(0) \cong \frac{\left\|\alpha_l^k(0)\right\| + \left\|\alpha_l^{k+1}(0)\right\|}{2} e^{i\theta_{0_l}}$	(5.71)
3	Doppler as an attenuation	$A_l^k(0) \cong \frac{\left\|\alpha_l^k(0)\right\| + \left\|\alpha_l^{k+1}(0)\right\|}{2} e^{i\pi\delta_{f_l}{}^k \cdot (N_{FFT}-1)} \frac{sin\left(\pi\delta_{f_l}{}^k N_{FFT}\right)}{sin\left(\pi\delta_{f_l}{}^k\right)}$	(5.72)
4	No Doppler	$A_l^k(0) \cong \frac{\left\|\alpha_l^k(0)\right\| + \left\|\alpha_l^{k+1}(0)\right\|}{2}$	(5.73)

Results are presented in Figure 5.26, Figure 5.27, Figure 5.28 and Figure 5.29 for case 1 to 4 respectively and for $P_e = -30\ dBW$. The comparison between the initial channel contribution model (5.70) in Figure 5.26 and the limited Doppler contribution channel model (5.71) in Figure 5.27 shows that the impact of the Doppler attenuation (phase evolution inside a symbol) is not responsible for the saturation effect of the Narrow-to-Wideband-Power-Ratio- C/N_0 estimator (since the saturation effect is still present when the Doppler attenuation factor has been removed).

The comparison between the initial channel contribution model (5.70) in Figure 5.26 and the case where the propagation channel is assumed to not have an evolving phase (Doppler effect only contributes to the attenuation) (5.72) in Figure 5.28 shows that the propagation channel phase evolution between symbols is responsible for the saturation of the Narrow-to-Wideband-Power-Ratio- C/N_0 estimator (since the saturation effect is no longer present when the Doppler-as-phase-evolution-between-symbols factor has been removed).

The behavior of the Narrow-to-Wideband-Power-Ratio- C/N_0 estimator for the Doppler free channel contribution model (in terms of phase evolution between symbols and inside a symbol) (5.73) is equivalent to the NWPR- C/N_0 estimator for the phase free channel contribution model (5.72). An expected observation since the Doppler attenuation (phase evolution inside a symbol) impact has been shown negligible from Figure 5.27.

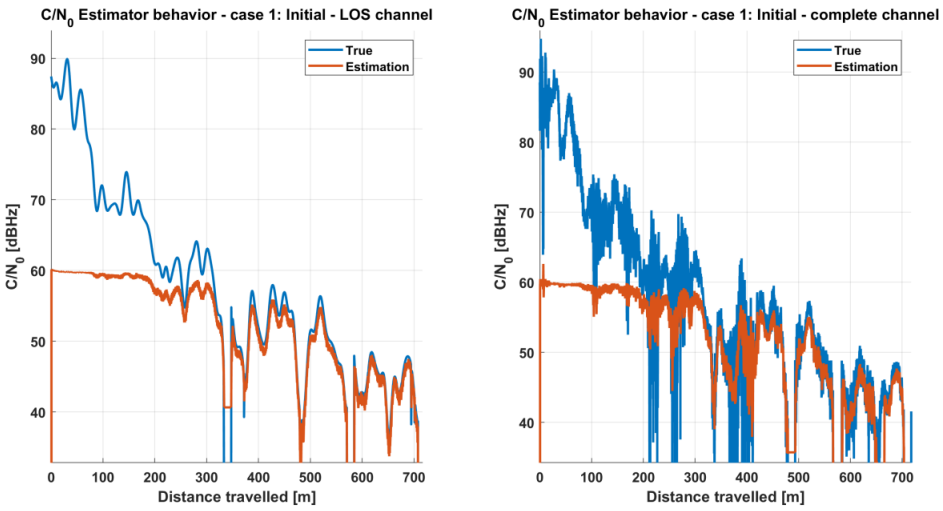

Figure 5.26 – Estimator behavior – Case 1

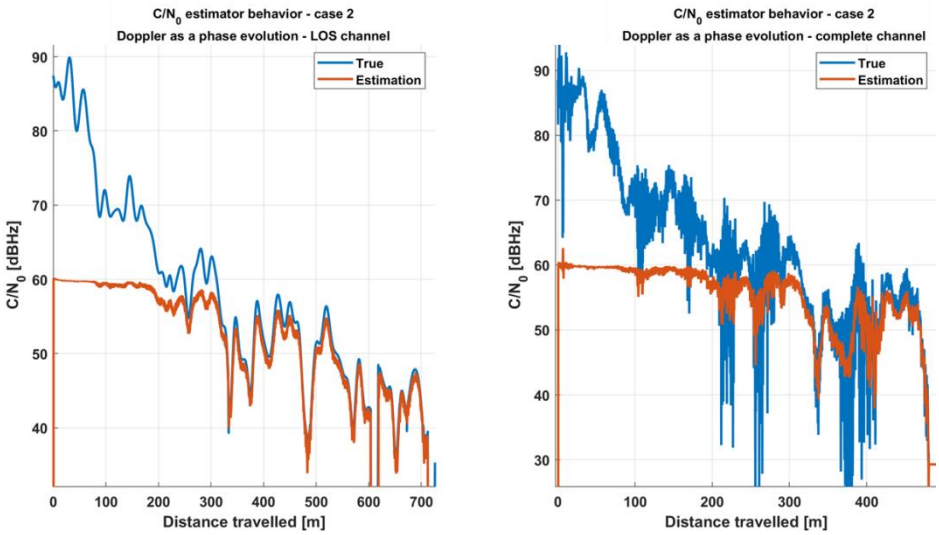

Figure 5.27 – Estimator behavior – Case 2

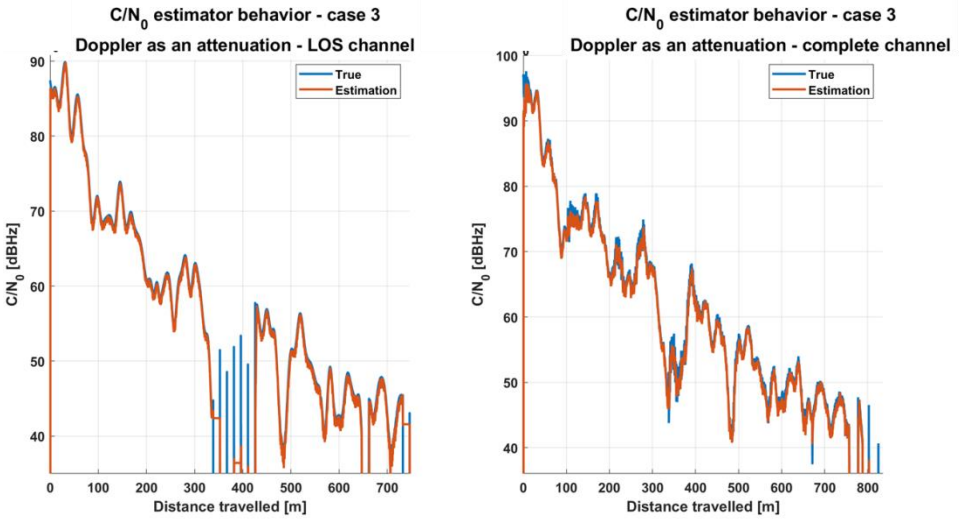

Figure 5.28 – Estimator behavior – Case 3

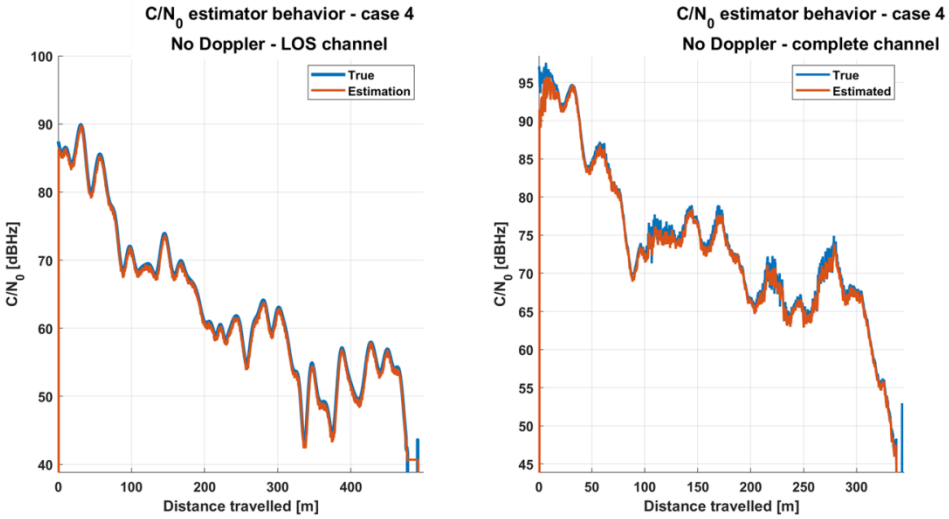

Figure 5.29 – Estimator behavior – Case 4

In conclusion, the Narrow-to-Wideband-Power-Ratio- C/N_0 estimator cannot correctly estimate high C/N_0 values since it saturates due to the phase evolution between symbols in the channel

contribution term. This limit was also identified in [55]. The estimator is actually phase sensitive due to the definition of NBP_k in (5.56).

5.3.2.3. Proposed C/N_0 estimators

Three solutions have been considered to overcome the Narrow-to-Wideband-Power-Ratio- C/N_0 estimator issue presented in the previous section. First, a C/N_0 estimator based on the method of moments has been tested which is, a priori, insensitive to the correlator outputs phase evolution. Second, since the limitation of the previous estimator is caused by the phase evolution between symbols, two new estimators have been derived by correcting this phase evolution.

5.3.2.3.1. Moment Method estimator

The C/N_0 estimator derived in section 5.3.2.1 depends on the correlators output phase evolution; it has been shown that this dependency is responsible for the observed saturation phenomenon. Therefore, another C/N_0 estimator candidate has been tested which is independent from the correlator outputs phase. This C/N_0 estimator is based on the method of moments.

The Moment Method estimator employs the second and forth order moments for the separate estimation of useful signal and noise powers. It is described in [55]; the equations are presented in (5.74) to (5.78).

$$\widehat{M}_2 = \frac{1}{N}\sum_{k=1}^{N}\left|R_P^{\mathrm{k}}(\varepsilon_\tau)\right|^2 \tag{5.74}$$

$$\widehat{M}_4 = \frac{1}{N}\sum_{k=1}^{N}\left|R_P^{\mathrm{k}}(\varepsilon_\tau)\right|^4 \tag{5.75}$$

$$\hat{P}_d = \sqrt{2\widehat{M}_2^2 - \widehat{M}_4} \tag{5.76}$$

$$\hat{P}_n = \widehat{M}_2 - \hat{P}_d \tag{5.77}$$

$$C/N_{0_{MM}} = \frac{\hat{P}_d}{\hat{P}_N \cdot B} \tag{5.78}$$

The behavior of this method of moment C/N_0 estimator has been studied for the radial trajectory in both the LOS case and the multipath case for 3 input SNRs for 3 different input emitter powers. Results are provided in Figure 5.30 for N=500, therefore for an integration time of $T_I = 0.0357\ s$.

For the LOS case corresponding to the left part of Figure 5.30, the Method of moments C/N_0 estimator works well for $C/N_0 < 85\ dBHz$. For the multipath case corresponding to the right part of Figure 5.30, the estimation is working properly for $C/N_0 < 60\ dBHz$. The estimation is not behaving as desired for higher C/N_0. Consequently, the method of moment C/N_0 estimator is not a good candidate for 5G signals in constrained propagation channels.

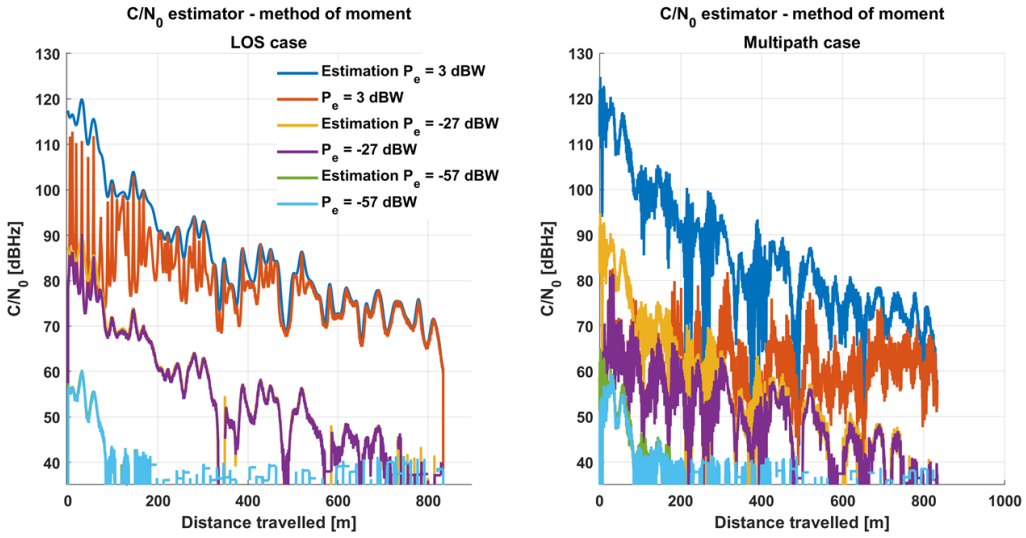

Figure 5.30 – C/N_0 method of moment estimator behavior

5.3.2.3.2. Correction of the phase for the NWPR C/N_0 estimator

The C/N_0 estimator derived in section 5.3.2.1 depends on the correlator output phase evolution; it has been shown that this dependency is responsible for the saturation phenomenon observed in section 5.3.2.2. The first attempt to correct this limit consists in testing a C/N_0 estimator that do not depends on the phase. Nevertheless, even if results are encouraging for channels without multipath, the estimation remains problematic for high C/N_0 values in the presence of multipath. Therefore, another method consisting in correcting the phase in the initial NWPR C/N_0 estimator has been tested.

This method actually leads to the behavior study of two C/N_0 estimators. In both estimators, the phase of the correlator output is corrected before the summations of the wide-band power and of the narrow-band power presented in (5.55) and (5.56). The difference is how the phase is estimated. In the first case, the phase is estimated by directly using the relationship of the I and Q correlator outputs. In the second one, the phase evolution is corrected by using a FLL.

The saturation phenomenon of the Narrow-to-Wideband-Power-Ratio- C/N_0 estimator is caused by the phase evolution in the propagation channel contribution (5.63). Therefore, an attempt to get a working C/N_0 estimator consists in correcting the correlator output used in the estimator, which model is reminded in (5.39), by an estimation of its phase, $\theta(n)$.

More specifically, the C/N_0 estimator presented in section 5.3.2.1 uses the real and imaginary parts of the prompt correlator output as detailed in (5.79).

$$R_P^k(\varepsilon_\tau) = Real\left(R_P^k(\varepsilon_\tau)\right) + 1i \cdot Imag\left(R_P^k(\varepsilon_\tau)\right) = I_k + 1i \cdot Q_k \tag{5.79}$$

In the corrected version of the C/N_0 estimator, the prompt correlator output can be decomposed into a modulus and a phase contributions as in (5.80).

$$R_P^k(\varepsilon_\tau) = \left|R_P^k(\varepsilon_\tau)\right| e^{i \cdot angle\left(R_P^k(\varepsilon_\tau)\right)} \tag{5.80}$$

The corrected correlator output is thus derived in (5.81). Consequently the C/N_0 estimator Wide Band and Narrow Band Power are computed following (5.82) and (5.83). This new estimator is now referred as the C/N_0 phase-corrected estimator.

$$R^{\mathrm{k}}_{P_{corrected}}(\varepsilon_\tau) = R^{\mathrm{k}}_{P}(\varepsilon_\tau)e^{-i\cdot\,\widehat{\phi}[k]} \tag{5.81}$$

$$WBP_k = \left(\sum_{i=1}^{M}\left(Real\left(R^{\mathrm{k}}_{P_{corrected}}(\varepsilon_\tau)\right)^2 + Imag\left(R^{\mathrm{k}}_{P_{corrected}}(\varepsilon_\tau)\right)^2\right)\right)_k \tag{5.82}$$

$$NBP_k = \left(\sum_{i=1}^{M} Real\left(R^{\mathrm{k}}_{P_{corrected}}(\varepsilon_\tau)\right)\right)^2_k + \left(\sum_{i=1}^{M} Imag\left(R^{\mathrm{k}}_{P_{corrected}}(\varepsilon_\tau)\right)\right)^2_k \tag{5.83}$$

Different types of NWPR C/N_0 phase-corrected estimators can be derived depending on the method used to determine the phase correction term.

5.3.2.3.2.1. 1st option – arctangent NWPR C/N_0 phase-corrected estimators

The first option proposed for a NWPR $\mathrm{C/N_0}$ phase-corrected estimator consist in estimating the phase correction term by using a typical arctangent discriminator as shown in (5.84). This estimator is denoted as arctangent-driven NWPR $\mathrm{C/N_0}$ phase-corrected estimator.

$$\widehat{\phi}[k] = \mathrm{atan}\left(\frac{Imag\left(R^{\mathrm{k}}_{P}(\varepsilon_\tau)\right)}{Real\left(R^{\mathrm{k}}_{P}(\varepsilon_\tau)\right)}\right) \tag{5.84}$$

The behavior of this arctangent NWPR C/N_0 phase-corrected estimator has been studied for the radial trajectory in both the LOS case and the multipath case for 3 emitter powers ($P_e = -57\ dBW$, $P_e = -27\ dBW$, $P_e = 3\ dBW$).

For the LOS case corresponding to the left part of Figure 5.31, the arctangent NWPR C/N_0 phase-corrected estimator works well since no saturation is observed. The tracking is lost for $C/N_0 < 50\ dBHz$, this is the reason why, no estimation are available below $50\ dBHz$, this must not be confused by a saturation. For the multipath case corresponding to the right part of Figure 5.31, the estimation works well for $C/N_0 < 95\ dBHz$ but it is still erroneous for higher C/N_0 values as can be seen on the blue and red curves in the right part of Figure 5.31.

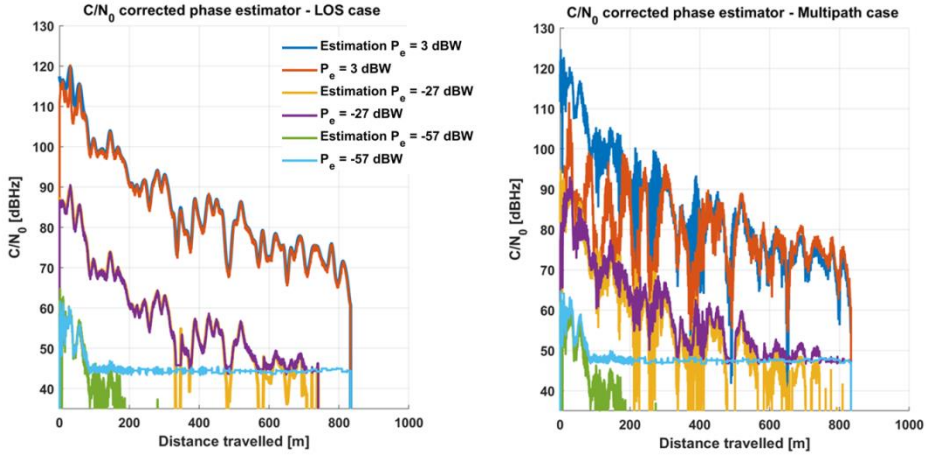

Figure 5.31 – C/N_0 corrected phase estimator behavior

In conclusion, the arctangent NWPR C/N_0 phase-corrected estimator is better than the NWPR-C/N_0 estimator. Nevertheless for $C/N_0 > 95\ dBHz$, the estimator is still not working optimally. However, as such, it is behaving well enough to determine whether the DLL is tracking the signal or not.

Regarding the tracking criterion, knowing that the C/N_0 is higher than 95 dBHz is sufficient to identify that a base station is tracked, the exact value is not required. Regarding the noise measurement covariance matrix definition, it is possible to assume that for C/N_0 values higher than 95 dBHz the noise measurement covariance is set to a constant value. This constant value will slightly over bound the noise measurement covariance. Nevertheless the consequences might be limited with regard to the occurrence of this situation.

5.3.2.3.2.2. 2nd option – FLL driven NWPR C/N_0 phase -corrected estimator

The second option proposed for a NWPR $\mathrm{C/N_0}$ phase-corrected estimator consists in estimating the phase correction term by using a FLL as shown in equation (5.85). Note that although the FLL is not able to provide the exact value of the phase, it is able to provide its time evolution. This estimator is denoted as FLL-driven NWPR $\mathrm{C/N_0}$ phase-corrected estimator.

$$\hat{\phi}[k] = \hat{\phi}[k-1] + 2\pi V_{c,FLL}(k) \tag{5.85}$$

In Figure 5.32 and Figure 5.33, the behavior of the FLL-driven NWPR C/N_0 phase-corrected estimator, when the FLL in section 5.2.7 is implemented, is compared to the arctangent NWPR C/N_0 phase-corrected estimator. Basically, both estimators present the same behavior and performance.

The FLL-driven NWPR C/N_0 phase-corrected estimator is better than the Narrow-to-Wideband-Power-Ratio- C/N_0 estimator. Nevertheless for $C/N_0 > 95dBHz$, the estimator is still not working optimally. However, as such, it is behaving well enough to determine whether the DLL is tracking the signal or not.

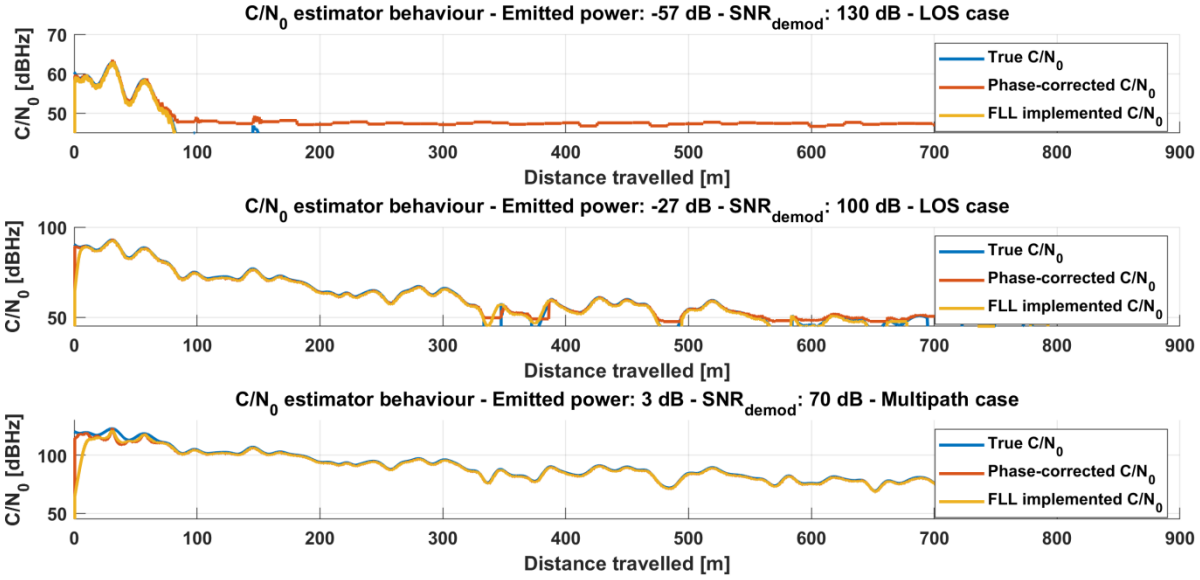

Figure 5.32 – C/N_0 estimators behavior in the LOS case: phase-corrected- C/N_0 vs FLL-implemented- C/N_0

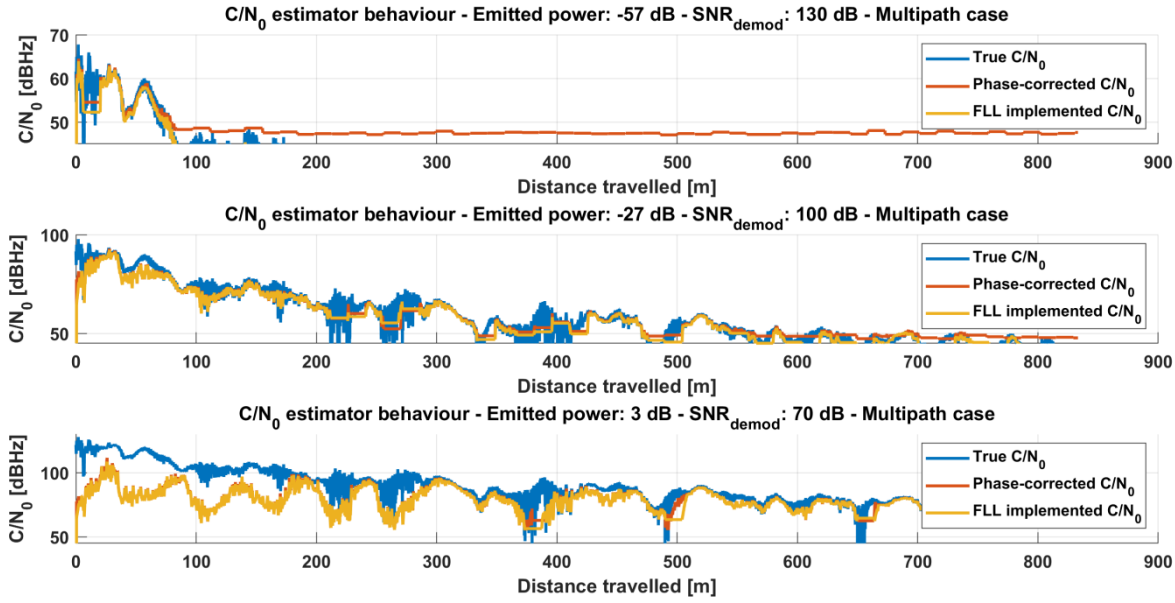

Figure 5.33 – C/N_0 estimators behavior in the LOS case: phase-corrected- C/N_0 vs FLL-implemented- C/N_0

5.3.2.4. Conclusion

In conclusion, it has been shown that the NWPR- C/N_0 estimator cannot be used to estimate the C/N_0. A saturation phenomenon has been observed and it is due to the phase evolution between symbols in the channel contribution term.

Remember that the estimation of the C/N_0 can be used for 2 purposes:

- the C/N_0 is typically used as an indicator to decide whether the tracking loops, DLL and FLL for example, are locked or not.
- the C/N_0 can also be used as the parameter which determines the pseudo range measurements error standard deviation to be used at each instant of time in the navigation solution filter.

Therefore, the C/N_0 estimation should be as accurate as possible and solutions to overcome the saturation phenomenon have been proposed.

According to section 5.3.2.3, the use of a phase-independent C/N_0 estimator (the method of moment estimator) does not permit to solve the identified issues. Therefore, two phase-corrected NWPR C/N_0 estimators have been proposed: one corrects the phase using an arctangent discriminator and the other uses an FLL to estimate the phase evolution. Their behavior is still not ideal for high C/N_0, $C/N_0 > 95\ dBHz$.

However, the NWPR C/N_0 estimator and its 2 C/N_0 estimator evolutions can still be used as a lock detector. Indeed, a closed-loop is declared locked if the C/N_0 is higher than a threshold; therefore, the most important situation is to estimate low C/N_0 values.

These evolutions can also be used in the navigation filter; in that case, the covariance noise coefficient is set to a constant value for $C/N_0 > 95\ dBHz$.

5.4. Conclusion

The objective of the chapter was to present the synchronization module proposed and implemented in the Ph.D. This synchronization module is basically composed of a DLL, a carrier frequency estimator and a

C/N_0 estimator (and a tracking lock detector simply based on the C/N0 estimation compared to a threshold).

As already stated in chapter 3 section 3.5.2, a Delay tracking loop is used; its architecture and performances are detailed in section 5.1. The same ranging module as the ranging module presented in chapter 3 section 3.5.2 is proposed. The reason is that, on one hand, chapter 3 ranging module was derived assuming an AWGN propagation channel. On the other hand, chapter 4 presented a complete correlator output model constituted of a noiseless useful part, equal to the one of an AWGN channel when no considering multipath, and of a Gaussian joint modelling of the noise and ICI terms. Therefore, the two models, without considering multipath, are equivalent from a stochastic process perspective. Therefore, note that this proposed ranging module is still not the optimal solution in the presence of multipath; this work has not tackled this optimization. An EMLP discriminator output is used in the DLL, its normalization factor as well as its linearity region have been precisely studied: the one-sided discriminator linearity zone is $D_{th} = 7/4$ samples. The performance of the DLL estimation error standard deviation in an AWGN channel using the correlator output mathematical models derived in Chapter 4 have been validated in simulation: as an example, the variance of the tracking error estimate for a $SNR_{demod} = 0\ dB$ equals $2.6 \cdot 10^{-4}\ m$

An analysis on the necessity of implementing a carrier frequency estimator is conducted in the second section. It has been proved theoretically and through simulations that the implementation of a carrier tracking loop, a FLL, does not improve the tracking performances of the ranging module for an AWGN. The method aims to study the degradation caused by a frequency estimation error on the time delay estimation conducted by the DLL. The method adopted to determine the necessity to implement a carrier frequency estimator consists in deriving the degradation of the time delay estimation performance as a function of the Signal to Noise Ratio (SNR) and the Carrier Frequency Offset (CFO). In order to conduct this study: first the impact of the CFO has been studied. Second the theoretical degradation of the SNR due to the CFO has been determined. In order to determined realistic values of the degradation, realistic SNR and Doppler variation values have been determined. Then the CFO degradation has been studied, followed by the theoretical degradation on the code delay estimation due to CFO. Finally, the theoretical derivation has been validated through simulations. Simulations assuming an AWGN channel have permitted to validate the theoretical degradation on the code delay estimation due to CFO; and has confirm the non-necessity of the implementation of a FLL. These simulations have been made assuming 3 configurations defined to represent realistic and generic 5G signal configurations. They have shown that for $SNR_{correlator} < 105\ dB$, the degradation due to a fractional CFO is lower than 0.5 dB and that the standard deviation of the tracking error estimate is of the order of the millimeters.

Additional simulations have been proposed for a complete channel in order to study the impact of the multipath degradation. These simulations have shown that when a complete propagation channel is considered (LOS+multipath), for a 1 Hz DLL loop bandwidth, the tracking performances are improved when the FLL is implemented. However, no improvements are observed for a 10 Hz DLL loop bandwidth.

The objective of the third section was to implement a C/N_0 estimator. The Narrow-to-Wideband-Power-Ratio- C/N_0 estimator tested has highlighted some limits for C/N_0 higher than 60 dBHz. More accurately, a saturation phenomenon is observed, and it is linked to the phase evolution between symbols of the propagation channel contribution term to the correlator outputs mathematical model. If there is no phase evolution (AWGN case), the saturation appears for C/N_0 higher than 120 dBHz; if the phase evolution is the highest (radial trajectory), the saturation appears for C/N_0 higher than 60 dBHz. Three solutions were tested to overcome this saturation phenomenon.

- First, since the Narrow-to-Wideband-Power-Ratio- C/N_0 estimator issues are due to the phase of the signal, another explored solution consisted in designing an estimator independent from the phase, the Method-of-Moments-C/N_0 estimator. Again, limits have been identified for $C/N_0 > 60\ dBHz$
- Second, two evolutions of the NWPR have been proposed to suppress the influence of the phase. This modified estimator is denoted as NWPR C/N_0 phase-corrected estimator since it corrects the phase of the correlator outputs before using them on the classical NWPR estimator. Two NWPR C/N_0 phase-corrected estimators are proposed depending on the method used to estimate the phase:
    - Arctangent NWPR C/N_0 phase-corrected estimator: A simple arctangent discriminator is used to estimate the correlator outputs phase.
    - FLL-driven NWPR C/N_0 phase-corrected estimator: the correlator output phase evolution is predicted / estimated with the use of a FLL.

  Both estimators behavior are more performing than the NWPR estimator but they still present limitations for $C/N_0 > 95dBHz$. There is no difference between the two NWPR C/N_0 phase-corrected estimators. Finally, it can be said that even if a FLL does not improve much the tracking performances, for a 10 Hz DLL loop bandwidth, it could permit a better estimation of the C/N_0. Therefore, the FLL will be kept for the rest of the Ph.D.

Chapter 6. Characterization of pseudo range measurement errors due to propagation channels

The propagation channels, SCHUN (for GNSS signals) and QuaDRiGa (for 5G signals), and the thermal noise introduce errors on the pseudo range measurements. Although these errors are characterized with a Gaussian distribution in an open sky environment, this assumption may not be fulfilled in urban environments: the expected distributions are positively biased and positively skewed.

However, the majority of navigation filters, such as the Kalman Filters (KF), assumes that the pseudo range measurement errors follow a Gaussian distribution even in urban environments. Therefore, if the true errors distribution is far from being Gaussian, the KF navigation solutions may provide a degraded performance with respect to the hypothetical case where the measurements errors follow a true Gaussian distribution.

One potential solution to cope with non-Gaussian distributions is to use filters adapted to any type of measurement errors distributions such as the Particle Filter (PF). Despite being the theoretical ideal solution, PF solutions are quite heavy computationally and may not be adapted to low-cost devices. Moreover, in order to evaluate the gain provided by PF solutions with respect to the increase of complexity they bring, it is important to first develop the best possible low-to-middle complexity navigation solutions to be used as reference or benchmark.

The general objective of this chapter is thus to allow the implementation of some potential best low-to-middle complexity navigation solutions, such as the KF solutions detailed in chapter 7, which assume Gaussian distributions for the measurement errors. Therefore, in this chapter, the pseudo range measurement errors due to the propagation channels and the thermal noise will be first accurately characterized in terms of mean, variance and probability density functions (PDF) and second, methods will be developed in order to approximate these PDFs by Gaussian distributions (in order to implement some potential best navigation solutions with low-to-middle complexity).

Another objective of this chapter is to find the more appropriate method to approximate the true PDF by a Gaussian distribution or, in other words, the method that will allow maximizing the performances of the KF filters. In this sense, two methods are considered: a Gaussian over bounding and a Gaussian fitting method.

Note that the characterization process of the pseudo range measurement errors is based on the analysis of tracking loops results when using the correlator output models described in Chapter 4 section 2 and when using the propagation channel simulators SCHUN for GNSS and QuaDRiGa for 5G.

A preliminary step, prior to characterize the pseudo range measurement errors, consists in describing accurately the pseudo range measurement (the range and the errors distorting it) considered in this work. And, in particular, since 2 systems (GNSS and 5G) are considered in this work it is of the utmost importance to express the pseudo range measurements with respect to the same reference time frame.

First the pseudo range measurement models and the synchronization between the different systems used in this thesis are precisely described. Second, the methods developed to over bound and to fit the distributions are presented. Third, the parameters of the envisioned characterization are presented. Then the obtained characterization for QuaDRiGa and SCHUN are presented. The characterization is made in function of the C/N_0 .

6.1. Synchronization between systems

In this work, measurements from three different systems are hybridized, GPS, Galileo and 5G systems, where each system has its own reference time frame. Therefore, in order to develop the hybrid navigation modules, it is of the utmost importance to express the measurements of each system in the same reference time frame; if this first action is not well conducted, the true ranges associated to each system pseudo-range measurements will not be consistent among them. The GPS time has been chosen to be the reference time frame for this analysis.

The pseudo ranges measurements for GNSS and 5G systems have been described in chapters 2 and 3 respectively. In this section, the objective is to express them with respect to the same time frame.

Two kinds of measurements are considered in this study: pseudo range code measurements for both 5G and GNSS systems and pseudo range rate measurements for GNSS systems only. According to the studies led in Chapter 5 section 5.2, and in order to considered generic navigation filters, no pseudo range rates for 5G system have been considered here. Indeed, Chapter 5 section 5.2 has shown that a FLL is not mandatory even if it can improve the performances for a 1 Hz DLL loop bandwidth. Note that in this chapter, pseudo range measurements are considered. Contrary to the pseudo range mathematical models, the pseudo range measurements include the thermal noise error, the propagation channel error, the measurement error, etc.

In the first three sections, the GPS, Galileo and 5G pseudo range models are presented respectively. In the fourth section a summary of these models is proposed and finally, the pseudo range and pseudo rate measurement models are presented.

6.1.1 GPS pseudo range model

The pseudo range is defined as the difference between the reception time and the transmission time. The pseudo range model of the j^{th} GPS satellite obtained by the user is expressed as (6.1). Note that equation (6.1) is denoted as model and not as measurement because it is assumed that there are no distorting elements corrupting the expression.

$$\rho_{GPS_j} = c \cdot \left(t_{user,RX} - t_{sat_{j,GPS},TX}\right) \tag{6.1}$$

Where:

- ρ_{GPS_j} is the pseudo-range model of the j^{th} GPS satellite obtained by the receiver
- c is the speed of the light
- $t_{user,RX}$ is the reception time expressed in the receiver clock time frame
- $t_{sat_{j,GPS},TX}$ is the GPS satellite j emission time expressed in the GPS satellite j clock time frame.

Expression (6.1) can be further developed by remembering that the receiver reference time frame and the GPS satellite time reference frame are not necessarily synchronized and that each time instant can also be expressed in the selected reference clock time frame: the GPS time frame.

The reception time is expressed in the reference time frame as (6.2) where $\Delta t_{GPS/user}$ is the time shift of the receiver clock with respect to the GPS clock time frame, Figure 6.1 helps visualizing this shift.

$$t_{user,RX} = t_{GPS,RX} + \Delta t_{GPS/user} \tag{6.2}$$

The emission time is expressed in the reference time frame as (6.3) where $\Delta t_{GPS/sat_{j,GPS}}$ is the time shift of the j^{th} GPS satellite clock time frame with respect to the GPS clock time frame, see Figure 6.1.

$$t_{sat_{j,GPS},TX} = t_{GPS,TX} + \Delta t_{GPS/sat_{j,GPS}} \tag{6.3}$$

Replacing (6.2) and (6.3) in (6.1), equation (6.4) is obtained.

$$\rho_{GPS_j} = c \cdot \left(t_{GPS,RX} - t_{GPS,TX} + \Delta t_{GPS/user} - \Delta t_{GPS/sat_{j,GPS}}\right) \tag{6.4}$$

This expression shows the value $c \cdot \left(t_{GPS,RX} - t_{GPS,TX}\right)$ which is equal to the geometric distance between the j^{th} GPS satellite and the receiver r_{GPS_j}.

The pseudo distance model of the j^{th} GPS satellite expressed in the GPS time frame is thus expressed as (6.5), Figure 6.1 illustrates the demonstration further details can be found in [56].

$$\rho_{GPS_j} = r_{GPS_j} + c \cdot \Delta t_{GPS/user} - c \cdot \Delta t_{GPS/sat_{j,GPS}} \tag{6.5}$$

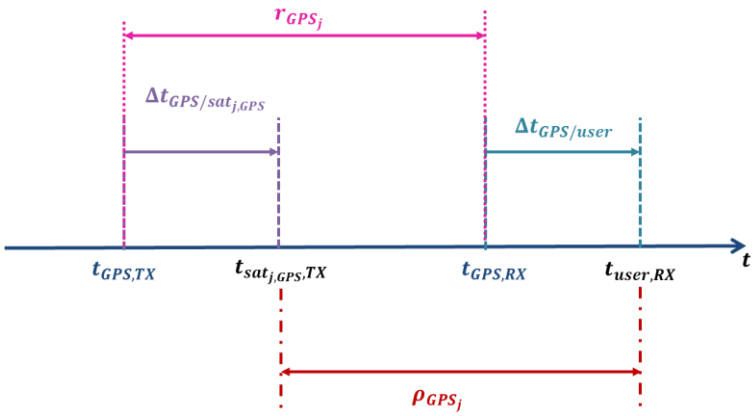

Figure 6.1 – GPS time frame synchronization

6.1.2 Galileo pseudo-range model

The pseudo range model of the j^{th} Galileo satellite obtained by the user is expressed as (6.6).

$$\rho_{Gal_j} = c \cdot \left(t_{user,RX} - t_{sat_j,Gal,TX}\right) \tag{6.6}$$

Where:

- ρ_{Gal_j} is the pseudo-range model of the j^{th} Galileo satellite obtained by the receiver
- c is the speed of the light
- $t_{user,RX}$ is the reception time expressed in the receiver clock time frame

- $t_{sat_j,Gal,TX}$ is the emission time expressed in the Galileo satellite j clock time frame

As well as before, expression (6.6) can be further developed by remembering that the receiver clock time frame and the satellite clock time frame are not necessarily synchronized. Moreover, remember that each time instant must be expressed in the selected reference clock time frame, the GPS clock time frame, in order to have all the pseudo range measurements expressed in the same reference time.

The reception time is expressed in the reference time frame as (6.7) where $\Delta t_{GPS/user}$ is the time shift of the receiver clock with respect to the GPS clock time frame, see Figure 6.2.

$$t_{user,RX} = t_{GPS,RX} + \Delta t_{GPS/user} \tag{6.7}$$

The emission time is expressed in the reference time frame as (6.8), where $\Delta t_{GPS/sat_{j,gal}}$ is the time shift of the j^{th} satellite clock with respect to the GPS clock time frame, see Figure 6.2.

$$t_{sat_j,Gal,TX} = t_{GPS,TX} + \Delta t_{GPS/sat_{j,gal}} \tag{6.8}$$

The pseudo range model of the j^{th} Galileo satellite obtained by the user in the GPS time frame is thus modeled as (6.9) where r_{Gal_j} is the geometric distance between the j^{th} Galileo satellite and the receiver.

$$\rho_{Gal_j} = r_{Gal_j} + c \cdot \Delta t_{GPS/user} - c \cdot \Delta t_{GPS/sat_{j,Gal}} \tag{6.9}$$

Finally, the time shift $\Delta t_{GPS/sat_{j,Gal}}$ can be expressed as: $\Delta t_{GPS/sat_{j,Gal}} = \Delta t_{GPS/Gal} + \Delta t_{Gal/sat_{j,Gal}}$; where $\Delta t_{GPS/Gal}$ represents the time shift between the GPS and Galileo systems and $\Delta t_{Gal/sat_{j,Gal}}$ is the time shift of the j^{th} Galileo satellite clock time frame with respect to the Galileo clock time frame, see Figure 6.2.

$$\rho_{Gal_j} = r_{Gal_j} + c \cdot \Delta t_{GPS/user} - c \cdot \Delta t_{GPS/Gal} - c \cdot \Delta t_{Gal/sat_{j,Gal}} \tag{6.10}$$

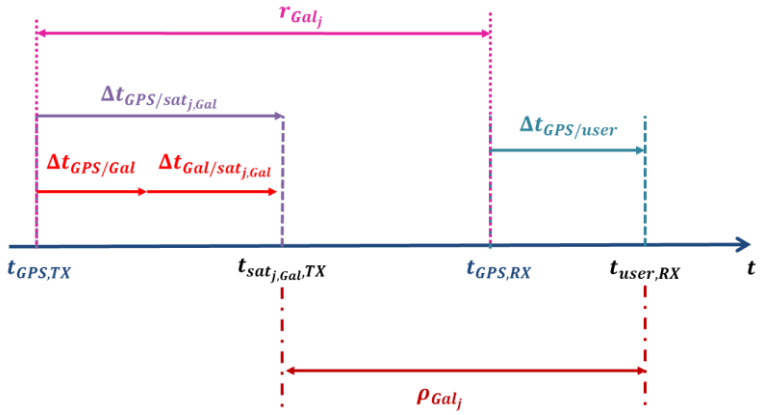

Figure 6.2 – Galileo time frame synchronization

6.1.3 5G pseudo-range model

The 5G pseudo range model of the j^{th} Base Station obtained by the user is expressed as (6.11), see Figure 6.3.

$$\rho_{5G_j} = c \cdot \left(t_{user,RX} - t_{BS_j,TX}\right) \tag{6.11}$$

Where:

- ρ_{5G_j} is the pseudo-range model of the j^{th} Base Station obtained by the receiver
- c is the speed of the light
- $t_{user,RX}$ is the reception time expressed in the receiver clock time frame
- $t_{BS_j,TX}$ is the emission time assumed by the receiver expressed in the 5G emitter j clock time frame

As well as before, expression (6.11) can be further developed by remembering that the receiver clock time frame and the Base Station time frame are not necessarily synchronized. Moreover, remember that each time instant must be expressed in the selected reference clock time frame, the GPS clock time frame, in order to have all the pseudo-range measurements expressed in the same reference time.

The reception time is expressed in the reference time frame as (6.12) where $\Delta t_{GPS/user}$ is the time shift of the receiver clock with respect to the GPS clock time frame, see Figure 6.3.

$$t_{user,RX} = t_{GPS,RX} + \Delta t_{GPS/user} \tag{6.12}$$

The emission time is expressed in the reference time frame as (6.13) where $\Delta t_{GPS/BS_j}$ is the time shift of the j^{th} Base station clock with respect to the GPS clock time frame.

$$t_{BS_j,TX} = t_{GPS,TX} + \Delta t_{GPS/BS_j} \tag{6.13}$$

The pseudo range model of the j^{th} Base Station obtained by the user in the GPS time frame is thus modeled as (6.14) where r_{5G_j} is the geometric distance between the j^{th} 5G base station and the receiver.

$$\rho_{5G_j} = r_{5G_j} + c \cdot \Delta t_{GPS/user} - c \cdot \Delta t_{GPS/BS_j} \tag{6.14}$$

Finally, the time shift $\Delta t_{GPS/BS_j}$ can be expressed as: $\Delta t_{GPS/BS_j} = \Delta t_{GPS/5G} + \Delta t_{5G/BS_j}$; where $\Delta t_{GPS/5G}$ represents the time shift between the GPS time and an hypothetical 5G system time frame, and $\Delta t_{5G/BS_j}$ is the time shift of the j^{th} 5G Base Station clock time frame with respect to the hypothetical 5G system time frame. See Figure 6.3.

$$\rho_{5G_j} = r_{5G_j} + c \cdot \Delta t_{GPS/user} - c \cdot \Delta t_{GPS/5G} - c \cdot \Delta t_{5G/BS_j} \tag{6.15}$$

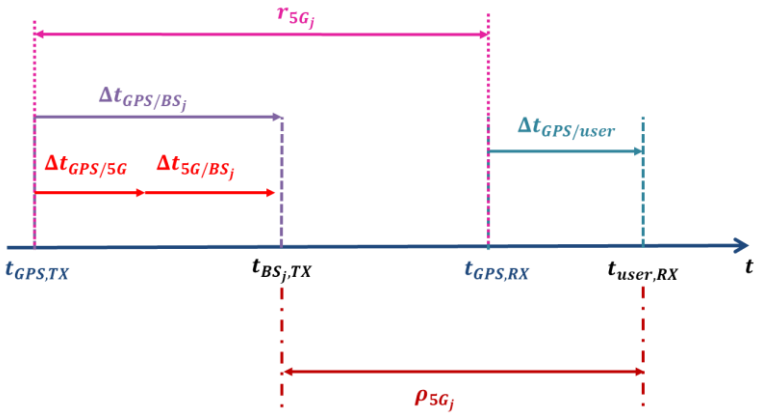

Figure 6.3 – 5G time frame synchronization

6.1.4 Pseudo ranges models summary

The set of considered pseudo ranges can be expressed as:

$$\begin{cases} \rho_{GPS_j} = r_{GPS_j} + c \cdot \Delta t_{GPS/user} - c \cdot \Delta t_{GPS/sat_{j,GPS}} & j = 1 \dots N_{GPS} \\ \rho_{Gal_j} = r_{Gal_j} + c \cdot \Delta t_{GPS/user} - c \cdot \Delta t_{GPS/Gal} - c \cdot \Delta t_{Gal/sat_{j,Gal}} & j = 1 \dots N_{Gal} \\ \rho_{5G_j} = r_{5G_j} + c \cdot \Delta t_{GPS/user} - c \cdot \Delta t_{GPS/5G} - c \cdot \Delta t_{5G/BS_j} & j = 1 \dots N_{5G} \end{cases} \quad (6.16)$$

Hypotheses have to be considered and tested regarding the biases and synchronization errors (equal to zero, constant, evolving, etc.). In particular, the following filters are derived assuming that GNSS measurements are corrected, ρ_{c,GPS_j} and ρ_{c,Gal_j}, that the offsets $\Delta t_{GPS/sat_{j,GPS}}$ and $\Delta t_{Gal/sat_{j,Gal}}$ are perfectly corrected and thus, that they are equal to 0. It is also assumed that the 5G network implements a synchronization process between all 5G base stations, so the time offset $\Delta t_{5G/BS_j}$ can be considered the same for all 5G base stations, can be considered constant over the observation duration (positioning calculation) and for simplification purposes it is set to 0. Consequently, the set of corrected pseudo ranges considered in the thesis are expressed in (6.17).

$$\begin{cases} \rho_{c,GPS_j} = \rho_{GPS_j} - \widehat{\Delta t}_{GPS/sat_{j,GPS}} = r_{GPS_j} + c \cdot \Delta t_{GPS/user} & j = 1 \dots N_{GPS} \\ \rho_{c,Gal_j} = \rho_{Gal_j} - \widehat{\Delta t}_{Gal/sat_{j,Gal}} = r_{Gal_j} + c \cdot \Delta t_{GPS/user} - c \cdot \Delta t_{GPS/Gal} & j = 1 \dots N_{Gal} \\ \rho_{5G_j} = r_{5G_j} + c \cdot \Delta t_{GPS/user} - c \cdot \Delta t_{GPS/5G} & j = 1 \dots N_{5G} \end{cases} \quad (6.17)$$

Where:

- $\widehat{\Delta t}_{GPS/sat_{j,GPS}}$ is the time shift of the j^{th} GPS satellite clock time frame with respect to the GPS clock time frame estimated by the GPS system and transmitted in the navigation message ($\approx \Delta t_{GPS/sat_{j,GPS}}$)
- $\widehat{\Delta t}_{Gal/sat_{j,GPS}}$ is the time shift of the j^{th} Galileo satellite clock time frame with respect to the Galileo clock time frame estimated by the Galileo system and transmitted in the navigation message ($\approx \Delta t_{Galileo/sat_{j,GPS}}$)

6.1.5 GNSS pseudo ranges rate models

As presented before, pseudo range rate measurements are also used for GNSS measurements. The general pseudo range rate model computed for a given satellite j (GPS or Galileo) is given below:

$$\dot{\rho}_j = \left(\dot{x}_{sat_j} - \dot{x}_{user}\right) \cdot a_{x_j} + \left(\dot{y}_{sat_j} - \dot{y}_{user}\right) \cdot a_{y_j} + \left(\dot{z}_{sat_j} - \dot{z}_{user}\right) \cdot a_{z_j} + c \cdot \dot{\Delta t}_{GPS/user} \quad (6.18)$$

Where:

- $\left(\dot{x}_{sat_j}, \dot{y}_{sat_j}, \dot{z}_{sat_j}\right)$ represents the j^{th} satellite velocity vector un the ECEF reference frame expressed in $\left[\frac{m}{s}\right]$
- $(\dot{x}_{user}, \dot{y}_{user}, \dot{z}_{user})$ represents the j^{th} user velocity vector un the ECEF reference frame expressed in $\left[\frac{m}{s}\right]$
- $a_{x_j} = \frac{\left(\dot{x}_{sat_j} - \dot{x}_{user}\right)}{\sqrt{\left(\dot{x}_{sat_j} - \dot{x}_{user}\right)^2 + \left(\dot{y}_{sat_j} - \dot{y}_{user}\right)^2 + \left(\dot{z}_{sat_j} - \dot{z}_{user}\right)^2}}$ denoted the LOS projection along the X-axis

- $\dot{\Delta}t_{GPS/user}$ is the receiver clock drift expressed as the clock bias derivative, the clock drift between GPS and Galileo is neglected $\dot{\Delta}t_{GPS/Gal}\sim 0$

6.1.6 Pseudo range and pseudo range rate measurements

The previously derived pseudo range and pseudo range rate equations are denoted as models and not as measurements because it is assumed that there are no distorting elements corrupting the expressions. Nevertheless, these distorting elements cannot be omitted; therefore, this section presents the pseudo range and pseudo range rated measurement models.

For the GNSS pseudo range measurement models, 5 types of errors are considered, [56]:

- The ionosphere error in $[m]$: ε_{iono}
- The troposphere error in $[m]$: ε_{tropo}
- The delay induced by the multipath effect in $[m]$: $\varepsilon_{multipath}$
- The receiver's thermal noise in $[m]$: ε_{noise}
- The ephemeris and satellite clock errors in $[m]$: $\varepsilon_{eph-sat}$

In Chapter 6, the multipath effect and the noise effect will be accurately characterized. Therefore, the code pseudo range measurement models for the j^{th} GPS and the j^{th} Galileo signals are

$$\rho_{c,GPS_j} = r_{GPS_j} + c\cdot\Delta t_{GPS/user} - c\cdot\Delta t_{GPS/sat_{j,GPS}} + \varepsilon_{iono_{j,GPS}} + \varepsilon_{tropo_{j,GPS}} + \varepsilon_{multipath_{j,GPS}} + \varepsilon_{noise_{j,GPS}} + \varepsilon_{eph-sat_{j,GPS}} \tag{6.19}$$

$$\rho_{c,Gal_j} = r_{Gal_j} + c\cdot\Delta t_{GPS/user} - c\cdot\Delta t_{GPS/sat_{j,Gal}} + \varepsilon_{iono_{j,Gal}} + \varepsilon_{tropo_{j,Gal}} + \varepsilon_{multipath_{j,Gal}} + \varepsilon_{noise_{j,Gal}} + \varepsilon_{eph-sat_{j,Gal}} \tag{6.20}$$

For the GNSS pseudo range rate measurement computed by the receiver for a given satellite j, the slow varying satellite clock and ephemeris error are neglected. Therefore, only 4 types of errors are considered:

- The time correlated errors induced by the ionospheric delay rate error in $\left[\frac{m}{s}\right]$: $\dot{\varepsilon}_{iono}$
- The time correlated errors induced by the tropospheric delay rate error in $\left[\frac{m}{s}\right]$: $\dot{\varepsilon}_{tropo}$
- The multipath effect on the pseudo range rate measurement in $\left[\frac{m}{s}\right]$: $\dot{\varepsilon}_{multipath}$
- The receiver's thermal noise effect on the pseudo range rate measurement in $\left[\frac{m}{s}\right]$: $\dot{\varepsilon}_{noise}$

Therefore, the pseudo range rate measurement models for the j^{th} GPS and the j^{th} Galileo signals are

$$\dot{\rho}_j = \left(\dot{x}_{sat_j} - \dot{x}_{user}\right)\cdot a_{x_j} + \left(\dot{y}_{sat_j} - \dot{y}_{user}\right)\cdot a_{y_j} + \left(\dot{z}_{sat_j} - \dot{z}_{user}\right)\cdot a_{z_j} + c\cdot\dot{\Delta}t_{GPS/user} + \dot{\varepsilon}_{iono_j} + \dot{\varepsilon}_{tropo_j} + \dot{\varepsilon}_{multipath_j} + \dot{\varepsilon}_{noise_j} \tag{6.21}$$

Note that in the following, the time correlated errors due to ionospheric and tropospheric are supposed to be null. The error due to multipath and the receiver thermal noise will be derived (characterized and approximated) in section 6.4.

For the 5G pseudo range measurement models, 2 types of errors are considered:

- The delay induced by the multipath effect in $[m]$: $\varepsilon_{multipath}$

- The receiver's thermal noise in $[m]$: ε_{noise}

These errors will be derived (characterized and approximated) in section 6.3. Therefore, the pseudo range measurement models for the j^{th} 5G Base station is

$$\rho_{5G_j} = r_{5G_j} + c \cdot \Delta t_{GPS/user} - c \cdot \Delta t_{GPS/5G} - c \cdot \Delta t_{5G/BS_j} + \varepsilon_{multipath_{5G_j}} + \varepsilon_{noise_{5G_j}} \quad (6.22)$$

6.1.7 Targeted solution for multipath and AWGN noise error component- modelling

In conclusion, in the rest of the Ph.D., only the errors due to the multipath and the receiver thermal noise are considered. More specifically, in chapter 6 for 5G and GNSS separately, these errors are gathered and considered as one single noise affecting the pseudo ranges.

This enhanced noise will be accurately derived in chapter 6 section 6.4. More accurately, the true distribution of the pseudo range measurements errors due to the propagation channel (SCHUN for GNSS and QuaDRiGa for 5G) and due to the thermal noise are first characterized (for 5G and GNSS independently). Second the distributions are approximated by Gaussian variable. The resulting derivation will be used in chapter 7 in the Kalman Filter to fill the measurement noise covariance matrix.

6.2. General methodology

As said during the introduction, the objective of this chapter is to derive Gaussian distributions for the pseudo range measurement errors obtained for 5G signals and GNSS signals. This derivation process is a two-step process, where the true PDF distributions of the pseudo range measurement errors are characterized and second the true PDF are approximate to a Gaussian distribution. In this section the derivation process is detailed and special attention is given to the Gaussian approximation methods, methods finding the Gaussian distribution which bests approximates a true distribution (minimization of a cost function), that will allow to maximize the performances of the KF navigation filers described in chapter 7 section 7.2.2.

First the description of the two-steps method is proposed. Second, the running example is presented. Third the first step of the method, namely the characterization step, is described and fourth the approximation step is described.

6.2.1 Description

In order to derive Gaussian distributions for the pseudo range measurements, a two-steps method has been developed:

1. To accurately characterize in terms of mean, variance and probability density functions (PDF) the pseudo range measurement errors due to the propagation channels and the thermal noise. This step is illustrated on the left part of Figure 6.4, where the PDF of the pseudo range errors obtained for a given C/N_0 (here 53 dBHz) is provided (the method to obtain this distribution is described later on).
2. To approximate these PDFs by Gaussian distributions. Two methods have been developed in this work: an over-bounding method and a fitting method. This step is illustrated on the right part of Figure 6.4, where the blue, red and yellow curves are Gaussian distributions approximating the true violet PDF (the method to obtain this approximation is described later on).

In order to allow for clear understanding of the notation on this chapter, the following concepts are defined and used along this chapter, the first step is referred as the “characterization” step, the second step is referred as the “approximation” step and finally, the whole process is referred as “derivation”. This nomenclature is illustrated in Figure 6.4.

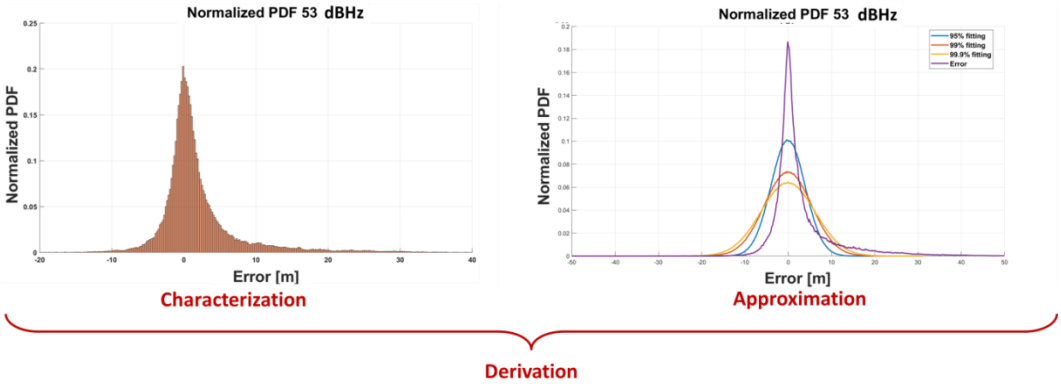

Figure 6.4 – Description of the method

6.2.2 Running example presentation

In Figure 6.5, the time series of the pseudo range measurement errors considered for the running example are presented. The pseudo ranges are generated from a 25 m-radius circle trajectory; the scenario selected is the QuaDRiGa 3GPP_38.901_UMi_LOS scenario which models a typical terrestrial pico-base stations deployed below the rooftops in densely populated urban areas covering carrier frequencies from 500 MHz to 100 GHz. Regarding the receiver processing, the considered OFDM numerology consists in a subcarrier spacing of 15 kHz and a carrier frequency of 2 GHz. The generated correlator outputs, derived in chapter 4 section 4.2.3, are used by the ranging module presented in chapter 5 section 5.1; the DLL considered uses an Early Minus Late Power (EMLP) discriminator, the loop bandwidth is set to 10 Hz and the correlator spacing is set to 4 samples. A second order DLL is considered. The frequency is assumed to be perfectly estimated, therefore, no FLL is implemented. The time series of the generated pseudo range measurement error is shown in Figure 6.5.

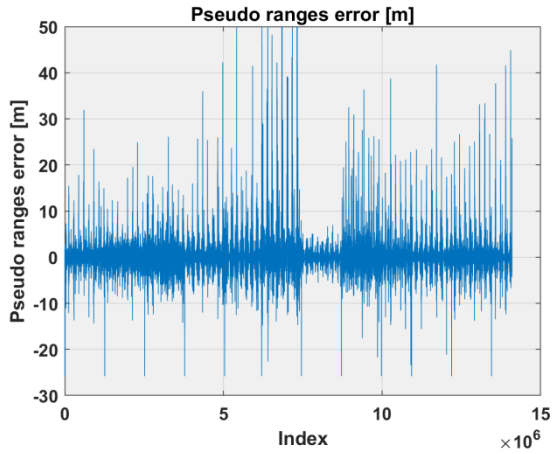

Figure 6.5 – Pseudo range errors

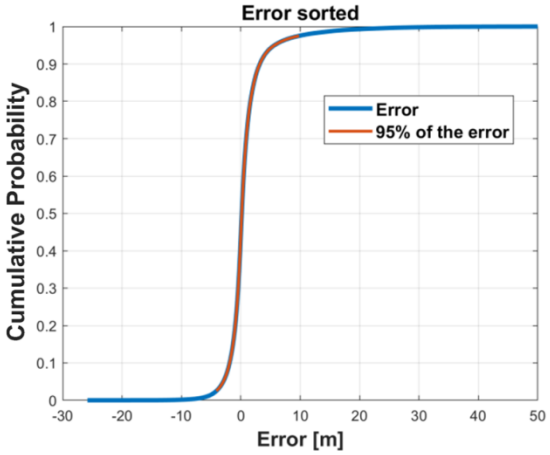

Figure 6.6 – Selection of the errors to be over bounded or fitted

6.2.3 Step 1: Characterization of the true distribution

The first step of the derivation method consists in characterizing the true distribution. The characterization can be conducted by either studying the PDF or the CDF of the pseudo ranges errors. The focus is made on the CDF in this work.

Inspecting the running example, in Figure 6.6 (blue curve), the Cumulative Density Function (CDF) of the pseudo range errors from Figure 6.5 is provided. The fitting and the over bounding are derived from the CDF.

6.2.4 Step 2: Approximation of the distribution

The second step of the derivation method consists in approximating the true distribution by Gaussian distributions. The principle of a Gaussian approximation method consists in selecting the Gaussian distribution which minimizes a given cost function, where the cost function depends on the Gaussian approximation method.

Two methods have been considered: a fitting method and an over-bounding method. There is no a priori reason to choose one over the other; therefore, the criterion selected to decide amongst the best approximation method is the navigation performance obtained in chapter 7 for the different tested navigation filters. The running example is used to graphically present an example of the application of each of the two methods with 5G pseudo ranges.

First the approximation parameters are described, second the over bounding method is presented, third the fitting method is described and finally, both methods are compared.

6.2.4.1 Approximation parameters

There are two parameters which completely determine a Gaussian variable: the mean and the variance, $N(\mu, \sigma)$. The key point of the two Gaussian approximation methods is the determination of the variance. In fact, the two methods calculate the mean using the same methodology, and the value of the mean might have a significant impact on the variance determination. In this work, three different mean μ values are inspected:

- $\mu = 0$
- $\mu = mean$, where $mean$ corresponds to the statistical mean value of the considered errors, i.e. the mean of the red curve in Figure 6.6

- $\mu = max$, where max corresponds to the index of the maximum of the histogram of the considered errors.

Another parameter which impacts the determination of the variance is the confidence bound. In fact, as their names indicate, the over-bounding and fitting methods are going to respectively over-bound and to fit the targeted CDF distribution over an interval defined by the confidence bound. The over-bounding and fitting process will thus depend on the selected confidence bound. In this work, 3 confidence bounds are tested: 95%, 99% and 99.9%. In order to approximate the distribution with a $X\%$ confidence bound, the errors kept correspond to the CDF errors inside the interval $\left[\left(\frac{100-X}{2}\right): \left(100 - \frac{100-X}{2}\right)\right]$.

These parameters are summarized in Table 6.1.

Table 6.1 – Approximation parameters

Confidence bound	95%	99%	99.9%
Mean	$N(0, \sigma)$	$N(mean, \sigma)$	$N(max, \sigma)$

Inspecting the running example, in Figure 6.6, in red are presented the error considered to find the 95% fitting/over-bounding distributions; it corresponds to the errors in the interval $[2.5\%: 97.5\%]$. For the example used along this section for illustration purposes, a 95% confidence over-bound is selected. Moreover, only the concerned errors inside confidence bound are shown.

6.2.4.2 Over bounding method

The objective of the over bounding method is to determine the minimal variance of the distribution that will permit to envelop the true distribution over the wanted confidence bound.

The over-bounding method consists in generating a Gaussian CDF initialized with a high variance value and to decrease the variance until the over bounding CDF envelop the CDF of the error to be over bounded.

Therefore the cost function to minimize corresponds to minimization of the approximation distribution variance $\sigma_{over\ bound}$ described in (6.23). Moreover, the cost function is subject to the conditions described in (6.23). In other word, the over bounding CDF must be above the CDF of the error for error values lower than the mean of the distributions; the over bounding CDF must be below the CDF of the error for error values higher than the mean of the distributions. (6.23) summarizes the method and Figure 6.7 illustrates the process.

$$\min \sigma_{over\ bound}$$
$$subject\ to \begin{cases} CDF_{overbounding}(Error) - CDF_{error}(Error) > 0 & for\ Error < \mu \\ CDF_{overbounding}(Error) - CDF_{error}(Error) < 0 & for\ Error > \mu \end{cases} \quad (6.23)$$

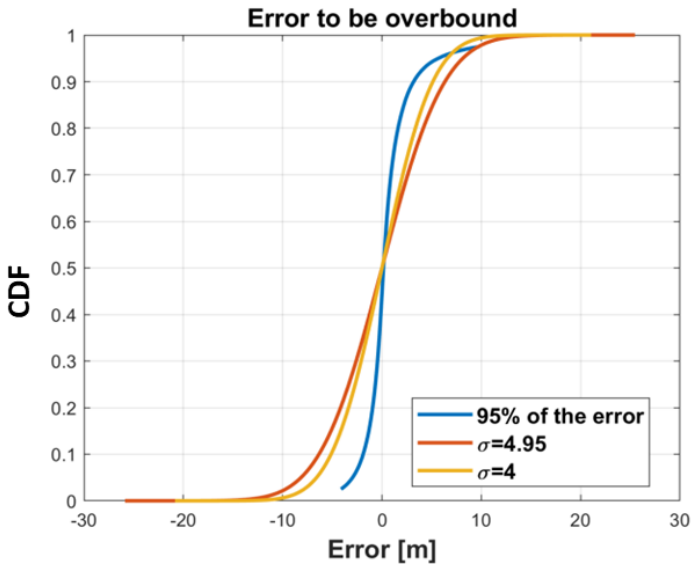

Figure 6.7 – Over bounding method – CDF

Inspecting the running example, in Figure 6.7, the CDF to be over bounded is the blue curve; the errors are over bounded by a zero mean Gaussian distribution. The red curve fulfils the over bounding conditions since the red curve is always at the right of the blue curve for positive error and at the left of the blue curve for the negative errors. Note that for values higher than 97.5% or lower than 2.5%, the blue curve is not plotted since the confidence bound is set to 95%; therefore, the red curve must only fulfill the criterion for the depicted blue curve. Finally, note that the yellow curve does not overlap entirely the positive errors.

6.2.4.3 Fitting method

The fitting method consist in generating a Gaussian CDF initialized with a small variance value and to increase the variance until the norm of the error over the abscises axis between the fitting CDF and the CDF of the error to be fitted is minimized.

The cost function of the fitting method is thus the difference between the CDF of the true distribution and the fitting CDF and is described in (6.24) over the whole confidence bound interval considered.

$$\underset{\sigma}{\text{Min}} \left|\left|CDF_{error} - CDF_{fitting}(\sigma)\right|\right| \; subject\ to\ the\ confidence\ bound\ interval \tag{6.24}$$

Where CDF_x represents the CDF vector of source x.

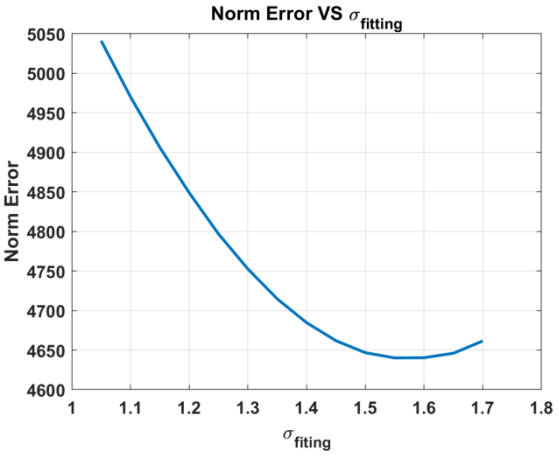

Figure 6.8 – Fitting method – minimum local

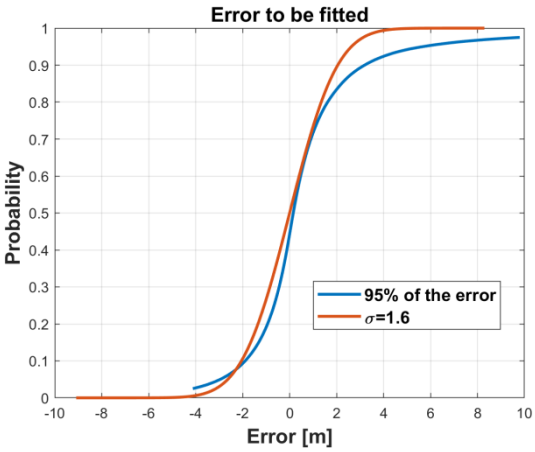

Figure 6.9 – Fitting method – CDF

Inspecting the running example, Figure 6.8 and Figure 6.9 allow to illustrate the process. As it can be observed from Figure 6.8, the norm of the error decreases as the value of the variance increases until it reaches a minimum local which corresponds to the fitting distribution illustrated in Figure 6.9.

6.2.4.4 Methods comparison

In this section the two methods are compared through their application to the running example. In Figure 6.10 and Figure 6.11, the resulting CDF and PFD of the fitting and over-bounding method applied to 95% of the initial error distribution are provided. As it can be seen, both methods provide very different results. Basically, the fitting method permits to correctly characterize the small errors, i.e. the center of the distribution. On the contrary, the over bounding method will allow to cover the tails of the distribution.

In this thesis, both methods are tested and compared in terms of positioning performances in chapter 7. Recommendations will be made according to the performances obtained.

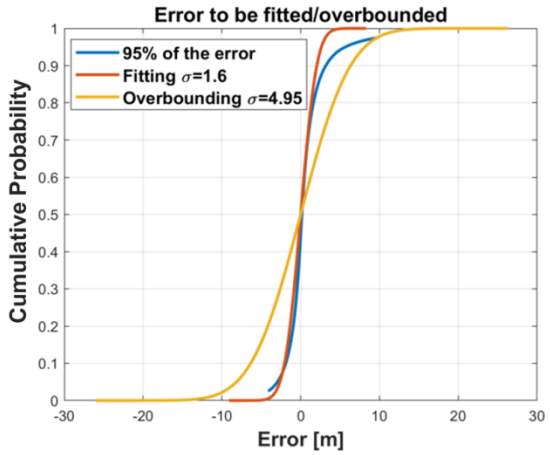

Figure 6.10 – Methods comparison – CDF

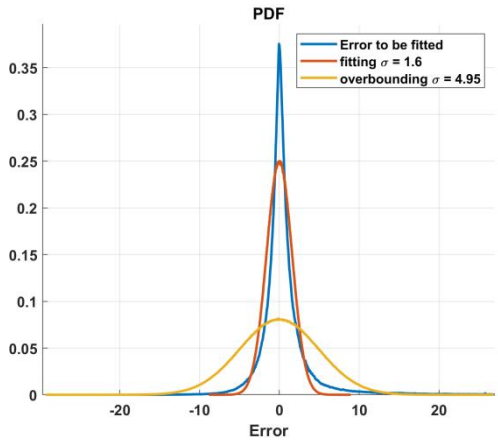

Figure 6.11 – Method comparison – PDF

6.3. Derivation of the QuaDRiGa pseudo range measurements errors Gaussian distribution

In this section the derivation of the pseudo range measurement error Gaussian distribution for 5G signals is provided. The errors of the pseudo range measurements are due to the thermal noise and the QuaDRiGa propagation channel (LOS shadowing and multipath). Therefore, first the generated scenarios are presented, second the over bounding and fitting results are provided.

6.3.1 Generated scenarios

As already presented in chapter 4 section 4.1.2, the scenario design of the propagation channel to be simulated by QuaDRiGa is made through the selection of 3 parameters: high-level scenario, receiver's trajectory and signal/receiver characteristics.

Regarding the high-level scenarios, the configurations used is referred as 3GPP_38.901_UMi_LOS. The configurations model typical terrestrial pico-base stations deployed below rooftop in densely populated urban areas covering carrier frequencies from 500 MHz to 100 GHz. The interest in choosing this high-level scenario is twofold. First, it follows the 3GPP standard on 5G propagation channel: TS.38.901, [49], especially regarding the frequency range. Second, it models Urban Micro-Cell environment which fits with the thesis problematic (constrained environment). The LOS scenario is a favorable case meaning that the LOS signal has higher power than multipath.

Regarding the trajectories, considering that the selected scenario simulates pico-base stations which have typically a 4-to-200 m-radius-size, 3 types of trajectories are considered. First a radial trajectory beginning at 20 m of the base station and going away linearly for 280 m, an illustration is provided in Figure 6.12. Second, a 500 m long 'chord' trajectory, consisting of a linear trajectory which passes at a minimum of 25 m from the Base Station; an illustration is provided in Figure 6.13. Finally, 12 circular trajectories have been studied, that lies in 10-to-250 m-radius-size; 3 of these trajectories are illustrated in Figure 6.14. The number of points generated per circular trajectory must be equal, in order to do so, the number of points required for the 200 m-radius circle is taken as the reference and the other circles are generated according to this number. By doing so, each circular trajectory is equivalently represented in the results. It means that the 100 m-radius-circle is travelled twice, and the 250 m-radius-circle is not complete as illustrated in Figure 6.14. The radiuses and lengths of the trajectories are a bit larger than the maximum pico-cell radius in order to increase the number of points at the edge of the pico-cell coverage. Indeed, the characterization is made with respect to the C/N_0 and the objective is to correctly characterize the pseudo range error even at low C/N_0 (when at the limit of the pico-cell).

As illustrated in Figure 6.12, Figure 6.13 and Figure 6.14, the trajectories are split into segments of about 25/30 m long. This is required for QuaDRiGa to simulate the time evolution of the propagation channel: at each segment a new random set of clusters is generated. Using a Monte Carlo approach, each trajectory is thus generated several times (between 800 and 1200 times) in order to increase this number of segments thus to increase the number of randomly generated sets of clusters and consequently improve the statistics.

The described trajectories are swept at a constant speed of 50 km/h.

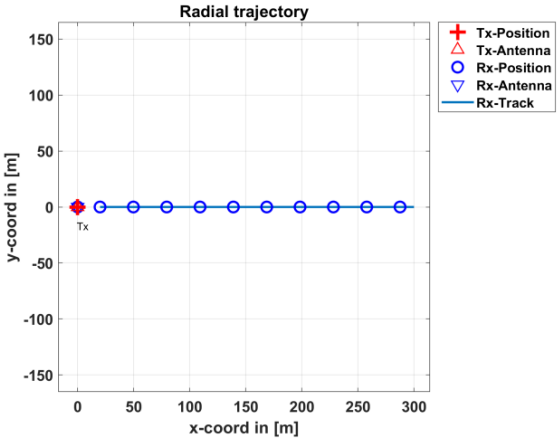

Figure 6.12 – Radial trajectory

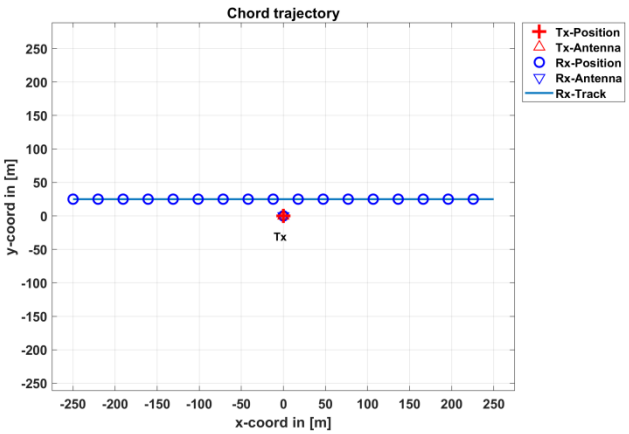

Figure 6.13 – Chord trajectory

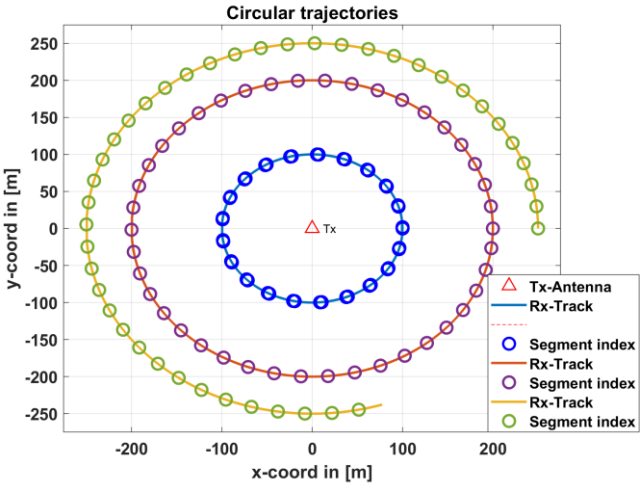

Figure 6.14 – Circular trajectories

Regarding the signal characteristics, the numerology of the OFDM signal considered consists in using a 15 kHz subcarrier spacing and a 2 GHz carrier frequency. Regarding the receiver characteristics, a second order DLL is used; two loop bandwidths are considered: 1 Hz and 10 Hz and the correlator spacing is set to 4 samples. The DLL characteristics are summarized in Table 6.2. Note that for simplification purposes, it is assumed that each consecutive symbol is identical and corresponds to the second symbol of the SSPBCH block described in chapter 3 section 3.3.6.3.2. Therefore, a simplified 5G frame is considered. All over the trajectory, the 5G frame is composed of one symbol repeated every symbol.

Table 6.2 – DLL characterization

Characteristics	Correlator spacing δ	Order	Update rate	Loop bandwidth
Adopted values	$\delta = 4\ samples$	2nd	$T_{update} = 7.1354 \cdot 10^{-5}\ s$	$B_l = 1\ Hz$ $B_l = 10\ Hz$

Table 6.3 is provided in order to summarize the configurations tested.

Table 6.3 – QuaDRiGa scenarios considered

QuaDRiGa scenario	Trajectory	High level Scenario	Carrier frequency	Subcarrier spacing
1	12 Circular	3GPP_38.901_UMi_LOS	2 GHz	15 kHz
2	Chord			
3	Radial			
4	12 Circular + Chord + Radial			

Finally, the last important point is the definition of the input SNR and the estimated C/N_0; remember that the driven idea was to be as realistic as possible. It is assumed that the useful transmitted power at the base station output is set to $C = 0\ dBm = -30\ dBW$. Note that according to 3GPP standards, the maximum transmitted power is $C_{max} = 23\ dBm$, in order to simulate a less ideal or more realistic case the transmitted power has been decreased to $C = 0\ dBm$. The noise power is defined using the GNSS receiver noise value already derived in chapter 5 section 5.3.1: $N_0 = -200\ dBW/Hz$ ($NF = 4dB$), and the bandwidth $B = \Delta f \cdot N_{FFT}$ where N_{FFT} is the FFT window size and Δf is the subcarrier spacing of the OFDM signal. The SNR at the demodulation input and without considering the propagation channel is thus $SNR_{demodulation} = \frac{C}{N_0 B} \cong 95\ dBHz$. The C/N_0 considered for the characterization is the true one as derived in equation (5.69).

The pseudo ranges are generated thanks to the simulator described in Annex A.

6.3.2 Results

The presentation of the results is split into 5 sections. In the first section, the obtained distributions (1st step of the methodology, the characterization process) as a function of the true C/N_0 are presented. The characterization is proposed to be made as a function of the C/N_0 as it is a usual available parameter in the receiver which can be estimated as proposed in Chapter 5 section 5.3.2. The approximation of the pseudo range error measurements is made using 3 Gaussians distributions differing from their mean as presented in section 6.1.4, the second section will present the impact of the mean selected for the approximation for both the over-bounding and the fitting methods (2nd step of the methodology, the Gaussian approximation process). The third section compares the over bounding and the fitting methods. Forth, the first 3 cases of Table 6.3 are compared in order to determine the impact of the trajectory on the characterization. The characterizations obtained for case 4 is presented in the last section.

6.3.2.1 Characterization of the pseudo range measurements errors

The objective here is not to define the best distribution to characterize the pseudo range errors since the Kalman filters require Gaussian approximation but to highlight the fact that other distributions could approximate more accurately these distributions.

In order to approximate the distribution by the fitting or the over bounding methods, it is required to work with the CDF, nevertheless in order to state the (non)-Gaussian aspect of the true distribution it is more convenient to work with the PDF.

The computation of the PDF is performed with respect to the true C/N_0. Considering the input SNR and the trajectories, the obtained C/N_0 lie in $C/N_0 \in [40\ 98]\ dBHz$. The characterization is made assuming

a $2\ dB$ binwidth; thus the characterization refered as the $97\ dBHz$-characterization corresponds to all errors generated for $C/N_0 \in [96\ \ 98]\ dBHz$.

In Figure 6.15 and Figure 6.16, two histograms of the errors obtained for the $53\ dBHz$-characterization (left) and the $67\ dBHz$-characterization (right) for the circular trajectories (case 1 in Table 6.3) are provided. As it can be seen, the histograms are not symmetrical, larger positive tails can be observed especially for the $53\ dBHz$-characterization. In fact, the lower the C/N_0, the larger the positive tails. This behavior is not specific to these two C/N_0 PDF estimations as illustrated in Figure 6.16. Similar observations can also be made for the radial and chord trajectories. Therefore the obtained distributions are not Gaussians.

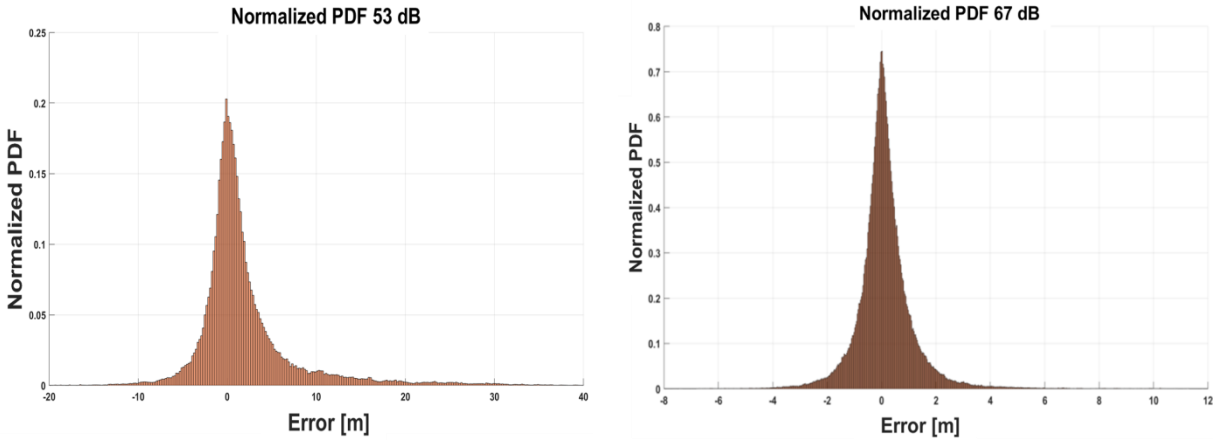

Figure 6.15 – Histogram of the errors for the $53\ dBHz$-characterization (left) and the $67\ dBHz$-characterization (right) – circular trajectories

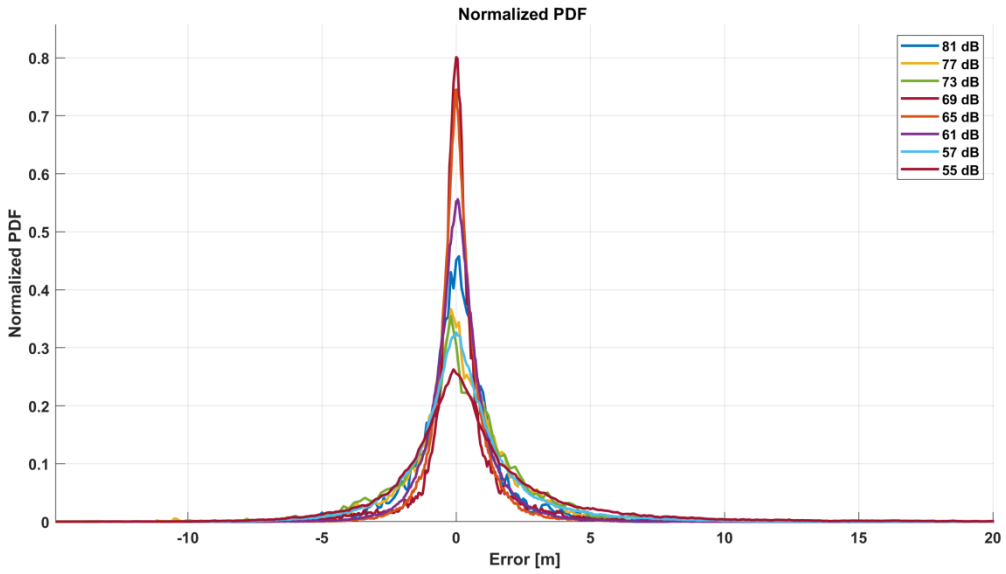

Figure 6.16 – PDF of the errors for several C/N_0 – circular trajectories

Remember that in this work, the navigation solutions are based on Kalman filters; Kalman filtering is based on the processing of Gaussian measurements as well as on Gaussian vector state noise. Therefore, in this work, the true distributions are over bounded and fitted by Gaussian distributions. Nevertheless, other distributions could be more appropriate to over bound and to fit the error distribution. As an example, in Figure 6.17, the Matlab distribution fitter app, [57], has been used to visualize the behavior of 3 fitting distributions:

- The Gaussian normal distribution: [58]
- The logistic distribution: [59]
- The non-parametric kernel distribution: [60]

There could be used in different navigation filters allowing non-Gaussian distributions (such as Particle Filters) in order to improve the performances of the navigation solution.

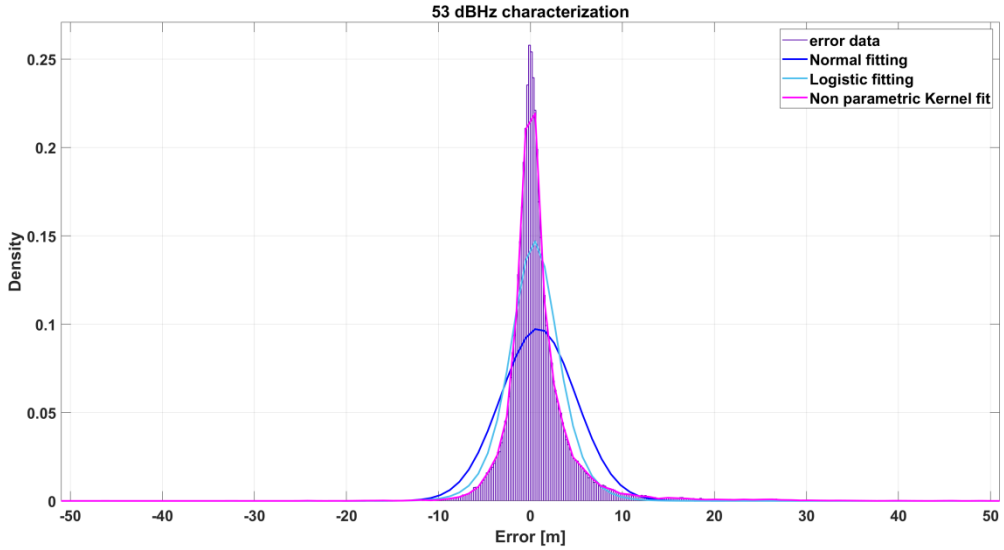

Figure 6.17 – Distribution fitter overview

6.3.2.2 Impact of the mean on the Gaussian approximation methods for the LOS scenario cases 1 to 3

The pseudo range measurement errors distributions are approximated by using the fitting and over-bounding method and by using three Gaussian distributions candidates as defined in section 6.1.4. These distributions differ from each other by the considered mean. In this section the impact of the mean on the obtained approximation of the variance is studied.

In Figure 6.18 and Figure 6.19, the fitting (defined in section 6.1.4.3) and over bounding (defined in section 6.1.4.2) approximations obtained for the circular trajectory and for a 95% confidence bound are provided.

First of all, the fitting and over bounding $N(0,\sigma)$ and $N(max,\sigma)$ distributions are barely identical. This is explained by the value of the max which is less than 0.1 m for any C/N_0 value; therefore, close to the zero mean of $N(0,\sigma)$.

Second, the statistical mean of the error increases along the C/N_0 decreases; this is why the difference between the $N(\mu,\sigma)$ and the two others distributions increases as the C/N_0 decreases. It must also be noted that the number of samples used for the characterization also decreases, which means that the results might be also biased due to the lack of samples.

Nevertheless, all 3 distributions provide comparable results. This behavior has also been observed for the radial and the chord trajectories. Consequently, in the following, the focus is made on the characterization by a $N(0,\sigma)$.

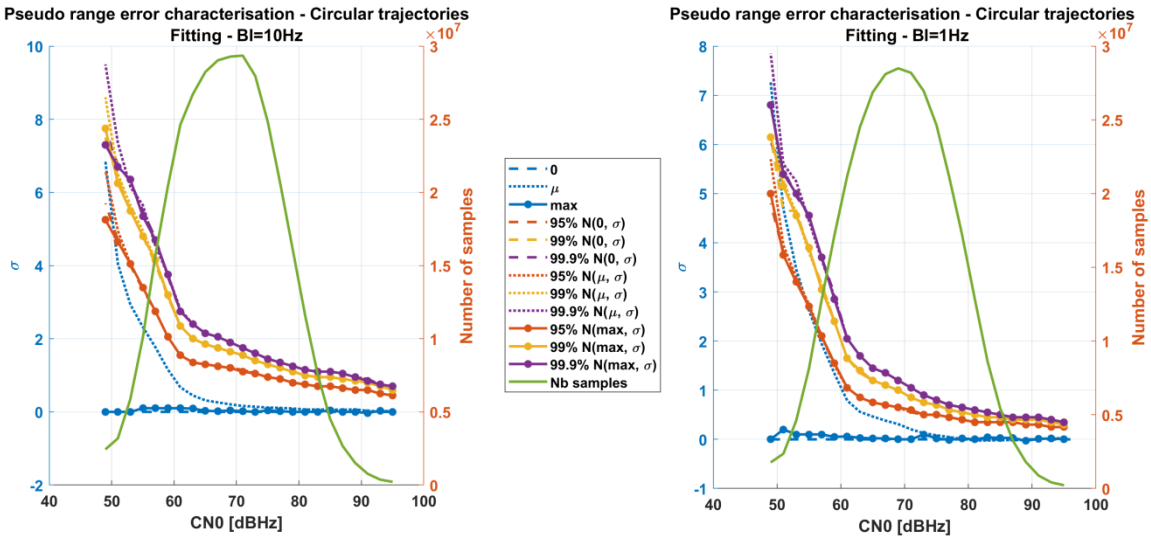

Figure 6.18 – Circular trajectories – fitting results for the 3 Gaussian distributions envisioned

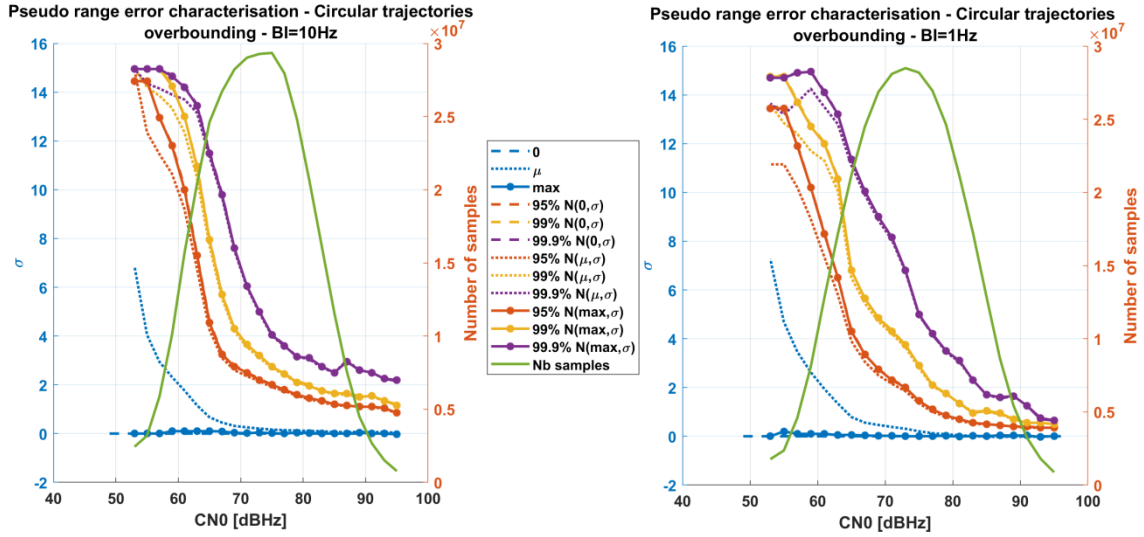

Figure 6.19 – Circular trajectories – Over bounding results for the 3 Gaussian distributions envisioned

6.3.2.3 *Fitting versus over bounding Gaussian approximation methods*

In section 6.1.4, two methods have been derived to approximate the pseudo range measurements errors true distribution with a Gaussian distribution: an over bounding method and a fitting method. In this section, the approximations obtained for the circular trajectories for the fitting and the over bounding cases are compared.

Figure 6.20 provides the over bounding and fitting results for both DLL configurations for the circular trajectories assuming a $N(0,\sigma)$ characterization.

This figure did not state whether a Gaussian approximation method is better than the other one, but it is clear that both the fitting and the over bounding methods have to be tested in order to determine the more appropriate one to be used for the application. The over bounding σ-values determined are much higher than the fitting σ-values. As an example for 55 dBHz the over bounding σ-values are three times higher than fitting σ-values.

In chapter 7, the performances of the Kalman filters will be studied for the Gaussian distribution derivations obtained for both methods: the fitting and over-bounding methods. Since KFs assume that the

errors follow centered Gaussian distributions, only the variances obtained for the $N(0,\sigma)$ for the fitting and over-bounding methods will be tested. The Gaussian distribution derivation obtained for the three confidence bounds will be tested. Then, recommendations will be provided on the appropriate method to adopt.

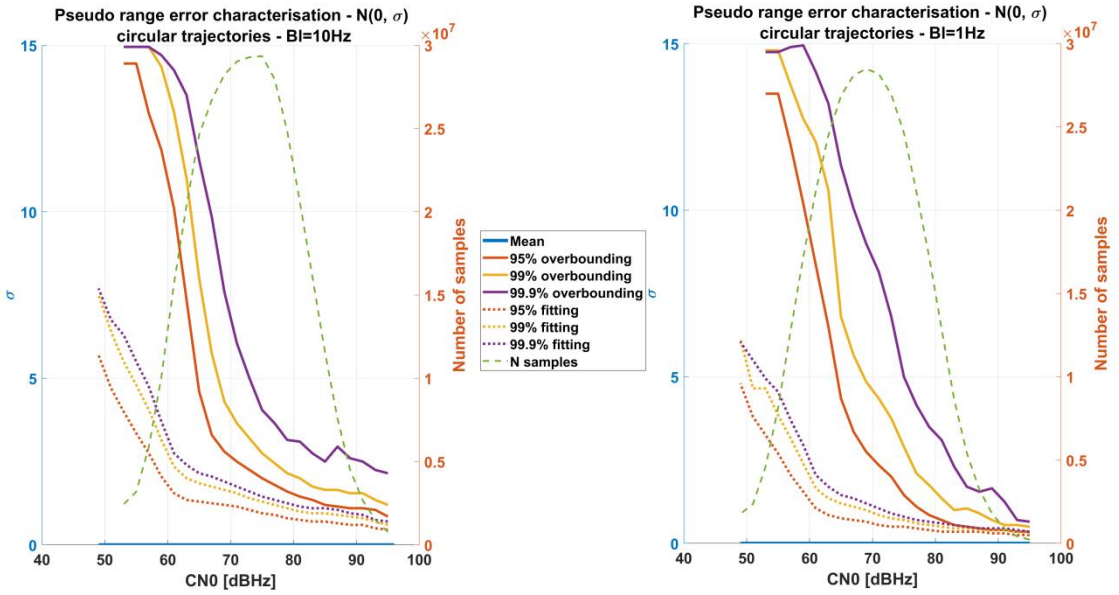

Figure 6.20 – Fitting versus over bounding characterization – circular trajectories

6.3.2.4 Impact of the trajectories

The impact of the trajectory on the obtained Gaussian distribution derivation has been studied. The first 3 cases presented in Table 6.3 differ only from the considered trajectory: radial, chord or circular trajectory. The Gaussian distribution derivation characterizations obtained for each trajectory are presented in this section.

In order to realistically compare the Gaussian distribution derivations obtained for each trajectory it is of the utmost importance to perform the derivation over the same number of samples. The green curves in Figure 6.21 to Figure 6.24, represent the number of samples considered for each trajectory in function of the C/N_0; as it can be seen, they are comparable and they are high enough to provide consolidate results.

In Figure 6.21, the fitting Gaussian distribution derivation is provided for the 3 trajectories (cases 1 to 3) and the 3 confidences bounds. According to the figure, the Gaussian distribution derivation seems both trajectory- and C/N_0-dependent.

The fitting Gaussian distribution derivation obtained for the circular trajectories is always below the fitting Gaussian distribution derivation obtained for the chord trajectories, meaning that, for any C/N_0, the observed error on the pseudo range has a lower standard deviation for circular trajectories than for chord trajectories. In Figure 6.21 it can be observed that for the 1 Hz DLL bandwidth, the 99.9% circular characterization is lower than the 95% chord characterization for $C/N_0 < 50\ dBHz$.

The fitting Gaussian distribution derivation obtained for the radial trajectory seems to behave as the chord trajectory for high C/N_0 and as the circular trajectories for low C/N_0.

In Figure 6.22, a focus is proposed on the 99.9% confidence bound for the fitting approximation. As already stated, the chord trajectory Gaussian distribution derivation provides the highest error standard deviation. However, the lowest obtained variance between the radial and the circular trajectories is C/N_0-dependent. For both DLL configurations the behavior of the radial trajectory Gaussian distribution

derivation is comparable. For high C/N_0 the radial Gaussian distribution derivation is comparable to the chord characterization ($C/N_0 > 85\ dBHz$ for the 10 Hz-DLL bandwidth and $C/N_0 > 80\ dBHz$ for the 1 Hz-DLL bandwidth) then it becomes lower than the circular Gaussian distribution derivation for low C/N_0 ($C/N_0 < 60\ dBHz$ for the 10 Hz-DLL bandwidth and $C/N_0 < 65\ dBHz$ for the 1 Hz-DLL bandwidth).

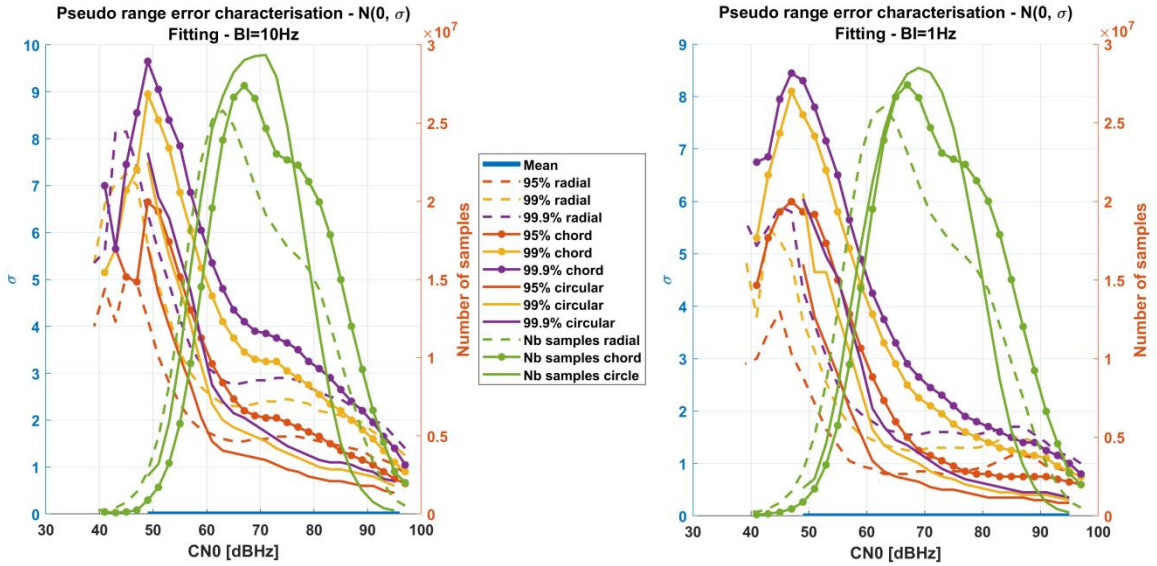

Figure 6.21 – Pseudo range characterization: trajectories impact – fitting

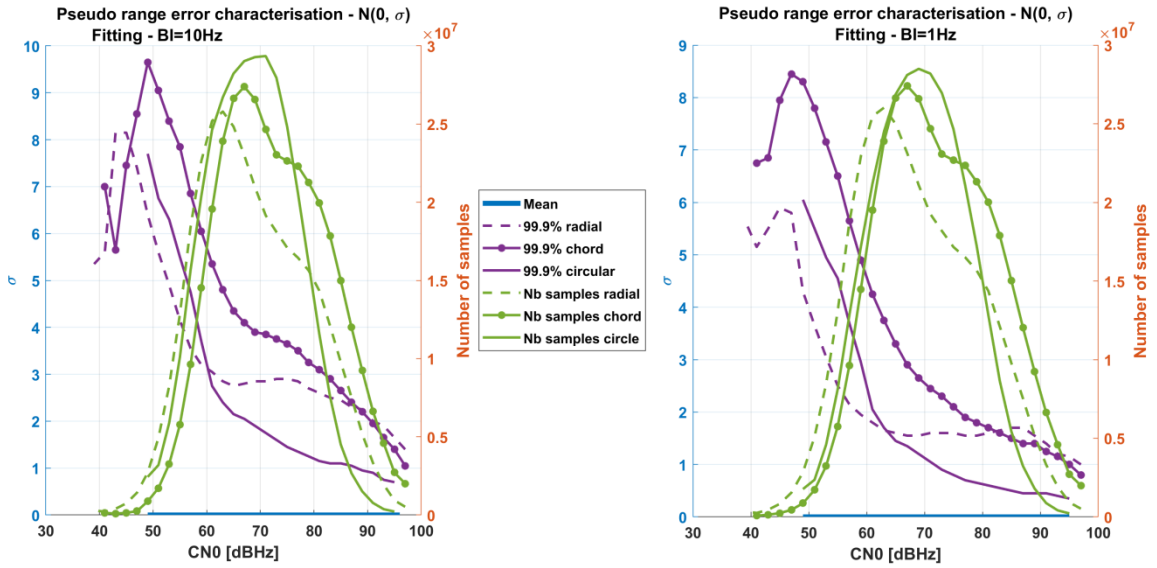

Figure 6.22 – Pseudo range characterization: trajectories impact – fitting – focus on the 99.9% confidence bound

The over bounding results are provided in Figure 6.23, a focus on the 99.9% approximation is proposed in Figure 6.24.

The description of the obtained Gaussian distribution derivation is less clear than for the fitting approximation, especially for the 1 Hz DLL bandwidth.

From Figure 6.23, for the 10 Hz DLL bandwidth, as for the fitting approximation, the chord Gaussian distribution derivation provides the higher σ-values. The lower σ-values are obtained for the circular trajectories for $C/N_0 > 65\ dBHz$. For $C/N_0 < 65\ dBHz$, the σ-values obtained for the 3 trajectory types tends to converge.

For the 1 Hz DLL bandwidth, the chord Gaussian distribution derivation provides the higher σ-values for $C/N_0 > 80\ dBHz$ and the circular trajectory provides the lowest σ-values. The situation is inverted for $C/N_0 < 73\ dBHz$.

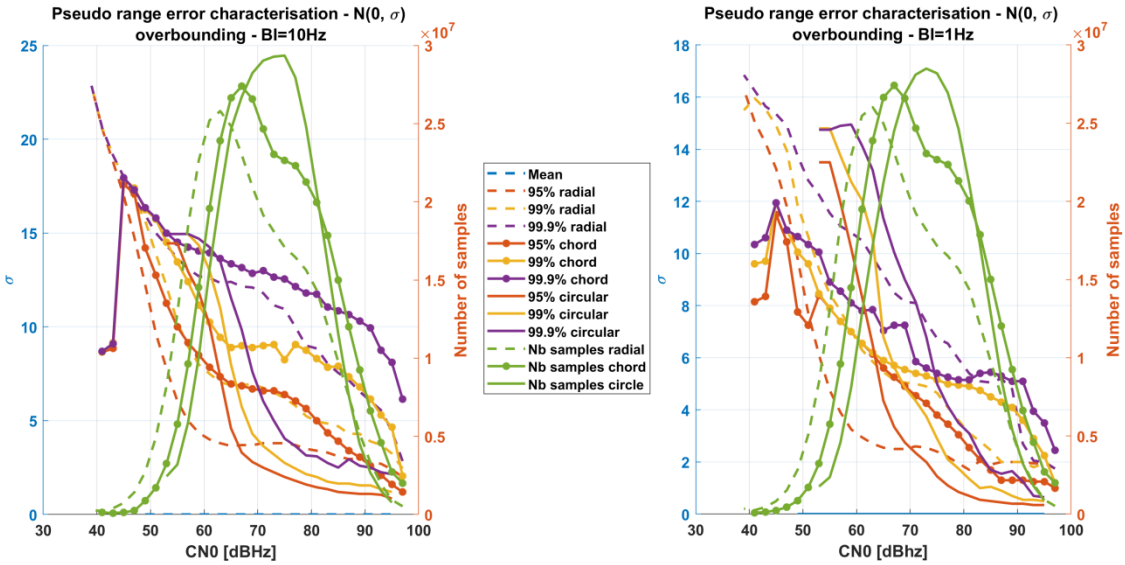

Figure 6.23 – Pseudo range characterization: trajectories impact – overbounding

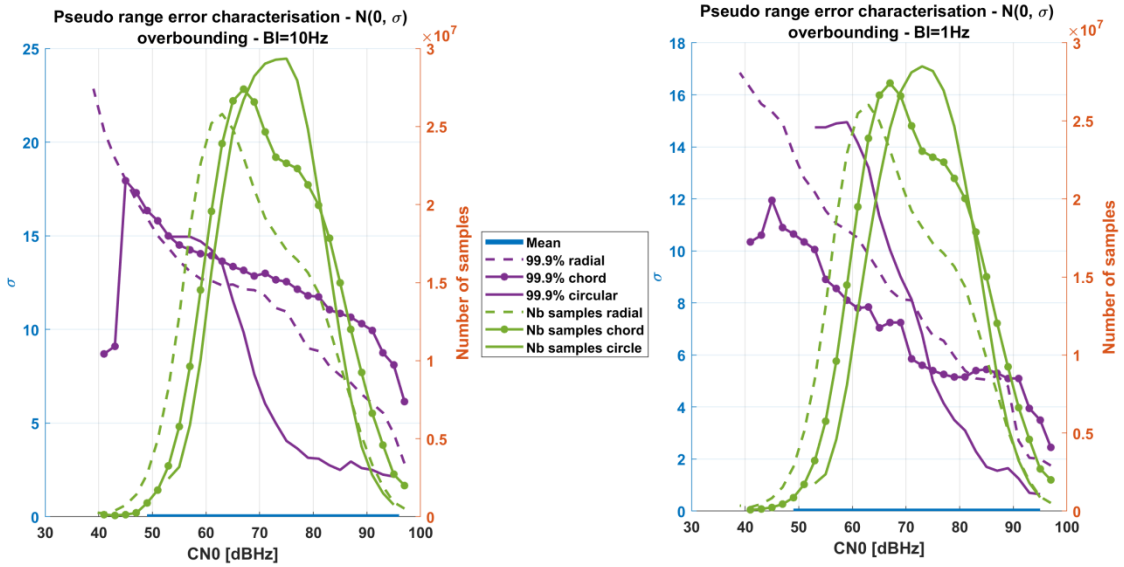

Figure 6.24 – Pseudo range characterization: trajectories impact – overbounding – focus on the 99.9% confidence bound

No definitive conclusions can be made from these pictures; nevertheless, the study highlights that the characterization is trajectory- and C/N_0-dependent.

6.3.2.5 *Results for the LOS scenario case 4*

The previous section has highlighted a link between the Gaussian distribution derivation results and the trajectory simulated; nevertheless, in the thesis a generic Gaussian distribution derivation, trajectory-independent has also been made. Therefore, the pseudo range errors obtained for the 3 trajectory types are gathered in order to provide one generic Gaussian distribution derivation for the LOS scenario at 2 GHz, case 4 in Table 6.3.

As it can be observed in Figure 6.25, Figure 6.26 and Figure 6.27, to gather the pseudo range errors generated for the three types of trajectory permit to average the σ-values all over the C/N_0. For the

fitting characterization, in Figure 6.25, the global characterization is lower than the chord characterization but higher than the circular characterization for high C/N_0 and higher than the radial characterization for low C/N_0.

The 95% distribution is provided in Figure 6.27 in order to ensure that the previous observations are not exclusively due to outlier pseudo range errors.

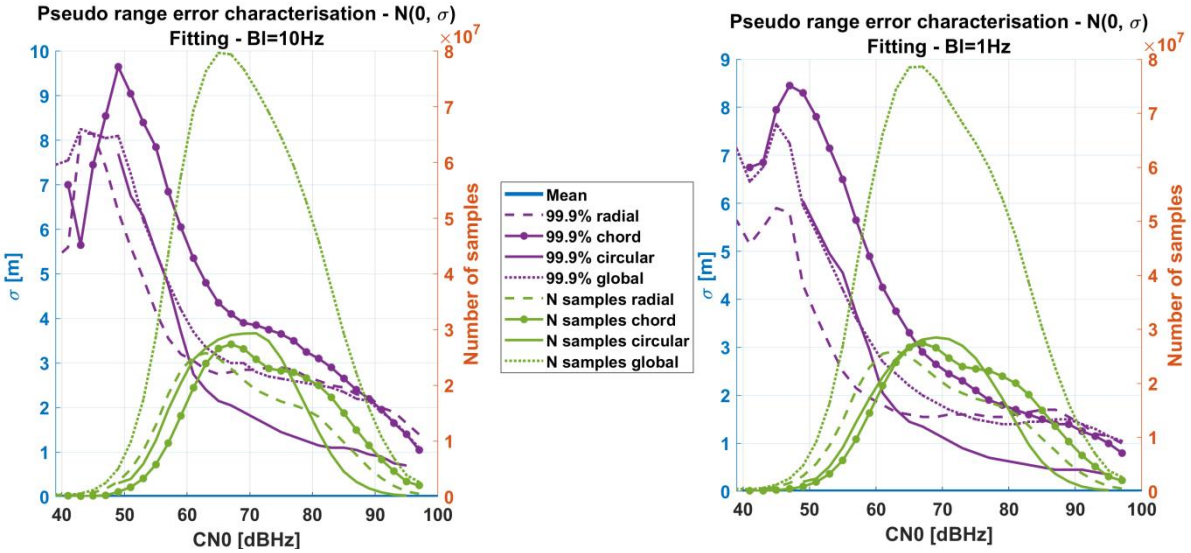

Figure 6.25 – pseudo range error characterization – Cases 1 to 4 – fitting – focus on 99.9% confidence level

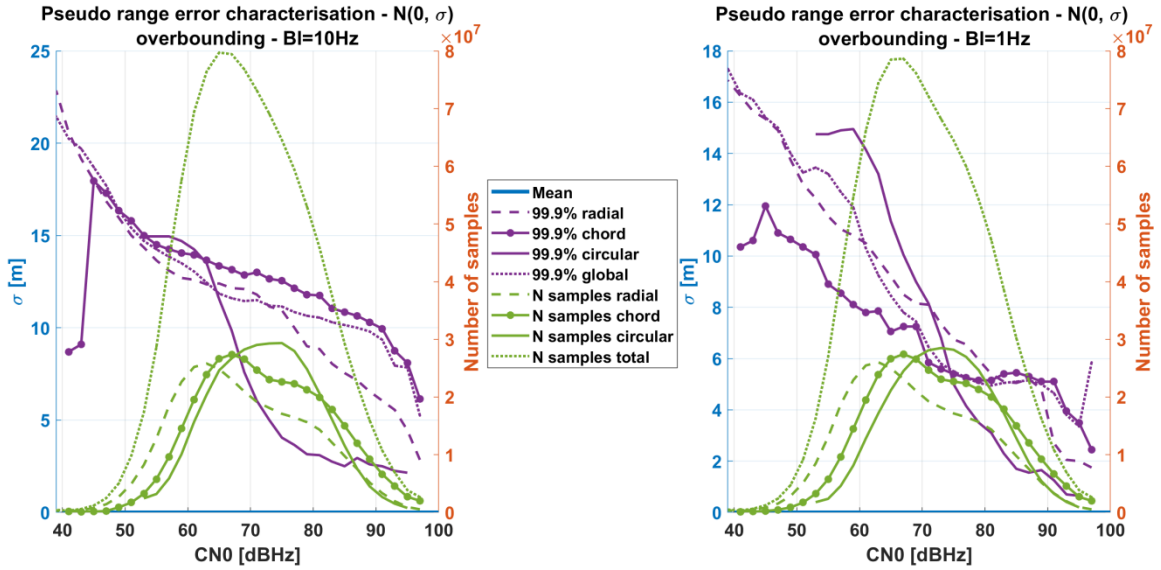

Figure 6.26 – pseudo range error characterization – Cases 1 to 4 – over bounding – focus on 99.9% confidence level

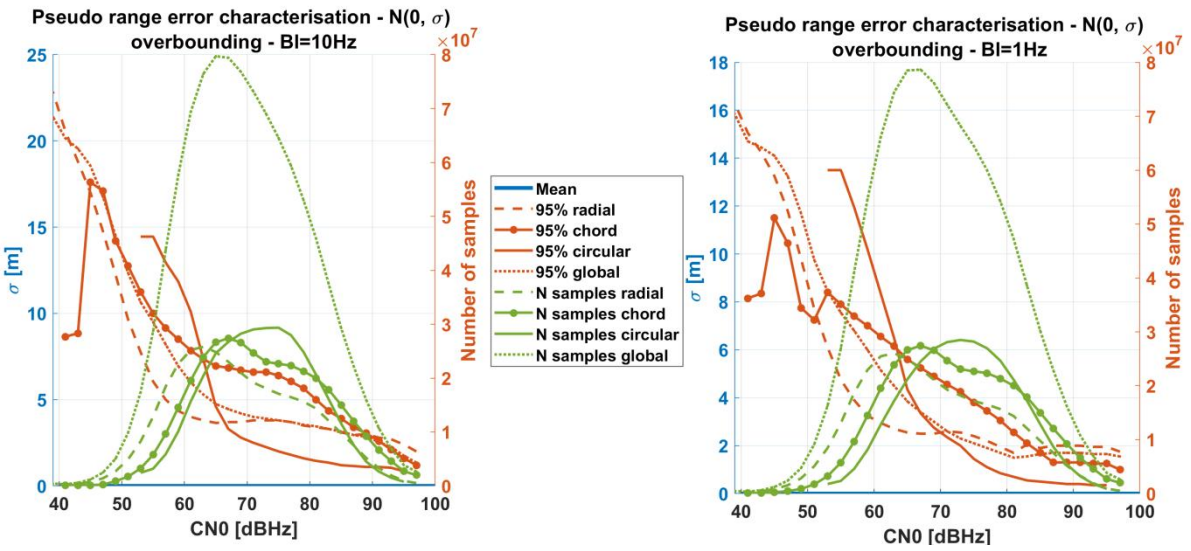

Figure 6.27 – pseudo range error characterization – Cases 1 to 4 – over bounding – focus on 95% confidence level

In Figure 6.28 and Table 6.4, a summary of the Gaussian distribution derivation candidates for the LOS case at 2 GHz (case 4) is provided. In Table 6.4, the σ-values obtained for the 99.9% confidence bound for the over bounding and fitting characterizations for both 10 Hz and 1 Hz DLL bandwidths are also provided. These σ-values will be tested in the navigation filters in Chapter 7.

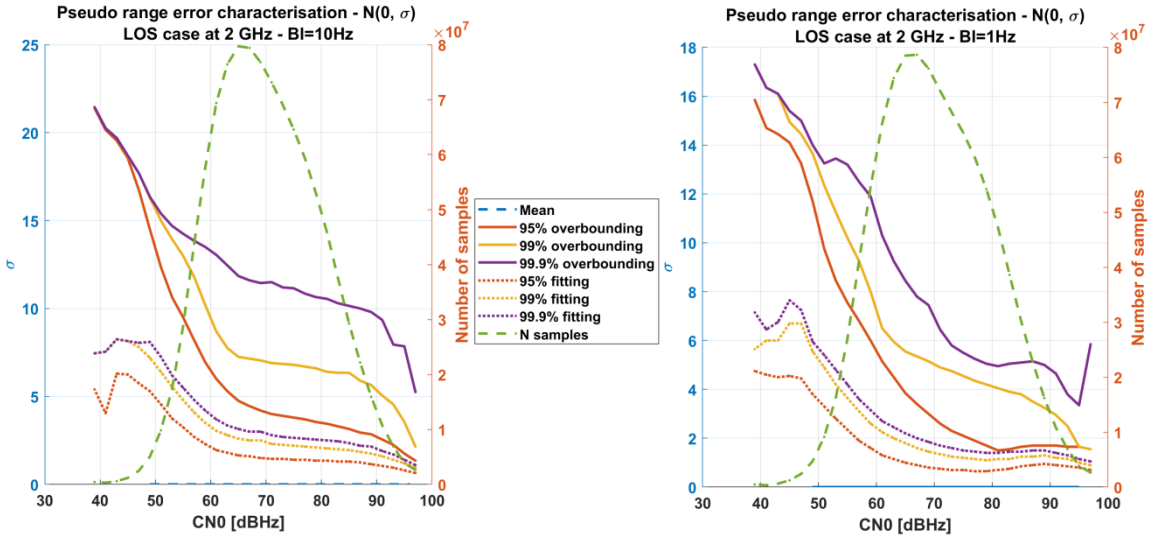

Figure 6.28 – pseudo range error characterization – Case 4

Table 6.4 – Characterization for the LOS scenario at 2 GHz – 99.9% confidence bound – $N(0, \sigma)$

C/N_0 $[dBHz]$	PR error σ [m]			
	Fitting (99.9%)		Over bounding (99.9%)	
	1 Hz	10 Hz	1 Hz	10 Hz
97	1.05	1.1	5.85	5.25
95	1.15	1.4	3.35	7.85
93	1.3	1.7	3.8	7.95
91	1.4	1.9	4.65	9.35
89	1.5	2.15	5.0	9.8
87	1.5	2.2	5.15	10.0
85	1.45	2.35	5.1	10.15
83	1.45	2.45	5.05	10.3

81	1.4	2.5	4.95	10.55
79	1.4	2.55	5.05	10.65
77	1.45	2.6	5.25	10.85
75	1.5	2.65	5.5	11.15
73	1.6	2.7	5.8	11.2
71	1.7	2.8	6.45	11.5
69	1.85	3.0	7.45	11.45
67	2.0	3.0	7.8	11.6
65	2.2	3.15	8.45	11.85
63	2.45	3.35	9.25	12.45
61	2.7	3.7	10.3	13.05
59	3.15	4.2	11.9	13.5
57	3.6	4.8	12.5	13.85
55	4.2	5.5	13.2	14.25
53	4.8	6.2	13.45	14.7
51	5.4	7.25	13.25	15.4
49	5.95	8.1	14.0	16.35
47	7.25	8.05	15.0	17.7
45	7.65	8.15	15.4	18.7
43	6.75	8.25	16.1	19.7
41	6.45	7.55	16.35	20.25
39	7.15	7.45	17.3	21.45

6.4. Derivation of the SCHUN pseudo range measurement errors distribution

In this section the derivation of the pseudo range measurement error Gaussian distribution for GNSS signals is provided. The errors on the pseudo ranges are due to the thermal noise and the SCHUN propagation channel. Therefore, first the generated scenario are presented; second the Gaussian distribution derivation results obtained when applying over bounding and fitting approximation methods are provided.

6.4.1 Method and scenario

The method used to obtain the GNSS pseudo range error characterization can be split in 3 steps.

1. The smart generation of the propagation channel with SCHUN, described in this section
2. The generation of the pseudo ranges: regarding the receiver characteristics, a first order Delay Lock Loop is adopted. An Early Minus Late Power discriminator is used with a 0.5 correlator spacing. The Phase Lock Loop used is a 3rd order Costas Loop. These pseudo ranges are generated thanks to the simulator described in Annex A. Note that the derivation of the Gaussian distributions is performed assuming that GPS pseudo ranges are generated. This means that the pseudo ranges considered are generated assuming a BPSK modulation. Remind that in chapter 2 it has been explained that Galileo E1 OS uses a BOC modulation; by using a BOC modulation, the Galileo signals should be more robust to multipath disturbance. Therefore, the derivation of Gaussian distribution for Galileo pseudo range measurement should provide lower σ-values. Consequently, the derivation proposed here slightly overestimate the actual σ-values for Galileo. Nevertheless, in order to save time, in chapter 7, the same Gaussian derivation is used for GPS and Galileo.
3. The Gaussian distribution derivation is presented in section 6.4.2.

In this section the generation of the SCHUN propagation channel is presented.

The SCHUN propagation channel is defined from three high-level choices:

a) The trajectory of the receiver
b) The satellites location in azimuth and elevation
c) The virtual city which is characterized by the building width, height, etc. All these parameters can be found in [22].

Moreover, note that the generation of propagation channel must be smartly conducted in order to allow the generation of a wide and representative variety of pseudo range errors with the simulator presented in Annex A. Therefore, it is of the utmost importance to verify that:

- All satellite locations in azimuth and elevation are represented during the SCHUN propagation channel generation. By doing so, it is certain that the pseudo range generation, and thus its later Gaussian distribution derivation will not be specific to one particular azimuth or elevation value.
- The virtual city and trajectory generated is identical for all generated satellite signal propagation channels in order to keep consistency and realism between the generated propagation channels.
- The SCHUN propagation channel is characterized by the satellite (transmitter) elevation and azimuth, consequently the relative azimuth between the receiver and the transmitter must be constant all over the simulation in order to guarantee that all elevation and azimuth angles are equally represented.

Therefore, from the previous considerations, the three high-level choices necessary to define the SCHUN propagation channel for the generation of a wide and significant pseudo range measurement errors set can be determined.

First, the trajectory generated is illustrated in Figure 6.29; by defining a linear trajectory, it ensures a constant relative azimuth all along the trajectory.

Second, the virtual city is always the same and is the one presented in Figure 6.29 with the parameters describe in Table 6.5.

Third, the generation of the satellites location, their azimuth and elevation, is conducted following random distribution over [0:360]° and [0:90]° respectively. In Figure 6.30, an example of the satellites generated between 2 consecutives Monte Carlo is provided. This process permits to generate all elevation and azimuth combinations over the Monte Carlo simulations.

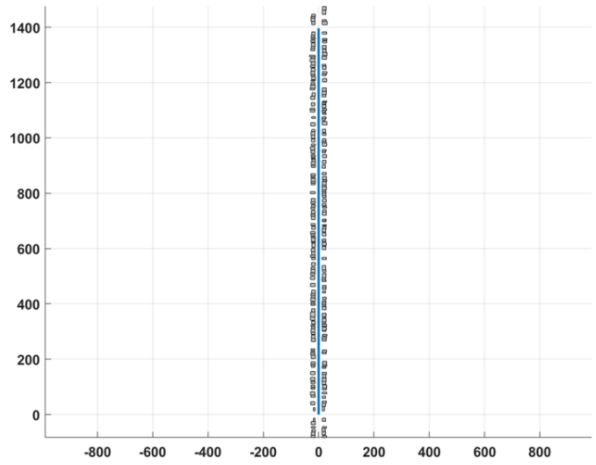

Figure 6.29 – trajectory considered – ENU coordinates

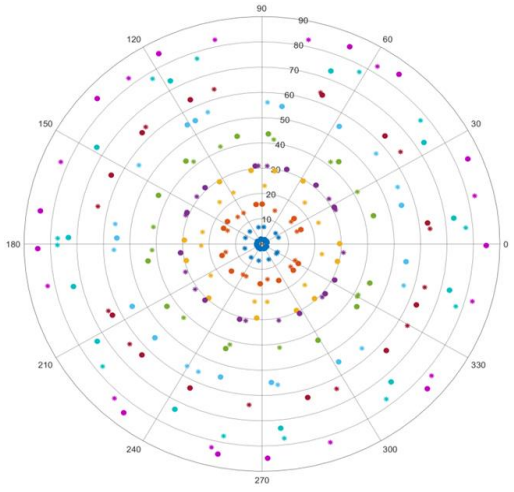

Figure 6.30 – Satellites generated from a monte carlo to the following one

Table 6.5 – SCHUN characterization: virtual city parameters

Parameters	Description	Format	Units	Value
Building density	The building occupation density in the virtual city	Float	0<index<1	0.75
Building height	The building height distribution assuming a Gaussian distribution	[Mean std]	[m]	[15 20]
Building width	The building width distribution assuming a Gaussian distribution	[Mean std]	[m]	[10 30]
Building depth	The building depth distribution assuming a Gaussian distribution	[Mean std]	[m]	[15 20]
Buiding space	Distance between buildings assuming a Gaussian distribution.	[Mean std]	[m]	[0 3]
Building back	The distance between the buildings and the street in meters	[Min Max]	[m]	[12 14]

6.4.2 Results

The Gaussian distribution derivation is made with respect to the estimated C/N_0. The C/N_0 is a parameter easily found in a classical GNSS receiver, thus it is easier to characterize the pseudo range measurement errors with respect to the C/N_0; note that it could have been possible to perform the Gaussian distribution derivation with respect to the azimuth and/or elevation. Results for the fitting approximation method are provided in the right part of Figure 6.31. Results for the over bounding approximation method are provided in the left part of Figure 6.31. As for the QuaDRiGa, there is not much difference between the 3 Gaussian distributions, $N(0,\sigma)$, $N(mean,\sigma)$ and $N(max,\sigma)$. A slight increase of the variances can be observed as the C/N_0 decreases.

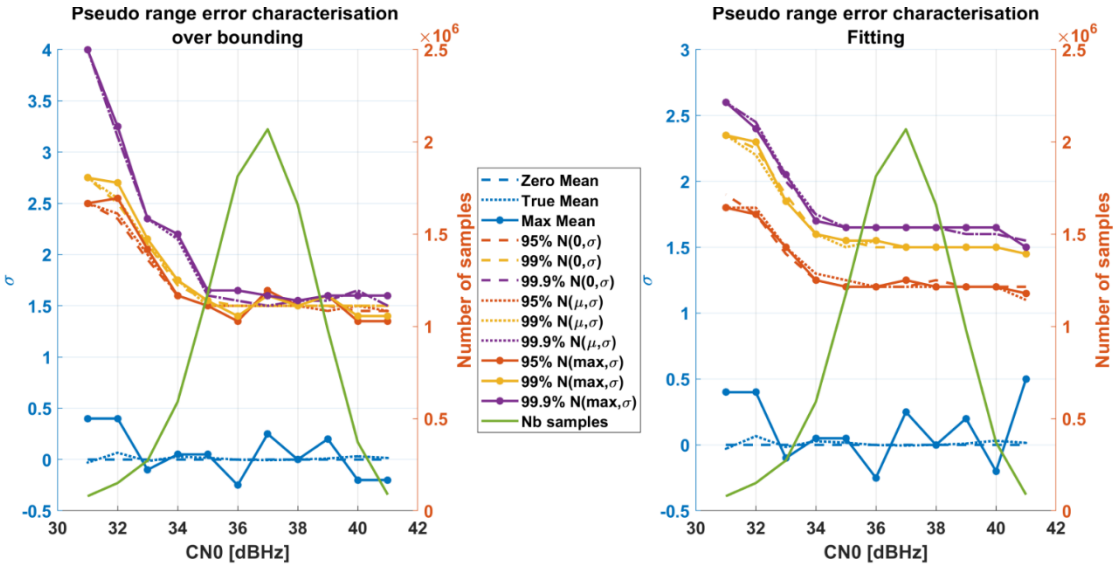

Figure 6.31 – GNSS characterization

In order to compare the behavior of the over bounding results and the fitting results, Figure 6.34 is provided. For C/N_0 lower than 35 dBHz, the over bounding variances are always larger than the fitting variances. The difference increases as the C/N_0 decreases. In Figure 6.32 and Figure 6.33, the PDFs obtained for $C/N_0 = 38\,dBHz$ and $C/N_0 = 32\,dBHz$ respectively are provided. In addition the fitting and over-bounding Gaussian distribution determined for these 2 cases for the 99.9% confidence bound are provided. It can be observe that the pseudo range measurement errors distribution for $C/N_0 = 38\,dBHz$ is closer to a Gaussian distribution than for $C/N_0 = 32\,dBHz$. This observation explains why

for high C/N_0, the fitting and over bounding approximation are equivalent; and why for low C/N_0, a slight difference can be observed between the two methods.

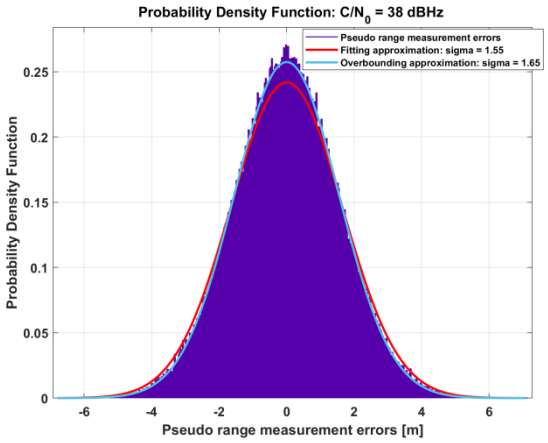

Figure 6.32 – PDF for a $C/N_0 = 38\ dBHz$

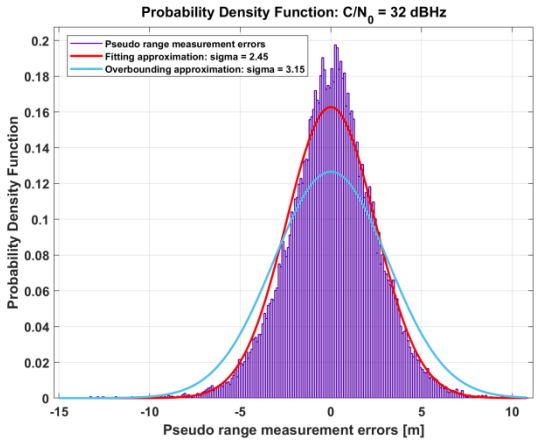

Figure 6.33 – PDF for a $C/N_0 = 32\ dBHz$

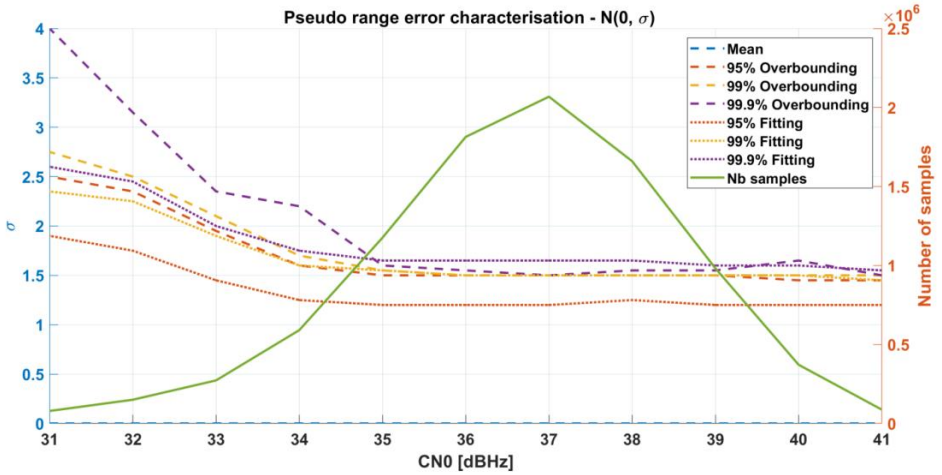

Figure 6.34 – GNSS characterization

In Table 6.6, the σ-values obtained for the $N(0,\sigma)$ are provided. They are used in the simulations of the next chapter. More specifically, in the simulation the σ-values used corresponds to the 99.9%-columns.

Table 6.6 – Characterization values obtained for a $N(0,\sigma)$

	PR error σ[m]					
	Overbounding			Fitting		
C/N_0 [dBHz]	95%	99%	99.9%	95%	99%	99.9%
41	1.45	1.5	1.5	1.2	1.45	1.55
40	1.45	1.5	1.65	1.2	1.5	1.6
39	1.5	1.5	1.55	1.2	1.5	1.6
38	1.5	1.5	1.55	1.25	1.5	1.65
37	1.5	1.5	1.5	1.2	1.5	1.65
36	1.5	1.5	1.55	1.2	1.5	1.65
35	1.5	1.55	1.6	1.2	1.55	1.65
34	1.6	1.7	2.2	1.25	1.6	1.75
33	1.95	2.1	2.35	1.45	1.9	2.0
32	2.35	2.5	3.15	1.75	2.25	2.45
31	2.5	2.75	4.0	1.9	2.35	2.6

6.5. Conclusion

In this chapter, the derivation of Gaussian distribution for the pseudo range measurement errors in presence of noise and multipath has been performed for both 5G and GNSS signals.

In order to design the 5G-GNSS hybrid navigation modules, a preliminary step consists in defining the pseudo range measurements of each system in the same reference time frame; if this first action is not conducted, the true ranges associated to each system pseud-range measurements are not consistent among them. The GPS time has been chosen to be the reference time frame for this analysis. The first section accurately defines the time shifts to be considered between each of the 3 system time frames and the GPS reference time frame.

Note that the pseudo range measurement errors are affected only by multipath and receiver thermal noise (no ionospheric effect, no tropospheric effect, etc.); both effects are assumed to be gathered as one enhanced noise which have been derived in this chapter. The method for the derivation of Gaussian distribution for the pseudo range measurement errors proposed in this chapter is divided in two steps:

1. The characterization of the pseudo range measurement error, or in other word, to obtain the true PDF distribution of the errors, which is based on the analysis of tracking loops results using the correlator output models described in Chapter 4 section 4.2.3 and using the propagation channel simulators SCHUN for GNSS and QuaDRiGa for 5G.
2. The approximation of the true distribution by a Gaussian distribution. In order to define the approximating distribution by Gaussian distribution, only two parameters have to be defined: the mean and the variance. Regarding the mean, three means have been considered: $\mu = 0$, $\mu = mean$ and $\mu = index$, where $index$ corresponds to the maximum of the characterized PDF. Three confidence bounds have been considered 99.9%, 99% and 95%. Finally, two approximation methods have been derived, namely a Gaussian over bounding and a Gaussian fitting method, parametrized by the amount of the actual simulated pseudo range error taken into account (95%, 99% and 99.9%) for the characterization.

In order to have statistically significant results, a high number of random drawings of the propagation channels and receiver noise were tested, using a Monte-Carlo approach.

The study has shown that for QuaDRiGa and for SCHUN, the assumption on the mean of the Gaussian distribution has a negligible influence for LOS scenario. It is proposed to assume a centered Gaussian distribution ($\mu = 0$). Moreover, the standard deviation of the Gaussian distribution depends on the C/N_0, which was expected.

The derivation of the Gaussian distributions for a QuaDRiGa channel has been made assuming a LOS sub-6 Ghz high level scenario, the derivation has been proposed for three independent trajectories and for all three trajectories gathered. A 2nd order DLL has been used for 2 DLL loop bandwidth (10 Hz and 1 Hz). This derivation has shown:

- The standard deviation of the Gaussian distribution depends on the type of trajectory. 3 types of trajectory were tested (radial, chord, circular), and led to sensibly different results, which was not expected. The final characterization does not keep this dependency and mixes the results from the 3 trajectory types. This dependency on the trajectory can be a potential future work.

- The receiver tracking parameter (mainly DLL bandwidth) has a slight impact. As expected, the lower the DLL bandwidth, the better accuracy.
- The fitting and the over bounding methodologies yield very different results, as expected. The recommendation between both methodologies will be given in Chapter 7.
- The distributions are not Gaussian, especially for 5G at low C/N_0, where the distribution tail for positive errors is larger (positively skewed).

The derivation of the Gaussian distributions for a SCHUN channel has been made assuming a LOS conditions. It has been made independently from the elevation and azimuth of the satellite. A first order Delay Lock Loop has been used assuming an Early Minus Late Power discriminator with a 0.5 correlator spacing. The Phase Lock Loop used is a 3rd order Costas Loop. The derivation has shown that:

- A slight increase of the variances can be observed as the C/N_0 decreases
- The distributions for $C/N_0 > 35\ dBHz$ are Gaussian
- Note that the derivation of the Gaussian distributions assumed that GPS pseudo ranges measurement. This means that the pseudo ranges considered have been generated assuming a BPSK modulation. Remind that in chapter 2 it has been explained that Galileo E1 OS uses a BOC modulation; by using a BOC modulation, the Galileo signals should be more robust to multipath disturbance. Therefore, the derivation of Gaussian distribution for Galileo pseudo range measurement should provide lower σ-values. Consequently, the derivation proposed here slightly overestimate the actual σ-values for Galileo. Nevertheless, in order to save time, in chapter 7, the same Gaussian derivation is used for GPS and Galileo.

The final output of this chapter is the model given in Table 6.4 and Table 6.6, respectively for 5G-LOS 2 GHz, and GNSS scenarios. These look-up tables will be used to model the pseudo range measurement standard deviation in the navigation filters studied in Chapter 7, more accurately, Table 6.4 is used for the cases assuming a 99.9% confidence bound.

Chapter 7. Positioning in urban environment using 5G and GNSS measurements

Over the past few years, the need for positioning, and thus the number of positioning services in general, has been in constant growth. This need for positioning has been increasingly focused on constrained environments, such as urban or indoor environments, where GNSS is known to have significant limitations: multipath as well as the lack of LOS satellite visibility degrades the GNSS positioning solution and makes it unsuitable for some urban or indoor applications. In order to improve the GNSS positioning performance in constrained environments, the envisioned solution in this work consists in using Signal of Opportunity and more specifically 5G signals and to hybridize them with GNSS signals. The objective is to determine the optimal solution combining both 5G and GNSS signals. The hybridization is expected to overcome the issues related to each signal: the degraded performances obtained on 3D for 5G and the lack of visibility and degraded performances in urban environment for GNSS. These problematics have been presented in Chapter 2 and 3.

In order to determine the most optimal signal processing techniques, it is of the utmost importance to precisely know the mathematical model of the transmitted signal for both GNSS and 5G systems. The generated signals go through the propagation channels which should also be carefully modelled in order to have a realistic mathematical model of the received signal. These propagation channels: SCHUN for GNSS and QuaDRIGa for 5G systems have been precisely described and modeled in chapter 2 and 4. GNSS are mature and mathematical models can easily be found in the literature, [56]. The correlator output mathematical models in multipath environment for 5G systems have been precisely derived in Chapter 4. These correlator outputs are then processed by the synchronization module; the 5G synchronization module has been described in Chapter 5, the GNSS synchronization module has been described in Chapter 2. The receiver permits the generation of pseudo range measurements; due to propagation channels and thermal noise, these pseudo ranges are affected by errors which have been precisely approximated by Gaussian variables in Chapter 6.

In this chapter, the objective is to develop hybrid 5G-GNSS navigation modules exploiting every studies led in the previous chapters (the mathematical model derivation, the pseudo range errors characterization, etc.). Two navigation modules are studied: an Extended Kalman Filter (EKF) and an Unscented Kalman Filters (UKF).

First the navigation modules are presented, second the simulation parameters are presented and third the results are presented.

7.1. Navigation module

Kalman Filtering (KF) is an estimation technique adapted to the estimation of the states of a dynamic system. It uses the history of the measurements instead of just a snapshot observation. In addition, KF uses a model of the evolution of the estimated states, called state transition model, in order to improve the overall estimation technique performance.

First a general overview of the Kalman Filtering process is provided, then 2 special cases are detailed: the Extended Kalman Filter in section 2 and the Unscented Kalman Filter in section 3. The filters theory is reminded in order to clearly state the differences between the two filters. The fourth section presents

these differences. Finally, the last section proposes an application of the filters to the hybrid GNSS/5G case.

7.1.1. General presentation

The Kalman Filter (KF) is a Bayesian estimation technique where all probability density functions are supposed Gaussian. It can be viewed as a sequential Minimum Mean Square Error (MMSE) estimator of a signal embedded in noise, where the signal is characterized by a dynamical or state model. It generalizes the sequential MMSE estimator, to allow the unknown parameters to evolve in time according to a dynamical model. If the signal and noise are jointly Gaussian, then the Kalman filter is an optimal MMSE estimator.

In other words, the Kalman Filter is a recursive estimator of the internal state of a dynamic system. This estimation technique is provided thanks to the knowledge of a measurement model and a state transition model. At each instant, the algorithm uses the best estimation obtained from the previous state (and propagated by the state transition model) and the latest measurement vector to provide the best estimation.

Consider the dynamic process X_{k+1} with the observations generated from the observation process Y_k defined as:

$$\begin{cases} X_{k+1} = f(X_k) + U_k + W_k \\ Y_{k+1} = h(X_{k+1}) + V_{k+1} \end{cases} \quad (7.1)$$

Where:

- f is the dynamic model function
- h is the observation function
- X_k is the state vector
- W_k is the state noise vector
- Y_{k+1} is the measurement vector
- V_{k+1} is the measurement noise vector
- The command vector U_k

The state noise vector represents the liberty of the system evolution with respect to the evolution model proposed by the state transition matrix. In other words, it represents the level of confidence put in the state transition model.

The following hypotheses are made:

- The measurement noise vector, V_k, and the state noise vector, W_k, are White Gaussian Centred Noise independent from each other
- Their covariance matrix is supposed known: $R_k = cov[V_k]$ and $Q_k = cov[W_k]$
- The initial state X_0 is a random Gaussian vector independent from V_k and W_k. Due to the recursive equation, the system state at any instant X_k is random and Gaussian as well as Y_k.

A general block diagram is provided in Figure 7.1, it summarizes the process of a general Kalman estimator and is fully detailed in [61]. As shown, the estimation process of a Kalman Filter can be divided into 3 steps: a prediction step, an observation step and an update step.

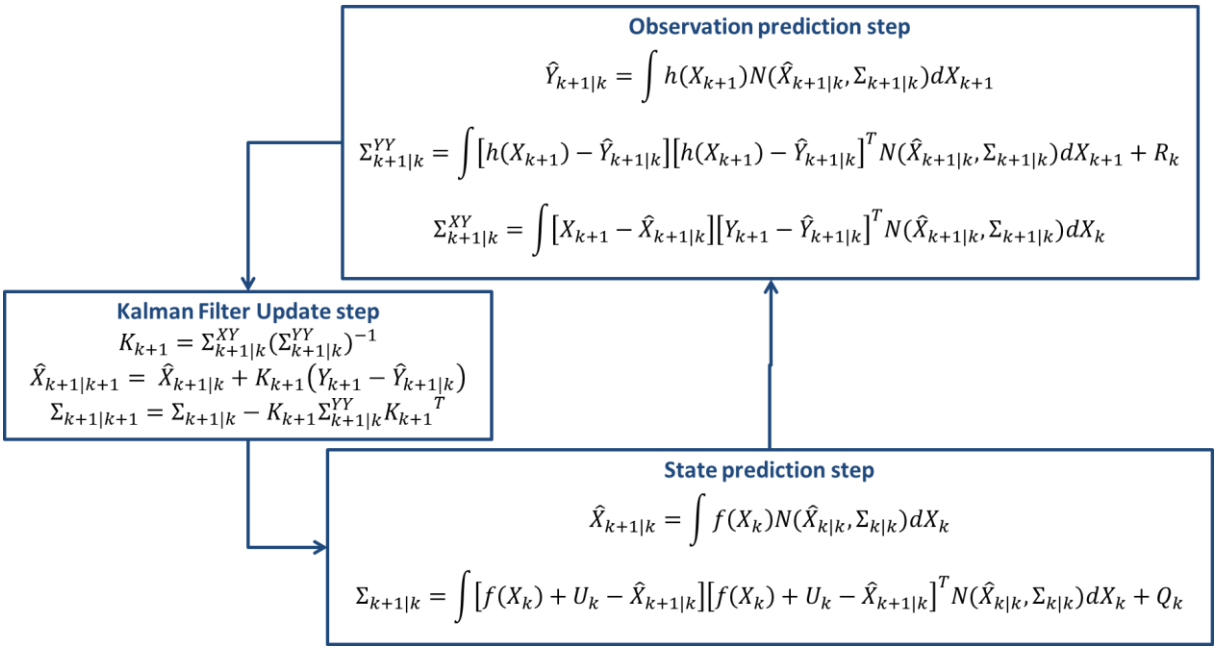

Figure 7.1 – Block diagram for a Bayesian estimator with Gaussian probability densities – extracted from [61]

The KF provides at each instant the MMSE estimator, which minimizes the mean square at every epoch. Therefore, the index k is used to define the epoch. In Figure 7.1, the prediction values at epoch $k+1$ are indexed by $k+1|k$; the estimates are indexed by $k+1|k+1$. Moreover, the function $N(\hat{X}_x, \Sigma_x)$ refers to a Gaussian distribution centred in $\hat{X}_x$ with a variance Σ_x, the subscript x depends on whether it is the state prediction ($N(\hat{X}_{k|k}, \Sigma_{k|k})$) or the observation prediction ($N(\hat{X}_{k+1|k}, \Sigma_{k+1|k})$).

This generic theory is now detailed for the 2 navigation filters considered in the Ph.D.: the Extended Kalman filter and the Unscented Kalman filter.

7.1.2. Extended Kalman Filter

First the motivations are reminded, second the equations of the EKF are reminded.

7.1.2.1. Motivation

The KF methods assume that all probability density functions are Gaussian variables; at each epoch the mean and variance must be determined. The idea of the EKF is to expand the nonlinear functions into Taylor polynomials around a single point; it is an analytical method to compute the integrals presented in Figure 7.1.

7.1.2.2. Linearization

In (7.1), the functions f and h are not linear and thus require a linearization which is limited to a first order in the thesis. Considering $\hat{X}_{k|k-1}$ and $\hat{X}_{k|k}$ recent and reasonably accurate approximations of X_k, it is possible to develop the functions f and h in Taylor series at the neighbourhood of $\hat{X}_{k|k-1}$ and $\hat{X}_{k|k}$.

$$\begin{cases} f(X_k) = f(\hat{X}_{k|k}) + \dfrac{\partial f}{\partial X_{k}}_{|X_k=\hat{X}_{k|k}} (X_k - \hat{X}_{k|k}) \\ h(X_k) = h(\hat{X}_{k|k-1}) + \dfrac{\partial h}{\partial X_{k}}_{|X_k=\hat{X}_{k|k-1}} (X_k - \hat{X}_{k|k-1}) \end{cases} \tag{7.2}$$

Classically, the following notation is used

$$\begin{cases} F_k = \dfrac{\partial f}{\partial X_{k}}_{|X_k=\hat{X}_{k|k}} \\ H_k = \dfrac{\partial h}{\partial X_{k}}_{|X_k=\hat{X}_{k|k-1}} \end{cases} \tag{7.3}$$

F_k and H_k are the Jacobian matrix of f and h, defined such that for a vector function of a vector variable (7.4), the Jacobian matrix is defined as

$$f: X = \begin{bmatrix} x_1 \\ \vdots \\ x_n \end{bmatrix} \rightarrow \begin{bmatrix} y_1 \\ \vdots \\ y_p \end{bmatrix} \tag{7.4}$$

$$\frac{\partial f}{\partial X} = \begin{bmatrix} \dfrac{\partial y_1}{\partial x_1} & \cdots & \dfrac{\partial y_1}{\partial x_n} \\ \vdots & \ddots & \vdots \\ \dfrac{\partial y_p}{\partial x_1} & \cdots & \dfrac{\partial y_p}{\partial x_n} \end{bmatrix} \tag{7.5}$$

Adopting this notation, the dynamic process X_{k+1} and the observations generated from the observation process Y_k can be redefined as (7.6). By adopting the notation proposed in (7.7), the linearized model is thus proposed in (7.8).

$$\begin{cases} X_{k+1} = f(\hat{X}_{k|k}) + F_k(X_k - \hat{X}_{k|k}) + U_k + W_k \\ Y_k = h(\hat{X}_{k|k-1}) + H_k\,(X_k - \hat{X}_{k|k-1}) + V_k \end{cases} \tag{7.6}$$

$$\begin{cases} \widetilde{U_k} = f(\hat{X}_{k|k}) - F_k \hat{X}_{k|k} \\ \widetilde{Y_k} = h(\hat{X}_{k|k-1}) - H_k \hat{X}_{k|k-1} \end{cases} \tag{7.7}$$

$$\begin{cases} X_{k+1} = F_k X_k + \widetilde{U_k} + U_k + W_k \\ Y_k - \widetilde{Y_k} = H_k\, X_k + V_k \end{cases} \tag{7.8}$$

7.1.2.3. Equations

With the linearized model, it is possible to adapt the equations used for the standard KF and derived in [61].

State prediction

$$\hat{X}_{k+1|k} = F_k \hat{X}_{k|k} \tag{7.9}$$

A priori covariance

$$\Sigma_{k+1|k} = F_k \Sigma_{k|k} {F_k}^T + Q_k \tag{7.10}$$

State update

$$\hat{X}_{k+1|k+1} = \hat{X}_{k+1|k} + K_{k+1}\left(Y_{k+1} - h\left(\hat{X}_{k+1|k}\right)\right) \tag{7.11}$$

Kalman Gain

$$K_{k+1} = \Sigma_{k+1|k} H_{k+1}^T \left(H_{k+1}\Sigma_{k+1|k}H_{k+1}^T + R_{k+1}\right)^{-1} \tag{7.12}$$

A posteriori covariance

$$\Sigma_{k+1|k+1} = \Sigma_{k+1|k} - K_{k+1}H_{k+1}\Sigma_{k+1|k} \tag{7.13}$$

The Kalman gain K_{k+1} defined in (7.12) is an important feature of the Kalman Filtering process. This gain permits to balance the information coming from the state prediction and the observations. If the state prediction is deemed good; the K_{k+1} will be small (the model is trusted). If the state prediction is deemed bad, the K_{k+1} will be large (more confidence is given to the measures).

From these equations, the EKF proceeds in 2 stages: a state prediction step and a measurement update step. At epoch $k+1$, there is an intermediate state estimate just after the prediction step, named the a priori state, which will be indexed by $k+1|k$. After a measurement update, the new estimate is called a posteriori state and will be indexed by $k+1|k+1$. Those steps are summarized in Figure 7.2.

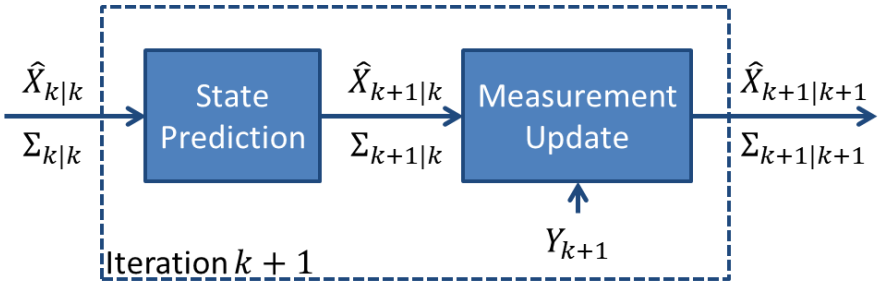

Figure 7.2 – Kalman Filter steps

7.1.3. Unscented Kalman Filter

First, the principle of the UKF is presented. Second, the summary of the UKF equations is given and finally, both the UKF and the EKF are theoretically compared. Remind that the system model considered is provided in (7.1).

7.1.3.1. UKF motivation

In the EKF all non-linear functions are expended in a Taylor polynomial about a single point, this is an analytical method for the evaluation of the integrals over the Gaussian weighted non-linear functions presented in Figure 7.1. The EKF gives reasonable estimation results if the nonlinearities are not very severe. If f and h are highly nonlinear, it is possible to extend the EKF by using the second order terms of the Taylor polynomial. However, this requires the computation of the Hessian of the functions which adds complexity to the method. In the EKF, the state distribution is propagated analytically through the first order linearization of the non-linear system, which could cause a corruption of the posterior mean and covariance.

The UKF is based on a statistical linearization technique; not an analytical one as for the EKF. This technique consists in the linearization of a nonlinear function of a random variable through a linear regression between n points drawn from the prior distribution of the random variable. In other words,

the UKF is based on a deterministic sampling approach; the state distribution is represented using a minimal set of carefully chosen sample points called sigma points.

The UKF is founded on the intuition that it is easier to approximate a probability distribution than it is to approximate an arbitrary nonlinear function or transformation. Each sigma point is then propagated through the nonlinearity yielding in the end in a cloud of transformed points. The new estimated mean and covariance are then computed based on their statistics. This process is called unscented transformation.

7.1.3.2. Linearization

7.1.3.2.1. Selection of the sigma points

The sigma points are chosen so that their mean and covariance to be exactly $\hat{X}_{k|k}$ and $\Sigma_{k|k}$. The set of sigma points is defined as (7.14) where n is the dimension of the state vector and w_i is the weight associated to point X_k^i.

$$X_k = \{(w_i, X_k^i), i = 0, \dots, 2n\} \tag{7.14}$$

There are several ways to select sigma point, in the following the unscented transformation is provided; the other main selection scheme is called the scaled unscented transformation, [61]. With the unscented transformation, the sigma points are defined such that:

$$\begin{cases} X_k^0 = \hat{X}_{k|k} \quad -1 < w_0 < 1 \\ X_k^i = \hat{X}_{k|k} + \left(\sqrt{\frac{n}{1-w_0}\Sigma_{k|k}}\right)_i \quad w_i = \frac{1-w_0}{2n} \quad \forall i = 1, \dots, n \\ X_k^i = \hat{X}_{k|k} - \left(\sqrt{\frac{n}{1-w_0}\Sigma_{k|k}}\right)_i \quad w_i = \frac{1-w_0}{2n} \quad \forall i = n+1, \dots, 2n \end{cases} \tag{7.15}$$

Where $\left(\sqrt{\frac{n}{1-w_0}\Sigma_{k|k}}\right)_i$ is the i^{th} row or column of the matrix $\sqrt{\frac{n}{1-w_0}\Sigma_{k|k}}$. The weights are such that: $\sum_{i=0}^{2n} w_i = 1$; the value of the initial weight, w_0, is left to the user, it must only fulfil the criteria: $-1 < w_0 < 1$.

7.1.3.2.2. Prediction step

The general expression of the state vector prediction equation is provided in (7.16). The UKF approximates this integral by a finite sum as presented in (7.17).

$$\hat{X}_{k+1|k} = \int f(X_k) N(\hat{X}_{k|k}, \Sigma_{k|k}) dX_k \tag{7.16}$$

$$\hat{X}_{k+1|k} \cong \sum_{j=0}^{2n} w_j f(X_k^j) \tag{7.17}$$

The general expression of the state vector covariance prediction equation is reminded in (7.18), the UKF uses the approximation provided in (7.19).

$$\Sigma_{k+1|k} = \int [f(X_k) - \hat{X}_{k+1|k}][f(X_k) - \hat{X}_{k+1|k}]^T N(\hat{X}_{k|k}, \Sigma_{k|k}) dX_k + Q_k \tag{7.18}$$

$$\Sigma_{k+1|k} \cong \sum_{j=0}^{2n} w_j [f(X_k^j) - \hat{X}_{k+1|k}][f(X_k^j) - \hat{X}_{k+1|k}]^T + Q_k \tag{7.19}$$

In a similar manner, the observation prediction equations given by Figure 7.1 are approximate by the UKF with equations (7.20), (7.21) and (7.22).

$$\hat{Y}_{k+1|k} \cong \sum_{j=0}^{2n} w_j h(X_k^j, V_k) \tag{7.20}$$

$$\Sigma_{k+1|k}^{YY} = \sum_{j=0}^{2n} w_j [h(X_k^j) - \hat{Y}_{k+1|k}][h(X_k^j) - \hat{Y}_{k+1|k}]^T + R_k \tag{7.21}$$

$$\Sigma_{k+1|k}^{XY} \cong \sum_{j=0}^{2n} w_j [f(X_k^j, W_k) - \hat{X}_{k+1|k}][h(X_k^j, V_k) - \hat{Y}_{k+1|k}]^T \tag{7.22}$$

7.1.3.2.3. Update step

The estimate of the state vector at time t_{k+1}, updated with the last observations Y_{k+1} is given by (7.23) and the estimate of the a posteriori covariance matrix is given by (7.24). The a posteriori covariance matrix determination requires the Kalman gain K_{k+1} which is defined as in (7.25).

$$\hat{X}_{k+1|k+1} = \hat{X}_{k+1|k} + K_{k+1}(Y_{k+1} - \hat{Y}_{k+1|k}) \tag{7.23}$$

$$\Sigma_{k+1|k+1} = \Sigma_{k+1|k} - K_{k+1}\Sigma_{k+1|k}^{YY}{K_{k+1}}^T \tag{7.24}$$

$$K_{k+1} = \Sigma_{k+1|k}^{XY}(\Sigma_{k+1|k}^{YY})^{-1} \tag{7.25}$$

7.1.3.3. Equation

A summary of the equations summarizing the UKF processing is provided below.

State prediction

$$\hat{X}_{k+1|k} \cong \sum_{j=0}^{2n} w_j f(X_k^j) \tag{7.26}$$

A priori covariance

$$\Sigma_{k+1|k} \cong \sum_{j=0}^{2n} w_j [f(X_k^j) - \hat{X}_{k+1|k}][f(X_k^j) - \hat{X}_{k+1|k}]^T + Q_k \tag{7.27}$$

State update

$$\hat{X}_{k+1|k+1} = \hat{X}_{k+1|k} + K_{k+1}(Y_{k+1} - \hat{Y}_{k+1|k}) \tag{7.28}$$

Kalman Gain

$$K_{k+1} = \Sigma_{k+1|k}^{XY}\left(\Sigma_{k+1|k}^{YY}\right)^{-1} \tag{7.29}$$

A posteriori covariance

$$\Sigma_{k+1|k+1} = \Sigma_{k+1|k} - K_{k+1}\Sigma_{k+1|k}^{YY}{K_{k+1}}^{T} \tag{7.30}$$

As for the EKF, the UKF is composed of a prediction step and a measurement update step. Before performing these steps another one is necessary: the sigma point determination step; see Figure 7.3. This part is based on [61], [62], [63], [64], [65].

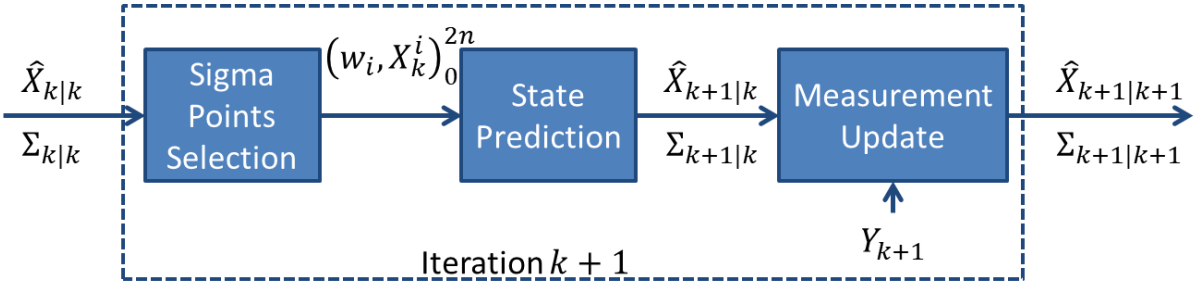

Figure 7.3 – UKF principle

7.1.4. A simple illustration of EKF and UKF fundamental difference

In Figure 7.4, a simple illustration, extracted from [64], of the difference between EKF and UKF processing is given. The experience conducted is the following one: a two dimensional Gaussian random variable is propagated through an arbitrary nonlinear transformation $f(x)$ and the optimally calculated mean and covariance of the transformed random variables are compared with those obtain with the EKF and the UKF. More specifically, a cloud of 5000 samples drawn from a Gaussian prior is propagated through $f(x)$ and the true posterior sample mean and covariance are calculated (this is shown in the left part of the figure).

On the left of the figure, the actual data are represented. The upper part represents the set of Gaussian variables. Those samples are propagated through $f(x)$ and the optimal statistics (mean and covariance) are determined. They are calculated with a Monte Carlo approach using 100000 samples drawn from the prior distribution and then propagated through the full nonlinear mapping.

$$\bar{y} = E[f(x)] = \frac{1}{N}\sum_{n=0}^{N} y_n \tag{7.31}$$

$$P_y = E[(y-\bar{y})(y-\bar{y})^T] = \frac{1}{N}\sum_{n=0}^{N}(y_n-\bar{y})^2 \tag{7.32}$$

In the middle of the figure the EKF process is illustrated. As a reminder, the EKF linearizes the system around a single point using a Taylor polynomial linearization.

In the right part of the figure, the UKF process is illustrated. A set of points is selected (5 here) and propagate through the non-linear system.

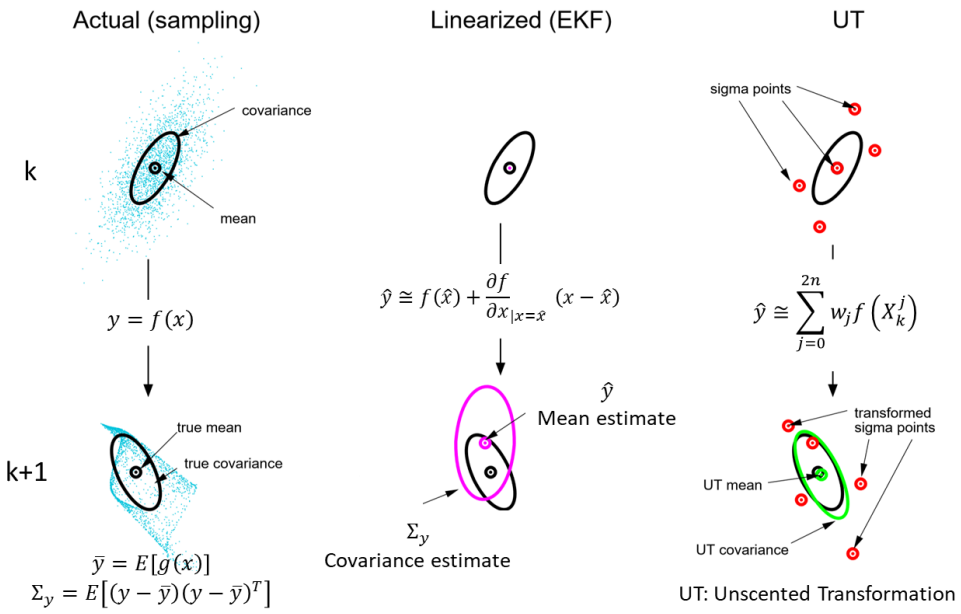

Figure 7.4 – Simple illustration of EKF and UKF – source [64]

It can be seen here that the UKF performs better than the EKF. It is generally the case when the system is highly non linear.

From a general point of view, the following comparison can be made between EKF and UKF.

- The EKF requires the computation of the Jacobian matrices which can be complex. This computational problem is not present in the UKF where a deterministic sampling approach is used. Hence, for the UKF, the non linear functions do not need to be differentiable.
- According to litterature, both the EKF and the UKF have slightly the same complexity.
- For linear models, UKF and EKF give the same results.
- For highly non linear model, the UKF outperforms the EKF.

7.1.5. Use case application

The hybrid KF navigation solutions envisioned in the thesis are presented in this section. First, the common step to EKF and UKF are presented. Second, the step particular to the EKF are detailed. Third the step particular to the UKF are detailed.

7.1.5.1. General model

7.1.5.1.1. State vector

Ten parameters have to be estimated: the user position $[x_k \quad y_k \quad z_k]$, the user velocity $[v_{x_k} \quad v_{y_k} \quad v_{z_k}]$, the time shifts between systems $b_{GPS/user} = c \cdot \Delta t_{GPS/user}$, $b_{GPS/GAL} = c \cdot \Delta t_{GPS/GAL}$, $b_{GPS/5G} = c \cdot \Delta t_{GPS/5G}$ and the receiver clock drift $\dot{b}_{GPS/user}$

The state vector considered in the hybrid navigation solution is thus provided in (7.33).

$$X = \left[x_k \quad v_{x_k} \quad y_k \quad v_{y_k} \quad z_k \quad v_{z_k} \quad b_{GPS/user} \quad \dot{b}_{GPS/user} \quad b_{GPS/Gal} \quad b_{GPS/5G}\right]^T \tag{7.33}$$

7.1.5.1.2. State transition matrix

In order to define the state transition matrix F_k, in the discrete time domain, it is assumed that x, y and z, in the continuous domain, are random walks processes which are the integration of white noise. In the continuous time domain, the state transition model is, according to the above mentioned hypothesis, defined as

$$\dot{X}(t) = f(t) \cdot X(t) + W(t) \tag{7.34}$$

$$\begin{bmatrix} \dot{x} \\ \dot{v_x} \\ \dot{y} \\ \dot{v_y} \\ \dot{z} \\ \dot{v_z} \\ \Delta\dot{t}_{GPS/user} \cdot c \\ \Delta\ddot{t}_{GPS/user} \cdot c \\ \Delta\dot{t}_{GPS/Gal} \cdot c \\ \Delta\dot{t}_{GPS/5G} \cdot c \end{bmatrix} = \begin{bmatrix} 0 & 1 & 0 & 0 & 0 & 0 & 0 & 0 & 0 & 0 \\ 0 & 0 & 0 & 0 & 0 & 0 & 0 & 0 & 0 & 0 \\ 0 & 0 & 0 & 1 & 0 & 0 & 0 & 0 & 0 & 0 \\ 0 & 0 & 0 & 0 & 0 & 0 & 0 & 0 & 0 & 0 \\ 0 & 0 & 0 & 0 & 0 & 1 & 0 & 0 & 0 & 0 \\ 0 & 0 & 0 & 0 & 0 & 0 & 0 & 0 & 0 & 0 \\ 0 & 0 & 0 & 0 & 0 & 0 & 0 & 1 & 0 & 0 \\ 0 & 0 & 0 & 0 & 0 & 0 & 0 & 0 & 0 & 0 \\ 0 & 0 & 0 & 0 & 0 & 0 & 0 & 0 & 0 & 0 \\ 0 & 0 & 0 & 0 & 0 & 0 & 0 & 0 & 0 & 0 \end{bmatrix} \begin{bmatrix} x \\ v_x \\ y \\ v_y \\ z \\ v_z \\ \mathrm{b_{GPS/user}} \\ \dot{\mathrm{b}}_{\mathrm{GPS/user}} \\ \mathrm{b_{GPS/Gal}} \\ \mathrm{b_{GPS/5G}} \end{bmatrix} + \begin{bmatrix} 0 \\ n_x \\ 0 \\ n_y \\ 0 \\ n_z \\ n_{\mathrm{b_{GPS-user}}} \\ n_{\dot{\mathrm{b}}_{\mathrm{GPS-user}}} \\ n_{\mathrm{b_{GPS-Gal}}} \\ n_{\mathrm{b_{GPS-5G}}} \end{bmatrix} \tag{7.35}$$

The sampled version of this equation is obtained by applying it the expectation. Remind that W_k is a White Gaussian Centred Noise, $E[W(t)] = 0$. Then, a first order Taylor series expansion is used around $t = kT_{update}$, for a small variation of time T_{update}.

$$\begin{aligned} X_{k+1} &\cong X_k + \frac{\partial}{\partial t} X_k \cdot T_{update} \cong X_k + f\left(kT_{update}\right) \cdot X_k \cdot T_s \cong \left(I + f\left(kT_{update}\right) \cdot T_{update}\right) \cdot X_k \\ &\cong F_k \cdot X_k \end{aligned} \tag{7.36}$$

$$\begin{bmatrix} x_{k+1} \\ v_{x_{k+1}} \\ y_{k+1} \\ v_{y_{k+1}} \\ z_{k+1} \\ v_{z_{k+1}} \\ \mathrm{b_{GPS-user}}_{k+1} \\ \dot{\mathrm{b}}_{\mathrm{GPS-user}_{k+1}} \\ \mathrm{b_{GPS-gal}}_{k+1} \\ \mathrm{b_{GPS-5G}}_{k+1} \end{bmatrix} = \begin{bmatrix} 1 & T_{update} & 0 & 0 & 0 & 0 & 0 & 0 & 0 & 0 \\ 0 & 1 & 0 & 0 & 0 & 0 & 0 & 0 & 0 & 0 \\ 0 & 0 & 1 & T_{update} & 0 & 0 & 0 & 0 & 0 & 0 \\ 0 & 0 & 0 & 1 & 0 & 0 & 0 & 0 & 0 & 0 \\ 0 & 0 & 0 & 0 & 1 & T_{update} & 0 & 0 & 0 & 0 \\ 0 & 0 & 0 & 0 & 0 & 1 & 0 & 0 & 0 & 0 \\ 0 & 0 & 0 & 0 & 0 & 0 & 1 & T_{update} & 0 & 0 \\ 0 & 0 & 0 & 0 & 0 & 0 & 0 & 1 & 0 & 0 \\ 0 & 0 & 0 & 0 & 0 & 0 & 0 & 0 & 1 & 0 \\ 0 & 0 & 0 & 0 & 0 & 0 & 0 & 0 & 0 & 1 \end{bmatrix} \begin{bmatrix} x_k \\ v_{x_k} \\ y_k \\ v_{y_k} \\ z_k \\ v_{z_k} \\ \mathrm{b_{GPS-user}}_k \\ \dot{\mathrm{b}}_{\mathrm{GPS-user}_k} \\ \mathrm{b_{GPS-gal}}_k \\ \mathrm{b_{GPS-5G}}_k \end{bmatrix} \tag{7.37}$$

Thus the state transition matrix is defined as

$$F_k = \begin{bmatrix} 1 & T_{update} & 0 & 0 & 0 & 0 & 0 & 0 & 0 & 0 \\ 0 & 1 & 0 & 0 & 0 & 0 & 0 & 0 & 0 & 0 \\ 0 & 0 & 1 & T_{update} & 0 & 0 & 0 & 0 & 0 & 0 \\ 0 & 0 & 0 & 1 & 0 & 0 & 0 & 0 & 0 & 0 \\ 0 & 0 & 0 & 0 & 1 & T_{update} & 0 & 0 & 0 & 0 \\ 0 & 0 & 0 & 0 & 0 & 1 & 0 & 0 & 0 & 0 \\ 0 & 0 & 0 & 0 & 0 & 0 & 1 & T_{update} & 0 & 0 \\ 0 & 0 & 0 & 0 & 0 & 0 & 0 & 1 & 0 & 0 \\ 0 & 0 & 0 & 0 & 0 & 0 & 0 & 0 & 1 & 0 \\ 0 & 0 & 0 & 0 & 0 & 0 & 0 & 0 & 0 & 1 \end{bmatrix} \tag{7.38}$$

Since the model is simple and linear, random walks, it is valid for both EKF and UKF. Therefore, for both UKF and EKF, the state transition matrix is identical.

7.1.5.1.3. Measurement noise covariance matrix

The measurement noise covariance matrix used in the EKF is a diagonal matrix presented in (7.39). The shape of the diagonal terms, Σ_{system}^{k}, where $system$ refers to the system considered (GPS, Galileo, 5G), is provided in (7.40). These values for pseudo range measurement have been derived in chapter 6.

$$R_k = \begin{bmatrix} \Sigma_{GPS}^{k} & 0 & 0 & 0 & 0 \\ 0 & \Sigma_{Gal}^{k} & 0 & 0 & 0 \\ 0 & 0 & \Sigma_{5G}^{k} & 0 & 0 \\ 0 & 0 & 0 & \dot{\Sigma}_{GPS}^{k} & 0 \\ 0 & 0 & 0 & 0 & \dot{\Sigma}_{Gal}^{k} \end{bmatrix} \tag{7.39}$$

$$\Sigma_{system}^{k} = \begin{bmatrix} \sigma^2_{system_{meas\,1}} & 0 & 0 \\ 0 & \ddots & 0 \\ 0 & 0 & \sigma^2_{system_{meas\,N_k}} \end{bmatrix} \tag{7.40}$$

7.1.5.1.4. State covariance matrix

As presented in section 7.2.2.1, the state covariance matrix is defined as $Q_k = cov[W_k]$ where W_k is the discrete white process noise sequence. Since a random walks is assumed for the Ph.D., the state covariance matrix is modelled as (7.41).

$$Q_k = \begin{bmatrix} \sigma_{vx}^2 \cdot \frac{T_{update}^3}{3} & \sigma_{vx}^2 \cdot \frac{T_{update}^2}{2} & 0 & 0 & 0 & 0 & 0 \\ \sigma_{vx}^2 \cdot \frac{T_{update}^2}{2} & \sigma_{vx}^2 \cdot T_{update} & 0 & 0 & 0 & 0 & 0 \\ 0 & 0 & \sigma_{vy}^2 \cdot \frac{T_{update}^3}{3} & \sigma_{vy}^2 \cdot \frac{T_{update}^2}{2} & 0 & 0 & 0 \\ 0 & 0 & \sigma_{vy}^2 \cdot \frac{T_{update}^2}{2} & \sigma_{vy}^2 \cdot T_{update} & 0 & 0 & 0 \\ 0 & 0 & 0 & 0 & \sigma_{vz}^2 \cdot \frac{T_{update}^3}{3} & \sigma_{vz}^2 \cdot \frac{T_{update}^2}{2} & 0 \\ 0 & 0 & 0 & 0 & \sigma_{vz}^2 \cdot \frac{T_{update}^2}{2} & \sigma_{vz}^2 \cdot T_{update} & 0 \\ 0 & 0 & 0 & 0 & 0 & 0 & Q_{clock_k} \end{bmatrix} \tag{7.41}$$

Where $\sigma_{vx}^2 = cov(n_x)$. For the simulations led in the following, $\sigma_{vx}^2 = \sigma_{vy}^2 = \sigma_{vz}^2 = 100$, and $T_{update} = 20\,ms$ Details can be found in [61]. The clock process noise part of the covariance matrix, Q_{clock_k}, is based on the Allan variance parameters, details can be found in [66].

$$Q_{clock_k} = \begin{bmatrix} \sigma_{b,discri}^2 & \sigma_{b-d,discri}^2 & 0 & 0 \\ \sigma_{b-d,discri}^2 & \sigma_{d,discri}^2 & 0 & 0 \\ 0 & 0 & 1 & 0 \\ 0 & 0 & 0 & 1 \end{bmatrix} \tag{7.42}$$

- The discrete-time oscillator's phase PSD is computed as: $\sigma_{b,discri}^2 = \frac{h_0}{2} T_{update} + 2h_{-1} T_{update}^2 + \frac{2}{3}\pi^2 h_{-2} T_{update}^3$
- $\sigma_{b-d,discri}^2 = h_{-1} T_{update} + \pi^2 h_{-2} T_{update}^2$ denotes the receiver's oscillator frequency PSD influence on the clock bias

- The discrete-time oscillator's frequency noise variance $\sigma^2_{d,discri}$ related to the receier's clock drift component is expressed as: $\sigma^2_{d,discri} = \frac{h_0}{2T_{update}} + 4h_{-1} + \frac{8}{3}\pi^2 h_{-2} T^2_{update}$
- h_0, h_{-1} and h_{-2} represent the Allan variance parameters

7.1.5.2. EKF customization

As presented before, the hybrid navigation solution uses pseudo ranges codes measurements from GPS, Galileo and 5G systems and pseudo range rates from GPS and Galileo systems. Therefore, the measurement model is $Y_k = h(X_k) + V_k$, where $h(X_k)$ is defined as:

$$h(X_k) = \begin{bmatrix} h^{(GPS)}(X_k) \\ h^{(Gal)}(X_k) \\ h^{(5G)}(X_k) \\ \dot{h}^{(Gal)}(X_k) \\ \dot{h}^{(Gal)}(X_k) \end{bmatrix} \tag{7.43}$$

Where h^X represents the pseudo range code measurements and $\dot{h}$ represents the pseudo range rate measurements. These sub-matrices are linearized in Taylor series, here after the definition of the Jacobian matrix H_k.

$$H_k = \frac{\partial h}{\partial X_k}_{|X_k = \hat{X}_{k+1|k}} = \begin{bmatrix} \frac{\partial h^{(GPS)}}{\partial X_k}_{|X_k = \hat{X}_{k+1|k}} \\ \frac{\partial h^{(Gal)}}{\partial X_k}_{|X_k = \hat{X}_{k+1|k}} \\ \frac{\partial h^{(5G)}}{\partial X_k}_{|X_k = \hat{X}_{k+1|k}} \\ \frac{\partial \dot{h}^{(GPS)}}{\partial X_k}_{|X_k = \hat{X}_{k+1|k}} \\ \frac{\partial \dot{h}^{(GPS)}}{\partial X_k}_{|X_k = \hat{X}_{k+1|k}} \end{bmatrix} \tag{7.44}$$

The complete derivations of each sub-matrices $\frac{\partial h^X}{\partial X_k}_{|X_k = \hat{X}_{k+1|k}}$ are provided in Annex G.

7.1.5.3. UKF customization

As already noted in 7.2.2.5.1.2, the dynamic model is quite simple and linear; therefore, in (7.26) and (7.27), the function $f(X_k)$ can be approximated by $f\left(X_k^j\right) = F_k \cdot X_k$

The UKF is based on a statistical linearization technique; not an analytical one as for the EKF. Therefore, the observation prediction equations are computed using the matrix $h(X_k)$ computed for each sigma point.

$$h(X_k) = \begin{bmatrix} h^{(GPS)}(X_k) \\ h^{(Gal)}(X_k) \\ h^{(5G)}(X_k) \\ \dot{h}^{(Gal)}(X_k) \\ \dot{h}^{(Gal)}(X_k) \end{bmatrix} \quad (7.45)$$

Where h^X represents the pseudo range code measurements and $\dot{h}$ represents the pseudo range rate measurements defined in section 7.1.

7.2. Simulation parameters

In order to compare the previously defined navigation filters, scenarios have to be defined. First the trajectory is presented, second the GNSS scenario is presented and finally the 5G scenario is presented.

7.2.1. Trajectory

In order to study the mathematical models developed all along this thesis, the scenario used is presented in Figure 7.5. An East North Up (ENU) representation is used. The trajectory lasts 60 seconds. The receiver is moving at a constant speed of $v = 50\ km/h$. This trajectory has been generated thanks to SCHUN and using the parameters provided in Table 7.1.

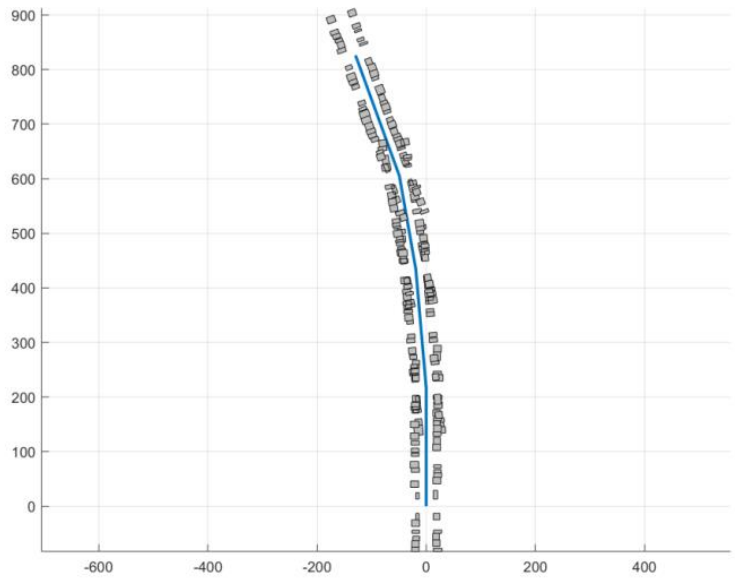

Figure 7.5 – Virtual city generated by SCHUN

Table 7.1 – SCHUN city virtual distribution

Parameters	Description	Format	Units	Value
Road crossing	Uniform distribution of the street lengths in meters	[Min Max]	[m]	[150 300]
Street orientation	Uniform distribution of the orientation in degrees between two consecutive streets.	[Min Max]	[m]	[-20 20]
Building density	The building occupation density in the virtual city	Float	0<index<1	0.75
Building height	The building height distribution assuming a Gaussian distribution	[Mean std]	[m]	[15 20]

Building width	The building width distribution assuming a Gaussian distribution	[Mean std]	[m]	[10 30]
Building depth	The building depth distribution assuming a Gaussian distribution	[Mean std]	[m]	[15 20]
Buiding space	Distance between buildings assuming a Gaussian distribution.	[Mean std]	[m]	[0 3]
Building back	The distance between the buildings and the street in meters	[Min Max]	[m]	[12 14]

7.2.2. GNSS scenario

Regarding the considered GNSS scenario, a randomly selected Almanac gives the sky plot provided in Figure 7.6 for location at Toulouse city center. Assuming the virtual city presented in Figure 7.5 and following the parameters presented in Table 7.1, a 50° elevation mask is used, illustrated by the blue disk in Figure 7.6. This mask angle permits to model the effect of buildings on the satellite visibility. Based on this, a maximum of 2 GPS satellites are visible and 3 Galileo satellites. The number of satellites from which exploitable pseudo range and pseudo range rate measurements are used can be lower than the number of visible satellites due to the propagation channel generated by SCHUN. The impact of the channel can make the receiver loose the tracking of the satellites.

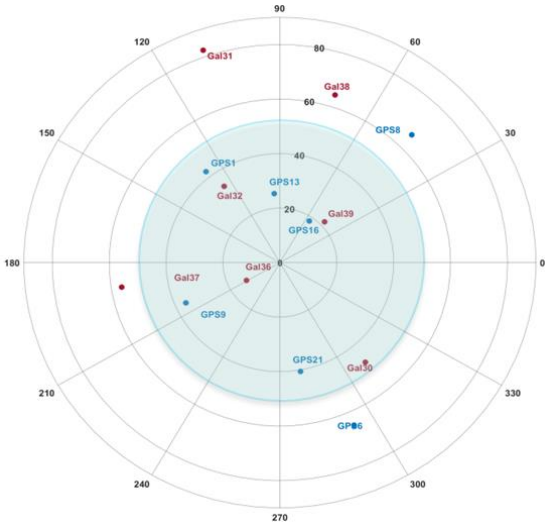

Figure 7.6 – GNSS sky plot

An example of the multipath additional path length with respect to the LOS path and of the multipath amplitude relative to the LOS path amplitude for GPS6 (in Figure 7.6) is provided in Figure 7.7 and Figure 7.8 respectively.

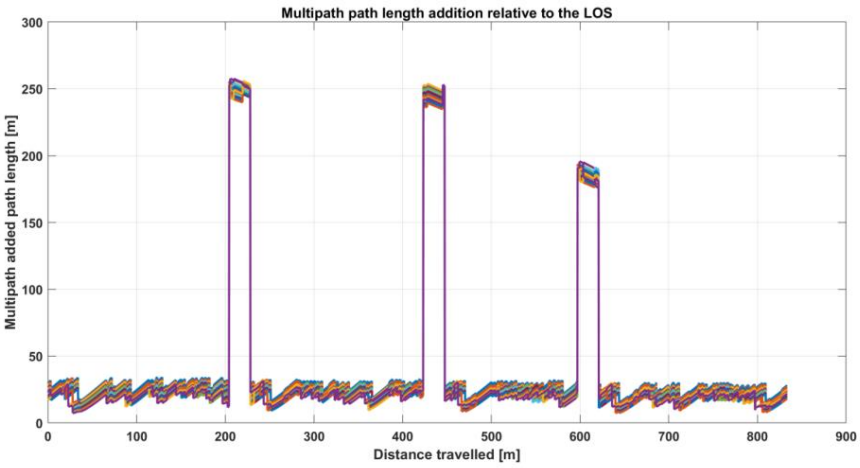

Figure 7.7 – Additional path length for GPS 6

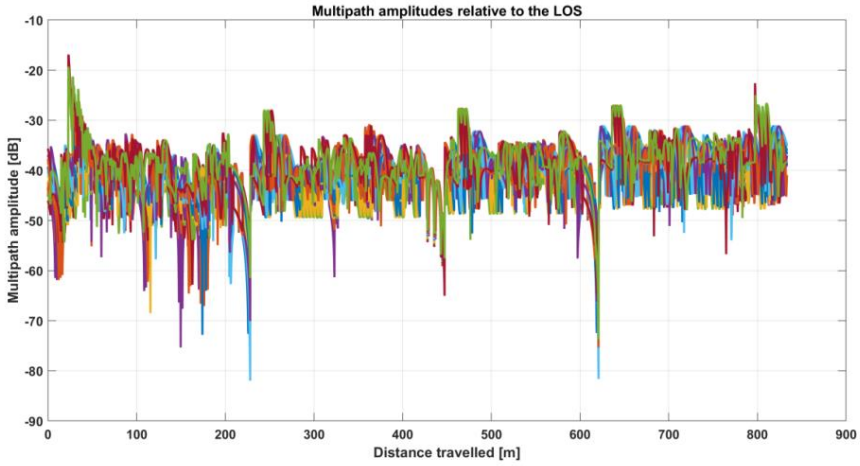

Figure 7.8 – Relative amplitude with respect to the LOS component for GPS 6

Note that the GNSS pseudo ranges generated by the simulator are affected by multipath and receiver thermal noise as presented in chapter 6 section 6.1 (no ionospheric or tropospheric effect, etc.).

7.2.3. 5G scenario

Regarding the 5G scenario adopted for the simulations, an Ultra Dense Network is assumed. Basically, the envisioned BS deployment scenario consists in BS located at each lamp post of the main and crossing streets. The ENU scheme is provided in Figure 7.9. The propagation channel is generated assuming the QuaDRiGa 3GPP_38.901_UMi_LOS high level scenario with a 2 GHz carrier frequency. BS are 15 m high.

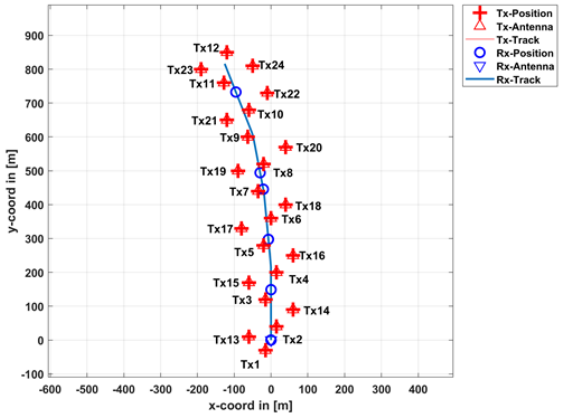

Figure 7.9 – Base Station location – UDN

In Figure 7.10 and Figure 7.11 the path delays and path power generated by QuaDRiGa for the Base Station 8 are provided for illustration.

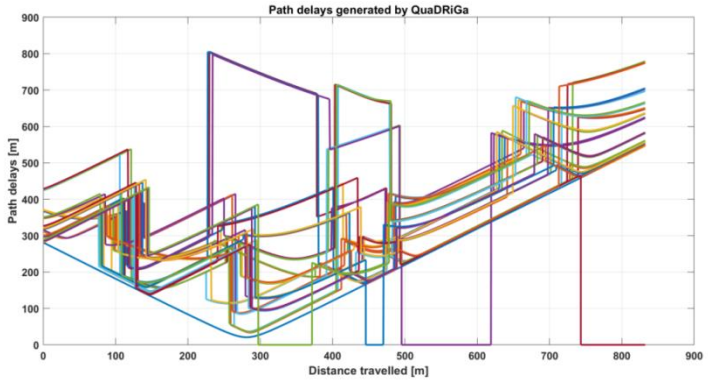

Figure 7.10 – Path delays generated by QuaDRiGa – Base Station 8

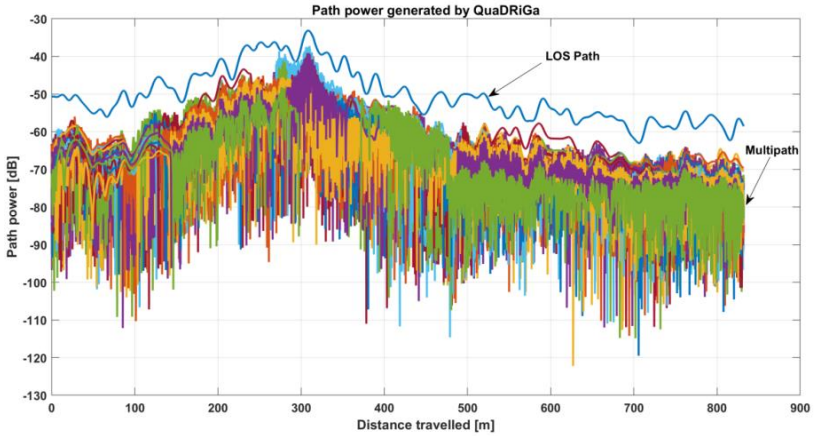

Figure 7.11 – Path powers generated by QuaDRiGa – Base Station 8

Note that for simplification purposes, it is assumed that each consecutive OFDM symbol is identical and corresponds to the second symbol of the SSPBCH block described in chapter 3. Therefore, a simplified 5G frame is considered. In other words, all over the trajectory, the 5G frame is composed of one symbol repeated every symbol.

Note that the 5G pseudo ranges generated by the simulator are affected by multipath and receiver thermal noise as presented in chapter 6 section 6.1.

7.2.4. Configurations tested

In order to clearly present the configurations tested in the following section; first the elements required to define a configuration are presented. Second, the nomenclature adopted in the following to refer to a particular configuration is presented and examples are provided to ease the reading. Finally, the tested configurations are presented.

7.2.4.1. Elements constituting a configuration

A configuration depends on 5 parameters: the considered channel, the adopted pseudo range measurement characterization, the defined synchronization module, the C/N_0 estimator used and the selected navigation solution module. Each of them is described in the section.

7.2.4.1.1. Channel

In order to characterize the performances of the navigation filters, three propagation channel cases are studied for 5G systems:

- AWGN: In order to have a reference or baseline performance; the channel is similar to a pure delay.
- LOS: The channel is assumed to be constituted of only one path, the LOS ray, the path parameters are evolving in time. Note that for the LOS case, only the LOS path is used of the 5G generated propagation channel from QuaDRiGa 3GPP_38.901_UMi_LOS high level scenario. This case will permit to study the influence of the multipath components.
- COMP: A complete channel is considered (LOS + multipath); this case allows to quantify the distortion due to the multipath by comparing it to the LOS case.

Two cases are considered for GNSS systems:

- AWGN case
- COMP: a complete propagation channel generated by SCHUN.

Note that in the AWGN case, QuaDRiGa and SCHUN propagation channel models are not used, and just simple direct rays with free space losses are considered. The AWGN case permits to have a reference or baseline performance to be compared to and the LOS case permits to quantify the impact of the multipath.

7.2.4.1.2. Pseudo range measurement error characterization

According to the studies provided in Chapter 6 section 6.1, the pseudo range measurement error characterization is made through 3 parameters:

- The method: Fitting (FG) and over bounding (OB) distribution pseudo range measurements error characterization. As presented in Chapter 6, both methods must be compared in order to select the more appropriate one and to provide recommendations.
- The confidence bounds: 99.9%, 99% or 95%, each of them must be tested in order to select the appropriate one.
- The trajectory: Circular (Ci), Radial (Ra), Chord (Ch) or Global (Gl). This will permit to determine whether the impact of the trajectory on the characterization impact the navigation filters performances. Therefore, it will permit to determine if it is required to design trajectory-dependent characterization and to define the measurement noise covariance matrix as a function of the receiver trajectory.

Table 7.2 summarizes the configuration parameters linked to the pseudo range measurement error characterization; basically, one parameter in each column is required to define a configuration.

Table 7.2 – Pseudo range measurement error characterization

Method	Confidence bound	Trajectory
Fitting: FG Over bounding: OB	99.9 % 99 % 95 %	Circular: Ci Radial: Ra Chord: Ch Global: Gl

7.2.4.1.3. C/N_0 estimator

In Chapter 5 section 5.3, several C/N_0 estimators have been studied. In this chapter, unless otherwise stated, the true C/N_0 is used. In section 7.3.3.4, the two phase-corrected NWPR C/N_0 estimators are tested and compared to the performances obtained using the true C/N_0.

7.2.4.1.4. Synchronization module

The synchronization module used for GNSS is composed of a code delay tracking with a second order DLL using a DLL loop bandwidth set to 1 Hz and a PLL set to 30 Hz.

For 5G signals, the synchronization module is composed of a DLL using either a 10 Hz DLL loop bandwidth or a 1 Hz DLL loop bandwidth. As presented in Chapter 5 section 5.2, a FLL, with a 10 Hz loop bandwidth, is also tested when the DLL loop bandwidth is set to 1 Hz.

Table 7.3 summarizes the configuration tested regarding the synchronization module.

Table 7.3 – Synchronization module configuration

Systems	DLL	Carrier tracking loop	
GNSS	1 Hz	Yes	30 Hz
5G	10 Hz	No	
	1 Hz	Yes	10 Hz
		No	

7.2.4.1.5. Navigation solution

The positioning performances obtained using the navigation filters described in section 7.2 are studied and compared for 5G or GNSS standalone navigation solution and hybrid navigation solution. By doing so, the performances of a 5G navigation solution with respect to a GNSS navigation solution can be compared. Moreover, the interest of the hybrid solution is to determine if the available GNSS measurements can improve the 5G standalone navigation solution. For each case, the navigation filters considered are detailed in Table 7.4.

Table 7.4 – Navigation filter configurations

Filters	Measurements	Notation
EKF	5G Standalone	SEKF5G
	GNSS Standalone	SEKFGNSS
	5G GNSS Hybrid	HEKF
UKF	5G Standalone	SUKF5G
	5G GNSS Hybrid	HUKF5G

The final configurations to be analyzed combine all the four previously described set of elements (channel, characterization, synchronization module, navigation solution). They are summarized in Table 7.6 and Table 7.7. In Table 7.6 the configurations tested for the GNSS systems are described, in Table 7.7 the configurations tested for the 5G systems are described.

7.2.4.2. Nomenclature adopted

In Table 7.6 and Table 7.7, a nomenclature has been derived to ease the identification of the configuration tested. For GNSS, since there are only 2 configurations, the AWGN case is identified by the name "AWGN-GNSS" and will be associated to the 5G AWGN case only. The GNSS configuration using a complete SCHUN propagation channel is identified by the name "COMP-GNSS" and will be associated to all the 5G configurations but the AWGN case. Regarding the 5G nomenclature, each 5G case is described by 6 parameters separated by dash signed. These parameters are described in Table 7.5.

Table 7.5 – 5G configuration tests nomenclature

Channel	Pseudo range error characterization			Synchronization module	Navigation filter
	Method	Confidence bound	Trajectory		
AWGN LOS COMP	Fitting: FG Over bounding: OB	99.9 % 99 % 95 %	Circular: Ci Radial: Ra Chord: Ch Global: Gl	DLL loop bandwidth FLL : used or not (5G system)	EKF 5G Standalone: SEKF5G EKF GNSS Standalone: SEKFGNSS EKF 5G GNSS Hybrid: HEKF UKF 5G Standalone: SUKF5G UKF GNSS Standalone: HUKF5G

For example, the case named "LOS-OB-99.9-Ci-10Hz" refers to the case where only the LOS path is used in the QuaDRiGa propagation channel, the pseudo range measurement error characterization method used is the over-bounding (OB), the confidence bound is equal to 99.9%, the characterization has been performed assuming a Circular trajectory (Ci) and a 5G 10Hz DLL loop bandwidth is used. Note that for a 10 Hz DLL loop bandwidth, a FLL is not required therefore, the nomenclature does not mention it.

A second example can be detailed: the case named "COMP-FG-95-Gl-1Hz-FLL" refers to the case where a complete QuaDRiGa propagation channel is used (LOS+multipath), the pseudo range measurement error characterization method used is the fitting method (FG), the confidence bound is equal to 95%, the characterization has been performed assuming the Global characterization (Gl) and the 5G synchronization uses a 1Hz DLL loop bandwidth and a FLL is implemented.

7.2.4.3. Configurations tested

The summary of all tested configuration is provided in Table 7.6 and Table 7.7. In Table 7.6 the configurations tested for the GNSS systems are described, in Table 7.7 the configurations tested for the 5G systems are described.

Remind that the AWGN-GNSS case is associated to the AWGN-5G only and all the others 5G configurations tested are associated to the COMP-GNSS case.

Moreover, each of the 5 navigation filters presented in Table 7.5 are tested for each configuration; therefore, there is no mention of them in the two following tables.

Table 7.6 – GNSS configurations tested

Case	Propagation channel model	Loop bandwidth	Characterization used
AWGN-GNSS	$\alpha(t,\tau) = \delta(\tau - \tau_0)$	DLL: 1 Hz FLL: 30 Hz	Thermal noise theoretical formula
COMP-GNSS	$\alpha(t,\tau) = \sum_{l=0}^{N} \gamma_l(t) e^{-j\Phi_l(t)} \delta(\tau - \tau_l(t))$	DLL: 1 Hz FLL: 30 Hz	Over bounding - $99.9\% - N(0,\sigma)$

Table 7.7 – 5G configurations tested

Case		Propagation channel model	Loop bandwidth		Characterization used $N(0,\sigma)$		
					Trajectory	Method	Confidence bound
1	AWGN-5G	$\alpha^k(t,\tau) = \delta(\tau - \tau_0)$	$B_l = 10Hz$		Thermal noise theoretical formula		
2	LOS-OB-99.9-Gl-10Hz	$\alpha^k(t,\tau) = \alpha^k(t) \cdot \delta\big(\tau - \tau_0(t)\big)$	$B_l = 10Hz$		Global	Over bounding	99.9%
3	COMP-OB-99.9-Ci-10Hz	$\alpha^k(t,\tau) = \sum_{l=0}^{L-1} \alpha_l^k(t) \cdot \delta\big(\tau - \tau_l(t)\big),\ 0 \le t \le T_{OFDM}$	$B_l = 10Hz$		Circular	Over bounding	99.9%
4	COMP-OB-99.9-Ra-10Hz				Radial		99.9%
5	COMP-OB-99.9-Ch-10Hz				Chord		99.9%
6	COMP-OB-99.9-Gl-10Hz				Global		99.9%
7	COMP-OB-99-Gl-10Hz				Global		99%
8	COMP-OB-95-Gl-10Hz				Global		95%
9	COMP-FG-99.9-Gl-10Hz				Global	Fitting	99.9%
10	COMP-FG-99-Gl-10Hz				Global		99%
11	COMP-FG-95-Gl-10Hz				Global		95%
12	COMP-OB-99.9-Ci-1Hz-NoFLL		$B_l = 1Hz$	No FLL	Circular	Over bounding	99.9%
13	COMP-OB-99.9-Ra-1Hz-NoFLL				Radial		99.9%
14	COMP-OB-99.9-Ch-1Hz-NoFLL				Chord		99.9%
15	COMP-OB-99.9-Gl-1Hz-NoFLL				Global		99.9%
16	COMP-OB-99-Gl-1Hz-NoFLL				Global		99%
17	COMP-OB-95-Gl-1Hz-NoFLL				Global		95%
18	COMP-FG-99.9-Gl-1Hz-NoFLL				Global	Fitting	99.9%
19	COMP-FG-99-Gl-1Hz-NoFLL				Global		99%
20	COMP-FG-95-Gl-1Hz-NoFLL				Global		95%
21	COMP-OB-99.9-Gl-1Hz-FLL			With FLL	Global	Over bounding	99.9%
22	COMP-OB-99-Gl-1Hz-FLL				Global		99%
23	COMP-OB-95-Gl-1Hz-FLL				Global		95%
24	COMP-FG-99.9-Gl-1Hz-FLL				Global	Fitting	99.9%
25	COMP-FG-99-Gl-1Hz-FLL				Global		99%
26	COMP-FG-95-Gl-				Global		95%

	1Hz-FLL						

7.3. Results

The results are split into 2 sections. First the performances of the EKF and UKF for all cases described in Table 7.6 and Table 7.7 are presented and compared in order to define the more appropriate tuning. Second, assuming the optimal tuning, different impact analyses are proposed (navigation filter, propagation channel, Gaussian approximation and C/N_0 estimation).

7.3.1. EKF and UKF tuning

In this section the performances of the EKF and UKF navigation solutions are studied in order to define the more appropriate tuning in term of characterization, synchronization module parameterization, etc. In order to characterize the performances of the navigation filters, the figure of merit selected is the Root Mean Square Error (RMSE) of the position error along the X, Y and Z axis expressed in the East North Up coordinate frame. The horizontal RMSE is also provided (X^2+Y^2).

In order to structure the results, the following outline is defined. First the impact of the trajectory on the filters performances is studied. Second, the impact of the confidence bound used for the characterization on the filters performances is studied. Third, the impact of the characterization method (fitting vs over-bounding) is studied. Forth, the impact of the synchronization module design is studied.

7.3.1.1. Impact of the trajectory used for the characterization on the filters performances

In this first subsection, the impact of the trajectory used for the pseudo range measurement error characterization on the filter performances is studied. Therefore, the objective is to determine the best characterization in term of trajectory to be used in the filters and the potential improvements to be made.

In Figure 7.12 histograms presenting the RMSE on the horizontal plane for cases 3, 4, 5 and 6 are presented. These 4 cases assumed an over bounding characterization for a 10 Hz DLL bandwidth (COMP-OB-99.9-XX-10Hz). Numerical values can be found in Table 7.8, Table 7.9, Table 7.10 and Table 7.11. From Figure 7.12 it can be said that the circular trajectory provides the worst results compared to the others. Obviously the considered trajectory (see Figure 7.5) is not circular at all but rather a chord or radial trajectory; this can explain why the characterization based on the circular trajectory provides the worst RMSE. The same behavior is observed for the 1 Hz DLL bandwidth, results are provided in Annex H.

The characterization obtained by mixing the 3 trajectories provided naturally averaged RMSEs compared to the other trajectory dependent characterizations. From these results, it is difficult to clearly state the impact of the trajectory used for the characterization on the navigation filter performances. Therefore, it is possible to use the global characterization without degrading a-priori the performances of the navigation filters. In order to clearly state the impact of the trajectory used for the characterization on the navigation solution, a solution could be to determine, at each instant and for each BS, the appropriate type of trajectory and associate the required characterization.

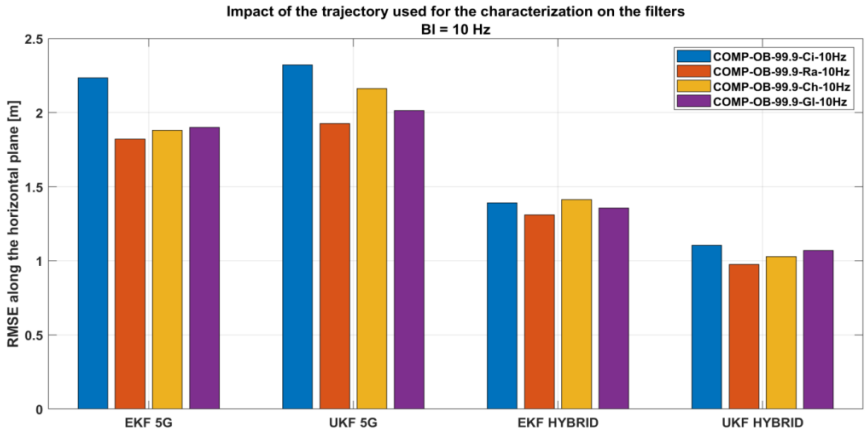

Figure 7.12 – Impact of the trajectory used for the characterization – overbounding method – 10 Hz – horizontal RMSE

Table 7.8 – Case 3: COMP-OB-99.9-Ci-10Hz

	X	Y	Z	X^2+Y^2
EKF GNSS	0.47	1.10	2.66	1.20
EKF 5G	1.41	1.74	5.82	2.23
UKF 5G	1.35	1.88	20.69	2.32
EKF HYBRID	0.51	1.29	2.41	1.39
UKF HYBRID	0.36	1.04	1.45	1.10

Table 7.9 – Case 4: COMP-OB-99.9-Ra-10Hz

	X	Y	Z	X^2+Y^2
EKF GNSS	0.47	1.10	2.66	1.20
EKF 5G	1.08	1.46	3.75	1.82
UKF 5G	1.11	1.57	8.38	1.93
EKF HYBRID	0.55	1.19	1.93	1.31
UKF HYBRID	0.29	0.93	1.45	0.98

Table 7.10 – Case 5: COMP-OB-99.9-Ch-10Hz

	X	Y	Z	X^2+Y^2
EKF GNSS	0.47	1.10	2.66	1.20
EKF 5G	0.98	1.61	3.63	1.88
UKF 5G	1.08	1.87	26.05	2.16
EKF HYBRID	0.58	1.29	2.27	1.41
UKF HYBRID	0.29	0.99	1.57	1.06

Table 7.11 – Case 6: COMP-OB-99.9-GI-10Hz

	X	Y	Z	X^2+Y^2
EKF GNSS	0.47	1.10	2.66	1.20
EKF 5G	0.93	1.64	3.76	1.89
UKF 5G	0.96	1.76	8.58	2.00
EKF HYBRID	0.54	1.31	2.16	1.42
UKF HYBRID	0.28	1.02	1.59	1.06

7.3.1.2. Impact of the confidence bound used for the characterization on the filters performances

In this subsection, the impact of the confidence bound used for the characterization on the filter performances is studied. In Figure 7.13 the histograms presenting the RMSE on the horizontal plane for cases 6 (COMP-OB-99.9-GI-10Hz), 7 (COMP-OB-99-GI-10Hz), 8 (COMP-OB-95-GI-10Hz) are presented. These 3 cases assume an over bounding characterization and a 10 Hz DLL bandwidth with respective confidence bound 99.9%, 99% and 95. Numerical values can be found in Table 7.11, Table 7.12 and Table 7.13.

Focusing on the horizontal RMSE, provided in Figure 7.13, it is clear that the confidence bound has a non-negligible impact on the filter performances. The RMSE decreases as the confidence bound increases; this tendency can also be observed for results obtained with a 1 Hz DLL loop bandwidth as proposed in Annex H. In average, by comparing the last column of Table 7.11 and Table 7.13 there is a difference of around 20 cm between the 99.9% and the 95% characterization. Although the results are a bit less clear for the RMSE along the Z axis, the tendency is confirmed.

In this section it has been proved that the confidence bound used for the characterization has a non-negligible impact on the filter behavior and that a 99.9% confidence bound provides globally the best results. Therefore, in the following the 99.9% confidence bound are kept.

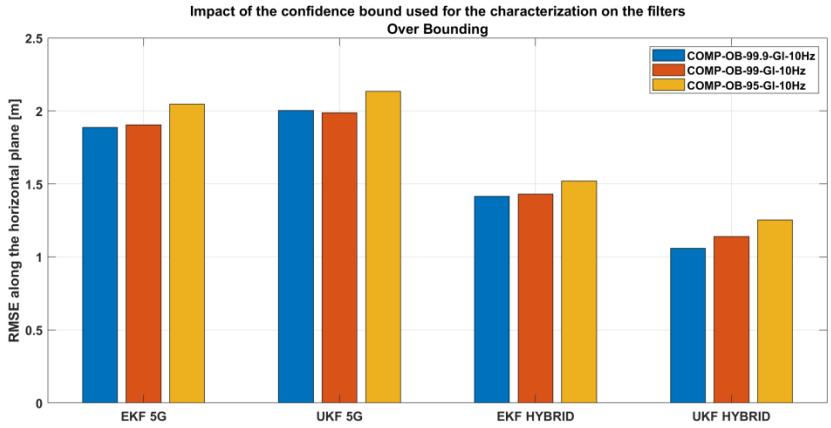

Figure 7.13 – Impact of the confidence bound used for the characterization of the filter performances – overbounding – horizontal plane

Table 7.12 – Case 7: COMP-OB-99-GI-10Hz

	X	Y	Z	X^2+Y^2
EKF GNSS	0.47	1.10	2.66	1.20
EKF 5G	0.94	1.66	16.21	1.90
UKF 5G	0.95	1.75	9.90	1.98
EKF HYBRID	0.49	1.34	2.14	1.43
UKF HYBRID	0.28	0.99	1.57	1.03

Table 7.13 – Case 8: COMP-OB-95-GI-10Hz

	X	Y	Z	X^2+Y^2
EKF GNSS	0.47	1.10	2.66	1.20
EKF 5G	1.02	1.78	8.75	2.05
UKF 5G	1.04	1.86	20.97	2.13
EKF HYBRID	0.54	1.42	2.23	1.52
UKF HYBRID	0.32	1.21	1.61	1.25

7.3.1.3. Impact of the over bounding and fitting characterization

In this subsection, the impact of the characterization method (over bounding or fitting) chosen on the filter performances is studied.

In Figure 7.14 the histograms presenting the RMSE on the horizontal plane for cases 6 (COMP-OB-99.9-GI-10Hz), 9 (COMP-FG-99.9-GI-10Hz), 15 (COMP-OB-99.9-GI-1Hz-NoFLL) and 18 (COMP-FG-99.9-GI-1Hz-NoFLL) are presented. Cases 6 and 15 assumed an over bounding characterization based on a 99.9% confidence bound for a 10 Hz and a 1 Hz DLL bandwidth respectively. Cases 9 and 18 assumed a fitting characterization for a 10 Hz and a 1 Hz DLL bandwidth respectively for the same 99.9% confidence bound. Numerical values can be found in Table 7.11, Table 7.14, Table 7.15 and Table 7.16.

From Figure 7.14 it is clear that the over bounding method is more appropriate than the fitting method. Results are even clearer for the hybrid filters where for the 1 Hz DLL bandwidth, the RMSE on the horizontal plane is around 60 cm worse for the fitting characterization than for the over bounding characterization (last two line of the last column of Table 7.15 and Table 7.16). The same tendency can be observed along the Z axis and for cases 21 and 25 when the FLL is implemented for a 1 Hz DLL loop bandwidth as presented in Annex H.

From these cases it is also possible to see that the DLL bandwidth used in the 5G ranging module has also a role that must be kept in mind. These observations are important since a 5G ranging module is still to be designed.

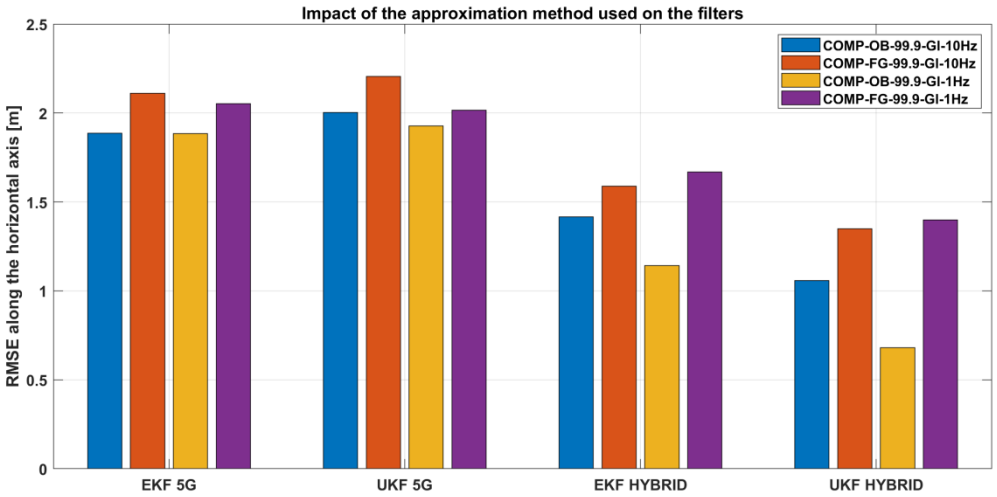

Figure 7.14 – Impact of the over bounding and fitting characterization – RMSE along the horizontal plane

Table 7.14 – Case 9: COMP-FG-99.9-GI-10Hz

	X	Y	Z	X^2+Y^2
EKF GNSS	0.47	1.10	2.66	1.20
EKF 5G	1.08	1.82	9.12	2.11
UKF 5G	1.11	1.91	21.13	2.21
EKF HYBRID	0.56	1.49	2.38	1.59
UKF HYBRID	0.37	1.30	1.66	1.35

Table 7.15 – Case 15: COMP-OB-99.9-GI-1Hz-NoFLL

	X	Y	Z	X^2+Y^2
EKF GNSS	0.47	1.10	2.66	1.20
EKF 5G	1.43	1.23	6.18	1.88
UKF 5G	1.52	1.19	18.68	1.93
EKF HYBRID	0.85	0.76	3.32	1.14
UKF HYBRID	0.44	0.51	0.87	0.68

Table 7.16 – Case 18: COMP-FG-99.9-GI-1Hz-NoFLL

	X	Y	Z	X^2+Y^2
EKF GNSS	0.47	1.10	2.66	1.20
EKF 5G	1.57	1.33	6.47	2.05
UKF 5G	1.60	1.23	11.91	2.01
EKF HYBRID	1.33	1.01	6.04	1.67
UKF HYBRID	1.15	0.80	1.24	1.40

7.3.1.4. Impact of the synchronization module

Regarding the synchronization, 2 parameters have to be studied:

- The impact of the DLL loop bandwidth: 10 Hz or 1 Hz when no FLL is considered
- The impact of the FLL for a 1 Hz DLL loop bandwidth

7.3.1.4.1. Impact of the DLL loop bandwidth

From the three previous sections it has been concluded that the best performances are obtained with the 99.9% over-bounding pseudo range measurement errors characterization; moreover, the global characterization can be kept without degrading the navigation filters performances. It must now be decided whether a 1 Hz DLL loop bandwidth or a 10 Hz DLL loop bandwidth is preferred. In order to compare the performances of the filters for these two configurations, the focus is made on cases 6 (COMP-OB-99.9-GI-10Hz) and 15 (COMP-OB-99.9-GI-1Hz-NoFLL). The numerical values are provided in Table 7.11 and Table 7.15 and are illustrated in Figure 7.15 and Figure 7.16 (red and blue bars). Keep in mind that these two cases do not considered the implementation of a FLL.

RMSE on the horizontal plane are lower for a 1 Hz DLL loop bandwidth than for a 10 Hz DLL loop bandwidth. The improvements are limited for standalone 5G navigation solution: lower than 10 cm for both Standalone 5G EKF and UKF navigation filter. However, the improvements are much more significant for the hybrid navigation solution: 30 cm lower for the EKF hybrid and 40 cm lower for the UKF hybrid.

Results on the vertical axis are much less convincing, the better performance of the 1 Hz DLL loop bandwidth can only be observed for the hybrid UKF navigation filter. Nevertheless, the 1 Hz DLL loop bandwidth is recommended after this study.

7.3.1.4.2. Impact of the FLL for a 1 Hz DLL loop bandwidth

It must now be decided whether a FLL is required or not. In order to study this parameter, the focus is made on case 15 (COMP-OB-99.9-Gl-1Hz-NoFLL) and case 21 (COMP-OB-99.9-Gl-1Hz-FLL). Both cases assumed an over bounding characterization using a 99.9% confidence bound and a 1 Hz DLL loop bandwidth. The numerical values are provided in Table 7.15 and Table 7.17 and are illustrated in Figure 7.15 and Figure 7.16 (red and yellow bars).

As it can be seen, the performances when a FLL is used are much better than when no FLL is implemented. The improvements are more important for the standalone 5G navigation: 80 to 90 cm improvement between the 1 Hz DLL loop bandwidth with and without the FLL for the RMSE along the horizontal plane.

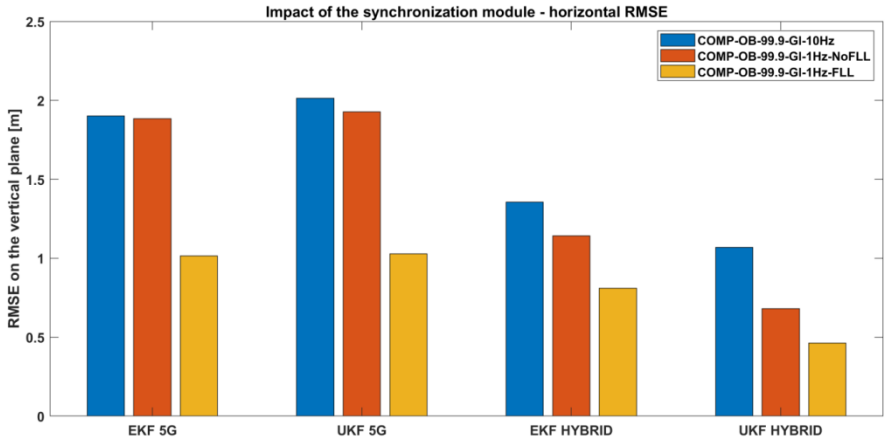

Figure 7.15 – Synchronization module impact – horizontal RMSE

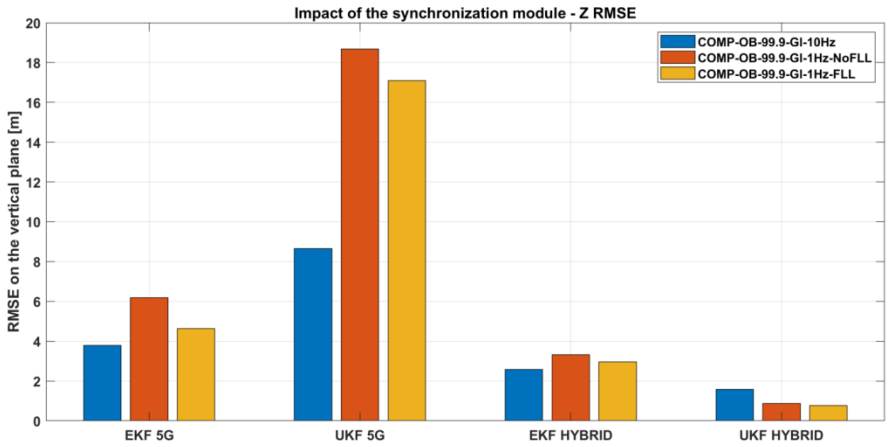

Figure 7.16 – Synchronization module impact – vertical RMSE

Table 7.17 – Case 21: COMP-OB-99.9-Gl-1Hz-FLL

	X	Y	Z	X^2+Y^2
EKF GNSS	0.47	1.10	2.66	1.20
EKF 5G	0.61	0.81	4.64	1.01
UKF 5G	0.67	0.78	17.09	1.03
EKF HYBRID	0.49	0.64	2.96	0.81
UKF HYBRID	0.43	0.38	0.75	0.58

7.3.1.5. Optimal solution identified

In conclusion, according to the study the tuning to adopt in order obtain the best navigation filter performances consist in using:

- An over bounding characterization
- A 99.9% confidence bound
- A 1 Hz DLL loop bandwidth with a FLL

7.3.2. Impact analysis over the best identified solution

The previous section has permitted to identify the best tuning for the KFs. It is now of interest to study the impact of the navigation filter (section 1), of the propagation channel (section 2), of the measurement error characterization (section 3) and on the C/N_0 estimation used (section 4) over the best solution defined in the previous section.

7.3.2.1. Impact of the navigation filter

The impact of the navigation filter is illustrated in Figure 7.18 for case 21, the optimal solution identified in section 7.3.2. Similar results can be observed for each simulated cases as presented in Annex H.

Regarding the performances of 5G standalone solution, there are no significant differences between the UKF and the EKF. Actually, this was predictable since for linear models UKF and EKF give the same results. Another important observation is the performances along the Z axis. The RMSE is much higher than for RMSE on the horizontal plane; as an example, it reaches 17.09 m for the standalone UKF in Figure 7.18. This behavior was also predictable since all BSs are at the same height; thus the geometry along the Z axis is not good enough. This is to be linked to the Dilution Of Precision (DOP) used for GNSS and studied for the 5G standalone WLS.

Another point is visible here: the hybrid navigation solution provides better solution than the standalone navigation solutions. In Figure 7.17 the number of measurements along the trajectory is provided. The number is obtained for a QuaDRiGa complete channel and a SCHUN channel. As illustrated in Figure 7.17, using only GNSS would not permit to compute a positioning solution since less than 5 satellites are in view after 500 m. Therefore, the use of the 5G signals improves the positioning solution availability in urban canyon. Nevertheless, by comparing the performances of the 5G standalone navigation solution and the hybrid navigation solution it can be seen than even if there are few GNSS satellites in view they still permit to improve the positioning precision.

Finally, the performances over the Z axis are much better in the hybrid navigation solution than in the 5G standalone solution.

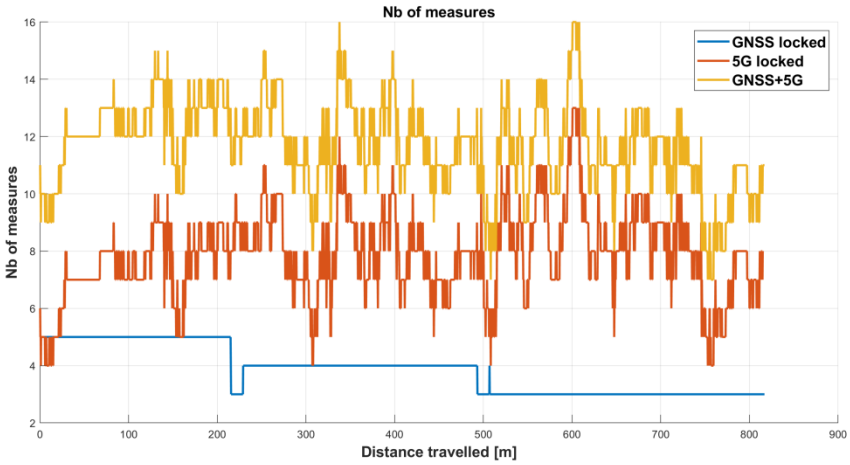

Figure 7.17 – Number of measures

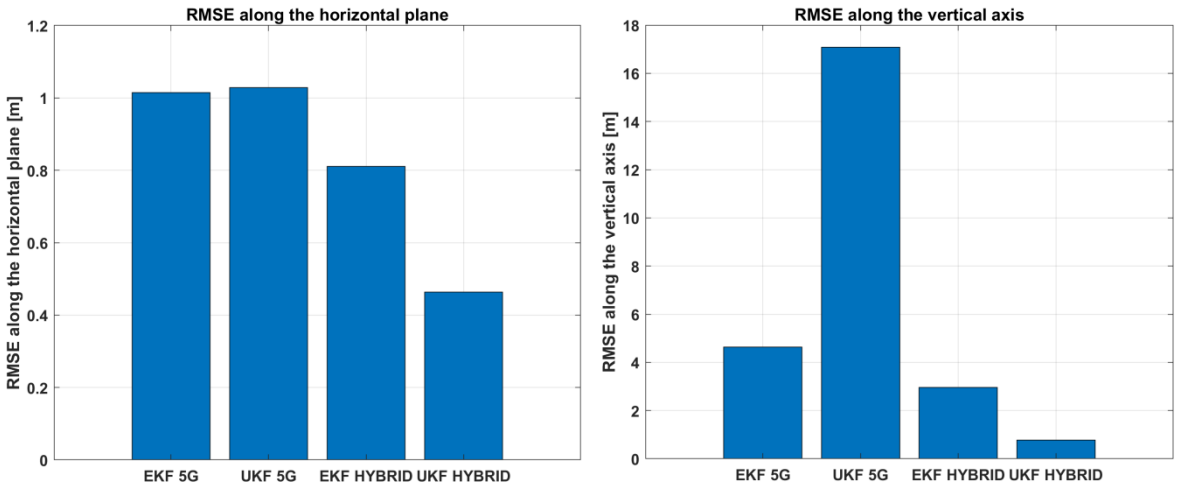

Figure 7.18 – Impact of the navigation filters used over the optimal solution

In conclusion, in this section it has been shown that it is possible to use the global trajectory characterization without degrading the navigation solution. In order to use a trajectory-dependent characterization it is required to determine at each instant and for each BS what is the correspondent trajectory and apply the required characterization. It has also been shown that the performances are better assuming an over bounding characterization using a 99.9% confidence bound. The synchronization module must use a 1 Hz DLL loop bandwidth and a FLL. Finally, the use of the hybrid navigation solution is recommended compared to the 5G standalone navigation solution; the use of the UKF is recommended compared to the EKF.

7.3.2.2. Impact of the propagation channel

This last section is dedicated to the study of the impact of the propagation channel on the navigation performance. In order to lead the study, Table 7.18 and Table 7.19 are provided. Table 7.18 presents the navigation filters RMSE in AWGN case. Table 7.19 presents the navigation filters RMSE in LOS case for a 10 Hz DLL loop bandwidth; note that the EKF GNSS presented in Table 7.19 assumed a complete propagation channel. According to the previous study, Table 7.17 is used to study the impact of the 5G complete channel. Figure 7.19 and Figure 7.20 illustrates these 3 cases.

First it can be seen that the difference between the LOS and the AWGN cases is really small compared to the impact of the complete propagation channel. The multipath component largely degrades the positioning performances along the vertical axis for the 5G standalone navigation filters; the error is increased from several meters.

Second, it can be seen from the horizontal plane RMSE that the hybrid navigation solutions outperform the standalone navigation solutions; an expected results since more measurements are used.

Table 7.18 – Case 1 – AWGN

	X	Y	Z	X^2+Y^2
EKF GNSS	0.37	0.46	0.76	0.59
EKF 5G	0.06	0.27	0.04	0.28
UKF 5G	0.007	0.007	0.07	0.01
EKF HYBRID	0.04	0.03	0.28	0.05
UKF HYBRID	0.06	0.27	0.29	0.28

Table 7.19 – Case 2: LOS-OB-99.9-GI-10Hz

	X	Y	Z	X^2+Y^2
EKF GNSS	0.47	1.10	2.66	1.20
EKF 5G	0.07	0.27	0.23	0.28
UKF 5G	0.04	0.05	0.25	0.06
EKF HYBRID	0.12	0.09	0.44	0.15
UKF HYBRID	0.11	0.27	0.51	0.29

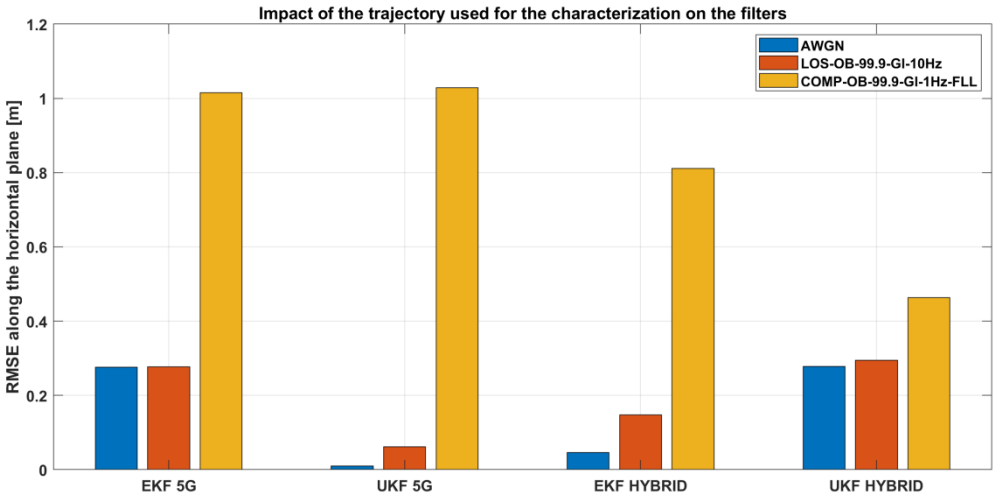

Figure 7.19 – Propagation channel impact – horizontal plane

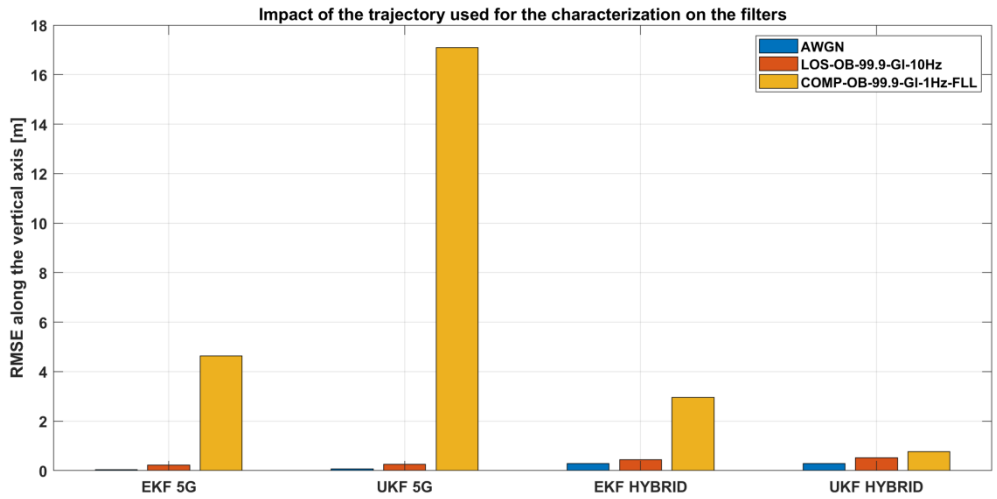

Figure 7.20 – Propagation channel impact – horizontal plane

7.3.2.3. Impact of the measurement error characterization

All along chapter 6, different methods have been defined in order to accurately approximate the true PDF of the pseudo range measurement errors by a Gaussian distribution. The objective of the chapter is to determine whether an accurate approximation permits to improve the KF performances or not.

In order to determine this, the optimal tuning determined in section 7.4.2 will be compared to a constant covariance case.

The optimal tuning corresponds to case 21 "COMP-OB-99.9-Gl-1Hz-FLL"; or in other words it corresponds to the approximation obtained by applying the 99.9% over bounding method for the Global trajectory. The DLL is a 1 Hz DLL loop bandwidth and the FLL is implemented. Results for this optimal case are provided in Table 7.17.

The constant covariance case also uses a 1 Hz DLL loop bandwidth and the FLL; however, the definition of the measurement noise covariance matrix does not depend on the approximation performed in chapter 6 but rather is composed of a constant value, independently from the C/N_0. In order to define the measurement noise covariance value used, the σ-values obtained in chapter 6 for the 1 Hz DLL loop bandwidth 99.9% over bounding case (Table 4) are averaged. Therefore, in the constant covariance case, the measurement noise covariance matrix is a diagonal matrix where all the diagonal terms are equal to $\sigma_{averaged} = 6.6\ m$. Results for this constant covariance case are provided in Table 7.20.

Table 7.20 – Impact of an accurate pseudo range error characterization

	X	Y	Z	X^2+Y^2
EKF GNSS	0.47	1.10	2.66	1.20
EKF 5G	0.75	0.92	5.81	1.19
UKF 5G	0.78	0.88	20.28	1.17
EKF HYBRID	0.64	0.64	3.50	0.91
UKF HYBRID	0.26	0.39	0.72	0.47

In order to compare Table 7.17 and Table 7.20, Figure 7.22 and Figure 7.21 are provided. In Figure 7.22, the RMSEs along the vertical axis for all 4 navigation filters are provided. In Figure 7.21, the RMSEs along the horizontal plane for all 4 navigation filters are provided.

Regarding the 5G standalone navigation solution, it can be observed that an accurate approximation of the pseudo range measurement errors improves the performances of the navigation filters by about 20 cm along the horizontal plane.

The improvement is less important for hybrid navigation solution, around 10 cm; this can be due to the fact that more measurements are available and therefore the filters performances are improved.

These results have to be balance with regards to section 7.3.1.1., which states that the use of a trajectory dependent approximation, assuming that at each instant and for each BS the appropriate type of trajectory is associated to the required approximation, could provide better results.

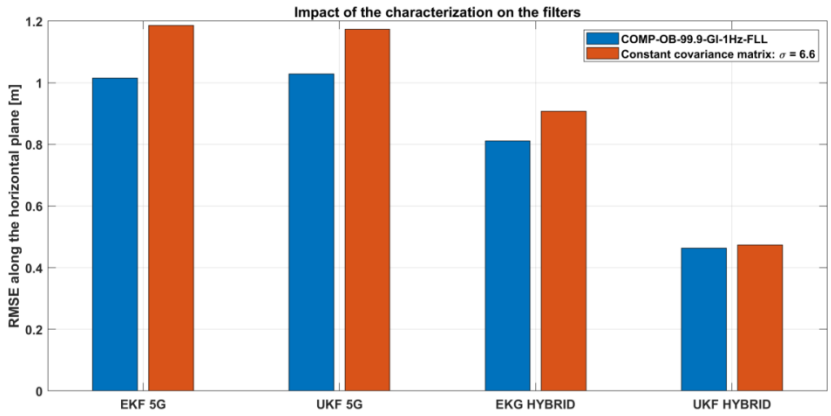

Figure 7.21 – Comparison of filters performance – characterization impact – RMSE along the horizontal plane

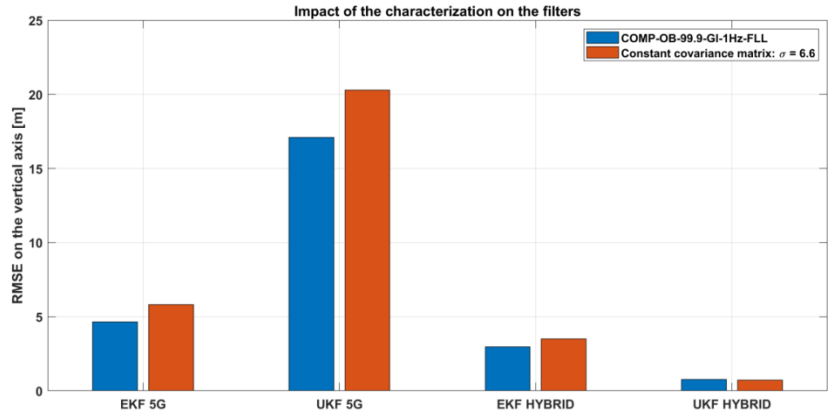

Figure 7.22 – Comparison of filters performance – characterization impact – RMSE along the vertical axis

7.3.2.4. Impact of the C/N_0 estimator

In chapter 5 section 5.3.2, C/N_0 estimators have been designed and studied. Remind that the C/N_0 is typically used as a lock detector, but the C/N_0 is also used as the parameter which determines the pseudo range measurements error standard deviation to be used at each instant of time in the navigation solution filter.

In chapter 6 and in all the navigation solutions cases tested and presented until now it has been assumed that the tracking conditions and the pseudo range measurements error standard deviation are determined by using the true C/N_0 as defined in (5.62). This section aims at determining the performances of the navigation filters assuming an estimated C/N_0.

More specifically, in chapter 5 section 5.3.2.3.2, 2 evolution of the NWPR C/N_0 estimator have been proposed:

- The arctangent NWPR C/N_0 phase-corrected estimator
- The FLL driven NWPR C/N_0 phase corrected estimator

In chapter 5 section 5.3.2, it has been shown that no C/N_0 estimators perfectly estimates the C/N_0 higher than 95 dBHz. Nevertheless this issues can be overcome by assuming that for C/N_0 higher than 95

dBHz, the σ-values required to approximate the distribution are constant to the σ-value obtained for $C/N_0 = 95\ dBHz$.

Therefore, in this section the performances of the navigation filters are studied depending on the C/N_0 used. More specifically 3 cases are compared:

1. The optimal tuning: the optimal tuning corresponds to case 21 "COMP-OB-99.9-Gl-1Hz-FLL"; or in other words it corresponds to the approximation obtained by applying the 99.9% over bounding method for the Global trajectory. The DLL is a 1 Hz DLL loop bandwidth and the FLL is implemented. The true C/N_0 is used. Results for this optimal case are provided in Table 7.17.
2. The arctangent NWPR C/N_0 phase-corrected estimator: in this case the DLL is a 1 Hz DLL loop bandwidth and no FLL is implemented. The pseudo range measurement errors approximation considered corresponds to the one obtained by applying the 99.9% over bounding method for the Global trajectory. The C/N_0 used is estimated by the phase corrected NWPR C/N_0 estimator. Results for this case are provided in Table 7.21.
3. The FLL driven NWPR C/N_0 phase corrected estimator: in this case the DLL is a 1 Hz DLL loop bandwidth and the FLL is implemented. The pseudo range measurement errors approximation considered corresponds to the one obtained by applying the 99.9% over bounding method for the Global trajectory. The C/N_0 used is estimated by the NWPR C/N_0 estimator. Results for this optimal case are provided in Table 7.22.

In order to compare Table 7.17, Table 7.21 and Table 7.22, Figure 7.23 and Figure 7.24 are provided. In Figure 7.24, the RMSEs along the vertical axis for all 4 navigation filters are provided. In Figure 7.23, the RMSEs along the horizontal plane for all 4 navigation filters are provided.

As it can be observed from the two figures, the performances obtained by using the true C/N_0 are better than those obtained by the estimated C/N_0. The estimated C/N_0, due to estimation errors, are mostly lower than the true C/N_0 and consequently the associated pseudo range measurements error standard deviation is higher (remind that the pseudo range measurements error standard deviation increases as the C/N_0 decreases).

It can also be observed that the performances obtained by using the FLL-driven NWPR C/N_0 phase-corrected estimator are better than the performances obtained by using the arctangent NWPR C/N_0 phase corrected estimator.

Finally, the 5G standalone navigation solutions are degraded by approximately 30 cm with the use of the FLL-driven NWPR C/N_0 phase corrected estimator and by approximately 1.30 m with the use of the arctangent NWPR C/N_0 phase corrected estimator along the horizontal plane.

The hybrid navigation solutions are degraded by less than 10 cm with the use of the FLL driven NWPR C/N_0 phase corrected estimator and by approximately 40 cm with the use of the arctangent NWPR C/N_0 phase corrected estimator along the horizontal plane.

Note that the degradation, due to an estimation error of the C/N_0, suppresses the improvement brought by the accurate characterization as shown with section 7.3.2.3. This study has shown the necessity to have a precise C/N_0 estimator. Nevertheless, it can also be said that for hybrid navigation solution the use of the FLL driven NWPR C/N_0 phase-corrected estimator can provide acceptable performances.

Table 7.21 – Phase corrected C/N_0 estimator

	X	Y	Z	X²+Y²
EKF GNSS	0.47	1.10	2.66	1.20
EKF 5G	1.98	1.25	15.97	2.34
UKF 5G	2.00	1.23	22.09	2.35
EKF HYBRID	1.18	0.95	4.06	1.52
UKF HYBRID	0.51	0.69	1.52	0.86

Table 7.22 – FLL C/N_0 estimator

	X	Y	Z	X²+Y²
EKF GNSS	0.47	1.10	2.66	1.20
EKF 5G	0.89	1.05	9.28	1.38
UKF 5G	0.88	0.95	23.13	1.29
EKF HYBRID	0.64	0.64	2.96	0.91
UKF HYBRID	0.32	0.39	0.93	0.51

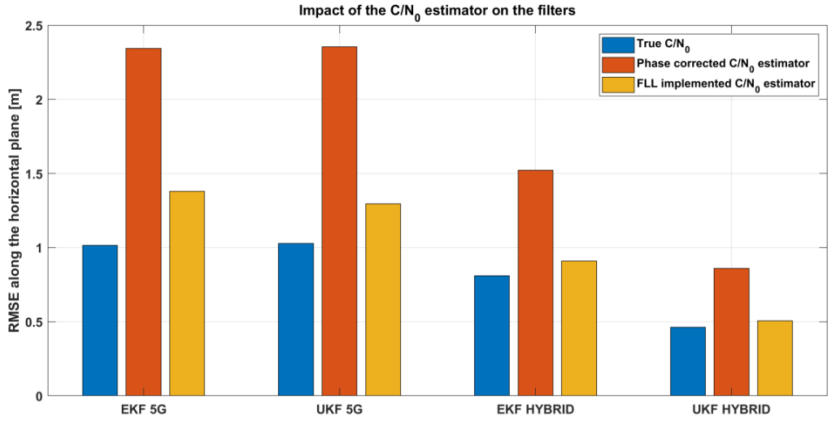

Figure 7.23 – Comparison of filters performance – C/N_0 estimator impact – RMSE along the horizontal plane

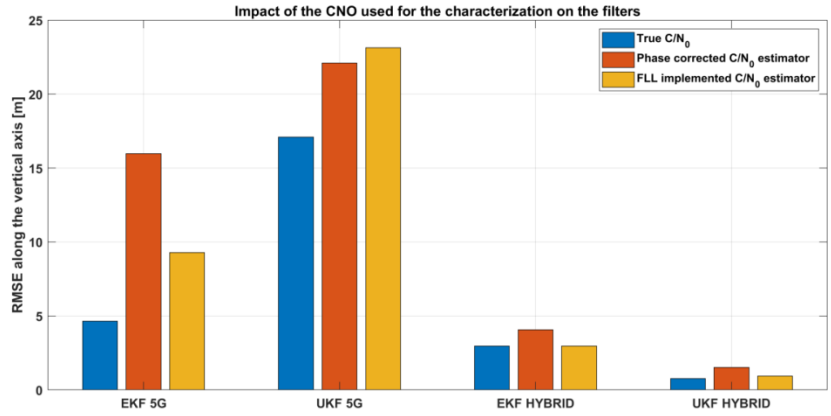

Figure 7.24 – Comparison of filters performance – C/N_0 estimator impact – RMSE along the vertical axis

7.4. Chapter conclusions

The objectives of the chapter are to design 5G-GNSS hybrid navigation filters and to provide recommendations regarding the best tuning for the filters.

In the first section the navigation filters envisioned in the thesis for the hybridization of 5G and GNSS measurements have been theoretically presented. Basically, two navigation filters have been studied. First, the Extended Kalman filters is detailed, and second the Unscented Kalman filters (UKF), a filter that could outperform the EKF is detailed.

In order to study the impact of the propagation channel and to design the more performant navigation filter several test configurations have been identified in section 7.2. These configurations depend on:

- The propagation channel: 3 cases have been identified, the AWGN case which represents the ideal or reference case. The LOS case, only the LOS path is used of the 5G generated propagation channel from QuaDRiGa, this case is also a reference against which the influence of the multipath

components can be compared. Finally, the COMP case, where the propagation channel is composed of LOS and multipath, which permits to study the impact of the multipath.

- The pseudo range measurement error characterization: in chapter 6, the pseudo range measurement error characterization has been defined according to several parameters:
    - The method. Two methods have been derived an over bounding and a fitting method
    - The confidence bound. Three confidence bounds have been detailed: 99.9%, 99% and 95%
    - The trajectory. The characterization has been designed as trajectory-dependent. More specifically, 3 trajectories have been designed in Chapter 6: circular, radial and chord. A global trajectory characterization has also been designed by gathering all previous three trajectories.

  Therefore, these three parameters have been studied in order to provide further recommendations
- the 5G synchronization module design: the 5G synchronization module defined in Chapter 5 uses a DLL and leave the possibility to use a FLL. Moreover, 2 DLL loop bandwidths have been identified to be studied: 1 Hz or 10 Hz DLL loop bandwidth. Therefore, configurations have been defined in order to determine whether a FLL improves the performances of the navigation filters or not and to determine which DLL loop bandwidth uses.
- The navigation filters: the configurations depend on the filter itself (EKF or UKF) and on the measurements used (standalone or hybrid)

Section 2 precisely describes all the configurations tested in the section 4.

Section 3 presents all the results obtained; these results have been split into 2 sections: first the determination of the optimal EKF and UKF tuning and second the study of the impact of the propagation channel.

The impact of several parameters has been studied in order to design the optimal EKF and UKF tuning. The following recommendations can be made:

- The characterizations proposed in Chapter 6 are trajectory-dependent; more specifically, 3 trajectories have been considered: circular, radial and chord. By comparing the performances obtained for each trajectory and for the global characterization, it is difficult to clearly state the impact of the trajectory used for the characterization on the navigation filter performances. Therefore, the global characterization is used without degrading a-priori the performances of the navigation filters. In order to clearly state the impact of the trajectory used for the characterization on the navigation solution, a solution could be to determine, at each instant and for each BS, the appropriate type of trajectory and associate the required characterization.
- The characterization proposed in Chapter 6 are made for 3 confidence bounds; the comparison made on section 7.4.2.2 has shown that better performances are obtained for a 99.9% confidence bound
- Two characterization methods have been proposed in Chapter 6; according to the results propose in section 7.4.2.3, the over bounding method is recommended.
- The synchronization module design has also been carefully studied. It has been shown that a 1 Hz DLL loop bandwidth is recommended with respect to the 10 Hz DLL loop bandwidth. Moreover, the use of the FLL improves the navigation filter performances.
- Regarding the impact of the navigation filters, first of all, the use of 5G measurements is highly recommended in constrained environment when there is a lack of GNSS measurements. Second,

if some GNSS measurements are available, a hybrid navigation solution is recommended since better performances, especially in the Z axis, can be expected. Finally, the UKF is recommended with respect to the EKF.

- The approximations performed in chapter 6 permit to improve the navigation filter performances with respect to a constant covariance characterization.
- The use of an estimated C/N_0 degrades the performances of the navigation filters with respect to the use of the true C/N_0. However, the use of the NWPR C/N_0 estimator with FLL permits to obtain satisfying results.
- KF filters outperform the 2D WLS filter

Assuming the above recommended tuning, the best performance among the simulated cases has a horizontal RMS of 58 cm.

Chapter 8. Conclusion

This chapter summarizes the main conclusions of the work conducted in this dissertation and provides several recommendations for future research in this field.

8.1. Conclusions

The work performed in this thesis is developed in the context of an urban positioning service based on the use of GNSS in urban environment. It has been reminded the challenges for GNSS in this urban environment. The multipath and direct signal blockage significantly affect the signal availability and its processing, and thus introduce great errors in the pseudo range and carrier measurements that further degrade the position accuracy and availability. In the worst case scenario, there might even be not enough measurements to compute a position. In order to overcome these issues, in the thesis, the use of a Signal of Opportunity is studied to improve the GNSS-based service. More specifically, the focus is on the use of 5G telecommunication signals since 5G system is a new and promising technology. A 5G ranging technique and its performance characterization in urban environment has been analyzed, as well as the impact of combining GNSS and 5G pseudo range measurements on a navigation filter performances.

The overall objective of the thesis is the design and performance characterization of a hybrid 5G and GNSS positioning receiver architecture.

Chapter 2 has provided a global overview of GNSS systems and has presented the signal processing techniques adopted in the receiver in order to obtain the required measurements. To achieve these objectives, the definition of the GNSS systems has been provided. As presented, there is a wide variety of GNSS systems, since the Ph.D. emphasis on 2 particular signals: GPS L1 C/A and Galileo E1 OS, only the description of these 2 signals have been provided. Before being processed by the user, the transmitted signal is disturbed by several sorts of interferences. These interferences have been modelled, in order to analyse the received signals, thanks to the definition of a propagation channel model. For the purpose of the thesis, the SCHUN propagation channel has been selected. SCHUN is a hybrid deterministic-statistical LMS propagation channel; the implementation of the statistical and deterministic modules optimizes the trade-off between accuracy and computational resource. The signal is then processed by the receiver, which has been presented. The main 3 signal processing functions of the receiver are based on the correlation operation: the acquisition, the tracking and the demodulation. The correlation aims to locally generate a replica perfectly synchronized with the incoming signal. Finally, the receiver provides pseudo range measurements which have been presented and used to allow the user to calculate its PVT solution. Then, a special care has been taken for a non-open sky environment since the conditions, with respect to an open sky, can be highly degraded.

Chapter 3 aims to provide a global overview of 5G systems and to present the signal processing techniques adopted in the receiver in order to obtain the required measurements when the 5G signal is transmitted through an AWGN channel. The chapter has provided a thorough description of the 5G systems. Since 5G is an emerging technology, the 5G systems history has been given as well as the envisioned use cases. Three radio-based positioning methods have been presented in the chapter: the signal strength based method, the Angle of Arrival method and the Time of Arrival method. The first two have not been selected for the Ph.D.; therefore the rest of the Ph.D. will be based on ToA measurements. The signal transmitted by 5G BS has been precisely described. In order to determine the most optimal signal processing techniques, it is of the utmost importance to precisely know the mathematical model of the received signal. And the received signal can be modelled from the transmission of the generated

signal through the propagation channel; therefore, the propagation channel should be carefully modelled in order to have a realistic mathematical model of the received signal. For realism purposes, a deep state of the art has been performed in order to identify the potential propagation channel projects that could be used for the Ph.D. The study has permitted to identify a 5G compliant and an easy-to-use propagation channel. QuaDRiGa, an open-source simulator following the 3GPP standard, [43], has been selected. It fulfills the 5G propagation channel requirements; moreover, it is a GSCM, thus proposes a fair trade between complexity and realism.

Then a description of the main techniques for ToA measurements on OFDM signals has been provided; more specifically, the ToA measurements are obtained at the output of a DLL, which uses correlator output. The correlation operation proposed is based on pilots signals present in the 5G frame; the focus has been made on the 5G synchronization signal SSPBCH. The envisioned 5G ranging module has been presented with a particular application for an AWGN case. Finally, the pseudo range model in AWGN channel has been derived. This model will be completed in later chapter with the impact of the multipaths.

The OFDM signal-type correlator output mathematical model presented in chapter 3 is derived by assuming a constant propagation channel over the duration of the correlation (which is performed over one OFDM symbol). Nevertheless, **Chapter 4** has shown that the CIR of a 5G signal propagation channel (QuaDRiGa) cannot be considered as constant over the duration of the correlation (channel coherence time of the CIR complex amplitude is smaller than the duration of the correlation) : the expected correlator output of a 5G signal is thus different between a time-evolving propagation channel and a constant one over the duration of an OFDM symbol. The ultimate goal of **Chapter 4** was thus to precisely derive the correlator output mathematical model of a 5G signal for ranging purposes; in other words, to improve the model presented in chapter 3. In order to derive this precise and realistic correlator output mathematical model, it is of the utmost importance to first precisely model the received 5G signal and, by extension, the interferences distorting the signal introduced by the propagation channel with as much realism as possible; or in other words, the CIR. Therefore, the method followed in **Chapter 4** is divided in two: the first step is the CIR characterization which has permitted to accurately model the propagation channel, the second step is the derivation of the correlator output mathematical model. The first step has permitted to conclude that the CIR-generation sampling rate required to simulate a realistic propagation channel by limiting as much as possible the generator computational burden / mathematical model is equal to 10CIR per OFDM symbol for the signal conditions considered relevant in the analysis of this work. The second step has permitted to provide the final correlator output mathematical model used in the Ph.D. This model is composed of the noiseless useful part for which a simplified model can be applied and an additive Gaussian variable. The Gaussian variables includes the noise and interference terms and can be seen as an enhanced noise power and thus as a potential decrease of the available SNR or C/N_0.

The aim of **Chapter 5** was to present the synchronization module proposed and implemented in the Ph.D. This synchronization module is basically composed of a DLL, a carrier frequency estimator and a C/N_0 estimator (and a tracking lock detector simply based on the C/N0 estimation compared to a threshold). The implemented Delay tracking loop has been carefully presented; its architecture and performances are detailed. An EMLP discriminator output is used in the DLL, its normalization factor as well as its linearity region have been precisely studied: the one-sided discriminator linearity zone is $D_{th} = 7/4$ samples. The performance of the DLL estimation error standard deviation in an AWGN channel using the correlator output mathematical models derived in Chapter 4 have been validated in simulation: as an example, the variance of the tracking error estimate for a $SNR_{demod} = 0\ dB$ equals $2.6 \cdot 10^{-4}\ m$. An analysis on the necessity of implementing a carrier frequency estimator is also conducted in the second section. It has

been theoretically proved and through simulations that the implementation of a carrier tracking loop, a FLL, does not improve the tracking performances of the ranging module for an AWGN. The principle used to theoretically prove this statement consists in studying the degradation caused by a frequency estimation error on the time delay estimation conducted by the DLL. More specifically, the method adopted to determine the necessity to implement a carrier frequency estimator consists in deriving the degradation of the time delay estimation performance as a function of the Signal to Noise Ratio (SNR) and the Carrier Frequency Offset (CFO). In order to determined realistic values of the degradation, realistic SNR and Doppler variation values have been determined. According to this, the SNR degradation caused by the CFO has been studied, followed by the theoretical degradation on the code delay estimation due to CFO. Finally, the theoretical derivation has been validated through simulations. Simulations assuming an AWGN channel have permitted to validate the theoretical degradation on the code delay estimation due to CFO; and has confirmed the non-necessity of the implementation of a FLL. These simulations have been made assuming 3 configurations defined to represent realistic and generic 5G signal configurations. They have shown that for $SNR_{correlator} < 105\ dB$, the degradation due to a fractional CFO is lower than 0.5 dB and that the standard deviation of the tracking error estimate is of the order of the millimeters. Additional simulations have been proposed for a complete channel in order to study the impact of the multipath degradation. These simulations have shown that when a complete propagation channel is considered (LOS+multipath), for a 1 Hz DLL loop bandwidth, the tracking performances are improved when the FLL is implemented. However, no improvements are observed for a 10 Hz DLL loop bandwidth. The objective of the third section was to implement a C/N_0 estimator. The Narrow-to-Wideband-Power-Ratio- C/N_0 estimator tested has highlighted some limits for C/N_0 higher than 60 dBHz. More accurately, a saturation phenomenon is observed, and it is linked to the phase evolution between symbols of the propagation channel contribution term to the correlator outputs mathematical model. If there is no phase evolution (AWGN case), the saturation appears for C/N_0 higher than 120 dBHz; if the phase evolution is the highest (radial trajectory), the saturation appears for C/N_0 higher than 60 dBHz. Three solutions were tested to overcome this saturation phenomenon: the Method-of-Moments-C/N_0 estimator (again, limits have been identified for $C/N_0 > 60\ dBHz$) and two evolutions of two evolutions of the NWPR (Arctangent NWPR C/N_0 phase-corrected estimator and FLL-driven NWPR C/N_0 phase-corrected estimator). Last 2 estimators are more performing than the NWPR estimator but they still present limitations for $C/N_0 > 95 dBHz$. There is no difference between the two NWPR C/N_0 phase-corrected estimators. Finally, it can be said that even if a FLL does not improve much the tracking performances, for a 10 Hz DLL loop bandwidth, it could permit a better estimation of the C/N_0. Therefore, the FLL will be kept for the rest of the Ph.D.

In **Chapter 6**, the derivation of a Gaussian distribution for the pseudo range measurement error component of the noise plus the multipath (joint modelling) has been performed for both 5G and GNSS signals. A preliminary step conducted on this chapter has consisted in the precise derivation of the pseudo range measurement models. Since 3 systems are considered in the thesis it is of the utmost importance to define each of them into the same reference time frame; therefore, this time frame synchronization has been precisely studied.

Then the derivation method has been proposed in this chapter and is divided in two steps:

1. The characterization of the pseudo range measurement error, or in other word, to obtain the true PDF distribution of the errors, which is based on the analysis of tracking loops results using the correlator output models described in chapter 4 and using the propagation channel simulators SCHUN for GNSS and QuaDRiGa for 5G.

2. The approximation of the true distribution by a Gaussian distribution. In order to define the approximating distribution by Gaussian distribution, only two parameters have to be defined: the mean and the variance. Regarding the mean, three means have been considered: $\mu = 0$, $\mu = mean$ and $\mu = index$, where $index$ corresponds to the maximum of the characterized PDF. Three confidence bounds have been considered 99.9%, 99% and 95%. Finally, two approximation methods have been derived, namely a Gaussian over bounding and a Gaussian fitting method, parametrized by the amount of the actual simulated pseudo range error taken into account (95%, 99% and 99.9%) for the characterization.

In order to have statistically significant results, a high number of random drawings of the propagation channels and receiver noise were tested, using a Monte-Carlo approach. The study has shown that for QuaDRiGa and for SCHUN, the assumption on the mean of the Gaussian distribution has a negligible influence for LOS scenario. It is proposed to assume a centered Gaussian distribution ($\mu = 0$). Moreover, the standard deviation of the Gaussian distribution depends on the C/N_0, which was expected. The derivation of the Gaussian distributions for a QuaDRiGa channel has been made assuming a LOS sub-6 Ghz high level scenario, the derivation has been proposed for three independent trajectories and for all three trajectories gathered. A 2nd order DLL has been used for 2 DLL loop bandwidth (10 Hz and 1 Hz). This derivation has shown:

- The standard deviation of the Gaussian distribution depends on the type of trajectory. 3 types of trajectory were tested (radial, chord, circular), and led to sensibly different results, which was not expected. The final characterization does not keep this dependency and mixes the results from the 3 trajectory types. This dependency on the trajectory can be a potential future work.
- The receiver tracking parameter (mainly DLL bandwidth) has a slight impact. As expected, the lower the DLL bandwidth, the better accuracy.
- The fitting and the over bounding methodologies yield very different results, as expected. The recommendation between both methodologies will be given in Chapter 7.
- The distributions are not Gaussian, especially for 5G at low C/N_0, where the distribution tail for positive errors is larger (positively skewed).

The derivation of the Gaussian distributions for a SCHUN channel has been made assuming a LOS conditions. It has been made independently from the elevation and azimuth of the satellite. A first order Delay Lock Loop has been used assuming an Early Minus Late Power discriminator with a 0.5 correlator spacing. The Phase Lock Loop used is a 3rd order Costas Loop. The pseudo ranges are generated assuming a BPSK modulation (GPS L1 C/A modulation) therefore the obtain results has served as over bounding for the Galileo signals since Galileo uses a BOC modulation assumed to be more robust in multipath environment. The derivation has shown that:

- A slight increase of the variances can be observed as the C/N_0 decreases
- The distributions for $C/N_0 > 35\ dBHz$ are Gaussian

In **Chapter 7**, two navigation filters have been derived: an Extended Kalman Filter and an Unscented Kalman Filter. Simulations have permitted to provide several recommendations. First, the use of 5G measurements is highly recommended in constrained environment when there is a lack of GNSS measurements. If some GNSS measurements are available, a hybrid navigation solution is recommended since better performances, especially in the Z axis, can be expected. The tuning of the 5G ranging module is important, according to the study a 1 Hz DLL loop bandwidth is recommended. The pseudo range

characterization has also a great importance and for the application the over bounding method provides better performances. Finally, the UKF is recommended with respect to the EKF.

Overall, the combination of a ranging module with a GNSS receiver brings an improvement of 45% on the position accuracy, compared to a GNSS only solution for an UKF navigation filter.

8.2. Main achievements

The main achievements of this Ph.D. studied are listed below:

- A description of the 5G physical layer, and notably the Synchronization Signal sent in the Physical Broadcast Channel (SS PBCH) (Chapter 3)
- The selection and mathematical model definition of a 5G compliant propagation channel. QuaDRiGa has been selected, studies have proved that the propagation channel cannot be considered as constant over the duration of the correction; therefore, methods have been designed to study these evolving parameters and to select the required propagation channel sampling rate generation.
- The development of mathematical models of 5G correlator outputs, taking into account the effects of non-constant propagation channel parameters, noise. (chapters 3,4)
- The proposition of a simplified model of 5G correlator outputs, which is valid in a LOS scenario for sub-6 GHz carrier frequency (chapter 4)
- The proposition of a statistical model for the interference term, which can be generate as a Gaussian variable with a mean and a variance derived in the study (chapter 4)
- The proposal of a ranging module composed of a DLL and proposing the use of a FLL for particular cases.
- A synchronization module based on a DLL and on a potential FLL has been derived. The FLL can improve the navigation solution for a 1 Hz DLL loop bandwidth but is not required. The synchronization module also implements a C/N_0 estimator.
- The development of a simulator, coded in C, providing ranging measurements from GNSS and 5G tracking loops, taking into account simulated multipath propagation channels
- The development of methods to characterize GNSS and 5G ranging measurement errors in urban environment. Methods have been proposed to generate realistic (regarding the carrier frequency adopted) and diverse (in terms of trajectories) scenarios so that the characterization obtained are as generic as possible.
- The proposition of Gaussian modeling of ranging measurements as a function of C/N_0
- The study of simulated positioning performances using different navigation filters (WLS, EKF, UKF) and various parameters. The parameters studied are:
    - the impact of the pseudo range measurement error characterization method adopted: the over bounding seems better performant than the fitting method
    - the impact of the confidence bound used for the pseudo range measurement error characterization: a 99.9% confidence bound provides better performance
    - the impact of the DLL loop bandwidth: a 1 Hz DLL loop bandwidth seems more performant.
- The work has been published in 2 conference papers:
    - ”Hybrid Navigation Filters Performances Between GPS, Galileo and 5G TOA Measurements in Multipath Environment” September, 23rd 2020 in the Session D1: Alternative Technologies for GNSS-Denied Environments 1 at ION GNSS + virtual conference, Anne-Marie TOBIE (TéSA), Axel GARCIA-PENA (ENAC), Paul THEVENON (ENAC), Marion AUBAULT (CNES), François Xavier MARMET (CNES)

- "Processed 5G Signals Mathematical Models for Positioning considering a Non-Constant Propagation Channel" Anne-Marie TOBIE (TéSA), Axel GARCIA-PENA (ENAC), Paul THEVENON (ENAC), Marion AUBAULT (CNES) – International Workshop on Reliable Ubiquitous Navigation in Smart Cities - co-located with the IEEE Vehicular Technology Conference (IEEE VTC-Fall 2019).

8.3. Perspectives

Starting from the research made in this Ph.D., further studies can be conducted on the correlator output mathematical model, on the pseudo range error characterization and on the positioning.

- Real data collect

In the Ph.D., the performance assessment of the proposed hybrid architecture was conducted in a simulated urban environment and for a simplified 5G signals. This offered the possibility to test and to analyze in detail the derived mathematical models. However, the use of real data would allow further tests crucial to finally validate the architecture and conclusions made on the thesis.

- Correlator output mathematical model

In the thesis, a propagation channel LOS scenario using a carrier frequency set to 2GHz is considered. The studies have proved that for this type of scenario, the interference term of the correlator output mathematical model can be neglected. Nevertheless, this is probably not the case for NLOS scenario. In the NLOS scenario, the pseudo range measurements quality will be degraded and consequently, the positioning solution obtained will be less accurate.

- Pseudo range error characterization

In the thesis the pseudo range error characterization has been made for the LOS scenario at 2 GHz. Nevertheless, in harsh urban environment, it would be interesting to derive the characterization for the NLOS scenario. As stated just before, in order to study the NLOS scenario, the interference term in the correlator output mathematical model must be included. Thus a first step would be the derivation, through simulations, of the statistics of the interference term. Then the method already derived in the thesis can be used to derive the characterization.

Since 5G systems will also use millimeter waves, the characterization should also be made for these frequencies. The propagation properties of mmW is highly different from the propagation in sub-6 GHz frequencies, the consequences on the pseudo range error distributions are probably different. Here again, the statistics of the interference term should be studied to correctly model the correlator outputs.

- Navigation solution

In the thesis, two Kalman filters have been derived. As stated, Kalman filters assume that these errors follow a Gaussian distribution; an assumption that may be too restrictive in urban environments. Indeed, for the LOS scenario in chapter 6 it has been shown that the errors distributions are not Gaussian, the positive tails are much larger. It could be interesting to find a more appropriate distribution to be used in more evolved navigation filters.

The development of other filters, such as Particle Filters (PF), could now be implemented. The main advantage of PF is that they do not rely on a Gaussian PDF approximation contrary to Kalman Filters; an a-priori information on the distributions must be provided, and such information has been derived in this study. Thus, by taking into account the true distribution for the PF better navigation filters performances could be obtained. Nevertheless, the complexity of such implementation will be higher.

Bibliography

[1] D. Serant, D. Kubrak, M. Monnerat, G. Artaud et L. Ries, «Field test performance assessment of GNSS/INS ultra-tight coupling scheme targeted to mass-market applications,» chez *2012 6th ESA Workshop on Satellite Navigation Technologies (Navitec 2012) & European Workshop on GNSS Signals and Signal Processing*, 2012.

[2] R. Broquet, N. Perrimon et B. Polle, «HiNAV Inertial/GNSS Hybrid Navigation Dystem for launchers and re-entry vehicles,» chez *2010 5th ESA Workshop on Satellite Navigation Technologies and European Workshop on GNSS Signals and Signal Processing (NAVITEC)*, 2010.

[3] K. Shamaei, J. Khalife et Z. Kassas, «Exploiting LTE Signals for Navigation: Theory to Implementation,» 2018.

[4] C. Mensing, S. Plass et A. Damman, «Synchronization algorithms for Positionning with OFDM Communication Signals,» 2007.

[5] C. Mensing et A. Dammann, « Positioning with OFDM based communications systems and GNSS in critical scenarios,» 2008.

[6] E. Staudinger, C. Klein et S. Sand, «A generic OFDM based TDoA positioing testbed with interference mitigation for subsample delay estimation,» 2011.

[7] P. Thevenon, D. Serant, O. Julien et C. Macabiau, «Positionning using mobile TV based on DVB-SH standard,» *Navigation, Institute of Navigation, 2011,58 (2), pp 71-90. ,* 2011.

[8] D. Serant, P. Thevenon, O. Julien et C. Macabiau, «Development and validation of an OFDM/DVB-T sensor for positioning,» 2010.

[9] J. Talvitie, M. Koivisto, T. Levanan, M. Valkama, G. Destino et H. Wymeersch, «High-Accuracy Joint Position and Orientation Estimation in Sparse 5G mmWave channel,» *Proc. IEEE International Conference on Communications (ICC),* 2019.

[10] A.-M. Tobie, A. Garcia-Pena, P. Thevenon et M. Aubault, «Processed 5G Signals Mathematical Models for Positioning considering a Non-Constant Propagation Channel.,» chez *VTC 2019-Fall2019 IEEE 90th Vehicular Technology Conference*, Honolulu, Sep 2019.

[11] 3GPP, «3GPP - The mobile Broadband Standard,» [En ligne]. Available: https://www.3gpp.org/DynaReport/38-series.htm.

[12] J. Del Peral-Rosado, J. Lopez-Salcedo, G. Seco-Granados, F. Zanier et M. Crisci, «Preliminary Analysis of the Positioning Capabilities of the Positioning Reference Signal of 3GPP LTE,» chez *Proceedings 5th Eur. Workshop on GNSS Signals and Signal Processing*, 2011.

[13] E. Kaplan et C. Hegarty, Understanding GPS/GNSS: Principles and Applications, 2107.

[14] 3GPP, «TS 38.211 Physical channels and modulation».

[15] W. J, Y. Z-X, P. C-Y, H. M et Y. L, «A combined code acquisition and symbol timing recovery method for TDS-OFDM,» *IEEE Transactions on Broadcasting,* 2003.

[16] M. Ait Ighil, J. Lemorton et al, «SCHUN - A hybrid and mobil satellite channel simulator enhanced for multipath modelling applied to satellite navigation systems,» *7th European Conference on Antennas and Propagation (EuCAP),* 2013.

[17] S. Jaeckel, L. Raschkowski, K. Börner et L. Thiele, «QuaDRiGa: A 3-D Multicell Channel Model with Time Evolution for Enabling Virtual Field Trials,» *IEEE Transactions on Antennas Propagation,* 2014.

[18] S. Jaeckel, L. Raschkowski et al, «QuaDRiGa: A 3-D Multicell Channel Model with Time Evolution for Enabling Virtual Field Trials,» *IEEE Transactions on Antennas Propagation,* 2014.

[19] «Navipedia,» [En ligne]. Available: https://gssc.esa.int/navipedia/index.php/Main_Page.

[20] I. GPS, «https://www.gps.gov/technical/icwg/,» [En ligne].

[21] I. Galileo, «https://www.gsc-europa.eu/electronic-library/programme-reference-documents,» [En ligne].

[22] M. Ait Ighil, «Ph.D. - Enhanced physical-statistical simulator of the land mobile satellite channel for multipath modelling applied to satellite navigation systems,» 2013.

[23] E. D. Kaplan et C. J. Hegarty, Understanding GPS principles and applications, second edition, 2006.

[24] 5GChampion, «5G Champion,» [En ligne]. Available: http://www.5g-champion.eu/Pages/Project-overview.aspx.

[25] ETSI, «ETSI - 5G standards,» [En ligne]. Available: https://www.etsi.org/technologies/mobile/5g.

[26] ITU, «World Radiocommunication Conference 2019 (WRC-19) Final Acts,» 2020.

[27] 3GPP, «TS 38.101_1 - Version 16.4.0 - NR; User Equipment (UE) radio transmission and reception; Part 1: Range 1 Standalone,» 07-2020.

[28] 3GPP, «TS 38.101_2 - version 16.4.0 - NR; User Equipment (UE) radio transmission and reception; Part 2: Range 2 Standalone,» 07-2020.

[29] ITU, «Setting the scene for 5G: opportunities and challenges,» 2018.

[30] R. W. H. J. a. N. González-Prelcic, «Fundamentals of mmWave Communication,» *Joint IEE and Eurasip summer school on signal processing for 5G wireless access,* 2017.

[31] E. Björnson, «Advanced Signal Processing for Massive MIMO,» *Joint IEEE SPS and EURASIP Summer School on Signal Processing for 5G Wireless Access,* 2017.

[32] S. P. a. J. S. E. Dahlman, 4G - LTE/LTE-advanced for mobile broadband, 2011.

[33] E. G. L. H. Y. a. H. Q. N. T. L. Marzetta, Fundamentals of Massive MIMO, 2016.

[34] L. D. a. J. Choi., «FDD massive MIMO for 5G,» *Joint IEEE and Eurasip summer school on signal*

processing for 5G wireless access, 2017.

[35] TUT, «Positioning and location awarness in future 5G networks,» [En ligne]. Available: http://www.tut.fi/5G/positioning/publications.html.

[36] M. Koivisto, H. Aki, M. Costa et J. Talviti, «Continuous high-acccuracy radio positioning of cars in Ultra Dense 5G Network,» *IEEE International wireless Communications and Mobile Computing Conference,* 2017.

[37] M. Koivisto, M. Costa, J. Werner, K. Heiska et J. Talvitie, «Joint Device Positioning and Clock Synchronization in 5G Ultra Dense Network,» *IEEE Transactions on Wireless Communications,* vol. 16, n° %15, 2017.

[38] M. Koivisto, A. Hakkarainen, M. Costa, K. Leppänen et M. Valkama, «Continuous Device Positioning and Synchronization in 5G Dense Networks with Skewed Clocks,» *IEEE International Workshop onSignal Processing Advances in Wireless Communication,* 2017.

[39] M. Koivisto, M. Costa et A. Hakkarainen, «Joint 3D Positioning and Network Synchronization in 5G Ultra-Dense Networks Using UKF and EKF,» *IEEE International Workshop on Localization and Tracking: Indoors, Outdoors, and Emerging Networks (GLOBECOM Workshops),* 2016.

[40] 3GPP, «TS 38.211 V15.0.0 Physical channel and modulation - Release 15,» 04/2018.

[41] P. Thevenon, S-band air interfaces for navigation systems: a focus on OFDM signals, 2010.

[42] 3GPP, «TS 38.211 Physical channels and modulation,» 2020.

[43] 3GPP, «3GPP TR 38.901 - Study on channel model for frequencies from 0.5 to 100 GHz,» 2017.

[44] 3GPP, «TS. 38.213 Physical layer procedures for control,» 2020.

[45] Fraunhofer Heinrich Hertz Institute, «Quasi Deterministic Radio Channel Generator User Manual and Documentation,» August 2017.

[46] K. M, H. A, C. M, K. P, L. K et V. M, «High-Efficiency Device Positioning and Location-Aware Communications in Dense 5G Networks,» *IEEE Communications Magazine,* vol. 55, n° %18, pp. 188--195, 2017.

[47] C. Mensing et S. Plass, «Positioning Algorithms for Cellular Networks Using TDOA,» chez *IEEE International Conference on Acoustics Speech and Signal Processing Proceedings*, 2006.

[48] J. Van de Beek, M. Sandell et P. Börjesson, «ML estimation of Time and Frequency Offset in OFDM Systems,» 1997.

[49] 3GPP, «TR 38.901 - Study on channel model for frequencies from 0.5 to 100GHz,» 2019.

[50] S. Stephens et J. Thomas, «Controlled-Root Formulation for Digital Phase-Locked Loop,» *IEEE Transactions on Aerospace and Electronic Systems,* 1995.

[51] D. Serant, p. Thevenon et al, «Development and validation of an OFDM/DVB-T sensor for positioning,» chez *IEEE/ION PLANS 2010, Position Location and Navigation Symposium, Indian Wells,*

United States. pp 988-1001, 2010.

[52] M. Morelli, J. Kuo et M. Pun, «Synchronization techniques for orthogonal frequency division multiple access (OFDMA): atutorial review,» *Proceedings of the IEEE,* vol. 95, n° %17, 2007.

[53] 3GPP, «TS 38.104 - Base Station radio transmission and reception - v16.4,» 2020.

[54] B. Parkinson et J. Spilker, Global Positioning System: Theory and Applications - Volume 1, 1996.

[55] M. Petovello, «Are C/N0 algorithms equivalent in all situations?,» *GNSS solution,* 2010.

[56] E. Kaplan et C. Hegarty, Understanding GPS: Principles and applications.

[57] Matlab, «Model data using the distribution fitter app,» [En ligne]. Available: https://www.mathworks.com/help/stats/model-data-using-the-distribution-fitting-tool.html.

[58] Matlab, «Normal Distribution,» [En ligne]. Available: https://www.mathworks.com/help/stats/normal-distribution.html.

[59] Matlab, «Logistic Distribution,» [En ligne]. Available: https://www.mathworks.com/help/stats/logistic-distribution.html.

[60] Matlab, «Kernel distribution,» [En ligne]. Available: https://www.mathworks.com/help/stats/kernel-distribution.html.

[61] H. A, Bayesian estimation and tracking: a practival guide, 2012.

[62] S. J. JULIER et J. K. UHLMANN, «Unscented Filtering and Nonlinear Estimation,» *Proceedings of the IEEE,* vol. 92, n° %13, pp. 401-422, 2004.

[63] G. A. TEREJANU, *Unscented Kalman Filter Tutorial.*

[64] R. Van der Merwe, Sigma point Kalman Filters for Probabilistic Inference in Dynamic State-Space Models, 2004.

[65] E. A. Wan et R. van der Merwe, The unscented Kalman Filter, in Kalman Filtering and Neural Networks (ed S. Haykin), New York, USA: John Wiley & Sons, Inc., 2001.

[66] R. Brown et P. Hwang, «Introduction to Random Signals and Applied Kalman Filtering,» 1996.

[67] O. Julien, «Design of Galileo L1F Receiver Tracking Loops,» 2005.

[68] J. Karedal, F. Tufvesson, N. Czink, J. Karedal, F. Tufvesson, N. Czink, A. Paier, C. Dumard, T. Zemen et C. F. Mecklenbr¨auker, «A Geometry Based Stochastic MIMO models for Vehicle-to-Vehicle communications,» *IEEE TRANSACTIONS ON WIRELESS COMMUNICATIONS, VOL. 8, NO. 7,* JULY 2009.

[69] P. Kyösti, J. Meinilä, L. Hentilä, X. Zhao, T. Jämsä, C. Schneider et M. Narandzić, «WINNER 2 Channel Models - D1.1.2 v1.2,» 2008.

[70] J. Meinilä, P. Kyösti, L. Hentilä, T. Jämsä, E. Suikkanen, E. Kunnari et M. Narandžić, «D5.3: WINNER+ Final Channel Models,» 2010.

[71] 3GPP, «3GPP TR 36.873 - Technical Specification Group Radio Access Network - study on 3D channel model,» 2017.

[72] ITU, «Report ITU-R M.2135-1 - Guideline for evaluation of radio interface technologies for IMT-Advanced,» 2009.

[73] L. Liu, C. Oestges, J. Poutanen, K. Haneda, P. Vainikainen, F. Quitin, F. Tufvesson et P. De Doncker, «The COST 2100 MIMO Channel Model,» 2012.

[74] A. MALTSEV, R. MASLENNIKOV, A. LOMAYEV, A. SEVASTYANOV et A. KHORYAEV, «Statistical Channel Model for 60 GHz WLAN Systems in Conference Room Environment,» *Radioengineering,* pp. 409-422, June 2011.

[75] V. N. (Nokia), A. K. (Aalto), A. R. (UOulu) et L. R. (. HHI), «METIS Channel Models - ICT-317669-METIS/D1.4,» 2015.

[76] A. J. Haug, Bayesian Estimation and Tracking, 2012.

Annexes

Annex A) General presentation of the simulator

In order to characterize the positioning performances of GNSS and 5G signals a simulator of 5G and GNSS signals has been designed. This annex aims at presenting the simulator used to test and validate all models presented until now. In order to do so, first the interest of a simulator is briefly reminded. Second, the process of the simulator is detailed.

A.1) Interest of a simulator

GNSS systems are mature and well known systems; however, 5G technology is being currently standardized and its positioning performance, as well as a potential generic receiver scheme to conduct positioning operations, is still under analysis. Therefore, to study the potential capabilities provided by 5G systems and to develop and to compare 5G, GNSS and hybrid 5G/GNSS signals generic positioning module schemes, one possible way forward consists in developing a controlled 5G and GNSS signals environment for positioning; or in other words, a 5G/GNSS signals positioning simulator. The main advantages of using a simulator instead of real signals are twofold. The first main advantage is the possibility to control the environment and thus to control the exact impairments the 5G and GNSS signals positioning module will have to overcome. The second main advantage is the possibility to control and to completely monitor the behavior of the implemented signal processing and positioning algorithms. However, the use of a simulator also entails some constraints: this controlled environment must be realistic enough in terms of 5G and GNSS simulated signals, which must be in accordance with the standards, and realistic enough in terms of propagation channel model; the simulated propagation channel must fulfil the 5G standard requirements defined in the 3GPP standards and the GNSS standards. One additional advantage of a simulator with respect to the process of real signals is the simplification or, directly, the removal of some signal processing stages if their output mathematical model is well characterized: instead of simulating the behavior of the signal processing stage, the output can be directly generated from its mathematical model.

A.2) Simulator architecture

The implemented simulator can be split into 3 modules as illustrated in Figure Annex 1

- A GNSS module named GeneIQ in Figure Annex 1
- A 5G module
- A navigation module

The implemented simulator generates 5G and GNSS correlator outputs in multipath environments from their mathematical models, reminded in chapter 4 and derived in [10] for 5G systems and in [11] for GNSS systems. In order to simplify the simulator and to remove computationally-heavy signal processing stages, only the correlator outputs are considered. Previous signal processing stages are not generated since their impact can be directly generated from the known correlator output mathematical model.

A.2.1) GeneIQ

In order to generate GNSS correlator outputs, the simulator first generates the observables or more specifically the delays between the receiver and satellites. To do so, the simulator computes the position of the satellites in view, based on the decoding of the provided Almanach. Then, based on the mask angle and the receiver position, it determines if the satellites are visible from the receiver. Based on models, an ionospheric, a tropospheric and a clock error delays are added to the true distance. Pseudo range code

and pseudo range rate measurements are then generated following $(A.1)$ and $(A.2)$. Thus the delays and phases of the input signals to be tracked are defined.

$$P_k^j = \rho_k^j + d_{Iono_k}^j + d_{Tropo}{}_k^j + c \cdot (\Delta t_{user-GPS_k} - \Delta t_{sat-GPS}^j) \quad (A.1)$$

$$\varphi_k^j = \rho_k^j - d_{Iono_k}^j + d_{Tropo}{}_k^j + c \cdot (\Delta t_{user-GPS_k} - \Delta t_{sat-GPS}^j) \quad (A.2)$$

Where:

- ρ_k^j is the geometric distance between the satellite and the user for sat j based on the Ephemerides information from the Almanach: $\rho_k^j = \sqrt{\left(x_{j_k} - x_{user_k}\right)^2 + \left(y_{j_k} - y_{user_k}\right)^2 + \left(z_{j_k} - z_{user_k}\right)^2}$
- $d_{Iono_k}^j$ is the Current true Ionospheric delay [m] for sat j
- $d_{Tropo_k}^j$ is the Current true tropospheric delay [m] for sat j
- $\Delta t_{user-GPS_k}$ is the Current user clock bias [s] – TCXO model
- $\Delta t_{sat-GPS}^j$ is the Current Satellite time clock error [s] – Rubidium model for sat j

Each satellite is then processed independently in order to compute correlator outputs. These correlator outputs are generated assuming a previously generated SCHUN propagation channel. The correlator outputs are then fed to a code and a carrier tracking loops allowing the estimation of delays and phases. The tracking loops delay and phase estimations are then used to generate pseudo range codes and pseudo range rates required to the design of the navigation modules. The process is illustrated in Figure Annex 1.

The pseudo ranges generated are used in the standalone navigation module; an Extended Kalman Filter (EKF) is implemented.

A.2.2) 5G module

In order to compute the correlator outputs, the simulator is provided with data files generated previously with QuaDRiGa. Two files are generated per Base Stations; one containing the delays information for each path, i.e., the delay between the BS and the receiver at each instant and for each path composing the propagation channel. The second file contains the complex amplitudes for each path at each instant.

Then correlator outputs are generated following $(A.3)$.

$$R(\varepsilon_\tau) = R_{useful}(\varepsilon_\tau) + R_{noise+interf}(\varepsilon_\tau) \quad (A.3)$$

Where $R_{useful}(\varepsilon_\tau)$ have been derived in (4.28), the simplified channel contribution term is used and $R_{noise+interf}(\varepsilon_\tau)$ is the a noise with an enhanced power. The correlator outputs are then fed to a time delay tracking loop allowing the estimation of delays; and a FLL is implemented if required by the simulation as explained in chapter 5 section 5.2.

The tracking loops delay estimations are then used to generate pseudo range codes required to the design of the navigation modules. The process is illustrated in Figure Annex 1. The pseudo ranges generated are used in the standalone navigation module; an EKF and an Unscented Kalman Filter (UKF) are implemented.

A.2.3) Hybrid navigation module

Based on the GNSS and 5G pseudo ranges generated, 2 hybrid navigation filters are designed: an EKF and an UKF. The process is illustrated in Figure Annex 1.

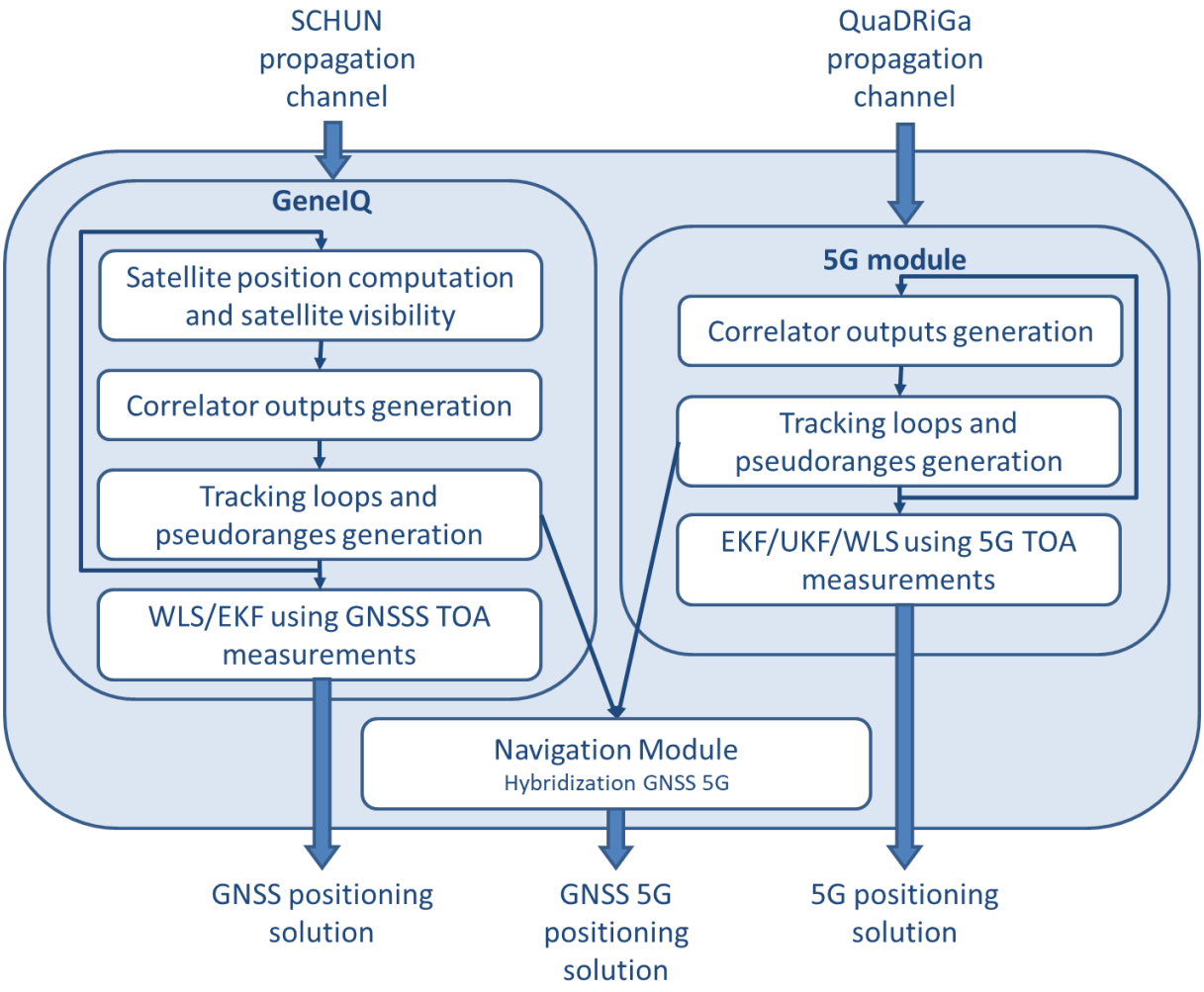

Figure Annex 1 – Simulator overview

A.3) Noise correlator output generation

This final subsection aims at presenting the method developed to simulate the noise correlator output terms. Indeed, the method to do so is not as obvious as it could be expected.

For the sake of simplicity, and with the will to be as generic as possible to adapt the method to any kind of generation of correlated samples, the correlation between correlator outputs spaced by a delay equal to $\Delta\tau$ presented in (4.49) is simplified as proposed in $(\mathrm{A}.4)$.

$$E[R_{noise}(\hat{\tau})R_{noise}{}^{*}(\hat{\tau}-\Delta\tau)] = \begin{cases} \dfrac{e^{\frac{i\pi\Delta\tau(2\beta+\gamma(N_P-1))}{N_{FFT}}}}{N_P^2}\dfrac{\sigma_{noise}^2}{N_{FFT}}\dfrac{sin\left(\frac{\pi\Delta\tau\gamma N_P}{N_{FFT}}\right)}{sin\left(\frac{\pi\Delta\tau\gamma}{N_{FFT}}\right)} & \Delta\tau \neq 0 \\ \dfrac{\sigma_{noise}^2}{N_{FFT}N_P} & \Delta\tau = 0 \end{cases} \quad (\mathrm{A}.4)$$

The method proposed to simulate correlated noise is based on Hurtz theory, [67]. In [67] the following matrix of correlated noise is generated.

$$C = \begin{bmatrix} R_{prompt} & R_{late} & R_{very\ late} \\ R_{early} & R_{prompt} & R_{late} \\ R_{very\ early} & R_{early} & R_{prompt} \end{bmatrix} \quad (A.5)$$

As complex number are generated with $E[R_{noise}(\hat{\tau})R_{noise}{}^{*}(\hat{\tau} - \Delta\tau)]$; this theory has to be adapted; and the following matrix is considered instead.

$$C = \begin{bmatrix} L_I L_I & L_I L_Q & L_I P_I & L_I P_Q & L_I E_I & L_I E_Q \\ L_Q L_I & L_Q L_Q & L_Q P_I & L_Q P_Q & L_Q E_I & L_Q E_Q \\ P_I L_I & P_I L_Q & P_I P_I & P_I P_Q & P_I E_I & P_I E_Q \\ P_Q L_I & P_Q L_Q & P_Q P_I & P_Q P_Q & P_Q E_I & P_Q E_Q \\ E_I L_I & E_I L_Q & E_I P_I & E_I P_Q & E_I E_I & E_I E_Q \\ E_Q L_I & E_Q L_Q & E_Q P_I & E_Q P_Q & E_Q E_I & E_Q E_Q \end{bmatrix} \quad (A.6)$$

Where:

$$R_{late} = L_I + jL_Q$$
$$R_{prompt} = P_I + jP_Q$$
$$R_{early} = E_I + jE_Q$$

The coefficient in C must verify the condition:

$$E[R(\varepsilon_\tau)R^{*}(\varepsilon_\tau - \Delta\tau)] = E[(N_I + jN_Q)(M_I + jM_Q)] \quad (A.7)$$

This lead to:

$$C = \begin{bmatrix} 1 & 0 & M_2\cos(\theta_2) & -M_2\sin(\theta_2) & M_1\cos(\theta_1) & -M_1\sin(\theta_1) \\ 0 & 1 & M_2\sin(\theta_2) & M_2\cos(\theta_2) & M_1\sin(\theta_1) & M_1\cos(\theta_1) \\ M_2\cos(\theta_2) & M_2\sin(\theta_2) & 1 & 0 & M_2\cos(\theta_2) & -M_2\sin(\theta_2) \\ -M_2\sin(\theta_2) & M_2\cos(\theta_2) & 0 & 1 & M_2\sin(\theta_2) & M_2\cos(\theta_2) \\ M_1\cos(\theta_1) & M_1\sin(\theta_1) & M_2\cos(\theta_2) & M_2\sin(\theta_2) & 1 & 0 \\ -M_1\sin(\theta_1) & M_1\cos(\theta_1) & -M_2\sin(\theta_2) & M_2\cos(\theta_2) & 0 & 1 \end{bmatrix} \quad (A.8)$$

Where

$$M_2 = \frac{1}{N_p}\frac{\sin\left(\frac{\pi\gamma d N_P}{2N_{FFT}}\right)}{\sin\left(\frac{\pi\gamma d}{2N_{FFT}}\right)}$$
$$M_1 = \frac{1}{N_p}\frac{\sin\left(\frac{\pi\gamma d N_P}{N_{FFT}}\right)}{\sin\left(\frac{\pi\gamma d}{N_{FFT}}\right)}$$
$$\theta_2 = \frac{\pi\gamma d(N_P - 1)}{2N_{FFT}}$$
$$\theta_1 = \frac{\pi\gamma d(N_P - 1)}{N_{FFT}}$$

The theory proposed in [67] says that, the noise added to the correlator outputs is such that

$$Noise = \sigma_{\text{noise}} \cdot V\sqrt{D}N_{norm} = \begin{bmatrix} Noise_{early} \\ Noise_{prompt} \\ Noise_{late} \end{bmatrix} \quad (A.9)$$

Where D and V are respectively the eigenvalues and eigenvectors of C.
Adapted to the matrix C developed above

$$V\sqrt{D}N_{norm} = \begin{bmatrix} N_{late_I} \\ N_{late_Q} \\ N_{Prompt_I} \\ N_{Prompt_Q} \\ N_{early_I} \\ N_{early_Q} \end{bmatrix} \quad (A.10)$$

$$Noise = \sigma_{\text{noise}} \cdot \begin{bmatrix} N_{late_I} + iN_{late_I} \\ N_{Prompt_I} + iN_{Prompt_Q} \\ N_{early_I} + iN_{early_Q} \end{bmatrix} \quad (A.11)$$

By doing so, the noise samples generated fulfil the correlation conditions (4.49).

Annex B) GNSS correlator outputs mathematical model in multipath environment

The objective of this annex is to derive the GNSS correlator outputs mathematical model in multipath environment

B.1) Complex envelop or low pass signal representation

The generic low pass signal transmitted by any GNSS system can be modeled as follow:

$$s_{lp}(t) = A \cdot d(t) \cdot c(t)$$

Where:

- A is the signal amplitude
- $d(t)$ is the navigation data bit
- $c(t)$ is the spreading code
- t is the GPS reference time

B.2) Propagation channel model SCHUN

The transmitted signal is disturbed by the propagation channel, the model adopted in the demonstration is the following one

$$h(t,\tau) = \sum_{l=0}^{N_{multi}-1} \gamma_l(t) e^{-i\Phi_l(t)} \delta\big(t - \tau_l(t)\big)$$

Where:

- N_{multi} is the number of path
- $\gamma_l(t)$ is the amplitude (real) of the l^{th} path
- $\Phi_l(t)$ is the phase of the l^{th} path
- $\tau_l(t)$is the delay of the l^{th} path
- τ is the convolution variable

B.3) Base band signal model

In order to obtain the base band signal model, the low pass transmitted signal is convoluted with the propagation channel

$$s(t) = s_{lp}(t) * h(t,\tau) = \sum_{l=0}^{N_{multi}-1} \gamma_l(t) e^{-i\Phi_l(t)} A \cdot d\big(t - \tau_l(t)\big) \cdot c\big(t - \tau_l(t)\big)$$

B.4) Real received signal

The signal is then modulated by a carrier frequency and the real part is then kept to model the received signal.

$$r(t) = Re\big\{s(t) e^{2i\pi f_c t}\big\}$$

Where:

- f_c is the carrier frequency

$$r(t) = \sum_{l=0}^{N_{multi}-1} \gamma_l(t) A \cdot d\big(t - \tau_l(t)\big) \cdot c\big(t - \tau_l(t)\big) \cdot \cos\big(2\pi f_c t - \Phi_l(t)\big)$$

Sampled phase model: $\Phi_{l_k} = 2\pi\Delta f_{d_l}\left(k - (\hat{\tau} + kT_I)\right) + \Phi_{l_{0_k}}$

Where:

- Δf_{d_l} is the Doppler frequency of the l^{th} path
- $\Phi_{l_{0_k}}$ is the phase of the l^{th} path at the instant $\hat{\tau} + kT_I$

B.5) Correlator output determination

The received signal is then correlated to a local replica (see section D)

B.5.1) Model in the time domain

$$I_P(k) = \frac{1}{T_I}\int_{\hat{\tau}+kT_I}^{\hat{\tau}+(k+1)T_I} r_{RF_{out}}(u)c_l(u-\hat{\tau})\cos\left(2\pi\left(f_c - \widehat{\Delta f_d}\right)u - \hat{\Phi}_k\right)du$$

Where:

- c_l is the spreading code local replica
- $\hat{\tau}$ is the estimated delay
- $\widehat{\Delta f_d}$ is the estimated Doppler
- $\hat{\Phi}_k$ is the estimated phase at the beginning of the interval
- $r_{RF_{out}}(u)$ is the received signal at the RF front end output

$$I_P(k) = \frac{1}{T_I}\int_{\hat{\tau}+kT_I}^{\hat{\tau}+(k+1)T_I}\sum_{l=0}^{N_{multi}-1}\gamma_{l_k}Ad_k\cdot c\left(u-\tau_{l_k}\right)\cdot c_l(u-\hat{\tau})$$
$$\cdot\cos\left(2\pi\left(f_c-\Delta f_{d_l}\right)u - \Phi_{l_{0_k}} + 2\pi\Delta f_{d_l}(\hat{\tau}+kT_I)\right)\cdot\cos\left(2\pi\left(f_c-\widehat{\Delta f_d}\right)u-\hat{\Phi}_k\right)du$$

$$I_P(k) = \sum_{l=0}^{N_{multi}-1}\frac{\gamma_{l_k}Ad_k}{T_I}\int_{\hat{\tau}+kT_I}^{\hat{\tau}+(k+1)T_I} c\left(u-\tau_{l_k}\right)\cdot c_l(u-\hat{\tau})$$
$$\cdot\cos\left(2\pi\left(f_c-\Delta f_{d_l}\right)u - \Phi_{l_{0_k}} + 2\pi\Delta f_{d_l}(\hat{\tau}+kT_I)\right)\cdot\cos\left(2\pi\left(f_c-\widehat{\Delta f_d}\right)u-\hat{\Phi}_k\right)du$$

Application of trigonometry function

$$cos(a)\,cos(b) = \frac{1}{2}(cos(a+b) + cos(a-b))$$

$$cos\left(2\pi\left(f_c-\Delta f_{d_l}\right)u - \Phi_{l_{0_k}} + 2\pi\Delta f_{d_l}(\hat{\tau}+kT_I)\right)\cdot cos\left(2\pi\left(f_c-\widehat{\Delta f_d}\right)u-\hat{\Phi}_k\right)$$
$$= \frac{1}{2}\left(cos\left(4\pi f_c u - 2\pi\left(\widehat{\Delta f_d} + \Delta f_{d_l}\right)u - \Phi_{l_{0_k}} + 2\pi\Delta f_{d_l}(\hat{\tau}+kT_I) - \hat{\Phi}_k\right)\right.$$
$$\left. + cos\left(2\pi\left(\Delta f_{d_l} - \widehat{\Delta f_d}\right)u + \Phi_{l_{0_k}} - 2\pi\Delta f_{d_l}(\hat{\tau}+kT_I) - \hat{\Phi}_k\right)\right)$$

The RF front end filters the high frequency, thus the previous term can be simplified as:

$$\left[\cos\left(2\pi\left(f_c-\Delta f_{d_l}\right)u - \Phi_{l_{0_k}} + 2\pi\Delta f_{d_l}(\hat{\tau}+kT_I)\right)\cdot\cos\left(2\pi\left(f_c-\widehat{\Delta f_d}\right)u-\hat{\Phi}_k\right)\right] * h_{RF_{out}}$$
$$= \frac{1}{2}\cos\left(2\pi\left(\Delta f_{d_l} - \widehat{\Delta f_d}\right)u + \Phi_{l_{0_k}} - 2\pi\Delta f_{d_l}(\hat{\tau}+kT_I) - \hat{\Phi}_k\right)$$

$$I_P(k) = \sum_{l=0}^{N_{multi}-1} \frac{\gamma_{l_k} A d_k}{2T_I} \int_{\hat{\tau}+kT_I}^{\hat{\tau}+(k+1)T_I} c\left(u-\tau_{l_k}\right)\cdot c_l(u-\hat{\tau}) \cdot \cos\left(2\pi\left(\Delta f_{d_l} - \widehat{\Delta f_d}\right)u + \Phi_{l_{0_k}} - 2\pi\Delta f_{d_l}(\hat{\tau}+kT_I) - \hat{\Phi}_k\right) du$$

B.5.2) Development of the frequency domain expression with a deterministic approach: using a rectangular impulse response

The integral over $[\hat{\tau}+kT_I, \hat{\tau}+(k+1)T_I]$ can be replace by an integral over R and a rectangle $\frac{1}{T_I} rect\left(\frac{u-\left(\hat{\tau}+\left(k+\frac{1}{2}\right)T_I\right)}{T_I}\right)$

$$I_P(k) = \sum_{l=0}^{N_{multi}-1} \frac{\gamma_{l_k} A d_k}{2} \int_{-\infty}^{+\infty} \frac{1}{T_I} rect\left(\frac{u-\left(\hat{\tau}+\left(k+\frac{1}{2}\right)T_I\right)}{T_I}\right)\cdot c\left(u-\tau_{l_k}\right)\cdot c_l(u-\hat{\tau}) \cdot \cos\left(2\pi\left(\Delta f_{d_l} - \widehat{\Delta f_d}\right)u + \Phi_{l_{0_k}} - 2\pi\Delta f_{d_l}(\hat{\tau}+kT_I) - \hat{\Phi}_k\right) du$$

$$I_P(k) = \sum_{l=0}^{N_{multi}-1} \frac{\gamma_{l_k} A d_k}{2} \int_{-\infty}^{+\infty} \frac{1}{T_I} rect\left(\frac{u-\frac{T_I}{2}-(\hat{\tau}+kT_I)}{T_I}\right)\cdot c\left(u-\tau_{l_k}\right)\cdot c_l(u-\hat{\tau}) \cdot \cos\left(2\pi\left(\Delta f_{d_l} - \widehat{\Delta f_d}\right)u + \Phi_{l_{0_k}} - 2\pi\Delta f_{d_l}(\hat{\tau}+kT_I) - \hat{\Phi}_k\right) du$$

Convolution product:

$$(f*g)(\tau) = \int_{-\infty}^{+\infty} f(t-\tau)g(t)\,dt = \int_{-\infty}^{+\infty} f(t)g(t-\tau)\,dt$$

$$I_P(k) = \sum_{l=0}^{N_{multi}-1} \frac{\gamma_{l_k} A d_k}{2} \int_{-\infty}^{+\infty} \underbrace{\frac{1}{T_I} rect\left(\frac{u-\left(\hat{\tau}+\left(k+\frac{1}{2}\right)T_I\right)}{T_I}\right)}_{f\left(u-\left(\hat{\tau}+\left(k+\frac{1}{2}\right)T_I\right)\right)} \cdot \underbrace{c\left(u-\tau_{l_k}\right)\cdot c_l(u-\hat{\tau}) \cdot \cos\left(2\pi\left(\Delta f_{d_l} - \widehat{\Delta f_d}\right)u + \Phi_{l_{0_k}} - 2\pi\Delta f_{d_l}(\hat{\tau}+kT_I) - \hat{\Phi}_k\right)}_{r_{prod}(u)} du$$

$$I_P(k) = \sum_{l=0}^{N_{multi}-1} \frac{\gamma_{l_k} A d_k}{2} \cdot (f * r_{prod})\left(\hat{\tau}+\left(k+\frac{1}{2}\right)T_I\right)$$

$$\overset{\rightleftarrows}{FT}$$

$$TF[I_P(k)](f) = \sum_{l=0}^{N_{multi}-1} \frac{\gamma_l A d_k}{2} \cdot F(f) R_{prod}(f)$$

Where:

- $f(t) = \frac{1}{T_I} rect\left(\frac{t}{T_I}\right) \cdot \overset{\rightleftarrows}{FT} F(f) = \mathrm{sinc}(\pi f T_I)$
- $r_{prod}(t) = c\left(t-\tau_{l_k}\right)\cdot c_l(t-\hat{\tau}) \cdot \cos\left(2\pi\left(\Delta f_{d_l} - \widehat{\Delta f_d}\right)t + \Phi_{l_{0_k}} - 2\pi\Delta f_{d_l}(\hat{\tau}+kT_I) - \hat{\Phi}_k\right)$

$$\overset{\rightleftarrows}{FT}$$

$$R_{prod}(f) = TF\left[c\left(t-\tau_{l_k}\right)\right](f) * TF[c_l(t-\hat{\tau})](f) * TF\left[\cos\left(2\pi\left(\Delta f_{d_l} - \widehat{\Delta f_d}\right)t + \Phi_{l_{0_k}} - 2\pi\Delta f_{d_l}(\hat{\tau}+kT_I) - \widehat{\Phi}_k\right)\right](f)$$

Fourier transform of a rectangle function:

$$F(f) = TF\left[\frac{1}{T_I} rect\left(\frac{u-\frac{T_I}{2}}{T_I}\right)\right](f) = \int_{-\infty}^{+\infty} \frac{1}{T_I} rect\left(\frac{u-\frac{T_I}{2}}{T_I}\right) e^{-2i\pi ft}\, dt$$

$$F(f) = \frac{1}{T_I}\int_{-\frac{T_I}{2}}^{\frac{T_I}{2}} e^{-2i\pi ft}\, dt = \frac{1}{2iT_I\pi f}\left[e^{-2i\pi ft}\right]_{-\frac{T_I}{2}}^{\frac{T_I}{2}} = \frac{\left(e^{-2i\pi f\frac{T_I}{2}} - e^{2i\pi f\frac{T_I}{2}}\right)}{2iT_I\pi f}$$

$$F(f) = \frac{1}{2iT_I\pi f}\left(e^{-i\pi fT_I} - e^{i\pi fT_I}\right)$$

$$F(f) = \frac{1}{T_I\pi f} sin(\pi fT_I)$$

$$F(f) = sinc(\pi fT_I)$$

B.5.3) Development of $R_{prod}(f)$

$$R_{prod}(f) = TF\left[c\left(t-\tau_{l_k}\right)\right](f) * TF[c_l(t-\hat{\tau})](f) * TF\left[\cos\left(2\pi\left(\Delta f_{d_l} - \widehat{\Delta f_d}\right)t + \Phi_{l_{0_k}} - 2\pi\Delta f_{d_l}(\hat{\tau}+kT_I) - \widehat{\Phi}_k\right)\right](f)$$

B.5.3.1) Development of $\boldsymbol{TF\left[\cos\left(2\pi\left(\Delta f_{d_l} - \widehat{\Delta f_d}\right)t + \Phi_{l_{0_k}} - 2\pi\Delta f_{d_l}(\hat{\tau}+kT_I) - \widehat{\Phi}_k\right)\right](f)}$

$$B(f) = TF\left[\cos\left(2\pi\left(\Delta f_{d_l} - \widehat{\Delta f_d}\right)t + \Phi_{l_{0_k}} - 2\pi\Delta f_{d_l}(\hat{\tau}+kT_I) - \widehat{\Phi}_k\right)\right](f) = \int_{-\infty}^{+\infty} \cos\left(2\pi\left(\Delta f_{d_l} - \widehat{\Delta f_d}\right)t + \Phi_{l_{0_k}} - 2\pi\Delta f_{d_l}(\hat{\tau}+kT_I) - \widehat{\Phi}_k\right) e^{-2i\pi ft}\, dt$$

Euler formula:

$$cos(x) = \frac{e^{ix} + e^{-ix}}{2}$$

$$cos\left(2\pi\left(\Delta f_{d_l} - \widehat{\Delta f_d}\right)t + \Phi_{l_{0_k}} - 2\pi\Delta f_{d_l}(\hat{\tau}+kT_I) - \widehat{\Phi}_k\right) = \frac{e^{i\left(2\pi\left(\Delta f_{d_l} - \widehat{\Delta f_d}\right)t + \Phi_{l_{0_k}} - 2\pi\Delta f_{d_l}(\hat{\tau}+kT_I) - \widehat{\Phi}_k\right)} + e^{-i\left(2\pi\left(\Delta f_{d_l} - \widehat{\Delta f_d}\right)t + \Phi_{l_{0_k}} - 2\pi\Delta f_{d_l}(\hat{\tau}+kT_I) - \widehat{\Phi}_k\right)}}{2}$$

$$B(f) = \frac{1}{2}\int_{-\infty}^{+\infty} e^{i\left(2\pi\left(\Delta f_{d_l} - \widehat{\Delta f_d}\right)t + \Phi_{l_{0_k}} - 2\pi\Delta f_{d_l}(\hat{\tau}+kT_I) - \widehat{\Phi}_k\right)} e^{-2i\pi ft}\, dt + \frac{1}{2}\int_{-\infty}^{+\infty} e^{-i\left(2\pi\left(\Delta f_{d_l} - \widehat{\Delta f_d}\right)t + \Phi_{l_{0_k}} - 2\pi\Delta f_{d_l}(\hat{\tau}+kT_I) - \widehat{\Phi}_k\right)} e^{-2i\pi ft}\, dt$$

$$B(f) = \frac{e^{i\left(\Phi_{l_{0_k}} - 2\pi\Delta f_{d_l}(\hat{\tau}+kT_I) - \hat{\Phi}_k\right)}}{2} \int_{-\infty}^{+\infty} e^{2i\pi\left(\Delta f_{d_l} - \widehat{\Delta f_d}\right)t} e^{-2i\pi ft}\, dt + \frac{e^{-i\left(\Phi_{l_{0_k}} - 2\pi\Delta f_{d_l}(\hat{\tau}+kT_I) - \hat{\Phi}_k\right)}}{2} \int_{-\infty}^{+\infty} e^{-2i\pi\left(\Delta f_{d_l} - \widehat{\Delta f_d}\right)t} e^{-2i\pi ft}\, dt$$

Fourier Transform of a Complex exponential:

$$\delta(t-\tau) \underset{FT}{\rightleftarrows} e^{-2i\pi f\tau}$$

$$\delta(f-f_0) \underset{FT}{\rightleftarrows} e^{2i\pi f_0 t}$$

$$B(f) = \frac{e^{i\left(\Phi_{l_{0_k}} - 2\pi\Delta f_{d_l}(\hat{\tau}+kT_I) - \hat{\Phi}_k\right)}}{2}\delta\left(f - \left(\Delta f_{d_l} - \widehat{\Delta f_d}\right)\right) + \frac{e^{-i\left(\Phi_{l_{0_k}} - 2\pi\Delta f_{d_l}(\hat{\tau}+kT_I) - \hat{\Phi}_k\right)}}{2}\delta\left(f + \left(\Delta f_{d_l} - \widehat{\Delta f_d}\right)\right)$$

B.5.3.2) Development of $TF[c_l(t)](f)$: hypothesis: periodic code

$$c_l(t) = \left[\sum_{n=0}^{L-1} c(n)\delta(t-nT_c)\right] * \sum_{j=-\infty}^{+\infty} \delta(t-jT_R) * m(t)$$

Where:

- $\{c(n)\}_{n\in L} = \pm 1$ are the data
- T_c is the sampling frequency
- L is the code length
- T_R is the period of repetition
- $m(t)$ is the waveform, for GPS L1 C/A, $m(t) = rect\left(\frac{t-\frac{T_C}{2}}{T_C}\right) \underset{FT}{\rightleftarrows} M(f) = T_C e^{-i\pi fT_C}\,\mathrm{sinc}(\pi fT_C)$

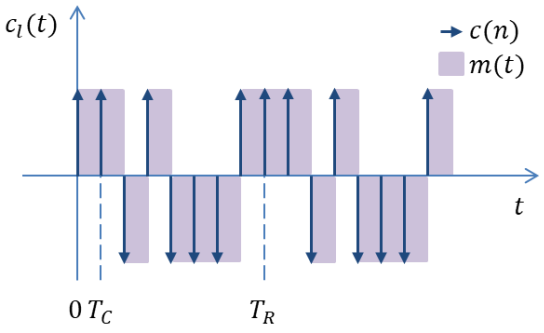

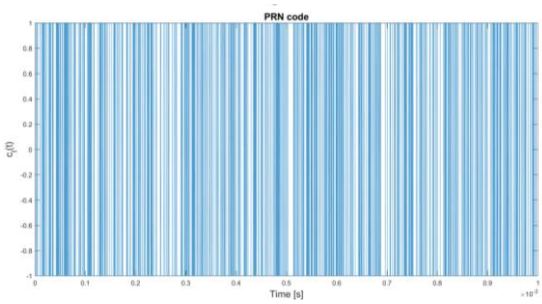

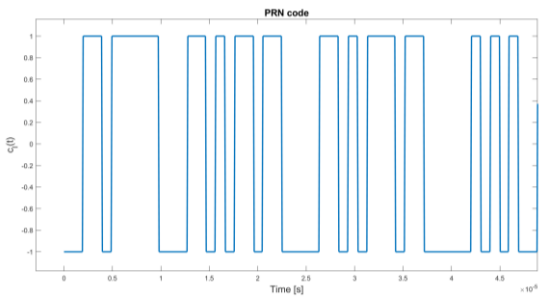

$$C_l(f) = TF[c_l(t)](f) = TF\left[\sum_{n=0}^{L-1} c(n)\delta(t - nT_c)\right](f) \cdot TF\left[\sum_{j=-\infty}^{+\infty} \delta(t - jT_R)\right](f) \cdot M(f)$$

Poisson formula

$$\sum_{j=-\infty}^{+\infty} \delta(t - jT_R) \underset{FT}{\rightleftarrows} \frac{1}{T_R} \sum_{j=-\infty}^{+\infty} \delta\left(f - \frac{j}{T_R}\right)$$

Fourier Transform of a series

$$TF\left[\sum_{n=0}^{L-1} c(n)\delta(t - nT_c)\right] = \sum_{n=0}^{L-1} c(n)e^{-2i\pi f n T_C}$$

$$C_l(f) = \sum_{n=0}^{L-1} c(n)e^{-2i\pi f n T_C} \cdot \frac{1}{T_R} \sum_{j=-\infty}^{+\infty} \delta\left(f - \frac{j}{T_R}\right) \cdot M(f)$$

This Fourier Transform is different from 0 only if $f = \frac{j}{T_r}$

$$C_l(f) = \frac{M(f)}{T_R} e^{-2i\pi f\hat{\tau}} \sum_{j=-\infty}^{+\infty} \sum_{n=0}^{L-1} c(n)e^{-2i\pi \frac{j}{T_R} n T_C} \ \delta\left(f - \frac{j}{T_R}\right)$$

Knowing that: $T_R = LT_C$

$$C_l(f) = \frac{M(f)}{T_R} e^{-2i\pi f\hat{\tau}} \sum_{j=-\infty}^{+\infty} \sum_{n=0}^{L-1} c(n)e^{-2i\pi \frac{j}{L} n} \ \delta\left(f - \frac{j}{T_R}\right)$$

$$C_l(f) = \frac{M(f)}{T_R} e^{-2i\pi f\hat{\tau}} \sum_{j=-\infty}^{+\infty} S_{c_l}(j)\delta\left(f - \frac{j}{T_R}\right)$$

Where $S_{c_l}(j) = \sum_{n=0}^{L-1} c(n)e^{-2i\pi \frac{j}{L} n}$

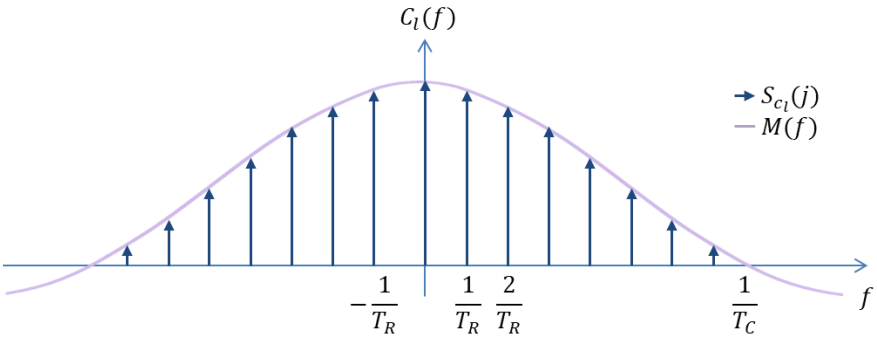

B.5.3.3) Back to the development of $R_{prod}(f)$

$$R_{prod}(f) = TF\left[c\left(t - \tau_{l_k}\right)\right](f) * TF[c_l(t - \hat{\tau})](f)$$
$$* TF\left[\cos\left(2\pi\left(\Delta f_{d_l} - \widehat{\Delta f_d}\right)t + \Phi_{l_{0_k}} - 2\pi\Delta f_{d_l}(\hat{\tau} + kT_I) - \widehat{\Phi}_k\right)\right](f)$$

$$R_{prod}(f) = \frac{M(f)}{T_R} e^{-2i\pi f \tau_{l_k}} \sum_{j=-\infty}^{+\infty} S_c(j)\delta\left(f - \frac{j}{T_R}\right) * \frac{M(f)}{T_R} e^{-2i\pi f \hat{\tau}} \sum_{j=-\infty}^{+\infty} S_{c_l}(j)\delta\left(f - \frac{j}{T_R}\right)$$
$$* \left[\frac{e^{i\left(\Phi_{l_{0_k}} - 2\pi\Delta f_{d_l}(\hat{\tau}+kT_I) - \hat{\Phi}_k\right)}}{2} \delta\left(f - \left(\Delta f_{d_l} - \widehat{\Delta f_d}\right)\right) \right.$$
$$\left. + \frac{e^{-i\left(\Phi_{l_{0_k}} - 2\pi\Delta f_{d_l}(\hat{\tau}+kT_I) - \hat{\Phi}_k\right)}}{2} \delta\left(f + \left(\Delta f_{d_l} - \widehat{\Delta f_d}\right)\right) \right]$$

Application of the Dirac distribution to the incoming code Fourier transform

$$R_{prod}(f) = \frac{e^{i\left(\Phi_{l_{0_k}} - 2\pi\Delta f_{d_l}(\hat{\tau}+kT_I) - \hat{\Phi}_k\right)}}{2T_R} \left(M\left(f - \left(\Delta f_{d_l} - \widehat{\Delta f_d}\right)\right) \cdot e^{-2i\pi\left(f - \left(\Delta f_{d_l} - \widehat{\Delta f_d}\right)\right)\tau_{l_k}} \right.$$
$$\left. \cdot \sum_{j=-\infty}^{+\infty} S_c(j)\delta\left(f - \left(\Delta f_{d_l} - \widehat{\Delta f_d}\right) - \frac{j}{T_R}\right) \right) * \left(M(f) e^{-2i\pi f \hat{\tau}} \sum_{j=-\infty}^{+\infty} S_{c_l}(j)\delta\left(f - \frac{j}{T_R}\right) \right)$$
$$+ \frac{e^{-i\left(\Phi_{l_{0_k}} - 2\pi\Delta f_{d_l}(\hat{\tau}+kT_I) - \hat{\Phi}_k\right)}}{2T_R} \left(M\left(f + \left(\Delta f_{d_l} - \widehat{\Delta f_d}\right)\right) \cdot e^{-2i\pi\left(f + \left(\Delta f_{d_l} - \widehat{\Delta f_d}\right)\right)\tau_{l_k}} \right.$$
$$\left. \cdot \sum_{j=-\infty}^{+\infty} S_c(j)\delta\left(f + \left(\Delta f_{d_l} - \widehat{\Delta f_d}\right) - \frac{j}{T_R}\right) \right) * \left(M(f) e^{-2i\pi f \hat{\tau}} \sum_{j=-\infty}^{+\infty} S_{c_l}(j)\delta\left(f - \frac{j}{T_R}\right) \right)$$

B.5.4) Study the Doppler impact

B.5.4.1) Hypothesis: No Doppler

$$r_{prod}(t) = c\left(t - \tau_{l_k}\right) \cdot c_l(t - \hat{\tau}) \overset{\rightleftarrows}{FT} R_{prod}(f) = TF\left[c\left(t - \tau_{l_k}\right)\right](f) * TF[c_l(t - \hat{\tau})](f)$$

$$r_{prod}(t) = c\left(t - \tau_{l_k}\right) \cdot c_l(t - \hat{\tau}) \overset{\rightleftarrows}{FT} R_{prod}(f)$$
$$= \left[\frac{M(f)}{T_R} e^{-2i\pi f \tau_{l_k}} \sum_{j=-\infty}^{+\infty} S_{c_l}(j)\delta\left(f - \frac{j}{T_R}\right) \right] * \left[\frac{M(f)}{T_R} e^{-2i\pi f \hat{\tau}} \sum_{j=-\infty}^{+\infty} S_{c_l}(j)\delta\left(f - \frac{j}{T_R}\right) \right]$$

$$R_{prod}(f) = \left[\frac{M(f)}{T_R} e^{-2i\pi f \tau_{l_k}} \sum_{j=-\infty}^{+\infty} S_c(j)\delta\left(f - \frac{j}{T_R}\right) \right] * \left[\frac{M(f)}{T_R} e^{-2i\pi f \hat{\tau}} \sum_{j=-\infty}^{+\infty} S_{c_l}(j)\delta\left(f - \frac{j}{T_R}\right) \right]$$

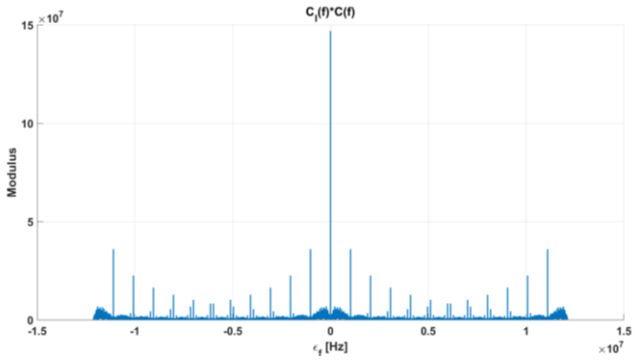

The convolution of a line spectrum by a line spectrum is a line spectrum where all lines are negligible except the one permitting a perfect synchronization between the 2 convoluted line spectrum.

$$R_{prod}(f) = K_{c,c_l}(\varepsilon_\tau) \cdot \delta(f)$$

B.5.4.2) Hypothesis: Doppler influence

$$R_{prod}(f) = \left[TF\left[c(t-\tau_{l_k})\right]\left(f - (\Delta f_{d_l} - \widehat{\Delta f_d})\right) + TF\left[c(t-\tau_{l_k})\right]\left(f - (\Delta f_{d_l} - \widehat{\Delta f_d})\right)\right] * TF[c_l(t-\hat{\tau})](f)$$

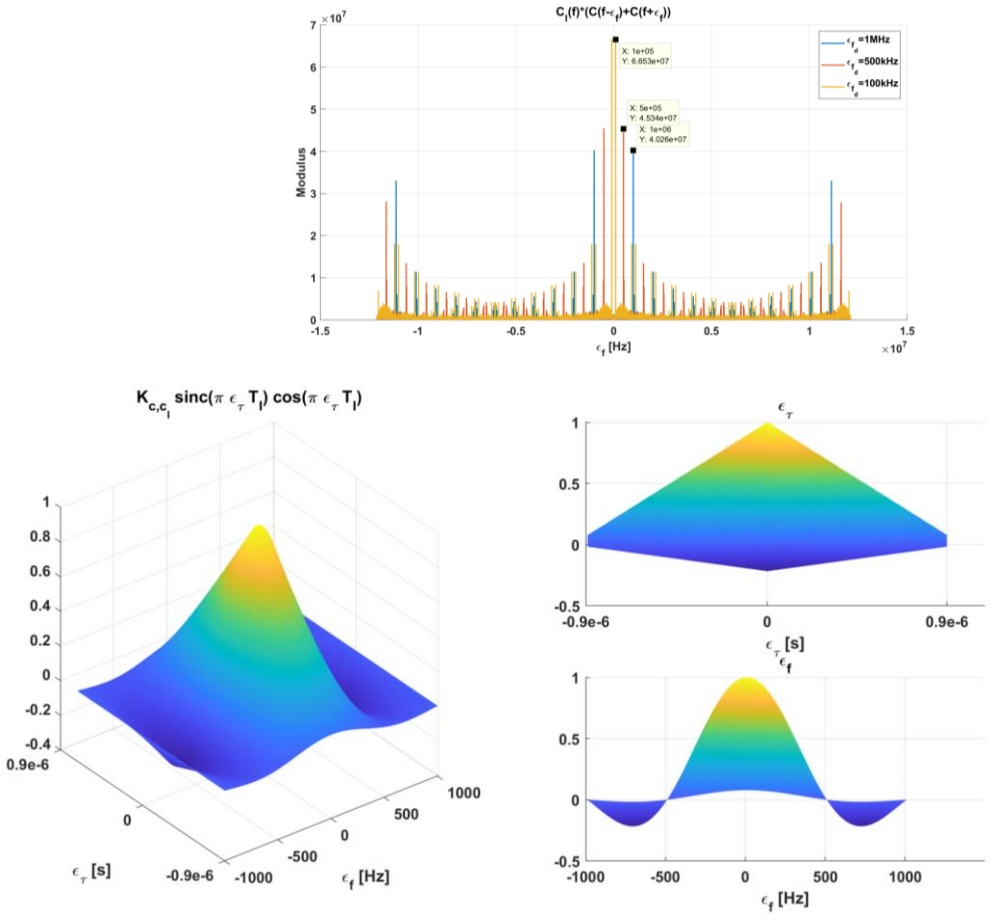

$$R_{prod}(f) = K_{c,c_l}(\varepsilon_{\tau_l}) \cdot \cos(\pi\varepsilon_{f_l}T_I + \varepsilon_\phi) \cdot \mathrm{sinc}(\pi\varepsilon_{f_l}T_I) \cdot \delta(f)$$

B.5.5) Back to the correlator output in the frequency domain

$$TF[I_P(k)](f) = \sum_{l=0}^{N_{multi}-1} \frac{\gamma_{l_k} A d_k}{2} \cdot F(f) R_{prod}(f)$$

$$TF[I_P(k)](f) = \sum_{l=0}^{N_{multi}-1} \frac{\gamma_{l_k} A d_k}{2} \mathrm{sinc}(\pi f T_I) \cdot K_{c,c_l}(\varepsilon_{\tau_l}) \cdot \cos(\pi\varepsilon_{f_l}T_I) \cdot \mathrm{sinc}(\pi\varepsilon_{f_l}T_I) \cdot \delta(f)$$

B.6) Correlator output final development

$$I_P(k) = \sum_{l=0}^{N_{multi}-1} \frac{\gamma_{l_k} A d_k}{2T_I} \int_{\hat{\tau}+kT_I}^{\hat{\tau}+(k+1)T_I} c(u-\tau_{l_k}) \cdot c_l(u-\hat{\tau}) \cdot \cos\left(2\pi(\Delta f_{d_l} - \widehat{\Delta f_d})u + \Phi_{l_{0_k}} - 2\pi\Delta f_{d_l}(\hat{\tau}+kT_I) - \hat{\Phi}_k\right) du$$

$$I_P(k) = \sum_{l=0}^{N_{multi}-1} \frac{\gamma_{l_k} A d_k}{2T_I} T_I \int_{\hat{\tau}+kT_I}^{\hat{\tau}+(k+1)T_I} c(u-\tau_{l_k}) c_l(u-\hat{\tau})\, du$$
$$\cdot \int_{\hat{\tau}+kT_I}^{\hat{\tau}+(k+1)T_I} \cos\left(2\pi(\Delta f_{d_l} - \widehat{\Delta f_d})u + \Phi_{l_{0_k}} - 2\pi\Delta f_{d_l}(\hat{\tau}+kT_I) - \hat{\Phi}_k\right) du$$

$$I_P(k) = \frac{1}{T_I} \sum_{l=0}^{N_{multi}-1} \frac{\gamma_{l_k} A d_k}{2} K_{c,c_l}(\varepsilon_{\tau_l}) \int_{\hat{\tau}+kT_I}^{\hat{\tau}+(k+1)T_I} \cos\left(2\pi(\Delta f_{d_l} - \widehat{\Delta f_d})u + \Phi_{l_{0_k}} - 2\pi\Delta f_{d_l}(\hat{\tau}+kT_I) - \hat{\Phi}_k\right) du$$

$$\int_{\hat{\tau}+kT_I}^{\hat{\tau}+(k+1)T_I} \cos\left(2\pi(\Delta f_{d_l} - \widehat{\Delta f_d})u + \Phi_{l_{0_k}} - 2\pi\Delta f_{d_l}(\hat{\tau}+kT_I) - \hat{\Phi}_k\right) du$$
$$= \frac{1}{2\pi(\Delta f_{d_l} - \widehat{\Delta f_d})} \left[sin\left(2\pi(\Delta f_{d_l} - \widehat{\Delta f_d})u + \Phi_{l_{0_k}} - 2\pi\Delta f_{d_l}(\hat{\tau}+kT_I) - \hat{\Phi}_k\right)\right]_{\hat{\tau}+kT_I}^{\hat{\tau}+(k+1)T_I}$$

$$\int_{\hat{\tau}+kT_I}^{\hat{\tau}+(k+1)T_I} \cos\left(2\pi(\Delta f_{d_l} - \widehat{\Delta f_d})u + \Phi_{l_{0_k}} - 2\pi\Delta f_{d_l}(\hat{\tau}+kT_I) - \hat{\Phi}_k\right) du$$
$$= \frac{1}{2\pi(\Delta f_{d_l} - \widehat{\Delta f_d})} \Big(sin\left(2\pi(\Delta f_{d_l} - \widehat{\Delta f_d})(\hat{\tau}+(k+1)T_I) + \Phi_{l_{0_k}} - 2\pi\Delta f_{d_l}(\hat{\tau}+kT_I)\right.$$
$$\left. - \hat{\Phi}_k\right) - sin\left(2\pi(\Delta f_{d_l} - \widehat{\Delta f_d})(\hat{\tau}+kT_I) + \Phi_{l_{0_k}} - 2\pi\Delta f_{d_l}(\hat{\tau}+kT_I) - \hat{\Phi}_k\right)\Big)$$

$$\sin(p) - \sin(q) = 2\cos\left(\frac{p+q}{2}\right)\sin\left(\frac{p-q}{2}\right)$$

$$\int_{\hat{\tau}+kT_I}^{\hat{\tau}+(k+1)T_I} \cos\left(2\pi(\Delta f_{d_l} - \widehat{\Delta f_d})u + \Phi_{l_{0_k}} - 2\pi\Delta f_{d_l}(\hat{\tau}+kT_I) - \hat{\Phi}_k\right) du$$
$$= \frac{1}{\pi\varepsilon_{f_l}} \cos\left(\pi(\Delta f_{d_l} - \widehat{\Delta f_d})T_I + \Phi_{l_{0_k}} - \hat{\Phi}_k - 2\pi\widehat{\Delta f_d}(\hat{\tau}+kT_I)\right) sin(\pi\varepsilon_{f_l} T_I)$$

$$\int_{\hat{\tau}+kT_I}^{\hat{\tau}+(k+1)T_I} \cos(2\pi\varepsilon_{f_l} u - \varepsilon_{\Phi_l})\, du = T_I \cos\left(\pi(\Delta f_{d_l} - \widehat{\Delta f_d})T_I + \Phi_{l_{0_k}} - \hat{\Phi}_k - 2\pi\widehat{\Delta f_d}(\hat{\tau}+kT_I)\right) sinc(\pi\varepsilon_{f_l} T_I)$$

Annex C) Addendum to 5G systems description

This annex provides addendum to the description of 5G systems. First, the OFDM symbol duration and CP duration are described for all numerology. Second, the time location of the SS PBCH synchronization block according to the cases derived in 3GPP standard is described. Third, a complement to the OFDM modulation description is provided. Forth, a complete definition of the synchronization signals is provided, finally, the complete study regarding the definition and selection of a 5G compliant propagation channel.

C.1) OFDM symbol and Cycle Prefix's duration

In chapter 3 section 3.3.4.4., the OFDM symbol and cycle prefix duration has been described for the first envisioned numerology of 5G systems, this annex provides the derivation for the other numerologies.

In this annex, the demonstration of the OFDM symbol and CP's durations is provided for all numerology. The FFT size is fixed at 2048.

The starting position of OFDM symbol l for subcarrier spacing configuration μ in a sub-frame is given by $(C.1)$.

$$t^{\mu}_{start,l} = \begin{cases} 0 & l = 0 \\ t^{\mu}_{start,l-1} + (N^{\mu}_{u} + N^{\mu}_{CP,l-1})T_c & otherwise \end{cases} \quad (C.1)$$

Where:

- $N^{\mu}_{u} = 2048\kappa.2^{-\mu}$
- $N^{\mu}_{CP,l} = \begin{cases} 512\kappa.2^{-\mu} & extended\ cyclic\ prefix \\ 144\kappa.2^{-\mu} + 16\kappa & normal\ cyclic\ prefix, l = 0\ and\ l = 7.2^{\mu} \\ 144\kappa.2^{-\mu} & normal\ cyclic\ prefix, l \neq 0\ and\ l \neq 7.2^{\mu} \end{cases}$

Note that the cycle prefix length is defined for a sub-frame and not for a slot. It does not influence the following example since the sub-frame contains only one slot.

C.1.1) $\mu = 0$

In this numerology, the following parameters are applied:

- $\Delta f = 15\ 000\ Hz$
- $N^{subframe}_{slot} = 1$
- $N^{slot}_{symb} = 14$

The basic unit time is: $T_s = \frac{1}{2048*15000} = \frac{1}{30\ 720\ 000} \approx 32.55\ ns$

A frame has duration of 10 ms: $T_{frame} = \frac{\Delta f_{max}\, N_f}{100} T_c = \frac{\Delta f_{max}\, N_f}{100} \frac{T_s}{\kappa} = 307\ 200 T_s = 10\ ms$

Each frame is composed of 10 sub-frames of duration 1 ms: $T_{subframe} = 30\ 720\ T_s$

For the case considered, there is only one slot in the sub-frame: $n_{Symbol} = 14$

The OFDM duration is fixed by the carrier spacing: $T_{OFDM} = 2048\ T_s \approx 66.67\ \mu s$

As it is shown in Figure Annex 2, a subframe is composed of 14 OFDM symbols and 14 cycle prefix.

$$T_{subframe} = 14\ T_{OFDM} + T_{CP}$$

Hence, to fully occupy the subframe, the cycle prefixes have to verify:

$$T_{CP} = (30\ 720 - 2048 * 14)\ T_s = 2048\ T_s$$

As 2048 is not a multiple of 14, it is necessary to define 2 CP lengths (the same principle is applied for 4G-LTE). As defined in [43], symbols 0 and 7 have extended length, we have:

$$2048 = 12 * 144 + 2 * 160$$

The length of the first and seventh OFDM symbols CP is then $160\,T_s \approx 5.208\,\mu s$ and the length of the remaining OFDM symbols CP is $144\,T_s \approx 4.687\,\mu s$.

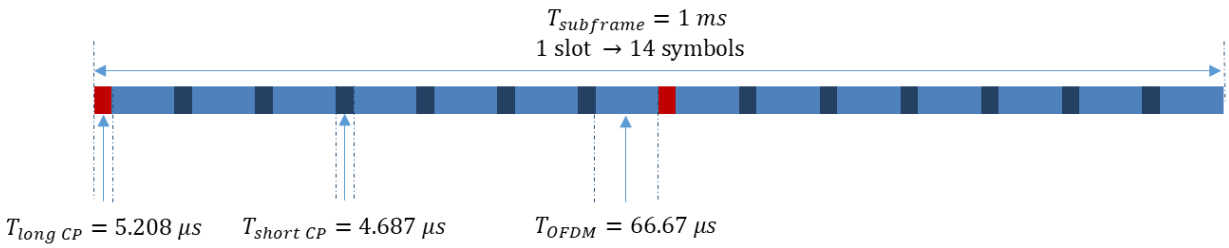

Figure Annex 2 – μ = 0

C.1.2) μ = 1

In this numerology, the following parameters are applied:

- $\Delta f = 30\,000\ Hz$
- $N_{slot}^{subframe} = 2$
- $N_{symb}^{slot} = 14$

The basic unit time is: $T_{s,\mu=1} = 2^{-\mu} T_s = \frac{2^{-1}}{2048*15000} = \frac{1}{61\,440\,000} \approx 16.28\ ns$

A frame has duration of 10 ms: $T_{frame} = \frac{\Delta f_{max}\, N_f}{100} T_c = \frac{\Delta f_{max}\, N_f}{100} \frac{T_{s,\mu=1}}{\kappa} = 614\,400 T_{s,\mu=1} = 10\ ms$

Each frame is composed of 10 sub-frames of duration 1 ms: $T_{subframe} = 61\,440\ T_{s,\mu=1}$

For the case considered, there are two slots in the sub-frame: $N_{Symbols} = 28$

The OFDM duration is fixed by the carrier spacing: $T_{OFDM} = 2048\ T_{s,\mu=1} = 1024 T_s \approx 33.34\ \mu s$

As it is shown in Figure Annex 3, a sub-frame is composed of 2 slots of 14 OFDM symbols and 14 cycle prefix each.

$$T_{subframe} = 28\ T_{OFDM} + T_{CP}$$

Hence, to fully occupy the slot, the cycle prefixes have to verify:

$$T_{CP} = (61440 - 28 * 2048)\ T_{s,\mu=1} = 4096 T_{s,\mu=1}$$

It is necessary to define 2 CP lengths (the same principle is applied for 4G-LTE). As defined in [43], symbols 0 and 14 have extended length, we have:

$$2048 = 26 * 144 + 2 * 176$$

The length of the first and seventh OFDM symbols CP is then $176 T_{s,\mu=1} \approx 2.865\ \mu s$ and the length of the remaining OFDM symbols CP is $144 T_{s,\mu=1} \approx 2.344\ \mu s$.

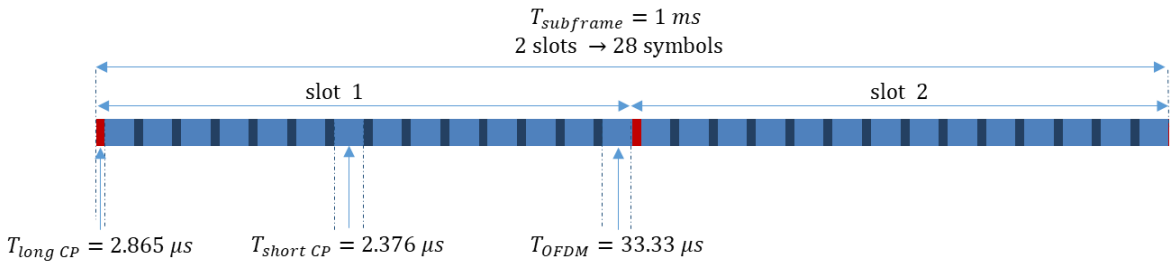

Figure Annex 3 – μ = 1

C.1.3) μ = 2

C.1.3.1) Normal CP

In this numerology, the following parameters are applied:

- $\Delta f = 60\ 000\ Hz$
- $N_{slot}^{subframe} = 4$
- $N_{symb}^{slot} = 14$

The basic unit time is: $T_{s,\mu=2} = 2^{-\mu} T_s = \frac{2^{-2}}{2048*15000} = \frac{1}{122\ 880\ 000} \approx 8.138\ ns$

A frame has duration of 10 ms: $T_{frame} = \frac{\Delta f_{max}\, N_f}{100} T_c = \frac{\Delta f_{max}\, N_f}{100} \frac{T_{s,\mu=2}}{\kappa} = 1\ 228\ 800 T_{s,\mu=2} = 10\ ms$

Each frame is composed of 10 sub-frames of duration 1 ms: $T_{subframe} = 122\ 880\ T_{s,\mu=2}$

For the case considered, there are four slots in the sub-frame: $N_{Symbol} = 56$

The OFDM duration is fixed by the carrier spacing: $T_{OFDM} = 2048\ T_{s,\mu=2} \approx 16.67\ \mu s$

As it is shown in Figure Annex 4, a sub-frame is composed of 4 slots of of 14 OFDM symbols and 14 cycle prefix each.

$$T_{subframe} = 56\ T_{OFDM} + T_{CP}$$

Hence, to fully occupy the slot, the cycle prefixes have to verify:

$$T_{CP} = (122\ 880 - 56 * 2048)\ T_{s,\mu=2} = 8\ 192 T_{s,\mu=2}$$

2 CP lengths are defined (the same principle is applied for 4G-LTE). As defined in [43], symbols 0 and 28 have extended length, we have:

$$8\ 192 = 54 * 144 + 2 * 208$$

The length of the first and seventh OFDM symbols CP is then $208 T_{s,\mu=2} \approx 1.692\ \mu s$ and the length of the remaining OFDM symbols CP is $144 T_{s,\mu=2} \approx 1.172\ \mu s$.

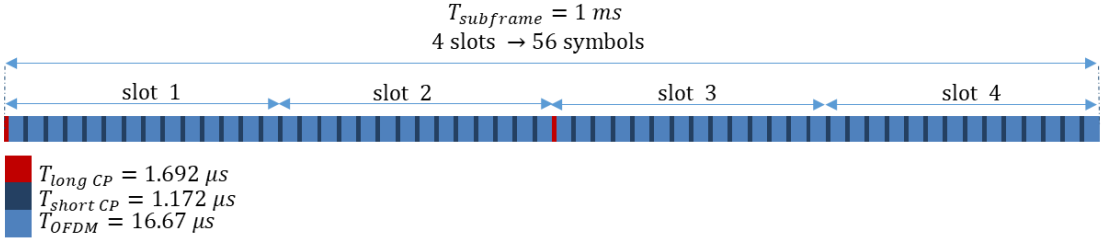

Figure Annex 4 – μ = 2 – normal CP

C.1.3.2) Extended CP

In this numerology, the following parameters are applied:

- $\Delta f = 60\,000\ Hz$
- $N_{slot}^{subframe} = 4$
- $N_{symb}^{slot} = 12$

The basic unit time is: $T_{s,\mu=2} = 2^{-\mu} T_s = \frac{2^{-2}}{2048*15000} = \frac{1}{122\,880\,000} \approx 8.138\ ns$

A frame has duration of 10 ms: $T_{frame} = \frac{\Delta f_{max}\, N_f}{100} T_c = \frac{\Delta f_{max}\, N_f}{100} \frac{T_{s,\mu=2}}{\kappa} = 1\,228\,800 T_{s,\mu=2} = 10\ ms$

Each frame is composed of 10 sub-frames of duration 1 ms: $T_{subframe} = 122\,880\ T_{s,\mu=2}$

For the case considered, there are four slots in the sub-frame: $T_{slot} = 30720 T_{s,\mu=2} = 250\ \mu s$

The OFDM duration is fixed by the carrier spacing: $T_{OFDM} = 2048\ T_{s,\mu=2} \approx 16.67\ \mu s$

As it is shown in Figure Annex 5, a slot is composed of 12 OFDM symbols and 12 cycle prefix.

$$T_{slot} = 12\ T_{OFDM} + T_{CP}$$

Hence, to fully occupy the slot, the cycle prefixes have to verify:

$$T_{CP} = (30\,720 - 12 * 2048)\ T_{s,\mu=2} = 6\,144 T_{s,\mu=2}$$

We have:

$$6\,144 = 12 * 512$$

The length of the OFDM symbols is then $512 T_{s,\mu=2,n} \approx 4.167 \mu s$.

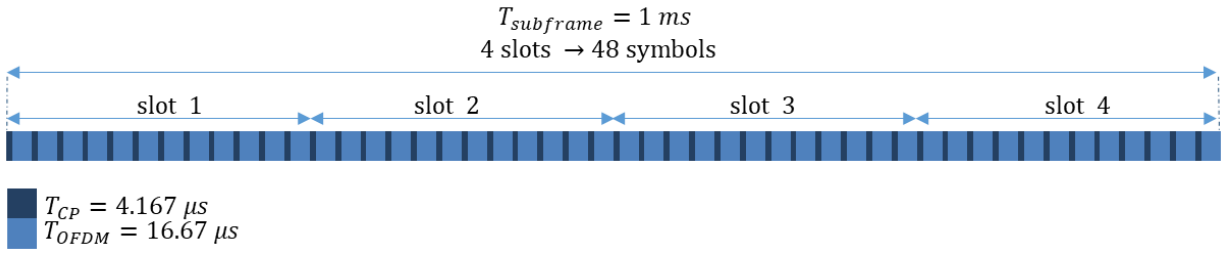

Figure Annex 5 – μ = 2 – extended CP

C.1.4) μ = 3

In this numerology, the following parameters are applied:

- $\Delta f = 120\,000\ Hz$
- $N_{slot}^{subframe} = 8$
- $N_{symb}^{slot} = 14$

The basic unit time is: $T_{s,\mu=3} = 2^{-\mu} T_s = \frac{2^{-3}}{2048*15000} = \frac{1}{245\,760\,000} \approx 4.069\ ns$

A frame has duration of 10 ms: $T_{frame} = \frac{\Delta f_{max}\, N_f}{100} T_c = \frac{\Delta f_{max}\, N_f}{100} \frac{T_{s,\mu=3}}{\kappa} = 2\,457\,600 T_{s,\mu=3} = 10\ ms$

Each frame is composed of 10 sub-frames of duration 1 ms: $T_{subframe} = 245\,760\ T_{s,\mu=3}$

For the case considered, there are eight slots in the sub-frame: $N_{Symbols} = 112$

The OFDM duration is fixed by the carrier spacing: $T_{OFDM} = 2048\, T_{s,\mu=3} \approx 8.333\ \mu s$

As it is shown in Figure Annex 6, a sub-frame is composed of eight slots of 14 OFDM symbols and 14 cycle prefix each.

$$T_{subframe} = 112\, T_{OFDM} + T_{CP}$$

Hence, to fully occupy the slot, the cycle prefixes have to verify:

$$T_{CP} = (245\,760 - 112 * 2048)\, T_{s,\mu=3} = 16\,384 T_{s,\mu=3}$$

2 CP lengths are defined (the same principle is applied for 4G-LTE). As defined in [43], symbols 0 and 56 have extended length, we have:

$$16\,384 = 110 * 144 + 2 * 272$$

The length of the first and seventh OFDM symbols CP is then $272 T_{s,\mu=3} \approx 1.106\ \mu s$ and the length of the remaining OFDM symbols CP is $144 T_{s,\mu=3} \approx 585.9\ ns$.

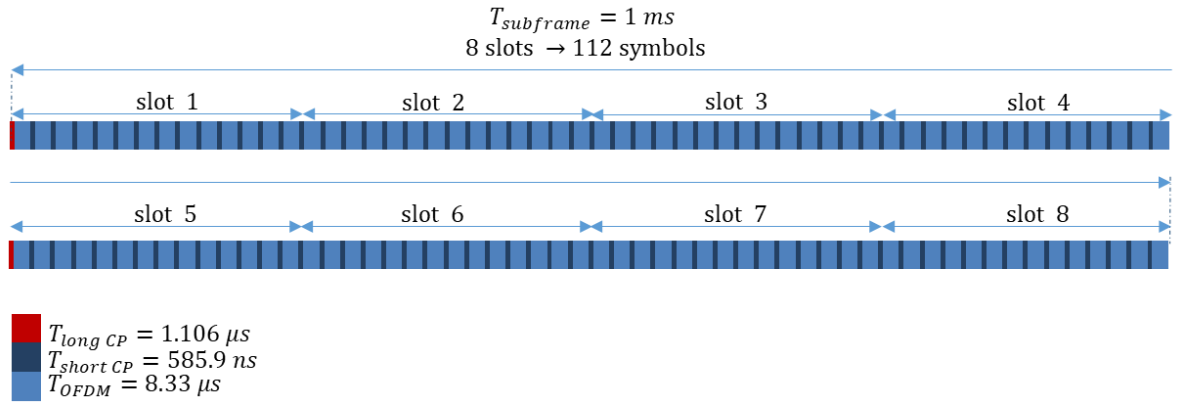

Figure Annex 6 – μ = 3

C.1.5) μ = 4

In this numerology, the following parameters are applied:

- $\Delta f = 240\,000\ Hz$
- $N_{slot}^{subframe} = 16$
- $N_{symb}^{slot} = 14$

The basic unit time is: $T_{s,\mu=4} = 2^{-\mu} T_s = \frac{2^{-4}}{2048*15000} = \frac{1}{491\,520\,000} \approx 2.034\ ns$

A frame has duration of 10 ms: $T_{frame} = \frac{\Delta f_{max}\, N_f}{100} T_c = \frac{\Delta f_{max}\, N_f}{100} \frac{T_{s,\mu=4}}{\kappa} = 4\,915\,200 T_{s,\mu=4} = 10\ ms$

Each frame is composed of 10 sub-frames of duration 1 ms: $T_{subframe} = 491\,520\, T_{s,\mu=4}$

For the case considered, there are sixteen slots in the sub-frame: $N_{Symbol} = 224$

The OFDM duration is fixed by the carrier spacing: $T_{OFDM} = 2048\, T_{s,\mu=4} \approx 4.167\ \mu s$

As it is shown in Figure Annex 7, a sub-frame is composed of sixteen slots of 14 OFDM symbols and 14 cycle prefix each.

$$T_{subframe} = 224\, T_{OFDM} + T_{CP}$$

Hence, to fully occupy the slot, the cycle prefixes have to verify:

$$T_{CP} = (491\,520 - 224 * 2048)\, T_{s,\mu=4} = 32\,768 T_{s,\mu=4}$$

2 CP lengths are defined (the same principle is applied for 4G-LTE). As defined in [43], symbols 0 and 112 have extended length, we have:

$$32\,768 = 222 * 144 + 2 * 400$$

The length of the first and seventh OFDM symbols CP is then $400T_{s,\mu=4} \approx 813.8\ ns$ and the length of the remaining OFDM symbols CP is $144T_{s,\mu=4} \approx 292.9\ ns$.

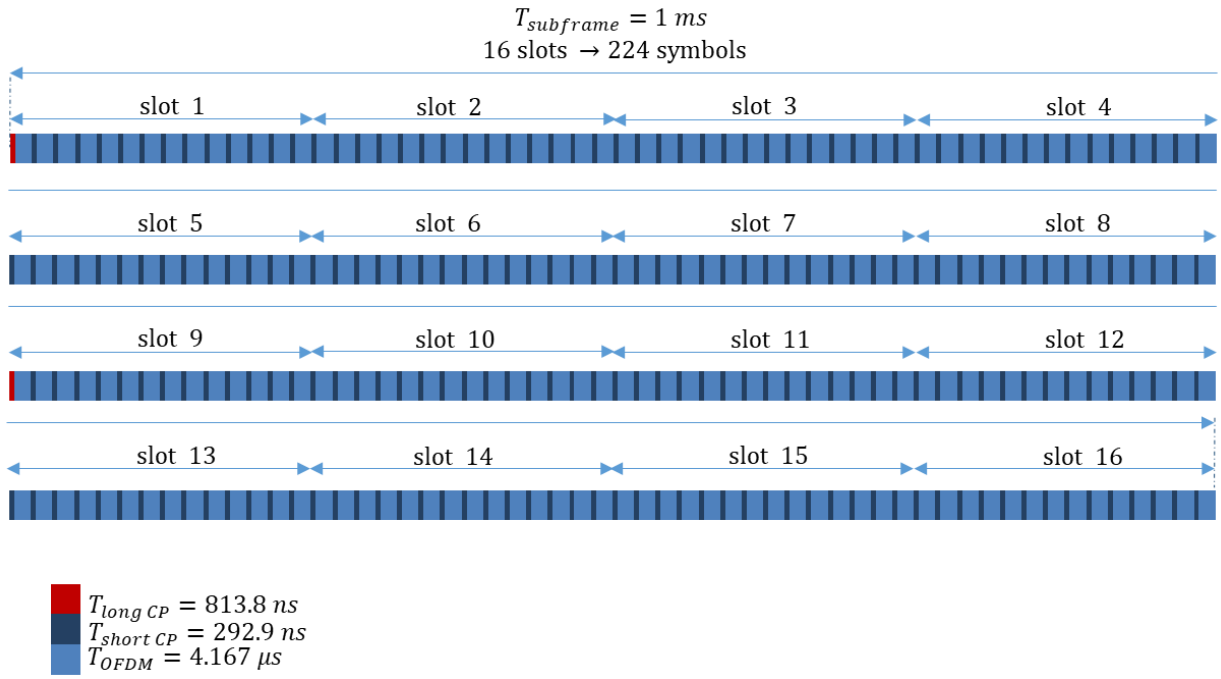

Figure Annex 7 – μ = 4

C.1.6) A.6 – Summary

μ	CP	Number of slot	OFDM symbol duration	1st and $(7.2^{\mu})^{th}$ CP duration	Other CP duration
0	Normal	1	66.67 µs	5.208 µs	4.687 µs
1	Normal	2	33.33 µs	2.865 µs	2.376 µs
2	Normal	4	16.67 µs	1.692 µs	1.172 µs
2	Extended	4	16.67 µs	4.167 µs	4.167 µs
3	Normal	8	8.333 µs	1.106 µs	585.9 ns
4	Normal	16	4.167 µs	813.8 ns	292.9 ns

C.2) Time location of SS/PBCH blocs

In this annex, the time location of the synchronization bloc is detailed. As explain in Chapter 3 section 3.3.6.3.2, 5 cases are defined in the standard according to the numerology and the carrier frequency used.

C.2.1) Case A

The standard specifies:

"For a half frame with SS/PBCH blocks, the number and first symbol indexes for candidate SS/PBCH blocks are determined according to the subcarrier spacing of SS/PBCH blocks as follows.

- *Case A: 15 kHz subcarrier spacing: the first symbols of the candidate SS/PBCH blocks have indexes of {2, 8} + 14*n. For carrier frequencies smaller than or equal to 3 GHz, n=0, 1. For carrier frequencies larger than 3 GHz and smaller than or equal to 6 GHz, n=0, 1, 2, 3."*

This visually can be represented as:

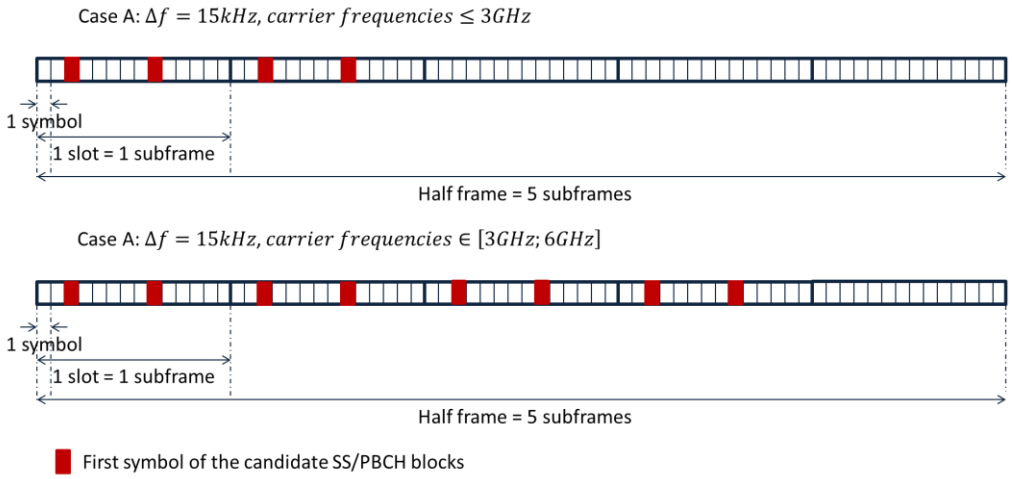

Figure Annex 8 – case A

C.2.2) Case B

The standard specifies:

"For a half frame with SS/PBCH blocks, the number and first symbol indexes for candidate SS/PBCH blocks are determined according to the subcarrier spacing of SS/PBCH blocks as follows.

- *Case B: 30 kHz subcarrier spacing: the first symbols of the candidate SS/PBCH blocks have indexes {4, 8, 16, 20} + 28*n. For carrier frequencies smaller than or equal to 3 GHz, n=0. For carrier frequencies larger than 3 GHz and smaller than or equal to 6 GHz, n=0, 1."*

This visually can be represented as:

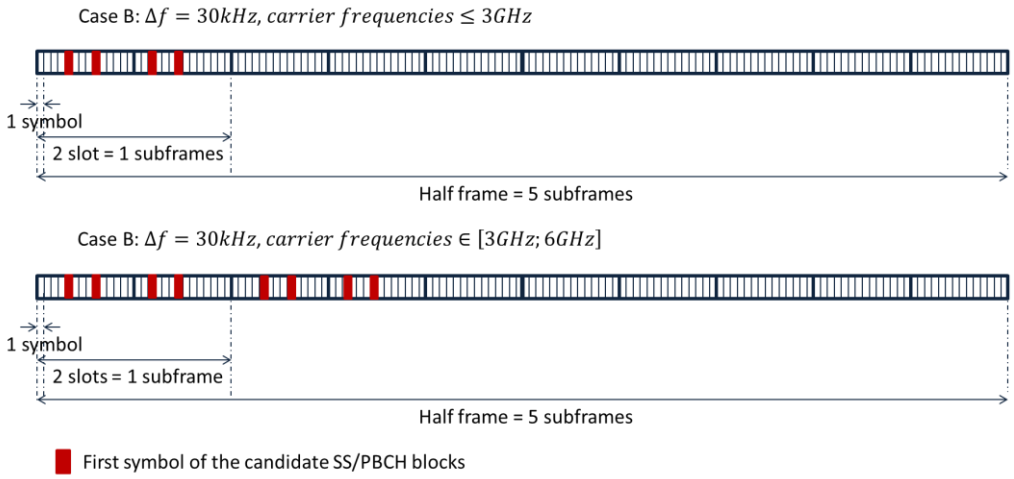

Figure Annex 9 – case B

C.2.3) Case C

The standard specifies:

"For a half frame with SS/PBCH blocks, the number and first symbol indexes for candidate SS/PBCH blocks are determined according to the subcarrier spacing of SS/PBCH blocks as follows.

- *Case C: 60 kHz subcarrier spacing: the first symbols of the candidate SS/PBCH blocks have indexes {2, 8} + 14*n. For carrier frequencies smaller than or equal to 3 GHz, n=0, 1. For carrier frequencies larger than 3 GHz and smaller than or equal to 6 GHz, n=0, 1, 2, 3."*

This visually can be represented as:

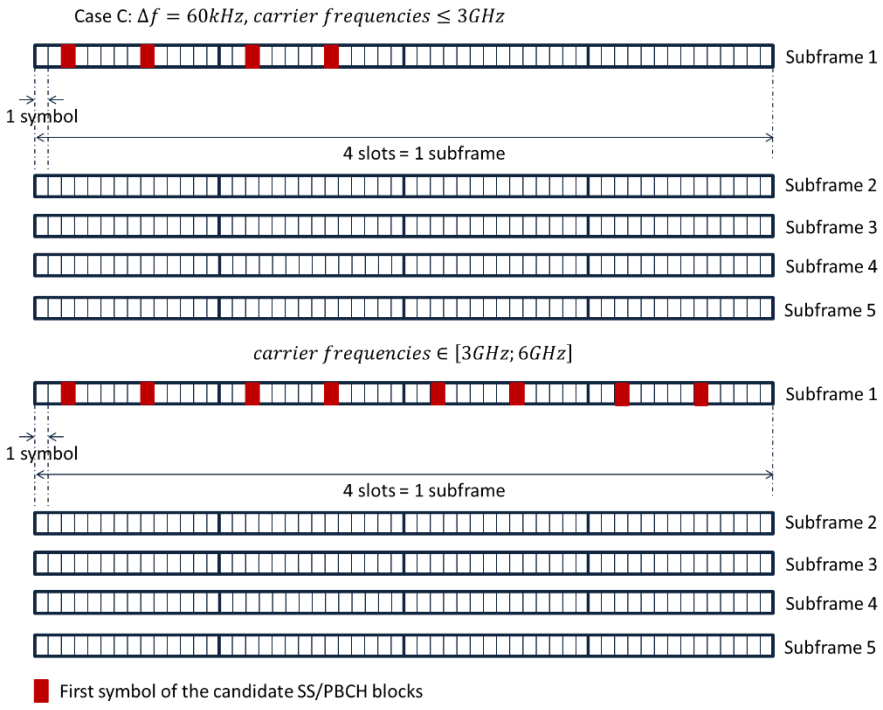

Figure Annex 10 – case C

C.2.4) Case D

The standard specifies:

"For a half frame with SS/PBCH blocks, the number and first symbol indexes for candidate SS/PBCH blocks are determined according to the subcarrier spacing of SS/PBCH blocks as follows.

- *Case D: 120 kHz subcarrier spacing: the first symbols of the candidate SS/PBCH blocks have indexes {4, 8, 16, 20} + 28*n. For carrier frequencies larger than 6 GHz, n=0, 1, 2, 3, 5, 6, 7, 8, 10, 11, 12, 13, 15, 16, 17, 18."*

This visually can be represented as:

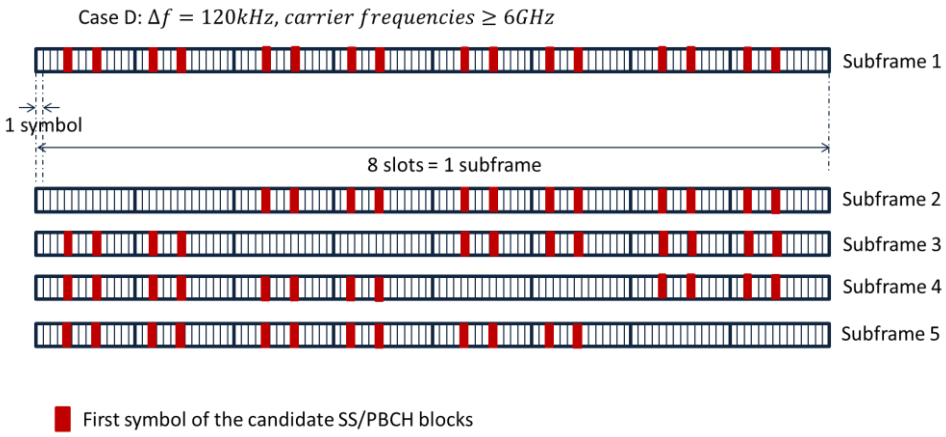

Figure Annex 11 – case D

C.2.5) Case E

The standard specifies:

"For a half frame with SS/PBCH blocks, the number and first symbol indexes for candidate SS/PBCH blocks are determined according to the subcarrier spacing of SS/PBCH blocks as follows.

- *Case E - 240 kHz subcarrier spacing: the first symbols of the candidate SS/PBCH blocks have indexes {8, 12, 16, 20, 32, 36, 40, 44} + 56*n. For carrier frequencies larger than 6 GHz, n=0, 1, 2, 3, 5, 6, 7, 8."*

This visually can be represented as:

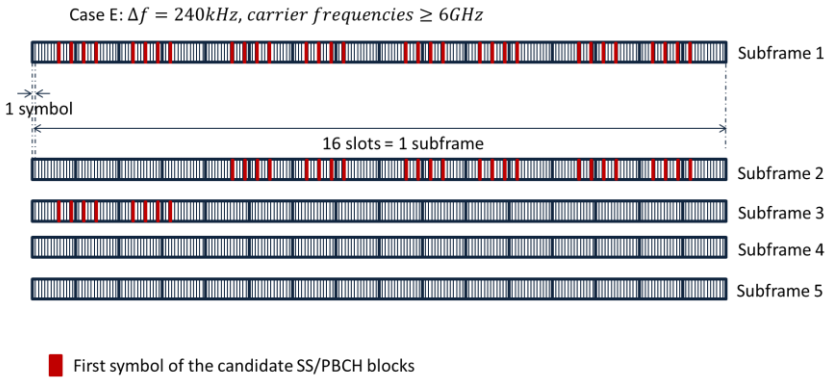

Figure Annex 12 – case E

C.3) Complement to the OFDM modulation description

For clarity reason, some properties of the OFDM modulation have not been explained in chapter 3. In this section the orthogonality of the OFDM modulation is demonstrate and second, the OFDM time dispersity property is reminded and complemented.

C.3.1) Orthogonality in OFDM

As said above, OFDM is based on orthogonal subcarriers. In other words, two modulated subcarriers s_{p_1} and s_{p_2} are mutually orthogonal over a symbol duration ($kT \leq t < (k+1)T$, where $T = \frac{1}{\Delta f}$ is the symbol duration). Mathematically, for 2 different integers, $p_1 \neq p_2$, equation $(C.2)$ demonstrates the orthogonality property.

$$\begin{aligned} < s_{p_1}, s_{p_2} > &= \int_{kT}^{(k+1)T} s_{p_1} s_{p_2}^* dt = \int_{kT}^{(k+1)T} d_{p_1}^k d_{p_2}^{*k} e^{i2\pi(p_1-p_2)\Delta f t} dt \\ &= \frac{d_{p_1}^k d_{p_2}^{*k}}{i2\pi(p_1-p_2)\Delta f} \left[e^{i2\pi(p_1-p_2)\Delta f t} \right]_{kT}^{(k+1)T} \\ &= \frac{d_{p_1}^k d_{p_2}^{*k}}{i2\pi(p_1-p_2)\Delta f} e^{i2\pi(p_1-p_2)k} \left[e^{i2\pi(p_1-p_2)} - 1 \right] = 0 \end{aligned} \qquad (C.2)$$

C.3.2) OFDM Time dispersity

The second main phenomenon linked to the multipath environment is time dispersity. Time dispersity is due to the spreading of the symbols' power in time. The solution usually adopted to correct this distortion is to introduce an interval between two consecutive symbols, to avoid inter-symbol interferences. In OFDM, the interval is filled with a cycle prefix before the OFDM actual symbol, see Figure Annex 13.

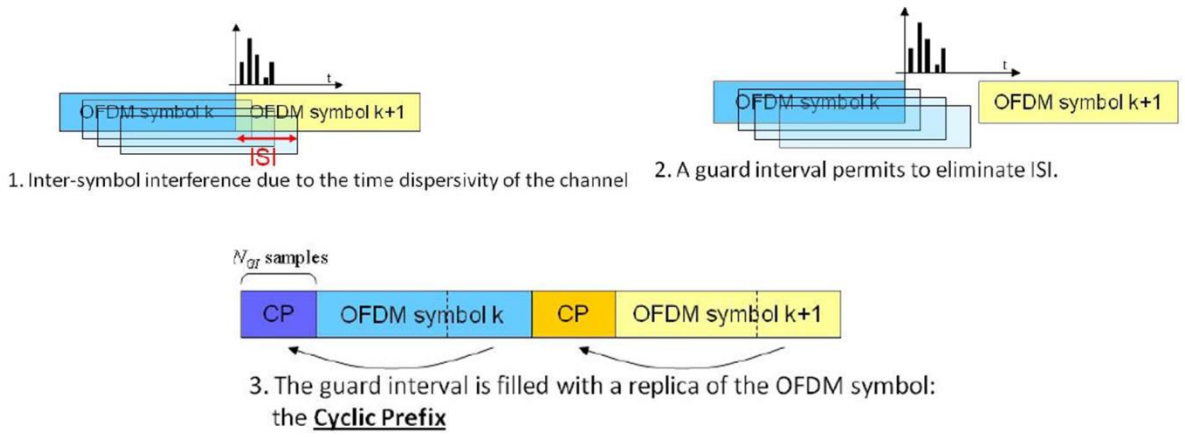

Figure Annex 13 – Cycle prefix introduction to combat time dispersity – source [41]

The cycle prefix is composed of the last N_{CP} samples of the OFDM symbol; hence the total length of the OFDM symbol becomes: $N_{CP} + N_{FFT}$. The samples belonging to the cycle prefix can be expressed as in $(C.3)$

$$s_n^k = s_{n+N_{FFT}}^k \; for - N_{CP} \leq n < 0 \qquad (C.3)$$

This property is interesting for the demodulation process. Indeed, the demodulation (i.e. the FFT) is done over N_{FFT} samples. In the ideal case, assuming a perfect synchronization process, the beginning of the FFT window would be placed just at the beginning of the symbol, (a) in Figure 3.19. If so, the received signal is expressed as in $(C.5)$.

$$r_{n\ with\ CP}^k = \sum_{p=-N_{CP}}^{N_{FFT}-1} s_p^k(nT_s) \qquad (C.4)$$

The cycle prefix is removed from the previous equation and therefore the received signal to be processed is given below.

$$r_n^k = \sum_{p=0}^{N_{FFT}-1} s_p^k(nT_s) \qquad (C.5)$$

Where $p = 0$ denotes the beginning of the OFDM symbol.

If there is a delay in the choice of the beginning of the FFT window (ie synchronization delay), case (b) in Figure 3.19, it will create a phase shift in the demodulation process. Indeed, let's consider the case (b); then noting N_s the advance in samples from the start of the OFDM symbol, the demodulated symbol is given in $(C.7)$. More specifically, the iFFT is performed as in $(C.6)$ with the sum over $n \in [0, N_{FFT}-1]$. Nevertheless, since there is a delay in the beginning of the FFT widow, the received signal is shifted from the delay N_s. Therefore, a change of variable is performed in order to obtain $(C.7)$.

$$\tilde{d}_{p'}^k = FFT_{N_{FFT}}(r_n^k)[p'] = \sum_{n=0}^{N_{FFT}-1} r_{n+N_s}^k \, e^{-i2\pi\frac{np'}{N_{FFT}}} \qquad (C.6)$$

$$\tilde{d}_{p'}^k = \sum_{n=-N_s}^{N_{FFT}-1-N_s} r_n^k \, e^{-i2\pi\frac{(n+N_s)p'}{N_{FFT}}} \qquad (C.7)$$

The sum can be split into two contributions (the samples that fall into the cycle prefix and the samples that fall into the OFDM symbol), as given in $(C.8)$.

$$\tilde{d}_{p'}^k = \sum_{n=-N_s}^{-1} r_n^k \, e^{-i2\pi\frac{(n+N_s)p'}{N_{FFT}}} + \sum_{n=0}^{N_{FFT}-1-N_s} r_n^k \, e^{-i2\pi\frac{(n+N_s)p'}{N_{FFT}}} \qquad (C.8)$$

Assuming an AWGN case, $r_n^k = s_n^k$, and using the property $s_n^k = s_{n+N_{FFT}}^k \; for - N_{CP} \leq n < 0$ the first sum can be rewritten as in $(C.9)$.

$$\begin{aligned} \tilde{d}_{p'}^k &= \sum_{n=-N_s}^{-1} s_{n+N_{FFT}}^k \, e^{-i2\pi\frac{(n+N_s)p'}{N_{FFT}}} + \sum_{n=0}^{N_{FFT}-1-N_s} s_n^k \, e^{-i2\pi\frac{(n+N_s)p'}{N_{FFT}}} \\ \tilde{d}_{p'}^k &= \sum_{n=N_{FFT}-N_s}^{N_{FFT}-1} s_n^k \, e^{-i2\pi\frac{(n+N_s-N_{FFT})p'}{N_{FFT}}} + \sum_{n=0}^{N_{FFT}-1-N_s} s_n^k \, e^{-i2\pi\frac{(n+N_s)p'}{N_{FFT}}} \end{aligned} \qquad (C.9)$$

The second sum of $(C.8)$ can be divided as proposed in $(C.10)$, which permits to simplify the first and third sums since the N_{FFT} term of the first sum complex exponential can be removed (equal to 2π multiple).

$$\begin{aligned} \tilde{d}_{p'}^k &= \sum_{n=N_{FFT}-N_s}^{N_{FFT}-1} s_n^k \, e^{-i2\pi\frac{(n+N_s-N_{FFT})p'}{N_{FFT}}} + \sum_{n=0}^{N_{FFT}-1} s_n^k \, e^{-i2\pi\frac{(n+N_s)p'}{N_{FFT}}} - \sum_{n=N_{FFT}-N_s}^{N_{FFT}-1} s_n^k \, e^{-i2\pi\frac{(n+N_s)p'}{N_{FFT}}} \\ \tilde{d}_{p'}^k &= \sum_{n=0}^{N_{FFT}-1} s_n^k \, e^{-i2\pi\frac{np'}{N_{FFT}}} e^{-i2\pi\frac{N_s p'}{N_{FFT}}} = e^{-i2\pi\frac{N_s p'}{N_{FFT}}} \sum_{n=0}^{N_{FFT}-1} s_n^k \, e^{-i2\pi\frac{np'}{N_{FFT}}} \end{aligned} \qquad (C.10)$$

C.4) Synchronization signal

3 synchronization signals are detailed in the 3GPP standard: the cell ID, the Primary Synchronization Signal and the Secondary Synchronization Signal. The last two are used to generate the SS PBCH synchronization block. Their mathematical models are provided here.

C.4.1) Cell ID

The physical cell ID is an identification of a cell at physical layer; it is determined by the Primary Synchronisation Signal (PSS) and the Secondary Synchronisation Signal (SSS).

There are 1008 unique physical-layer cell identities given by $(C.11)$.

$$N_{ID}^{cell} = 3N_{ID}^{(1)} + N_{ID}^{(2)} \qquad (C.11)$$

Where:

- $N_{ID}^{(1)} \in \{0,1,\dots,335\}$ represents the cell group number (335 kinds of Secondary Synchronisation Sequence)
- $N_{ID}^{(2)} \in \{0,1,2\}$ represents the cell number (3 kinds of Primary Synchronisation Sequence)

C.4.2) PSS

In this section, the Primary Synchronisation Signal is presented. The sequence $d_{PSS}(n)$ for the PSS is defined as in $(C.12)$

$$\begin{gathered} d_{PSS}(n) = 1 - 2x(m) \\ m = \left(n + 43N_{ID}^{(2)}\right) mod 127 \\ 0 \le n \le 127 \end{gathered} \qquad (C.12)$$

Where:

- $x(i+7) = \big(x(i+4) + x(i)\big) mod 2$
- $[x(6) \quad x(5) \quad x(4) \quad x(3) \quad x(2) \quad x(1) \quad x(0)] = [1 \quad 1 \quad 1 \quad 0 \quad 1 \quad 1 \quad 0]$

C.4.3) SSS

In this section, the Secondary Synchronisation Signal is presented. The sequence $d_{SSS}(n)$ for the SSS is defined as in $(C.13)$.

$$\begin{gathered} d_{SSS}(n) = \big[1 - 2x_0\big((n + m_0) mod 127\big)\big]\big[1 - 2x_1\big((n + m_1) mod 127\big)\big] \\ m_0 = 15\left\lfloor \frac{N_{ID}^{(1)}}{112} \right\rfloor + 5N_{ID}^{(2)} \\ m_1 = N_{ID}^{(1)} mod 112 \\ 0 \le n \le 127 \end{gathered} \qquad (C.13)$$

Where:

- $x_0(i+7) = \big(x_0(i+4) + x_0(i)\big) mod 2$
- $x_1(i+7) = \big(x_1(i+1) + x_1(i)\big) mod 2$
- $[x_0(6) \quad x_0(5) \quad x_0(4) \quad x_0(3) \quad x_0(2) \quad x_0(1) \quad x_0(0)] = [0 \quad 0 \quad 0 \quad 0 \quad 0 \quad 0 \quad 1]$
- $[x_1(6) \quad x_1(5) \quad x_1(4) \quad x_1(3) \quad x_1(2) \quad x_1(1) \quad x_1(0)] = [0 \quad 0 \quad 0 \quad 0 \quad 0 \quad 0 \quad 1]$

C.5) Propagation channel

C.5.1) 5G requirements

The 5G requirements in term of transmission channel depend on several parameters: the scenarios in which the radio system is expected to be used (indoor, outdoor, rural, and urban), the frequencies used, the bandwidths, the antenna, etc. In the following, the main challenges with 5G systems are presented.

C.5.1.1) Expected scenarios

The main objective of 5G systems is to provide services to anyone and anything anywhere and anytime. In that perspective, 5G must be available all the time everywhere and so a wide range of propagation scenarios must be modelled. The wireless network must serve from stationary users to mobile users, and

the mobile-to-mobile links. The wireless system should work reliably in any environment, including indoor, outdoor-to-indoor, dense urban, wide area, highway, shopping mall, stadium, etc. The network topologies should support not only cellular, but also direct device-to-device (D2D), machine-to-machine (M2M) and vehicle-to-vehicle (V2V) links as well as full mesh networks.

C.5.1.2) Spectrum considerations

In addition to the frequency bands traditionally used be current mobile telecommunication systems (sub-6 GHz bands), 5G systems will use millimetre waves which are electromagnetic waves typically defined to lie within the frequency range of 30–300 GHz. Those frequencies are very promising; they make it possible to implement very small antennas and even massive array antennas in relatively small volume. In addition to that, the spectrum at mmW frequencies is rather unused, which means that wider bandwidths are available. However, note that the propagation properties for these frequencies are not perfectly known.

To summarize, it is necessary to define propagation effects for the full frequency range from 350 MHz up to 100 GHz.

C.5.1.3) Antenna considerations

Current channel models assume plane wave propagation and that the size of an array antenna is small. An important technology component of 5G mobile communications is the use of very large array antennas: massive MIMO. For these highly directive antennas or large array antennas, huge performance gains are expected. These large arrays require non-planar wave modelling replacing the commonly used plane wave approximation.

C.5.1.4) Spatial consistency and mobility

Another technical direction of 5G systems is the use of denser network. Traditional networks use macro cells and microcells, with 5G systems pico-cells and femto-cells are expected to be use. The femto-cells have the shortest range of small cell types, usually deployed in homes or small enterprises. Femtocells have maximum range of less than 10 meters. Pico-cells are usually installed in larger indoor areas like shopping malls, workplaces and airport or stations they can accommodate up to 100 users at a time and ranges under 200 meters.

Moreover, with 5G systems, scenarios where both ends of the links are moving (for example D2D scenario) are envisioned. The traffic is also expected to grow exponentially leading to a growing number of links. Hence, these features bring new requirements to channel modelling in terms of spatial consistency and mobility. The term spatial consistency means that the channel evolves smoothly without discontinuities when the transmitter and/or receiver moves or turns. It also means that channel characteristics are similar in closely located links.

C.5.1.5) Propagation considerations

The use of higher bandwidth and higher number of antennas will increase the delay and spatial resolution of the receiver. Hence, the propagation effects must be more precisely modelled. Particularly, for 5G systems, the channel modelling should consider realistic modelling of specular paths.

C.5.1.6) Complexity and accuracy

As presented earlier, a wide range of scenarios has to be modelled, each having different requirements in terms of model accuracy and complexity. In other words, the model must be realistic enough to represent the scenario and not too complicated to be applicable.

C.5.1.7) D2D communication

D2D connections are today an important part of modern radio communications. However, channel models for D2D connections are not perfectly known.

C.5.2) State of the art

In the previous section, the main requirements for 5G channel model have been presented. In this section, an overview of the main models currently used is provided to identify a suitable candidate for 5G propagation channel exploited for positioning purposes.

C.5.2.1) Channel modelling

There are three main ways to model a channel: a deterministic, a stochastic and geometry based stochastic way (see [68] for more details).

C.5.2.1.1) Deterministic channel modelling

Deterministic channel modelling is used for site specific channel modelling. The deterministic channel model can be divided into parts, an environment model and a wave propagation model. The environment model describes the position, the geometry, the material composition and the surface properties of the relevant objects and obstacles. The wave propagation model consists in computing Maxwell equations when taking into account the environment model. Maxwell's equations are often approximated by using ray tracing techniques, which are methods that are valid as long as the light waves propagate through and around objects whose dimensions are much greater than the light's wavelength. Deterministic channel modelling requires such intensive computation that it is almost impossible to use.

C.5.2.1.2) Stochastic channel modelling

Stochastic channel modelling provides the statistics of the power received with a certain Doppler shift, delay, Angle of Arrival (AOA), etc. These types of channel modelling require much less computation resources than the deterministic channel modelling, but they will not reproduce exactly the behaviour of a site/environment.

C.5.2.1.3) Geometry based stochastic modelling

The principle of Geometry based Stochastic Channel Models (GSCM) consists in first placing diffuse or discrete scatterers randomly according to certain statistical distribution and assigning them scattering properties. Contrary to the deterministic channel modelling the GSCM generates randomly the environment. Second, the signal contribution of the scatterers is determined from a greatly simplified ray tracing, and finally, the total signal is summed up at the receiver. There are several advantages of such modelling. First it can easily handle non-stationary channels; it also provides not only delay and Doppler spectra but inherently models the MIMO properties of the channel, it represents wideband channels. Therefore, it is possible to easily change the antenna influence by simply including a different antenna pattern. The environment can also be easily changed and statistically generated. Finally, it is much faster than deterministic ray tracing since only single scattering needs to be simulated.

When designing a wireless transmission system, it is useful to evaluate its performance over at least a minimum number of channel realizations. The high computational complexity of deterministic modelling prohibits the intensive link or system level simulation required during system design. This is one of the main reasons why GSCM modelling is the most used type of propagation channel model in practice.

In Figure Annex 14, the global evolution of GSCM models is presented. In the next section, they are briefly described and references are provided to further study each model.

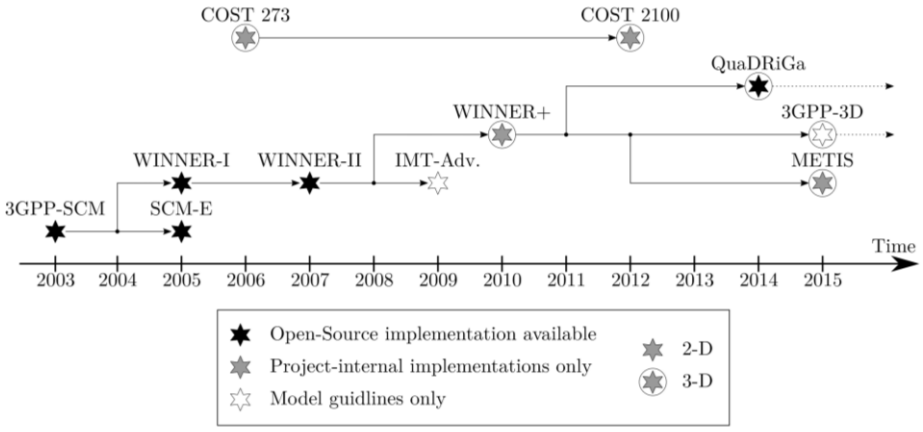

Figure Annex 14 – GSCM evolution – source [45]

C.5.2.2) Literature review

Focusing on GSCM and with the objective of finding a usable 5G propagation channel for positioning purposes, five main projects/models, presenting 5G propagation channel models, can be cited:

- The WINNER propagation channel model: The Wireless world INitiative for New Radio (WINNER) project had as goal to develop a single ubiquitous radio access system adaptable to a comprehensive range of mobile communication scenarios from short range to wide area. It is a GSCM model. It is scalable in terms of carrier bandwidth and carrier frequency range. The channel parameters for individual snapshots are determined stochastically, based on statistical distribution extracted from channel measurement. Channel realisation are generated with geometrical principle by summing contributions of rays (plane waves) with specific small scale parameters like delay, power angle of arrival and departure. The WINNER channel model is a widely used propagation channel model. More details can be found in [69] and [70].
  Based on this model, three evolution of the WINNER project have been developed: the METIS project, the QuaDRiGa project and the 3GPP 3D project. These models are presented as 5G-compliant propagation channel model:
  - The METIS project: This model is used at Tampere University of Technology (TUT) for their work on 5G positioning; however, no public implementation is available
  - The 3GPP 3D model: The time line does not go after 2015, however, an implementation is available in matlab in the LTE Toolbox
  - The QuaDRIGa project which provides an open source implementation of the channel model.
- The 3GPP LTE 3D channel model: the 3GPP LTE 3D model, developed for the Long Term Evolution (LTE) systems, is a GSCM. Several propagation scenarios described in this standard from urban micro cell environment with high UE density, the BS is placed below surrounding buildings to indoor hotspot cell environment with high UE density, etc. The frequency range in which the model is usable is 2GHz to 3.5GHz. However, the path loss models developed for the model can only be used for frequencies in the range 2GHz to 6GHz. The 3GPP 3D channel model provides additional flexibility for the elevation dimension, allowing modelling for 2D antenna systems. More details can be found in [71].
- The International Mobile Telecommunication Advanced models: the IMT Advanced models present compatible use case scenarios with 5G; the IMT advanced models can be applied are indoor, micro cellular, macro cellular, and high speed scenarios. It supports low to high mobility application and a wide range of data rates in accordance with users and service demands in multiple environments. Key features of these models are:

- high degree of commonality of functionality worldwide while retaining the flexibility to support a wide range of services and application in a cost efficient manner
- Compatibility of services within IMT and with fixed networks
- Capability of interworking with other radio access systems
- High quality mobile services
- UE suitable for worldwide use
- User friendly application, services and equipment
- Worldwide roaming capability
- Enhanced peak data rates to support advanced services and applications

More details can be found in [72].

- The COST 2100 propagation channel model: the COST 2100 is a GSCM model well suited for MIMO simulation and already designed for telecommunication system, especially for 4G networks. Contrary to the previous models, in the COST models, the clusters (scattering objects) are defined as being present in the environment and are not specific to one single link. Each cluster is described by a visibility region and is visible to UE located within this region. This enables closely located users to see partly similar environments. Spherical waves and smooth time evolution of the channel is supported because the clusters have their location fixed. The principle of this model is the following one. The whole environment is first generated and the movement of the UE in this simulation causes the visibility of different clusters to change as the UE enters and leaves different visibility regions resulting implicitly in non-stationary channel simulation. For most of the propagation scenarios envisioned with the COST 2100 models (macro/micro/pico-cellular, outdoor rural environments), the frequency used is 400MHz. For indoor pico-cellular scenarios it is at 3.6GHz and 5.3GHz. More details can be found in [73].
- Wireless Local Area Networks (WLAN): This model is defined for 60GHz, frequencies envisioned for 5G, where very high data rates are required. It is a cluster based model and is parameterized for three indoor scenarios: Living room, Conference room and cubicle. Since the model parameters are created deterministically, the parameterisation for each scenario is site specific and may not be valid for other similar environments. More details can be found in [74].

C.5.2.3) Deficiencies of current models

The previously presented channel models present interesting characteristics for 5G: the WINNER and the 3GPP 3D models are already used for mobile telecommunications, the WLAN deals with millimeter wave frequencies, the COST 2100 is well suited for MIMO simulations, etc. Nevertheless, none of them completely fulfills the 5G requirements. This section aims at presenting the deficiencies of the previously presented propagation channel models.

C.5.2.3.1) General comment

The WINNER, the 3GPP and the IMT-Advanced models present the same deficiencies. They are designed for a fixed BS, it means that they cannot be applied for D2D scenarios or if BS is moving or in ultra-dense network (UDN) where closely located BS sees partly the same environment. Other problems are the lack of support for spherical waves and consistent modelling of closely located users in other words there is poor realism when high spatial realism is needed (in particular for MIMO). The last important limitation is that, the frequency range where these models can be applicable is limited to sub 6GHz; far from the mmW expected with 5G systems.

The COST 2100 model also presents a set of deficiencies that makes it unusable for 5G systems. First the model is limited to sub-6GHz frequency range. Second, the BSs are at fixed location making the model unusable for D2D scenarios. Finally, it is difficult to parameterized different environments.

C.5.2.3.2) Back to 5G requirements

The deficiencies of current models regarding 5G requirements are summarized below.

- Most of the models are 2D models. Hence considering that 3D beamforming will be an important feature of 5G systems, they cannot be used.
- The frequency range is limited. Most of currently used models have been concentrated to sub-6GHz frequency range and around 60GHz for IEEE 802.11 model. 5G systems are envisioned to use from 350 MHz up to 100 GHz.
- The bandwidth is limited. Millimetre waves spectrum is rather unused, hence wider bandwidth are available, the propagation model must be adapted to these large bandwidth.
- Some propagation scenarios are not considered. More specifically, it misses the mass events scenarios and the D2D scenarios. Indeed, traditional model supposed that the BS is fixed and only the UE is moving; however, D2D is an important feature of 5G systems.
- Spherical modelling is missing. 5G systems will use very large array antennas which require both high resolution and realistic distribution. Hence, propagation waves need to be modelled spherical whereas they are planar in the currently used models.

More details can be found in [75], to summarize, the following table has been extracted from [75].

Feature	3GPP Stochastic Channel Model	WINNER II/ WINNER +	IMT-Advanced	3GPP D2D	3GPP 3D	IEEE 802.11	COST 2100
Frequency range (GHz)	1-3	1-6	0.45-6	1-4	1-4	60-66	0.4-6
Bandwidth (MHz)	5	100	100	100	100	2000	100
Support mMIMO	No	Limited	No	No	No	Yes	Yes
Support spherical waves	No	No	No	No	No	No	Yes
Support extremely large arrays	No	No	No	No	No	No	No
Support dual mobility	No	No	No	Limited	No	No	No
Support 3D	No	Yes	No	No	Yes	Yes	No
Support mmw	No	No	No	No	No	Yes	No
Dynamic modelling	No	Very limited	No	No	No	Limited	Yes

Table 23 – Models comparison – source [75]

Based on these observations, only the three models evolved from the WINNER project are 5G compliant propagation channel model. They fulfill the main requirements identified for 5G regarding:

- Frequency range. For each models, millimeter waves as well as sub-6 GHz carrier frequency can be modelled
- Envisioned scenarios: dense urban as well as indoor environment can be modelled
- Antenna considerations: MIMO antennas can be modelled

At the time the research for a 5G compliant propagation channel was led (Mid 2018), the LTE toolbox did not allow the definition of a precise trajectory, the receiver was fixed. This was a serious limit for the Ph.D. since no path delay evolution can be modelled. Moreover, the toolbox is not open accessed.

The METIS project is not a free open source project, therefore not usable for the Ph.D.

The QuaDRiGa project is an open free project, allowing the design of particular trajectory and high level scenario propagation. Therefore, the propagation channel model adopted for the rest of the Ph.D. is QuaDRiGa.

Annex D) Determination of the CIR sampling interval for accurate modeling of symbol demodulation

D.1) Addentum to 4.1.5 – comparison with respect to the demodulated symbols and the correlator

Remind that in section 4.1.5, the following method is applied to determine the required CIR sampling interval of a 5G signal propagation channel with complex amplitude evolving over 1 OFDM symbol. Remind that this CIR sampling interval is required in section 4.2 to determine the correlator output mathematical model for ranging purposes.

1. The second or fourth 5G SSPBCH reference OFDM symbols presented in Figure 3.28 is generated (pilots and random data).
2. The propagation channel is generated considering 1, 10, 20 and 100 CIR and applied to the generated symbol.
3. The demodulated symbols, (3.28), and the correlator, (3.29)., obtained with each considered X CIR sampling rate, are compared to the 100 CIR samples case per symbol (reference). The comparison metrics is presented in section 4.1.5.2.
4. The results are analyzed with respect to the first criterion, described in section 4.1.5.3, to complete the study proposed in section 4.1.5.4

In Table 4.4 and Table 4.5, the first selection criterion presented in in section 4.1.5 is inspected. On these tables, the averaged mean and standard deviation of the RE (for the demodulation and correlation part) are provided. Results are provided for all trajectories in both LOS (Table 4.4) and NLOS (Table 4.5) scenarios. The color code adopted for all tables represents the following conditions:

- in red, differences between reference and tested X-CIR sampling rate are deemed unacceptable
- in orange, differences between reference and tested X-CIR sampling rate are deemed at the acceptance limit
- in blue, differences between reference and tested X-CIR sampling rate fulfill the criteria and the CIR configuration is the selected one
- in green, differences between reference and tested X-CIR sampling rate are better than the criteria

From Table 4.4, the first relevant conclusion of the CIR sampling rate determination can be extracted for the LOS scenario: 10CIR per OFDM symbol is suitable candidate for all cases. However, results are less convincing for 10CIR as seen in Table 4.5 for the NLOS scenario. In fact, no CIR generation sampling rate is satisfying except for a small group of cases.

Table 24 – LOS scenario – CIR generation rate impact on the demodulation, the correlation and the discriminator output

Trajectory			Trajectory 1		Trajectory 2		Trajectory 3		Trajectory 4	
Scenario			LOS		LOS		LOS		LOS	
Case			1	2	1	2	1	2	1	2
Demodulation RE (100%)	μ	1	0,74	2,90	0,43	0,47	0,65	0,54	0,16	2,27
		10	0,06	0,27	0,04	0,04	0,05	0,04	0,01	0,22
		20	0,03	0,13	0,01	0,02	0,02	0,02	0,00	0,09
	σ	1	0,34	0,71	0,28	0,13	0,46	0,12	0,09	0,68
		10	0,02	0,06	0,02	0,01	0,03	0,01	0,00	0,05
		20	0,01	0,02	0,01	0,00	0,01	0,00	0,00	0,02
o n	μ	1	0,31	0,68	0,41	0,28	0,44	0,29	0,16	0,48

		10	0,02	0,05	0,03	0,02	0,03	0,02	0,01	0,04
		20	0,01	0,02	0,01	0,01	0,01	0,01	0,00	0,02
	σ	1	0,29	0,40	0,29	0,18	0,34	0,18	0,11	0,22
		10	0,02	0,03	0,02	0,01	0,02	0,01	0,00	0,02
		20	0,01	0,01	0,00	0,00	0,01	0,00	0,00	0,01
Discriminator AE (m)	μ	1	0,12	0,21	0,08	0,05	0,18	0,04	0,06	0,37
		10	0,00	0,02	0,00	0,00	0,01	0,00	0,00	0,04
		20	0,00	0,00	0,00	0,00	0,00	0,00	0,00	0,01
	σ	1	0,28	0,18	0,09	0,09	0,14	0,03	0,05	0,65
		10	0,02	0,02	0,00	0,00	0,01	0,00	0,00	0,13
		20	0,00	0,00	0,00	0,00	0,00	0,00	0,00	0,03

Table 25 – NLOS scenario – CIR generation rate impact on the demodulation, the correlation and the discriminator output

Trajectory			Trajectory 1		Trajectory 2		Trajectory 3		Trajectory 4	
Scenario			NLOS		NLOS		NLOS		NLOS	
Case			1	2	1	2	1	2	1	2
Demodulation RE (100%)	μ	1	1,24	3,11	1,10	4,29	1,16	2,99	1,13	4,05
		10	0,11	0,29	0,09	0,40	0,10	0,28	0,10	0,39
		20	0,05	0,13	0,04	0,17	0,04	0,13	0,04	0,17
	σ	1	1,00	1,57	2,28	1,69	1,08	2,53	1,10	0,98
		10	0,08	0,14	0,08	0,15	0,08	0,24	0,10	0,09
		20	0,04	0,06	0,03	0,06	0,03	0,11	0,04	0,04
Correlation RE (100%)	μ	1	0,87	1,74	0,87	2,33	0,78	2,06	0,82	1,38
		10	0,07	0,17	0,07	0,19	0,07	0,20	0,08	0,13
		20	0,03	0,07	0,03	0,09	0,03	0,08	0,03	0,05
	σ	1	0,84	1,35	1,04	1,73	0,70	2,05	0,92	0,91
		10	0,06	0,12	0,08	0,14	0,06	0,19	0,08	0,08
		20	0,03	0,05	0,03	0,06	0,02	0,08	0,03	0,03
Discriminator AE (m)	μ	1	0,72	1,40	0,75	2,20	1,98	13,4	2,39	17,0
		10	0,04	0,29	0,05	0,61	0,15	1,36	0,36	1,43
		20	0,01	0,09	0,02	0,07	0,05	0,56	0,15	1,44
	σ	1	1,99	6,93	4,79	21,9	16,0	24,4	56,4	289,
		10	0,19	4,30	0,32	14,2	1,73	18,4	9,04	29,0
		20	0,08	0,73	0,17	0,63	0,49	7,26	3,69	35,9

However, these results are corrupted by outliers and must be further inspected. In order to do so, the following finer criterion is proposed: the discriminator output AE is satisfying when its value is lower than 0.5m 95% of time and lower than 1m 99% of time. In Table 4.6, the percentage of time when the discriminator output AE is less than 0.5m (upper part) and less than 1m (lower part) is presented. These criteria are satisfied when using 10CIR per OFDM symbol for the 0.5m criterion, and when using 20CIR per OFDM symbol for the 1m criterion; for all cases but the NLOS case 2.

D.2) Addentum to 4.1.5 – comparison with different DLL tuning

In this annex the discriminator output AE are provided for 4 DLL configurations; they are described in Table 26.

Table 26 – DLL configurations tested

	Configuration 1	Configuration 2	Configuration 3	Configuration 4
DLL loop bandwidth	10Hz	1Hz	1Hz	10Hz
Correlator spacing	4 samples	6 samples	4 samples	6 samples

The criterion used are reminded: the discriminator output AE is satisfying when it is lower than 0.5m 95% of time and lower than 1m 99% of time. In the following tables, the percentage of time when the discriminator output AE is less than 0.5m and less than 1m is presented.

The color code adopted for all tables represents these criteria:

- in red, differences between reference and tested X-CIR sampling rate are deemed unacceptable
- in orange, differences between reference and tested X-CIR sampling rate are deemed at the acceptance limit
- in blue, differences between reference and tested X-CIR sampling rate fulfill the criteria and the CIR configuration is the selected one
- in green, differences between reference and tested X-CIR sampling rate are better than the criteria

D.2.1) DLL configuration 1

Discriminator output AE <0.5m	radial				50m				100m				150m			
	LOS		*NLOS*		*LOS*		*NLOS*		*LOS*		*NLOS*		*LOS*		*NLOS*	
	1	*2*	*1*	*2*	*1*	*2*	*1*	*2*	*1*	*2*	*1*	*2*	*1*	*2*	*1*	*2*
1CIR	96.5	91.8	65.8	54.5	99.7	99.3	77.8	36.4	96.1	100	65.8	1.93	99.9	78.3	62.9	8.2
10CIR	100	100	99.1	91.6	100	100	98.5	66.7	100	100	96.6	72.8	100	99.6	91.1	84.6
20CIR	100	100	99.8	97.6	100	100	99.1	72.9	100	100	98.9	94.1	100	99.8	95.7	84.2
Initial	99.7	76.1	98.2	55.3	100	99.6	97.9	6.02	100	100	77.3	66.8	100	19.5	83.2	3.8
simplified	99.9	76.1	98.2	54.9	100	99.7	98.5	30.9	100	100	78.1	68.9	100	19.7	85.3	4.6

Discriminator output AE <1m	radial				50m				100m				150m			
	LOS		*NLOS*		*LOS*		*NLOS*		*LOS*		*NLOS*		*LOS*		*NLOS*	
	1	*2*	*1*	*2*	*1*	*2*	*1*	*2*	*1*	*2*	*1*	*2*	*1*	*2*	*1*	*2*
1CIR	98.8	99.7	81.5	74.1	99.9	99.6	89.0	55.1	99.9	100	78.5	4.2	100	94.8	79.8	15.7
10CIR	100	100	99.7	95.7	100	100	99.2	71.1	100	100	98.4	87.9	100	99.8	94.7	91.0
20CIR	100	100	99.9	99.2	100	100	99.5	74.9	100	100	99.4	96.2	100	99.9	98.8	89.3
Initial	100	97.9	99.7	74.5	100	99.9	99.2	10.9	100	100	86.4	83.8	100	38.4	89.1	8.2
simplified	100	97.9	99.7	74.3	100	99.9	99.4	50.6	100	100	86.8	84.7	100	38.4	91.8	9.2

D.2.2) DLL configuration 2

Discriminator output AE <0.5m	radial				50m				100m				150m			
	LOS		*NLOS*		*LOS*		*NLOS*		*LOS*		*NLOS*		*LOS*		*NLOS*	
	1	*2*	*1*	*2*	*1*	*2*	*1*	*2*	*1*	*2*	*1*	*2*	*1*	*2*	*1*	*2*
1CIR	96.7	100	78.1	87.4	98.4	100	84.2	81.8	94.3	100	86.7	84.0	99.9	100	73.0	42.1
10CIR	100	100	98.4	97.7	100	100	97.9	96.5	100	100	98.8	97.8	100	100	98.4	84.2
20CIR	100	100	99.2	98.5	100	100	98.6	97.8	100	100	99.4	98.6	100	100	99.3	89.6
Initial	100	100	94.9	95.8	100	100	97.0	92.6	100	100	98.5	94.3	100	100	97.1	9.56
simplified	100	100	95.9	95.9	100	100	96.9	93.0	100	100	98.9	94.9	100	100	97.8	9.50

Discriminator output AE <1m	radial				50m				100m				150m			
	LOS		NLOS		*LOS*		NLOS		*LOS*		NLOS		*LOS*		NLOS	
	1	*2*	*1*	2	*1*	*2*	*1*	2	*1*	*2*	*1*	2	*1*	*2*	*1*	2
1CIR	98.3	100	88.3	93.0	99.9	100	92.9	88.8	98.7	100	93.2	92.5	100	100	87.8	58.9
10CIR	100	100	99.2	98.5	100	100	98.6	97.6	100	100	99.3	98.5	100	100	99.2	89.7
20CIR	100	100	99.5	99.1	100	100	99.0	98.6	100	100	99.6	99.1	100	100	99.4	92.9
Initial	100	100	97.7	97.6	100	100	98.0	95.2	100	100	99.1	97.2	100	100	98.7	17.6
simplified	100	100	98.2	97.7	100	100	98.1	95.5	100	100	99.3	97.2	100	100	99.1	17.6

D.2.3) DLL configuration 3

Discriminator output AE <0.5m	radial				50m				100m				150m			
	LOS		*NLOS*		*LOS*		*NLOS*		*LOS*		*NLOS*		*LOS*		*NLOS*	
	1	*2*	*1*	*2*	*1*	*2*	*1*	*2*	*1*	*2*	*1*	*2*	*1*	*2*	*1*	*2*
1CIR	96.9	100	82.4	89.3	98.3	100	84.4	82.9	92.5	100	87.3	88.7	99.9	100	72.5	48.4
10CIR	100	100	98.1	98.5	100	100	98.5	97.8	100	100	98.8	98.7	100	100	98.8	89.8
20CIR	100	100	99.0	98.9	100	100	99.2	98.6	100	100	99.3	99.3	100	100	99.6	94.3
Initial	100	100	97.0	96.9	100	100	96.6	91.8	100	100	98.5	95.8	100	100	97.8	9.0
simplified	100	100	96.9	97.2	100	100	96.8	92.0	99.9	100	98.4	95.9	100	100	97.7	8.9

Discriminator output AE <1m	Radial				50m				100m				150m			
	LOS		*NLOS*		*LOS*		*NLOS*		*LOS*		*NLOS*		*LOS*		*NLOS*	
	1	*2*	*1*	*2*	*1*	*2*	*1*	*2*	*1*	*2*	*1*	*2*	*1*	*2*	*1*	*2*
1CIR	98.5	100	90.2	94.7	99.9	100	93.1	90.8	97.3	100	93.6	94.9	100	100	87.7	68.5
10CIR	100	100	99.0	99.0	100	100	99.2	98.6	100	100	99.3	99.2	100	100	99.5	94.0

20CIR	100	100	99.4	99.5	100	100	99.7	99.1	100	100	99.6	99.5	100	100	99.7	96.9
Initial	100	100	98.4	98.3	100	100	98.6	95.9	100	100	99.1	97.7	100	100	99.1	17.8
simplified	100	100	98.3	98.4	100	100	98.7	95.9	100	100	99.0	97.7	100	100	99.2	17.8

D.2.4) DLL configuration 4

Discriminator output AE <0.5m	radial				50m				100m				150m			
	LOS		*NLOS*		*LOS*		*NLOS*		*LOS*		*NLOS*		*LOS*		*NLOS*	
	1	*2*	*1*	*2*	*1*	*2*	*1*	*2*	*1*	*2*	*1*	*2*	*1*	*2*	*1*	*2*
1CIR	96.8	100	78.9	86.5	98.9	100	84.4	82.3	93.8	100	86.7	85.8	99.9	100	78.8	48.5
10CIR	99.8	100	97.7	98.1	100	100	98.4	96.6	100	100	99.3	97.8	100	100	97.7	86.2
20CIR	100	100	99.3	98.7	100	100	99.2	97.9	100	100	99.6	98.8	100	100	99.1	91.3
Initial	99.9	100	97.3	94.9	100	100	97.9	93.1	100	100	98.3	95.8	100	100	96.3	12.1
simplified	99.9	100	97.1	95.2	100	100	97.7	93.3	100	100	98.3	95.5	100	100	96.0	12.2
Discriminator output AE <1m	Radial				50m				100m				150m			
	LOS		*NLOS*		*LOS*		*NLOS*		*LOS*		*NLOS*		*LOS*		*NLOS*	
	1	*2*	*1*	*2*	*1*	*2*	*1*	*2*	*1*	*2*	*1*	*2*	*1*	*2*	*1*	*2*
1CIR	98.3	100	90.4	93.3	99.9	100	90.9	88.9	98.2	100	94.3	92.8	100	100	87.6	65.1
10CIR	100	100	98.6	98.7	100	100	99.0	97.8	100	100	99.6	98.7	100	100	99.0	90.8
20CIR	100	100	99.6	99.4	100	100	99.4	98.8	100	100	99.7	99.3	100	100	99.4	94.1
Initial	100	100	98.4	97.0	100	100	98.7	95.4	100	100	99.1	97.5	100	100	98.2	21.4
simplified	100	100	98.3	97.1	100	100	98.7	95.4	100	100	99.2	97.4	100	100	97.9	21.4

D.3) Addentum to 4.2.1.5 – comparison with respect to the correlator

In order to validate the simplification of the correlator output useful term, a comparison is performed between the correlation operation using 10 CIR for a complete channel, the initial derived correlator output mathematical model (4.28) using 10 CIR and the proposed simplification (4.42) with respect to the correlation operation using 100 CIR. The correlation operation corresponds to the actual correlation between the received signal and the local replica. The comparison method which has been used is: for the four trajectories defined in section 4.1.2 case 1 and 2, in both LOS/NLOS conditions, the four correlation output time series are computed over 5000 symbols over the main peak of the correlation; then for each symbol the RE of the three models to be compared with the reference (correlation operation using 100 CIR) are computed. Finally, these REs are averaged with respect to the 5000 symbols and with respect to the main peak of the correlation. In Table 27, the averaged REs are provided.

In chapter 4 section 4.2.1.5, the DLL outputs are inspected but in terms of AE.

Table 27 – Comparison of the correlator relative evolution

Trajectory			Trajectory 1				Trajectory 2			
Scenario			LOS		NLOS		LOS		NLOS	
Case			1	2	1	2	1	2	1	2
Correlation RE (100%)	μ	10	0,02	0,05	0,07	0,17	0,03	0,02	0,07	0,19
		Initial	0,11	0,53	0,17	0,30	0,07	0,04	0,16	0,73
		Simplified	0,11	0,52	0,16	0,30	0,06	0,04	0,15	0,67
	σ	10	0,02	0,03	0,06	0,12	0,02	0,01	0,08	0,14
		Initial	0,05	0,31	0,16	0,20	0,05	0,02	0,13	0,53
		Simplified	0,04	0,30	0,14	0,19	0,04	0,02	0,12	0,50
Trajectory			Trajectory 3				Trajectory 4			
Scenario			LOS		NLOS		LOS		NLOS	
Case			1	2	1	2	1	2	1	2
Correlation RE (100%)	μ	10	0,03	0,02	0,07	0,20	0,01	0,04	0,08	0,13
		Initial	0,07	0,10	0,11	0,39	0,02	1,98	0,12	5,49
		Simplified	0,06	0,09	0,10	0,23	0,01	1,99	0,11	5,48
	σ	10	0,02	0,01	0,06	0,19	0,00	0,02	0,08	0,08
		Initial	0,05	0,05	0,07	0,36	0,01	1,07	0,13	3,27
		Simplified	0,04	0,04	0,07	0,17	0,01	1,07	0,12	3,27

Annex E) Noise theoretical development

E.1) Correlation between two demodulated symbols

The statistics between two demodulated symbols of noise are provided here. The generated noise symbols follow $(E.1)$, the demodulated noise symbol can thus be expressed as $(E.2)$. After derivation, the correlation between two demodulated symbols is expressed in $(E.9)$.

$$b_n^k \sim N\left(0,\ \sigma_{noise}^2\right) \tag{E.1}$$

$$b_p^k = \frac{1}{N_{FFT}} \sum_{n=0}^{N_{FFT}-1} b_n^k e^{-\frac{2i\pi pn}{N_{FFT}}} \tag{E.2}$$

$$E\left[b_p^k b_q^{k*}\right] = E\left[\left(\frac{1}{N_{FFT}} \sum_{n=0}^{N_{FFT}-1} b_n^k e^{-\frac{2i\pi pn}{N_{FFT}}}\right)\left(\frac{1}{N_{FFT}} \sum_{n'=0}^{N_{FFT}-1} b_{n'}^k e^{-\frac{2i\pi qn'}{N_{FFT}}}\right)^*\right] \tag{E.3}$$

$$E\left[b_p^k b_q^{k*}\right] = \frac{1}{{N_{FFT}}^2} E\left[\sum_{n=0}^{N_{FFT}-1} \sum_{n'=0}^{N_{FFT}-1} b_{n'}^{k*}\, b_n^k e^{-\frac{2i\pi(pn-qn')}{N_{FFT}}}\right] \tag{E.4}$$

$$E\left[b_p^k b_q^{k*}\right] = \frac{1}{{N_{FFT}}^2} \sum_{n=0}^{N_{FFT}-1} \sum_{n'=0}^{N_{FFT}-1} E\left[b_{n'}^{k*} b_n^k\right] e^{-\frac{2i\pi(pn-qn')}{N_{FFT}}} \tag{E.5}$$

$$E\left[b_{n'}^{k*} b_n^k\right] = \begin{cases} 0 & n \neq n' \\ \sigma_{noise}^2 & n = n' \end{cases} \tag{E.6}$$

$$E\left[b_p^k b_q^{k*}\right] = \frac{\sigma_{noise}^2}{{N_{FFT}}^2} \sum_{n=0}^{N_{FFT}-1} e^{-\frac{2i\pi(p-q)n}{N_{FFT}}} \tag{E.7}$$

$$E\left[b_p^k b_q^{k*}\right] = \begin{cases} \frac{\sigma_{noise}^2}{N_{FFT}^2} e^{-\frac{i\pi(p-q)}{N_{FFT}}} \frac{\sin\left(\pi(p-q)\right)}{\sin\left(\frac{\pi(p-q)}{N_{FFT}}\right)} = 0 & if\ p \neq q \\ \frac{\sigma_{noise}^2}{N_{FFT}} & if\ p = q \end{cases} \tag{E.8}$$

$$E\left[b_p^k b_q^{k*}\right] = \begin{cases} 0 & if\ p \neq q \\ \frac{\sigma_{noise}^2}{N_{FFT}} & if\ p = q \end{cases} \tag{E.9}$$

In conclusion the expectancy of the correlation between two noise symbols is null, the variance equals $\frac{\sigma_{noise}^2}{N_{FFT}}$ and the covariance is null. Therefore, two noise symbols are uncorrelated.

E.2) Correlation with local replica

The statistics of the correlation between a noise symbol and the local replica are derived in this section. After derivation, the correlation between a noise symbol and the local replica is expressed in $(E.12)$.

$$R(\tau) = \frac{1}{N_P} \sum_{p \in P} b_p^k p_p^{k*} e^{\frac{2i\pi\tau p}{N_{FFT}}} \tag{E.10}$$

$$R(\tau) = \frac{1}{N_P} \sum_{p=0}^{N_P-1} b_p^k p_p^{k*} e^{\frac{2i\pi\tau(4p+P_0)}{N_{FFT}}} \tag{E.11}$$

$$R(\tau) = \frac{e^{\frac{2i\pi\tau P_0}{N_{FFT}}}}{N_P} \sum_{p=0}^{N_P-1} b_p^k p_p^{k*} e^{\frac{2i\pi\tau 4p}{N_{FFT}}} \tag{E.12}$$

The expectancy of the $(E.12)$ is derived in $(E.16)$.

$$E[R(\tau)] = E\left[\frac{e^{\frac{2i\pi\tau P_0}{N_{FFT}}}}{N_P}\sum_{p=0}^{N_P-1} b_p^k p_p^{k*} e^{\frac{2i\pi\tau 4p}{N_{FFT}}}\right] \quad (E.13)$$

$$E[R(\tau)] = \frac{e^{\frac{2i\pi\tau P_0}{N_{FFT}}}}{N_P}\sum_{p=0}^{N_P-1} E\left[b_p^k\right] p_p^{k*} e^{\frac{2i\pi\tau 4p}{N_{FFT}}} \quad (E.14)$$

$$E\left[b_p^k\right] = 0 \quad (E.15)$$

$$E[R(\tau)] = 0 \quad (E.16)$$

The expectancy of the $(E.12)$ is derived in $(E.25)$

$$Var[R(\tau)] = E[(R(\tau) - E[R(\tau)])^2] \quad (E.17)$$

$$Var[R(\tau)] = E\left[\left(R(\tau)\right)^2\right] \quad (E.18)$$

$$Var[R(\tau)] = E[R(\tau)R^*(\tau)] \quad (E.19)$$

$$Var[R(\tau)] = E\left[\frac{e^{\frac{2i\pi\tau P_0}{N_{FFT}}}}{N_P}\sum_{p=0}^{N_P-1} b_p^k p_p^{k*} e^{\frac{2i\pi\tau 4p}{N_{FFT}}}\left(\frac{e^{\frac{2i\pi\tau P_0}{N_{FFT}}}}{N_P}\sum_{p=0}^{N_P-1} b_p^k p_p^{k*} e^{\frac{2i\pi\tau 4p}{N_{FFT}}}\right)^*\right] \quad (E.20)$$

$$Var[R(\tau)] = \frac{1}{N_P^2}E\left[\sum_{p=0}^{N_P-1}\sum_{p'=0}^{N_P-1} b_p^k b_{p'}^{k*} p_{p'}^k p_p^{k*} e^{-\frac{2i\pi\tau 4(p'-p)}{N_{FFT}}}\right] \quad (E.21)$$

$$Var[R(\tau)] = \frac{1}{N_P^2}\sum_{p=0}^{N_P-1}\sum_{p'=0}^{N_P-1} E\left[b_p^k b_{p'}^{k*}\right] p_{p'}^k p_p^{k*} e^{-\frac{2i\pi\tau 4(p'-p)}{N_{FFT}}} \quad (E.22)$$

$$E\left[b_p^k b_{p'}^{k*}\right] = \begin{cases} 0 & if\ p \neq p' \\ \dfrac{\sigma_{noise}^2}{N_{FFT}} & if\ p = p' \end{cases} \quad (E.23)$$

$$Var[R(\tau)] = \frac{1}{N_P^2}\frac{\sigma_{noise}^2}{N_{FFT}}\sum_{p=0}^{N_P-1} p_p^k p_p^{k*} \quad (E.24)$$

$$Var[R(\tau)] = \frac{\sigma_{noise}^2\sigma_{local}^2}{N_{FFT}N_P} \quad (E.25)$$

E.3) Correlation of the noise generated between two correlator outputs

Finally, it is required to determine the correlation of the noise generated between two correlator outputs spaced by a delay equal to $\Delta\tau$. The complete derivation is provided here.

$$E[R(\tau)R^*(\tau-\Delta\tau)] = E\left[\frac{e^{\frac{2i\pi\tau P_0}{N_{FFT}}}}{N_P}\sum_{p=0}^{N_P-1} b_p^k p_p^{k*} e^{\frac{2i\pi\tau 4p}{N_{FFT}}}\left(\frac{e^{\frac{2i\pi(\tau-\Delta\tau)P_0}{N_{FFT}}}}{N_P}\sum_{p=0}^{N_P-1} b_p^k p_p^{k*} e^{\frac{2i\pi(\tau-\Delta\tau)4p}{N_{FFT}}}\right)^*\right] \quad (E.26)$$

$$E[R(\tau)R^*(\tau-\Delta\tau)] = E\left[\frac{e^{\frac{2i\pi\tau P_0}{N_{FFT}}}}{N_P}\frac{e^{-\frac{2i\pi(\tau-\Delta\tau)P_0}{N_{FFT}}}}{N_P}\sum_{p=0}^{N_P-1} b_p^k p_p^{k*} e^{\frac{2i\pi\tau 4p}{N_{FFT}}}\sum_{p=0}^{N_P-1} b_p^{k*} p_p^k e^{-\frac{2i\pi(\tau+\Delta\tau)4p}{N_{FFT}}}\right] \quad (E.27)$$

$$E[R(\tau)R^*(\tau-\Delta\tau)] = E\left[\frac{e^{\frac{2i\pi\Delta\tau P_0}{N_{FFT}}}}{N_P^2}\sum_{p=0}^{N_P-1}\sum_{p'=0}^{N_P-1} b_{p'}^{k*} p_{p'}^k e^{-\frac{2i\pi(\tau+\Delta\tau)4p'}{N_{FFT}}} b_p^k p_p^{k*} e^{\frac{2i\pi\tau 4p}{N_{FFT}}}\right] \quad (E.28)$$

$$E[R(\tau)R^*(\tau-\Delta\tau)] = E\left[\frac{e^{\frac{2i\pi\Delta\tau P_0}{N_{FFT}}}}{N_P^2}\sum_{p=0}^{N_P-1}\sum_{p'=0}^{N_P-1} b_{p'}^{k*} b_p^k p_{p'}^k p_p^{k*} e^{-\frac{2i\pi\tau 4(p'-p)}{N_{FFT}}} e^{\frac{2i\pi\Delta\tau 4p'}{N_{FFT}}}\right] \quad (E.29)$$

$$E[R(\tau)R^*(\tau-\Delta\tau)] = \frac{e^{\frac{2i\pi\Delta\tau P_0}{N_{FFT}}}}{N_P^2}\sum_{p=0}^{N_P-1}\sum_{p'=0}^{N_P-1} E\left[b_{p'}^{k*}b_p^k\right]p_{p'}^k p_p^{k*} e^{-\frac{2i\pi\tau 4(p'-p)}{N_{FFT}}} e^{\frac{2i\pi\Delta\tau 4p'}{N_{FFT}}} \quad (E.30)$$

$$E\left[b_p^k b_{p'}^{k*}\right] = \begin{cases} 0 & if\ p \neq p' \\ \dfrac{\sigma^2}{N_{FFT}} & if\ p = p' \end{cases} \quad (E.31)$$

$$E[R(\tau)R^*(\tau-\Delta\tau)] = \frac{e^{\frac{2i\pi\Delta\tau P_0}{N_{FFT}}}}{N_P^2}\frac{\sigma^2}{N_{FFT}}\sum_{p=0}^{N_P-1} p_p^k p_p^{k*} e^{-\frac{2i\pi\tau 4(p-p)}{N_{FFT}}} e^{\frac{2i\pi\Delta\tau 4p}{N_{FFT}}} \quad (E.32)$$

$$p_p^k p_p^{k*} = 1 \quad (E.33)$$

$$E[R(\tau)R^*(\tau-\Delta\tau)] = \frac{e^{\frac{2i\pi\Delta\tau P_0}{N_{FFT}}}}{N_P^2}\frac{\sigma^2}{N_{FFT}}\sum_{p=0}^{N_P-1} e^{\frac{2i\pi\Delta\tau 4p}{N_{FFT}}} \quad (E.34)$$

$$\sum_{p=0}^{N_P-1} e^{\frac{2i\pi\Delta\tau 4p}{N_{FFT}}} \quad (E.35)$$

$$= \begin{cases} \dfrac{1-e^{\frac{2i\pi\Delta\tau 4N_P}{N_{FFT}}}}{1-e^{\frac{2i\pi\Delta\tau 4}{N_{FFT}}}} = e^{\frac{i\pi\Delta\tau 4(N_P-1)}{N_{FFT}}}\dfrac{e^{-\frac{i\pi\Delta\tau 4N_P}{N_{FFT}}}-e^{\frac{i\pi\Delta\tau 4N_P}{N_{FFT}}}}{e^{-\frac{i\pi\Delta\tau 4}{N_{FFT}}}-e^{\frac{i\pi\Delta\tau 4}{N_{FFT}}}} = e^{\frac{i\pi\Delta\tau 4(N_P-1)}{N_{FFT}}}\dfrac{\sin\left(\frac{\pi\Delta\tau 4N_P}{N_{FFT}}\right)}{\sin\left(\frac{\pi\Delta\tau 4}{N_{FFT}}\right)} & \Delta\tau \neq 0 \\ N_P & \Delta\tau = 0 \end{cases}$$

$$E[R(\tau)R^*(\tau-\Delta\tau)] = \begin{cases} \dfrac{e^{\frac{2i\pi\Delta\tau P_0}{N_{FFT}}}}{N_P^2}\dfrac{\sigma^2}{N_{FFT}}e^{\frac{i\pi\Delta\tau 4(N_P-1)}{N_{FFT}}}\dfrac{\sin\left(\frac{\pi\Delta\tau 4N_P}{N_{FFT}}\right)}{\sin\left(\frac{\pi\Delta\tau 4}{N_{FFT}}\right)} & \Delta\tau \neq 0 \\ e^{\frac{2i\pi\Delta\tau P_0}{N_{FFT}}}\dfrac{\sigma^2}{N_{FFT}N_P} & \Delta\tau = 0 \end{cases} \quad (E.36)$$

Annex F) Addentum to DLL study

This annex permits to complete the description of the Time delay estimator of section 5.1. First the derivation of the normalization factor is provided.

F.1) Normalization Factor derivation

In this Annex, the Normalization factor of the EMLP discriminator defined in chapter 5 section 1 is derived.

The EMLP discriminator defined in (5.1) is normalized by a factor K_{norm}, such that $D_{EMLP}^{norm}(\varepsilon_\tau) \approx \varepsilon_\tau$ for ε_τ close to 0, its expression is now derived. In order to simplify the derivation, only one path is considered from now on; thus, the correlator output model is

$$R_{useful}(\varepsilon_\tau) = \frac{A_l^k(0)}{N_{FFT}} \frac{1}{N_P} e^{\frac{i2\pi\beta\varepsilon_{\tau_l}}{N_{FFT}}} \frac{sin\left(\frac{\pi\gamma\varepsilon_{\tau_l}N_P}{N_{FFT}}\right)}{sin\left(\frac{\pi\gamma\varepsilon_{\tau_l}}{N_{FFT}}\right)} e^{\frac{i\pi\gamma(N_P-1)\varepsilon_{\tau_l}}{N_{FFT}}} \quad (F.1)$$

The expression of the normalization factor, K_{norm}, is such that

$$D_{EMLP}^{norm}(\varepsilon_\tau) \sim_0 \varepsilon_\tau \quad (F.2)$$

Supposing ε_τ is closed to 0, the normalized correlator output $(F.1)$ can be simplified into $(F.6)$, by using $(F.4)$.

$$D_{EMLP}^{norm}(\varepsilon_\tau) = \frac{\left(\frac{sin\left(\frac{\pi\gamma\left(\varepsilon_\tau-\frac{\delta}{2}\right)N_P}{N_{FFT}}\right)}{\frac{\pi\gamma\left(\varepsilon_\tau-\frac{\delta}{2}\right)}{N_{FFT}}}\right)^2 - \left(\frac{sin\left(\frac{\pi\gamma\left(\varepsilon_\tau+\frac{\delta}{2}\right)N_P}{N_{FFT}}\right)}{\frac{\pi\gamma\left(\varepsilon_\tau+\frac{\delta}{2}\right)}{N_{FFT}}}\right)^2}{K_{norm}\left(\frac{sin\left(\frac{\pi\gamma\varepsilon_\tau N_P}{N_{FFT}}\right)}{\frac{\pi\gamma\varepsilon_\tau}{N_{FFT}}}\right)^2} \quad (F.3)$$

$$\frac{sin\left(\frac{\pi\gamma\varepsilon_\tau N_P}{N_{FFT}}\right)}{\frac{\pi\gamma\varepsilon_\tau}{N_{FFT}}} \sim_0 1 \quad (F.4)$$

$$D_{EMLP}^{norm}(\varepsilon_\tau) = \frac{\left(sin\left(\frac{\pi\gamma\left(\varepsilon_\tau-\frac{\delta}{2}\right)N_P}{N_{FFT}}\right)\right)^2}{K_{norm}\left(\frac{\pi\gamma\left(\varepsilon_\tau-\frac{\delta}{2}\right)}{N_{FFT}}\right)^2} - \frac{\left(sin\left(\frac{\pi\gamma\left(\varepsilon_\tau+\frac{\delta}{2}\right)N_P}{N_{FFT}}\right)\right)^2}{K_{norm}\left(\frac{\pi\gamma\left(\varepsilon_\tau+\frac{\delta}{2}\right)}{N_{FFT}}\right)^2} \quad (F.5)$$

$$D_{EMLP}^{norm}(\varepsilon_\tau) = \frac{\left(\varepsilon_\tau+\frac{\delta}{2}\right)^2\left(sin\left(\frac{\pi\gamma\left(\varepsilon_\tau-\frac{\delta}{2}\right)N_P}{N_{FFT}}\right)\right)^2 - \left(\varepsilon_\tau-\frac{\delta}{2}\right)^2\left(sin\left(\frac{\pi\gamma\left(\varepsilon_\tau+\frac{\delta}{2}\right)N_P}{N_{FFT}}\right)\right)^2}{K_{norm}\left(\varepsilon_\tau-\frac{\delta}{2}\right)^2\left(\frac{\pi\gamma}{N_{FFT}}\right)^2\left(\varepsilon_\tau+\frac{\delta}{2}\right)^2} \quad (F.6)$$

Using the trigonometric formula $(F.7)$ leads to $(F.8)$, then after development it leads to $(F.9)$ and $(F.10)$.

$$\sin(x)^2 = \frac{1-\cos(2x)}{2} \tag{F.7}$$

$$D_{EMLP}^{norm}(\varepsilon_\tau) = \frac{\left(\varepsilon_\tau+\frac{\delta}{2}\right)^2\left(1-\cos\left(2\frac{\pi\gamma\left(\varepsilon_\tau-\frac{\delta}{2}\right)N_P}{N_{FFT}}\right)\right)-\left(\varepsilon_\tau-\frac{\delta}{2}\right)^2\left(1-\cos\left(2\frac{\pi\gamma\left(\varepsilon_\tau+\frac{\delta}{2}\right)N_P}{N_{FFT}}\right)\right)}{2K_{norm}\left(\varepsilon_\tau-\frac{\delta}{2}\right)^2\left(\frac{\pi\gamma}{N_{FFT}}\right)^2\left(\varepsilon_\tau+\frac{\delta}{2}\right)^2} \tag{F.8}$$

$$D_{EMLP}^{norm}(\varepsilon_\tau) = \frac{\left(\varepsilon_\tau+\frac{\delta}{2}\right)^2-\left(\varepsilon_\tau+\frac{\delta}{2}\right)^2\cos\left(2\frac{\pi\gamma\left(\varepsilon_\tau-\frac{\delta}{2}\right)N_P}{N_{FFT}}\right)-\left(\varepsilon_\tau-\frac{\delta}{2}\right)^2+\left(\varepsilon_\tau-\frac{\delta}{2}\right)^2\cos\left(2\frac{\pi\gamma\left(\varepsilon_\tau+\frac{\delta}{2}\right)N_P}{N_{FFT}}\right)}{2K_{norm}\left(\varepsilon_\tau-\frac{\delta}{2}\right)^2\left(\frac{\pi\gamma}{N_{FFT}}\right)^2\left(\varepsilon_\tau+\frac{\delta}{2}\right)^2} \tag{F.9}$$

$$\begin{aligned} D_{EMLP}^{norm}(\varepsilon_\tau) = {} & \frac{2\varepsilon_\tau\delta+\left(\varepsilon_\tau^2+\frac{\delta^2}{4}\right)\left[\cos\left(\frac{\pi\gamma(2\varepsilon_\tau+\delta)N_P}{N_{FFT}}\right)-\cos\left(\frac{\pi\gamma(2\varepsilon_\tau-\delta)N_P}{N_{FFT}}\right)\right]}{2K_{norm}\left(\varepsilon_\tau-\frac{\delta}{2}\right)^2\left(\frac{\pi\gamma}{N_{FFT}}\right)^2\left(\varepsilon_\tau+\frac{\delta}{2}\right)^2} \\ & -\frac{\varepsilon_\tau\delta\left[\cos\left(\frac{\pi\gamma(2\varepsilon_\tau-\delta)N_P}{N_{FFT}}\right)+\cos\left(\frac{\pi\gamma(2\varepsilon_\tau+\delta)N_P}{N_{FFT}}\right)\right]}{2K_{norm}\left(\varepsilon_\tau-\frac{\delta}{2}\right)^2\left(\frac{\pi\gamma}{N_{FFT}}\right)^2\left(\varepsilon_\tau+\frac{\delta}{2}\right)^2} \end{aligned} \tag{F.10}$$

Using the trigonometric formula $(F.11)$ and $(F.12)$ leads to $(F.13)$.

$$\cos(p)+\cos(q) = 2\cos\left(\frac{p+q}{2}\right)\cos\left(\frac{p-q}{2}\right) \tag{F.11}$$

$$\cos(p)-\cos(q) = -2\sin\left(\frac{p+q}{2}\right)\sin\left(\frac{p-q}{2}\right) \tag{F.12}$$

$$D_{EMLP}^{norm}(\varepsilon_\tau) = \frac{2\varepsilon_\tau\delta-2\left(\varepsilon_\tau^2+\frac{\delta^2}{4}\right)\sin\left(\frac{\pi\gamma 4\varepsilon_\tau N_P}{N_{FFT}}\right)\sin\left(\frac{\pi\gamma 2\delta N_P}{N_{FFT}}\right)-2\varepsilon_\tau\delta\cos\left(\frac{\pi\gamma 4\varepsilon_\tau N_P}{N_{FFT}}\right)\cos\left(\frac{\pi\gamma 2\delta N_P}{N_{FFT}}\right)}{2K_{norm}\left(\varepsilon_\tau-\frac{\delta}{2}\right)^2\left(\frac{\pi\gamma}{N_{FFT}}\right)^2\left(\varepsilon_\tau+\frac{\delta}{2}\right)^2} \tag{F.13}$$

Using $(F.14)$ permits to develop the normalization discriminator as $(F.15)$.

$$\frac{\sin(kX)}{X} \xrightarrow[X\to 0]{} k \tag{F.14}$$

$$\frac{D_{EMLP}^{norm}(\varepsilon_\tau)}{\varepsilon_\tau} \xrightarrow[\varepsilon_\tau\to 0]{} \frac{1-\frac{\delta\pi\gamma N_P}{N_{FFT}}\sin\left(\frac{\pi\gamma 2\delta N_P}{N_{FFT}}\right)-\varepsilon_\tau\cos\left(\frac{\pi\gamma 2\delta N_P}{N_{FFT}}\right)}{K_{norm}\left(\frac{\pi\gamma}{N_{FFT}}\right)^2\frac{\delta^3}{2^4}} \tag{F.15}$$

Finally, the normalization factor is provided in $(F.16)$.

$$K_{norm} = \frac{1 - \frac{\delta\pi\gamma N_P}{N_{FFT}} \sin\left(\frac{\pi\gamma 2\delta N_P}{N_{FFT}}\right) - \varepsilon_\tau \cos\left(\frac{\pi\gamma 2\delta N_P}{N_{FFT}}\right)}{\left(\frac{\pi\gamma}{N_{FFT}}\right)^2 \frac{\delta^3}{2^4}} \quad (F.16)$$

Where

- δ is the correlator spacing
- γ is determining the pilot architecture as presented in chapter 3 section 3.3.6.3.2

F.2) Variance of the tracking error estimate – chapter 5 section 5.1.3

In this annex, the variance of the discriminator output required to determine the tracking criterion in section 5.1.3 is derived.

The discriminator adopted for the thesis is the Early Minus Late Power which expression is reminded in $(F.17)$.

$$D_{EMLP}^{norm}(\varepsilon_\tau) = \frac{\left|R\left(\varepsilon_\tau - \frac{\delta}{2}\right)\right|^2 - \left|R\left(\varepsilon_\tau + \frac{\delta}{2}\right)\right|^2}{K_{norm}|R(\varepsilon_\tau)|^2} \quad (F.17)$$

In order to derive the statistics of the discriminator output the following hypothesis are assumed. First the discriminator normalization by the prompt correlator is supposed perfect, i.e. it is assumed that there is no noise component on the value of $R(\tau)$. Second, the tracking error is supposed close to zero $\varepsilon_\tau \cong 0$.

The correlator output mathematical model adopted is presented below. It corresponds to the model derived for an AWGN case in chapter 3. Both are reminded below.

$$R(\varepsilon_\tau) = R_{useful}(\varepsilon_\tau) + R_{noise}(\varepsilon_\tau) \quad (F.18)$$

$$R_{useful}(\varepsilon_\tau) = \frac{1}{N_P}\sum_{q=0}^{N_p-1} e^{\frac{2i\pi\varepsilon_\tau\gamma q}{N}} = \begin{cases} \frac{1}{N_P} e^{\frac{i\pi\varepsilon_\tau\gamma(N_p-1)}{N_{FFT}}} \frac{\sin\left(\frac{\pi\varepsilon_\tau\gamma N_P}{N_{FFT}}\right)}{\sin\left(\frac{\pi\varepsilon_\tau\gamma}{N_{FFT}}\right)} & \varepsilon_\tau \neq 0 \\ 1 & \varepsilon_\tau = 0 \end{cases} \quad (F.19)$$

$$R_{noise}(\varepsilon_\tau) = \frac{1}{N_P}\sum_{q=0}^{N_P-1} b_q^k p_q^{k*} e^{\frac{2i\pi\hat{\tau}\gamma q}{N_{FFT}}} \quad (F.20)$$

Where:

- p_p^{k*} is the sequence of pilots
- b_p^k is the sequence of demodulated noise symbols
- P is the set of pilots defined by $P \in \{\gamma n\}, n = 0, \dots, N_P$ in that case
- N_P is the number of pilots
- N_{FFT} is the FFT window size

F.2.1) Statistics of the noise term

The statistics of the correlator output noise term are derived. First the mean of the noise correlator output is derived in $(F.22)$ and $(F.23)$. Since QPSK symbols are generated, their mean is equal to zero, $E\left[b_p^k\right] = 0$ thus the mean of the noise term is equal to zero.

$$E[R_{noise}(\varepsilon_\tau)] = E\left[\frac{1}{N_P}\sum_{q=0}^{N_P-1} b_q^k p_q^{k*} e^{\frac{2i\pi\hat{\tau}\gamma q}{N_{FFT}}}\right] \quad (F.22)$$

$$E[R_{noise}(\varepsilon_\tau)] = \frac{1}{N_P}\sum_{p=0}^{N_P-1} E\left[b_p^k\right] p_p^{k*} e^{\frac{2i\pi\tau\alpha p}{N}} \quad (F.23)$$

$$\mathrm{E}[R_{noise}(\varepsilon_\tau)] = 0 \quad (F.24)$$

Second, the variance of the noise correlation function is derived from equation $(F.25)$ to $(F.31)$; one must keep in mind the statistics of QPSK symbols: $E\left[b_p^k b_{p'}^{k*}\right] = \begin{cases} 0 & if\ p \neq p' \\ \frac{\sigma_{noise}^2}{N_{FFT}} & if\ p = p' \end{cases}$. In the equation, the variance of the pilots is noted $E\left[p_q^k p_q^{k*}\right] = \sigma_{local}^2$.

$$Var[R_{noise}(\varepsilon_\tau)] = E[(R_{noise}(\varepsilon_\tau) - E[R_{noise}(\varepsilon_\tau)])^2] \quad (F.25)$$

$$Var[R_{noise}(\varepsilon_\tau)] = E\left[\left(R_{noise}(\varepsilon_\tau)\right)^2\right] = E[R_{noise}(\varepsilon_\tau)R_{noise}^*(\varepsilon_\tau)] \quad (F.26)$$

$$Var[R_{noise}(\varepsilon_\tau)] = E\left[\frac{1}{N_P}\sum_{q=0}^{N_P-1} b_q^k p_q^{k*} e^{\frac{2i\pi\hat{\tau}\gamma q}{N_{FFT}}}\left(\frac{1}{N_P}\sum_{p=0}^{N_P-1} b_q^k p_q^{k*} e^{\frac{2i\pi\hat{\tau}\gamma q}{N_{FFT}}}\right)^*\right] \quad (F.27)$$

$$Var[R_{noise}(\varepsilon_\tau)] = \frac{1}{N_P^2} E\left[\sum_{q=0}^{N_P-1}\sum_{q'=0}^{N_P-1} b_q^k b_{q'}^{k*} p_{q'}^k p_q^{k*} e^{-\frac{2i\pi\hat{\tau}\gamma(q'-q)}{N_{FFT}}}\right] \quad (F.28)$$

$$Var[R_{noise}(\varepsilon_\tau)] = \frac{1}{N_P^2}\sum_{q=0}^{N_P-1}\sum_{q'=0}^{N_P-1} E\left[b_q^k b_{q'}^{k*}\right] p_{q'}^k p_q^{k*} e^{-\frac{2i\pi\hat{\tau}\gamma(q'-q)}{N_{FFT}}} \quad (F.29)$$

$$Var[R_{noise}(\varepsilon_\tau)] = \frac{1}{N_P^2}\frac{\sigma_{noise}^2\sigma_{local}^2}{N_{FFT}}\sum_{q=0}^{N_P-1} p_q^k p_q^{k*} \quad (F.30)$$

$$Var[R_{noise}(\varepsilon_\tau)] = \frac{\sigma_{noise}^2\sigma_{local}^2}{N_{FFT}N_P} \quad (F.31)$$

F.2.2) Non normalized EMLP discriminator output

First the Non-normalized discriminator output is studied

$$D_{EMLP}(\varepsilon_\tau) = \left|R\left(\varepsilon_\tau - \frac{\delta}{2}\right)\right|^2 - \left|R\left(\varepsilon_\tau + \frac{\delta}{2}\right)\right|^2 \quad (F.32)$$

The expression of the first term is:

$$\left|R\left(\varepsilon_\tau - \frac{\delta}{2}\right)\right|^2 = R\left(\varepsilon_\tau - \frac{\delta}{2}\right)R\left(\varepsilon_\tau - \frac{\delta}{2}\right)^* \quad (F.33)$$

$$\left|R\left(\varepsilon_\tau-\frac{\delta}{2}\right)\right|^2=\left|R_{useful}\left(\varepsilon_\tau-\frac{\delta}{2}\right)\right|^2+R_{useful}\left(\varepsilon_\tau-\frac{\delta}{2}\right)R_{noise}\left(\varepsilon_\tau-\frac{\delta}{2}\right)^*+R_{noise}\left(\varepsilon_\tau-\frac{\delta}{2}\right)R_{useful}\left(\varepsilon_\tau-\frac{\delta}{2}\right)^*+\left|R_{noise}\left(\varepsilon_\tau-\frac{\delta}{2}\right)\right|^2 \quad (F.34)$$

Similarly, the expression of the second term is:

$$\left|R\left(\varepsilon_\tau+\frac{\delta}{2}\right)\right|^2=\left|R_{useful}\left(\varepsilon_\tau+\frac{\delta}{2}\right)\right|^2+R_{useful}\left(\varepsilon_\tau+\frac{\delta}{2}\right)R_{noise}\left(\varepsilon_\tau+\frac{\delta}{2}\right)^*+R_{noise}\left(\varepsilon_\tau+\frac{\delta}{2}\right)R_{useful}\left(\varepsilon_\tau+\frac{\delta}{2}\right)^*+\left|R_{noise}\left(\varepsilon_\tau+\frac{\delta}{2}\right)\right|^2 \quad (F.35)$$

Noting:

$$N(\varepsilon_\tau)=R_{useful}(\varepsilon_\tau)R_{noise}(\varepsilon_\tau)^*+R_{noise}(\varepsilon_\tau)R_{useful}(\varepsilon_\tau)^*+|R_{noise}(\varepsilon_\tau)|^2 \quad (F.36)$$

$$\begin{cases}\left|R\left(\varepsilon_\tau-\frac{\delta}{2}\right)\right|^2=\left|R_{useful}\left(\varepsilon_\tau-\frac{\delta}{2}\right)\right|^2+N\left(\varepsilon_\tau-\frac{\delta}{2}\right)\\ \left|R\left(\varepsilon_\tau+\frac{\delta}{2}\right)\right|^2=\left|R_{useful}\left(\varepsilon_\tau+\frac{\delta}{2}\right)\right|^2+N\left(\varepsilon_\tau+\frac{\delta}{2}\right)\end{cases} \quad (F.37)$$

$$D_{EMLP}(\varepsilon_\tau)=\left|R_{useful}\left(\varepsilon_\tau-\frac{\delta}{2}\right)\right|^2-\left|R_{useful}\left(\varepsilon_\tau+\frac{\delta}{2}\right)\right|^2+N\left(\varepsilon_\tau-\frac{\delta}{2}\right)-N\left(\varepsilon_\tau+\frac{\delta}{2}\right) \quad (F.38)$$

Noting:

$$\Omega=N\left(\varepsilon_\tau-\frac{\delta}{2}\right)-N\left(\varepsilon_\tau+\frac{\delta}{2}\right) \quad (F.39)$$

$$D_{EMLP}(\varepsilon_\tau)=\left|R_{useful}\left(\varepsilon_\tau-\frac{\delta}{2}\right)\right|^2-\left|R_{useful}\left(\varepsilon_\tau+\frac{\delta}{2}\right)\right|^2+\Omega \quad (F.40)$$

F.2.3) Study of Ω

The objective is to determine the variance of the non-normalized discriminator output, in order to do so, the statistics of the previous expression has to be defined.

F.2.3.1) Expectancy of Ω

By definition:

$$\mathrm{E}[\Omega]=E\left[N\left(\varepsilon_\tau-\frac{\delta}{2}\right)-N\left(\varepsilon_\tau+\frac{\delta}{2}\right)\right] \quad (F.41)$$

$$\mathrm{E}[\Omega]=E\left[N\left(\varepsilon_\tau-\frac{\delta}{2}\right)\right]-E\left[N\left(\varepsilon_\tau+\frac{\delta}{2}\right)\right] \quad (F.42)$$

$$E[N(\varepsilon_\tau)]=E\left[R_{useful}(\varepsilon_\tau)R_{noise}(\varepsilon_\tau)^*+R_{noise}(\varepsilon_\tau)R_{useful}(\varepsilon_\tau)^*+|R_{noise}(\varepsilon_\tau)|^2\right] \quad (F.43)$$

$$E[N(\varepsilon_\tau)]=E\left[R_{useful}(\varepsilon_\tau)R_{noise}(\varepsilon_\tau)^*\right]+E\left[R_{noise}(\varepsilon_\tau)R_{useful}(\varepsilon_\tau)^*\right]+E[|R_{noise}(\varepsilon_\tau)|^2] \quad (F.44)$$

$$E[N(\varepsilon_\tau)] = E\left[R_{useful}(\varepsilon_\tau)\right]E[R_{noise}(\varepsilon_\tau)^*] + E[R_{noise}(\varepsilon_\tau)]E\left[R_{useful}(\varepsilon_\tau)^*\right] + E[|R_{noise}(\varepsilon_\tau)|^2] \quad (F.45)$$

The statistics of the noise correlation have been derived above. It has been proved that:

$$\mathrm{E}[\mathrm{R}_{noise}(\varepsilon_\tau)] = 0 \quad (F.46)$$

$$E[N(\varepsilon_\tau)] = E[|R_{noise}(\varepsilon_\tau)|^2] = \frac{\sigma_{noise}^2 \sigma_{local}^2}{N_{FFT} N_P} \quad (F.47)$$

Thus, the expectation of Ω is

$$\mathrm{E}[\Omega] = E\left[N\left(\varepsilon_\tau - \frac{\delta}{2}\right)\right] - E\left[N\left(\varepsilon_\tau + \frac{\delta}{2}\right)\right] = 0 \quad (F.48)$$

F.2.3.2) Variance of Ω

By definition:

$$Var[\Omega] = E[(\Omega - E[\Omega])^2] = E[\Omega\Omega^*] - E[\Omega](E[\Omega])^* = E[\Omega\Omega^*] \quad (F.49)$$

$$E[\Omega\Omega^*] = \left(N\left(\varepsilon_\tau - \frac{\delta}{2}\right) - N\left(\varepsilon_\tau + \frac{\delta}{2}\right)\right)\left(N\left(\varepsilon_\tau - \frac{\delta}{2}\right) - N\left(\varepsilon_\tau + \frac{\delta}{2}\right)\right)^* \quad (F.50)$$

$$E[\Omega\Omega^*] = E\left[\left|N\left(\varepsilon_\tau - \frac{\delta}{2}\right)\right|^2\right] + E\left[\left|N\left(\varepsilon_\tau + \frac{\delta}{2}\right)\right|^2\right] - 2Re\left(E\left[N\left(\varepsilon_\tau - \frac{\delta}{2}\right)N\left(\varepsilon_\tau + \frac{\delta}{2}\right)^*\right]\right) \quad (F.51)$$

First step, the variance of $N(\varepsilon_\tau)$ is defined as:

$$E[|N(\varepsilon_\tau)|^2] = E[N(\varepsilon_\tau)N(\varepsilon_\tau)^*] \quad (F.52)$$

$$E[|N(\varepsilon_\tau)|^2] = E\left[\left(R_{useful}(\varepsilon_\tau)R_{noise}(\varepsilon_\tau)^* + R_{noise}(\varepsilon_\tau)R_{useful}(\varepsilon_\tau)^* + |R_{noise}(\varepsilon_\tau)|^2\right)\left(R_{useful}(\varepsilon_\tau)R_{noise}(\varepsilon_\tau)^* + R_{noise}(\varepsilon_\tau)R_{useful}(\varepsilon_\tau)^* + |R_{noise}(\varepsilon_\tau)|^2\right)^*\right] \quad (F.53)$$

$$\begin{aligned} E[|N(\varepsilon_\tau)|^2] = {} & E\left[\left|R_{useful}(\varepsilon_\tau)\right|^2 |R_{noise}(\varepsilon_\tau)^*|^2\right] + E\left[R_{useful}(\varepsilon_\tau)^2 R_{noise}(\varepsilon_\tau)^{*2}\right] \\ & + E\left[R_{useful}(\varepsilon_\tau)R_{noise}(\varepsilon_\tau)^* |R_{noise}(\varepsilon_\tau)|^{2*}\right] + E\left[R_{useful}(\varepsilon_\tau)^{2*} R_{noise}(\varepsilon_\tau)^2\right] \\ & + E\left[\left|R_{useful}(\varepsilon_\tau)^*\right|^2 |R_{noise}(\varepsilon_\tau)|^2\right] \\ & + E\left[R_{noise}(\varepsilon_\tau)R_{useful}(\varepsilon_\tau)^* |R_{noise}(\varepsilon_\tau)|^{2*}\right] \\ & + E\left[R_{useful}(\varepsilon_\tau)R_{noise}(\varepsilon_\tau)^* |R_{noise}(\varepsilon_\tau)|^2\right] \\ & + E\left[R_{noise}(\varepsilon_\tau)R_{useful}(\varepsilon_\tau)^* |R_{noise}(\varepsilon_\tau)|^2\right] \\ & + E[|R_{noise}(\varepsilon_\tau)|^2 |R_{noise}(\varepsilon_\tau)|^2] \end{aligned} \quad (F.54)$$

- R_{noise} is a centered complex variable, the following can be used: $E[R_{noise}(\varepsilon_\tau)R_{noise}(\varepsilon_\tau)] = 0$
- $E\left[R_{noise}(\varepsilon_\tau)^{(*)}R_{noise}(\varepsilon_\tau)^{(*)}R_{noise}(\varepsilon_\tau)^{(*)}\right] = 0$ (the third order moment of a complex normal variable is null)

The application of the two above mentioned simplifications leads to:

$$E[|N(\varepsilon_\tau)|^2] = 2\left|R_{useful}(\varepsilon_\tau)\right|^2 E[|R_{noise}(\varepsilon_\tau)^*|^2] + E[|R_{noise}(\varepsilon_\tau)|^4] \quad (F.55)$$

Using this result, the first term of the variance formula $E\left[\left|N\left(\tau - \frac{\delta}{2}\right)\right|^2\right]$ can be developed:

$$E\left[\left|N\left(\varepsilon_\tau - \frac{\delta}{2}\right)\right|^2\right] = 2\left|R_{useful}\left(\varepsilon_\tau - \frac{\delta}{2}\right)\right|^2 E\left[\left|R_{noise}\left(\varepsilon_\tau - \frac{\delta}{2}\right)^*\right|^2\right] + E\left[\left|R_{noise}\left(\varepsilon_\tau - \frac{\delta}{2}\right)\right|^4\right] \quad (F.56)$$

As previously presented, the useful correlation formula is:

$$R_{useful}\left(\varepsilon_\tau - \frac{\delta}{2}\right) = \frac{\sigma_{pilot}\sigma_{local}}{N_P} e^{\frac{i\pi\left(\varepsilon_\tau - \frac{\delta}{2}\right)\gamma(N_p-1)}{N_{FFT}}} \frac{\sin\left(\frac{\pi\left(\varepsilon_\tau - \frac{\delta}{2}\right)\gamma N_P}{N_{FFT}}\right)}{\sin\left(\frac{\pi\left(\varepsilon_\tau - \frac{\delta}{2}\right)\gamma}{N_{FFT}}\right)} \quad (F.57)$$

By applying $\varepsilon_\tau = 0$, it leads to

$$R_u\left(-\frac{\delta}{2}\right) = \frac{\sigma_{pilot}\sigma_{local}}{N_P} e^{-\frac{i\pi\frac{\delta}{2}\alpha(N_p-1)}{N_{FFT}}} \frac{\sin\left(\frac{\pi\delta\gamma N_P}{2N_{FFT}}\right)}{\sin\left(\frac{\pi\delta\gamma}{2N_{FFT}}\right)} \quad (F.58)$$

$$E[|R_{noise}(\varepsilon_\tau)|^4] = E[|R_{noise}(\varepsilon_\tau)|^2 |R_{noise}(\varepsilon_\tau)|^2] \quad (F.59)$$

$$E[|R_{noise}(\varepsilon_\tau)|^4] = E[(R_{noise}(\varepsilon_\tau)R_{noise}(\varepsilon_\tau)^*)(R_{noise}(\varepsilon_\tau)R_{noise}(\varepsilon_\tau)^*)] \quad (F.60)$$

Using the property of 4 normal random variables N_1, N_2, N_3, N_4 (Isserlis' theorem)

$$E[N_1N_2N_3N_4] = E[N_1N_2]E[N_3N_4] + E[N_1N_3]E[N_2N_4] + E[N_1N_4]E[N_2N_3] \quad (F.61)$$

$$\begin{aligned} E[|R_{noise}(\varepsilon_\tau)|^4] = {} & E[R_{noise}(\varepsilon_\tau)R_{noise}(\varepsilon_\tau)^*]E[R_{noise}(\varepsilon_\tau)R_{noise}(\varepsilon_\tau)^*] \\ & + E[R_{noise}(\varepsilon_\tau)R_{noise}(\varepsilon_\tau)]E[R_{noise}(\varepsilon_\tau)^*R_{noise}(\varepsilon_\tau)^*] \\ & + E[R_{noise}(\varepsilon_\tau)R_{noise}(\varepsilon_\tau)^*]E[R_{noise}(\varepsilon_\tau)^*R_{noise}(\varepsilon_\tau)] \end{aligned} \quad (F.62)$$

$$\begin{aligned} E[|R_N(\tau)|^4] = {} & E[|R_{noise}(\varepsilon_\tau)|^2]E[|R_{noise}(\varepsilon_\tau)|^2] \\ & + \underbrace{E[R_{noise}(\varepsilon_\tau)R_{noise}(\varepsilon_\tau)]}_{0}\underbrace{E[R_{noise}(\varepsilon_\tau)^*R_{noise}(\varepsilon_\tau)^*]}_{0} \\ & + E[|R_{noise}(\varepsilon_\tau)|^2]E[|R_{noise}(\varepsilon_\tau)|^2] \end{aligned} \quad (F.63)$$

$$E[|R_{noise}(\varepsilon_\tau)|^4] = 2E[|R_{noise}(\varepsilon_\tau)|^2]^2 \quad (F.64)$$

Thus, the first term of the variance formula $E\left[\left|N\left(\varepsilon_\tau - \frac{\delta}{2}\right)\right|^2\right]$ is

$$E\left[\left|N\left(\varepsilon_\tau - \frac{\delta}{2}\right)\right|^2\right] = 2\frac{\sigma_{pilot}^2\sigma_{local}^2}{N_P^2}\left(\frac{\sin\left(\frac{\pi\delta\gamma N_P}{2N_{FFT}}\right)}{\sin\left(\frac{\pi\delta\gamma}{2N_{FFT}}\right)}\right)^2 \frac{\sigma_{noise}^2\sigma_{local}^2}{N_{FFT}N_P} + 2\frac{\sigma_{noise}^4\sigma_{local}^4}{N_{FFT}^2N_P^2} \quad (F.65)$$

Similarly, the second term of the variance formula $E\left[\left|N\left(\varepsilon_\tau+\frac{\delta}{2}\right)\right|^2\right]$

$$E\left[\left|N\left(\varepsilon_\tau+\frac{\delta}{2}\right)\right|^2\right]=2\frac{\sigma_{pilot}^2\sigma_{local}^2}{N_P^2}\left(\frac{\sin\left(\frac{\pi\delta\gamma N_P}{2N_{FFT}}\right)}{\sin\left(\frac{\pi\delta\gamma}{2N_{FFT}}\right)}\right)^2\frac{\sigma_{noise}^2\sigma_{local}^2}{N_{FFT}N_P}+2\frac{\sigma_{noise}^4\sigma_{local}^4}{N_{FFT}^2N_P^2} \qquad (F.66)$$

The third term of the variance formula $E\left[N\left(\varepsilon_\tau-\frac{\delta}{2}\right)N\left(\varepsilon_\tau+\frac{\delta}{2}\right)^*\right]$ can be expressed as

$$\begin{aligned}E\left[N\left(\varepsilon_\tau-\frac{\delta}{2}\right)N\left(\varepsilon_\tau+\frac{\delta}{2}\right)^*\right]&\\ =\ E\Bigg[\Bigg(&R_{useful}\left(\varepsilon_\tau-\frac{\delta}{2}\right)R_{noise}\left(\varepsilon_\tau-\frac{\delta}{2}\right)^*\\ &+R_{noise}\left(\varepsilon_\tau-\frac{\delta}{2}\right)R_{useful}\left(\varepsilon_\tau-\frac{\delta}{2}\right)^*\\ &+\left|R_{noise}\left(\varepsilon_\tau-\frac{\delta}{2}\right)\right|^2\Bigg)\Bigg(R_{useful}\left(\varepsilon_\tau+\frac{\delta}{2}\right)R_{noise}\left(\varepsilon_\tau+\frac{\delta}{2}\right)^*\\ &+R_{noise}\left(\varepsilon_\tau+\frac{\delta}{2}\right)R_{useful}\left(\varepsilon_\tau+\frac{\delta}{2}\right)^*+\left|R_{noise}\left(\varepsilon_\tau+\frac{\delta}{2}\right)\right|^2\Bigg)^*\Bigg]\end{aligned} \qquad (F.67)$$

Remind that:

- R_N is a centered complex variable, the following can be used $E[R_{noise}(\varepsilon_\tau)R_{noise}(\varepsilon_\tau)]=0$
- $E\left[R_{noise}(\varepsilon_\tau)^{(*)}R_{noise}(\varepsilon_\tau)^{(*)}R_{noise}(\varepsilon_\tau)^{(*)}\right]=0$ (the third order moment of a complex normal variable is null)

Applying these results, the third term of the variance: $E\left[N\left(\varepsilon_\tau-\frac{\delta}{2}\right)N\left(\varepsilon_\tau+\frac{\delta}{2}\right)^*\right]$ becomes:

$$\begin{aligned}E\left[N\left(\varepsilon_\tau-\frac{\delta}{2}\right)N\left(\varepsilon_\tau+\frac{\delta}{2}\right)^*\right]&\\ =R_{useful}\left(\varepsilon_\tau-\frac{\delta}{2}\right)R_{useful}\left(\varepsilon_\tau+\frac{\delta}{2}\right)^*&E\left[R_{noise}\left(\varepsilon_\tau-\frac{\delta}{2}\right)^*R_{noise}\left(\varepsilon_\tau+\frac{\delta}{2}\right)\right]\\ +R_{useful}\left(\varepsilon_\tau-\frac{\delta}{2}\right)^*R_{useful}\left(\varepsilon_\tau+\frac{\delta}{2}\right)&E\left[R_{noise}\left(\varepsilon_\tau-\frac{\delta}{2}\right)R_{noise}\left(\varepsilon_\tau+\frac{\delta}{2}\right)^*\right]\\ +E\left[\left|R_{noise}\left(\varepsilon_\tau-\frac{\delta}{2}\right)\right|^2\right.&\left.\left|R_{noise}\left(\varepsilon_\tau+\frac{\delta}{2}\right)\right|^2\right]\end{aligned} \qquad (F.68)$$

Regarding the useful terms contribution in the first two part of the formula:

- $$R_{useful}\left(\varepsilon_\tau-\frac{\delta}{2}\right)R_{useful}\left(\varepsilon_\tau+\frac{\delta}{2}\right)^*=\frac{\sigma_{local}^2\sigma_{pilot}^2}{N_P^2}e^{-\frac{i\pi\delta\gamma(N_p-1)}{N_{FFT}}}\left(\frac{\sin\left(\frac{\pi\frac{\delta}{2}\gamma N_P}{N_{FFT}}\right)}{\sin\left(\frac{\pi\frac{\delta}{2}\gamma}{N_{FFT}}\right)}\right)^2 \qquad (F.69)$$

- $R_{useful}\left(\varepsilon_\tau - \frac{\delta}{2}\right)^* R_{useful}\left(\varepsilon_\tau + \frac{\delta}{2}\right) = \frac{\sigma_{local}^2 \sigma_{pilot}^2}{N_P^2} e^{\frac{i\pi\delta\gamma(N_p-1)}{N_{FFT}}} \left(\frac{\sin\left(\frac{\pi\frac{\delta}{2}\gamma N_P}{N_{FFT}}\right)}{\sin\left(\frac{\pi\frac{\delta}{2}\gamma}{N_{FFT}}\right)}\right)^2 \quad (F.70)$

Regarding the noise terms contribution in the first two part of the formula:

- Noise term 1

$$E\left[R_{noise}\left(\varepsilon_\tau - \frac{\delta}{2}\right)^* R_{noise}\left(\varepsilon_\tau + \frac{\delta}{2}\right)\right] = E\left[\frac{1}{N_P}\sum_{p=0}^{N_P-1} b_p^{k*} p_p^k e^{-\frac{2i\pi\left(\varepsilon_\tau - \frac{\delta}{2}\right)\gamma p}{N_{FFT}}} \frac{1}{N_P}\sum_{p=0}^{N_P-1} b_p^k p_p^{k*} e^{\frac{2i\pi\left(\varepsilon_\tau + \frac{\delta}{2}\right)\gamma p}{N_{FFT}}}\right] \quad (F.71)$$

$$= \frac{1}{N_P^2}\frac{\sigma_{noise}^2\sigma_{pilot}^2}{N_{FFT}}\sum_{p=0}^{N_P-1} e^{\frac{2i\pi\delta\gamma p}{N_{FFT}}}$$

$$E\left[R_{noise}\left(\varepsilon_\tau - \frac{\delta}{2}\right)^* R_{noise}\left(\varepsilon_\tau + \frac{\delta}{2}\right)\right] = \frac{1}{N_P^2}\frac{\sigma_{noise}^2\sigma_{pilot}^2}{N_{FFT}} e^{\frac{i\pi\delta\gamma(N_P-1)}{N_{FFT}}} \frac{\sin\left(\frac{\pi\delta\gamma N_P}{N_{FFT}}\right)}{\sin\left(\frac{\pi\delta\gamma}{N_{FFT}}\right)} \quad (F.72)$$

- Noise term 2

$$E\left[R_{noise}\left(\varepsilon_\tau - \frac{\delta}{2}\right) R_{noise}\left(\varepsilon_\tau + \frac{\delta}{2}\right)^*\right] = \frac{1}{N_P^2}\frac{\sigma_{noise}^2\sigma_{pilot}^2}{N_{FFT}} e^{-\frac{i\pi\delta\gamma(N_P-1)}{N_{FFT}}} \frac{\sin\left(\frac{\pi\delta\gamma N_P}{N_{FFT}}\right)}{\sin\left(\frac{\pi\delta\gamma}{N_{FFT}}\right)} \quad (F.73)$$

Regarding the third term: $E\left[\left|R_{noise}\left(\varepsilon_\tau - \frac{\delta}{2}\right)\right|^2 \left|R_{noise}\left(\varepsilon_\tau + \frac{\delta}{2}\right)\right|^2\right]$: Using the property of 4 normal random variables N_1, N_2, N_3, N_4 (Isserlis' theorem). It leads to

$$E\left[R_{noise}\left(\varepsilon_\tau - \frac{\delta}{2}\right) R_{noise}\left(\varepsilon_\tau - \frac{\delta}{2}\right)^* R_{noise}\left(\varepsilon_\tau + \frac{\delta}{2}\right) R_{noise}\left(\varepsilon_\tau + \frac{\delta}{2}\right)^*\right] = \left(\frac{\sigma_{noise}^2\sigma_{pilot}^2}{N_{FFT}N_P}\right)^2 \left(1 + \frac{1}{N_P^2}\left(\frac{\sin\left(\frac{\pi\delta\gamma N_P}{N_{FFT}}\right)}{\sin\left(\frac{\pi\delta\gamma}{N_{FFT}}\right)}\right)^2\right) \quad (F.74)$$

Finally:

$$E\left[N\left(\varepsilon_\tau-\frac{\delta}{2}\right)N\left(\varepsilon_\tau+\frac{\delta}{2}\right)^*\right]$$
$$=2\frac{\sigma_{local}^2\sigma_{pilot}^2}{N_P^4}\frac{\sigma_{noise}^2\sigma_{pilot}^2}{N_{FFT}}\left(\frac{\sin\left(\frac{\pi\delta\gamma N_P}{2N_{FFT}}\right)}{\sin\left(\frac{\pi\delta\gamma}{2}\right)}\right)^2\frac{\sin\left(\frac{\pi\delta\gamma N_P}{N_{FFT}}\right)}{\sin\left(\frac{\pi\delta\gamma}{N_{FFT}}\right)} \quad (F.75)$$
$$+\left(\frac{\sigma_{noise}^2\sigma_{pilot}^2}{N_{FFT}N_P}\right)^2\left(1+\frac{1}{N_P^2}\left(\frac{\sin\left(\frac{\pi\delta\gamma N_P}{N_{FFT}}\right)}{\sin\left(\frac{\pi\delta\gamma}{N_{FFT}}\right)}\right)^2\right)$$

As a reminder the objective is to determine the variance of Ω , which is defined as:

$$E[\Omega\Omega^*]=E\left[\left|N\left(\varepsilon_\tau-\frac{\delta}{2}\right)\right|^2\right]-2Re\left(E\left[N\left(\varepsilon_\tau-\frac{\delta}{2}\right)N\left(\varepsilon_\tau+\frac{\delta}{2}\right)^*\right]\right)+E\left[\left|N\left(\varepsilon_\tau+\frac{\delta}{2}\right)\right|^2\right] \quad (F.76)$$

Where:

- $E\left[\left|N\left(\varepsilon_\tau-\frac{\delta}{2}\right)\right|^2\right]=2\frac{\sigma_{local}^2\sigma_{pilot}^2}{N_P^2}\left(\frac{\sin\left(\frac{\pi\delta\gamma N_P}{2N_{FFT}}\right)}{\sin\left(\frac{\pi\delta\gamma}{2N_{FFT}}\right)}\right)^2\frac{\sigma_{noise}^2\sigma_{pilot}^2}{N_{FFT}N_P}+2\frac{\sigma_{noise}^4\sigma_{pilot}^4}{{N_{FFT}}^2N_P^2}$ $(F.77)$

- $2Re\left(E\left[N\left(\varepsilon_\tau-\frac{\delta}{2}\right)N\left(\varepsilon_\tau+\frac{\delta}{2}\right)^*\right]\right)=$
$4\frac{\sigma_{lcoal}^2\sigma_{pilot}^2}{N_P^4}\frac{\sigma_{noise}^2\sigma_{pilot}^2}{N_{FFT}}\left(\frac{\sin\left(\frac{\pi\delta\gamma N_P}{2N_{FFT}}\right)}{\sin\left(\frac{\pi\delta\gamma}{2N_{FFT}}\right)}\right)^2\frac{\sin\left(\frac{\pi\delta\gamma N_P}{N_{FFT}}\right)}{\sin\left(\frac{\pi\delta\gamma}{N_{FFT}}\right)}+2\left(\frac{\sigma_{noise}^2\sigma_{pilot}^2}{N_{FFT}N_P}\right)^2\left(1+\right.$ $(F.78)$
$\left.\frac{1}{N_P^2}\left(\frac{\sin\left(\frac{\pi\delta\gamma N_P}{N_{FFT}}\right)}{\sin\left(\frac{\pi\delta\gamma}{N_{FFT}}\right)}\right)^2\right)$

Then :

$$E[\Omega\Omega^*]=2\frac{\sigma_{noise}^2\sigma_{pilot}^2}{NN_P}\left[2\frac{\sigma_{local}^2\sigma_{pilot}^2}{N_P^2}\left(\frac{\sin\left(\frac{\pi\delta\alpha N_P}{2N}\right)}{\sin\left(\frac{\pi\delta\alpha}{2N}\right)}\right)^2\left(1-\frac{1}{N_P}\frac{\sin\left(\frac{\pi\delta\alpha N_P}{N}\right)}{\sin\left(\frac{\pi\delta\alpha}{N}\right)}\right)\right.$$
$$\left.+\frac{\sigma_{noise}^2\sigma_{pilot}^4}{NN_P}\left(1-\frac{1}{N_P^2}\left(\frac{\sin\left(\frac{\pi\delta\alpha N_P}{N}\right)}{\sin\left(\frac{\pi\delta\alpha}{N}\right)}\right)^2\right)\right] \quad (F.79)$$

F.2.4) Non - Normalized discriminator output variance

As a reminder, the objective is to determine the variance of the non-normalized discriminator output

$$D_{EMLP}(\varepsilon_\tau)=\left|R_{useful}\left(\varepsilon_\tau-\frac{\delta}{2}\right)\right|^2-\left|R_{useful}\left(\varepsilon_\tau+\frac{\delta}{2}\right)\right|^2+\Omega \quad (F.80)$$

The useful contribution is:

$$R_{useful}\left(\varepsilon_\tau - \frac{\delta}{2}\right) = \frac{\sigma_{local}\sigma_{pilot}}{N_P} e^{-\frac{i\pi\frac{\delta}{2}\gamma(N_p-1)}{N_{FFT}}} \frac{\sin\left(\frac{\pi\delta\gamma N_P}{2N_{FFT}}\right)}{\sin\left(\frac{\pi\delta\gamma}{2N_{FFT}}\right)} \quad (F.81)$$

Thus

$$\left|R_{useful}\left(\varepsilon_\tau - \frac{\delta}{2}\right)\right|^2 = \left|R_{useful}\left(\varepsilon_\tau + \frac{\delta}{2}\right)\right|^2 = \frac{\sigma_{local}^2\sigma_{pilot}^2}{N_P^2}\left(\frac{\sin\left(\frac{\pi\delta\gamma N_P}{2N_{FFT}}\right)}{\sin\left(\frac{\pi\delta\gamma}{2N_{FFT}}\right)}\right)^2 \quad (F.82)$$

It leads to :

$$D_{EMLP}(\varepsilon_\tau) = \Omega \quad (F.83)$$

Thus the variance of the non-normalized discriminator output is equal to the variance of Ω

$$\begin{aligned} var\left(D_{EMLP}(\varepsilon_\tau)\right) = 2\frac{\sigma_{noise}^2\sigma_{pilot}^2}{N_{FFT}N_P}\Bigg[2\frac{\sigma_{local}^2\sigma_{pilot}^2}{N_P^2}\left(\frac{\sin\left(\frac{\pi\delta\gamma N_P}{2N_{FFT}}\right)}{\sin\left(\frac{\pi\delta\gamma}{2N_{FFT}}\right)}\right)^2\left(1-\frac{1}{N_P}\frac{\sin\left(\frac{\pi\delta\gamma N_P}{N_{FFT}}\right)}{\sin\left(\frac{\pi\delta\gamma}{N_{FFT}}\right)}\right) \\ + \frac{\sigma_{noise}^2\sigma_{pilot}^2}{N_{FFT}N_P}\left(1-\frac{1}{N_P^2}\left(\frac{\sin\left(\frac{\pi\delta\gamma N_P}{N_{FFT}}\right)}{\sin\left(\frac{\pi\delta\gamma}{N_{FFT}}\right)}\right)^2\right)\Bigg] \end{aligned} \quad (F.84)$$

F.2.5) Normalized discriminator output variance

The variance of the normalized discriminator output is

$$\begin{aligned} var\left(D_{EMLP}^{norm}(\varepsilon_\tau)\right) &= var\left(\frac{D_{EMLP}(\varepsilon_\tau)}{K_{norm}\left|R_{useful}(\varepsilon_\tau)\right|^2}\right) = \frac{var\left(D_{EMLP}(\varepsilon_\tau)\right)}{K_{norm}^2\left|R_{useful}(\varepsilon_\tau)\right|^4} \\ &= \frac{var\left(D_{EMLP}(\varepsilon_\tau)\right)}{K_{norm}^2\sigma_{local}^4\sigma_{pilot}^4} \end{aligned} \quad (F.85)$$

Where:

$$K_{norm} = \frac{1-\frac{\delta}{2}\pi\beta\sin(\pi\beta\delta)-\cos(\pi\beta\delta)}{\frac{(\pi\beta)^2\delta^3}{16}} \quad (F.86)$$

$$\begin{aligned} &var\left(D_{EMLP}^{norm}(\varepsilon_\tau)\right) \\ &= \frac{1}{K_{norm}^2\sigma_{local}^2}2\frac{\sigma_{noise}^2}{N_{FFT}N_P}\Bigg[2\frac{1}{N_P^2}\left(\frac{\sin\left(\frac{\pi\delta\gamma N_P}{2N_{FFT}}\right)}{\sin\left(\frac{\pi\delta\gamma}{2N_{FFT}}\right)}\right)^2\left(1-\frac{1}{N_P}\frac{\sin\left(\frac{\pi\delta\gamma N_P}{N}\right)}{\sin\left(\frac{\pi\delta\gamma}{N}\right)}\right) \\ &+ \frac{\sigma_{noise}^2}{N_{FFT}N_P\sigma_{local}^2}\left(1-\frac{1}{N_P^2}\left(\frac{\sin\left(\frac{\pi\delta\gamma N_P}{N_{FFT}}\right)}{\sin\left(\frac{\pi\delta\gamma}{N_{FFT}}\right)}\right)^2\right)\Bigg] \end{aligned} \quad (F.87)$$

Posing $SNR = \frac{\sigma^2_{local}}{\frac{\sigma^2_{noise}}{N}}$

$$var\left(D^{norm}_{EMLP}(\varepsilon_\tau)\right) = \frac{1}{N_P SNR}\frac{4}{K^2_{norm}}\frac{1}{N_P^2}\left(\frac{\sin\left(\frac{\pi\delta\gamma N_P}{2N_{FFT}}\right)}{\sin\left(\frac{\pi\delta\gamma}{2N_{FFT}}\right)}\right)^2\left(1-\frac{1}{N_P}\frac{\sin\left(\frac{\pi\delta\gamma N_P}{N_{FFT}}\right)}{\sin\left(\frac{\pi\delta\gamma}{N_{FFT}}\right)}\right) \cdot\left[1+\frac{1}{N_P SNR}\frac{\left(1+\frac{1}{N_P}\frac{\sin\left(\frac{\pi\delta\gamma N_P}{N_{FFT}}\right)}{\sin\left(\frac{\pi\delta\gamma}{N_{FFT}}\right)}\right)}{2\frac{1}{N_P^2}\left(\frac{\sin\left(\frac{\pi\delta\gamma N_P}{2N_{FFT}}\right)}{\sin\left(\frac{\pi\delta\gamma}{2N_{FFT}}\right)}\right)^2}\right] \quad (F.88)$$

$$var\left(D^{norm}_{EMLP}(\varepsilon_\tau)\right) = \frac{K_1}{N_P SNR}\left(1+\frac{K_2}{N_P SNR}\right) \quad (F.89)$$

$$K_1 = \frac{4}{K^2_{norm}}\frac{1}{N_P^2}\left(\frac{\sin\left(\frac{\pi\delta\gamma N_P}{2N_{FFT}}\right)}{\sin\left(\frac{\pi\delta\gamma}{2N_{FFT}}\right)}\right)^2\left(1-\frac{1}{N_P}\frac{\sin\left(\frac{\pi\delta\gamma N_P}{N_{FFT}}\right)}{\sin\left(\frac{\pi\delta\gamma}{N_{FFT}}\right)}\right) \quad (F.90)$$

$$K_2 = \frac{1}{2}\frac{\left(1+\frac{1}{N_P}\frac{\sin\left(\frac{\pi\delta\gamma N_P}{N_{FFT}}\right)}{\sin\left(\frac{\pi\delta\gamma}{N_{FFT}}\right)}\right)}{\frac{1}{N_P^2}\left(\frac{\sin\left(\frac{\pi\delta\gamma N_P}{2N_{FFT}}\right)}{\sin\left(\frac{\pi\delta\gamma}{2N_{FFT}}\right)}\right)^2} \quad (F.91)$$

F.3) Annex C – SNR tracking threshold derivation

The tracking loss criterion is such that the 3-sigma value of the tracking error becomes greater than the linearity zone of the discriminator, $(F.92)$.

$$3\sqrt{var[\varepsilon_\tau]} < \frac{7}{4} \quad (F.92)$$

The variance of the tracking error estimate is expressed as $(F.93)$, its derivation is provided in the previous section.

$$var[\varepsilon_\tau] = \frac{2B_l T_s K_1}{N_P SNR}\left(1+\frac{K_2}{N_P SNR}\right) \quad (F.93)$$

Where:

- B_l is the DLL loop bandwidth
- T_s is the OFDM symbol duration
- N_P is the number of pilots

- $K_1 = \frac{4}{K_{norm}^2}\frac{1}{N_P^2}\left(\frac{\sin\left(\frac{\pi\delta\alpha N_P}{2N}\right)}{\sin\left(\frac{\pi\delta\alpha}{2N}\right)}\right)^2\left(1-\frac{1}{N_P}\frac{\sin\left(\frac{\pi\delta\alpha N_P}{N}\right)}{\sin\left(\frac{\pi\delta\alpha}{N}\right)}\right)$
- $K_2 = \frac{1}{2}\frac{\left(1+\frac{1}{N_P}\frac{\sin\left(\frac{\pi\delta\alpha N_P}{N}\right)}{\sin\left(\frac{\pi\delta\alpha}{N}\right)}\right)}{\frac{1}{N_P^2}\left(\frac{\sin\left(\frac{\pi\delta\alpha N_P}{2N}\right)}{\sin\left(\frac{\pi\delta\alpha}{2N}\right)}\right)^2}$
- $K_{norm} = \frac{1-\frac{\delta\pi\gamma N_P}{N_{FFT}}\sin\left(\frac{\pi\gamma 2\delta N_P}{N_{FFT}}\right)-\varepsilon_\tau\cos\left(\frac{\pi\gamma 2\delta N_P}{N_{FFT}}\right)}{\left(\frac{\pi\gamma}{N_{FFT}}\right)^2\frac{\delta^3}{2^4}}$ is the normalization factor which derivation is provided in Annex F1.
    - δ is the correlator spacing
    - γ is determining the pilot architecture as presented in chapter 3

By replacing the variance in $(F.92)$ by its expression $(F.93)$, we have

$$3\sqrt{\frac{2B_lT_sK_1}{N_PSNR}\left(1+\frac{K_2}{N_PSNR}\right)} < \frac{7}{4} \qquad (F.94)$$

$$\frac{2B_lT_sK_1}{N_PSNR}\left(1+\frac{K_2}{N_PSNR}\right) < \frac{7^2}{12^2} \qquad (F.95)$$

$$\frac{2B_lT_sK_1}{N_P}\frac{12^2}{7^2} < \frac{SNR}{\left(1+\frac{K_2}{N_PSNR}\right)} \qquad (F.96)$$

$$\frac{2B_lT_sK_1}{N_P}\frac{12^2}{7^2} < \frac{SNR}{\frac{N_pSNR+K_2}{N_PSNR}} \qquad (F.97)$$

$$\frac{2B_lT_sK_1}{N_P}\frac{12^2}{7^2} < \frac{N_PSNR^2}{N_pSNR+K_2} \qquad (F.98)$$

$$\frac{2B_lT_sK_1}{N_P}\frac{12^2}{7^2}\left(N_pSNR+K_2\right) < N_PSNR^2 \qquad (F.99)$$

$$-N_PSNR^2+\frac{12^2}{7^2}2B_lT_sK_1SNR+\frac{2B_lT_sK_1K_2}{N_P}\frac{12^2}{7^2} < 0 \qquad (F.100)$$

$$SNR^2-\frac{12^2}{7^2}\frac{2B_lT_sK_1}{N_p}SNR-\frac{2B_lT_sK_1K_2}{N_P^2}\frac{12^2}{7^2} < 0 \qquad (F.101)$$

As a reminder, the solutions of a second order equation $ax^2+bx+c=0$ are $\frac{-b\pm\sqrt{b^2-4ac}}{2a}$

Then, the threshold SNR is

$$SNR = \frac{\frac{12^2}{7^2}\frac{2B_lT_sK_1}{N_p}\pm\sqrt{\left(\frac{12^2}{7^2}\frac{2B_lT_sK_1}{N_p}\right)^2+4\frac{2B_lT_sK_1K_2}{N_P^2}\frac{12^2}{7^2}}}{2} \qquad (F.102)$$

$$SNR = \frac{12^2}{2 \cdot 7^2}\frac{2B_l T_s K_1}{N_p} \pm \frac{1}{2}\frac{12^2}{7^2}\frac{2B_l T_s K_1}{N_p}\sqrt{1 + \frac{4\frac{2B_l T_s K_1 K_2}{N_P^2}\frac{12^2}{7^2}}{\left(\frac{12^2}{7^2}\frac{2B_l T_s K_1}{N_p}\right)^2}} \quad (F.103)$$

$$SNR = \frac{12^2}{2 \cdot 7^2}\frac{2B_l T_s K_1}{N_p} \pm \frac{1}{2}\frac{12^2}{7^2}\frac{2B_l T_s K_1}{N_p}\sqrt{1 + \frac{4K_2}{\frac{12^2}{7^2}2B_l T_s K_1}} \quad (F.104)$$

$$SNR = \frac{12^2}{7^2}\frac{B_l T_s K_1}{N_p}\left(1 \pm \sqrt{1 + \frac{2 \cdot 7^2 K_2}{12^2 B_l T_s K_1}}\right) \quad (F.105)$$

$$SNR_{th} = \frac{12^2}{7^2}\frac{B_l T_s K_1}{N_p}\left(1 \pm \sqrt{1 + \frac{2 \cdot 7^2 K_2}{12^2 B_l T_s K_1}}\right) \quad (F.106)$$

Where:

- $K_1 = \frac{4}{K_{norm}^2}\frac{1}{N_P^2}\left(\frac{\sin\left(\frac{\pi\delta\alpha N_P}{2N}\right)}{\sin\left(\frac{\pi\delta\alpha}{2N}\right)}\right)^2\left(1 - \frac{1}{N_P}\frac{\sin\left(\frac{\pi\delta\alpha N_P}{N}\right)}{\sin\left(\frac{\pi\delta\alpha}{N}\right)}\right)$
- $K_2 = \frac{1}{2}\frac{\left(1+\frac{1}{N_P}\frac{\sin\left(\frac{\pi\delta\alpha N_P}{N}\right)}{\sin\left(\frac{\pi\delta\alpha}{N}\right)}\right)}{\frac{1}{N_P^2}\left(\frac{\sin\left(\frac{\pi\delta\alpha N_P}{2N}\right)}{\sin\left(\frac{\pi\delta\alpha}{2N}\right)}\right)^2}$
- δ, the correlator spacing
- $T_s = \frac{N_{FFT}+N_{CP}}{\Delta f N_{FFT}}$, the OFDM symbol duration
- Δf, the subcarrier spacing
- N_{CP}, the Cycle Prefix length
- B_l, the loop bandwidth

Annex G)Derivation of the observation matrix in the hybrid navigation filter

In this annex, the complete derivation of the observation matrix Jacobian used in Chapter 7 is described here.

G.1) 5G Pseudo ranges code measurements

$$h^{(5G)}(X_k) = \begin{bmatrix} h_1^{(5G)}(X_k) \\ \dots \\ h_{N_{5G}}^{(5G)}(X_k) \end{bmatrix} = \begin{bmatrix} \sqrt{\left(x_k - x_{BS_1}\right)^2 + \left(y_k - y_{BS_1}\right)^2 + \left(z_k - z_{BS_1}\right)^2} + \mathrm{b}_{GPS/user} - \mathrm{b}_{GPS/5G} \\ \dots \\ \sqrt{\left(x_k - x_{BS_{N_{5G}}}\right)^2 + \left(y_k - y_{BS_{N_{5G}}}\right)^2 + \left(z_k - z_{BS_{N_{5G}}}\right)^2} + \mathrm{b}_{GPS/user} - \mathrm{b}_{GPS/5G} \end{bmatrix}$$

$$h^{(5G)}(X_k) = \begin{bmatrix} h_1^{(5G)}(X_k) \\ \dots \\ h_{N_{5G}}^{(5G)}(X_k) \end{bmatrix} = \begin{bmatrix} d_{measure}{}_1^{(5G)} + c \cdot \mathrm{b}_{GPS/user} - c \cdot \mathrm{b}_{GPS/5G} \\ \dots \\ d_{measure}{}_{N_{5G}}^{(5G)} + c \cdot \mathrm{b}_{GPS/user} - c \cdot \mathrm{b}_{GPS/5G} \end{bmatrix}$$

Where $d_{predicted}{}_j^{(5G)} = \sqrt{\left(\hat{x}_k - x_{BS_j}\right)^2 + \left(\hat{y}_k - y_{BS_j}\right)^2 + \left(\hat{z}_k - z_{BS_j}\right)^2}$

The Jacobian matrix of $h^{(5G)}(X_k)$ is $\frac{\partial h^{(5G)}}{\partial X_k}_{|X_k = \hat{X}_{k+1|k}}$, where:

$$\hat{X}_{k+1|k} = \begin{bmatrix} \hat{x}_{k+1|k} \\ \widehat{v_x}_{k+1|k} \\ \hat{y}_{k+1|k} \\ \widehat{v_y}_{k+1|k} \\ \hat{z}_{k+1|k} \\ \widehat{v_z}_{k+1|k} \\ \hat{b}_{GPS-user}{}_{k+1|k} \\ \hat{\mathrm{b}}_{GPS-user}{}_{k+1|k} \\ \hat{\mathrm{b}}_{GPS-Gal}{}_{k+1|k} \\ \hat{\mathrm{b}}_{GPS-5G}{}_{k+1|k} \end{bmatrix}^T$$

Then

$$\frac{\partial h^{(5G)}}{\partial X_k}_{|X_k=\hat{X}_{k+1|k}} = \begin{bmatrix} \frac{\partial h_1^{(5G)}(X_k)}{\partial \hat{x}_{k+1|k}} & \cdots & \frac{\partial h_{N_{5G}}^{(5G)}(X_k)}{\partial \hat{x}_{k+1|k}} \\ \frac{\partial h_1^{(5G)}(X_k)}{\partial \widehat{v_x}_{k+1|k}} & \cdots & \frac{\partial h_{N_{5G}}^{(5G)}(X_k)}{\partial \widehat{v_x}_{k+1|k}} \\ \frac{\partial h_1^{(5G)}(X_k)}{\partial \hat{y}_{k+1|k}} & \cdots & \frac{\partial h_{N_{5G}}^{(5G)}(X_k)}{\partial \hat{y}_{k+1|k}} \\ \frac{\partial h_1^{(5G)}(X_k)}{\partial \widehat{v_y}_{k+1|k}} & \cdots & \frac{\partial h_{N_{5G}}^{(5G)}(X_k)}{\partial \widehat{v_y}_{k+1|k}} \\ \frac{\partial h_1^{(5G)}(X_k)}{\partial \hat{z}_{k+1|k}} & \cdots & \frac{\partial h_{N_{5G}}^{(5G)}(X_k)}{\partial \hat{z}_{k+1|k}} \\ \frac{\partial h_1^{(5G)}(X_k)}{\partial \widehat{v_z}_{k+1|k}} & \cdots & \frac{\partial h_{N_{5G}}^{(5G)}(X_k)}{\partial \widehat{v_z}_{k+1|k}} \\ \frac{\partial h_1^{(5G)}(X_k)}{\partial \left(\hat{b}_{GPS-user_{k+1|k}}\right)} & \cdots & \frac{\partial h_{N_{5G}}^{(5G)}(X_k)}{\partial \left(\hat{b}_{GPS-user_{k+1|k}}\right)} \\ \frac{\partial h_1^{(5G)}(X_k)}{\partial \left(\hat{\mathrm{b}}_{GPS-user_{k+1|k}}\right)} & \cdots & \frac{\partial h_{N_{5G}}^{(5G)}(X_k)}{\partial \left(\hat{\mathrm{b}}_{GPS-user_{k+1|k}}\right)} \\ \frac{\partial h_1^{(5G)}(X_k)}{\partial \left(\hat{\mathrm{b}}_{GPS-Gal_{k+1|k}}\right)} & \cdots & \frac{\partial h_1^{(5G)}(X_k)}{\partial \left(\hat{b}_{GPS-Gal_{k+1|k}}\right)} \\ \frac{\partial h_1^{(5G)}(X_k)}{\partial \left(\hat{\mathrm{b}}_{GPS-5G_{k+1|k}}\right)} & \cdots & \frac{\partial h_1^{(5G)}(X_k)}{\partial \left(\hat{b}_{GPS-5G_{k+1|k}}\right)} \end{bmatrix}^T$$

Then, the coefficient of the matrix H_{k+1}

$$\frac{\partial h_j^{(5G)}(X_k)}{\partial \hat{x}_{k+1|k}} = \frac{\partial}{\partial \hat{x}_{k+1|k}}\left[d_{predicted_j} + c \cdot \widehat{\Delta t}_{GPS-user_{k+1|k}} - c \cdot \widehat{\Delta t}_{GPS/5G_{k+1|k}}\right] = \frac{\hat{x}_{k+1|k} - x_{BS_j}}{d_{predicted_j}^{(5G)}}$$

$$\frac{\partial h_j^{(5G)}(X_k)}{\partial \widehat{v_x}_{k+1|k}} = 0$$

$$\frac{\partial h_j^{(5G)}(X_k)}{\partial \hat{y}_{k+1|k}} = \frac{\hat{y}_{k+1|k} - y_{BS_j}}{d_{predicted_j}^{(5G)}}$$

$$\frac{\partial h_j^{(5G)}(X_k)}{\partial \widehat{v_y}_{k+1|k}} = 0$$

$$\frac{\partial h_j^{(5G)}(X_k)}{\partial \hat{z}_{k+1|k}} = \frac{\hat{z}_{k+1|k} - z_{BS_j}}{d_{predicted_j}^{(5G)}}$$

$$\frac{\partial h_j^{(5G)}(X_k)}{\partial \widehat{v_z}_{k+1|k}} = 0$$

$$\frac{\partial h_j^{(5G)}(X_k)}{\partial \left(c \cdot \widehat{\Delta t}_{GPS-user_{k+1|k}}\right)} = 1$$

$$\frac{\partial h_j^{(5G)}(X_k)}{\partial\left(c\cdot\widehat{\Delta t}_{GPS-user_{k+1|k}}\right)}=0$$

$$\frac{\partial h_j^{(5G)}(X_k)}{\partial\left(c\cdot\widehat{\Delta t}_{GPS-Gal_{k+1|k}}\right)}=0$$

$$\frac{\partial h_j^{(5G)}(X_k)}{\partial\left(c\cdot\widehat{\Delta t}_{GPS-5G_{k+1|k}}\right)}=-1$$

$$\frac{\partial h^{(5G)}}{\partial X_k}_{|X_k=\hat{X}_{k+1|k}}=\begin{bmatrix}\frac{\hat{x}_{k+1|k}-x_{BS_1}}{d_{predicted}{}_1^{(5G)}} & 0 & \frac{\hat{y}_{k+1|k}-y_{BS_1}}{d_{predicted}{}_1^{(5G)}} & 0 & \frac{\hat{z}_{k+1|k}-z_{BS_1}}{d_{predicted}{}_1^{(5G)}} & 0 & 1 & 0 & 0 & -1\\ \vdots & \vdots & \vdots & \vdots & \vdots & \vdots & \vdots & \vdots & \vdots & \vdots\\ \frac{\hat{x}_{k+1|k}-x_{BS_{N_{5G}}}}{d_{predicted}{}_1^{(5G)}} & 0 & \frac{\hat{y}_{k+1|k}-y_{BS_{N_{5G}}}}{d_{predicted}{}_1^{(5G)}} & 0 & \frac{\hat{z}_{k+1|k}-z_{BS_{N_{5G}}}}{d_{predicted}{}_1^{(5G)}} & 0 & 1 & 0 & 0 & -1\end{bmatrix}$$

G.2) GPS Pseudo ranges code measurements

Similarly for GPS pseudo range measurements

$$h^{(GPS)}(X_k)=\begin{bmatrix}h_1^{(GPS)}(X_k)\\ \dots\\ h_{N_{GPS}}^{(GPS)}(X_k)\end{bmatrix}=\begin{bmatrix}d_{predicted}{}_1^{(GPS)}+c\cdot\widehat{\Delta t}_{GPS/user}\\ \dots\\ d_{predicted}{}_{N_{GPS}}^{(GPS)}+c\cdot\widehat{\Delta t}_{GPS/user}\end{bmatrix}$$

Where $d_{predicted}{}_j^{(GPS)}=\sqrt{\left(\hat{x}_{k+1|k}-x_{GPS_j}\right)^2+\left(\hat{y}_{k+1|k}-y_{GPS_j}\right)^2+\left(\hat{z}_{k+1|k}-z_{GPS_j}\right)^2}$

$$\frac{\partial h^{(GPS)}}{\partial X_k}_{|X_k=\hat{X}_{k+1|k}}=\begin{bmatrix}\frac{\hat{x}_{k+1|k}-x_{GPS_1}}{d_{predicted}{}_1^{(GPS)}} & 0 & \frac{\hat{y}_{k+1|k}-y_{GPS_1}}{d_{predicted}{}_1^{(GPS)}} & 0 & \frac{\hat{z}_{k+1|k}-z_{GPS_1}}{d_{predicted}{}_1^{(GPS)}} & 0 & 1 & 0 & 0 & 0\\ \vdots & \vdots & \vdots & \vdots & \vdots & \vdots & \vdots & \vdots & \vdots & \vdots\\ \frac{\hat{x}_{k+1|k}-x_{GPS_{N_{GPS}}}}{d_{predicted}{}_{N_{GPS}}^{(GPS)}} & 0 & \frac{\hat{y}_{k+1|k}-y_{GPS_{N_{GPS}}}}{d_{predicted}{}_{N_{GPS}}^{(GPS)}} & 0 & \frac{\hat{z}_{k+1|k}-z_{GPS_{N_{GPS}}}}{d_{predicted}{}_{N_{GPS}}^{(GPS)}} & 0 & 1 & 0 & 0 & 0\end{bmatrix}$$

G.3) Galileo Pseudo ranges code measurements

Similarly for Galileo pseudo range measurements

$$h^{(Gal)}(X_k)=\begin{bmatrix}h_1^{(Gal)}(X_k)\\ \dots\\ h_{N_{Gal}}^{(Gal)}(X_k)\end{bmatrix}=\begin{bmatrix}d_{predicted}{}_1^{(Gal)}+c\cdot\widehat{\Delta t}_{GPS/user}-c\cdot\widehat{\Delta t}_{GPS/Gal}\\ \dots\\ d_{predicted}{}_{N_{GPS}}^{(Gal)}+c\cdot\widehat{\Delta t}_{GPS/user}-c\cdot\widehat{\Delta t}_{GPS/Gal}\end{bmatrix}$$

Where $d_{predicted}{}_j^{(Gal)}=\sqrt{\left(\hat{x}_{k+1|k}-x_{Gal_j}\right)^2+\left(\hat{y}_{k+1|k}-y_{Gal_j}\right)^2+\left(\hat{z}_{k+1|k}-z_{Gal_j}\right)^2}$

$$\frac{\partial h^{(Gal)}}{\partial X_k}_{|X_k=\hat{X}_{k+1|k}}=\begin{bmatrix}\frac{\hat{x}_{k+1|k}-x_{Gal_{j_1}}}{d_{predicted}{}_1^{(Gal)}} & 0 & \frac{\hat{y}_{k+1|k}-y_{Gal_1}}{d_{predicted}{}_1^{(Gal)}} & 0 & \frac{\hat{z}_{k+1|k}-z_{Gal_1}}{d_{predicted}{}_1^{(Gal)}} & 0 & 1 & 0 & -1 & 0\\ \vdots & \vdots & \vdots & \vdots & \vdots & \vdots & \vdots & \vdots & \vdots & \vdots\\ \frac{\hat{x}_{k+1|k}-x_{Gal_{N_{Gal}}}}{d_{predicted}{}_{N_{GPS}}^{(Gal)}} & 0 & \frac{\hat{y}_{k+1|k}-y_{Gal_{N_{Gal}}}}{d_{predicted}{}_{N_{GPS}}^{(Gal)}} & 0 & \frac{\hat{z}_{k+1|k}-z_{Gal_{N_{Gal}}}}{d_{predicted}{}_{N_{GPS}}^{(Gal)}} & 0 & 1 & 0 & -1 & 0\end{bmatrix}$$

G.4) GPS Pseudo ranges rate measurements

$$h^{(\dot{GPS})}(X_k) = \begin{bmatrix} h_1^{(\dot{GPS})}(X_k) \\ \dots \\ h_{N_{GPS}}^{(\dot{GPS})}(X_k) \end{bmatrix}$$

$$= \begin{bmatrix} \left(\widehat{v_x}_{k+1|k} - v_{x_{GPS_1}}\right) \cdot \dfrac{\hat{x}_{k+1|k} - x_{GPS_1}}{d_{predicted}{}_1^{(GPS)}} + \left(\widehat{v_y}_{k+1|k} - v_{y_{GPS_1}}\right) \cdot \dfrac{\hat{y}_{k+1|k} - y_{GPS_1}}{d_{predicted}{}_1^{(GPS)}} \\ + \left(\widehat{v_z}_{k+1|k} - v_{z_{GPS_1}}\right) \cdot \dfrac{\hat{z}_{k+1|k} - z_{GPS_1}}{d_{predicted}{}_1^{(GPS)}} + c \cdot \dot{\Delta t}_{GPS/user} \\ \dots \\ \left(\widehat{v_x}_{k+1|k} - v_{x_{GPS_{N_{GPS}}}}\right) \cdot \dfrac{\hat{x}_{k+1|k} - x_{GPS_{N_{GPS}}}}{d_{predicted}{}_{N_{GPS}}^{(GPS)}} + \left(\widehat{v_y}_{k+1|k} - v_{y_{GPS_{N_{GPS}}}}\right) \cdot \dfrac{\hat{y}_{k+1|k} - y_{GPS_{N_{GPS}}}}{d_{predicted}{}_{N_{GPS}}^{(GPS)}} \\ + \left(\widehat{v_z}_{k+1|k} - v_{z_{GPS_{N_{GPS}}}}\right) \cdot \dfrac{\hat{z}_{k+1|k} - z_{GPS_{N_{GPS}}}}{d_{predicted}{}_{N_{GPS}}^{(GPS)}} + c \cdot \dot{\Delta t}_{GPS/user} \end{bmatrix}$$

The Jacobian matrix of $h^{(\dot{GPS})}(X_k)$ is $\frac{\partial h^{(\dot{GPS})}}{\partial X_k}_{|X_k = \hat{X}_{k+1|k}}$, where:

Then, the coefficient of the matrix H_{k+1}

$$\frac{\partial h_j^{(\dot{GPS})}(X_k)}{\partial \hat{x}_{k+1|k}} = \frac{\partial}{\partial \hat{x}_{k+1|k}} \left[\left(\widehat{v_x}_{k+1|k} - v_{x_{GPS_j}}\right) \cdot \frac{\hat{x}_{k+1|k} - x_{GPS_j}}{d_{predicted}{}_j^{(GPS)}} + \left(\widehat{v_y}_{k+1|k} - v_{y_{GPS_j}}\right) \cdot \frac{\hat{y}_{k+1|k} - y_{GPS_j}}{d_{predicted}{}_j^{(GPS)}} \right.$$
$$\left. + \left(\widehat{v_z}_{k+1|k} - v_{z_{GPS_j}}\right) \cdot \frac{\hat{z}_{k+1|k} - z_{GPS_j}}{d_{predicted}{}_j^{(GPS)}} + c \cdot \dot{\Delta t}_{GPS/user} \right]$$

$$\frac{\partial h_j^{(\dot{GPS})}(X_k)}{\partial \hat{x}_{k+1|k}} = \left(\widehat{v_x}_{k+1|k} - v_{x_{GPS_j}}\right) \frac{\partial}{\partial \hat{x}_{k+1|k}} \left[\frac{\hat{x}_{k+1|k} - x_{GPS_j}}{d_{predicted}{}_j^{(GPS)}} \right]$$
$$+ \left[\left(\widehat{v_y}_{k+1|k} - v_{y_{GPS_j}}\right) \cdot \left(\hat{y}_{k+1|k} - y_{GPS_j}\right) + \left(\widehat{v_z}_{k+1|k} - v_{z_{GPS_j}}\right) \right.$$
$$\left. \cdot \left(\hat{z}_{k+1|k} - z_{GPS_j}\right) \right] \frac{\partial}{\partial \hat{x}_{k+1|k}} \left[\frac{1}{d_{predicted}{}_j^{(GPS)}} \right]$$

$$\frac{\partial}{\partial \hat{x}_{k+1|k}} \left[\frac{\hat{x}_{k+1|k} - x_{GPS_j}}{d_{predicted}{}_j^{(GPS)}} \right] = \frac{1}{d_{predicted}{}_j^{(GPS)}} - \frac{\left(\hat{x}_{k+1|k} - x_{GPS_j}\right)^2}{d_{predicted}{}_j^{(GPS)^3}}$$

$$\frac{\partial}{\partial \hat{x}_{k+1|k}} \left[\frac{1}{d_{predicted}{}_j^{(GPS)}} \right] = \frac{\left(\hat{x}_{k+1|k} - x_{GPS_j}\right)}{d_{predicted}{}_j^{(GPS)^3}}$$

$$\frac{\partial h_j^{(\dot{GPS})}(X_k)}{\partial \hat{x}_{k+1|k}} = \frac{\left(\widehat{v_x}_{k+1|k} - v_{x_{GPS_j}}\right)}{d_{predicted}{}_j^{(GPS)}}$$
$$- \left[\left(\widehat{v_x}_{k+1|k} - v_{x_{GPS_j}}\right) \left(\hat{x}_{k+1|k} - x_{GPS_j}\right) + \left(\widehat{v_y}_{k+1|k} - v_{y_{GPS_j}}\right) \cdot \left(\hat{y}_{k+1|k} - y_{GPS_j}\right) \right.$$
$$\left. + \left(\widehat{v_z}_{k+1|k} - v_{z_{GPS_j}}\right) \cdot \left(\hat{z}_{k+1|k} - z_{GPS_j}\right) \right] \frac{\left(\hat{x}_{k+1|k} - x_{GPS_j}\right)}{d_{predicted}{}_j^{(GPS)^3}}$$

The following notation is adopted for the rest of the report:

$$\widehat{V_{k_j}} = \frac{\left[\left(\widehat{v_x}_{k+1|k} - v_{x_{GPS_j}}\right)\left(\hat{x}_{k+1|k} - x_{GPS_j}\right) + \left(\widehat{v_y}_{k+1|k} - v_{y_{GPS_j}}\right)\cdot\left(\hat{y}_{k+1|k} - y_{GPS_j}\right) + \left(\widehat{v_z}_{k+1|k} - v_{z_{GPS_j}}\right)\cdot\left(\hat{z}_{k+1|k} - z_{GPS_j}\right)\right]}{d_{predicted_j}^{(GPS)}}$$

$$\frac{\partial h_j^{(\dot{GPS})}(X_k)}{\partial \hat{x}_{k+1|k}} = \frac{\left(\widehat{v_x}_{k+1|k} - v_{x_{GPS_j}}\right)}{d_{predicted_j}^{(GPS)}} - \widehat{V_{k_j}}\frac{\left(\hat{x}_{k+1|k} - x_{GPS_j}\right)}{d_{predicted_j}^{(GPS)^2}}$$

$$\frac{\partial h_j^{(5G)}(X_k)}{\partial \widehat{v_x}_{k+1|k}} = \frac{\left(\hat{x}_{k+1|k} - x_{GPS_j}\right)}{d_{predicted_j}^{(GPS)}}$$

$$\frac{\partial h_j^{(\dot{GPS})}(X_k)}{\partial \hat{y}_{k+1|k}} = \frac{\left(\widehat{v_y}_{k+1|k} - v_{y_{GPS_j}}\right)}{d_{predicted_j}^{(GPS)}} - \widehat{V_{k_j}}\frac{\left(\hat{y}_{k+1|k} - y_{GPS_j}\right)}{d_{predicted_j}^{(GPS)^2}}$$

$$\frac{\partial h_j^{(5G)}(X_k)}{\partial \widehat{v_y}_{k+1|k}} = \frac{\left(\hat{y}_{k+1|k} - y_{GPS_j}\right)}{d_{predicted_j}^{(GPS)}}$$

$$\frac{\partial h_j^{(\dot{GPS})}(X_k)}{\partial \hat{z}_{k+1|k}} = \frac{\left(\widehat{v_z}_{k+1|k} - v_{z_{GPS_j}}\right)}{d_{predicted_j}^{(GPS)}} - \widehat{V_{k_j}}\frac{\left(\hat{z}_{k+1|k} - z_{GPS_j}\right)}{d_{predicted_j}^{(GPS)^2}}$$

$$\frac{\partial h_j^{(\dot{GPS})}(X_k)}{\partial \widehat{v_z}_{k+1|k}} = \frac{\left(\hat{z}_{k+1|k} - z_{GPS_j}\right)}{d_{predicted_j}^{(GPS)}}$$

$$\frac{\partial h_j^{(\dot{GPS})}(X_k)}{\partial\left(c\cdot\widehat{\Delta t}_{GPS-user_{k+1|k}}\right)} = 0$$

$$\frac{\partial h_j^{(\dot{GPS})}(X_k)}{\partial\left(c\cdot\widehat{\dot{\Delta t}}_{GPS-user_{k+1|k}}\right)} = 1$$

$$\frac{\partial h_j^{(\dot{GPS})}(X_k)}{\partial\left(c\cdot\widehat{\Delta t}_{GPS-Gal_{k+1|k}}\right)} = 0$$

$$\frac{\partial h_j^{(\dot{GPS})}(X_k)}{\partial\left(c\cdot\widehat{\Delta t}_{GPS-5G_{k+1|k}}\right)} = 0$$

$$\frac{\partial h^{(\dot{GPS})}}{\partial X_k}_{|X_k=\hat{X}_{k+1|k}}$$

$$= \begin{bmatrix} \frac{\left(\widehat{v_x}_{k+1|k} - v_{x_{GPS_1}}\right)}{d_{predicted_1}^{(GPS)}} - \widehat{V_k}_1 \frac{\left(\hat{x}_{k+1|k} - x_{GPS_1}\right)}{d_{predicted_1}^{(GPS)^2}} & \cdots & \frac{\left(\widehat{v_x}_{k+1|k} - v_{x_{GPS_{N_{GPS}}}}\right)}{d_{predicted_{N_{GPS}}}^{(GPS)}} - \widehat{V_k}_{N_{GPS}} \frac{\left(\hat{x}_{k+1|k} - x_{GPS_{N_{GPS}}}\right)}{d_{predicted_{N_{GPS}}}^{(GPS)^2}} \\ \frac{\left(\hat{x}_{k+1|k} - x_{GPS_1}\right)}{d_{predicted_1}^{(GPS)}} & \cdots & \frac{\left(\hat{x}_{k+1|k} - x_{GPS_{N_{GPS}}}\right)}{d_{predicted_{N_{GPS}}}^{(GPS)}} \\ \frac{\left(\widehat{v_y}_{k+1|k} - v_{y_{GPS_1}}\right)}{d_{predicted_1}^{(GPS)}} - \widehat{V_k}_1 \frac{\left(\hat{y}_{k+1|k} - y_{GPS_1}\right)}{d_{predicted_1}^{(GPS)^2}} & \cdots & \frac{\left(\widehat{v_y}_{k+1|k} - v_{y_{GPS_{N_{GPS}}}}\right)}{d_{predicted_{N_{GPS}}}^{(GPS)}} - \widehat{V_k}_{N_{GPS}} \frac{\left(\hat{y}_{k+1|k} - y_{GPS_{N_{GPS}}}\right)}{d_{predicted_{N_{GPS}}}^{(GPS)^2}} \\ \frac{\left(\hat{y}_{k+1|k} - y_{GPS_1}\right)}{d_{predicted_1}^{(GPS)}} & \cdots & \frac{\left(\hat{y}_{k+1|k} - y_{GPS_{N_{GPS}}}\right)}{d_{predicted_{N_{GPS}}}^{(GPS)}} \\ \frac{\left(\widehat{v_z}_{k+1|k} - v_{z_{GPS_1}}\right)}{d_{predicted_1}^{(GPS)}} - \widehat{V_k}_1 \frac{\left(\hat{z}_{k+1|k} - z_{GPS_1}\right)}{d_{predicted_1}^{(GPS)^2}} & \cdots & \frac{\left(\widehat{v_z}_{k+1|k} - v_{z_{GPS_{N_{GPS}}}}\right)}{d_{predicted_{N_{GPS}}}^{(GPS)}} - \widehat{V_k}_{N_{GPS}} \frac{\left(\hat{z}_{k+1|k} - z_{GPS_{N_{GPS}}}\right)}{d_{predicted_{N_{GPS}}}^{(GPS)^2}} \\ \frac{\left(\hat{z}_{k+1|k} - z_{GPS_1}\right)}{d_{predicted_1}^{(GPS)}} & \cdots & \frac{\left(\hat{z}_{k+1|k} - z_{GPS_{N_{GPS}}}\right)}{d_{predicted_{N_{GPS}}}^{(GPS)}} \\ 0 & \cdots & 0 \\ 1 & \cdots & 1 \\ 0 & \cdots & 0 \\ 0 & \cdots & 0 \end{bmatrix}^T$$

G.5) Galileo Pseudo ranges rate measurements

As for GPS pseudo range rates measurements

$$\frac{\partial h^{(Galileo)}}{\partial X_k}_{|X_k=\hat{X}_{k+1|k}}$$

$$= \begin{bmatrix} \frac{\left(\widehat{v_x}_{k+1|k} - v_{x_{Gal_1}}\right)}{d_{predicted_1}^{(Gal)}} - \widehat{V_k}_1 \frac{\left(\hat{x}_{k+1|k} - x_{Gal_1}\right)}{d_{predicted_1}^{(Gal)^2}} & \cdots & \frac{\left(\widehat{v_x}_{k+1|k} - v_{x_{Gal_{N_{Gal}}}}\right)}{d_{predicted_{N_{Gal}}}^{(Gal)}} - \widehat{V_k}_{N_{Gal}} \frac{\left(\hat{x}_{k+1|k} - x_{Gal_{N_{Gal}}}\right)}{d_{predicted_{N_{Gal}}}^{(Gal)^2}} \\ \frac{\left(\hat{x}_{k+1|k} - x_{Gal_1}\right)}{d_{predicted_1}^{(Gal)}} & \cdots & \frac{\left(\hat{x}_{k+1|k} - x_{Gal_{N_{Gal}}}\right)}{d_{predicted_{N_{Gal}}}^{(Gal)}} \\ \frac{\left(\widehat{v_y}_{k+1|k} - v_{y_{Gal_1}}\right)}{d_{predicted_1}^{(Gal)}} - \widehat{V_k}_1 \frac{\left(\hat{y}_{k+1|k} - y_{Gal_1}\right)}{d_{predicted_1}^{(Gal)^2}} & \cdots & \frac{\left(\widehat{v_y}_{k+1|k} - v_{y_{Gal_{N_{Gal}}}}\right)}{d_{predicted_{N_{Gal}}}^{(Gal)}} - \widehat{V_k}_{N_{GPS}} \frac{\left(\hat{y}_{k+1|k} - y_{Gal_{N_{Gal}}}\right)}{d_{predicted_{N_{Gal}}}^{(Gal)^2}} \\ \frac{\left(\hat{y}_{k+1|k} - y_{Gal_1}\right)}{d_{predicted_1}^{(GPS)}} & \cdots & \frac{\left(\hat{y}_{k+1|k} - y_{Gal_{N_{Gal}}}\right)}{d_{predicted_{N_{Gal}}}^{(Gal)}} \\ \frac{\left(\widehat{v_z}_{k+1|k} - v_{z_{Gal_1}}\right)}{d_{predicted_1}^{(Gal)}} - \widehat{V_k}_1 \frac{\left(\hat{z}_{k+1|k} - z_{Gal_1}\right)}{d_{predicted_1}^{(Gal)^2}} & \cdots & \frac{\left(\widehat{v_z}_{k+1|k} - v_{z_{Gal_{N_{Gal}}}}\right)}{d_{predicted_{N_{Gal}}}^{(Gal)}} - \widehat{V_k}_{N_{Gal}} \frac{\left(\hat{z}_{k+1|k} - z_{Gal_{N_{Gal}}}\right)}{d_{predicted_{N_{Gal}}}^{(Gal)^2}} \\ \frac{\left(\hat{z}_{k+1|k} - z_{Gal_1}\right)}{d_{predicted_1}^{(Gal)}} & \cdots & \frac{\left(\hat{z}_{k+1|k} - z_{Gal_{N_{Gal}}}\right)}{d_{predicted_{N_{Gal}}}^{(Gal)}} \\ 0 & \cdots & 0 \\ 1 & \cdots & 1 \\ 0 & \cdots & 0 \\ 0 & \cdots & 0 \end{bmatrix}^T$$

Annex H) Addentum results chapter 7

The following tables corresponds to the cases not presented in chapter 7.

Table H.1 – Case 10: COMP-FG-99-Gl-10Hz

	X	Y	Z	X^2+Y^2
EKF GNSS	0.47	1.10	2.66	1.20
EKF 5G	1.12	1.85	19.63	2.16
UKF 5G	1.13	1.94	19.59	2.25
EKF HYBRID	0.68	1.47	2.69	1.62
UKF HYBRID	0.40	1.34	1.68	1.40

Table H.2.28– Case 11: COMP-FG-95-Gl-10Hz

	X	Y	Z	X^2+Y^2
EKF GNSS	0.47	1.10	2.66	1.20
EKF 5G	1.15	1.97	19.48	2.28
UKF 5G	1.17	2.07	19.59	2.38
EKF HYBRID	0.60	1.61	2.84	1.72
UKF HYBRID	0.47	1.49	1.78	1.56

Table H.3 – Case 12: COMP-OB-99.9-Ci-1Hz-NoFLL

	X	Y	Z	X^2+Y^2
EKF GNSS	0.47	1.10	2.66	1.20
EKF 5G	1.11	1.02	10.95	1.51
UKF 5G	1.12	0.93	20.67	1.46
EKF HYBRID	0.73	0.69	2.67	1.00
UKF HYBRID	0.82	0.49	1.24	0.96

Table H.4 – Case 13: COMP-OB-99.9-Ra-1Hz-NoFLL

	X	Y	Z	X^2+Y^2
EKF GNSS	0.47	1.10	2.66	1.20
EKF 5G	1.51	1.27	11.13	1.97
UKF 5G	1.69	1.38	21.12	2.18
EKF HYBRID	0.77	0.78	2.68	1.10
UKF HYBRID	0.48	0.46	0.95	0.67

Table H.5 – Case 14: COMP-OB-99.9-Ch-1Hz-NoFLL

	X	Y	Z	X^2+Y^2
EKF GNSS	0.47	1.10	2.66	1.20
EKF 5G	1.57	1.34	11.34	2.06
UKF 5G	1.62	1.32	15.24	2.09
EKF HYBRID	0.84	0.84	2.66	1.19
UKF HYBRID	0.45	0.56	0.93	0.72

Table H.6 – Case 16: COMP-OB-99-Gl-1Hz-NoFLL

	X	Y	Z	X^2+Y^2
EKF GNSS	0.47	1.10	2.66	1.20
EKF 5G	1.61	1.35	6.63	2.10
UKF 5G	1.63	1.26	10.31	2.06
EKF HYBRID	1.00	0.84	4.56	1.31
UKF HYBRID	0.66	0.62	1.01	0.91

Table H.7 – Case 17: COMP-OB-95-Gl-1Hz-NoFLL

	X	Y	Z	X^2+Y^2
EKF GNSS	0.47	1.10	2.66	1.20
EKF 5G	1.32	1.22	11.41	1.79
UKF 5G	1.34	1.07	10.57	1.72
EKF HYBRID	1.03	0.86	5.11	1.34
UKF HYBRID	0.83	0.65	0.97	1.06

Table H.8 – Case 19: COMP-FG-99-Gl-1Hz-NoFLL

	X	Y	Z	X^2+Y^2
EKF GNSS	0.47	1.10	2.66	1.20
EKF 5G	1.62	1.33	6.53	2.09
UKF 5G	1.64	1.24	14.64	2.06
EKF HYBRID	1.42	0.99	9.32	1.73
UKF HYBRID	1.24	0.83	1.34	1.49

Table H.9 – Case 20: COMP-FG-95-Gl-1Hz-NoFLL

	X	Y	Z	X^2+Y^2
EKF GNSS	0.47	1.10	2.66	1.20
EKF 5G	1.87	1.40	21.00	2.34
UKF 5G	1.90	1.33	20.80	2.32
EKF HYBRID	1.77	1.12	10.89	2.09
UKF HYBRID	1.55	0.94	1.74	1.81

Table H.10 – Case 22: COMP-OB-99-Gl-1Hz-FLL

	X	Y	Z	X^2+Y^2
EKF GNSS	0.47	1.10	2.66	1.20
EKF 5G	0.64	0.85	5.01	1.07
UKF 5G	0.63	0.75	10.11	0.98
EKF HYBRID	0.58	0.64	3.48	0.87
UKF HYBRID	0.43	0.38	0.75	0.58

Table H.11 – Case 23: COMP-OB-95-Gl-1Hz-FLL

	X	Y	Z	X^2+Y^2
EKF GNSS	0.47	1.10	2.66	1.20
EKF 5G	0.66	0.84	4.80	1.07
UKF 5G	0.65	0.74	5.21	0.99
EKF HYBRID	0.45	0.64	3.51	0.78
UKF HYBRID	0.55	0.48	0.77	0.73

Table H.12 – Case 24: COMP-FG-99.9-Gl-1Hz-FLL

	X	Y	Z	X^2+Y^2
EKF GNSS	0.47	1.10	2.66	1.20
EKF 5G	0.69	0.88	5.48	1.12
UKF 5G	0.68	0.86	15.82	1.09
EKF HYBRID	0.46	0.63	4.07	0.78
UKF HYBRID	0.53	0.51	0.70	0.74

Table H.13 – Case 25: COMP-FG-99-Gl-1Hz-FLL

	X	Y	Z	X^2+Y^2
EKF GNSS	0.47	1.10	2.66	1.20
EKF 5G	0.71	0.90	17.99	1.14
UKF 5G	0.70	0.80	17.99	1.06
EKF HYBRID	0.51	0.65	4.17	0.83
UKF HYBRID	0.53	0.53	0.71	0.75

Table H.14 – Case 26 : COMP-FG-95-Gl-1Hz-FLL

	X	Y	Z	X^2+Y^2
EKF GNSS	0.47	1.10	2.66	1.20
EKF 5G	0.76	0.92	18.02	1.19
UKF 5G	0.75	0.84	17.99	1.13
EKF HYBRID	0.52	0.72	4.48	0.89
UKF HYBRID	0.52	0.56	0.95	0.77

H.1) Impact of the trajectory used for the characterization on the filters performances

In this first subsection, the impact of the trajectory used for the pseudo range measurement error characterization on the filter performances is studied. Therefore, the objective is to determine the best characterization in term of trajectory to be used in the filters and the potential improvements to be made.

In Figure 7.12 and Figure H.1, histograms presenting the RMSE on the horizontal plane and along the Z axis for cases 3, 4, 5 and 6 are presented. These 4 cases assumed an over bounding characterization for a 10 Hz DLL bandwidth (COMP-OB-99.9-XX-10Hz). Numerical values can be found in Table 7.8, Table 7.9, Table 7.10 and Table 7.11.

In Figure H.2 and Figure H.4 histograms presenting the RMSE on the horizontal plane and along the Z axis for cases 3, 4, 5 and 6 are presented. These 4 cases assumed an over bounding characterization for a 1 Hz DLL bandwidth. Numerical values can be found in Table H., Table H., Table and Table H..

From Figure 7.12 and Figure H.1 it can be said that the circular trajectory provides the worst results compared to the others. Obviously the considered trajectory (see Figure 7.5) is not circular at all but rather a chord or radial trajectory; this can explain why the characterization based on the circular trajectory provides the worst RMSE. Nevertheless, this behavior is not observed for the 1 Hz DLL bandwidth.

The characterization obtained by mixing the 3 trajectories provided naturally averaged RMSEs compared to the other trajectory dependent characterizations. From these results, it is difficult to clearly state the impact of the trajectory used for the characterization on the navigation filter performances. Therefore, it is possible to use the global characterization without degrading a-priori the performances of the navigation filters.

In order to clearly state the impact of the trajectory used for the characterization on the navigation solution, a solution could be to determine, at each instant and for each BS, the appropriate type of trajectory and associate the required characterization.

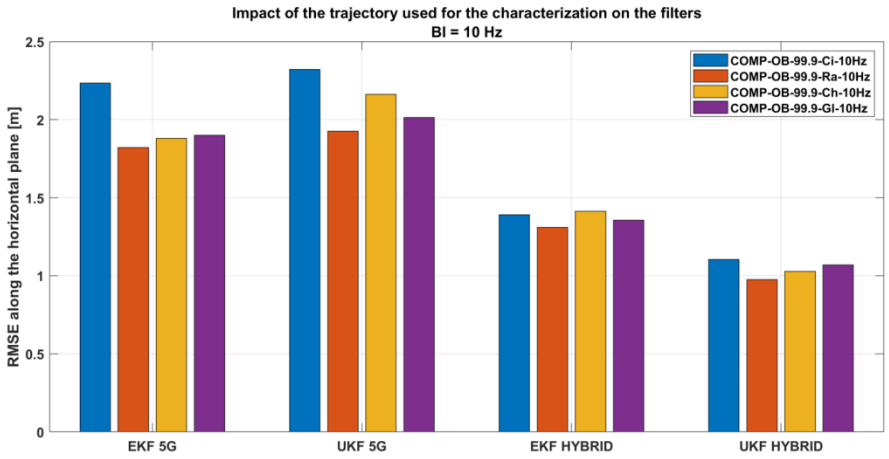

Figure H.1 – Impact of the trajectory used for the characterization – overbounding method – 10 Hz – horizontal RMSE

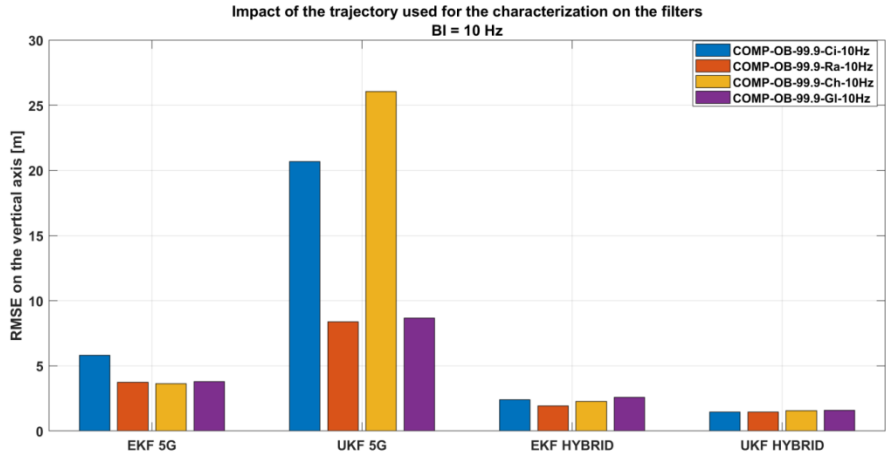

Figure H.2 – Impact of the trajectory used for the characterization – overbounding method – 10 Hz – Z axis RMSE

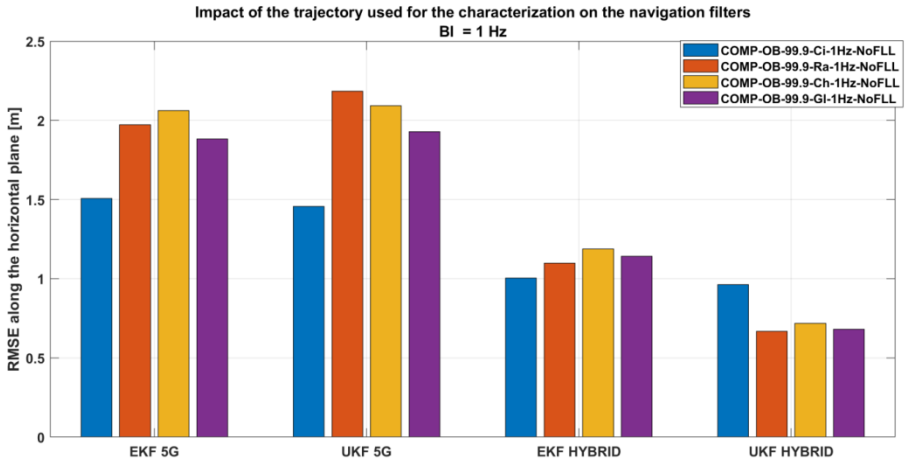

Figure H.3 – Impact of the trajectory used for the characterization – over bounding method – 1 Hz – horizontal RMSE

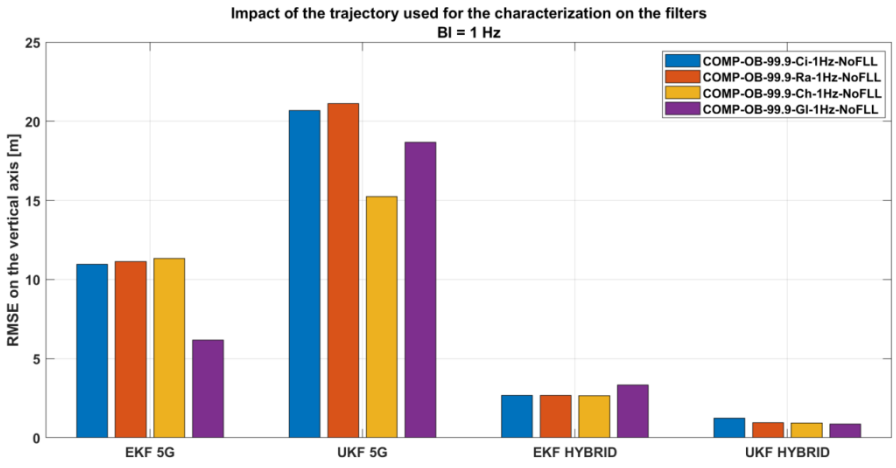

Figure H.4 – Impact of the trajectory used for the characterization – over bounding method – 1 Hz – Z axis RMSE

H.2) Impact of the confidence bound used for the characterization on the filters performances

In this subsection, the impact of the confidence bound used for the characterization on the filter performances is studied.

In Figure H.5 and Figure H.6 histograms presenting the RMSE on the horizontal plane and along the Z axis for cases 9 (COMP-FG-99.9-GI-10Hz), 10 (COMP-FG-99-GI-10Hz), 11 (COMP-FG-95-GI-10Hz), 18 (COMP-FG-99.9-GI-1Hz-NoFLL), 19 (COMP-FG-99-GI-1Hz-NoFLL) and 10 (COMP-FG-95-GI-1Hz-NoFLL) are presented. These 6 cases assume a fitting characterization; cases 9, 10 and 11 assume a 10 Hz DLL bandwidth case 18, 19 and 20 assume a 1Hz DLL bandwidth.

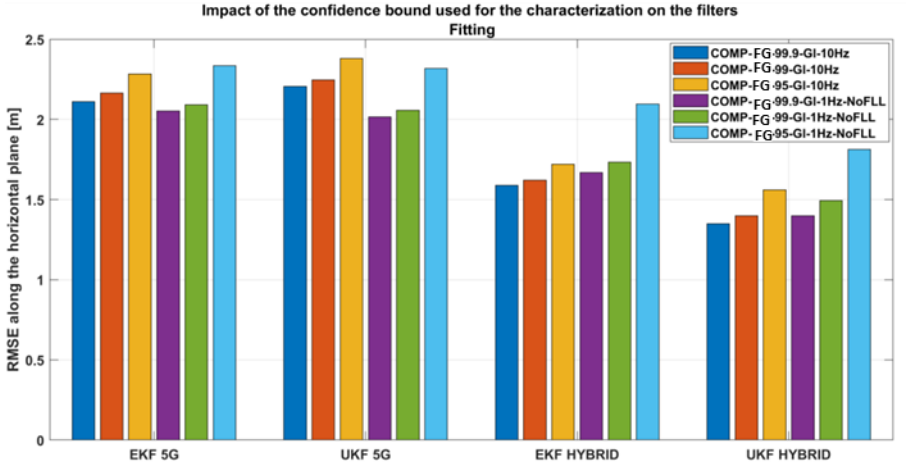

Figure H.5 – Impact of the confidence bound used for the characterization of the filter performances – fitting – horizontal plane

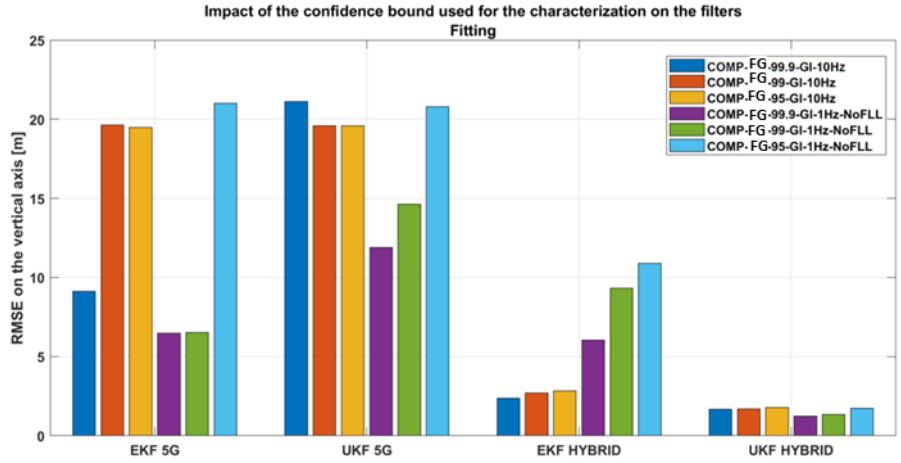

Figure H.6 – Impact of the confidence bound used for the characterization of the filter performances – fitting – Z axis

Annex I) Résumé

Cette dernière annexe propose un résume de la thèse en français.

I.1) Introduction

I.1.1) Contexte et motivation

Ces dernières années, les besoins en terme de positionnement sont en constante augmentation, en particulier en environnement contraints, tels que les environnements urbains ou en intérieurs. Dans de tels environnements, les systèmes GNSS (Global Navigation Satellite System) sont très limités principalement à cause des multi trajets et de l'absence de visibilité directe des satellites (LOS).

Plus précisément, un récepteur GNSS a besoin d'au moins 4 signaux LOS pour fournir une position. Cependant, cette situation idéale est rarement remplie dans les canyons urbains. D'une part, en raison des bâtiments élevés et des rues étroites, beaucoup de signaux satellites sont obstrués. Ce blocage a une incidence sur la géométrie des satellites vus par le récepteur : la plupart des signaux satellites provenant de « l'autre côté de la rue » sont bloqués, ne laissant que ceux « le long de la rue ». Le résultat est donc une dégradation de la dilution de précision (DOP) de la solution.

D'autre part, la présence de bâtiments élevés et de rues étroites favorisent l'apparition de multi trajets. Le phénomène de multi trajets est produit par la superposition du signal direct avec ses répliques réfléchies ou diffractées. Le chemin parcouru par un multi trajet étant, par définition, plus long que le chemin direct, il est toujours reçu après le chemin direct et son impact sur la poursuite du signal dépendra de son retard, de sa phase et de son amplitude relative. Si le délai du multi trajet est très important, il peut être facilement supprimé. En effet, la fonction de corrélation entre le signal reçu (chemin direct et multi trajet) et la réplique locale laissera le pic principal (correspondant au chemin direct) « propre » ou, en d'autres termes, non déformé. Cependant, si le délai est court, la fonction de corrélation sera déformée ce qui compliquera la poursuite du signal, allant d'une erreur sur les mesures de pseudo distance jusqu'à causer la perte de la poursuite.

Qui plus est, la combinaison des deux précédents phénomènes peut même entrainer une situation pire encore. Le signal transmis par satellite ne peut être reçu que par réflexion : un biais constant est ajouté à la mesure de pseudo-portée qui, à son tour, crée un biais sur la solution de positionnement. Ce phénomène est connu sous le nom de réception NLOS.

En résumé, à cause du phénomène de multi trajet, du manque de satellite en visibilité directe et du phénomène de réception NLOS, la solution de positionnement GNSS peut être grandement dégradée et inutilisable pour certaines applications urbaines ou indoor.

Il existe de nombreuses solutions pour améliorer les performances du positionnement GNSS en milieu contraint : l'hybridation avec des capteurs additionnels, [1], [2] ou l'utilisation de signaux d'opportunités par exemple, [3], [4], [5], [6], [7], [8]. Concernant les signaux d'opportunité, les signaux de communication mobiles, comme la 4G LTE (Long Term Evolution) ou la 5G, sont naturellement envisagés pour faire du positionnement, [3], [9], [10]. En effet, une grande majorité des utilisateurs est « connectée », de plus la 5G offre d'intéressantes opportunités.

La 5G est actuellement en court de standardisation au 3GPP [11]; la première version des spécifications 5G, la Release-15, a été transmise à la communauté scientifique en mars 2018. La 5G est une technologie émergente et ses performances en terme de positionnement, ainsi qu'un schéma de récepteur générique

potentiel pour mener des opérations de positionnement, sont toujours à l'étude. Afin d'étudier les capacités potentielles de la 5G et de développer un schéma de module de positionnement générique basé sur la 5G, la première étape fondamentale consiste à développer les modèles mathématiques des signaux 5G à chaque étape du récepteur pour des canaux de propagation réalistes. Dans cette thèse, l'accent est mis sur l'opération de corrélation qui est la fonction de base mise en œuvre par les modules de positionnement typiques pour les signaux 4G LTE [12], les signaux DVB [7], [8], et les signaux GNSS [13]. La connaissance des modèles mathématiques de sorties de corrélateurs permettrait effectivement le développement de techniques de traitement du signal 5G optimales pour faire du positionnement.

Des études précédentes ont été menées et ont permis de définir les modèles mathématiques aux différentes étapes du traitement pour des signaux similaires aux signaux 5G, c'est-à-dire basé sur une modulation OFDM (Orthogonal Frequency Division Multiplexing) comme envisagé par le standard 3GPP [14]. Des modèles mathématiques de sorties de corrélateur ainsi que des techniques d'acquisition pour des signaux de type OFDM ont été développés dans [7], [15]. A cela, dans [8], [15], des techniques de poursuite du signal ont été proposées, analysées et testées en utilisant les modèles mathématiques de sorties de corrélateurs proposés dans [7]. Cependant, ces modèles ont été développés en supposant que le canal de propagation est constant sur la durée de la corrélation. Malheureusement, quand la réponse impulsionnelle du canal (Channel Impulse Response (CIR)) fournie par un canal de propagation réaliste ne peut pas être considéré comme constante sur la durée de corrélation, les modèles mathématiques de sortie de corrélateur sont légèrement différent des modèles proposés dans [7], [8].

Par conséquent, le premier point considéré dans la thèse consiste au développement de modèles mathématiques de sorties de corrélateurs de signaux 5G pour le positionnement. Afin d'obtenir des modèles mathématiques précis, l'étude de l'impact de l'évolution temporelle d'un canal de propagation conforme à la norme 5G est de la plus haute importance. Notez que, dans cette thèse, la CIR continue sera approchée par une CIR discrète, et l'évolution temporelle continue sera remplacée par la notion d'échantillonnage de la génération de canaux de propagation. Cette approximation fait sens puisque, dans une chaine de transmission/réception classique, le signal continu reçu est échantillonné à la sortie du filtre Radio Fréquence (RF). Ainsi, avant de développer des modèles mathématiques précis de signaux 5G, il est nécessaire de déterminer le taux d'échantillonnage le plus approprié pour le canal de propagation sélectionné pour la thèse : QuaDRiGA. QuaDRiGA, en plus de vérifier les critères 5G, propose un compromis entre réalisme et complexité. La réduction de la complexité est particulièrement importante dans le cas des canaux de propagation compatible 5G (émetteur et récepteur multi antennes, et multi trajets très important). C'est pourquoi, l'impact de l'évolution temporelle du canal de propagation à l'intérieur d'un symbole OFDM est étudié. Une méthode pour sélectionner le taux d'échantillonnage le plus approprié pour précisément modéliser le canal est proposée.

Les modèles mathématiques de sorties de corrélateurs développés pour des environnements multi trajets réalistes pour le GNSS et la 5G sont ensuite utilisés pour développer des modules de positionnement ; c'est le second objective de cette thèse. Ces modules de positionnement permettent la génération de mesures de pseudo distances nécessaire au développement de solution de navigation. Le module de positionnement proposé pour les signaux 5G est basé sur l'utilisation d'une boucle de poursuite de retard (DLL) et d'une boucle de poursuite de fréquence (FLL) (dont l'utilité sera statuée dans cette thèse). Un estimateur de C/N_0 est également proposé, il a pour objectif de déterminer si un signal peut être poursuivi et de remplir la matrice de covariance du bruit dans les filtres de navigation.

Afin d'améliorer la disponibilité du positionnement et les performances du positionnement GNSS en milieu urbain grâce à l'exploitation des signaux 5G, les deux systèmes, GNSS et 5G, doivent être combinés de manière optimale. En fait, pour obtenir cette combinaison optimale, les deux types de signaux doivent être traités de façon optimale et les modèles mathématiques de mesures de pseudo-distances doivent être caractérisés avec précision. Le troisième objectif de cette thèse vise donc à caractériser de manière réaliste les modèles mathématiques de mesure de pseudo-distance GNSS et 5G et à développer des modules de navigation hybrides adaptés aux modèles mathématiques de mesure de pseudo-distance dérivés. Afin de valider les modèles mathématiques développés dans cette thèse, un simulateur est conçu. Il intègre un module de traitement de récepteur GNSS typique et une proposition de module de traitement de signal 5G; en outre, afin de parvenir à une caractérisation réaliste, le simulateur met en œuvre des canaux de propagation très réalistes pour le GNSS, SCHUN [16], et pour la 5G, QuaDRiGa [18]. Les modules de navigation hybrides implémentés et comparés dans ce travail sont un filtre Kalman étendu (EKF), un filtre classique utilisé dans la littérature et un filtre Kalman Unscented (UKF), qui pourrait surpasser l'EKF. Les performances de ces modules de navigation hybrides sont ensuite étudiées pour quantifier les améliorations apportées par les mesures 5G TOA.

I.1.2) Objectifs

L'objectif global de la thèse est la conception de modules de navigation hybrides utilisant à la fois des mesures GNSS et 5G. Pour ce faire, la thèse est divisée en 4 phases :

- Le développement de sorties de corrélateurs 5G très réalistes pour faire du positionnement en considérant un canal de propagation réaliste
    - Le réalisme du canal de propagation est de la plus haute importance; il doit être soigneusement sélectionné et modélisé. QuaDRiGa, [18], est sélectionné dans la thèse. Des études ont montré que le canal de propagation généré par QuaDRiGa ne peut pas être considéré comme constant pendant la durée d'un symbole OFDM. Par conséquent, une méthodologie complète a été dérivée afin de déterminer : les paramètres changeants du canal de propagation et le taux d'échantillonnage de génération requis pour modéliser avec précision le canal de propagation.
    - Détermination d'un modèle mathématique de sortie de corrélateur très réaliste. Le modèle dérivé peut être divisé en un terme utile et un terme d'interférence. Toutefois, le modèle complet qui en résulte est assez complexe et il pourrait être utile, à des fins pratiques, d'en tirer un modèle simplifié, par exemple en mettant en œuvre des simulations moins longues. Ce modèle simplifié sera moins précis mais plus facile à manipuler ; sa dérivation est divisée en une simplification du terme utile et une modélisation du terme interférence.
    - Un modèle simplifié pour la contribution utile dans le modèle présenté précédemment a été proposé et validé dans la thèse
    - Des études statistiques ont montré la possibilité de modéliser l'interférence et le terme de bruit par une variable gaussienne additive.
- Développement de modules de positionnement
    - L'objectif du module de positionnement de signaux 5G est d'estimer le temps d'arrivée (TOA) du signal.
    - Le module de positionnement de signal 5G proposé est basé sur l'utilisation d'une boucle de poursuite de délai classique (DLL); une FLL est également proposée et les configurations pour laquelle elle est utile sont décrites.
    - Des études ont été menées pour évaluer la nécessité de mettre en œuvre un estimateur de fréquence porteuse, une FLL par exemple. En fait, il sera démontré que la mise en

œuvre d'une FLL n'est pas nécessaire pour améliorer l'estimation de poursuite, mais qu'elle peut tout de même être utilisée dans certains cas.

- La caractérisation précise des erreurs sur les pseudo-distances dues aux canaux de propagation
    - Dérivation des méthodes. En l'absence de méthodes précises dans la littérature, deux méthodes ont été conçues pour caractériser les erreurs sur les pseudo-distances dues aux canaux de propagation et au bruit thermique appelés overbounding et fitting.
    - Définition des scénarios et détermination des caractéristiques. Deux systèmes sont pris en compte dans la thèse : les systèmes GNSS et 5G; les deux avec un canal de propagation approprié : SCHUN pour GNSS et QuaDRiGa pour 5G. Des scénarios d'utilisation ont été définis afin de dériver à travers des simulations les caractérisations
- Le développement de modules de navigation hybrides adaptés aux modèles mathématiques de mesures de pseudo-distances dérivés.
    - 2 filtres de navigation ont été étudiés dans la thèse : un filtre Kalman étendu (EKF) et un filtre Kalman unscented (UKF).
    - Détermination des avantages des mesures 5G dans un module de navigation. L'EKF et l'UKF ont été étudiés pour les cas 5G autonome et hybrides GNSS/5G. L'avantage de l'utilisation de la mesure 5G a été prouvé

I.2) Conclusion

Cette section résume les principales conclusions du travail mené dans le manuscrit et propose plusieurs recommandations pour de futures recherches dans ce domaine.

I.2.1) Conclusions

Les travaux de cette thèse sont développés dans le cadre d'un service de positionnement basé sur l'utilisation du GNSS en milieu urbain. Les défis liés à l'usage du GNSS dans cet environnement urbain ont été rappelé. Le blocage du signal direct et les nombreux multi-trajets affectent de manière significative la disponibilité du signal et son traitement, et introduisent ainsi de grandes erreurs sur les mesures de pseudo-distances et sur les mesures porteuses ceux qui dégradent davantage la précision et la disponibilité de la position. Dans le pire des cas, il pourrait même ne pas y avoir assez de mesures pour calculer une position en utilisant les données GNSS uniquement. Afin de surmonter ces problèmes, dans la thèse, l'utilisation d'un signal d'opportunité est étudiée pour améliorer le service basé sur le GNSS. Plus précisément, l'accent est mis sur l'utilisation des signaux de télécommunication 5G puisque la technologie 5G est nouvelle et prometteuse. Un module de positionnement 5G a été développé et ses performances caractérisées, ainsi que l'impact de la combinaison de mesures GNSS et 5G sur les performances d'un filtre de navigation.

L'objectif globale de la thèse est le design et l'étude des performances d'un récepteur hybride GNSS/5G.

Le chapitre 2 a donné un aperçu global des systèmes GNSS et a présenté les techniques de traitement du signal adoptées dans le récepteur afin d'obtenir les mesures requises. Pour atteindre ces objectifs, la définition des systèmes GNSS a été fournie. Tel que présenté, il existe une grande variété de systèmes GNSS, la thèse se focalisant sur 2 signaux particuliers : GPS L1 C/A et Galileo E1 OS, seule la description de ces 2 signaux a été fournis. Avant d'être traité par l'utilisateur, le signal transmis est perturbé par plusieurs sortes d'interférences. Ces interférences ont été modélisées, afin d'analyser les signaux reçus, grâce à la définition d'un modèle de canal de propagation. Pour les besoins de la thèse, le canal de propagation SCHUN a été sélectionné.

SCHUN est un canal de propagation LMS déterministe-statistique hybride; la mise en œuvre des modules statistiques et déterministes optimise le compromis entre la précision et la charge de calcul. Le signal est

ensuite traité par le récepteur, qui a été présenté. Les 3 principales fonctions de traitement du signal du récepteur sont basées sur l'opération de corrélation : l'acquisition, la poursuite et la démodulation. La corrélation vise à générer localement une réplique parfaitement synchronisée avec le signal entrant. Enfin, le récepteur fournit des mesures de pseudo-distance qui ont été présentées et utilisées pour permettre à l'utilisateur de calculer sa solution PVT. Ensuite, un soin particulier a été apporté à un environnement contraint (non-open sky) puisque les conditions, par rapport à un environnement ouvert, peuvent être très dégradées.

Le chapitre 3 vise à fournir une vue d'ensemble des systèmes 5G et à présenter les techniques de traitement du signal adoptées dans le récepteur afin d'obtenir les mesures requises lorsque le signal 5G est transmis par un canal AWGN. Le chapitre fournit une description complète des systèmes 5G. Étant donné que la 5G est une technologie émergente, l'historique des systèmes 5G a été présenté ainsi que les cas d'utilisation envisagés. Trois méthodes de radio positionnement ont été présentées dans le chapitre : la méthode basée sur la puissance du signal, la méthode basée sur l'angle d'arrivée et la méthode basée sur le temps d'arrivée. Les deux premiers n'ont pas été sélectionnés pour la thèse ; par conséquent, le reste de la thèse sera basé sur les mesures de ToA. Le signal transmis par la station de base 5G a été décrit avec précision. Afin de déterminer les techniques de traitement du signal les plus optimales, il est de la plus haute importance de connaître précisément le modèle mathématique du signal reçu. Le signal reçu peut être modélisé à partir de la transmission du signal généré par le canal de propagation; par conséquent, le canal de propagation doit être soigneusement modélisé afin d'avoir un modèle mathématique réaliste du signal reçu. À des fins de réalisme, un état l'art précis a été réalisé afin d'identifier les projets potentiels de canaux de propagation qui pourraient être utilisés pour la thèse. L'étude a permis d'identifier un canal de propagation conforme aux standards 5G et facile à utiliser. QuaDRiGa, un simulateur open source conforme à la norme 3GPP, [43] , a été sélectionné. Il répond aux exigences du canal de propagation 5G ; de plus, il s'agit d'un GSCM, proposant ainsi un commerce équitable entre complexité et réalisme.

Ensuite, une description des principales techniques de mesures ToA sur les signaux OFDM a été fournie ; plus spécifiquement, les mesures ToA sont obtenues à la sortie d'une DLL, qui utilise les sorties de corrélateurs. L'opération de corrélation proposée est basée sur les signaux des pilotes présents dans la trame 5G ; l'accent a été mis sur le signal de synchronisation 5G SSPBCH. Le module de positionnement 5G envisagé a été présenté avec une application particulière pour un cas AWGN. Enfin, le modèle de pseudo distance pour un canal AWGN a été dérivé. Ce modèle sera complété dans le chapitre suivant avec l'impact des multi trajets.

Le modèle mathématique de sortie de corrélateurs pour un signal de type OFDM présenté au chapitre 3 est dérivé en supposant un canal de propagation constant sur la durée de la corrélation (qui est effectuée sur un symbole OFDM). Néanmoins, le chapitre 4 a montré que la CIR d'un canal de propagation compatible 5G (QuaDRiGa) ne peut pas être considérée comme constante pendant la durée de la corrélation (le temps de cohérence du canal de l'amplitude complexe de la CIR est inférieur à la durée de la corrélation) : la sortie de corrélation attendue pour un signal 5G est donc différente entre un canal de propagation à évolution temporelle et un canal constant sur la durée d'un symbole OFDM.

Le but ultime du chapitre 4 était donc de dériver précisément le modèle mathématique de sortie corrélateur d'un signal 5G à des fins de positionnement, c'est-à-dire d'améliorer le modèle présenté au chapitre 3. Afin de dériver ce modèle mathématique de sortie corrélateur précis et réaliste, il est de la plus haute importance de modéliser d'abord précisément le signal 5G reçu et, par extension, les interférences faussant le signal et introduit par le canal de propagation avec autant de réalisme que possible; ou en d'autres termes, la CIR. Par conséquent, la méthode suivie au chapitre 4 est divisée en

deux : la première étape est la caractérisation de la CIR qui a permis de modéliser avec précision le canal de propagation, la deuxième étape est la dérivation du modèle mathématique de sortie du corrélateur. La première étape a permis de conclure que pour la CIR, le taux d'échantillonnage de production nécessaire pour simuler un canal de propagation réaliste en limitant autant que possible la charge de calcul/le modèle mathématique du générateur est égal à 10CIR par symbole OFDM pour les conditions de signal jugées pertinentes dans l'analyse de ce travail. La deuxième étape a permis de fournir le modèle mathématique de sortie du corrélateur final utilisé dans la thèse. Ce modèle est composé de la partie utile sans bruit pour laquelle un modèle simplifié peut être appliqué et d'une variable gaussienne additive. La variable gaussienne inclue les termes de bruit et d'interférence et peut être considérées comme une puissance sonore accrue et donc comme une diminution potentielle du SNR ou C/N_0 disponible.

L'objectif du chapitre 5 était de présenter le module de synchronisation proposé et mis en œuvre dans le Ph.D. Ce module de synchronisation est composé d'une DLL, d'un estimateur de fréquence porteuse et d'un estimateur C/N_0 (et un détecteur de verrouillage de poursuite basé simplement sur l'estimation C/N_0 par rapport à un seuil). La boucle de poursuite de temps mise en œuvre a été soigneusement présentée ; son architecture et ses performances ont été détaillées. Un discriminateur EMLP est utilisé dans la DLL, son facteur de normalisation ainsi que sa zone de linéarité ont été étudiés avec précision : la zone de linéarité unilatérale est $D_{th} = 7/4$ échantillons. La performance sur l'écart-type de l'erreur d'estimation de la DLL pour un canal AWGN utilisant les modèles mathématiques de sortie du corrélateur dérivés au chapitre 4 a été validée en simulation : par exemple, la variance de l'estimation de l'erreur de suivi pour un $SNR_{demod} = 0\ dB$ égale $2.6 \cdot 10^{-4}\ m$. Une analyse de la nécessité de mettre en œuvre un estimateur de fréquence porteuse est également effectuée dans la deuxième section. Il a été prouvé théoriquement et par des simulations que la mise en œuvre d'une boucle de poursuite de porteuse, une FLL, n'améliore pas les performances de poursuite du module de positionnement pour un canal AWGN. Le principe utilisé pour prouver théoriquement cette déclaration consiste à étudier la dégradation causée par une erreur d'estimation de fréquence sur l'estimation de délai effectuée par la DLL. Plus précisément, la méthode adoptée pour déterminer la nécessité de mettre en œuvre un estimateur de fréquence porteuse consiste à dériver la dégradation de la performance d'estimation du délai en fonction du rapport signal-bruit (SNR) et du décalage de fréquence porteuse (CFO). Afin de déterminer des valeurs réalistes de la dégradation, des valeurs de variation SNR et Doppler réalistes ont été déterminées. Selon ce rapport, la dégradation du SNR causée par le CFO a été étudiée, suivie de la dégradation théorique sur l'estimation du retard de code due au CFO. Enfin, la dérivation théorique a été validée par des simulations. Les simulations supposant un canal AWGN ont permis de valider la dégradation théorique de l'estimation du retard de code due au CFO ; et ont confirmé la non-nécessité de la mise en œuvre d'une FLL. Ces simulations ont été effectuées pour 3 configurations définies pour représenter des configurations de signaux 5G réalistes et génériques. Elles ont montré que pour $SNR_{correlator} < 105\ dB$, la dégradation due à un CFO fractionnaire est inférieure à 0,5 dB et que l'écart-type de l'estimation de l'erreur de suivi est de l'ordre des millimètres.

Des simulations supplémentaires ont été proposées pour un canal complet afin d'étudier l'impact de la dégradation liée aux multi trajets. Ces simulations ont montré que lorsqu'un canal de propagation complet est considéré (LOS+multipath), pour une bande de boucle DLL de 1 Hz, les performances de la poursuite sont améliorées lorsque la FLL est mise en œuvre. Cependant, aucune amélioration n'est observée pour une bande de boucle de 10 Hz DLL. L'objectif de la troisième section était de mettre en œuvre un estimateur de C/N_0. L'estimateur considéré, le Narrow-to-Wideband-Power-Ratio- estimateur de C/N_0, a mis au jour des limites pour des C/N_0 supérieur à 60 dBHz. Plus précisément, un phénomène de saturation est observé, il est lié à l'évolution de phase entre les symboles du terme de contribution de canal de propagation au modèle mathématique de sorties de corrélateur. S'il n'y a pas d'évolution de

phase (cas AWGN), la saturation apparaît pour C/N_0 supérieure à 120 dBHz ; si l'évolution de phase est la plus élevée (trajectoire radiale), la saturation apparaît pour des C/N_0 supérieurs à 60 dBHz. Trois solutions ont été testées pour surmonter ce phénomène de saturation : l'estimateur de C/N_0 basé sur la méthode des moments (là encore, des limites ont été identifiées pour $C/N_0 > 60\ dBHz$) et deux évolutions de deux évolutions du NWPR (Arctangent NWPR C/N_0 phase-corrected estimator et FLL-driven NWPR C/N_0 phase-corrected estimateur). Les deux derniers estimateurs sont plus performants que l'estimateur NWPR, mais ils présentent toujours des limites pour $C/N_0 > 95dBHz$. Il n'y a pas de différence entre les 2 estimateurs à correction de phase NWPR. Enfin, on peut dire que même si une FLL n'améliore pas beaucoup les performances de poursuite, pour une bande de boucle DLL de 10 Hz, il pourrait permettre une meilleure estimation du C/N_0. Par conséquent, le FLL sera conservé pour le reste de la thèse.

Dans le chapitre 6, les erreurs sur les mesures de pseudo distance dues au bruit thermique et aux multi trajets ont été caractérisées par une distribution gaussienne pour les signaux 5G et GNSS. Une étape préliminaire menée sur ce chapitre a consisté en la dérivation précise des modèles de mesure de pseudo-distance. Étant donné que 3 systèmes sont considérés dans la thèse, il est de la plus haute importance de définir chacun d'entre eux dans le même temps de référence; par conséquent, cette synchronisation de temps a été étudiée avec précision.

Ensuite, la méthode de dérivation a été proposée dans ce chapitre et est divisée en deux étapes :

1. La caractérisation de l'erreur de mesure de la pseudo-distance, ou en d'autres termes, pour obtenir la distribution PDF réelle des erreurs, qui repose sur l'analyse des résultats des boucles de poursuite à l'aide des modèles de sortie du corrélateur décrits au chapitre 4 et à l'aide des simulateurs de canaux de propagation SCHUN pour GNSS et QuaDRiGa pour 5G.
2. L'approximation de la distribution réelle par une distribution gaussienne. Pour définir la distribution des erreurs par une distribution gaussienne, seuls deux paramètres doivent être définis : la moyenne et la variance. En ce qui concerne la moyenne, trois moyennes ont été envisagés :$\mu = 0$, $\mu = mean$ et $\mu = index$, ou $index$ correspond au maximum de la PDF caractérisée. Trois bornes de confiance ont été considérées 99.9%, 99% et 95%. Enfin, deux méthodes d'approximation ont été dérivées, à savoir une méthode d'overbounding gaussienne et une méthode de fitting gaussienne, paramétrée par l'erreur de pseudo-distance simulée réelle prise en compte (95 %, 99 % et 99,9 %) pour la caractérisation.

Afin d'obtenir des résultats statistiquement significatifs, un grand nombre de générations aléatoires des canaux de propagation et du bruit du récepteur ont été testés en utilisant une approche Monte-Carlo. L'étude a montré que pour QuaDRiGa et pour SCHUN, l'hypothèse sur la moyenne de la distribution gaussienne a une influence négligeable sur le scénario LOS. Il est proposé de supposer une distribution gaussienne centrée (μ=0). De plus, l'écart-type de la distribution gaussienne dépend du C/N_0, ce qui était prévu. La dérivation des distributions gaussiennes pour un canal QuaDRiGa a été effectuée en supposant un scénario LOS sous-6 Ghz, la dérivation a été proposée pour trois trajectoires indépendantes et pour les trois trajectoires rassemblées. Une DLL de 2e ordre a été utilisée pour 2 bandes boucles DLL (10 Hz et 1 Hz). Cette dérivation a montré :

- L'écart-type de la distribution gaussienne dépend du type de trajectoire. Trois types de trajectoires ont été testés (radiale, corde, circulaire) et ont donné des résultats sensiblement différents, ce qui n'était pas prévu. La caractérisation finale ne conserve

pas cette dépendance et moyenne les résultats des 3 types de trajectoires. Cette dépendance à l'égard de la trajectoire peut être un travail futur potentiel.

- Les paramètres de la poursuite du récepteur (principalement la bande passante DLL) a un léger impact. Comme prévu, plus la bande passante DLL est faible, meilleure est la précision.
- Les méthodologies de fitting et d'overbounding donnent des résultats très différents, comme prévu. La recommandation entre les deux méthodologies sera présentée au chapitre 7.
- Les distributions ne sont pas gaussiennes, en particulier pour la 5G à faible C/N_0, où la queue de distribution pour les erreurs positives est plus grande (positivement asymétrique).

La dérivation des distributions gaussiennes pour un canal SCHUN a été faite en supposant des conditions LOS. Elle a été réalisée indépendamment de l'altitude et de l'azimut du satellite. Une boucle de poursuite de délai de premier ordre a été utilisée en supposant un EMLP avec un espacement corrélateur de 0,5. La boucle de poursuite de phase utilisée est une boucle Costas de 3e ordre. Les pseudo-distances sont générées en supposant une modulation BPSK (modulation GPS L1 C/A) donc les résultats obtenus ont servi de bornes hautes pour les signaux Galileo puisque Galileo utilise une modulation BOC supposée plus robuste en environnement multi trajets. La dérivation a montré que :

- La variance augmente légèrement quand le C/N_0 décroit
- Les distributions pour des $C/N_0 > 35\ dBHz$ sont Gaussiennes

Dans le chapitre 7, deux filtres de navigation ont été dérivés : un Filtre Kalman étendu et un Filtre Kalman Unscented. Les simulations ont permis de fournir plusieurs recommandations. Tout d'abord, l'utilisation de mesures 5G est fortement recommandée dans un environnement contraint en l'absence de mesures GNSS. Si certaines mesures GNSS sont disponibles, une solution de navigation hybride est recommandée car de meilleures performances, en particulier sur l'axe Z, peuvent être attendues. Le réglage du module de mesure 5G est important, selon l'étude, une bande de boucle DLL de 1 Hz est recommandée. La caractérisation de la pseudo distance a également une grande importance et pour l'application la méthode overbounding fournit de meilleures performances. Enfin, l'UKF est recommandée par rapport à l'EKF.

Dans l'ensemble, la combinaison d'un module de positionnement 5G avec un récepteur GNSS apporte une amélioration de 45% sur la précision de position, par rapport à une solution GNSS uniquement pour un filtre de navigation UKF.

I.2.2) Main achievements

Les principales réalisations de ce doctorat sont énumérées ci-dessous:

- Une description de la couche physique 5G, et notamment du signal de synchronisation envoyé dans le canal PBCH (SS PBCH) (chapitre 3)
- La sélection et la définition mathématique d'un canal de propagation conforme à la 5G. QuaDRiGa a été sélectionné, des études ont prouvé que le canal de propagation ne peut pas être considéré comme constant pendant la durée de la corrélation. Par conséquent, des méthodes ont été conçues pour étudier ces paramètres évolutifs et sélectionner le taux d'échantillonnage du canal de propagation requis.
- Le développement de modèles mathématiques de sorties de corrélateurs 5G, en tenant compte des effets des paramètres de canaux de propagation non constants, du bruit. (chapitres 3,4)

- La proposition d'un modèle simplifié de sorties de corrélateur 5G, qui est valide dans un scénario LOS pour la fréquence porteuse inférieure à 6 GHz (chapitre 4)
- La proposition d'un modèle statistique pour le terme d'interférence, qui peut être généré sous forme de variable gaussienne avec une moyenne et une variance dérivées dans l'étude (chapitre 4)
- La proposition d'un module de positionnement composé d'une DLL et proposant l'utilisation d'une FLL pour des cas particuliers.
- Un module de synchronisation basé sur une DLL et sur une potentielle FLL a été dérivé. La FLL peut améliorer la solution de navigation pour une bande passante de boucle DLL de 1 Hz mais n'est pas nécessaire. Le module de synchronisation implémente également un estimateur C/N_0.
- Le développement d'un simulateur, codé en C, fournissant des mesures de pseudo distances issues des boucles de poursuite GNSS et 5G, en tenant compte des canaux de propagation simulés.
- Le développement de méthodes pour caractériser les erreurs de mesure GNSS et 5G en milieu urbain. Des méthodes ont été proposées pour générer des scénarios réalistes (concernant la fréquence porteuse adoptée) et divers (en termes de trajectoires) afin que la caractérisation obtenue soit aussi générique que possible.
- La proposition de modélisation gaussienne des mesures de pseudo distances en fonction de C/N_0
- L'étude des performances de positionnement simulées à l'aide de différents filtres de navigation (EKF, UKF) et de divers paramètres. Les paramètres étudiés sont :
    - l'impact de la méthode de caractérisation des erreurs de mesure de pseudo-distance adoptée : l'overbounding semble plus performant que le fitting
    - l'impact de la borne de confiance utilisée pour la caractérisation de l'erreur de mesure de la pseudo-distance : une borne de confiance de 99,9 % offre de meilleures performances
    - l'impact de la bande passante de la boucle DLL : une bande passante de boucle DLL de 1 Hz semble plus performante.
- Le travail a été publié dans 2 papiers:
    - "Hybrid Navigation Filters Performances Between GPS, Galileo and 5G TOA Measurements in Multipath Environment" September, 23rd 2020 dans la Session D1: Alternative Technologies for GNSS-Denied Environments 1 at ION GNSS + virtual conference, Anne-Marie TOBIE (TéSA), Axel GARCIA-PENA (ENAC), Paul THEVENON (ENAC), Marion AUBAULT (CNES), François Xavier MARMET (CNES)
    - "Processed 5G Signals Mathematical Models for Positioning considering a Non-Constant Propagation Channel" Anne-Marie TOBIE (TéSA), Axel GARCIA-PENA (ENAC), Paul THEVENON (ENAC), Marion AUBAULT (CNES) – International Workshop on Reliable Ubiquitous Navigation in Smart Cities - co-located with the IEEE Vehicular Technology Conference (IEEE VTC-Fall 2019).

I.2.3) Perspectives

À partir des recherches effectuées dans cette thèse, d'autres études peuvent être menées sur le modèle mathématique de sortie du corrélateur, sur la caractérisation des erreurs de pseudo-distance et sur le positionnement.

- Campagne de collecte de données

Dans cette thèse, l'évaluation des performances de l'architecture hybride proposée a été effectuée dans un environnement urbain simulé et pour un signal 5G simplifié. Cela a permis de tester et d'analyser en

détail les modèles mathématiques dérivés. Cependant, l'utilisation de données réelles permettrait d'autres tests cruciaux pour finalement valider l'architecture et les conclusions faites sur la thèse.

- Modèle mathématique de sortie de corrélateur

Dans la thèse, un scénario de canal de propagation LOS utilisant une fréquence porteuse de 2GHz est considéré. Les études ont prouvé que pour ce type de scénario, le terme d'interférence du modèle mathématique de sortie du corrélateur peut être négligé. Néanmoins, ce n'est probablement pas le cas pour le scénario NLOS. Dans le scénario NLOS, la qualité des mesures de pseudo-distance sera dégradée et, par conséquent, la solution de positionnement obtenue sera moins précise.

- Caractérisation des erreurs de pseudo distances

Dans la thèse, la caractérisation de l'erreur de pseudo-distance a été effectuée pour le scénario LOS à 2 GHz. Néanmoins, dans un environnement urbain difficile, il serait intéressant de déterminer la caractérisation du scénario NLOS. Comme nous l'avons dit tout à l'heure, pour étudier le scénario du NLOS, il faut inclure le terme interférence dans le modèle mathématique de sortie du corrélateur. Ainsi une première étape serait la dérivation, à travers des simulations, des statistiques du terme d'interférence. Ensuite, la méthode déjà dérivée dans la thèse peut être utilisée pour dériver la caractérisation.

Étant donné que les systèmes 5G utiliseront également des ondes millimétriques, la caractérisation devrait également être faite pour ces fréquences. Les propriétés de propagation de mmW sont très différentes de la propagation dans les fréquences inférieures à 6 GHz, les conséquences sur les distributions d'erreurs de pseudo-distance sont probablement différentes. Là encore, les statistiques du terme d'interférence devraient être étudiées pour modéliser correctement les sorties du corrélateur.

- Solution de navigation

Dans la thèse, deux filtres Kalman ont été dérivés. Comme indiqué, les filtres Kalman supposent que ces erreurs suivent une distribution gaussienne, une hypothèse qui peut être trop restrictive dans les environnements urbains. En effet, pour le scénario LOS au chapitre 6, il a été démontré que les distributions d'erreurs ne sont pas gaussiennes, les queues positives sont beaucoup plus grandes. Il pourrait être intéressant de trouver une distribution plus appropriée pour être utilisée dans des filtres de navigation plus évolués.

Le développement d'autres filtres, tels que les filtres à particules (PF), pourrait maintenant être mis en œuvre. Le principal avantage de PF est qu'ils ne s'appuient pas sur une approximation PDF gaussienne contrairement à Kalman Filters; des informations a priori sur les distributions doivent être fournies, et de telles informations ont été dérivées dans cette étude. Ainsi, en tenant compte de la répartition réelle pour le PF, on pourrait obtenir de meilleures performances des filtres de navigation. Néanmoins, la complexité de cette mise en œuvre sera plus grande.